

FINAL REPORT OF THE MAJOR RESEARCH PROJECT

*STUDIES ON TWO PHASE GAS LIQUID (NEWTONIAN AND NON-
NEWTONIAN) FLOW THROUGH PIPING COMPONENTS COILS AND FLOW
PHENOMENA USING CFD TECHNIQUE*

UGC Reference No. : F-33-387/2007(S.R.) Dt. 29.02.2008

Submitted to

UNIVERSITY GRANTS COMMISSION
BAHADUR SHAH ZAFAR MARG
NEW DELHI – 110002



By
Dr. S. K. Das
Principal Investigator
Department of Chemical Engineering,
University of Calcutta,
92, A. P.C. Road, Kolkata-700009

UNIVERSITY GRANTS COMMISSION
BAHADUR SHAH ZAFAR MARG
NEW DELHI – 110002

Annual Report of the work done on the major research Project (report to be submitted within 6 weeks after completion of each year)

1. Project report No. 1st / 2nd / Final : **Final**
2. UGC Reference No. : F-33-387/2007(S.R.) Dt. 29.02.2008
3. Period of report from : 1.7.2008 to 30.06.2011 & 6 months extension thereafter
4. Title of research project : Studies on Two Phase Gas Liquid (Newtonian and Non-Newtonian) Flow through piping Components coils and flow Phenomena using CFD Technique
5. (a) Name of the Principal Investigator : Dr.S.K. Das

(b) Dept. and University / College where work is progressed:

Department of Chemical Engineering,
University of Calcutta,
92, A. P.C. Road,
Kolkata-700009
6. Effective date of starting of the project : 1.7.2008
7. Grant approved and expenditure incurred during the period of the report :

Please see the Audited Statement of Account
8. Consolidated audited account :

Please see the Audited Statement of Account
9. Final Consolidated audited account certificate :

Please see the Audited Statement of Account

10. One copy of final progress report along with CD in pdf. Format

Attached

11. Details of expenditure incurred on Field Work duly signed and sealed by the Registrar/Principal & Principal Investigator :

Not Applicable

12. Month-wise and Year-wise detailed statement of expenditure towards salary of staff appointed under the project :

Not Applicable

13. A **Certificate** from the Head of the Institute is mandatory that final report of the work done has been kept in the **library** of the respective University/College and the executive summary of the evaluated final report of work done on the project has been placed on the **website** of the Institute :

Attached

14. HRA Certificate in the prescribed format, if applicable, duly signed by the Registrar/Principal :

Not Applicable

15. Bank interest, if any, accrued by the Institution :

Please see in the audited statement of account

16. Refund unspent balance :

17. Ph.D. thesis completed

Tarun Kanti Bandyopadhyay - *Studies on liquid and gas – liquid flow through piping components and coils using CFD technique, 2012*

18. Report of the work done

(a) Brief objective of the project:

- (1) To generate the experimental data on the gas-non-Newtonian liquid flow through helical coils of different tube and coils diameters, different helix angles for vertical orientation.
- (2) To generate the experimental data on the gas-non-Newtonian liquid flow through helical coils of different tube and coil diameters, different helix angles for horizontal orientation.
- (3) The complex two-phase hydrodynamics was explained by using computational fluid dynamics, i.e. by Fluent 6.2 Software.

(b) Work done so far and results achieved and publication if any, resulting from the work (Give details of the title of the papers and names of the journal in which it has been published or accepted for publication) :

- (1) All experiments were completed and few data was analysed by CFD techniques using Fluent 6.2 Software.
- (2) Studies on liquid and gas-liquid flow through piping components and coils using CFD technique: Tarun Kanti Bandyopadhyay – Ph. D. completed, University of Calcutta.

(3) Publications :

- i. Ph. D. Thesis - *Studies on liquid and gas – liquid flow through piping components and coils using CFD technique : Tarun Kanti Bandyopadhyay, 2012.*

Other publications

1. T. K. Bandyopadhyay, A. B. Biswas, and S. K. Das, Gas-Non-Newtonian liquid flow through helical coils—pressure drop and CFD analysis, *AIP Conf. Proc.* 1298, 98-102 (2010); doi: 10.1063/1.3516433.
2. Tarun Kanti Bandyopadhyay, Tapan Ghosh, and Sudip Kumar Das, Water and airwater flow through U-bends—experiments and CFD analysis, *AIP Conf. Proc.* 1298, (2010) 110-114, doi: 10.1063/1.3516285.
3. T. K. Bandyopadhyay and S. K. Das, Non-Newtonian and Gas-non-Newtonian Liquid Flow through Elbows – CFD Analysis, *Journal of Applied Fluid Mechanics*, 6(1) (2013) 131-141.
4. Tarun Kanti Bandyopadhyay and Sudip Kumar Das, Non-Newtonian Liquid Flow through Small Diameter Piping Components: CFD Analysis, *J. Inst. Eng. India Ser. E*., 97(2) (2016) 131-141.

Sudip
22/9/19

(PRINCIPAL INVESTIGATOR)

Sudip Kumar Das, Ph. D.
Professor
Chemical Engineering Department
University of Calcutta
92, A. P. C. Road, Kolkata - 700009

[Signature]

(REGISTRAR/PRINCIPAL)

(Seal)

Registrar
University of Calcutta



भारतीय प्रौद्योगिकी संस्थान (भारतीय खनि विद्यापीठ) धनबाद
INDIAN INSTITUTE OF TECHNOLOGY (INDIAN SCHOOL OF MINES) DHANBAD
धनबाद-826004, झारखण्ड, भारत
DHANBAD-826004, JHARKHAND, INDIA

Dr. Tarun Kumar Naiya
Assistant Professor

+91-326-2235879; +91 9471191367

Fax: +91-326-2296632

Email: trn2711@yahoo.com

No : PE/6/17

Dt : 30.08.2017

To
Prof. S. K. Das
Department of Chemical Engineering
University of Calcutta

Dear Sir,

Please find the report on the UGC Major Project titled **Studies on two phase gas liquid (Newtonian and non-Newtonian) flow through piping components coils and flow phenomena using CFD technique** in the attached file.

With regards ,

(T. K. Naiya)

1926 से राष्ट्र की सेवा में

In service of the Nation since 1926

INDIAN INSTITUTE OF TECHNOLOGY (INDIAN SCHOOL OF MINES) DHANBAD

Phone: (0326) 2296-559 to 562 (4 Lines); Fax: (0326) 2296563

Email: exam@ismdhanbad.ac.in Website: www.ismdhanbad.ac.in

Report on the UGC Project titled **Studies on two phase gas liquid (Newtonian and non-Newtonian) flow through piping components coils and flow phenomena using CFD technique.**

The objective of the work is clearly stated and the work demonstrated the fulfillment of the objectives.

The hydrodynamics of single and two-phase gas-liquid flow have received extensive treatment during few decades because of their widespread application in industry. It occurs in boiler tubes, distillation columns, oil and gas wells, transportation system of crudes and refined products, all key pieces of equipment in refineries, petrochemical industries, polymer processing, nuclear engineering and large number of chemical reactor applications. With the development in polymer processing, mineral recovery, food processing, biomedical engineering, biochemical engineering, gas-liquid-solid reactions, hydraulic transportation the liquids most often be non-Newtonian in nature. Hence, there is a need to study the flow of non-Newtonian and gas-non-Newtonian liquid flow through piping components and helical coils. The computational fluid dynamics (CFD) is a powerful tool to evaluate the frictional losses and estimate the other flow characteristics can be visualized to aid in better understanding of the flow phenomenon and it can be applied to improve flow characteristics and equipment design.

The project deals with the CFD modelling of different flow system using gas-liquid (Newtonian and non-Newtonian), non-Newtonian flow through different piping components, like straight pipe, elbows, bends, valves and coils and the CFD modelling is verified with the experimental data either reported in the report or their previous experimental data. The report is divided into different independent chapters starting with fundamentals of piping components and CFD, and CFD analysis in different systems.

It is also pleased to see that Mr. Tarun Kanti Bandyopadhyay is completed his Ph.D. thesis in this area and now he is the one of the CFD expert in the Eastern Region.

Finally I must mention that the report is an excellent demonstration of CFD work in small diameter piping components and coils in single and two-phase flow system. I congratulate Prof. S. K. Das and UGC to support the project.

Deeja
20/8/17

Report of the UGC Major Project titled *Studies on Two Phase Gas Liquid (Newtonian and Non-Newtonian) Flow through piping Components coils and flow Phenomena using CFD Technique*

The hydrodynamics of single and two-phase gas-liquid flow have received extensive treatment during few decades because of their widespread application in industry. It occurs in almost all key equipments in any process industries. The fluid used is often non-Newtonian in nature. So, there is a need to study the flow of non-Newtonian and gas-non-Newtonian liquid flow through piping components and helical coils. The computational fluid dynamics (CFD) is a powerful tool to evaluate the frictional losses and estimate the other flow characteristics which can be visualized to understand the flow phenomenon and it can be applied to improve flow characteristics and equipment design.

Thus in view of the importance of the single-phase and two-phase gas-liquid flow through piping components and helical coils, and the CFD simulation used a commercial software Fluent 6.3.

The report presented in eight different chapters consisting of basic fundamentals of CFD, importance of CFD analysis in piping components, some experimentation and their CFD analysis. Author used CFD analysis for gas-non-Newtonian flow through helical coils and applicability was verified from their earlier published data.

The entire report is very well written and fulfills the objectives of the project.

1
D. M. Srinivasan
27/9/17

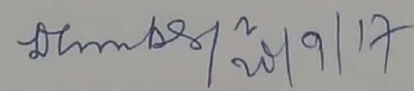
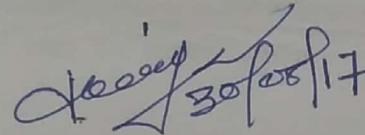
Final Report Assessment / Evaluation Certificate
(Two Members Expert Committee Not Belonging to the Institute of Principal Investigator)
(To be submitted with the final report)

It is certified that the final report of Major Research Project entitled “**Studies on two phase Gas Liquid (Newtonian and Non-Newtonian) flow through piping components coils and flow phenomena using CFD Technique**” by Prof. Sudip Kumar Das Dept. of Chemical Engineering has been assessed by the committee consisting the following members for final submission of the report to the UGC, New Delhi under the scheme of Major Research Project.

Comments/Suggestions of the Expert Committee:-

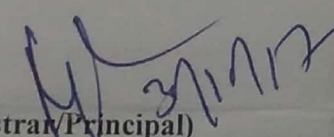
See attached sheet

Name & Signatures of Experts with Date:-

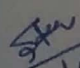
Name of Expert	University/College name	Signature with Date
1. Prof. Dulal Chandra Mukherjee	Heritage Institute of Technology	 20/9/17
2. Dr. Tarun Kumar Naiya	Indian Institute Technology (ISM, Dhanbad)	 30/08/17

It is certified that the final report has been uploaded on UGC-MRP portal on

It is also certified that final report, Executive summary of the report, Research documents, monograph academic papers provided under Major Research Project have been posted on the website of the University/College.


(Registrar/Principal)
Seal

Registrar
University of Calcutta


22/9/17
Sudip Kumar Das, Ph. D.
Professor
Chemical Engineering Department
University of Calcutta
92, A. P. C. Road, Kolkata - 700009

PREFACE

This is to certify that the project entitled *Studies on Two Phase Gas Liquid (Newtonian and Non-Newtonian) Flow through piping Components coils and flow Phenomena using CFD Technique* submitted by Dr. S. K. Das is submitted herewith. In the present investigation some experimental studies have been carried out on the hydrodynamics of single-phase and two-phase gas-liquid flow through piping components and coils and some experimental data taken from earlier published report from our laboratory for the simulation purpose. Commercial Fluent 6.3 software has been used for the simulation purpose. The simulation gives the details flow field inside the piping components and coils. The simulated results agree well with the experimental data.

CONTENTS

	Page No.
Preface	
Content	11
List of Tables	vii
	x
List of Figures	xxxix
Synopsis	2
Chapter 1 Introduction	6
1.1 Introduction	
1.2 Objective of the present work	
Chapter 2 CFD methodology	
2.1 Theoretical consideration	9
2.2 Mathematical model	10
2.2.1 Single phase water flow	10
2.2.2 Mathematical Model for Air - water system	11
2.3 Mathematical Model	12
2.3.1 Single phase non-Newtonian fluid	12
2.3.2 For air-non-Newtonian fluid system	12
2.3.3 Estimation of the mesh cell size adjacent to the wall	15
2.4 Numerical approach	17
2.4.1 CFD procedure	17
2.4.2 Solver	19

2.4.3	Convergence	19
2.5	Conclusion	19
Chapter 3 Water and air-water flow through U-bends		
3.1	Introduction	22
3.2	The experimental set up	25
3.3	Evaluation of frictional pressure drop across the U-bend	26
3.4	CFD Procedure	27
3.4.1	Assumptions for air-water flow through U-bends	28
3.5	Results and discussion	29
3.5.1	Convergence and grid independency	29
3.5.2	CFD analysis for water flow through U-bends	30
3.5.3	CFD analysis for air-water flow through U-bends	34
3.6	Conclusions	37
Chapter 4 Non-Newtonian fluid flow through piping components – experimental investigation		
4.1	Introduction	113
4.2	The experimental set up	115
4.3	Results and discussion	116
4.3.1	Evaluation of the pressure drop across the piping components	116
4.3.2	Effect of non-Newtonian characteristics on the pressure drop across the piping components	117
4.3.3	Problem analysis	117
4.3.3.1	Elbow	118
4.3.3.2	Orifice	119

4.3.3.3 Valves	120
4.3.4 Pressure drop	120
4.3.4.1 Analysis of the Experimental pressure drop	120
4.3.4.2 Stream-wise pressure drop due to pipe fittings	123
4.4 Conclusions	123
Chapter 5 Non-Newtonian liquid flow through small diameter piping components - CFD analysis	
5.1 Introduction	141
5.2 Experimental	143
5.3 Mathematical Model	143
5.4 CFD Procedure	144
5.5 Results and discussion	146
5.5.1 Convergence and grid independency	146
5.5.2 Straight pipe	147
5.5.3 Elbows	147
5.5.4 Orifices	150
5.5.5 Gate valve	150
5.5.6 Globe valve	151
5.6 Conclusions	151
Chapter 6 CFD analysis on two-phase gas-non-Newtonian liquid flow through piping components	
6.1 Introduction	196
6.2 The Experimental setup	198
6.3 Mathematical Model	199

6.3.1	CFD Procedure	199
6.3.2	Assumptions for air-SCMC flow through piping components	201
6.4	Results and discussion	202
6.4.1	Convergence and grid independency	202
6.4.2	CFD analysis for air-non-Newtonian flow through straight pipe	203
6.4.3	Computational fluid dynamics (CFD) analysis for air-non-Newtonian liquid flow through elbows	204
6.4.4	CFD analysis for air-non-Newtonian liquid flow through orifices	206
6.4.5	CFD analysis for air-non-Newtonian flow through gate Valve	207
6.4.6	CFD analysis for air-non-Newtonian flow through globe Valve	209
6.5	Conclusions	210
Chapter 7 Non-Newtonian liquid flow through helical coils - CFD analysis		
7.1	Introduction	283
7.2	The experimental setup	284
7.3	Mathematical Model	286
7.4	Computational fluid dynamics (CFD) Procedure	287
7.5	Results and discussion	289
7.5.1	Convergence and grid independency	289
7.5.2	Computational fluid dynamics (CFD) analysis	289
7.6	Comparison with the data available in the literature	293
7.7	Conclusions	294

**Chapter 8 Gas-non-Newtonian liquid flow
through helical coils - CFD analysis**

8.1	Introduction	339
8.2	Experimental	341
8.3	Mathematical Model	342
	8.3.1 CFD Procedure	342
	8.3.2 Assumptions for air-SCMC flow through helical coils	344
8.4	Results and discussion	345
	8.4.1 Convergence and grid independency	345
	8.4.2 CFD analysis	346
8.5	Conclusions	351
	Nomenclature	395
	References	400

LIST OF TABLES

Table No.	Title	Page No.
2.1	General property ϕ for general transport equation	20
2.2	Empirical constants in K- ϵ turbulence model	20
3.1	Dimensions of the U-bends used in the experiments	109
3.2	Range of variables used in the experiment	109
3.3	Comparison of the pressure drop across the U-bends, experimental and CFD analysis data	110
3.4	Comparison of the two-phase pressure drop across the U-bends, experimental and CFD analysis	111
4.1	Dimension of the piping components	138
4.2	Physical properties of the SCMC solution	138
4.3	Range of variables	139
5.1	Comparison of experimental and CFD analysis data for straight pipe	190
5.2	Comparison of experimental and CFD analysis data for elbows, Concentration of SCMC solution (kg/m^3): 0.2	191
5.3	Comparison of experimental and CFD analysis data for orifice, Concentration of SCMC solution (kg/m^3): 0.8	192
5.4	Comparison of experimental and CFD analysis data for gate valve, Concentration of SCMC solution (kg/m^3): 0.8	193
5.5	Comparison of experimental and CFD analysis data	194

	for globe valve, Concentration of SCMC solution (kg/m ³): 0.8	
6.1	Range of variables	272
6.2	Comparison of the experimental and CFD analysis data of two-phase pressure drop through straight pipe for different flow rate	273
6.3	Comparison of the experimental and CFD analysis data of two-phase pressure drop through straight pipe for different SCMC concentration	274
6.4	Comparison of the experimental and CFD analysis data of two-phase pressure drop through elbows for different liquid flow rate	275
6.5	Comparison of the experimental and CFD analysis data of two-phase pressure drop through elbows at different elbow angle	276
6.6	Comparison of the experimental and CFD analysis data of two-phase pressure drop through orifices at different liquid flow rate	277
6.7	Comparison of the experimental and CFD analysis data of two-phase pressure drop through orifices at different orifice diameter ratio	278
6.8	Comparison of the experimental and CFD analysis data of two-phase pressure drop through gate valve at different flow rate	279
6.9	Comparison of the experimental and CFD analysis data of two-phase pressure drop at different opening of gate valve	280
6.10	Comparison of the experimental and CFD analysis data of two-phase pressure drop at different opening of globe valve	281
7.1	Range of variables investigated	334

7.2	Comparison of the experimental and CFD analysis data for the frictional pressure drop across the coil for different liquid concentration	335
7.3	Comparison of the experimental and CFD analysis data for frictional pressure across the coil for liquid concentration of 0.8 kg/m^3 and different coil diameter	336
7.4	Comparison of the experimental and calculated data for friction factor across the coil for different liquid (SCMC) concentration	337
8.1	Range of variables investigated	391
8.2	Comparison of the experimental and CFD analysis data for frictional pressure drop across the coil for liquid (SCMC concentration) of 0.8 kg/m^3	392
8.3	Comparison of the experimental and CFD analysis data for frictional pressure drop across the coil at different liquid (SCMC) concentrations	393
8.4	Comparison of the experimental and CFD analysis data for frictional pressure drop across the coil for liquid (SCMC) concentration of 0.8 kg/m^3 for different coil diameters	394

LIST OF FIGURES

Figure No.	Title
2.1	Discretized cell
3.1	Schematic diagram of experimental set up
3.2	Pressure distributions along pipeline with a bend
3.3	Typical static pressure distribution curve
3.4	Grid for U-bends
3.5	Plot of Velocity vector for U-bend for water velocity (m/s): 0.933
3.6	Plot of velocity vector in the bend portion i.e. helicity for U-bends for water velocity (m/s): 0.933
3.7	Contour plot of velocity vector at different points in the bend at water velocity (m/s): 0.933 and radius of curvature (m): 0.06
3.8	Contour plot of velocity vector at angular coordinates in the bend for water velocity (m/s): 0.933 and radius of curvature (m): 0.06
3.9	Contour plot of velocity at different points in the bend for water velocity (m/s): 0.933 and radius of curvature (m): 0.06
3.10	Contour plot of velocity at angular coordinates in the bend for water velocity (m/s): 0.933 and radius of curvature (m): 0.06
3.11	Contour plot of velocity at radial coordinates in the bend for water velocity (m/s): 0.933 and radius of curvature (m): 0.06
3.12	Contour plot of cell Reynolds number at different points in the bend for water velocity (m/s): 0.933 and radius of curvature (m): 0.06
3.13	Contour plot of cell Reynolds number at angular coordinates in the bend for water velocity (m/s): 0.933 and radius of curvature (m): 0.06
3.14	Contour plot of cell Reynolds number at radial coordinates in the bend for water velocity (m/s): 0.933 and radius of curvature (m): 0.06

-
- 3.15 Contour plot of tangential velocity at different points in the bend for water velocity (m/s): 0.933 and radius of curvature (m): 0.06
- 3.16 Contour plot of tangential velocity at angular coordinates in the bend for water velocity (m/s): 0.933 and radius of curvature (m): 0.06
- 3.17 Contour plot of radial velocity at different points in the bend for water velocity (m/s): 0.933 and radius of curvature (m): 0.06
- 3.18 Contour plot of radial velocity at angular coordinates in the bend for water velocity (m/s): 0.933 and radius of curvature (m): 0.06
- 3.19 Contours plot of static pressure for U-bend for water velocity (m/s): 0.933
- 3.20 Contour plot of static pressure at different points in the bend for water velocity (m/s): 0.933 and radius of curvature (m): 0.06
- 3.21 Contour plot of static pressure at angular coordinates in the bend for water velocity (m/s): 0.933 and radius of curvature (m): 0.06
- 3.22 Contour plot of static pressure at radial coordinates in the bend for water velocity (m/s): 0.933 and radius of curvature (m): 0.06
- 3.23 Contour velocity plot inside the different points of U-bend water velocity: 0.933 m/s, radius of curvature: 0.06 m
- 3.24 Contour velocity plot inside the different angular points of U-bend water velocity: 0.933 m/s, radius of curvature: 0.06 m
- 3.25 Experimental and CFD static pressure distribution
- 3.26 Contours plot of wall shear stress for U-bend for water velocity (m/s): 0.933
- 3.27 Contour plot of wall shear stress at different points in the bend water velocity: 0.933 m/s, radius of curvature: 0.06 m
- 3.28 Contour plot of wall shear stress at angular coordinates in the bend for water velocity (m/s): 0.933, radius of curvature(m): 0.06
- 3.29 Contour plot of wall shear stress at radial coordinates in the bend for water velocity (m/s): 0.933, radius of curvature(m): 0.06
- 3.30 Contours plot of strain rate for U-bend for water velocity (m/s):

-
- 0.933
- 3.31 Contour plot of wall strain rate at different points in the bend for water velocity (m/s): 0.933, radius of curvature(m): 0.06
- 3.32 Contour plot of strain rate at angular coordinates in the bend for water velocity (m/s): 0.933, radius of curvature (m): 0.06
- 3.33 Contour plot of strain rate at radial coordinates in the bend for water velocity (m/s): 0.933, radius of curvature (m): 0.06
- 3.34 Contour plot of helicity at different points in the bend for water velocity (m/s): 0.933, radius of curvature (m): 0.06
- 3.35 Contour plot of helicity at angular coordinates in the bend for water velocity (m/s): 0.933, radius of curvature (m): 0.06
- 3.36 Contour plot of helicity at radial coordinates in the bend for water velocity (m/s): 0.933, radius of curvature (m): 0.06
- 3.37 Contour plot of vorticity at different points in the bend for water velocity (m/s): 0.933, radius of curvature (m): 0.06
- 3.38 Contour plot of vorticity at angular coordinates in the bend for water velocity (m/s): 0.933, radius of curvature (m): 0.06
- 3.39 Contour plot of vorticity at radial coordinates in the bend for water velocity (m/s): 0.933, radius of curvature (m): 0.06
- 3.40 Contour plot of turbulent kinetic energy at different points in the bend for water velocity (m/s): 0.933, radius of curvature (m): 0.06
- 3.41 Contour plot of turbulent kinetic energy at angular coordinates in the bend for water velocity (m/s): 0.933, radius of curvature (m): 0.06
- 3.42 Contour plot of turbulent kinetic energy at radial coordinates in the bend for water velocity (m/s): 0.933, radius of curvature (m): 0.06
- 3.43 Contour plot of turbulent intensity at different points in the bend for water velocity (m/s): 0.933, radius of curvature (m): 0.06
- 3.44 Contour plot of turbulent intensity at angular coordinates in the bend for water velocity (m/s): 0.933, radius of curvature (m): 0.06
- 3.45 Contour plot of turbulent intensity at radial coordinates in the

-
- bend for water velocity (m/s): 0.933, radius of curvature (m): 0.06
- 3.46 Contour plot of turbulent dissipation rate at different points in the bend for water velocity (m/s): 0.933, radius of curvature (m): 0.06
- 3.47 Contour plot of turbulent dissipation rate at angular coordinates in the bend for water velocity (m/s): 0.933, radius of curvature (m): 0.06
- 3.48 Contour plot of turbulent dissipation rate at radial coordinates in the bend for water velocity (m/s): 0.933, radius of curvature (m): 0.06
- 3.49 Contour plot of production of k at different points in the bend for water velocity (m/s): 0.933, radius of curvature (m): 0.06
- 3.50 Contour plot of production of k at angular coordinates in the bend for water velocity (m/s): 0.933, radius of curvature (m): 0.06
- 3.51 Contour plot of turbulent viscosity at different points in the bend for water velocity (m/s): 0.933, radius of curvature (m): 0.06
- 3.52 Contour plot of turbulent viscosity at angular coordinates in the bend for water velocity (m/s): 0.933, radius of curvature (m): 0.06
- 3.53 Contour plot of turbulent viscosity at radial coordinates in the bend for water velocity (m/s): 0.933, radius of curvature (m): 0.06
- 3.54 Contour plot of mass imbalance at radial coordinates in the bend for water velocity (m/s): 0.933, radius of curvature (m): 0.06
- 3.55 Comparison plot of the experimental data and CFD modeling for water flow
- 3.56 Contour plot of velocity vector for U-bend, water velocity (m/s): 0.933, gas velocity (m/s): 1.365, gas fraction, α_g : 0.59
- 3.57a Contour plot of velocity vector for air-water mixture at different points in the bend, radius of curvature 0.06 m, water velocity (m/s): 0.933, gas velocity (m/s): 1.365, gas fraction, α_g : 0.59
- 3.57b Contour plot of velocity vector for water in the mixture at different points in the bend, radius of curvature 0.06 m, water velocity (m/s): 0.933, gas velocity (m/s): 1.365, gas fraction, α_g : 0.59

-
- 3.57c Contour plot of velocity vector for air in the mixture at different points in the bend, radius of curvature 0.06 m, water velocity (m/s): 0.933, gas velocity (m/s): 1.365, gas fraction, α_g : 0.5
- 3.58 Contour plot of velocity, mixture for U-bend at radius of curvature 0.06 m at different points in the bend, water velocity (m/s): 0.933, gas velocity (m/s): 1.365, gas fraction, α_g : 0.59
- 3.59 Contour plot of velocity, mixture for U-bend at radius of curvature 0.06 m at different angular points in the bend, water velocity (m/s): 0.933, gas velocity (m/s): 1.365, gas fraction, α_g : 0.59
- 3.60 Contour plot of static pressure for U-bends, water velocity (m/s): 0.933, gas velocity (m/s): 1.365, gas fraction, α_g : 0.59
- 3.61 Contour plot of static pressure, mixture for U-bend at radius of curvature 0.06 m at different points in the bend, water velocity (m/s): 0.933, Gas velocity (m/s): 1.365, gas fraction, α_g : 0.59
- 3.62 Contour plot of static pressure, mixture for U-bend at radius of curvature 0.06 m at different angular points in the bend, water velocity (m/s): 0.933, gas velocity (m/s): 1.365, Gas fraction, α_g : 0.59
- 3.63 Contour velocity plot inside the different points of U-bend water velocity: 0.933 m/s, gas velocity (m/s): 1.365, Gas fraction, α_g : 0.59, radius of curvature: 0.06 m
- 3.64 Contour velocity plot inside the different angular points of U-bend water velocity: 0.933 m/s, gas velocity (m/s): 1.365, Gas fraction, α_g : 0.59, radius of curvature: 0.06 m
- 3.65 Experimental and CFD static pressure distribution
- 3.66a Contour plot of volume fraction for water at different points in the bend, radius of curvature 0.06 m, water velocity (m/s): 0.933, gas velocity (m/s): 1.365, gas fraction, α_g : 0.59
- 3.66b Contour plot of volume fraction for air at different points in the bend, radius of curvature 0.06 m, water velocity (m/s): 0.933, gas

-
- velocity (m/s): 1.365, gas fraction, α_g : 0.59
- 3.67a Contour plot of volume fraction for water at different angular points in the bend, radius of curvature 0.06 m, water velocity (m/s): 0.933, gas velocity (m/s): 1.365, gas fraction, α_g : 0.59
- 3.67b Contour plot of volume fraction for air at angular coordinates in the bend, radius of curvature 0.06 m, water velocity (m/s): 0.933, gas velocity (m/s): 1.365, gas fraction, α_g : 0.59
- 3.68 Contour plot of shear stress and shear strain for U-bend at radius of curvature 0.06 m at different points in the bend, water velocity (m/s): 0.933, Gas velocity (m/s): 1.365, Gas fraction, α_g : 0.59
- 3.69 Comparison plot of the experimental data and CFD modeling for two – phase air–water flow
- 3.70 Comparison of the two-phase pressure drop across the U-bends, experimental and CFD analysis
- 4.1 Schematic diagram of the experimental setup
- 4.2 Static pressure distribution curve across the valve
- 4.3 Typical static pressure distribution curve for elbow
- 4.4 Typical static pressure distribution curve for orifice
- 4.5 Typical static pressure distribution curve for gate valve
- 4.6 Typical static pressure distribution curve for globe valve
- 4.7 Variation of the pressure drop across the elbow with liquid flow rate
- 4.8 Variation of the pressure drop across the orifice with liquid flow rate
- 4.9 Variation of the pressure drop across the gate valve with liquid flow rate
- 4.10 Variation of the pressure drop across the globe valve with liquid flow rate
- 4.11 Comparison of the experimental pressure drop across 45° elbow

-
- with Turian et al. (1998) correlation
- 4.12 Comparison of the experimental pressure drop across 90° elbow with Edwards et al. (1985) and Telis-Romero et al. (2000) correlation
- 4.13 Comparison of the experimental pressure drop across gate valve with Edwards et al. (1985) and Turian et al. (1998) correlation
- 4.14 Comparison of the experimental pressure drop across globe valve with Edwards et al. (1985) and Turian et al. (1998) correlation
- 5.1 Unstructured boundary layer hexahedral grid of straight pipe
Grid Size: No. of cells = 200633; No. of faces = 615032, No. of nodes = 214428, 1 cell zone, 4 face zones
- 5.2 Contour plot of static pressure for straight pipe
Concentration of SCMC (kg/m^3): 0.8, Liquid velocity (m/s): 0.3199
- 5.3 Plot of velocity vector for straight pipe
Concentration of SCMC (kg/m^3): 0.8, Liquid velocity (m/s): 0.3199
- 5.4 Comparison of the experimental data and CFD modeling for straight pipe
- 5.5 Mesh geometry – unstructured t-grid (tetrahedral)
(a) 45° elbow
Grid Size: No. of cells = 25985; No. of faces = 57149, No. of nodes = 7310, 1 cell zone, 4 face zones
(b) 90° elbow
Grid Size: No. of cells = 29157; No. of faces = 64167, No. of nodes = 8208, 1 cell zone, 4 face zones
(c) 135° elbow
Grid Size: No. of cells = 4427; No. of faces = 9778, No. of nodes = 1279, 1 cell zone, 4 face zones
(d)
- 5.6 Plot of velocity vector
(a) 45° elbow
Concentration of SCMC solution (kg/m^3): 0.2, Liquid velocity (m/s): 0.296
(b) 90° elbow
Concentration of SCMC solution (Kg/m^3): 0.2, Liquid velocity (m/s): 0.296 m/s
(c) 135° elbow
Concentration of SCMC solution (Kg/m^3): 0.8, Liquid velocity (m/s): 1.733m/s

-
- 5.7a Contours plot of velocity vector inside the different points of 45⁰ elbow, Concentration of SCMC solution (kg/m³): 0.8, Liquid flow rate, Q_1 (m³/s): 21.94×10^{-5} , Liquid velocity, V_1 (m/s): 1.733
- 5.7b Contour plot of velocity vector inside the different points of 90⁰ elbow, Concentration of SCMC solution (kg/m³): 0.8, Liquid flow rate, Q_1 (m³/s): 21.94×10^{-5} , Liquid velocity, V_1 (m/s): 1.733
- 5.7c Contour plot of velocity vector inside the different points of 135⁰ elbow, Concentration of SCMC solution (kg/m³): 0.8, Liquid flow rate, Q_1 (m³/s): 21.94×10^{-5} , Liquid velocity, V_1 (m/s): 1.733
- 5.8a Contours plot of velocity magnitude inside the different points of 45⁰ elbow, Concentration of SCMC solution (kg/m³): 0.8, Liquid flow rate, Q_1 (m³/s): 21.94×10^{-5} , Liquid velocity, V_1 (m/s): 1.733
- 5.8b Contour plot of velocity magnitude inside the different points of 90⁰ elbow, Concentration of SCMC solution (kg/m³): 0.8, Liquid flow rate, Q_1 (m³/s): 21.94×10^{-5} , Liquid velocity, V_1 (m/s): 1.733
- 5.8c Contour plot of velocity magnitude inside the different points of 135⁰ elbow, Concentration of SCMC solution (kg/m³): 0.8, Liquid flow rate, Q_1 (m³/s): 21.94×10^{-5} , Liquid velocity, V_1 (m/s): 1.733
- 5.9a Contour plot of X-velocity inside the different points of 45⁰ elbow, Concentration of SCMC solution (kg/m³): 0.8, Liquid flow rate, Q_1 (m³/s): 21.94×10^{-5} , Liquid velocity, V_1 (m/s): 1.733
- 5.9b Contour plot of X-velocity inside the different points of 90⁰ elbow, Concentration of SCMC solution (kg/m³): 0.8, Liquid flow rate, Q_1 (m³/s): 21.94×10^{-5} , Liquid velocity, V_1 (m/s): 1.733
- 5.9c Contour plot of X-velocity inside the different points of 135⁰ elbow, Concentration of SCMC solution (kg/m³): 0.8, Liquid flow rate, Q_1 (m³/s): 21.94×10^{-5} , Liquid velocity, V_1 (m/s): 1.733
- 5.10 Contour plot of static pressure
(a) 45⁰ elbow
Concentration of SCMC solution (kg/m³): 0.2, Liquid velocity (m/s): 0.296
(b) 90⁰ elbow
Concentration of SCMC solution (Kg/m³): 0.2 Liquid velocity (m/s): 0.296
(c) 135⁰ elbow
Concentration of SCMC solution (Kg/m³): 0.4, Liquid velocity

-
- (m/s): 0.296
- 5.11a Contours plot of static pressure inside the different points of 45⁰ elbow, Concentration of SCMC solution (kg/m³): 0.8, Liquid flow rate, Q_1 (m³/s): 21.94×10^{-5} , Liquid velocity, V_1 (m/s): 1.733
- 5.11b Contours plot of static pressure inside the different points of 90⁰ elbow, Concentration of SCMC solution (kg/m³): 0.8, Liquid flow rate, Q_1 (m³/s): 21.94×10^{-5} , Liquid velocity, V_1 (m/s): 1.733
- 5.11c Contour plot of static pressure inside the different points of 135⁰ elbow, Concentration of SCMC solution (kg/m³): 0.8, Liquid flow rate, Q_1 (m³/s): 21.94×10^{-5} , Liquid velocity, V_1 (m/s): 1.733
- 5.12a Contour plot of total pressure inside the different points of 45⁰ elbow, Concentration of SCMC solution (kg/m³): 0.8, Liquid flow rate, Q_1 (m³/s): 21.94×10^{-5} , Liquid velocity, V_1 (m/s): 1.733
- 5.12b Contour plot of total pressure inside the different points of 135⁰ elbow, Concentration of SCMC solution (kg/m³): 0.8, Liquid flow rate, Q_1 (m³/s): 21.94×10^{-5} , Liquid velocity, V_1 (m/s): 1.733
- 5.13 Comparison of the experimental and CFD for 45⁰ elbow
- 5.14 Comparison of the experimental data and CFD modeling for elbows
- 5.15 Unstructured boundary layer hexahedral grid of orifice, $D_0/D_t = 0.5984$ Grid Size: No. of cells = 4427; No. of faces = 9778, No. of nodes = 1279, 1 cell zone, 4 face zones
- 5.16 Contour plot of static pressure for $D_0/D_t = 0.4646$ orifice Concentration of SCMC solution (kg/m³): 0.8, Liquid velocity (m/s): 0.3199
- 5.17 Contour plot of static pressure at different points of $D_0/D_t = 0.5984$ orifice Concentration of SCMC solution (kg/m³): 0.8, Liquid velocity (m/s): 1.2772
- 5.18 Plot of velocity vector for $D_0/D_t = 0.4646$ orifice Concentration of SCMC solution (kg/m³): 0.8, Liquid velocity (m/s): 0.3199
- 5.19 Plot of velocity vector at different points of $D_0/D_t = 0.5984$ orifice Concentration of SCMC solution (kg/m³): 0.8, Liquid velocity (m/s): 1.2772

-
- 5.20 Plot of velocity magnitude for $D_0/D_t = 0.5984$ orifice Concentration of SCMC solution (kg/m^3): 0.8, Liquid velocity (m/s): 1.2772
- 5.21 Comparison plot of experimental and CFD for orifice
- 5.22 Comparison of the experimental data and CFD modeling for orifices
- 5.23 Grid for 50% opening gate valve
- 5.24 Plot of static pressure for 50% opening gate valve Concentration of SCMC solution (kg/m^3): 0.8, Liquid velocity (m/s): 1.5142
- 5.25 Plot of total pressure for 50% opening gate valve Concentration of SCMC solution (kg/m^3): 0.8, Liquid velocity (m/s): 1.5142
- 5.26 Plot of velocity magnitude for 50% opening gate valve Concentration of SCMC solution (kg/m^3): 0.8, Liquid velocity (m/s): 1.5142
- 5.27 Plot of velocity vector for 50% opening gate valve Concentration of SCMC solution (kg/m^3): 0.8, Liquid velocity (m/s): 0.8033
- 5.28 Comparison plot of experimental and CFD for gate valve
- 5.29 Comparison of the experimental data and CFD modeling for gate valves
- 5.30 Unstructured boundary layer hexahedral grid of 75% opening globe valve Grid Size: No. of cells = 348633; No. of faces = 1077668, No. of nodes = 381741, 1 cell zone, 4 face zones
- 5.31 Plot of velocity vector for 75% opening globe valve Concentration of SCMC solution (kg/m^3): 0.8, Liquid velocity (m/s): 0.8033
- 5.32 Comparison plot of experimental and CFD for globe valve
- 5.33 Comparison of the experimental data and CFD modeling for globe valves
- 6.1 Schematic diagram of the experimental setup

-
- 6.2 Contour plot of velocity vector in the air-SCMC mixture at different points of straight pipe, concentration of SCMC solution (kg/m^3): 0.8, Liquid velocity (m/s): 1.2772, Gas velocity (m/s): 1.9842, Gas fraction, α_g : 0.3086
- 6.3 Plot of velocity vector for SCMC phase in the mixture at different points of straight pipe, concentration of SCMC solution (kg/m^3): 0.8, Liquid velocity (m/s): 1.2772, Gas velocity (m/s): 1.9842, Gas fraction, α_g : 0.3086
- 6.4 Contour plot of velocity vector for air phase in the mixture at different points of straight pipe, concentration of SCMC solution (kg/m^3): 0.8, Liquid velocity (m/s): 1.2772, Gas velocity (m/s): 1.9842, Gas fraction, α_g : 0.3086
- 6.5 Contour plot of velocity magnitude in air-SCMC mixture at different points of straight pipe, concentration of SCMC solution (kg/m^3): 0.8, Liquid velocity (m/s): 1.2772, Gas velocity (m/s): 1.9842, Gas fraction, α_g : 0.3086
- 6.6 Contour plot of axial velocity inside the different points of straight pipe, concentration of SCMC solution (kg/m^3): 0.8, Liquid velocity (m/s): 1.2772, Gas velocity (m/s): 1.9842, Gas fraction, α_g : 0.3086
- 6.7 Contours of static pressure inside the different points of straight pipe, concentration of SCMC solution (kg/m^3): 0.8, Liquid velocity (m/s): 1.2772, Gas velocity (m/s): 1.9842, Gas fraction, α_g : 0.3086
- 6.8 Contours of total pressure inside the different points of straight pipe, concentration of SCMC solution (kg/m^3): 0.8, Liquid velocity (m/s): 1.2772, Gas velocity (m/s): 1.9842, Gas fraction, α_g : 0.3086
- 6.9 Contours of SCMC phase volume fraction at different points of straight pipe, concentration of SCMC solution (kg/m^3): 0.8, Liquid velocity (m/s): 1.2772, Gas velocity (m/s): 1.9842, Gas fraction, α_g : 0.3086
- 6.10 Contours of air phase volume fraction at different points of

-
- straight pipe, concentration of SCMC solution (kg/m^3): 0.8, Liquid velocity (m/s): 1.2772, Gas velocity (m/s): 1.9842, Gas fraction, α_g : 0.3086
- 6.11 Comparison of the experimental data and CFD modeling for straight pipe varying with liquid flow rate
- 6.12 Comparison of the experimental data and CFD modeling for straight pipe varying with SCMC solution concentration
- 6.13 Comparison of experimental results with CFD simulated results for different liquid flow rate
- 6.14 Contour plot of velocity vector for air-SCMC mixture at different points in 45° elbow, concentration of SCMC solution (kg/m^3): 0.8, Liquid velocity (m/s): 1.733, Gas velocity (m/s): 3.167, Gas fraction, α_g : 0.64
- 6.15 Contour plot of velocity in the air-SCMC mixture at different points of elbows, concentration of SCMC solution (kg/m^3): 0.8, Liquid velocity (m/s): 1.733 (a) 45° , Gas velocity (m/s): 3.167, Gas fraction, α_g : 0.64 (b) 90° , Gas velocity (m/s): 2.3933, Gas fraction, α_g : 0.58 (c) 135° , Gas velocity (m/s): 2.867, Gas fraction, α_g : 0.62
- 6.16 Contour plot of velocity vector for SCMC in the mixture at different points in 45° elbow, concentration of SCMC solution (kg/m^3): 0.8, Liquid velocity (m/s): 1.733, Gas velocity (m/s): 3.167, Gas fraction, α_g : 0.64
- 6.17 Contour plot of velocity vector for air in the mixture at different points in 90° elbow, concentration of SCMC solution (kg/m^3): 0.8, Liquid velocity (m/s): 1.733, Gas velocity (m/s): 2.3933, Gas fraction, α_g : 0.5
- 6.18 Contours plot of static pressure for elbows, concentration of SCMC solution (kg/m^3): 0.8, liquid velocity (m/s): 1.733 (a) 45° , Gas velocity (m/s): 3.167, Gas fraction, α_g : 0.64 (b) 90° , Gas velocity (m/s): 2.3933, Gas fraction, α_g : 0.58 (c) 135° , Gas velocity (m/s): 2.867, Gas fraction, α_g : 0.62

-
- 6.19 Contour plot of static pressure, at different points in the elbows, concentration of SCMC solution (kg/m^3): 0.8, Liquid velocity (m/s): 1.733 (a) 45° , Gas velocity (m/s): 3.167, Gas fraction, α_g : 0.64
(b) 90° , Gas velocity (m/s): 2.3933, Gas fraction, α_g : 0.58
(c) 135° , Gas velocity (m/s): 2.867, Gas fraction, α_g : 0.62
- 6.20 Contour velocity plot inside different points of 45° elbow concentration of SCMC solution (kg/m^3): 0.8, Liquid velocity (m/s): 1.733, Gas velocity (m/s): 3.167, Gas fraction, α_g : 0.64
- 6.21 Contours of volume fraction for 90° elbow, concentration of SCMC solution (kg/m^3): 0.8, Liquid velocity (m/s): 1.733, gas velocity (m/s): 2.3933, gas fraction, α_g : 0.58 (a) SCMC phase and (b) air phase
- 6.22 Comparison plot of static pressure experimental and CFD for 45° elbow
- 6.23 Comparison of experimental results with CFD simulated results at different elbow angle
- 6.24 Contour plot of velocity vector for $D_0/D_t = 0.4646$ orifice Concentration of SCMC solution (kg/m^3): 0.8, Liquid velocity (m/s): 0.8033, Gas velocity (m/s): 0.3552, Gas fraction, α_g : 0.30
- 6.25 Contour plot of velocity vector for $D_0/D_t = 0.5984$ orifice Concentration of SCMC solution (kg/m^3): 0.8, Liquid velocity (m/s): 0.8033, Gas velocity (m/s): 0.3552, Gas fraction, α_g : 0.30
- 6.26 Contour plot of velocity vector for $D_0/D_t = 0.7087$ orifice Concentration of SCMC solution (kg/m^3): 0.8, Liquid velocity (m/s): 1.2772, Gas velocity (m/s): 2.4304, Gas fraction, α_g : 0.65
- 6.27 Contour plot of static pressure for $D_0/D_t = 0.4646$ orifice Concentration of SCMC solution (kg/m^3): 0.8, Liquid velocity (m/s): 0.8033, Gas velocity (m/s): 0.3552, Gas fraction, α_g : 0.30
- 6.28 Contour plot of static pressure for $D_0/D_t = 0.5984$ orifice Concentration of SCMC solution (kg/m^3): 0.8, Liquid velocity

- (m/s): 0.8033, Gas velocity (m/s): 0.3552, Gas fraction, α_g : 0.30
- 6.29 Contour plot of static pressure for $D_0/D_t = 0.7087$ orifice
Concentration of SCMC solution (kg/m^3): 0.8, Liquid velocity (m/s): 1.2772, Gas velocity (m/s): 2.4304, Gas fraction, α_g : 0.65
- 6.30 Contour plot of velocity vector in air-SCMC mixture at different points for $D_0/D_t = 0.4646$ orifice Concentration of SCMC solution (kg/m^3): 0.8, Liquid velocity (m/s): 1.2772, Gas velocity (m/s): 1.1508, Gas fraction, α_g : 0.46
- 6.31 Contour plot of velocity vector plot of SCMC-phase in the mixture at different points for $D_0/D_t = 0.4646$ orifice Concentration of SCMC solution (kg/m^3): 0.8, Liquid velocity (m/s): 1.2772, Gas velocity (m/s): 1.1508, Gas fraction, α_g : 0.46
- 6.32 Contour plot of velocity vector plot of air-phase in the mixture at different points for $D_0/D_t = 0.4646$ orifice Concentration of SCMC mixture (kg/m^3): 0.8, Liquid velocity (m/s): 1.2772, Gas velocity (m/s): 1.1508, Gas fraction, α_g : 0.46
- 6.33 Contours plot of velocity magnitude in the air-SCMC mixture at different points for $D_0/D_t = 0.4646$ orifice Concentration of SCMC solution (kg/m^3): 0.8, Liquid velocity (m/s): 1.2772, Gas velocity (m/s): 1.1508, Gas fraction, α_g : 0.46
- 6.34 Contours plot of velocity in the air-SCMC mixture inside the different points for $D_0/D_t = 0.4646$ orifice Concentration of SCMC solution (kg/m^3): 0.8, Liquid velocity (m/s): 1.2772, Gas velocity (m/s): 1.1508, Gas fraction, α_g : 0.46
- 6.35 Contours plot of static pressure in the air-SCMC mixture inside the different points for $D_0/D_t = 0.4646$ orifice Concentration of SCMC solution (kg/m^3): 0.8, Liquid velocity (m/s): 1.2772, Gas velocity (m/s): 1.1508, Gas fraction, α_g : 0.46
- 6.36 Contours plot of total pressure in the air-SCMC mixture inside the different points for $D_0/D_t = 0.4646$ orifice Concentration of SCMC solution (kg/m^3): 0.8, Liquid velocity (m/s): 1.2772, Gas velocity (m/s): 1.1508, Gas fraction, α_g : 0.46
- 6.37 Contours plot of SCMC phase volume fraction in the mixture inside the different points of $D_0/D_t = 0.4646$ orifice Concentration of SCMC solution (kg/m^3): 0.8, Liquid velocity (m/s): 1.2772, Gas velocity

-
- (m/s): 1.1508, Gas fraction, α_g : 0.46
- 6.38 Contours of air phase volume fraction in the mixture inside the different points of $D_0/D_t = 0.4646$ orifice Concentration of SCMC solution (kg/m^3): 0.8, Liquid velocity (m/s): 1.2772, Gas velocity (m/s): 1.1508, Gas fraction, α_g : 0.46
- 6.39 Comparison of the experimental result with CFD simulated result with different liquid flow rate and fixed liquid concentration, fixed orifice dimension
- 6.40 Comparison of the experimental result with CFD simulated result with different orifice dimension and fixed liquid concentration, fixed liquid flow rate
- 6.41 Comparison of experimental results with CFD simulated results for different liquid flow rates
- 6.42 Comparison of experimental results with CFD simulated results for different Orifice diameter ratios
- 6.43 Contours plot of velocity vector in the air-SCMC mixture at the different points of 50% opening gate valve, Concentration of SCMC solution (kg/m^3): 0.8, Liquid velocity (m/s): 1.5142, Gas velocity (m/s): 3.0516, Gas fraction, α_g : 0.668
- 6.44 Contours plot of velocity magnitude in the air-SCMC mixture at the different points of 50% opening gate valve, Concentration of SCMC solution (kg/m^3): 0.8, Liquid velocity (m/s): 1.5142, Gas velocity (m/s): 3.0516, Gas fraction, α_g : 0.6683
- 6.45 Contours plot of velocity in the air-SCMC mixture at the different points of 50% opening gate valve, Concentration of SCMC solution (kg/m^3): 0.8, Liquid velocity (m/s): 1.5142, Gas velocity (m/s): 3.0516, Gas fraction, α_g : 0.6683
- 6.46 Contours plot of static pressure in the air-SCMC mixture at the different points of 50% opening gate valve, Concentration of SCMC solution (kg/m^3): 0.8, Liquid velocity (m/s): 1.5142, Gas velocity (m/s): 3.0516, Gas fraction, α_g : 0.6683
- 6.47 Contours plot of total pressure in the air-SCMC mixture at the different points of 50% opening gate valve, Concentration of SCMC solution (kg/m^3): 0.8, Liquid velocity (m/s): 1.5142, Gas velocity (m/s): 3.0516, Gas fraction, α_g : 0.6683

-
- 6.48 Contours plot of SCMC phase volume fraction in the air-SCMC mixture at the different points of 50% opening gate valve, Concentration of SCMC solution (kg/m^3): 0.8, Liquid velocity (m/s): 1.5142, Gas velocity (m/s): 3.0516, Gas fraction, α_g : 0.6683
- 6.49 Contours plot of air phase volume fraction in the air-SCMC mixture at the different points of 50% opening gate valve, Concentration of SCMC solution (kg/m^3): 0.8, Liquid velocity (m/s): 1.5142, Gas velocity (m/s): 3.0516, Gas fraction, α_g : 0.6683
- 6.50 Comparison of experimental results with CFD simulated results for different liquid flow rates
- 6.51 Comparison of experimental results with CFD simulated results for different % opening of Gate valve
- 6.52 Contours plot of velocity vector in the air-SCMC mixture for 50% opening globe valve, Concentration of SCMC solution (kg/m^3): 0.8, Liquid velocity (m/s): 1.5142, Gas velocity (m/s): 1.7265, Gas fraction, α_g : 0.5
- 6.53 Contours plot of velocity vector in the air-SCMC mixture at the different points of 50% opening globe valve, Concentration of SCMC solution (kg/m^3): 0.8, Liquid velocity (m/s): 1.5142, Gas velocity (m/s): 1.7265, Gas fraction, α_g : 0.5
- 6.54 Contours plot of velocity vector for SCMC phase in the air-SCMC mixture at the different points of 50% opening globe valve, Concentration of SCMC solution (kg/m^3): 0.8, Liquid velocity (m/s): 1.5142, Gas Velocity (m/s): 1.7265, Gas fraction, α_g : 0.5
- 6.55 Contours plot of velocity vector for air phase in the air-SCMC mixture at the different points of 50% opening globe valve, Concentration of SCMC solution (kg/m^3): 0.8, Liquid Velocity (m/s): 1.5142, Gas velocity (m/s): 1.7265, Gas fraction, α_g : 0.5
- 6.56 Contours of velocity magnitude in the air-SCMC mixture at the different points of 50% opening globe valve, Concentration of SCMC solution (kg/m^3): 0.8, Liquid velocity (m/s): 1.5142, Gas velocity (m/s): 1.7265, Gas fraction, α_g : 0.5

-
- 6.57 Contours of axial velocity in the air-SCMC mixture at the different points of 50% opening globe valve, Concentration of SCMC solution (kg/m^3): 0.8, Liquid velocity (m/s): 1.5142, Gas velocity (m/s): 1.7265, Gas fraction, α_g : 0.5
- 6.58 Contours of static pressure in the air-SCMC mixture at the different points of 50% opening globe valve, Concentration of SCMC solution (kg/m^3): 0.8, Liquid velocity (m/s): 1.5142, Gas velocity (m/s): 1.7265, Gas fraction, α_g : 0.5
- 6.59 Contours plot of total pressure in the air-SCMC mixture at the different points of 50% opening globe valve, Concentration of SCMC solution (kg/m^3): 0.8, Liquid velocity (m/s): 1.5142, Gas velocity (m/s): 1.7265, Gas fraction, α_g : 0.5
- 6.60 Contours plot of SCMC phase volume fraction in the air-SCMC mixture at the different points of 50% opening globe valve, Concentration of SCMC solution (kg/m^3): 0.8, Liquid velocity (m/s): 1.5142, Gas velocity (m/s): 1.7265, Gas fraction, α_g : 0.5
- 6.61 Contours plot of air phase volume fraction in the air-SCMC mixture at the different points of 50% opening globe valve, Concentration of SCMC solution (kg/m^3): 0.8, Liquid velocity (m/s): 1.5142, Gas velocity (m/s): 1.7265, Gas fraction, α_g : 0.5
- 6.62 Comparison of experimental and CFD simulated result at different liquid flow rate and fixed liquid concentration, fixed opening of the Globe valve
- 6.63 Comparison of experimental results with CFD simulated results for different liquid flow rates
- 6.64 Comparison of experimental results with CFD simulated results for different % opening of globe valve
- 7.1 Schematic diagram of helical coil
- 7.2 Schematic geometry of the coil, pitch = 0
- 7.3 Co-ordinate of the coiled tube

-
- 7.4 Tetrahedral grid for coil
Coil dimension D_t : 0.00933 m, D_t/D_c : 0.0529, D_c : 0.2662 m,
Total length: 5.01 m, Turn: 6
- 7.5 Hexahedral grid for coil
Coil dimension D_t : 0.00933 m, D_t/D_c : 0.0529, D_c : 0.2662 m,
Total length: 5.01 m, Turn: 6
- 7.6 Contour plot of static pressure at (a) hexahedral (b) tetrahedral
grid, Coil dimension, D_t : 0.00933 m, D_t/D_c : 0.0529, D_c : 0.2662
m, Total length: 5.01 m, Turn: 6, Liquid velocity (m/s): 1.7086
and concentration of SCMC solution (kg/m^3): 0.8
- 7.7 Contour plot of total pressure at hexahedral grid, Coil dimension,
 D_t : 0.00933 m, D_t/D_c : 0.0529, D_c : 0.2662 m, Total length: 5.01
m, Turn: 6, Liquid velocity (m/s): 1.7086 and concentration of
SCMC solution (kg/m^3): 0.8
- 7.8 Contour plot of static pressure at various planes along the length
of the at hexahedral grid, Coil dimension, D_t : 0.00933 m, D_t/D_c :
0.0529, D_c : 0.2662 m, Total length: 5.01 m, Turn: 6, Liquid
velocity (m/s): 1.7086 and concentration of SCMC solution
(kg/m^3): 0.8
- 7.9 Contour plot of total pressure at various planes along the length
of the coil at hexahedral grid, Coil dimension, D_t : 0.00933 m,
 D_t/D_c : 0.0529, D_c : 0.2662 m, Total length: 5.01 m, Turn: 6,
Liquid velocity (m/s): 1.7086 and concentration of SCMC
solution (kg/m^3): 0.8
- 7.10 Contour plot of static pressure at the different angular plane and
at different turn of the coil, D_t : 0.00933 m, D_t/D_c : 0.0529, D_c :
0.2662 m, Total length: 5.01 m, Turn: 6, Liquid velocity (m/s):
1.7086 and concentration of SCMC solution (kg/m^3): 0.8
- 7.11 Contour plot of total pressure at the different angular plane and at
different turn of the coil at hexahedral grid of dimension, D_t :
0.00933 m, D_t/D_c : 0.0529, D_c : 0.2662 m, Total length: 5.01 m,
Turn: 6, Liquid velocity (m/s): 1.7086 and concentration of
SCMC solution (kg/m^3): 0.8
- 7.12 Contour plot of static pressure at the different angular plane and
at the fixed turn1 of the coil, Coil dimension, D_t : 0.00933 m,
 D_t/D_c : 0.0529, D_c : 0.2662 m, Total length: 5.01 m, Turn: 6,

-
- Liquid velocity (m/s): 1.7086 and concentration of SCMC solution (kg/m^3): 0.8
- 7.13 Contour plot of total pressure at the different angular plane and at the fixed turn1 of the coil, Coil dimension, D_t : 0.00933 m, D_t/D_c : 0.0529, D_c : 0.2662 m, Total length: 5.01 m, Turn: 6, Liquid velocity (m/s): 1.7086 and concentration of SCMC solution (kg/m^3): 0.8
- 7.14 Contour plot of dynamic pressure at Hexahedral grid for helical coil, Coil dimension, D_t : 0.00933 m, D_t/D_c : 0.0529, D_c : 0.2662 m, Total length: 5.01 m, Turn: 6, Liquid velocity (m/s): 1.7086 and concentration of SCMC solution (kg/m^3): 0.8
- 7.15 Contour plot of dynamic pressure at various planes along the length coil for hexahedral grid, Coil dimension, D_t : 0.00933 m, D_t/D_c : 0.0529, D_c : 0.2662 m, Total length: 5.01 m, Turn: 6, Liquid velocity (m/s): 1.7086 and concentration of SCMC solution (kg/m^3): 0.8
- 7.16 Contour plot of dynamic pressure at the different angular plane and at different turn or length of the coil at hexahedral grid, Coil dimension, D_t : 0.00933 m, D_t/D_c : 0.0529, D_c : 0.2662 m, Total length: 5.01 m, Turn: 6, Liquid velocity (m/s): 1.7086 and concentration of SCMC solution (kg/m^3): 0.8
- 7.17 Contour plot of dynamic pressure at the different angular plane and at different turn or length of the coil at hexahedral grid, Coil dimension, D_t : 0.00933 m, D_t/D_c : 0.0529, D_c : 0.2662 m, Total length: 5.01 m, Turn: 6, Liquid velocity (m/s): 1.7086 and concentration of SCMC solution (kg/m^3): 0.8
- 7.18 Contour plot of dynamic pressure at the different angular plane and at the fixed turn1 of the coil at hexahedral grid, Coil dimension, D_t : 0.00933 m, D_t/D_c : 0.0529, D_c : 0.2662 m, Total length: 5.01 m, Turn: 6, Liquid velocity (m/s): 1.7086 and concentration of SCMC (kg/m^3): 0.8
- 7.19 Contour plot of dynamic pressure at the different angular plane and at the fixed turn1 of the coil at hexahedral grid, Coil dimension, D_t : 0.00933 m, D_t/D_c : 0.0529, D_c : 0.2662 m, Total length: 5.01 m, Turn: 6, Liquid velocity (m/s): 1.7086 and concentration of SCMC solution (kg/m^3): 0.8
- 7.20 Contour plot of velocity magnitude for helical coil at hexahedral

-
- grid, Coil dimension, D_t : 0.00933 m, D_t/D_c : 0.0529, D_c : 0.2662 m, Total length: 5.01 m, Turn: 6, Liquid velocity (m/s): 1.7086 and concentration of SCMC solution (kg/m^3): 0.8
- 7.21 Contour plot of velocity magnitude at various planes along the length coil at hexahedral grid, Coil dimension, D_t : 0.00933 m, D_t/D_c : 0.0529, D_c : 0.2662 m, Total length: 5.01 m, Turn: 6, Liquid velocity (m/s): 1.7086 and concentration of SCMC solution (kg/m^3): 0.8
- 7.22 Contour plot of velocity magnitude at various planes along the length coil at hexahedral grid, Coil dimension, D_t : 0.00933 m, D_t/D_c : 0.0529, D_c : 0.2662 m, Total length: 5.01 m, Turn: 6, Liquid velocity (m/s): 1.7086 and concentration of SCMC solution (kg/m^3): 0.8
- 7.23 Contour plot of velocity magnitude at various planes along the length coil at hexahedral grid, Coil dimension, D_t : 0.00933 m, D_t/D_c : 0.0529, D_c : 0.2662 m, Total length: 5.01 m, Turn: 6, Liquid velocity (m/s): 1.7086 and concentration of SCMC solution (kg/m^3): 0.8
- 7.24 Contour plot of velocity magnitude at the different angular plane and at different turn or length of the coil at hexahedral grid, Coil dimension, D_t : 0.00933 m, D_t/D_c : 0.0529, D_c : 0.2662 m, Total length: 5.01 m, Turn: 6, Liquid velocity (m/s): 1.7086 and concentration of SCMC solution (kg/m^3): 0.8
- 7.25 Contour plot of velocity magnitude at the different angular plane and at the fixed turn1 of the coil at hexahedral grid, Coil dimension, D_t : 0.00933 m, D_t/D_c : 0.0529, D_c : 0.2662 m, Total length: 5.01 m, Turn: 6, Liquid velocity (m/s): 1.7086 and SCMC concentration (kg/m^3): 0.8
- 7.26 Contour of velocity magnitude at the different angular plane and at the fixed turn1 of the coil at hexahedral grid, Coil dimension, D_t : 0.00933 m, D_t/D_c : 0.0529, D_c : 0.2662 m, Total length: 5.01 m, Turn: 6, Liquid velocity (m/s): 1.7086 and concentration of SCMC solution (kg/m^3): 0.8
- 7.27 Contour plot of velocity for helical coil at hexahedral grid, Coil dimension, D_t : 0.00933 m, D_t/D_c : 0.0529, D_c : 0.2662 m, Total length: 5.01 m, Turn: 6, Liquid velocity (m/s): 1.7086 and concentration of SCMC solution (kg/m^3): 0.8

-
- 7.28 Contour plot of velocity at various planes along the length coil for helical coil at hexahedral grid, Coil dimension, D_t : 0.00933 m, D_t/D_c : 0.0529, D_c : 0.2662 m, Total length: 5.01 m, Turn: 6, Liquid velocity (m/s): 1.7086 and concentration of SCMC solution (kg/m^3): 0.8
- 7.29 Contour plot of velocity at the different angular plane and at different turn or length of the coil at hexahedral grid, Coil dimension, D_t : 0.00933 m, D_t/D_c : 0.0529, D_c : 0.2662 m, Total length: 5.01 m, Turn: 6, Liquid velocity (m/s): 1.7086 and SCMC concentration (kg/m^3): 0.8
- 7.30 Contour plot of velocity at the different angular plane and at different turn or length of the coil at hexahedral grid, Coil dimension, D_t : 0.00933 m, D_t/D_c : 0.0529, D_c : 0.2662 m, Total length: 5.01 m, Turn: 6, Liquid velocity (m/s): 1.7086 and concentration of SCMC solution (kg/m^3): 0.8
- 7.31 Contour plot of velocity at the different angular plane and at the fixed turn1 of the coil at hexahedral grid, Coil dimension, D_t : 0.00933 m, D_t/D_c : 0.0529, D_c : 0.2662 m, Total length: 5.01 m, Turn: 6, Liquid velocity (m/s): 1.7086 and concentration of SCMC solution (kg/m^3): 0.8
- 7.32 Contour plot of velocity at the different angular plane and at the fixed turn1 of the coil at hexahedral grid, Coil dimension, D_t : 0.00933 m, D_t/D_c : 0.0529, D_c : 0.2662 m, Total length: 5.01 m, Turn: 6, Liquid velocity (m/s): 1.7086 and concentration of SCMC solution (kg/m^3): 0.8
- 7.33 Contour plot of velocity vector for helical coil at (a) hexahedral grid (b) tetrahedral grid, Coil dimension, D_t : 0.00933 m, D_t/D_c : 0.0529, D_c : 0.2662 m, Total length: 5.01 m, Turn: 6, Liquid velocity (m/s): 1.7086 and concentration of SCMC solution (kg/m^3): 0.8
- 7.34 Contour plot of velocity vector at the different angular plane of the coil at hexahedral grid, Coil dimension, D_t : 0.00933 m, D_t/D_c : 0.0529, D_c : 0.2662 m, Total length: 5.01 m, Turn: 6, Liquid velocity (m/s): 1.7086 and concentration of SCMC solution (kg/m^3): 0.8

-
- 7.35 Contour plot of velocity vector at the different angular plane and at different turn or length of the coil at hexahedral grid, Coil dimension, D_t : 0.00933 m, D_t/D_c : 0.0529, D_c : 0.2662 m, Total length: 5.01 m, Turn: 6, Liquid velocity (m/s): 1.7086 and concentration of SCMC solution (kg/m^3): 0.8
- 7.36 Contour plot of velocity vector at the different angular plane and at the fixed turn of the coil at hexahedral grid, Coil dimension, D_t : 0.00933 m, D_t/D_c : 0.0529, D_c : 0.2662 m, Total length: 5.01 m, Turn: 6, Liquid velocity (m/s): 1.7086 and concentration of SCMC solution (kg/m^3): 0.8
- 7.37 Contour plot of helicity for helical coil at hexahedral grid, Coil dimension, D_t : 0.00933 m, D_t/D_c : 0.0529, D_c : 0.2662 m, Total length: 5.01 m, Turn: 6, Liquid velocity (m/s): 1.7086 and concentration of SCMC solution (kg/m^3): 0.8
- 7.38 Contour plot of vorticity for helical coil at hexahedral grid, Coil dimension, D_t : 0.00933 m, D_t/D_c : 0.0529, D_c : 0.2662 m, Total length: 5.01 m, Turn: 6, Liquid velocity (m/s): 1.7086 and concentration of SCMC solution (kg/m^3): 0.8
- 7.39 Contour plot of cell Reynolds number for helical coil at hexahedral grid, Coil dimension, D_t : 0.00933 m, D_t/D_c : 0.0529, D_c : 0.2662 m, Total length: 5.01 m, Turn: 6, Liquid velocity (m/s): 1.7086 and concentration of SCMC solution (kg/m^3): 0.8
- 7.40 Contour plot of strain rate at hexahedral grid, Coil dimension, D_t : 0.00933 m, D_t/D_c : 0.0529, D_c : 0.2662 m, Total length: 5.01 m, Turn: 6, Liquid velocity (m/s): 1.7086 and concentration of SCMC (kg/m^3) solution : 0.8
- 7.41 Contour plot of strain rate at the different angular plane along the length of the coil at hexahedral grid, Coil dimension, D_t : 0.00933 m, D_t/D_c : 0.0529, D_c : 0.2662 m, Total length: 5.01 m, Turn: 6, Liquid velocity (m/s): 1.7086 and concentration of SCMC solution (kg/m^3): 0.8
- 7.42 Contour plot of shear stress for helical coil at hexahedral grid, Coil dimension, D_t : 0.00933 m, D_t/D_c : 0.0529, D_c : 0.2662 m, Total length: 5.01 m, Turn: 6, Liquid velocity (m/s): 1.7086 and concentration of SCMC solution (kg/m^3): 0.8
- 7.43 Contour plot of shear stress at the different angular plane along

- the length of the coil at hexahedral grid, Coil dimension, D_t : 0.00933 m, D_t/D_c : 0.0529, D_c : 0.2662 m, Total length: 5.01 m, Turn: 6, Liquid velocity (m/s): 1.7086 and concentration of SCMC solution (kg/m^3): 0.8
- 7.44 Comparison plot of helical coil at different SCMC concentration
- 7.45 Comparison plot of helical coil at different coil diameter
- 7.46 Comparison of present prediction with the experimental data (a) dimensionless shear stress (b) pressure drop
- 7.47 Development of axial velocity profile at different cross-sectional planes in curved tube at curvature ratio = 28, coil turn = 2, $V_L = 1.7086$ m/s, SCMC conc. (kg/m^3) = 0.8 in (a) horizontal centerline and (b) vertical centerline
- 7.48 Effect of liquid velocity on development of axial velocity profile in curved tube at curvature ratio = 28, coil turn = 2
- 7.49 Effect of coil turn or coil length, H on the development of axial velocity profile in (a) horizontal centerline (b) vertical centerline
- 7.50 Effect of curvature ratio on the development of axial velocity profile in (a) horizontal centerline (b) vertical centerline, $V_L = 1.7086$ m/s, SCMC conc. (kg/m^3) = 0.8
- 7.51 Comparison plot of the experimental and calculated data for friction factor across the coil for different liquid (SCMC) concentration
- 8.1 Schematic diagram of helical coil
- 8.2 Contour plot of static pressure mixture at (a) hexahedral and (b) tetrahedral grid, Coil dimension, D_t : 0.00933 m, D_t/D_c : 0.0431, D_c : 0.2162 m, Total length: 6.10 m, Turn: 9, Concentration of SCMC solution: 0.8 kg/m^3 , Liquid velocity: 1.9531 m/s, Gas velocity: 0.7218 m/s, Gas Fraction, α_g : 0.231
- 8.3 Contour plot of static pressure at (a) hexahedral and (b) tetrahedral grid, Coil dimension, D_t : 0.00933 m, D_t/D_c : 0.0350, D_c : 0.2662 m, Total length: 5.01 m, Turn: 6, Concentration of SCMC solution: 0.8 kg/m^3 , Liquid velocity: 1.7086 m/s, Gas

velocity: 0.9282 m/s, Gas fraction, α_g : 0.3750

- 8.4 Contour plot of static pressure mixture at various planes along the length of the coil at hexahedral grid, Coil dimension, D_t : 0.00933 m, D_t/D_c : 0.0431, D_c : 0.2162 m, Total length: 6.10 m, Turn: 9, Concentration of SCMC solution: 0.8 kg/m³, Liquid velocity: 1.9531 m/s, Gas velocity: 0.7218 m/s, Gas Fraction: 0.231
- 8.5 Contour plot of static pressure, mixture at hexahedral boundary layer grid varying with coil turn or coil length and angle of coil, Coil dimension, D_t : 0.00933 m, D_t/D_c : 0.0431, D_c : 0.2162 m, Total length: 6.10 m, Turn: 9, Concentration of SCMC solution (kg/m³): 0.8, Liquid Velocity, V_L (m/s):1.9531, Gas velocity, V_g (m/s) :0.7218, Gas Fraction, α_g :0.2310
- 8.6 Contour plot of static pressure (mixture) varying with angle at the first turn of the coil, Coil of dimension, D_t : 0.00933 m, D_t/D_c : 0.0431, D_c : 0.2162 m, Total length: 6.10 m, Turn: 9, Concentration of SCMC solution (kg/m³): 0.8, Liquid velocity, V_L (m/s): 1.9531, Gas velocity, V_g (m/s) :0.7218, Gas Fraction, α_g :0.2310
- 8.7 Contour plot of static pressure at the selected plane along the length of the coil varying angle and turn of the coil , from 1-9, coil of dimension, D_t : 0.00933 m, D_t/D_c : 0.0431, D_c : 0.2162 m, Total length: 6.10 m, Turn: 9, Concentration of SCMC solution (kg/m³): 0.8, Liquid velocity, V_L (m/s): 1.9531, Gas velocity, V_g (m/s):0.7218, Gas Fraction, α_g :0.2310
- 8.8 Contour plot of static pressure varying with angle and number of turn of the coil, Coil dimension, Tube diameter (m): 0.00933, D_t/D_c : 0.0431, D_c : 0.2162 m, Total length: 6.10 m, Turn: 9, Concentration of SCMC solution (kg/m³): 0.8, Liquid velocity (m/s): 1.037, Gas velocity (m/s): 1.9531, Gas fraction, α_g : 0.2310 Turn: 9
- 8.9 Contour plot of static pressure at different angle and fixed turn of the coil, from 1-8 at the selected plane along the length of the coil, Coil dimension, Tube diameter (m): 0.00933, D_t/D_c : 0.0431, D_c : 0.2162 m, Total length: 6.10 m, Turn: 9, Concentration of SCMC solution (kg/m³): 0.8, Liquid flow rate (m³/s): 13.34x10⁻⁵, Gas flow rate (m³/s): 4.93x10⁻⁵, Gas fraction, α_g : 0.2310

-
- 8.10 Contours plot of total pressure varying with angle and coil height
Coil dimension, D_t : 0.00933 m, D_t/D_c : 0.0350, D_c : 0.2662 m,
Total length: 5.01 m, Turn: 6, Concentration of SCMC solution:
 0.8 kg/m^3 , Liquid velocity: 1.7086 m/s, Gas velocity: 0.9282 m/s,
Gas fraction, α_g : 0.3750
- 8.11 Contours plot of total pressure (mixture) at the first turn of the
coil varying with angle grid at the selected plane along the of the
helical coil, Coil dimension, D_t : 0.00933 m, D_t/D_c : 0.0350, D_c :
0.2662 m, Total length: 5.01 m, Turn: 6, Concentration of SCMC
solution: 0.8 kg/m^3 , Liquid velocity: 1.7086 m/s, Gas velocity:
0.9282 m/s, Gas fraction, α_g : 0.3750
- 8.12 (a) Contours plot of velocity magnitude for mixture and (b)
Contours plot of velocity magnitude at various planes along the
length of the coil at hexahedral grid, Coil dimension, D_t : 0.00933
m, D_t/D_c : 0.0431, D_c : 0.2162 m, Total length: 6.10 m, Turn: 9,
Concentration of SCMC solution : 0.8 kg/m^3 , Liquid velocity:
1.9531 m/s, Gas velocity: 0.7218 m/s, Gas fraction, α_g : 0.231
- 8.13 Contour plot of velocity at the selected plane along the length of
the coil varying with angle and turn of the coil from 1-9 , Coil
dimension: D_t : 0.00933 m, D_t/D_c : 0.0431, D_c : 0.2162 m, Total
length: 6.10 m, Turn: 9, Concentration of SCMC solution:
 0.8 kg/m^3 , Liquid velocity: 1.9531 m/s, Gas velocity: 0.7218 m/s,
Gas fraction, α_g : 0.231
- 8.14 Contour plot of velocity magnitude at the different angular plane
and at any fixed turn of the coil, Coil dimension, D_t : 0.00933 m,
 D_t/D_c : 0.0350, D_c : 0.2662 m, Total length: 5.01 m, Turn: 6,
Concentration of SCMC solution: 0.8 kg/m^3 , Liquid velocity:
1.7086 m/s, Gas velocity: 0.9282 m/s, Gas fraction, α_g : 0.3750
- 8.15 (a) Contour plot of velocity magnitude for air phase at various
planes along the length of the coil (b) Contours plot of velocity
magnitude for air phase varying with angle and coil height, Coil
dimension, D_t : 0.00933 m, D_t/D_c : 0.0350, D_c : 0.2662 m, Total
length: 5.01 m, Turn: 6, Concentration of SCMC solution: 0.8
 kg/m^3 , Liquid velocity: 1.7086 m/s, Gas velocity: 0.9282 m/s,
Gas fraction, α_g : 0.3750

-
- 8.16 Contours plot of velocity magnitude for air phase at the first turn of the coil varying with angle for hexahedral grid at the selected plane along the length of the coil, Coil dimension, D_t : 0.00933 m, D_t/D_c : 0.0350, D_c : 0.2662 m, Total length: 5.01 m, Turn: 6, Concentration of SCMC solution: 0.8 kg/m^3 , Liquid velocity: 1.7086 m/s, Gas velocity: 0.9282 m/s, Gas fraction, α_g : 0.3750
- 8.17 (a) Contour plot of velocity magnitude for liquid phase at various planes along the length of the coil
(b) Contours plot of velocity magnitude for liquid phase varying with angle and coil height at hexahedral grid, Coil dimension, D_t : 0.00933 m, D_t/D_c : 0.0350, D_c : 0.2662 m, Total length: 5.01 m, Turn: 6, Concentration of SCMC solution: 0.8 kg/m^3 , Liquid velocity: 1.7086 m/s, Gas velocity: 0.9282 m/s, Gas fraction, α_g : 0.3750
- 8.18 Contours plot of velocity magnitude for liquid phase at the first turn of the coil varying with angle for hexahedral grid at the selected plane along the length of the coil, Coil dimension, D_t : 0.00933 m, D_t/D_c : 0.0350, D_c : 0.2662 m, Total length: 5.01 m, Turn: 6, Concentration of SCMC solution: 0.8 kg/m^3 , Liquid velocity: 1.7086 m/s, Gas velocity: 0.9282 m/s, Gas fraction, α_g : 0.3750
- 8.19 Contour plot of velocity vector at (a) hexahedral and (b) tetrahedral grid, Coil dimension, D_t : 0.00933 m, D_t/D_c : 0.0431, D_c : 0.2162 m, Total length: 6.10 m, Turn: 9, Concentration of SCMC solution: 0.8 kg/m^3 , Liquid velocity: 1.9531 m/s, Gas velocity: 0.7218 m/s, Gas fraction, α_g : 0.231
- 8.20 Contour plot of velocity vector varying with angle and coil turn or height at hexahedral grid, Coil dimension, D_t : 0.00933 m, D_t/D_c : 0.0350, D_c : 0.2662 m, Total length: 5.01 m, Turn: 6, Concentration of SCMC solution: 0.8 kg/m^3 , Liquid velocity: 1.7086 m/s, Gas velocity: 0.9282 m/s, Gas fraction, α_g : 0.3750
- 8.21 Contours plot of velocity vector at the first turn of the coil varying with angle for hexahedral grid at the selected plane of the coil, Coil dimension, D_t : 0.00933 m, D_t/D_c : 0.0350, D_c : 0.2662 m, Total length: 5.01m, Turn: 6, Concentration of SCMC solution: 0.8 kg/m^3 , Liquid velocity: 1.7086 m/s, Gas velocity: 0.9282 m/s, Gas fraction, α_g : 0.3750

-
- 8.22 Contour plot of velocity vector for liquid phase at hexahedral grid, Coil dimension, D_t : 0.00933m, D_t/D_c : 0.0529, D_c : 0.2662 m, Total length: 5.01 m, Turn: 6, Concentration of SCMC solution: 0.8 kg/m^3 , Liquid velocity: 1.7086 m/s, Gas velocity: 0.9282 m/s, Gas fraction, α_g : 0.3750
- 8.23 Contour plot of velocity vector for liquid phase varying with angle and coil height at hexahedral grid, Coil dimension, D_t : 0.00933 m, D_t/D_c : 0.0350, D_c : 0.2662 m, Total length: 5.01 m, Turn: 6, Concentration of SCMC solution: 0.8 kg/m^3 , Liquid velocity: 1.7086 m/s, Gas velocity: 0.9282 m/s, Gas fraction, α_g : 0.3750
- 8.24 Contour plot of velocity vector for liquid phase varying with angle and coil turn1 at hexahedral grid at the selected plane of the coil, Coil dimension, D_t : 0.00933 m, D_t/D_c : 0.0350, D_c : 0.2662 m, Total length: 5.01 m, Turn: 6, Concentration of SCMC solution: 0.8 kg/m^3 , Liquid velocity: 1.7086 m/s, Gas velocity: 0.9282 m/s, Gas fraction, α_g : 0.3750
- 8.25 (a) Contour plot of velocity vector for air phase and (b) Velocity vector plot for air phase at various plane along the length of the coil at hexahedral grid, Coil dimension, D_t : 0.00933 m, D_t/D_c : 0.0529, D_c : 0.2662 m, Total length: 5.01 m, Turn: 6, Concentration of SCMC solution : 0.8 kg/m^3 , Liquid velocity: 1.7086 m/s, Gas velocity: 0.9282 m/s, Gas fraction, α_g : 0.3750
- 8.26 Contour plot of velocity vector for air phase varying with angle and coil height at hexahedral grid, Coil dimension, D_t : 0.00933 m, D_t/D_c : 0.0350, D_c : 0.2662 m, Total length: 5.01 m, Turn: 6, Concentration of SCMC solution: 0.8 kg/m^3 , Liquid velocity: 1.7086 m/s, Gas velocity: 0.9282 m/s, Gas fraction, α_g : 0.3750
- 8.27 Contours plot of velocity vector for air phase at the first turn of the coil varying with angle at hexahedral grid at the selected plane along the length of the coil, Coil dimension, D_t : 0.00933 m, D_t/D_c : 0.0350, D_c : 0.2662 m, Total length: 5.01 m, Turn: 6, Concentration of SCMC solution: 0.8 kg/m^3 , Liquid velocity: 1.7086 m/s, Gas velocity: 0.9282 m/s, Gas fraction, α_g : 0.3750
- 8.28 Contour plot of volume fraction at the selected plane for air-

-
- SCMC phase varying with angle and coil turn at hexahedral boundary layer grid, Coil dimension, D_t : 0.00933 m, D_t/D_c : 0.0431, D_c : 0.2162 m, Total length: 6.10 m, Turn: 9, Concentration of SCMC solution (kg/m^3): 0.8, Liquid velocity, V_L (m/s): 1.9531, Gas velocity, V_g (m/s): 0.7218, Gas Fraction, α_g : 0.2310
- 8.29 (a) Contours plot of volume fraction for liquid phase and (b) Contour plot of volume fraction for liquid phase at various planes along the length of the coil at hexahedral grid at the selected plane along the length of the coil, Coil dimension, D_t : 0.00933 m, D_t/D_c : 0.0350, D_c : 0.2662 m, Total length: 5.01 m, Turn: 6, Concentration of SCMC solution: 0.8 kg/m^3 , Liquid velocity: 1.7086 m/s, Gas velocity: 0.9282 m/s, Gas fraction, α_g : 0.3750
- 8.30 Contours plot of volume fraction for liquid phase at the first turn of the coil varying with angle at hexahedral grid at the selected plane along the length of the coil, Coil dimension, D_t : 0.00933 m, D_t/D_c : 0.0350, D_c : 0.2662 m, Total length: 5.01 m, Turn: 6, Concentration of SCMC solution: 0.8 kg/m^3 , Liquid velocity: 1.7086 m/s, Gas velocity: 0.9282 m/s, Gas fraction, α_g : 0.3750
- 8.31 Contours plot of volume fraction for liquid phase varying with angle and coil height at hexahedral grid, Coil dimension, D_t : 0.00933 m, D_t/D_c : 0.0350, D_c : 0.2662 m, Total length: 5.01 m, Turn: 6, Concentration of SCMC solution: 0.8 kg/m^3 , Liquid velocity: 1.7086 m/s, Gas velocity: 0.9282 m/s, Gas fraction, α_g : 0.3750,
- 8.32 (a) Contour plot of volume fraction for air phase (b) Contours of volume fraction for air phase at various planes along the length of the coil at hexahedral grid, Coil dimension, D_t : 0.00933 m, D_t/D_c : 0.0431, D_c : 0.2162 m, Total length: 6.10 m, Turn: 9, Concentration of SCMC solution: 0.8 kg/m^3 , Liquid velocity: 1.9531 m/s, Gas velocity: 0.7218 m/s, Gas fraction, α_g : 0.231
- 8.33 Contour plot of volume fraction for air phase at the first turn of the coil varying with angle at hexahedral grid at the selected plane along the length of the helical coil, Coil dimension, D_t : 0.00933 m, D_t/D_c : 0.0529, D_c : 0.2662 m, Total length: 5.01 m, Turn: 6, Concentration of SCMC solution: 0.8 kg/m^3 , Liquid velocity: 1.7086 m/s, Gas velocity: 0.9282 m/s, Gas fraction, α_g :

0.3520

- 8.34 Contours plot of volume fraction for air phase varying with angle and coil height grid, Coil dimension, D_t : 0.00933 m, D_t/D_c : 0.0350, D_c : 0.2662 m, Total length: 5.01 m, Turn: 6, Concentration of SCMC solution: 0.8 kg/m³, Liquid velocity: 1.7086 m/s, Gas velocity: 0.9282 m/s, Gas fraction, α_g : 0.3750
- 8.35 Path lines of particle ID mixture
- 8.36 Comparison plot for helical coil
- 8.37 Comparison plot for helical coil at different SCMC concentration
- 8.38 Comparison plot of experimental data and CFD analysis for helical coil for two-phase frictional pressure drop per unit length of the coil with gas flow rate at constant liquid flow rate and constant SCMC solution for different coil diameter
- 8.39 Comparison of present prediction with the experimental data: (a) pressure drop (b) void fraction
- 8.40 Effect of gas and liquid velocity on liquid volume fraction in curved tube at curvature ratio = 18, coil turn = 2
- 8.41 Effect of gas and liquid velocity on development of axial velocity profile in curved tube at curvature ratio 18, coil turn = 2, $V_L=1.9531$ m/s, in horizontal centerline
- 8.42 Effect of coil turns or coil length on the development of axial velocity profile in (a) horizontal centerline and (b) vertical centerline
- 8.43 Effect of angle on the development of axial velocity profile in (a) horizontal centerline and (b) vertical centerline
- 8.44 Effect of curvature ratio on the development of axial velocity profile in (a) horizontal centerline and (b) vertical centerline, at $V_G=0.8433$ m/s, $V_L=1.9531$ m/s

SYNOPSIS

The hydrodynamics of single and two-phase gas-liquid flow have received extensive treatment during few decades because of their widespread application in industry. It occurs in boiler tubes, distillation columns, oil and gas wells, transportation system of crudes and refined products, all key pieces of equipment in refineries, petrochemical industries, polymer processing, nuclear engineering and large number of chemical reactor applications. With the development in polymer processing, mineral recovery, food processing, biomedical engineering, biochemical engineering, gas-liquid-solid reactions, hydraulic transportation the liquids most often be non-Newtonian in nature. Hence, there is a need to study the flow of non-Newtonian and gas-non-Newtonian liquid flow through piping components and helical coils.

The computational fluid dynamics (CFD) is a powerful tool to evaluate the frictional losses and estimate the other flow characteristics can be visualized to aid in better understanding of the flow phenomenon and it can be applied to improve flow characteristics and equipment design. However, the simulation models are generally empirical in nature and caution must be exercised in their application to practical cases which may involve detailed investigation of all the involved assumptions and limitations. Such modeling would always require fine tuning by comparison with reliable experimental data.

Thus in view of the importance of the single-phase and two-phase gas-liquid flow through piping components and helical coils, and the CFD simulation using a commercial software Fluent 6.3, a research programme has been undertaken in investigate the following aspects,

-
1. Experimental studies and CFD analysis for water and air–water flow through U – bends,
 2. Experimental studies and CFD simulation on the non-Newtonian fluid flow through piping components,
 3. CFD analysis on the gas-non-Newtonian liquid flow through piping components,
 4. Experimental studies and CFD analysis on the non-Newtonian liquid flow through helical coils,
 5. CFD simulation on the Gas- non–Newtonian liquid flow through helical coils.

The thesis has been presented in the eight chapters :

Chapter – 1 : It presents an overview and importance of the existing information in the flow of liquid and gas-liquid flow through piping components and helical coils. The importance of the computational Fluid Dynamics (CFD) is also highlighted.

Chapter – 2 : It describes the CFD methodology used for the simulation.

Chapter – 3 : It consists of the experimental studies on the pressure loss for water and air-water flow through four different U-bends of different radius of curvatures. The range of flow rate used for air and water in the experiments are $5.936 \times 10^{-5} - 56.1189 \times 10^{-5} \text{ m}^3/\text{s}$ and $2.000 \times 10^{-4} - 4.6500 \times 10^{-4} \text{ m}^3/\text{s}$ respectively. The CFD simulations are carried out using κ - ϵ model and standard mixture κ - ϵ model for water and air-water flow through U-bends. The simulated result gives the detail flow phenomena inside the U-bends for water and air-water flow. The CFD simulated pressure drop agrees well the experimental data.

Chapter – 4 : It consists of experimental studies on the non-Newtonian liqui flow through piping components. Dilute aqueous solutions of Sodium salt of carboxymethyl

cellulose (SCMC) is used as non-Newtonian liquids. Piping components used for the experiment are elbows of three different angles, orifices, gate valves and globe valves. The flow rates used for the experiment are $3.75 \times 10^{-5} - 29.83 \times 10^{-5} \text{ m}^3/\text{s}$. Empirical correlations have been developed to predict the pressure losses across the piping components.

Chapter – 5 : It consists of the CFD analysis of non-Newtonian liquid flow through piping components. Single phase laminar non-Newtonian power law model is used for the simulation. The CFD analysis gives the insight of the flow phenomena of the piping components. The CFD simulated pressure drop data matches well with the experimental data.

Chapter – 6 : It consists of the CFD analysis on two-phase gas-non-Newtonian liquid flow through piping components. Laminar non-Newtonian power law Eulerian multiphase model have been used for simulation. The simulated results gives the insight flow phenomena, velocity magnitude, velocity vector, static pressure, volume fraction of different phases. The simulated two-phase pressure drop data matches well with our earlier published experimental data.

Chapter - 7 : It consists of the experiment and CFD analysis of non-Newtonian liquid flow through helical coils. Dilute aqueous solution of sodium salt of carboxymethyl cellulose (SCMC) used as non-Newtonian liquids. The range of liquid flow rates used for the experiments is $3.334 \times 10^{-5} - 15.003 \times 10^{-5} \text{ m}^3/\text{s}$. Single phase laminar non-Newtonian power law model is used for the CFD simulation. The CFD simulation gives the insight of velocity and pressure field of the coil. The CFD simulated results matches well with

the experimental results. The experimental and CFD simulated results are compare with the other values obtained from literature.

Chapter – 8 : It consists of the CFD analysis of gas-non-Newtonian liquid flow through helical coils. Laminar non-Newtonian power law Eulerian multiphase model have been used for CFD simulation. The simulation gives the insight flow phenomena of velocity magnitude, velocity vector, static pressure, volume fraction of the different phases. The two-phase CFD simulated pressure drop data matches well with the experimental data obtained earlier in our laboratory. It is also noted that simulated data at hexahedral grid gives the better result than tetrahedral grid.

Chapter 1

Introduction

The hydrodynamics of single-phase and gas-liquid two-phase flows have received extensive treatment during last few decades because of their widespread application in industry. This chapter deals with the importance of the hydrodynamics studies and the computational Fluid Dynamics (CFD). Here the literature review attempted is not breadth or depth of coverage but is focused mainly on the importance of the flow studies.

1.1 Introduction

Pipe fittings such as elbows, bends, valves, orifices are integral part of any piping system. The flow in fittings is considerably more complex than in a straight pipe. The problem of determining the pressure losses in pipe fittings is important in design and analysis of the fluid machinery. Forcing a fluid through pipe fittings consumes energy detected by the drop in pressure across the fittings. The friction between the fluid and the fitting wall causes this pressure drop. The problem of predicting pressure losses in pipe fittings is much more uncertain than for the pipe because,

- i. The mechanism of flow is not clearly defined. At least two types of losses are superposed – skin friction and the loss due to change in flow direction, and
- ii. There are very few experimental data available in the literature.

Two-phase flow through pipe fittings are even much more complex than that of straight pipes and only few experimental data are available in literature (Mandal and Das, 2003). When fluid flows through a curved pipe, it generates secondary flows due to the interaction between centrifugal and viscous forces. The secondary flow fields become more complex due to the combined effects of the coriolis force (due to torsion of the tube centerline) and the centrifugal force (due to the curvature), i.e., simultaneous effect of curvature and torsion on the flow. When two-phase flow enters the curved portion, the

heavier density phase is subjected to a large centrifugal force, which causes the liquid to move away from the centre of curvature, whereas the gas flows towards the center of the curvature. Separation of phases in this way is likely to give rise to significant slip between the phases. This process is a continuous function of the coil geometry. Despite various applications, the literature on two-phase flow through coiled tubes is rather meager (Biswas, 2008).

Fluid flows play the key roles in the working process of many modern engineering devices. Designing of these devices for the required operational parameters is impossible without reliable prediction of characteristics of these flows. As many engineering devices are very expensive and labour intensive in their manufacturing process, so their physical modeling with experimental determination of their working parameters at different possible models, as a rule, requires large temporal and financial expenses. Besides, due to restricted possibilities of modern experimental sensors and measuring instruments, experimental observations do not give complete information about the investigated phenomena. Due to the nature of fluid medium itself, fluid flows often occur in very complex manner, with the presence of transitional effects, stagnation zones, vortex structures, and at supersonic velocities – their possibilities of generation of compression shock waves. The situation is still very complex when heat and mass transfer is present, when considering flow of a mixture of gas-liquid, liquid-liquid, slurry etc., free surface flows, flows with cavitation, boiling, condensation, combustion, chemical reaction etc. are present. All these factors explain the growing interest for the software tools for simulation of fluid flow allowing for the prediction of characteristics of these flows and the working parameters of engineering devices at the stage of designing,

before the manufacturing. The branch of science dealing with simulation of fluid flows with heat and mass transfer in various engineering and natural objects is computational fluid dynamics (CFD).

The computational power of computers grew and at the same time, their prices become reduce and affordable for more and more users, since the 70s of XX century, rapid development of commercial CFD software has started. Till the beginning of 90s the cheap personal computers have become as powerful as those of workstations, and CFD software packages designed for PC have started.

Today dozens of software packages intended for solution of fluid flow problems are available. A complete list is given at the site www.cfd-online.com. Among the CFD software most recognized worldwide are Fluent, CFX, STAR-CD, Numeca etc. Initially computational fluid dynamics was developed for solution of problems of aerospace industry – simulation of processes in combustion chambers of rocket engines, simulation of phesico-chemical processes in the flow around rocket airframe and supersonic aircrafts. Today the field of application of CFD is essentially extended in all fields of engineering where fluid flows occur.

In the field of chemical engineering the design of process equipment involves specifying the configuration of the equipment and its operating protocols, which must be acceptable in safety, environment and economic point of view. A wide variety of process equipment and operating protocols/codes are used in practice. The major driving force of these different designs are energy efficient and more control of the reactants, the process and the easy removal of the products. In chemical or physical transformation process requires the addition or removal of different materials and energy in right place and also

in right time. This can be achieved by controlling basic fluid dynamics. So the understanding of the process and its requirements and identification of the actual or desired fluid dynamic characteristics is essential. The CFD models are expected to help in this direction.

Design engineers use CFD models for two purposes; “design” models, which attempt to provide a quantitative relationship between the hardware and performance, and “learning” models, which provide a basic understanding of different underlying processes (Joshi and Ranade, 2003). With the help of CFD designer could predict what could or would happen as a result of a specific design, thereby steering the design in promising directions. It also help to end up with a new design concepts which often get sidelined due to lack of resources like experimental facilities, time, funding etc. to test them.

The Vision 2020 document for the U. S. chemical industry (<http://www.chemicalvision2020.org/pdfs/compfluid.pdf>) entitled Technology roadmap for CFD identified the following performance targets for CFD,

- i. Shorten the lead times (from research to final plant design) to 3-5 years.
- ii. Reduce plant downtimes to 1%.
- iii. Reduce the separation energy and improve the separation efficiency by 20%.
- iv. Increase the reliability of the design (reduce risk).
- v. Reduce/eliminate design errors.
- vi. Promote innovation.
- vii. Reduce fuel consumption per unit of product.
- viii. Improve heat transfer (waste heat recovery).

- ix. Optimize processes to increase yield and aid incremental expansion.

According to Joshi and Ranade (2003) this document is justified for the fulfillment of the target because of the advancement in numerical methods and computers help to minimize the errors due to numerical inaccuracies.

So basically computational fluid dynamics (CFD) is the science of predicting fluid flow, heat and mass transfer, chemical reactions and related phenomena by solving numerically the set of governing mathematical equations (conservation of mass, momentum, energy). The results of CFD analysis are used for studies of new design, product development, trouble shooting and redesign. CFD analysis complements testing and experiments, reduces the total effort required in the experiment design and data acquisition. Hence, the CFD analysis gives substantial reduction of times and costs of new designs (Ranade, 2002).

A commercial fluent 6.3 solver is used to solve the basic governing mathematical equation numerically based on the finite volume method in the present analysis presented in the thesis. Geometries are created in Gambit 6.3 preprocessor. Geometries are imported into Fluent 6.2/6.3 in a cartesian co-ordinate system. Fluent 6.2/6.3 solved the governing equations in 3-D geometry. The use of CFD yields a very detailed solution containing the local values of relevant variables, such as pressure, velocity, temperature, viscosity, shear stress and so on.

1.2 Objective of the present work

Few experiments are conducted and other experimental data collected from past Ph. D. thesis worked in our laboratory used for the present CFD analysis,

1. Experimental studies and CFD analysis for water and air–water flow through U–bends.
2. Experimental studies and CFD simulation on the non-Newtonian fluid flow through piping components,
3. CFD analysis on the gas-non-Newtonian liquid flow through piping components,
4. Experimental studies and CFD analysis on the non-Newtonian liquid flow through helical coils,
5. CFD simulation on the Gas- non–Newtonian liquid flow through helical coils.

Chapter 2

CFD methodology

This chapter provides information on the working theory behind the simulation package used to model the flow phenomena in the subsequent chapters.

2.1 Theoretical consideration

This chapter deals with the theoretical consideration used for the CFD analysis using commercial software Fluent 6.3.

Fluent solvers are based on the finite volume method. Details have been discussed by Chung (2002), Ferziger and Peric (1997), Fluent 6.2 and 6.3 User's guide.

Domain (fluid region) is discretized into a finite set of control volumes (mesh) or cells.

General transport equation for mass, momentum, energy, etc. is applied to each cell and discretized. For cell p,

$$\frac{\partial}{\partial t} \int_V w dV + \int_A w u \cdot dA = \int_A \Gamma \nabla w \cdot dA + \int_V S_w dV \quad (2.1)$$

Unsteady convection diffusion generation

Table 2.1 represents general property w for general transport equation. Partial differential equations are discretized into a system of algebraic equations (SIMPLE algorithm originally developed by Patanker, 1980). All algebraic equations are then solved numerically to render the solution field. Each transport equation is discretized into algebraic form. Fig. 2.1 represents the discretized cell. For cell p,

$$\frac{(\dots)_p^{n+\Delta t} - (\dots)_p^n}{\Delta t} \Delta V + \sum_{faces} w_j u_j A_j = \sum_{faces} \Gamma_j (\nabla w)_j A_j + S_w \Delta V \quad (2.2)$$

Discretized equations require information at cell centers and faces.

Field data (material properties, velocities, etc.) are stored at cell centers.

Face values are interpolated in terms of local and adjacent cell values.

Discretization accuracy depends upon ‘stencil’ size.

The discretized equation can be expressed simply as:

$$a_p W_p + \sum_{nb} a_{nb} W_{nb} = b_p \quad (2.3)$$

Equation is written out for every control volume in domain resulting in equation set.

2.2 Mathematical model

2.2.1 Single phase water flow

Conservation of mass:

$$\nabla \cdot (\dots u) = 0 \quad (2.4)$$

where u is velocity vector.

Conservation of momentum:

$$\nabla \cdot (\dots uu) - \nabla \cdot (\tilde{\tau}_{eff} \nabla u) = -\nabla p + \nabla \cdot (\tilde{\tau}_{eff} (\nabla u^T)) + B \quad (2.5)$$

where B is a body force, p is the pressure, and ^T stands for transpose.

High Reynolds number k- ν turbulence model:

$$\tilde{\tau}_{eff} = \tilde{\tau} + \tilde{\tau}_t \quad \text{and} \quad \tilde{\tau}_t = C_\mu \frac{k^2}{\nu} \quad (2.6)$$

The transport equations for the turbulent kinetic energy (k) and turbulent dissipation (ν) are

$$\nabla \cdot (\dots uk) - \nabla \cdot \left(\left(\tilde{\tau} + \frac{\tilde{\tau}_t}{\Gamma_k} \right) \nabla k \right) = \tilde{\tau}_{eff} \nabla u \cdot (\nabla u + (\nabla u)^T) - \frac{2}{3} \nabla \cdot u (\tilde{\tau}_{eff} \nabla u + \dots k) - \dots \nu \quad (2.7)$$

$$\nabla \cdot (\dots u\nu) - \nabla \cdot \left(\left(\tilde{\tau} + \frac{\tilde{\tau}_t}{\Gamma_\nu} \right) \nabla \nu \right) = C_1 \frac{\nu}{k} (\tilde{\tau}_{eff} \nabla u \cdot (\nabla u + (\nabla u)^T)) - \frac{2}{3} \nabla \cdot u (\tilde{\tau}_{eff} \nabla u + \dots k) - C_2 \dots \nu \quad (2.8)$$

Table 2.1 represents the empirical constants in k- ν turbulence model.

2.2.2 Mathematical Model for Air–water system

Governing equations and numerical methods

Standard k- ν turbulence model is used for single-phase water flow and mixture standard k- ν multiphase model equations are used for two-phase air–water flow through U-bends.

This approach allows for simulation of multi-phase flows when the substances of different phases can intermix and do not form the free surface. In order to simulate the flow of two or several phases, this model uses one continuity equation, one set of momentum equations and one energy equation that are written with regard to mass-averaged velocity and density of the mixture. Thus continuity equation in this model looks as follows,

Solves one equation for Continuity of the mixture,

$$\frac{\partial \rho_m}{\partial t} + \nabla \cdot (\rho_m \mathbf{u}_m) = m \quad (2.9)$$

Solves for the transport of volume fraction of each secondary phase

$$\frac{\partial}{\partial t} (\alpha_k) + \nabla \cdot (\alpha_k \mathbf{u}_m) = -\nabla \cdot (\alpha_k \mathbf{u}'_k) \quad (2.10)$$

This model uses the conception of drift velocities to take account that motion of different phases occurs with different velocities. This allows for simulation.

Solves one equation for the momentum of the mixture

$$\frac{\partial}{\partial t} (\rho_m \mathbf{u}_m) + \nabla \cdot (\rho_m \mathbf{u}_m \mathbf{u}_m) = -\nabla p + \nabla \cdot [\rho_m (\nabla \mathbf{u}_m + \nabla \mathbf{u}'_m)] + \rho_m \mathbf{g} + F + \nabla \cdot \left(\sum_{k=1}^n \alpha_k \rho_k \mathbf{u}'_k \mathbf{u}'_k \right) \quad (2.11)$$

Drift velocity $\mathbf{u}'_k = \mathbf{u}_k - \mathbf{u}_m$

Where mixture properties are defined as

$$\rho_m = \sum_{k=1}^n r_k \rho_k \quad \mu_m = \sum_{k=1}^n r_k \mu_k \quad u_m = \frac{\sum_{k=1}^n r_k u_k}{\rho_m} \quad (2.12)$$

The standard $k - \epsilon$ belong to high-Reynolds number models, which are primarily valid for turbulent core flow while they neglect the effects of viscosity in the near-wall region.

These models necessitate the use of a wall function or a two-phase zonal approach.

2.3 Mathematical Model

2.3.1 Single phase non-Newtonian fluid

Governing equations and numerical methods

Dilute solution of SCMC follows the laminar non-Newtonian pseudo plastic Power law model. In general for non-Newtonian liquids the effective viscosity is used for calculation and defined as,

$$\mu_{eff} = K \left(\frac{8u}{d} \right)^{n'-1} \quad (2.13)$$

The governing equation is the Navier – Stokes equation as,

$$\rho \frac{\partial u}{\partial t} + \rho u \cdot \nabla u = \mu_{eff} \nabla^2 u - \nabla P \quad (2.14)$$

and the continuity equation is

$$\nabla u = 0 \quad (2.15)$$

where,
$$\nabla = i \frac{\partial}{\partial x} + j \frac{\partial}{\partial y} + k \frac{\partial}{\partial z} \quad (2.16)$$

2.3.2 For air-non-Newtonian fluid system

Eulerian multiphase model equations

Volume fraction equation

The volume of phase q is defined as

$$V_q = \int_v r_q dV \quad (2.17)$$

Where r_q is volume fraction of phase q, and

$$\sum_{q=1}^n r_q = 1 \quad (2.18)$$

where n is number of phases.

Eulerian multiphase model equations

Two-phase flow was modeled with the Eulerian-Eulerian approach, where the phases are assumed to be interpenetrating continua. One of the phases defined as continuous and the other as dispersed, the phases sum up to the unity. The pressure and gravity vectors are shared by both phases, whereas other variables are phase specific. The only notable change to the one phase solution is the presence of interfacial forces.

This model is the most general and the most complex among all the models of multi-phase flow. The substance of each phase is assumed to form continuous medium. Its motion is simulated with own system of Navier–Stokes equations, continuity equation and energy equation. According to this model, the equations written for each phase are solved jointly. At high values of r_g , the dispersed particles strongly influence the carrier flow, and only the multi-phase Eulerian model should be used for adequate simulation of such flows.

Continuity

$$\frac{\partial}{\partial t} r_{q \dots q} + \nabla \cdot (r_{q \dots q} u_q) = \sum_{p=1}^n m_{pq} \quad \text{Where } r_q = \text{fraction for the } q\text{-th phase} \quad (2.19)$$

Momentum for q-th phase

$$\frac{\partial}{\partial t}(\rho_q \dots u_q) + \nabla \cdot (\rho_q \dots u_q u_q) = -\rho_q \nabla p + \rho_q \dots g + \nabla \cdot \overline{\tau}_q + \sum_{p=1}^n (R_{pq} + m_{pq} u_q) + \rho_q \dots (F_q + F_{lift,q} + F_{vm,q})$$

Transient convective pressure body shear interphase external, lift, and Forces and mass virtual mass forces Exchange

(2.20)

The inter-phase exchange forces are expressed as

$$R_{pq} = K_{pq} (u_p - u_q) \text{ where } K_{pq} = \text{fluid - fluid exchange coefficient}$$

(2.21)

As the flow of liquid is laminar, non-Newtonian Power Law model is used as viscous model and Eulerian model is used as multiphase model for the CFD analysis.

Where u_p is the velocity of phase p, and K_{pq} is the interphase momentum exchange coefficient which can be written in the following general form:

$$K_{pq} = \frac{\rho_q \rho_q \dots f}{\tau_p}$$

(2.22)

where ρ_p the volume fraction of phase p is, ρ_p is the density of phase p, f is the drag function, and τ_p is the particulate relaxation time which is defined as:

$$\tau_p = \frac{\rho_p d_p^2}{18 \mu_p}$$

(2.23)

where, d_p is the diameter of the bubbles of phase p, and μ_p is the viscosity of phase p.

The drag function, f , can be expressed as (Schiller and Naumann, 1935),

$$f = \frac{C_D \text{Re}}{24}$$

(2.24)

where

$$C_D = \left\{ 24 \left(1 + 0.15 \text{Re}^{0.657} \right) / \text{Re} \right\} \text{Re} \leq 1000$$

$$= \{0.44\} \text{Re} \geq 1000 \quad (2.25)$$

Where C_D the drag coefficient and Re is the relative Reynolds number which can be obtained from:

$$\text{Re} = \frac{\dots_q |u_p - u_q| d_p}{\sim_q} \quad (2.26)$$

And \sim_q is the viscosity of phase q.

2.3.3 Estimation of the mesh cell size adjacent to the wall

The distance from the wall to the centroid of the first mesh cell (Δy) can be estimated by choosing a desired y^+ (ideally, $y^+=1$) with the estimated bulk Reynolds number as (ANSYS Fluent Inc., 2008).

$$\frac{\Delta y}{y^+} = 5.06 d_h \text{Re}_b^{-7/11} \quad (2.27)$$

where y^+ is a dimensionless number, d_h is the hydraulic diameter, and Re_b is the bulk Reynolds number. These equations are solved subject to the following boundary conditions,

- (i) The piping components and coil walls are assumed rigid and a no-slip condition is imposed.
- (ii) At the outlet, the velocities are free but the normal and tangential stresses are constrained to be zero and the gauge pressure is set to zero.
- (iii) At the inlet, a uniform velocity profile is used with a time varying forcing function representative of flow in the left portion of the bend.

A three-dimensional computational grid was generated for each geometry studied using the package GAMBIT 6.3. The geometry was drawn using Gambit. An unstructured tetrahedral and boundary layer hexahedral mesh with nearly 5×10^3 - 20×10^4 were used. Inlet and outlet are located at each end of the system. The inlet is used to specify the inlet velocity and outlet is used to specify pressure outlet. The commercially available CFD code, FLUENT Version 6.3, which is based on the finite-volume method, was used.

Geometries are imported into FLUENT 6.3 in a Cartesian coordinate system. In the simulation, the governing equations are solved for a full 3-D geometry. For flow phenomena associated with single-phase non-Newtonian, water and two-phase air-non-Newtonian, air - water flow, we have chosen laminar non-Newtonian power law model for single-phase non-Newtonian and K-epsilon model for single-phase water flow. For two-phase air-water flow we have chosen k-epsilon mixture model and two-phase air-non-Newtonian flow we have chosen laminar Eulerian model. The model solves for momentum equation and prescribes relative velocities to describe the dispersed phases. Continuity equations for the gas phase coupled with a single continuity equation for the liquid phase. In addition simulations were carried out with constant bubble size of 1mm using mixture $k-v$ and Eulerian model. The governing equations are non linear and several iterations of loop must be performed before a convergent solution is obtained. These equations solved sequentially by Segregated Solver. The standard $k-v$ model is used to solve the air-water flow and Eulerian model to solve air-non-Newtonian flow. The first-order upwind scheme is used in the discretization of set of governing equations.

Since there is significant difference in the velocities of two phases, slip velocity is turned on in mixture parameters.

2.4 Numerical approach

The governing equations for the multiphase flow in piping components and coils will be solved by the Eulerian–Eulerian approach. This approach treats different phases as interpenetrating continua, and solves the momentum and continuity equations for each phase individually. The phase coupling is achieved through the pressure and interphase exchange coefficients.

2.4.1 CFD procedure

A general procedure to simulate gas mixing in piping components and coils based on Gambit 6.3 and Fluent 6.3 software (ANSYS Fluent Inc., 2008) is outlined below,

- i. Perform meshing under Gambit 6.3 - Create a computational domain at the flow region, using tetrahedral and boundary layer hexahedral meshes where possible to generate grids, and controlling a smooth change in the mesh size by size functions. The boundary and continuum types should be specified. Examine the mesh to ensure that the high skewness is below 0.5.
- ii. Import the mesh file to Fluent 6.3 and check the mesh.
- iii. Define a 3-D, unsteady, implicit, and pressure-based solver.
- iv. Activate the Eulerian multiphase model.
 1. Define a standard k- ν model including slip velocity.
 2. Enable the water properties with turbulent flow conditions and non-Newtonian fluid properties with laminar flow conditions using the text command:
define/models/viscous/turbulence

3. Define the phases by setting water (or a non-Newtonian fluid) as the primary phase and gas as the secondary phase, and keeping the default selection of Schiller-Naumann drag model in the phase interaction panel.
4. Define the operating conditions by turning on gravity and specify the operating density.
5. Define the boundary conditions.

Solution control methodology-Under-relaxation factors - 0.3 for pressure, 0.3 for momentum, 0.1-0.9 for volume fraction, and default values for the other parameters. Discretization schemes - standard for pressure, momentum and volume fraction, and first-order upwind for other variables: momentum, turbulent kinetic energy, turbulent dissipation rate. Easiest to converge, only first-order accurate.

6. Pressure-velocity SIMPLE coupling used.
7. Initialize the solution-velocity.
8. Enable the plotting of residuals during the calculation, and keep the default convergence criteria (10^{-5} for energy and 10^{-3} for continuity).
9. Enable a volume monitor for the volume-weighted average velocity of liquid phase.
10. Set the time step size that can be estimated as a ratio of mesh cell size and gas inlet velocity, and run a simulation until achieving a steady-state solution.

2.4.2 Solver

The segregated (implicit) solver is preferred in all other cases, due to lower memory requirements than coupled implicit solver. Segregated approach provides flexibility in solution procedure

2.4.3 Convergence

All discrete conservation equations (momentum, energy, etc.) are obeyed in all cells to a specified tolerance.

Solution no longer changes with more iteration.

Overall mass, momentum, energy, and scalar balances are achieved.

Monitoring convergence with residuals history:

Generally, a decrease in residuals by 3 orders of magnitude indicates at least qualitative convergence.

Major flow features established.

Scaled energy residual must decrease to 10^{-6} for segregated solver.

Scaled species residual may need to decrease 10^{-5} to achieve species balance.

2.5 Conclusion

Basic fundamentals of CFD are discussed in this chapter.

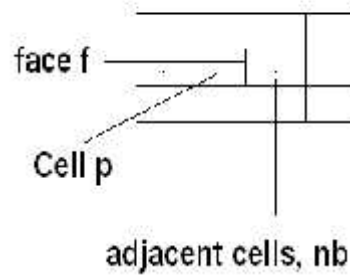


Fig. 2.1 Discretized cell

Table 2.1 General property w for general transport equation

Equation	w
continuity	1
x-momentum	u
y-momentum	v
energy	h

Table 2.2 Empirical constants in K- ϵ turbulence model

C_μ	\dagger_K	\dagger_ν	C_1	C_2
0.09	1.0	1.3	1.44	1.92

Chapter 3

Water and air-water flow through U-bends

Experimental investigation has been carried out in order to study the water and air-water flow through four different U-bends. Numerical modeling is carried using Fluent 6.3 software to find its applicability.

3.1 Introduction

Bends are an integral part of any pipeline transport processes, and the flow patterns developed are more complex than those of straight tubes. Fluid motion in a bend is not parallel to the curved axis of the bend. When fluid flows through a curved pipe, the presence of curvature generates a centrifugal force that acts right angles to the main flow, resulting in secondary flow. The strength of secondary flow depends on the curvature of the surface, i.e., radius of curvature of the bend. Information on flows in curved pipes is highly important for many engineering applications in connection with confined curved flows through bends, headers, cooling ducts and blade passages of turbines. Lack of information, however, exists in spite of a lot of investigations which have been made by many researchers.

Thomson (1876) first observed the curvature effects of bends on flows. Eustice (1910) also observed the existence of secondary flows by injecting ink into water passing through a coiled pipe. Wilson et al. (1922) observed that the pressure drop is dependent on the flow Reynolds number and Dean (1928 a, b) studied the stability of a curved pipe flow and identified the condition for the onset of secondary vortices. Ito (1959) indicated that secondary flows can cause a rapid rise in friction and lead to a much increased pressure drop. Tunstall and Harvey (1968) observed the presence of a main or primary flow recirculation at the inner wall for tight bends ($\theta < 3$). Berger et al. (1983) and Das (1996) have provided a comprehensive review of literature on flows through curved

pipes. The intensity of such secondary flows depends on the combination of the main flow Reynolds number (Re) and the curvature ratio ($\kappa = R_b/R_t$) and can be characterized by the dimensionless number called the Dean Number.

Enayet et al. (1982) measured, in a range of Reynolds numbers, Re , 500 to 4.6×10^6 , longitudinal components of mean and fluctuating velocities for the turbulent water flow in a circular 90° bend using laser Doppler velocimeter. Azzola et al. (1986) reported the computations method using the standard $k-\epsilon$ model and measurements of developed turbulent flow in a 180° bend. Anwer et al. (1989) measured mean velocities and Reynolds stresses in the horizontal and a normal plane in an 180° bend using hot wire anemometer. Bend flows have been extensively studied experimentally by Kim and Simon (1988), Al-Rafai et al. (1990), Cheng and Farokhi (1992), Anwer and So (1993), Sudo et al. (1998) and Sudo et al. (2000).

The Computer simulations provide an efficient approach for studying flows through curved pipes under various conditions. Practical simulations can also be performed by solving the filtered Navier-Stokes equation using a Large-Eddy Simulation (LES) or by solving the Reynolds Average Navier-Stokes (RANS) equation with an appropriate closure model for the Reynolds stress (Pui et al., 1987; Van de Vosse et al., 1989; Jayanti et al., 1990; Brockmann, 1993; Bergstrom et al., 1998; Wang and Shirazi, 2001; Breuer et al., 2006; Berrouk and Laurence, 2008; and Zhang et al., 2009, 2010, etc.).

Two phase flow has got an enormous application in industry starting from reboiler, Nuclear reactor to pipeline transportation, chemical, petrochemical, petroleum refineries, and pharmaceutical industries. The need for reliable design methods has been

the driving force behind a very large effort in two-phase gas-liquid flow over past few decades. When a fluid flows through a bend the presence of curvature generates a centrifugal force across the bend that acts right angle to main flow and results in secondary flow. The strength of the secondary flow depends on the curvature of the surface. This results in a pressure gradient between maximum pressure at the outer wall and a minimum pressure at the inner wall. A secondary flow is superimposed on the main flow and the point of maximum velocity is moved towards the outer wall. Two-phase gas-liquid flow through bends is much more complex in nature. When flow enters the curved portion, the heavier density phase is subjected to a larger centrifugal force and this force causes the liquid to move away from the centre of curvature, while the lower density phase gas flows toward the centre of curvature. Number of different flow regime exist in gas-liquid two-phase flow and is gives added complexity.

Two-phase flow pressure drop in return bends in refrigeration systems have been experimentally investigated by several authors and for other gas-liquid flow system only few literatures are available. Pierre (1964) reported the pressure drop of R-12 in return bends with two-phase flow for the oil-free medium and oil refrigerant mixtures. Geary (1975) had carried out an investigation of the two-phase adiabatic flow pressure drop in return bends based on R-22 data using tube diameter ranging from 11.05 mm to 11.63 mm with curvature ratios ranging from 2.317 to 6.54. He proposed two-phase pressure drop correlation used typically in the design purpose for air-conditioning application. Chisholm (1980) developed equations for pressure drop prediction based on the two-phase multiplier for 90° and 180° bend. Experimental observations of the flow structure and pressure drop have been presented by Hoang and Davis (1984) for air-water froth

flow in the entrance of 180° bends. They observed that the overall loss coefficients were substantially larger than those in single-phase flow, particularly for bends with a larger radius of curvature, and the flow structure was almost stratified. Das et al. (1991a) studied gas non-Newtonian liquid flow through bends and developed empirical correlation to predict two-phase friction factor. Mandal and Das (2001) studied pressure losses for two-phase gas-Newtonian liquid flow in different types of bends (45° – 180°) in the horizontal plane. They proposed empirical correlation to predict the two-phase friction factor. Wang et al. (2003) studied air-water two-phase flow and the flow pattern by visual observation through smooth horizontal return bends. They proposed three flow pattern maps to describe the effects of return bends on the transition of the two-phase flow pattern. Chen et al. (2004) studied the two-phase frictional pressure drop for R-410A in four small diameter U-type return bends. They modified Geary (1975) correlation for the two-phase friction factor. Wang et al. (2005) studied the air-water slug flow across vertical U-type return bends. They proposed dimensionless correlations to describe the variation of transitional velocity within the return bends. Domanski and Christian (2008) proposed empirical correlation to determine the two-phase pressure drop in 180° return bends for R-22 and R-410A.

3.2 The experimental setup

The experimental setup is shown in Fig. 3.1. It consists of 3.0 m upstream straight tube, a U-bend, and 3.0 m downstream straight tube, a tank (0.45 m³ capacity), pump, gas-liquid separator, pressure and temperature instruments, control devices for flow etc. The internal diameter of the tubes and the bends was 0.01905 m. The reason for having long horizontal upstream and downstream portion before and after the bend was to

achieve fully developed flow conditions to facilitate the measurement of pressure drop across the bend. The bend portion of the test section was connected to the upstream and downstream portions with the help of flanges. The entrance and exit lengths were 2.0 m and 1.4 m respectively, which is more than 50 pipe diameters to ensure fully developed flow. Before the test section, a 0.5 m length Perspex tube of the same diameter was incorporated in the system to visualize the flow pattern. The rest of the test section was fabricated from mild steel. The test section was fitted horizontally with the help of leveling gauge. It was provided with pressure taps (piezometric ring) at different points in the upstream and downstream sections of the pipe and bends. Four different radius of curvature of the U-bends have been used for the experiments and their dimensions are given in Table 3.1. The U-bends used for the experiment were specially manufactured in order to ensure uniform internal diameter, constant curvature and roundness. The range of flow rate used for air and water in the experiments are $5.936 \times 10^{-5} - 56.1189 \times 10^{-5} \text{ m}^3/\text{s}$ and $2.000 \times 10^{-4} - 4.6500 \times 10^{-4} \text{ m}^3/\text{s}$ respectively. The range of variable investigated is shown in Table 3.2. Experiments were repeated a number of times to ensure reproducibility of the data. The observed flow pattern was intermittent at the inlet of the bend. The temperature of the water and air used in the experiments was maintained at $30 \pm 2^\circ\text{C}$, i.e. ambient temperature.

3.3 Evaluation of frictional pressure drop across the U-bend

Variation in the static pressure along the tube is schematically shown in Fig. 3.2, in which AC and DF correspond to the upstream and the downstream portion of the test section, and CD corresponds to the bend. The curve a-b-c-d-e-f is the static pressure distribution in the straight upstream portion, the bend portion and the straight

downstream portion of the test section. The curves a-b'-c' and d''-e''-f are the extended portions of the pressure distribution curve in the upstream and downstream portions of the fully developed flow region, respectively. The pressure loss due to the bend, P_b , was obtained from the difference in static pressure of the upstream and the downstream fully developed flow regions, ignoring the physical presence of the bend. The pressure can be expressed graphically as the vertical segment c'c'' in the pressure distribution curve. Thus

P_b includes the frictional pressure drop for the two-phase mixture flowing through a passage the same length as the axis of the bend, and the additional pressure loss due to the turbulent motion promoted by the change of flow direction. A typical static pressure distribution curve is shown in Fig. 3.3. Few experimental data are tabulated in Tables 3.3 – 3.4.

3.4 Computational fluid dynamics (CFD) Procedure

The fundamental of the k- model is discussed in Chapter 2. The general procedure to simulate water and air-water flow through four different U-bends based on Gambit 6.3 and Fluent 6.3 software is outlined below,

1. Perform meshing under Gambit 6.3 :
 - Create a computational domain at the flow region,
 - The grids were generated using boundary layer hexahedral meshes,
 - Controlling a smooth change in the mesh size by size functions,
 - Specify boundary and continuum types,
 - Examine the mesh to ensure that the high skewness is below 0.5.
2. Import the mesh file to Fluent 6.3 and check the mesh.
3. Define a 3-D, unsteady, implicit, and pressure-based solver.

4. Activate the mixture multiphase model.
5. Define a standard k- ν model. Slip velocity is added.
6. Enable the water properties with turbulent flow conditions using the text command: `define/models/viscous/turbulence`.
7. Define the phases by setting water as the primary phase and gas as the secondary phase in case of two-phase flow, and keeping the default selection of Schiller-Naumann drag model in the phase interaction panel.
8. Define the operating conditions by turning on gravity and specify the operating density.
9. Solution control methodology – Under relaxation factors – 0.5 for pressure, 0.3 for momentum, 0.2 for volume fraction, and default values for the other parameters. Standard schemes – STANDARD for momentum and volume fraction, and 1st order upwind for other variables. Pressure-velocity SIMPLE coupling used;
10. Initialize the solution – velocity;

Enable the plotting of residuals during the calculation, and kept the default convergence criteria, 1×10^{-5} for all residuals except for the transport equation which residual was set at 10^{-3} .

3.4.1 Assumptions for air-water flow through U-bends

The following concepts and assumptions were made:

1. A single pressure is shared by both phases
2. Momentum and continuity equations are solved for each phase

3. The secondary phase consists of uniform and unchanging bubbles dispersed in a continuous phase
4. The bubbles size is assumed to be small, 0.1mm spherical in size
5. Two-phase mixture k- model is used
6. Physical properties are uniform throughout.

3.5 Results and discussion

3.5.1 Convergence and grid independency

Grid refinement study was conducted to obtain grid independent solution. The study indicated that a large number of grid points were required to obtain accurate solution for this three dimensional simulation. To verify accuracy of the simulations, the results from CFD were first compared to experimental data. Mesh refinement does not produce important improvements of the simulated result. The convergence criterions were set at 10^{-5} for all equations except for the transport equation which residual was set at 10^{-3} . A computational domain L 200D was used to ensure fully developed flow results could be obtained for all U-bends. In general the final results depend upon mesh geometries. Subsequent decrement and increment in mesh resolution by 50% were applied to evaluate if the employed mesh resolution was adequate to obtain accurate solutions. It was observed that when the mesh resolution was decreased by 50% the axial velocity profile was 5-12% of the currently employed mesh velocity profile for different U-bends. As the present mesh resolution was increased by 50% the axial velocity profile changes 1-3% for different U-bends. These results suggest that the current mesh resolution is sufficient to obtained grid independent solutions for the proposed model.

3.5.2 Computational fluid dynamics (CFD) analysis for water flow through U-bends

Fig. 3.4 shows mesh for U-bend. An unstructured boundary layer hexahedral cooper mesh with nearly 5×10^3 - 25×10^3 was used.

Fig. 3.5 shows plot of velocity vector. It indicates that liquid velocity is higher from middle to inner side of the bend portion and liquid velocity is lower at outer and inner wall. It also indicates smaller bend radius of curvature results faster dispersion of rope and shorter developing flow. Fig. 3.6 shows the velocity vector and helicity for U-bend. It is clear that the helicity effect on velocity is more for bend radius of curvature 0.06m. Its effect gradually decreases from bend radius of curvature 0.06m to 0.20m, i.e., velocity is more dispersed from bend radius of curvature 0.06m to 0.20m. Fig. 3.7 shows that velocity vector plot of water at different points in the bend. It shows that velocity is high at centre and up to near the inner wall of the bend. Fig. 3.8 shows the velocity vector plot in angular coordinate. It also indicates that the velocity is high at the centre and up to near wall of the bend. It is due to turbulent nature of the water flow and nearly a flat velocity profile is observed. The velocity at the wall is zero and increases to maximum within a very short distance from the wall. Fig. 3.9 shows that contour plot of velocity at different points in the bend. It is observed from the figure that the inlet velocity profile changes with passing through the bend and the maximum water velocity is shifted towards the outer wall. Similar result also obtained in the contour plot of velocity at angular and radial coordinate in the bend as shown in Figs. 3.10 – 3.11. Figs. 3.12 – 3.14 show the contour plots for cell Reynolds number for different coordinate systems. These figures show the similar trend with the contour velocity plot. Figs. 3.15 – 3.16 show that contour plot of tangential velocity at different points in the bend. It indicates that

tangential velocity is more near the wall and less at the centre position. Fig. 3.17 shows that contour plot of radial velocity at different points in the bend. It indicates that radial velocity is less at the inlet of the bend and more at the outlet of the bend. But at the U-bend centre portion velocity is distributed radially. Similar results are shown in Fig. 3.18 at angular coordinates.

Fig. 3.19 shows a comparison of the static pressure profile for U-bends. A smaller radius of curvature bend results in an increase in pressure drop, a faster dispersion of rope and a shorter developing flow and larger bend radius of curvature results in slower dispersion of rope and longer developing flow. Fig.3.20 shows that contour plot of static pressure at different points in the bend. It shows that pressure is high at the outer wall due to centrifugal force water flows towards the outer wall. Similar features are clearly demonstrated in Figs. 3.21 – 3.22 in angular and radial coordinate system. Just after the bend exit a transverse pressure difference and is due to existence of pair of vortices.

Figs. 3.23 shows contour plot inside the different points of U-bend and Fig. 3.24 shows the contour plot at different angular position. Just before the inlet of the bend the velocity profile is concentrically distributed and then the water is slightly accelerated near the inner wall (Figs. 3.8 and 3.24). The acceleration of water in this region causes a weak secondary water stream flowing from an outer to inner wall over the cross section (Fig. 3.23). As the flow progresses water experiences centrifugal force and the static pressure in the fluid increases toward the outer wall (Figs. 3.19 – 3.22). At the inlet of the bend the pressure gradient is more in the inner wall and gradually shifted towards the outer wall, the water near the inner wall accelerated and de-accelerated near the outer wall. As the flow progresses through the bend the strong pressure gradient along the inner wall makes

the water in the inner wall further accelerated, and the vortices are formed in the cross section by the action of the large pressure difference between the inner and outer wall (Fig. 3.21). Due the centrifugal force the water in the central portion of the bend moved outward direction and the water near the upper and lower walls moves inward along the walls by the pressure gradient (Fig. 3.7). On further flow of water through the bend the two vortices in the cross section are developed and the water at high velocity near the inner wall is transported toward the outer wall by the action of the secondary flow. The water at the upper and lower wall has the low velocity is forced inwardly along the wall by the secondary flow and then gradually brought towards the inner wall and the static pressure rises again. On further water flow the high velocity region of the flow observed in the central region but slightly close to the outer wall (Fig. 3.9) and the intensive turbulence appeared. At the bend exit a new pair of vortices appears in the outer half cross section (Figs. 3.23 – 3.24) and diminishes rapidly and the down stream the flow returns slowly to the proper flow in a straight pipe so it needs a longer distance for recovery. Similar phenomena also observed by the Rowe (1970), Azzola et al. (1986), and Sudo et al. (2000).

Fig. 3.25 shows the static pressure distribution in the upstream, bend and downstream portion of the tube, obtained from experiments and CFD simulation. It is clear from the figure CFD simulated values matches very well with the experimental values. The static pressure starts to deviate from steady value within 15 pipe diameter in the upstream of the inlet of the U-bends, depending on the flow rate. In the downstream of the U-bend, the pressure recovery lengths were found to be within 20 pipe diameter for all U-bends, depending on the flow rate.

Fig. 3.26 shows that contours plot of wall shear stress for U-bends. Figs. 3.27 – 3.29 illustrate the contour plot of wall shear stress for different coordinate systems. It is clear from this plots that at inlet the inner wall has the maximum stress and at the outlet the maximum stress at the outer wall. This is due to the centrifugal force acting on water while passing through the curve surface of the U-bend. In general the stress at the wall is high compare to the centre portion.

Fig. 3.30 shows that contours plot of strain rate for U-bends. Figs. 3.31 – 3.33 illustrate the contour plot of strain rate for different coordinate systems. It indicates that strain rate is high at the near inner and outer wall position of bends and low at the centre.

Figs. 3.34 - 3.39 show the contour plot of helicity and vorticity at different points in the bend. It indicates that helicity and vorticity effect is more at the centre and near the inner side wall of the U-bend.

Figs. 3.40 - 3.46 shows contour plot of turbulent kinetic energy and its intensity at different points in the bend. It indicates that at inlet of the bend the turbulent kinetic energy is less and outlet is more. Both effects are large from centre to outer wall of the bend. The kinetic energy effect is modified with the change of radius of curvature. Similar observation confirmed by Cheng and Farokhi (1992) and Pruvost et al. (2004).

Figs. 3.47 - 3.49 show that contour plot of turbulent dissipation rate. It indicates that turbulent dissipation rate is more near outer and inner wall of the bend and less at the centre.

Figs. 3.49 - 3.50 show that contour plot of production of kinetic energy. It shows that at the inlet portion of the kinetic energy is low and just crossing the bend portion the kinetic energy value increases at the centre and again decreases at the outlet. As kinetic

energy term is directly related to the velocity term due to centrifugal action it changes accordingly.

Figs. 3.51 - 3.53 show that contour plot of turbulent viscosity at different points in the bend. It indicates that at inlet turbulent viscosity is low and gradually increases in the outlet. It is also observed from these figures that turbulent viscosity gradually increases at the centre position of the bend from inlet to outlet.

Fig. 3.54 show that contour plot of mass imbalance at different points in the bend. This imbalance arises due to centrifugal force acting on the water particle while passing through the bend.

Fig. 3.55 shows the variation of frictional pressure drop with water flow rate. As water flow rate increases pressure drop also increases. The CFD simulation also gives the good agreement with the experimental results as shown in the figure. Few experimental and CFD simulated data is shown in Table 3.3.

3.5.3 Computational fluid dynamics (CFD) analysis for air-water flow through U-bends

Fig. 3.56 shows plot of velocity vector for air-water mixture. Figs. 3.57a – c illustrate the contour plot of mixture, water and air respectively. Figs. 3.58 – 3.59 show that contour plot of velocity at different points in the bend and in angular coordinate. It is clear from these figures the mixture velocity is higher at the centre position and inner side of the bend and lower at the outer wall. As the mixture enters to the bend due to centrifugal action heavier density phase that is water moves to the outer wall and lower density phase, air moves to the inner wall. Fig. 3.57b clearly demonstrates that the water velocity is higher at the outer wall. Fig. 3.57c illustrates that the air velocity at the inner wall is higher and practically zero at the outer wall. The inlet flow regime is intermittent

in nature (plug and slug). At inlet the existence of air is at the top. Due to slip exist between the water and air and the existence of the pressure gradient across the cross-section air velocity increases compare to water velocity, due to centrifugal action the water is shifted towards the outer wall and a stratified flow condition attain within the bend. Fig. 3.57c clearly demonstrates these phenomena. Due to increase in air velocity in the inner side of the bend the mixture velocity also increase as it demonstrated in the Fig. 3.57a. The water velocity at the outer wall is much higher than the inner wall due to centrifugal force and is clearly illustrate in the Fig. 3.57b.

Fig. 3.60 shows the static pressure profile U-bend. A smaller bends radius of curvature results in an increase in pressure drop due to faster dispersion of rope and a shorter developing flow exist compare to the larger bend radius of curvature. Figs. 3.61 – 3.62 show that contour plot of static pressure at different points in the bend and in angular coordinate. It shows that pressure is high at outer wall as heavier density water phase goes to outer wall due to centrifugal force and low at the inner wall when the air phase exists. Due to this pressure gradient at any cross section of the bend the air is accelerated more than the water phase. Due to this acceleration maximum velocity is shifted for the mixer.

Similar to the water flow experiments as stated earlier, the secondary flow originated in a pair of counter rotating vortices at the just inside of the bend as shown in Figs. 3.63 – 3.64. These vortices continue up to the downstream of the bend, merged in the just outlet of the bend and downstream flow return slowly to the steady state. Similar phenomena observed by Usui et. al (1983) and Supa – Amorkul et. al (2005).

Fig. 3.65 illustrates the experimental and CFD simulated static pressure distribution curve. It is clear that the both curves match very well.

The static pressure starts to deviate from steady value within 30 pipe diameter in the upstream of the inlet of the U-bends, depending on the air-water flow rate. In the downstream of the U-bend, the pressure recovery lengths were found to be within 35 pipe diameter for all U-bends, depending on the air-water flow rate.

Figs. 3.66a-b – 3.67a-b show that volume fraction of the water and air at different point in the bend and in angular coordinate system. It shows that heavier density phase water goes to outer wall side and lighter air goes to inner wall side due to centrifugal force.

Fig. 3.68 shows that contour plot of shear stress and shear strain at different points in the bend. Shear stress and shear strain is high at the wall side and small at centre.

Fig. 3.69 illustrates the typical two-phase frictional pressure drop across the bend as the function of air velocity. As the air velocity increases, the two phase pressure drop across the bend gradually increases. The CFD simulated values are also plotted in this graph, it gives the good agreement with the experimental values. Fig. 3.70 illustrates the typical experimental and CFD simulated pressure drop across the U-bends as a function of air velocity. It is clear from the graph that for a constant liquid flow rate the pressure drop across the bend is higher for small radius of curvature of U-bend. . Few experimental and CFD simulated data is shown in Table 3.4.

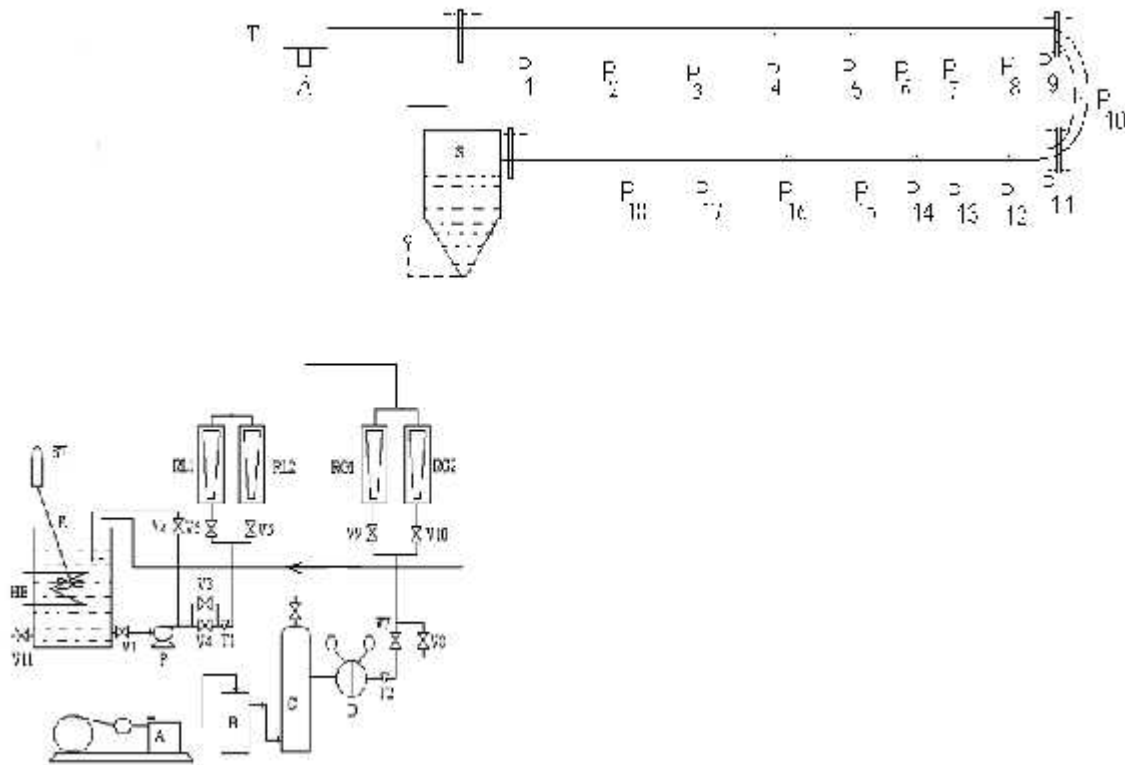
3.6 Conclusions

Experimental investigations for water and air-water flow through four different U-bends in the horizontal plane are reported. Computational fluid dynamic simulation using Fluent 6.3 is studied to investigate inside of the flow phenomena.

The pressure drop across the bends measured for water flow in turbulent condition. The CFD simulations are carried out using standard k- model. The simulated results predicts the flow structure, cell Reynolds number, static pressure, shear stress, shear strain, turbulent kinetic energy, turbulent intensity, dissipation losses, vorticity, helicity. The experimental pressure drop across the bends matches well with the simulated values.

The two-phase pressure drop across the bends measured experimentally for air-water flow. The CFD simulations are carried out using standard mixture-k- model. The simulated results predicts the flow structure, mixture, water and air-phase static pressure, volume fraction of water and air phase, shear stress, shear strain. The experimental pressure drop across the bends matches well with the simulated values.

Thus, CFD can be useful tool for designing bend for industrial practice.



A: Compressor, B: Oil Tray, C: Gas Cylinder, D: Gas Regulator, E: Storage Tank, H: Drier, HE: Heat Exchanger, LC: Level Controller, P: Pump, P1 – P18: Pressure Tap, RL – RG: Rota meters, S: Gas – Liquid Separator, T: Joint, T1 – T2: Thermometers, V1 – V12: Valve

Fig. 3.1 Schematic diagram of experimental set up

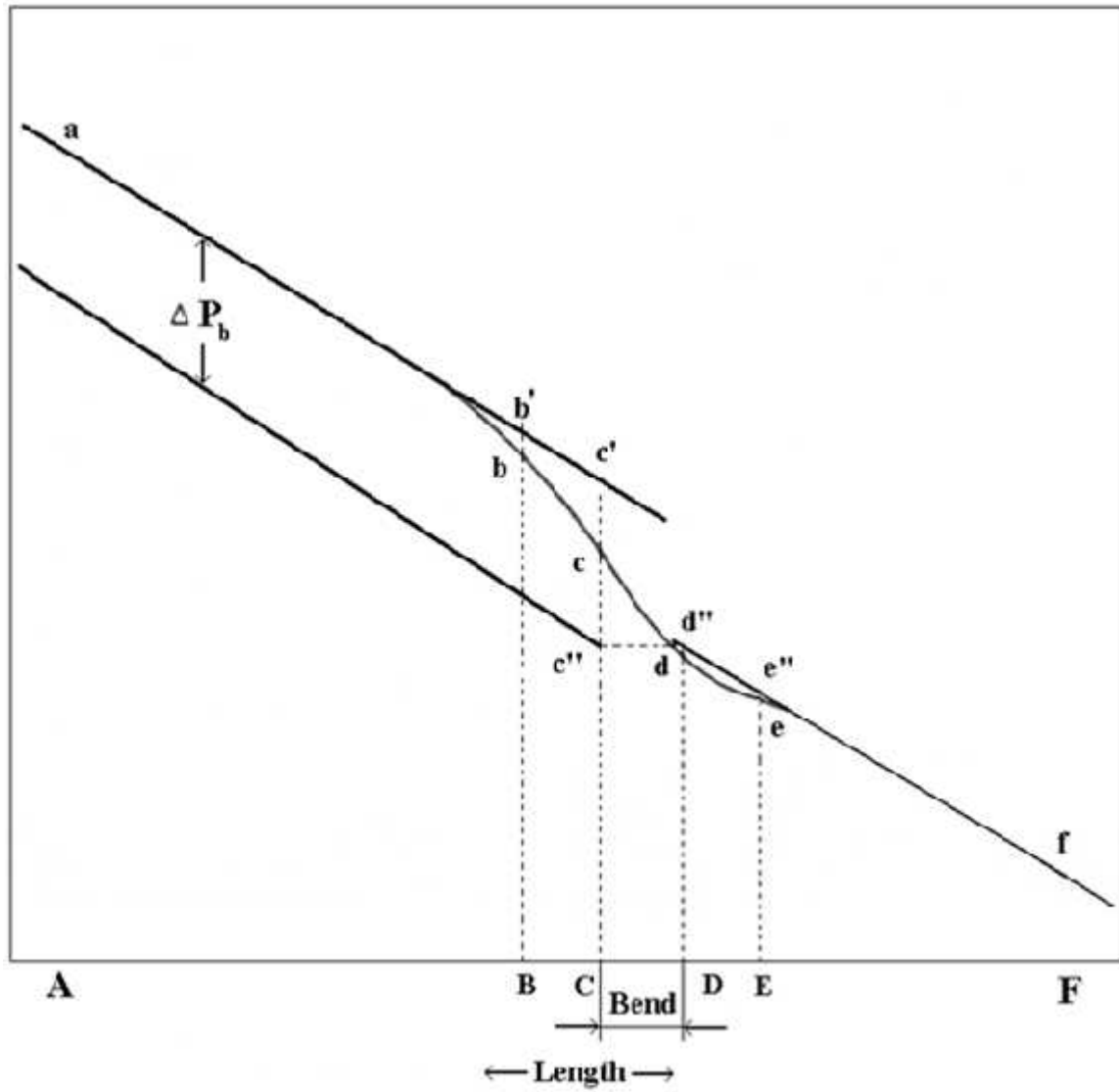


Fig. 3.2 Pressure distributions along pipeline with a bend

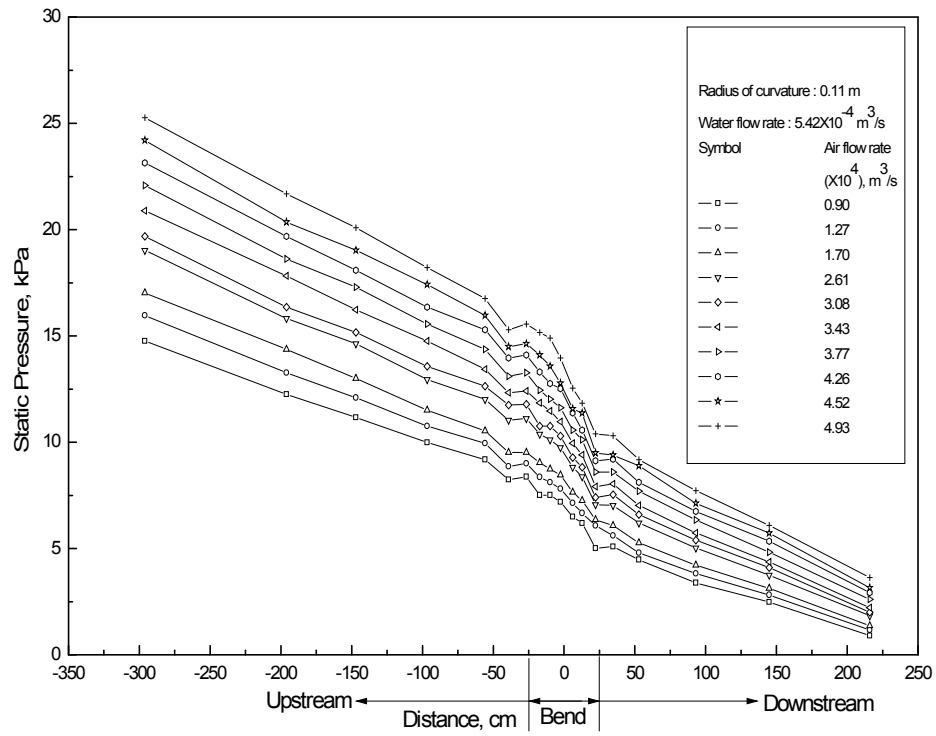
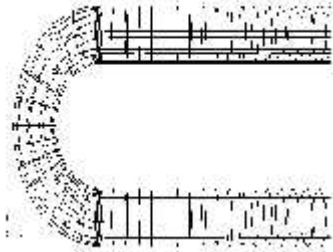
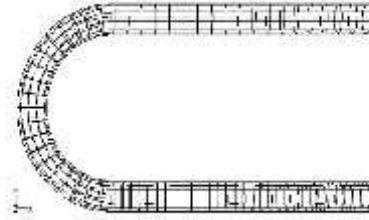


Fig. 3.3 Typical static pressure distribution curve



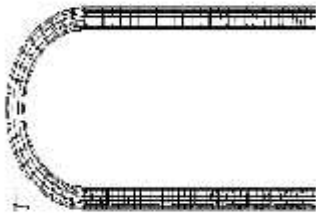
Grid Size: Level: 0; Cells: 21344;
Faces: 65930; Nodes: 23616
Partitions: 1; 1 cell zone,
4 face zones

(a) Radius of curvature 0.06 m



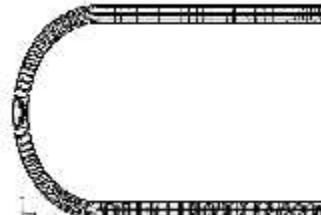
Grid Size: Level: 0; Cells: 5076;
Faces: 16656; Nodes: 6792;
Partitions: 1; 1 cell zone,
4 face zones

(b) Radius of curvature 0.11 m



Grid Size: Level: 0; Cells: 5076;
Faces: 16656; Nodes: 6792;
Partitions: 1; 1 cell zone, 4 face zones

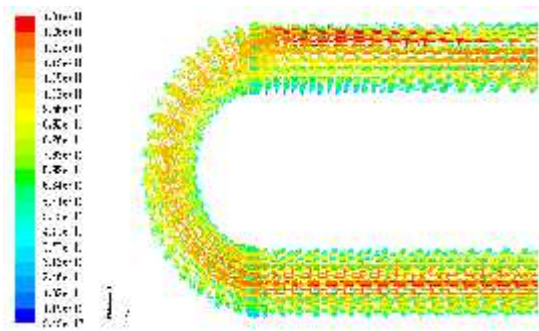
(c) Radius of curvature 0.15 m



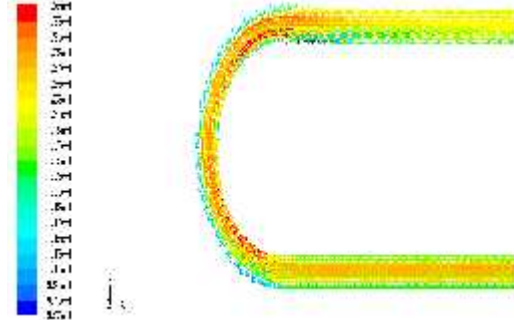
Grid Size: Level: 0; Cells: 20240;
Faces: 65364; Nodes: 25355;
Partitions: 1; 1 cell zone,
4 face zones

(d) Radius of curvature 0.20 m

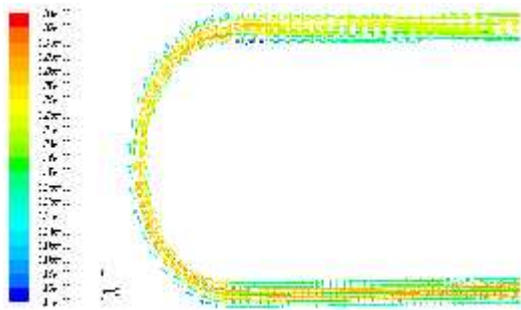
Fig. 3.4 Grid for U-bends



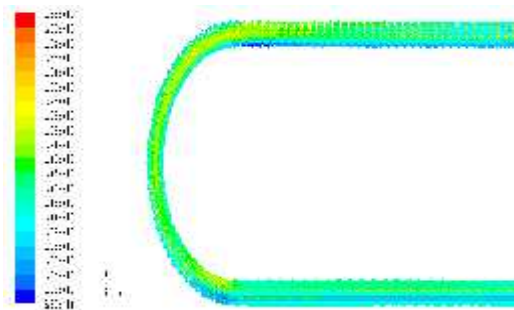
(a) Radius of curvature 0.06 m



(b) Radius of curvatures 0.1 m



(c) Radius of curvature 0.15 m



(d) Radius of curvatures 0.2 m

Fig. 3.5 Plot of velocity vector for U-bend for water velocity (m/s): 0.933

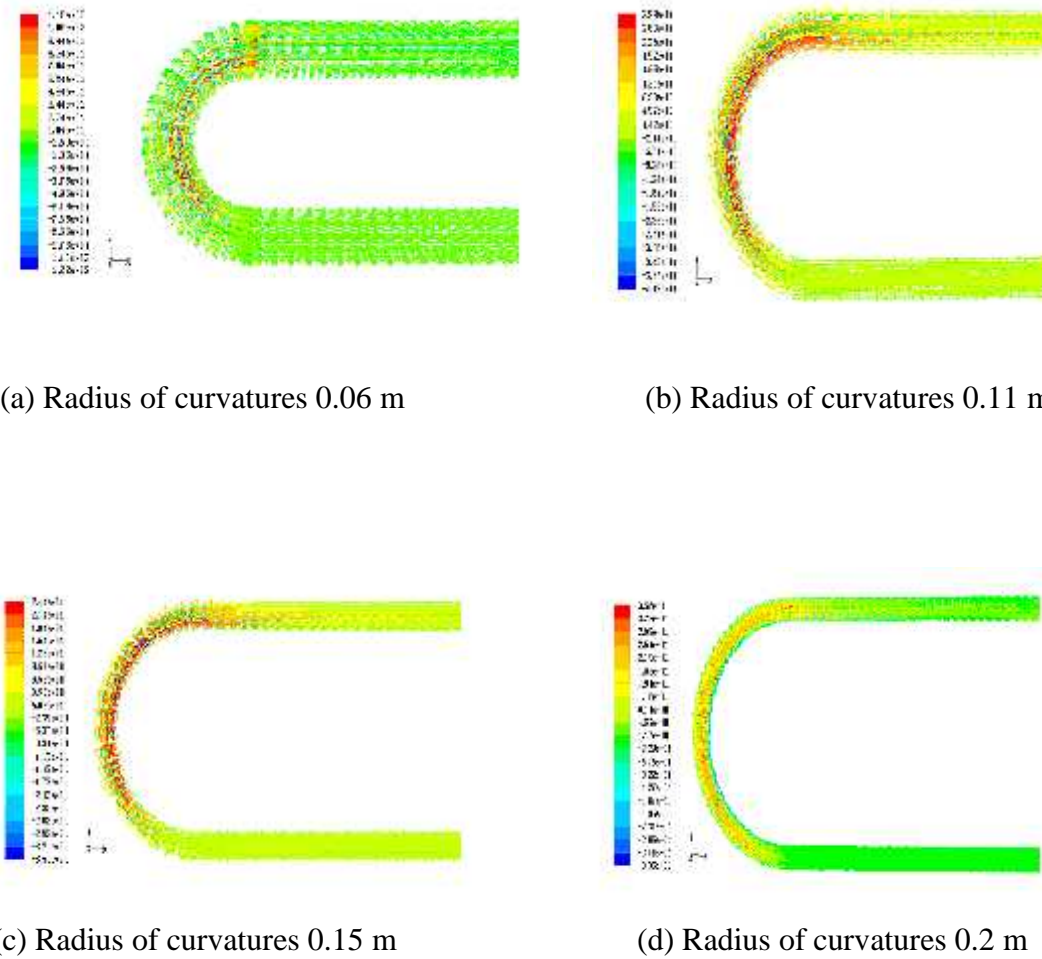


Fig. 3.6 Plot of velocity vector in the bend portion, i.e., helicity for U-bends for water velocity (m/s): 0.933

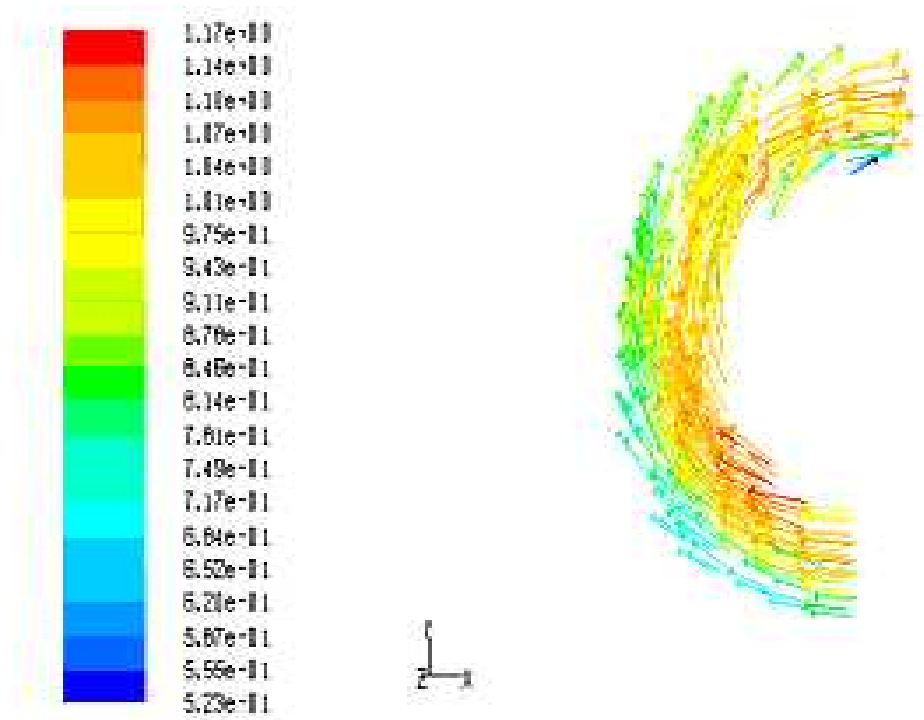


Fig. 3.7 Contour plot of velocity vector at different points in the bend at water velocity (m/s): 0.933 and radius of curvature (m): 0.06

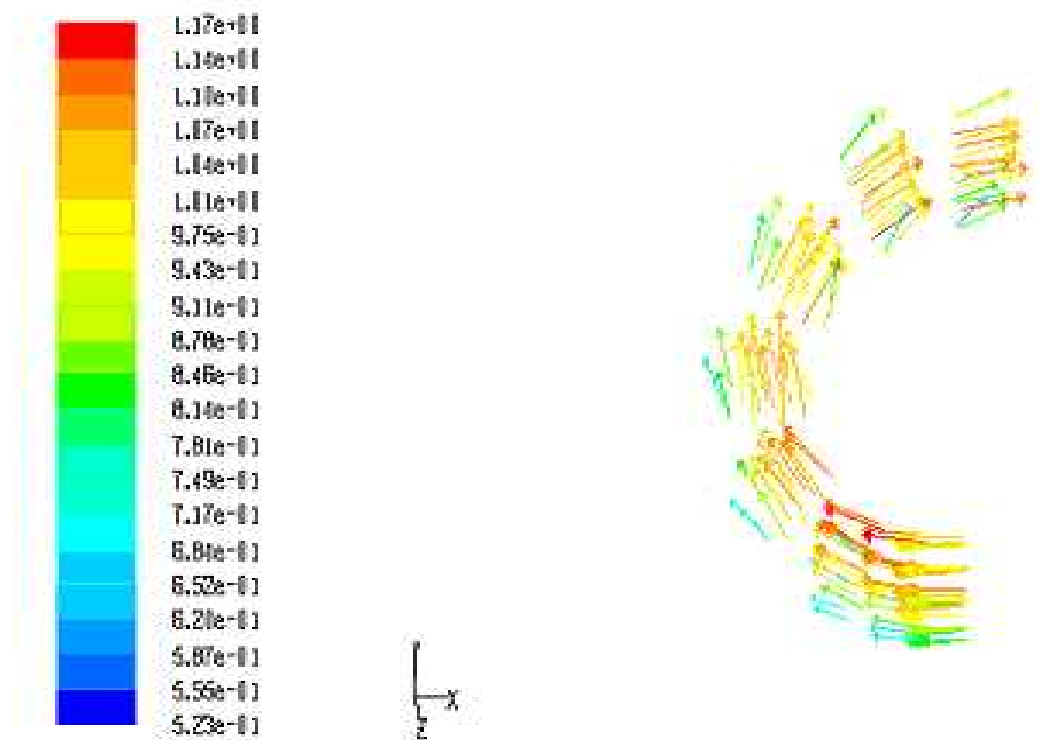


Fig. 3.8 Contour plot of velocity vector at angular coordinates in the bend for water velocity (m/s): 0.933 and radius of curvature (m): 0.06

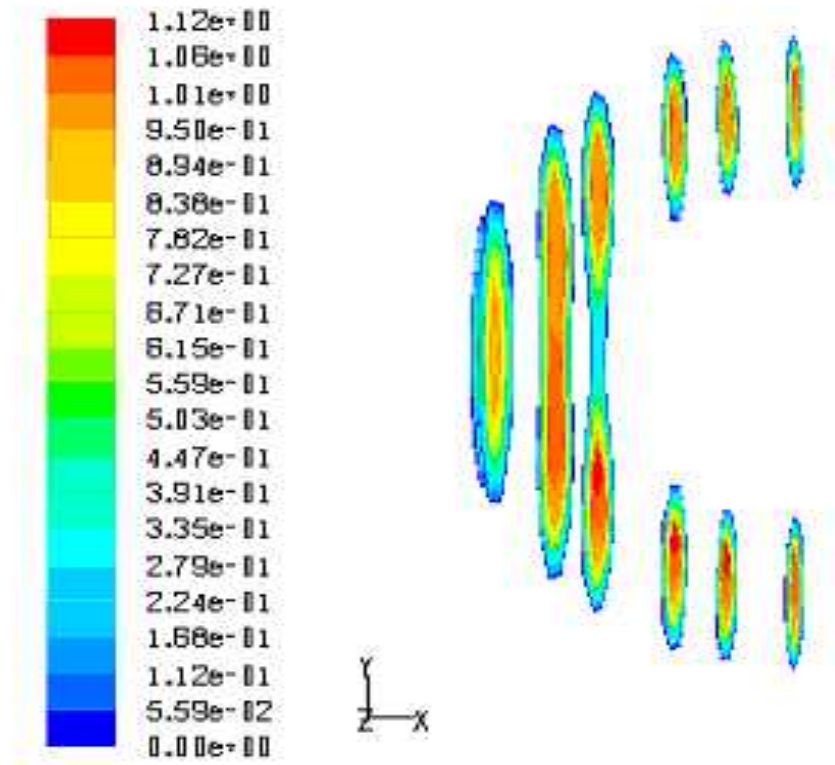


Fig. 3.9 Contour plot of velocity at different points in the bend for water velocity (m/s): 0.933 and radius of curvature (m): 0.06

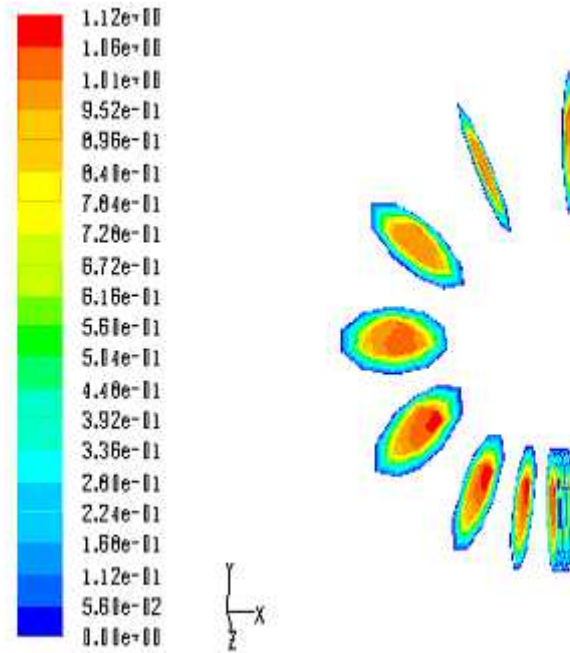


Fig. 3.10 Contour plot of velocity at angular coordinates in the bend for water velocity (m/s): 0.933 and radius of curvature (m): 0.06

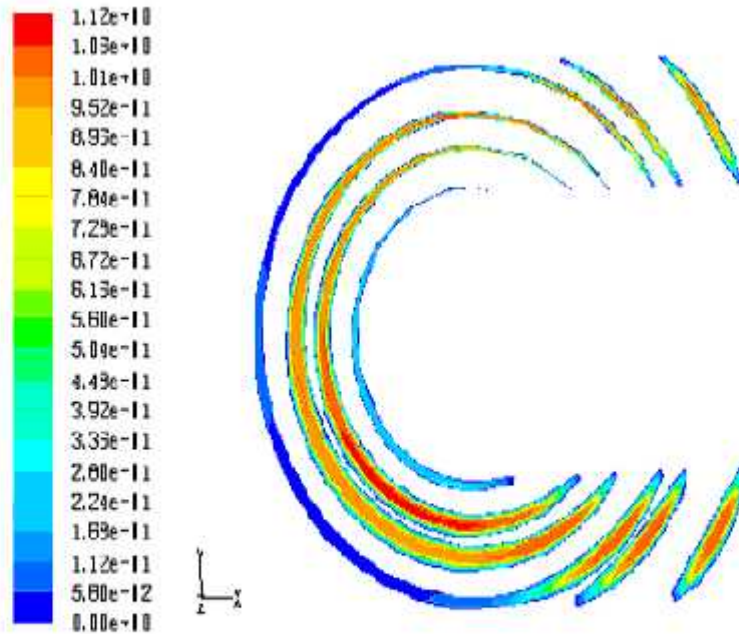


Fig. 3.11 Contour plot of velocity at radial coordinates in the bend for water velocity (m/s): 0.933 and radius of curvature (m): 0.06

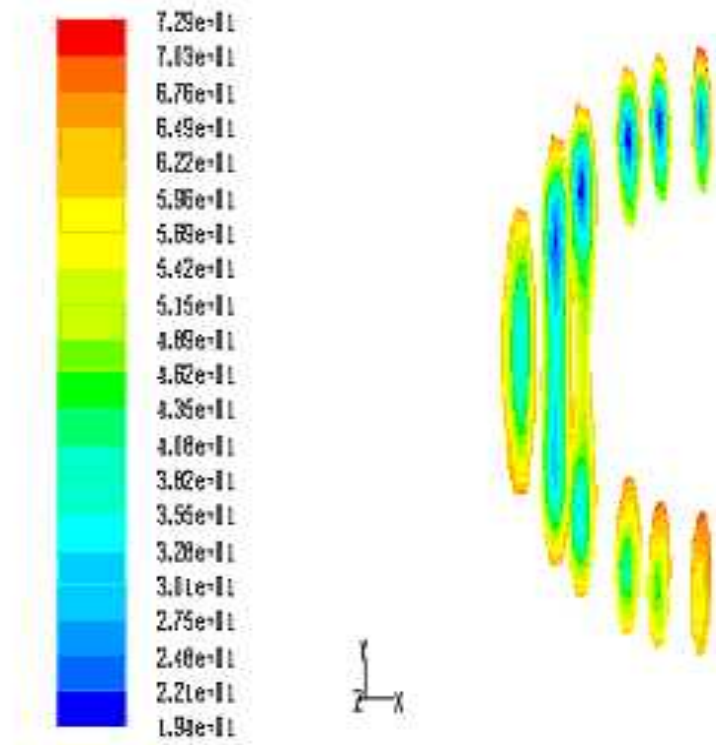


Fig. 3.12 Contour plot of cell Reynolds number at different points in the bend for water velocity (m/s): 0.933 and radius of curvature (m): 0.06

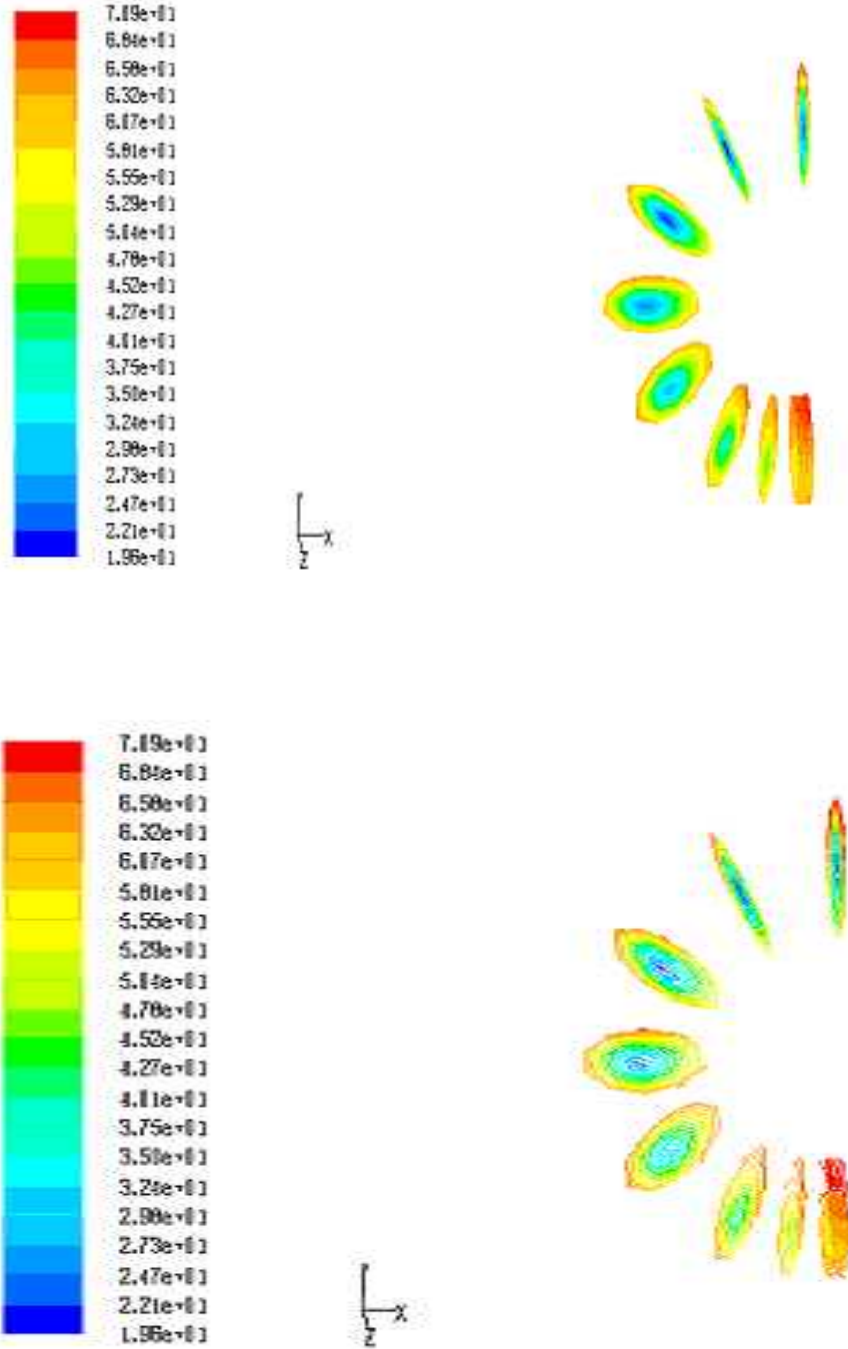


Fig. 3.13 Contour plot of cell Reynolds number at angular coordinates in the bend for water velocity (m/s): 0.933 and radius of curvature (m): 0.06

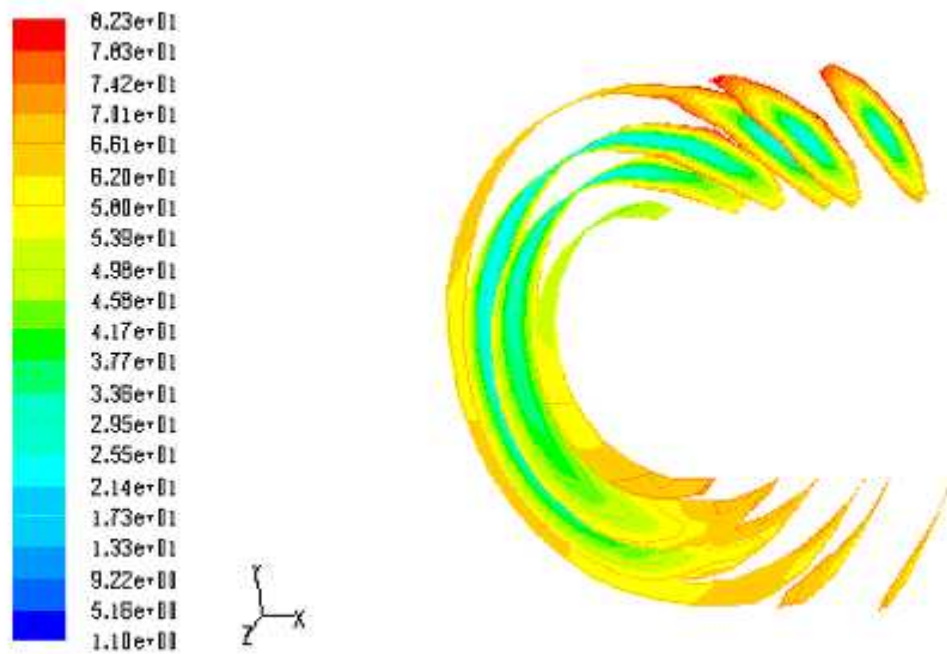


Fig. 3.14 Contour plot of cell Reynolds number at radial coordinates in the bend for water velocity (m/s): 0.933 and radius of curvature (m): 0.06

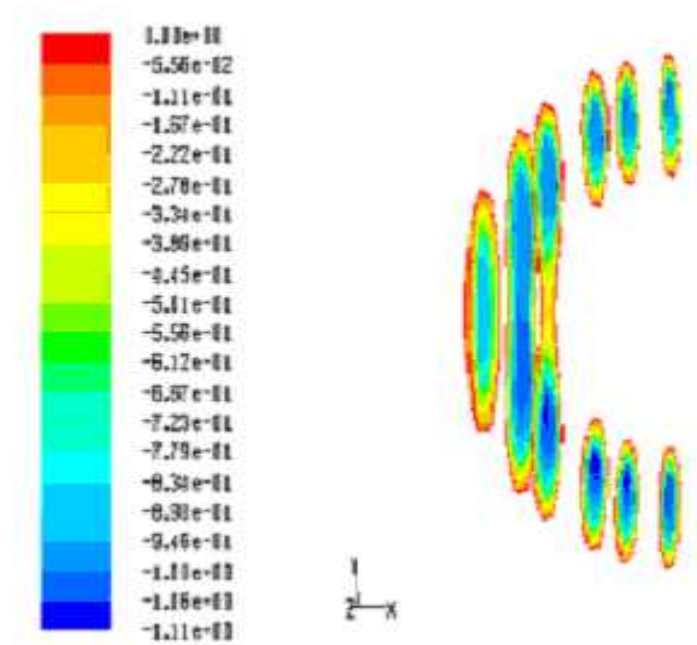


Fig. 3.15 Contour plot of tangential velocity at different points in the bend for water velocity (m/s): 0.933 and radius of curvature (m): 0.06

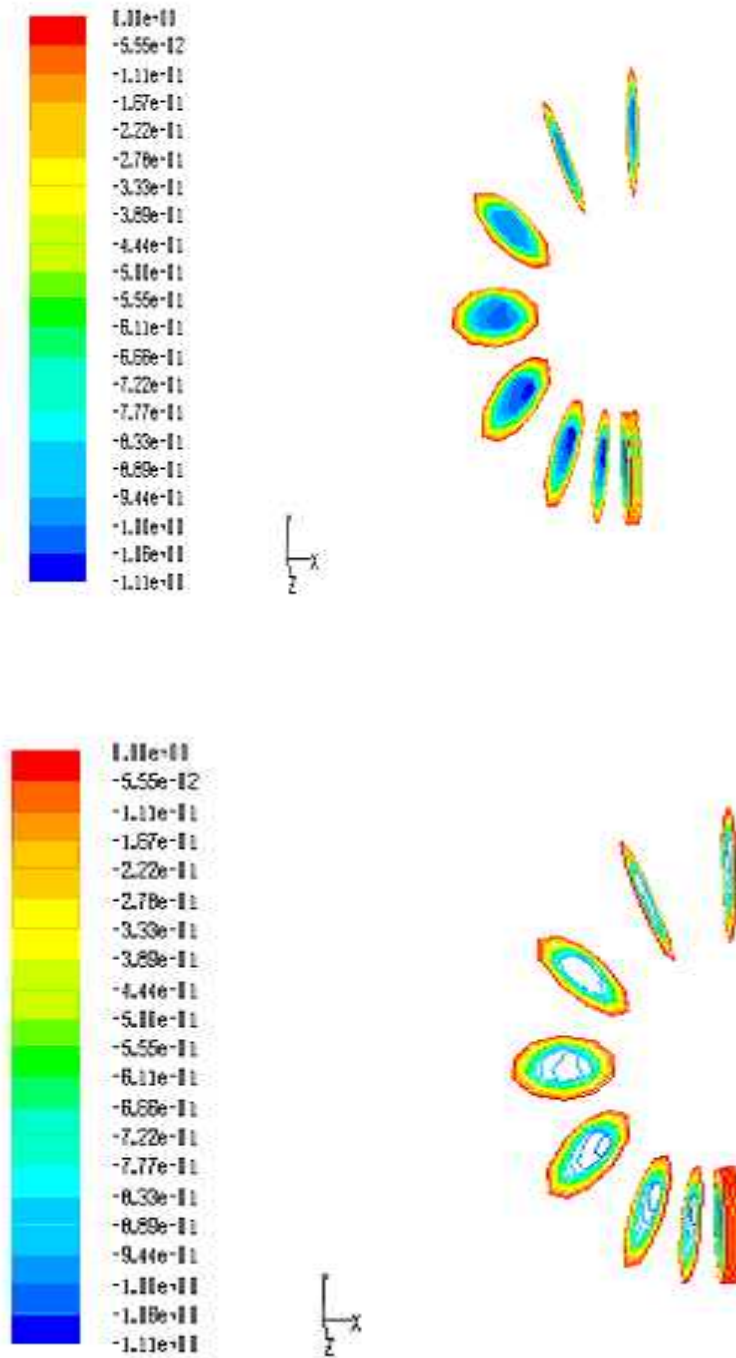


Fig. 3.16 Contour plot of tangential velocity at angular coordinates in the bend for water velocity (m/s): 0.933 and radius of curvature (m): 0.06

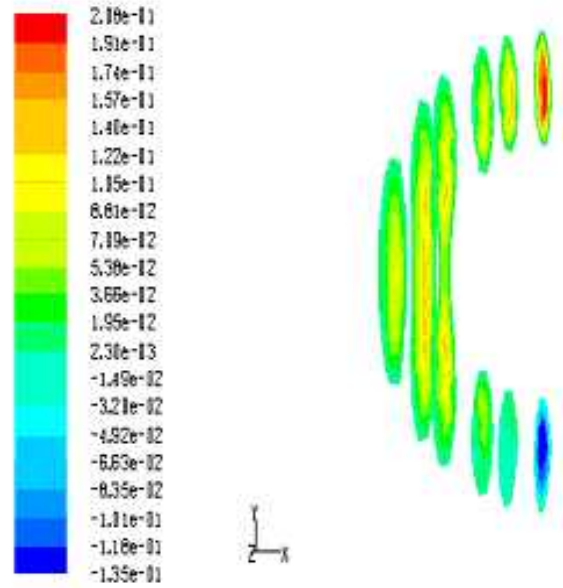


Fig. 3.17 Contour plot of radial velocity at different points in the bend for water velocity (m/s): 0.933 and radius of curvature (m): 0.06

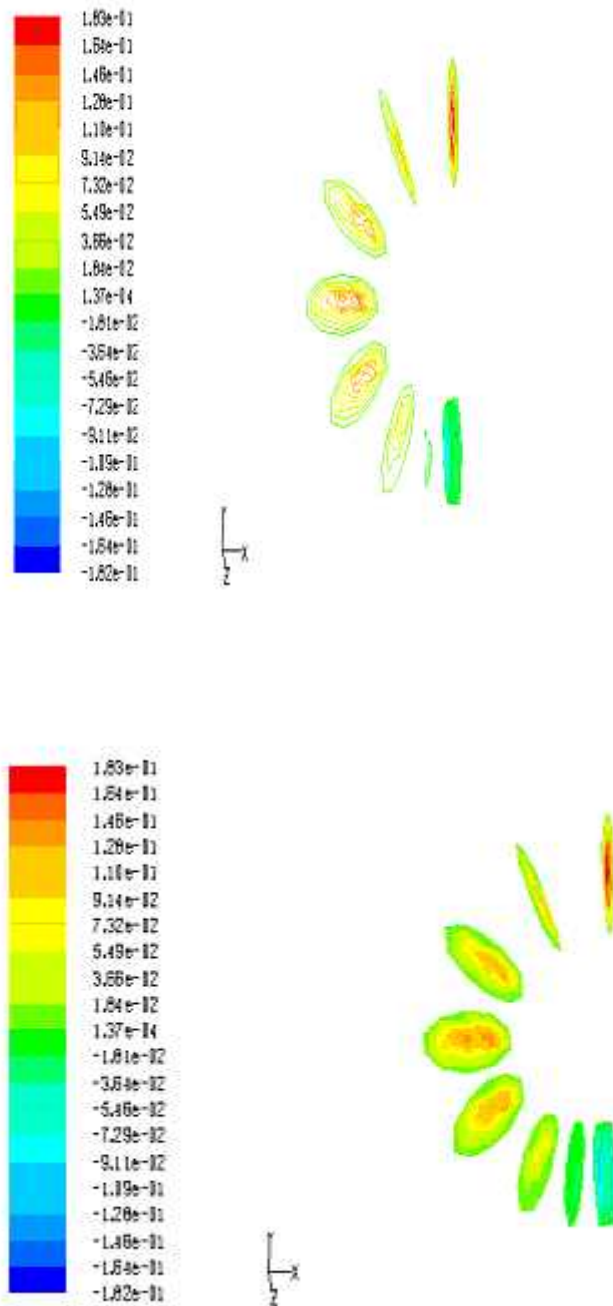
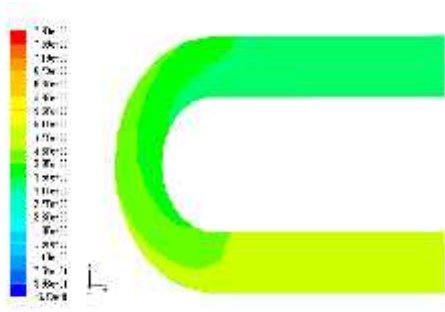
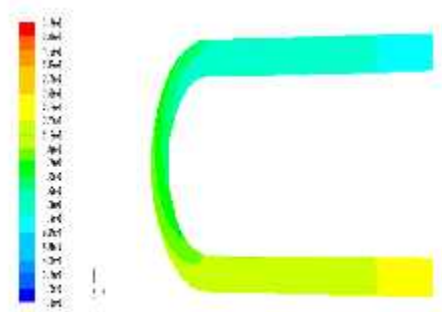


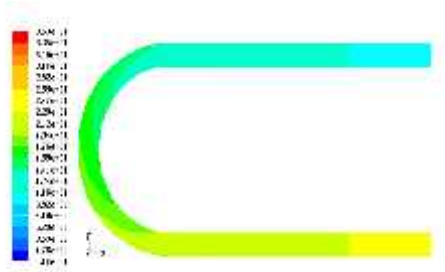
Fig. 3.18 Contour plot of radial velocity at angular coordinates in the bend for water velocity (m/s): 0.933 and radius of curvature (m): 0.06



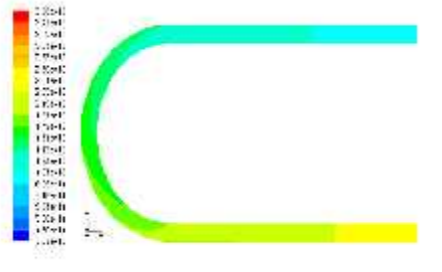
(a) Radius of curvatures 0.06 m



(b) Radius of curvatures 0.11 m



(c) Radius of curvatures 0.15 m



(d) Radius of curvatures 0.2 m

Fig. 3.19 Contours plot of static pressure for U-bend for water velocity (m/s): 0.933

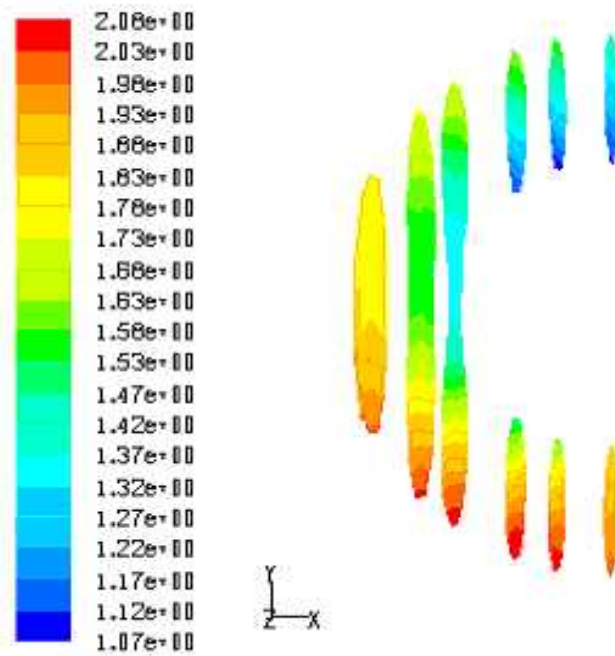


Fig. 3.20 Contour plot of static pressure at different points in the bend for water velocity (m/s): 0.933 and radius of curvature (m): 0.06

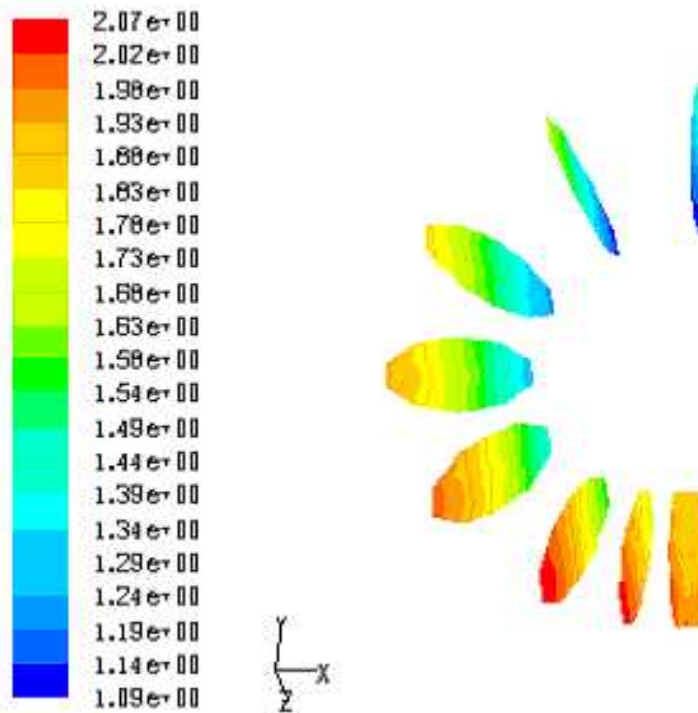


Fig. 3.21 Contour plot of static pressure at angular coordinates in the bend for water velocity (m/s): 0.933 and radius of curvature (m): 0.06

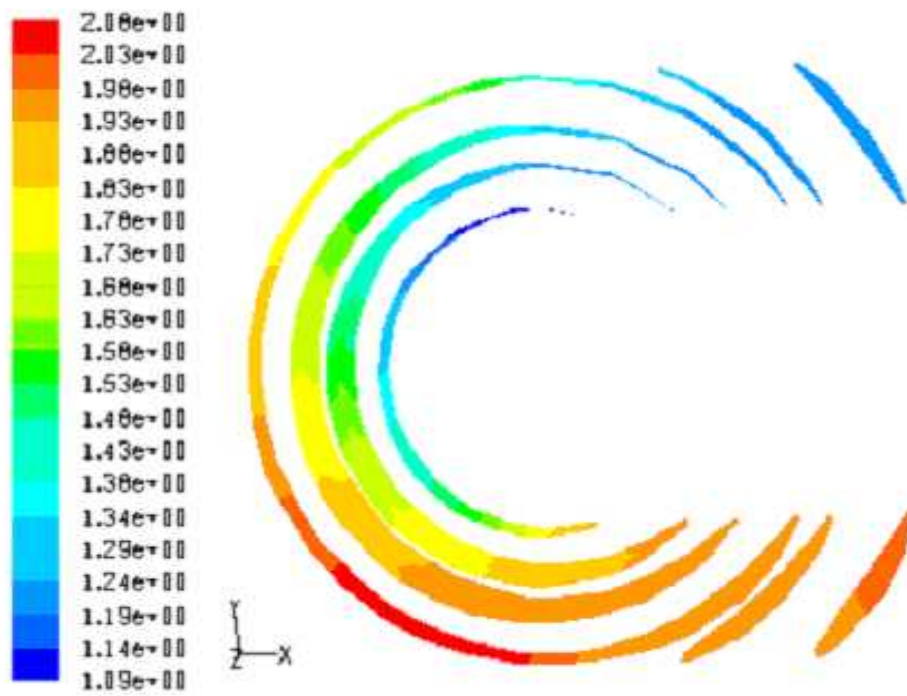


Fig. 3.22 Contour plot of static pressure at radial coordinates in the bend for water velocity (m/s): 0.933 and radius of curvature (m): 0.06

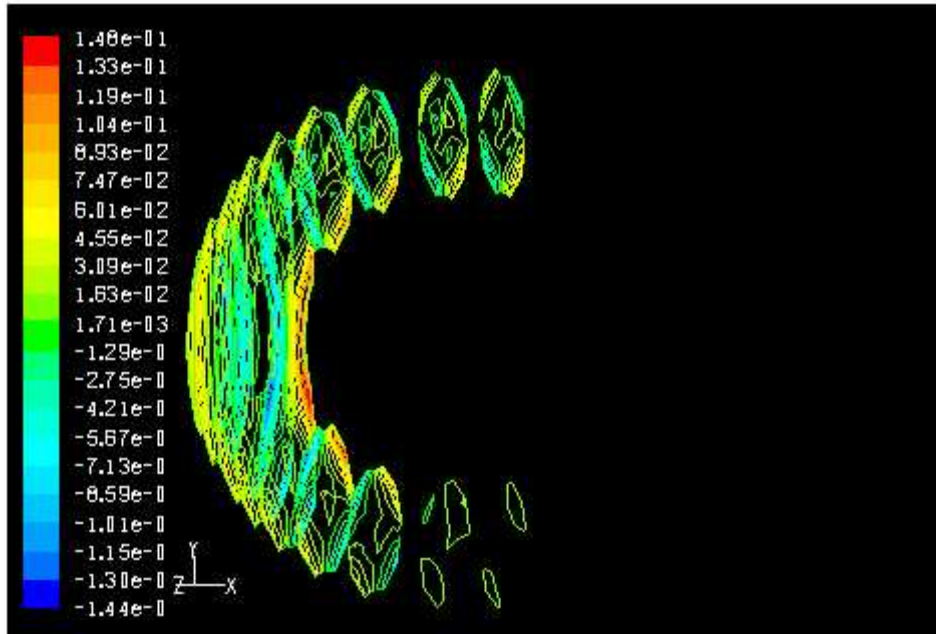


Fig. 3.23 Contour velocity plot inside the different points of U-bend for water velocity: 0.933 m/s, radius of curvature: 0.06 m

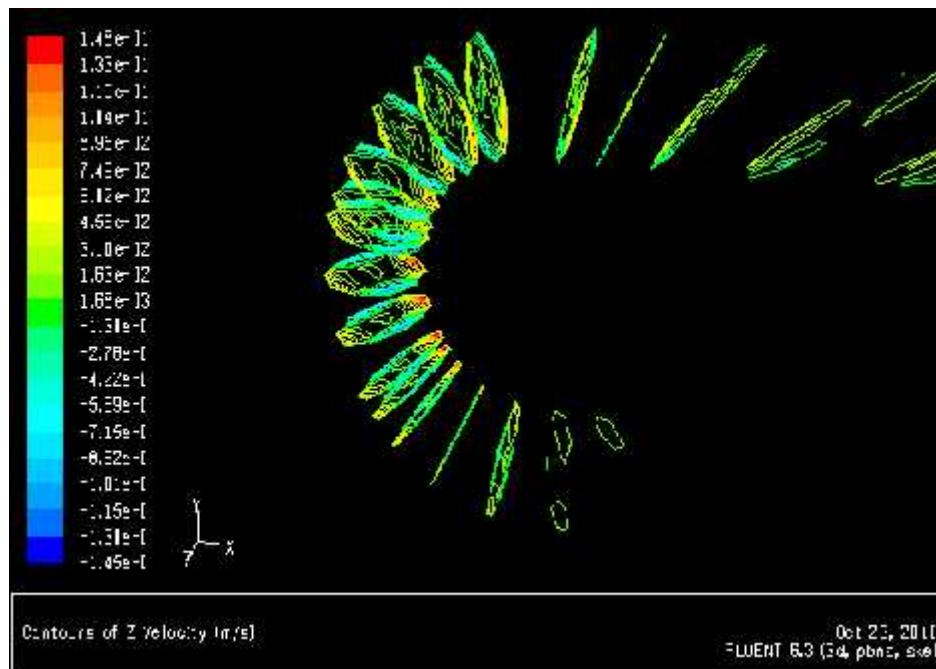


Fig. 3.24 Contour velocity plot inside the different angular points of U-bend for water velocity: 0.933 m/s, radius of curvature: 0.06 m

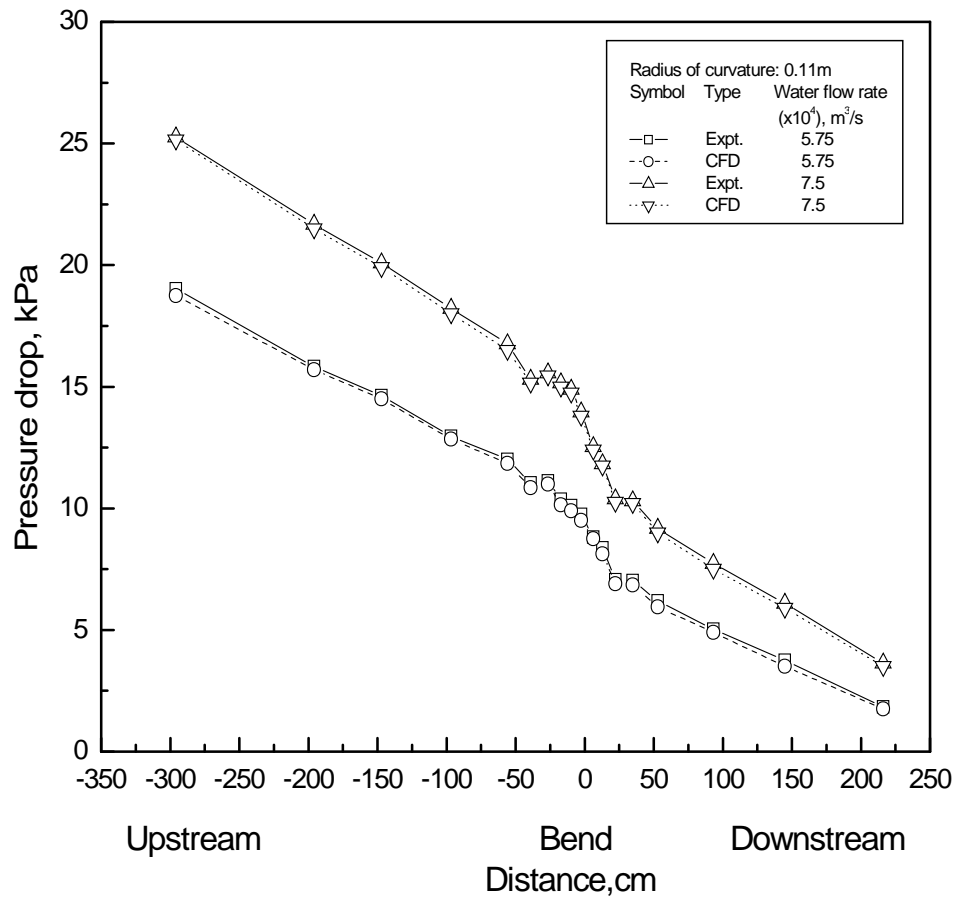
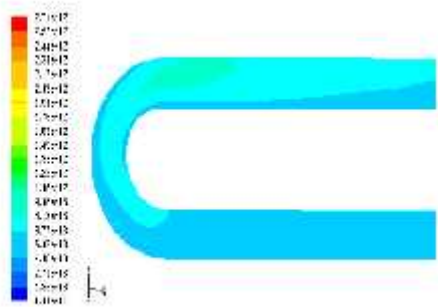
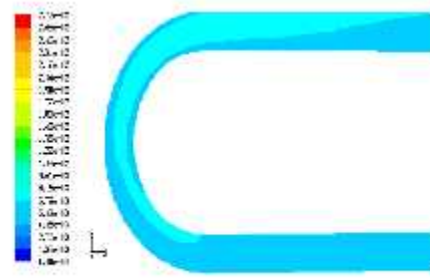


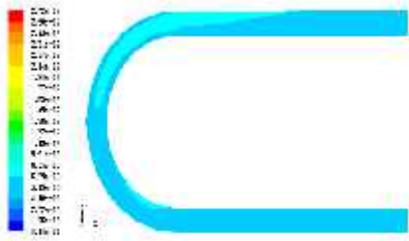
Fig. 3.25 Experimental and CFD static pressure distribution



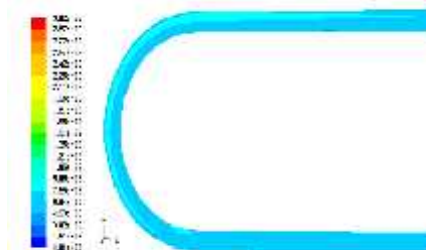
(a) Radius of curvatures 0.06 m



(b) Radius of curvatures 0.11 m



(c) Radius of curvatures 0.15 m



(d) Radius of curvatures 0.2 m

Fig. 3.26 Contours plot of wall shear stress for U-bend for water velocity (m/s): 0.933

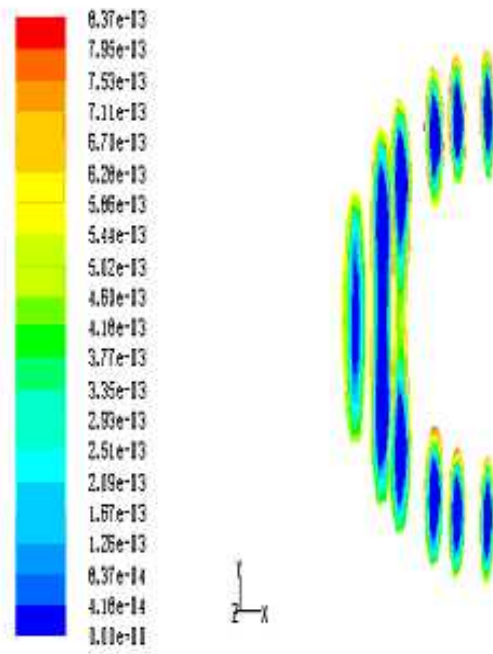


Fig. 3.27 Contour plot of wall shear stress at different points in the bend for water velocity: 0.933 m/s, radius of curvature: 0.06 m

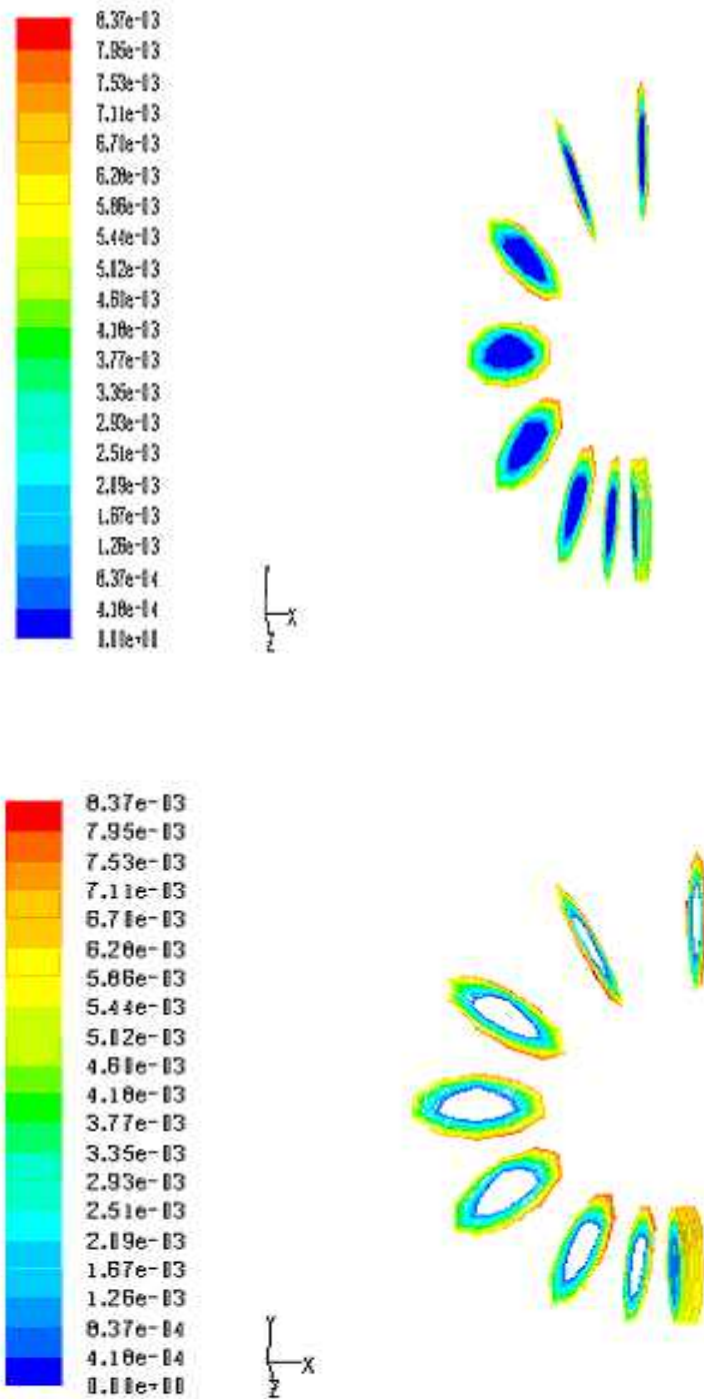


Fig. 3.28 Contour plot of wall shear stress at angular coordinates in the bend for water velocity (m/s): 0.933, radius of curvature (m): 0.06

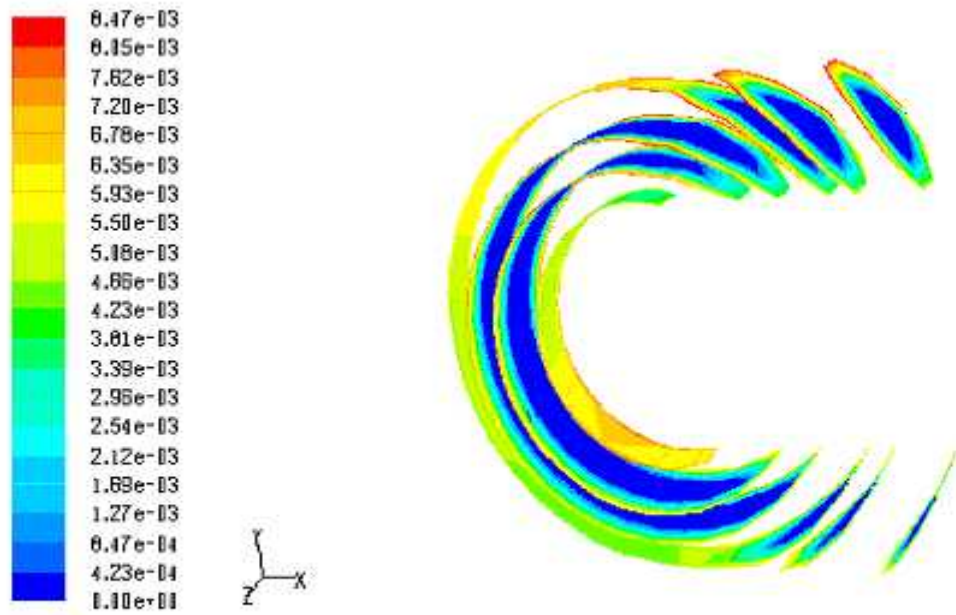
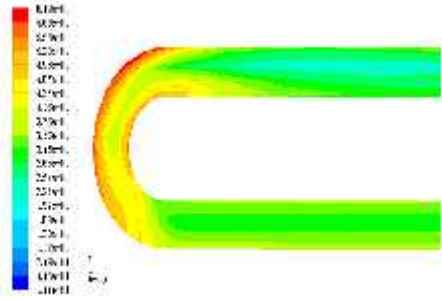
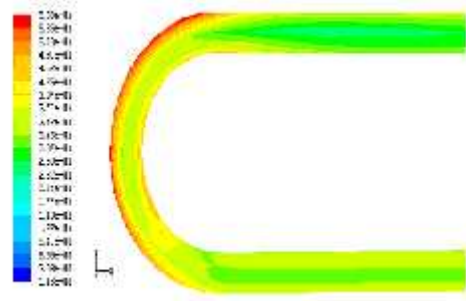


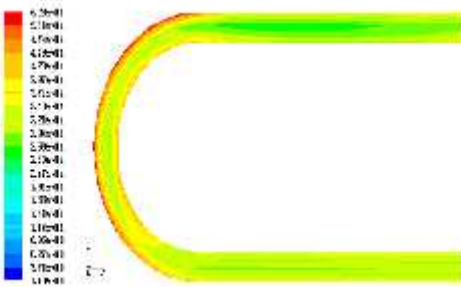
Fig. 3.29 Contour plot of wall shear stress at radial coordinates in the bend for water velocity (m/s): 0.933, radius of curvature (m): 0.06



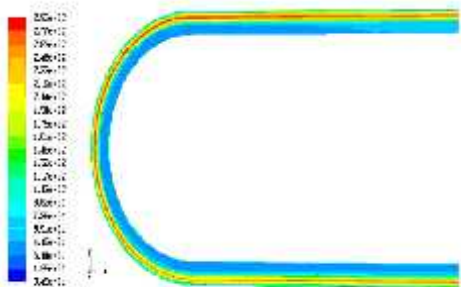
(a) Radius of curvatures 0.06 m



(b) Radius of curvatures 0.11 m



(c) Radius of curvatures 0.15 m



(d) Radius of curvatures 0.20 m

Fig. 3.30 Contours plot of strain rate for U-bend for water velocity (m/s): 0.933

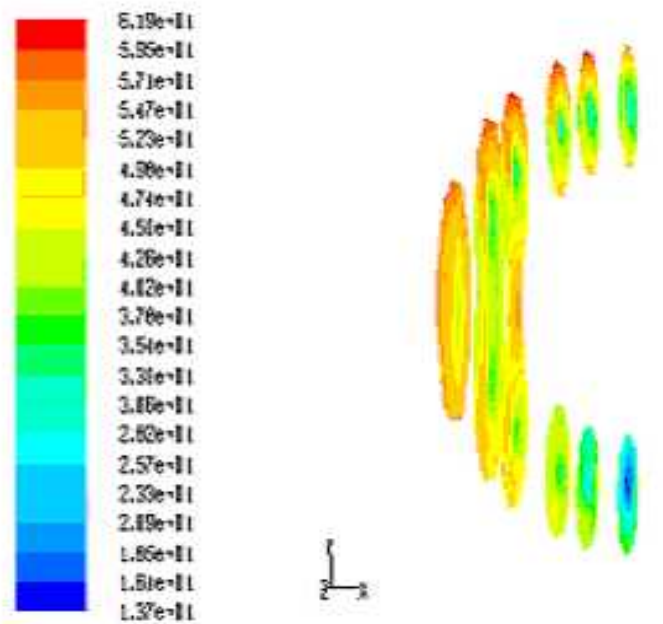
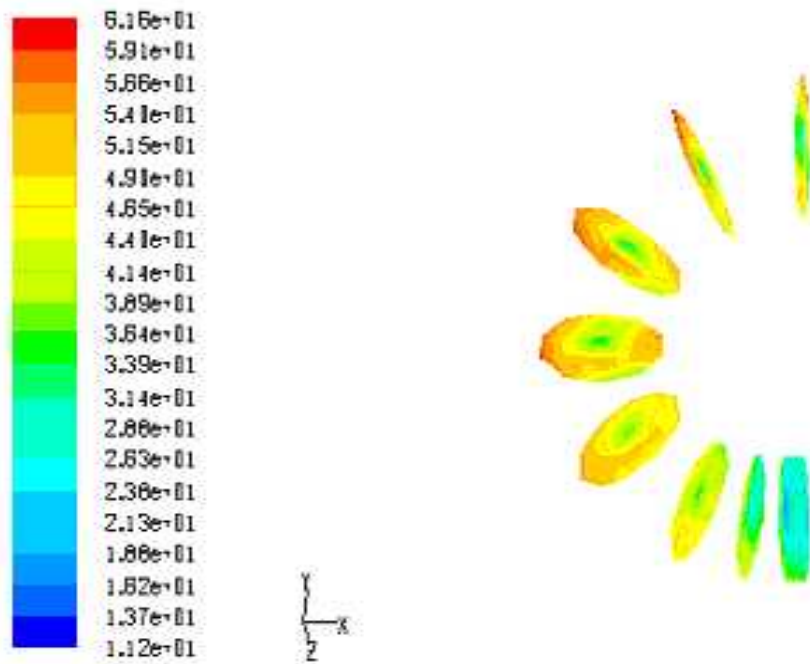


Fig. 3.31 Contour plot of wall strain rate at different points in the bend for water velocity (m/s): 0.933, radius of curvature (m): 0.06



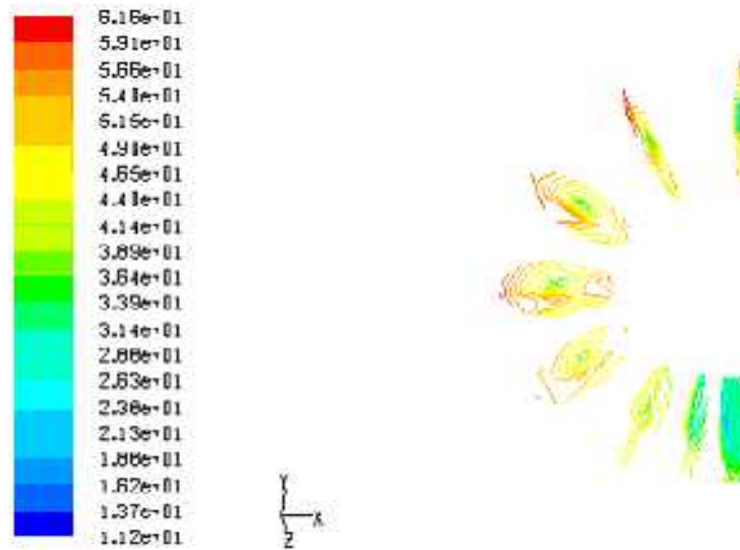


Fig. 3.32 Contour plot of strain rate at angular coordinates in the bend for water velocity (m/s): 0.933, radius of curvature (m): 0.06

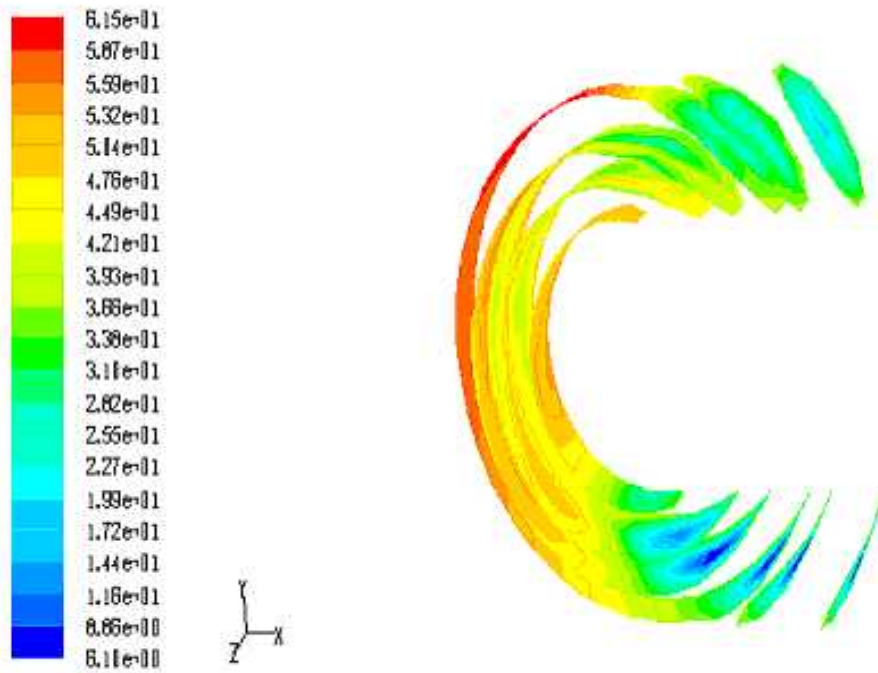


Fig.3.33 Contour plot of strain rate at radial coordinates in the bend for water velocity (m/s): 0.933, radius of curvature (m): 0.06

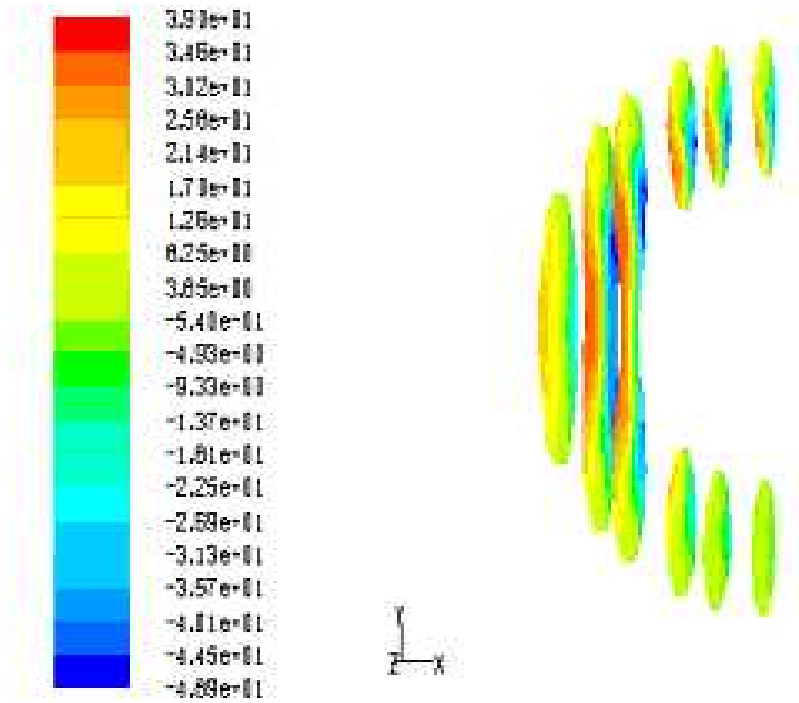


Fig. 3.34 Contour plot of helicity at different points in the bend for water velocity (m/s): 0.933, radius of curvature (m): 0.06

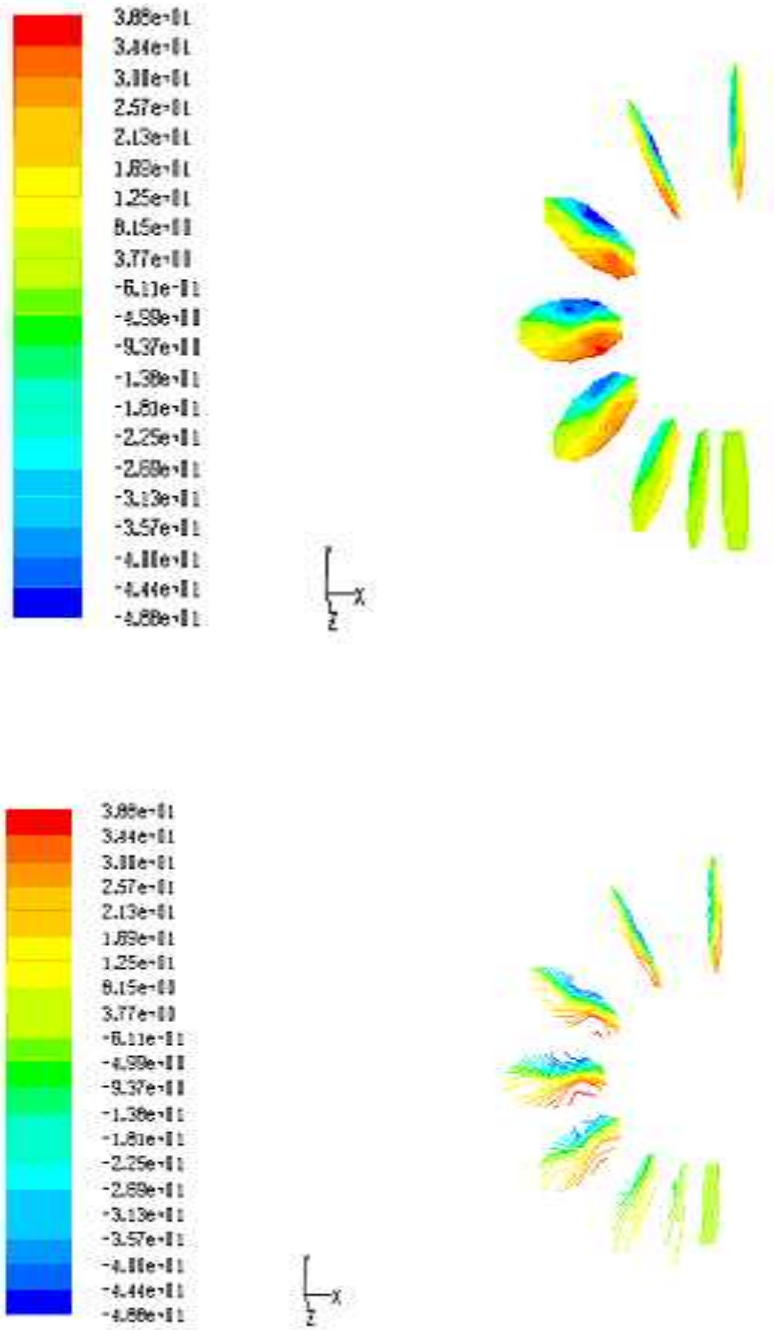


Fig. 3.35 Contour plot of helicity at angular coordinates in the bend for water velocity (m/s): 0.933, radius of curvature (m): 0.06

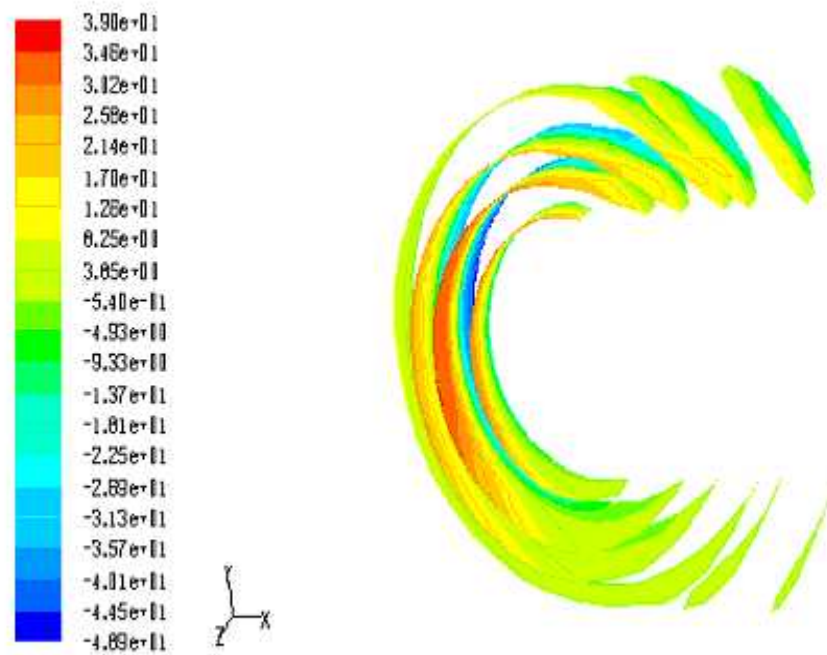


Fig. 3.36 Contour plot of helicity at radial coordinates in the bend for water velocity (m/s): 0.933, radius of curvature (m): 0.06

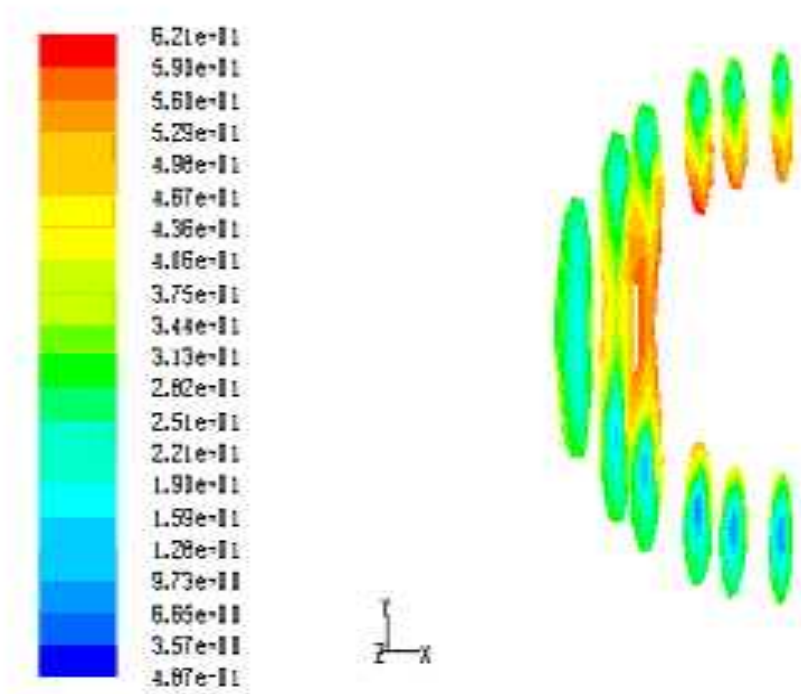


Fig. 3.37 Contour plot of vorticity at different points in the bend for water velocity (m/s): 0.933, radius of curvature (m): 0.06

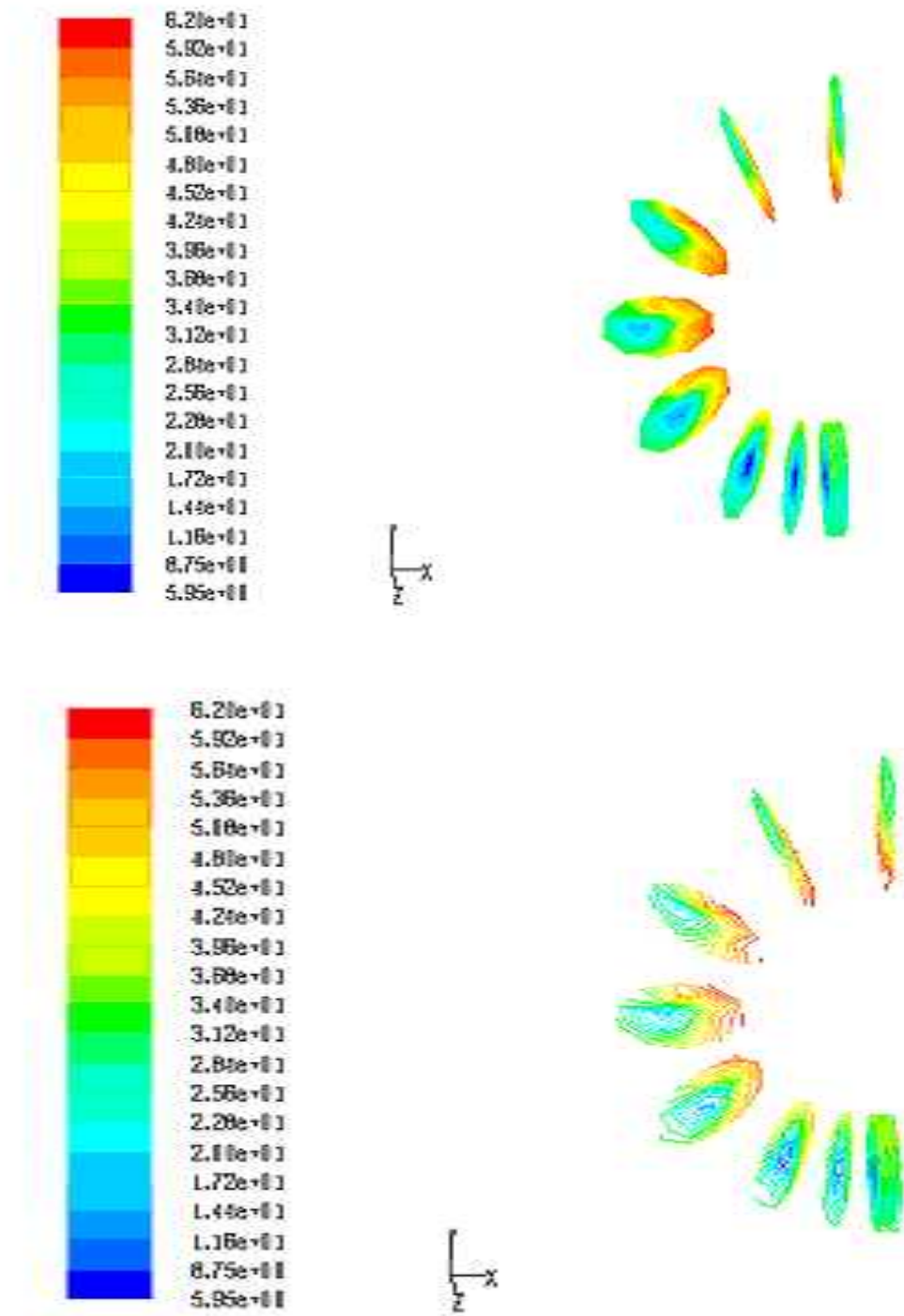


Fig. 3.38 Contour plot of vorticity at angular coordinates in the bend for water velocity (m/s): 0.933, radius of curvature (m): 0.06

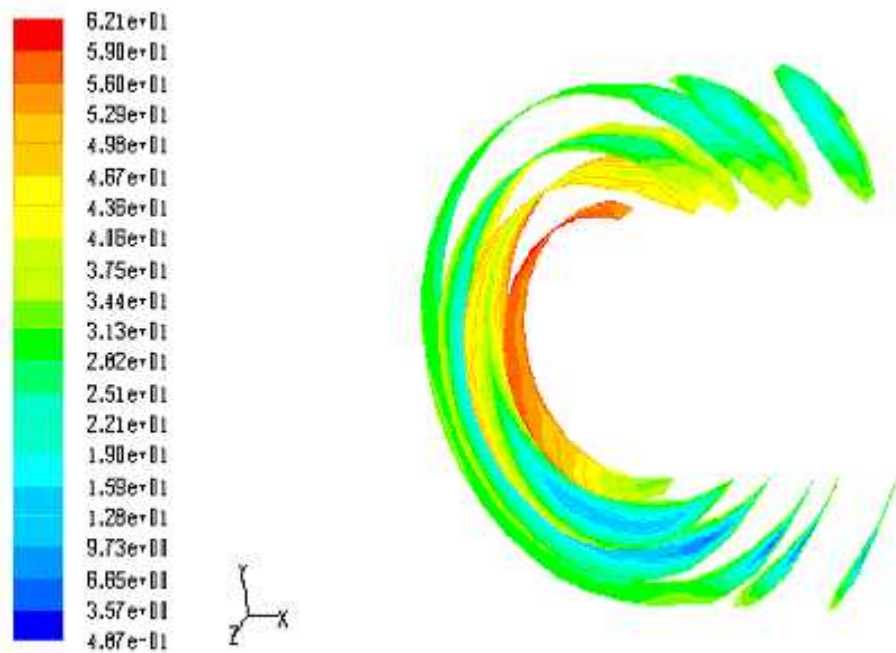


Fig. 3.39 Contour plot of vorticity at radial coordinates in the bend for water velocity (m/s): 0.933, radius of curvature (m): 0.06

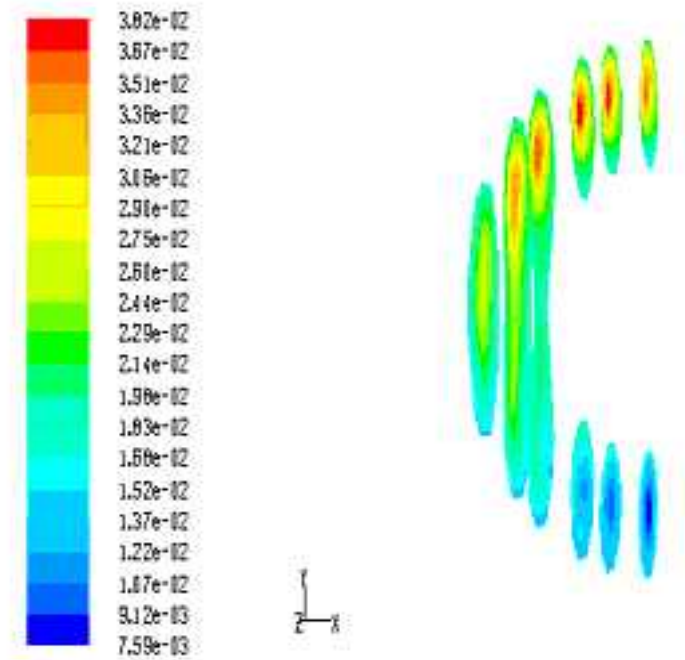


Fig. 3.40 Contour plot of turbulent kinetic energy at different points in the bend for water velocity (m/s): 0.933, radius of curvature (m): 0.06

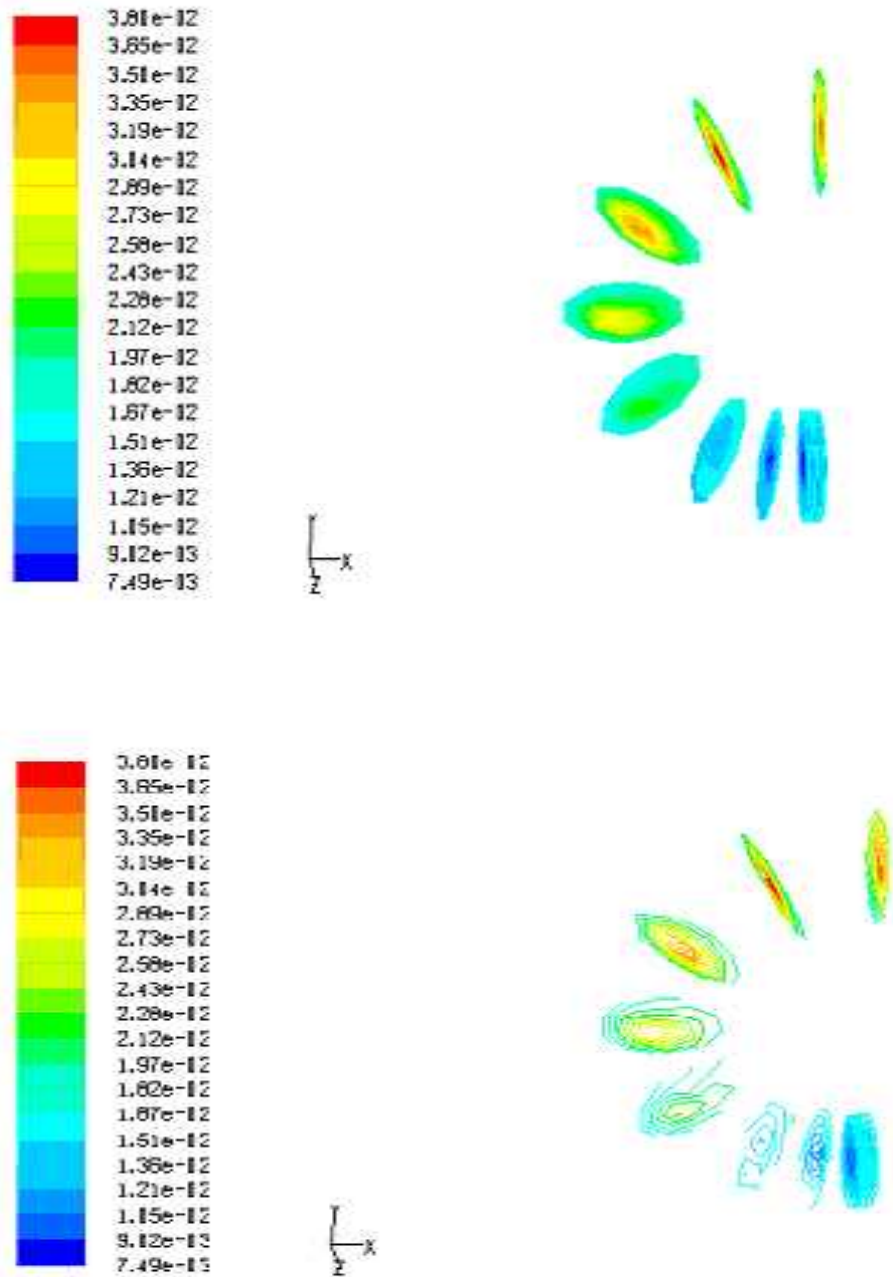


Fig. 3.41 Contour plot of turbulent kinetic energy at angular coordinates in the bend for water velocity (m/s): 0.933, radius of curvature (m): 0.06

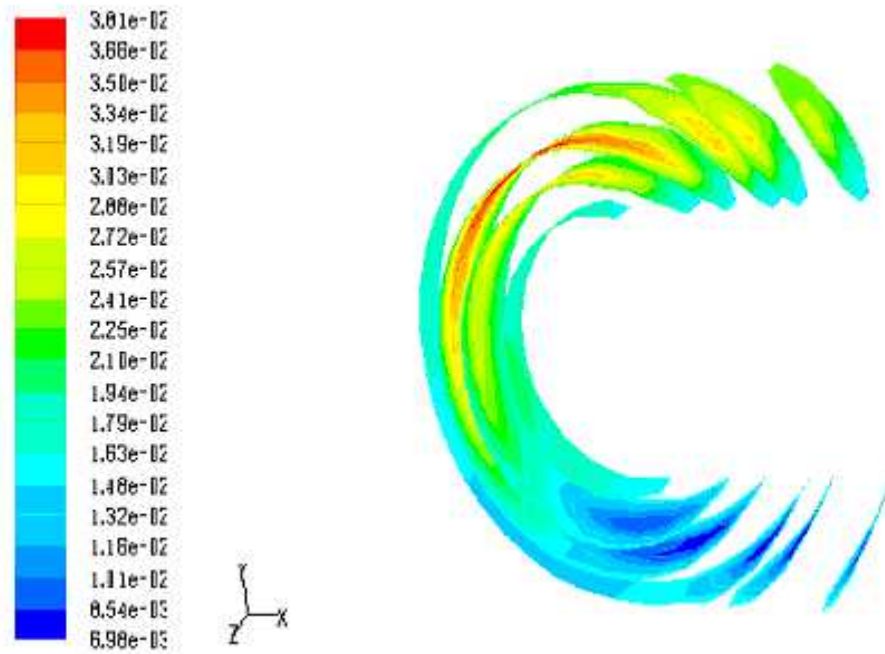


Fig. 3.42 Contour plot of turbulent kinetic energy at radial coordinates in the bend for water velocity (m/s): 0.933, radius of curvature (m): 0.06

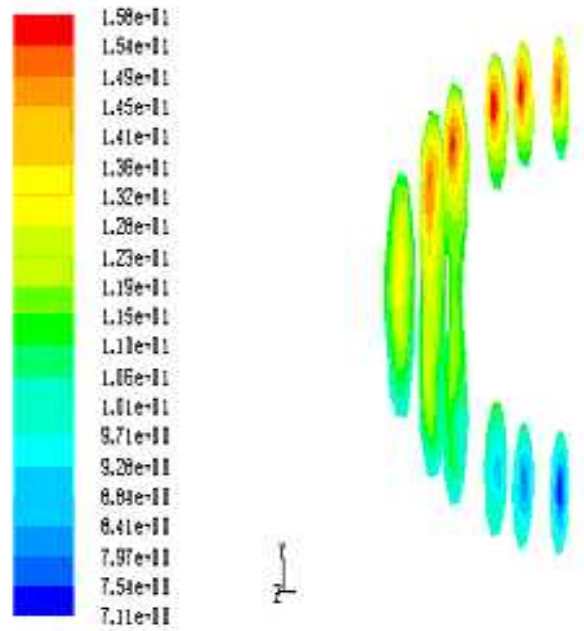


Fig. 3.43 Contour plot of turbulent intensity at different points in the bend for water velocity (m/s): 0.933, radius of curvature (m): 0.06

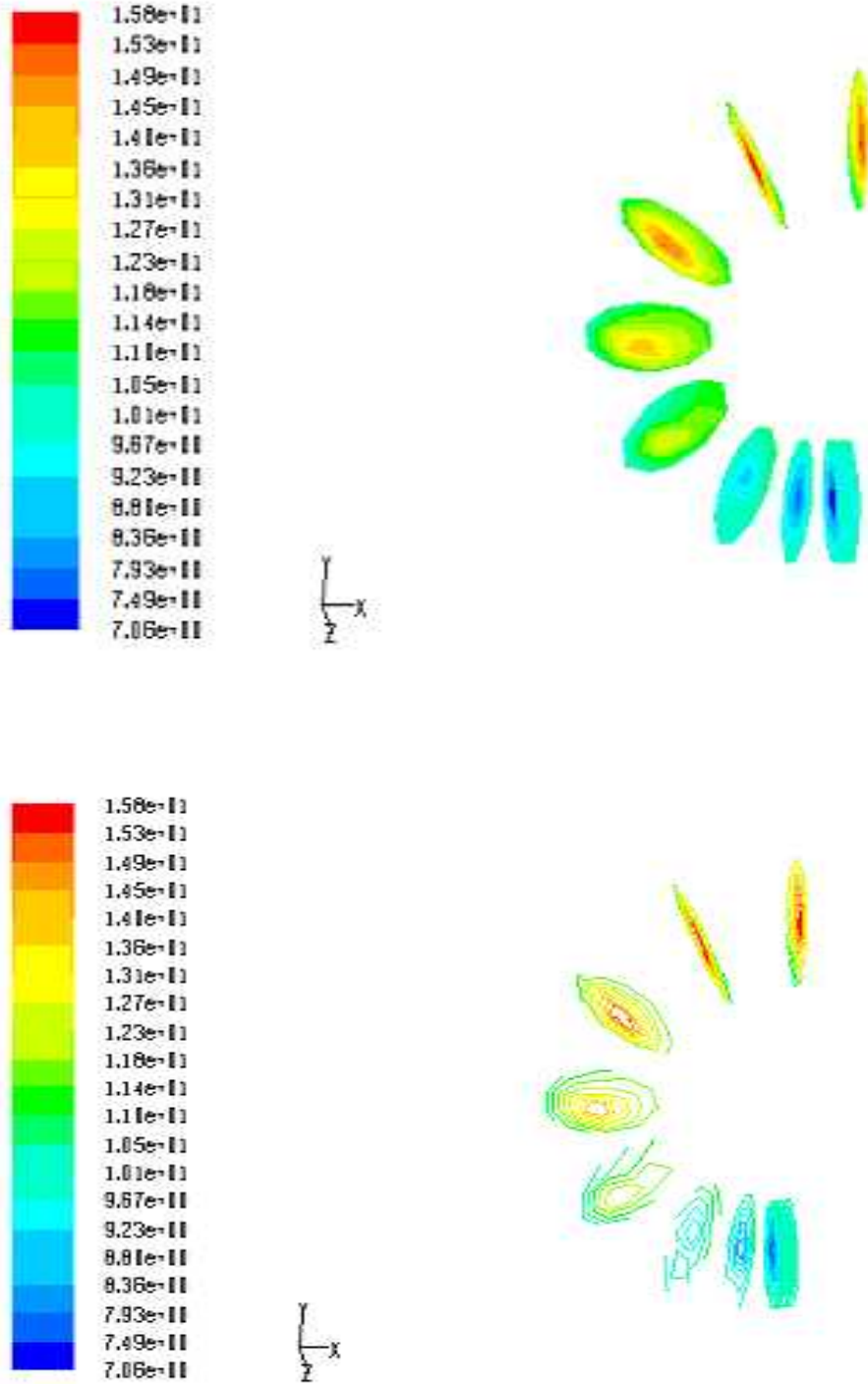


Fig. 3.44 Contour plot of turbulent intensity at angular coordinates in the bend for water velocity (m/s): 0.933, radius of curvature (m): 0.06

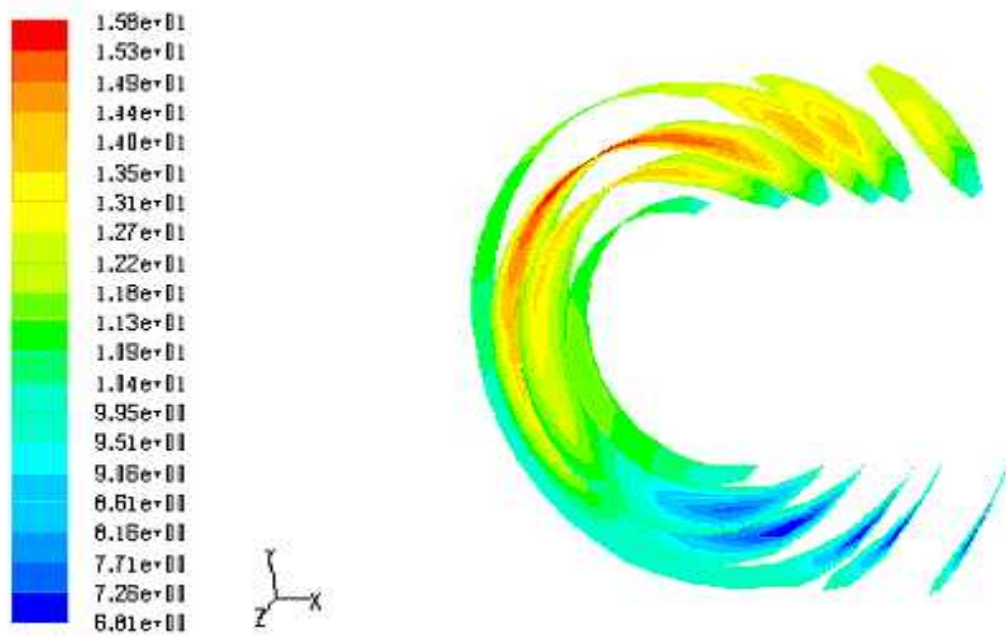


Fig. 3.45 Contour plot of turbulent intensity at radial coordinates in the bend for water velocity (m/s): 0.933, radius of curvature (m): 0.06

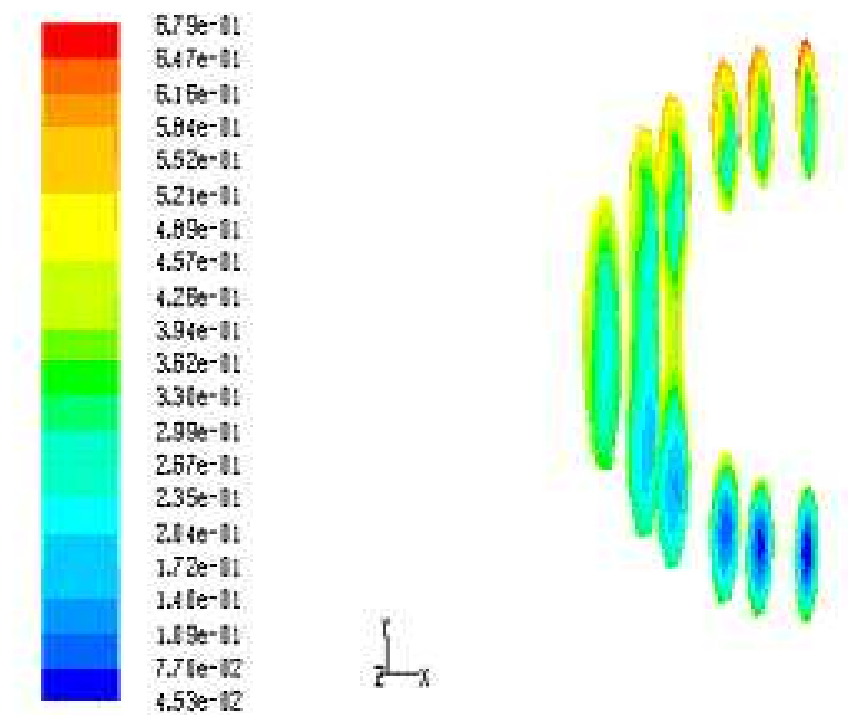


Fig. 3.46 Contour plot of turbulent dissipation rate at different points in the bend for water velocity (m/s): 0.933, radius of curvature (m): 0.06

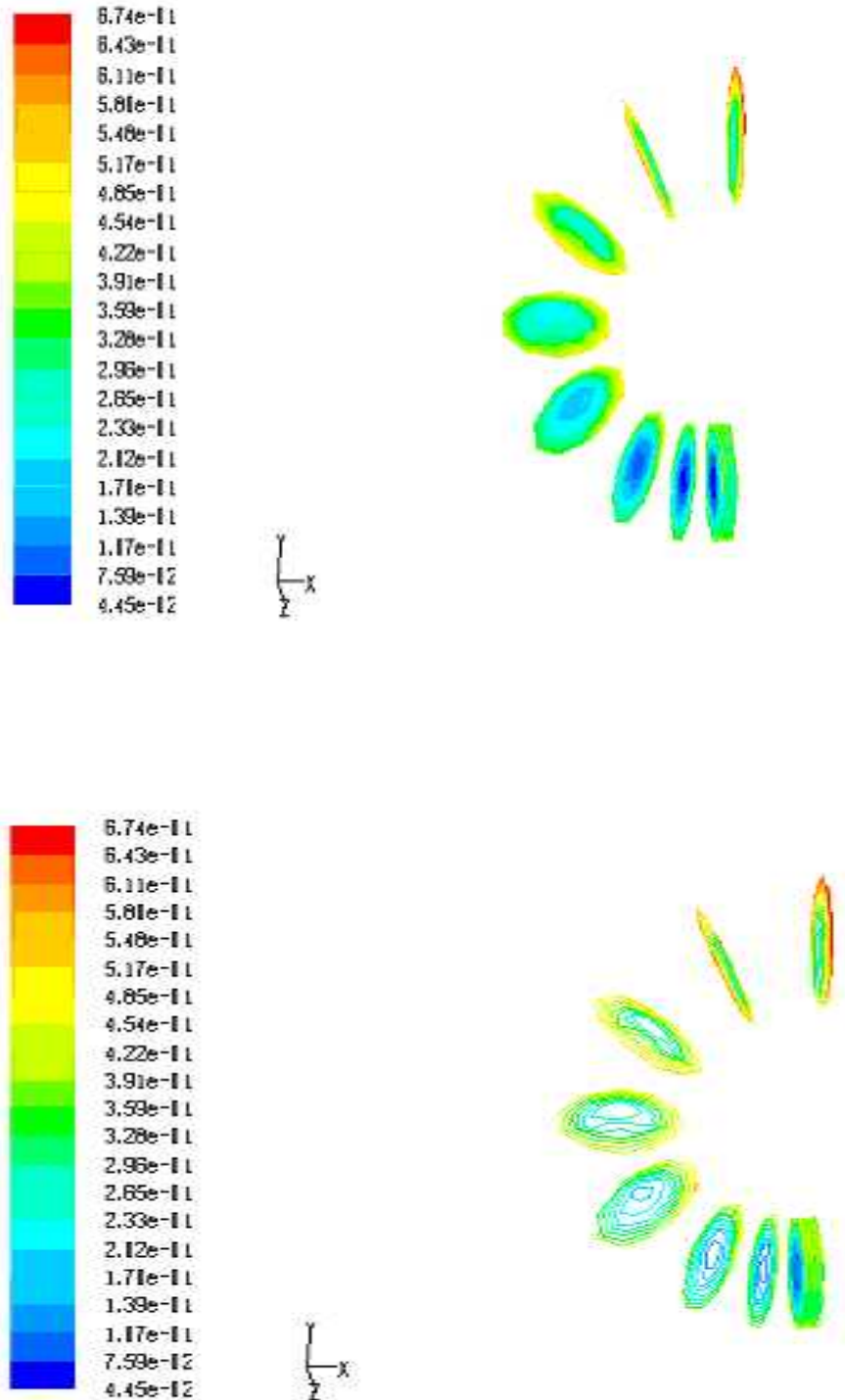


Fig. 3.47 Contour plot of turbulent dissipation rate at angular coordinates in the bend for water velocity (m/s): 0.933, radius of curvature (m): 0.06

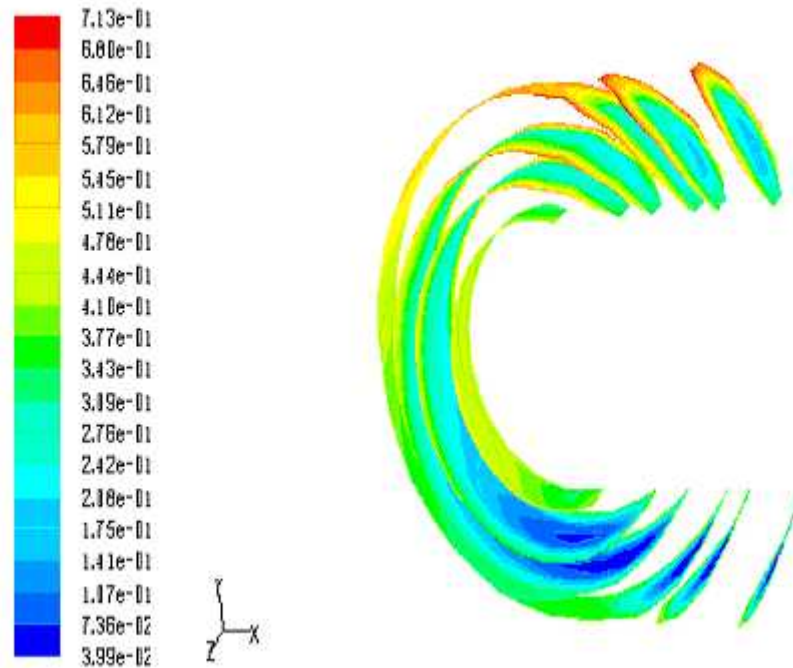


Fig. 3.48 Contour plot of turbulent dissipation rate at radial coordinates in the bend for water velocity (m/s): 0.933, radius of curvature (m): 0.06

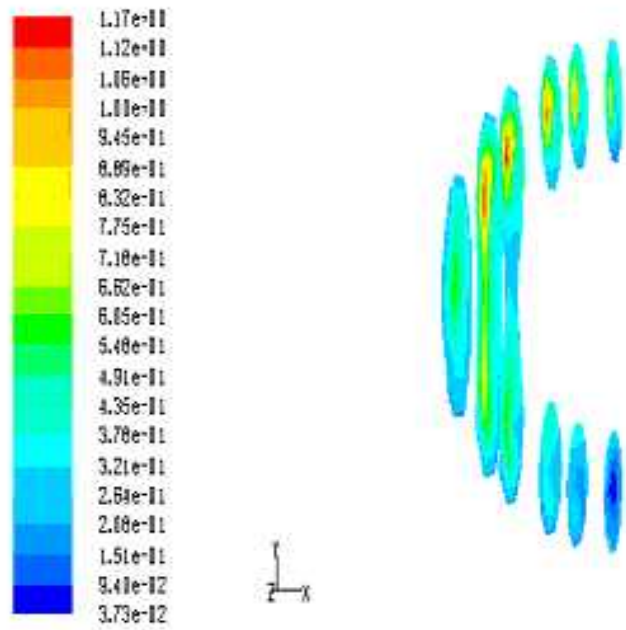


Fig. 3.49 Contour plot of production of k at different points in the bend for water velocity (m/s): 0.933, radius of curvature (m): 0.06

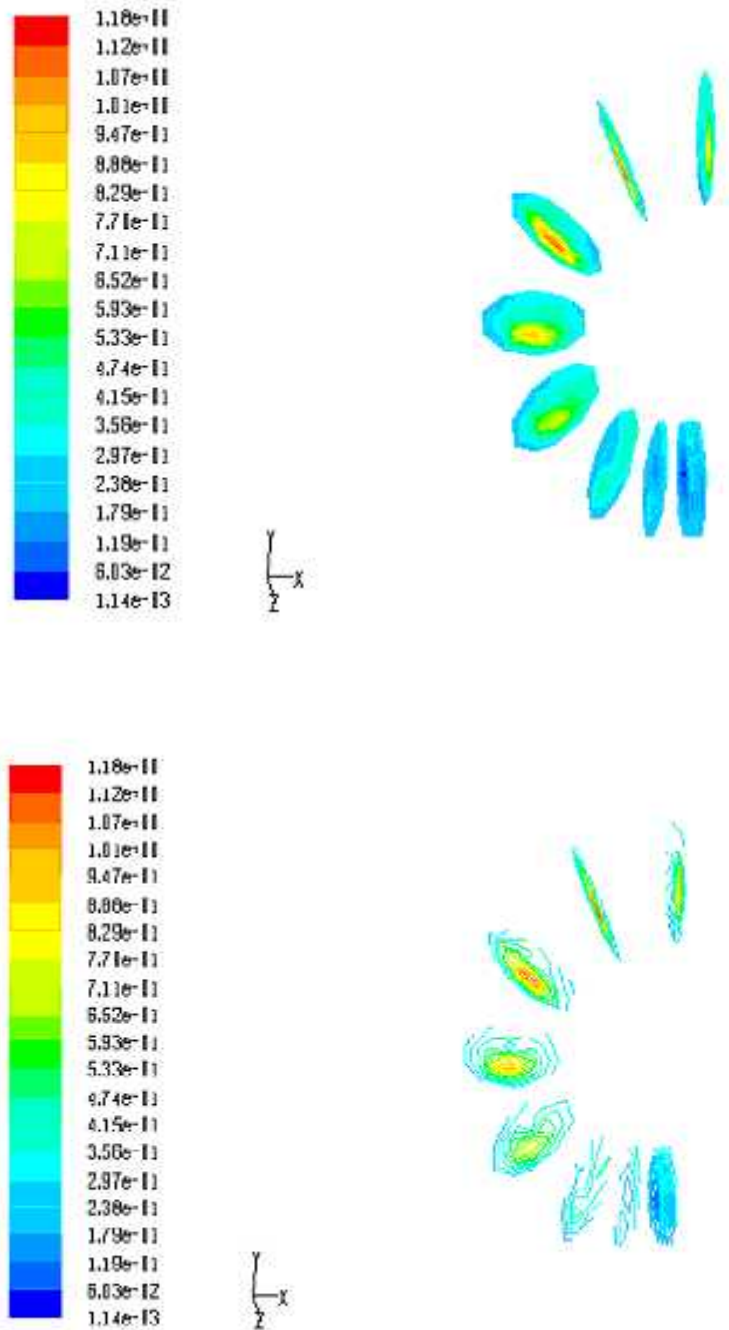


Fig. 3.50 Contour plot of production of k at angular coordinates in the bend for water velocity (m/s): 0.933, radius of curvature (m): 0.06

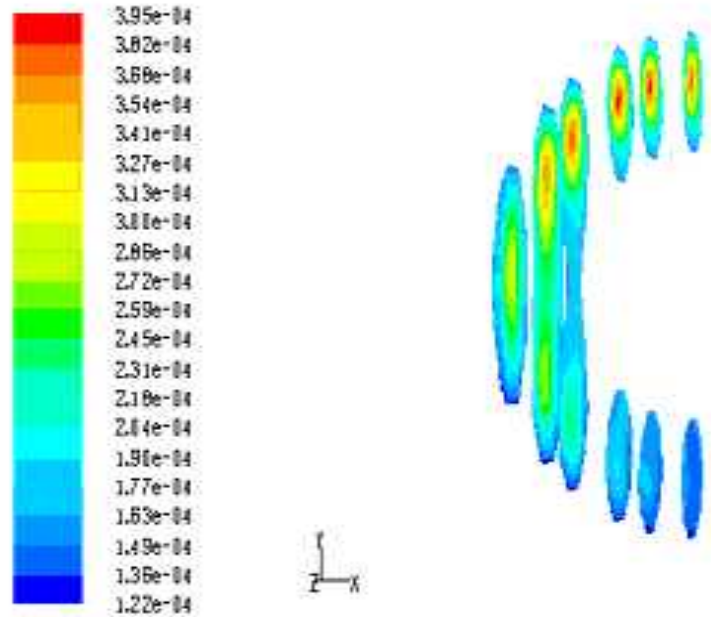


Fig. 3.51 Contour plot of turbulent viscosity at different points in the bend for water velocity (m/s): 0.933, radius of curvature (m): 0.06

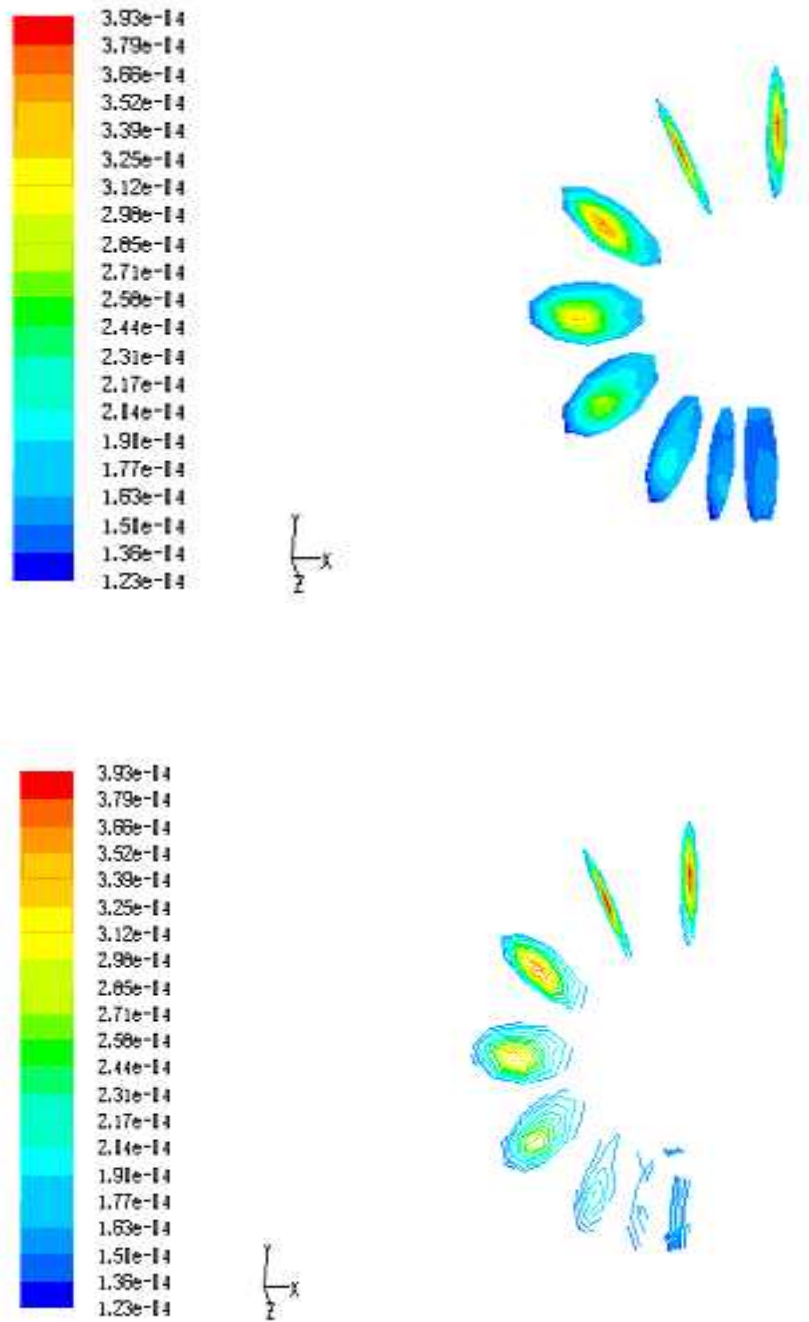


Fig. 3.52 Contour plot of turbulent viscosity at angular coordinates in the bend for water velocity (m/s): 0.933, radius of curvature (m): 0.06

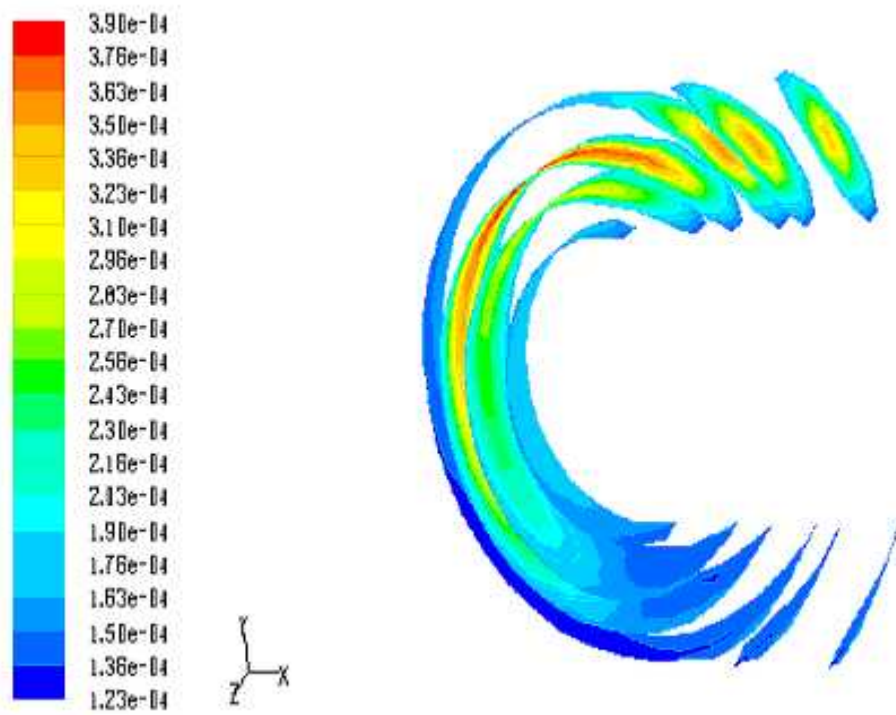


Fig. 3.53 Contour plot of turbulent viscosity at radial coordinates in the bend for water velocity (m/s): 0.933, radius of curvature (m): 0.06

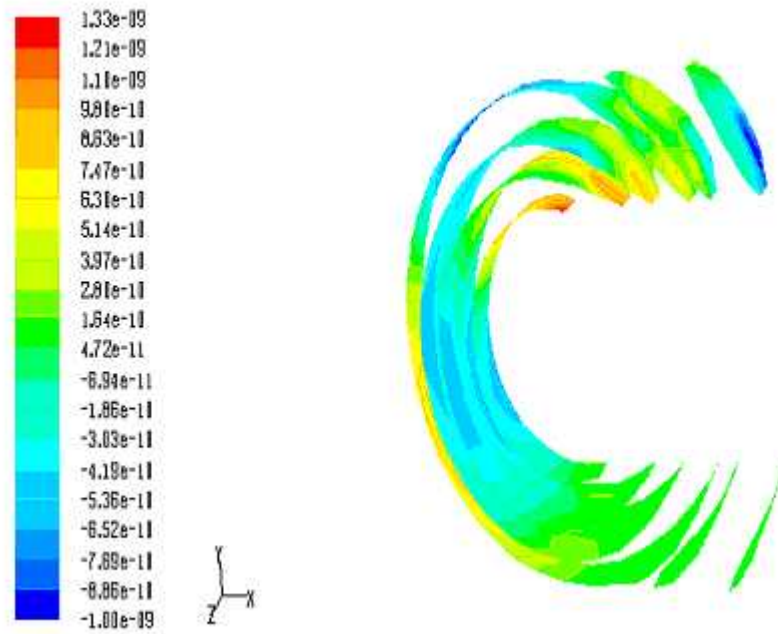


Fig. 3.54 Contour plot of mass imbalance at radial coordinates in the bend for water velocity (m/s): 0.933, radius of curvature (m): 0.06

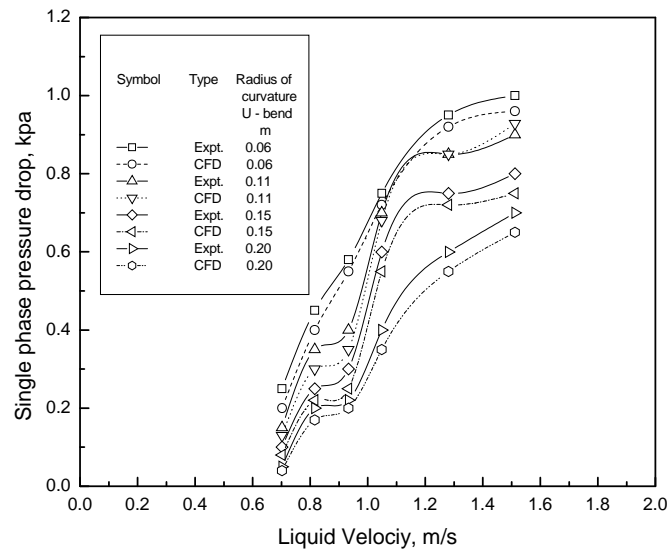
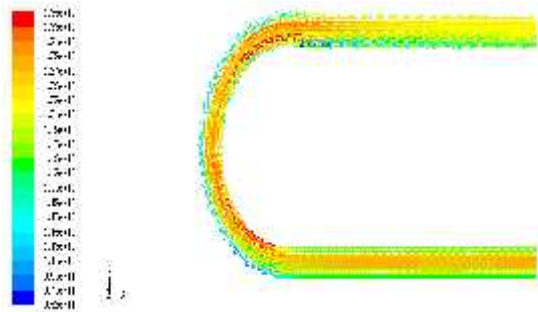
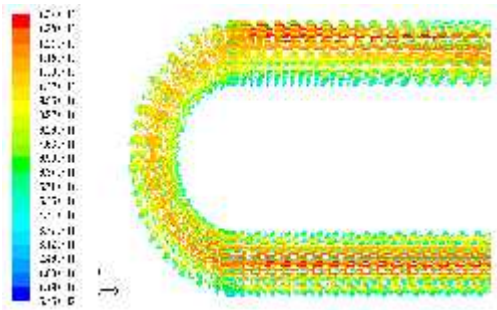
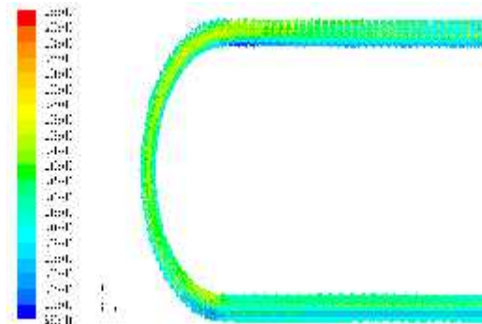
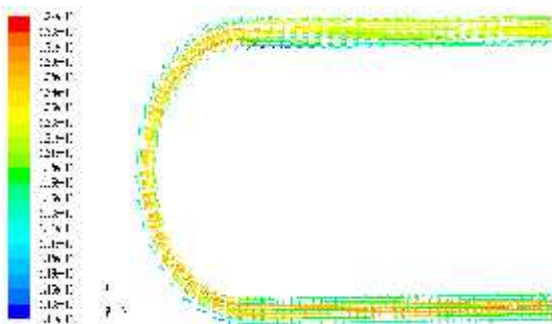


Fig. 3.55 Comparison plot of the experimental data and CFD modeling for water flow



(a) Radius of curvature 0.06 m

(b) Radius of curvatures 0.11 m



(c) Radius of curvature 0.15 m

(d) Radius of curvatures 0.2 m

Fig. 3.56 Contour plot of velocity vector for U-bend, water velocity (m/s): 0.933, gas velocity (m/s): 1.365, gas fraction, Γ_g : 0.59

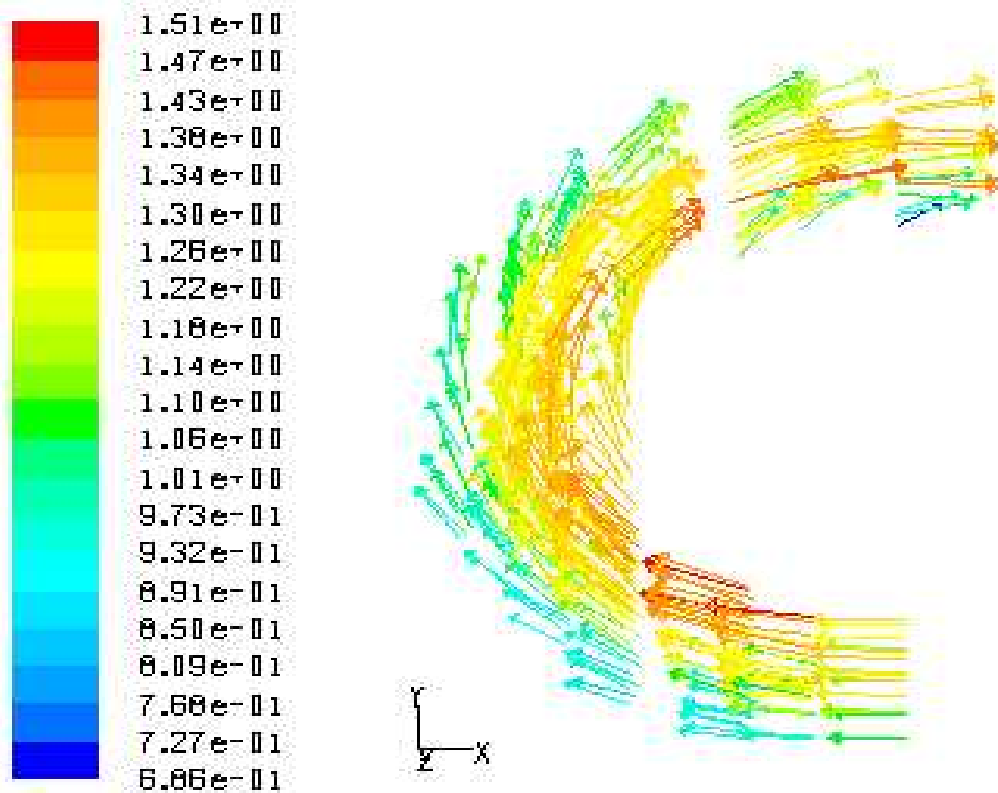


Fig. 3.57a Contour plot of velocity vector for air-water mixture at different points in the bend,

radius of curvature 0.06 m, water velocity (m/s): 0.933,
 gas velocity (m/s): 1.365, gas fraction, Γ_g : 0.5

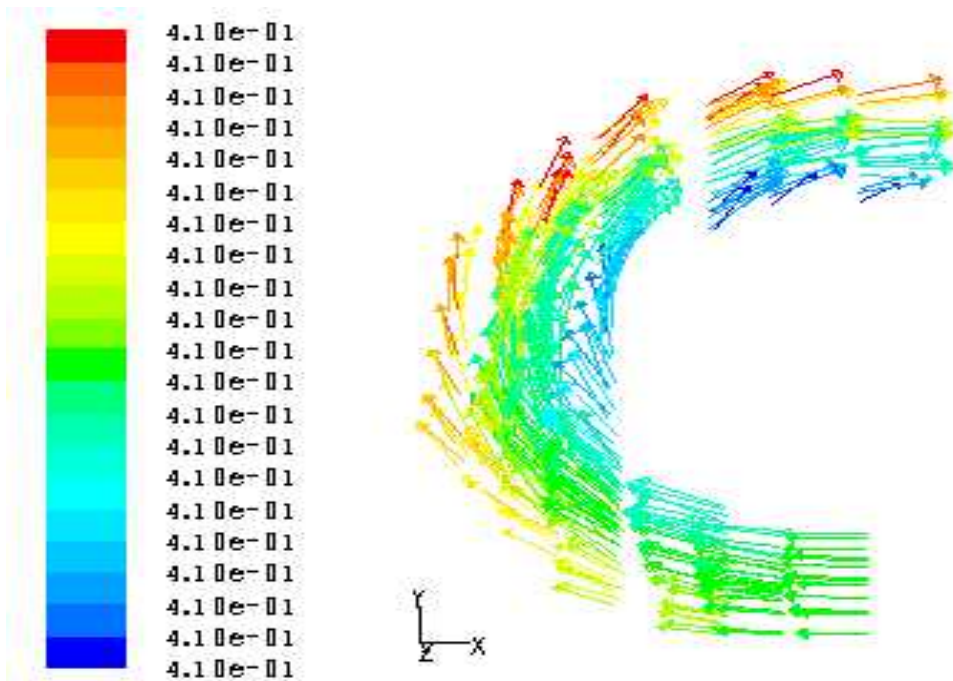


Fig. 3.57b Contour plot of velocity vector for water in the mixture at different points in the bend,
radius of curvature 0.06 m, water velocity (m/s): 0.933,
gas velocity (m/s): 1.365, gas fraction, r_g : 0.59

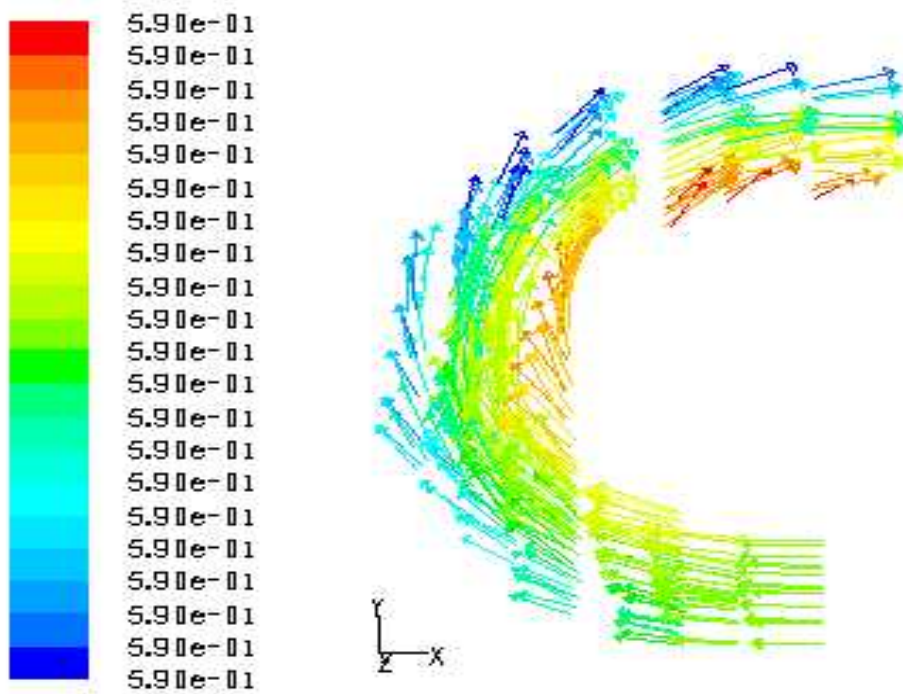


Fig. 3.57c Contour plot of velocity vector for air in the mixture at different points in the bend,
radius of curvature 0.06 m, water velocity (m/s): 0.933,

gas velocity (m/s): 1.365, gas fraction, r_g : 0.59

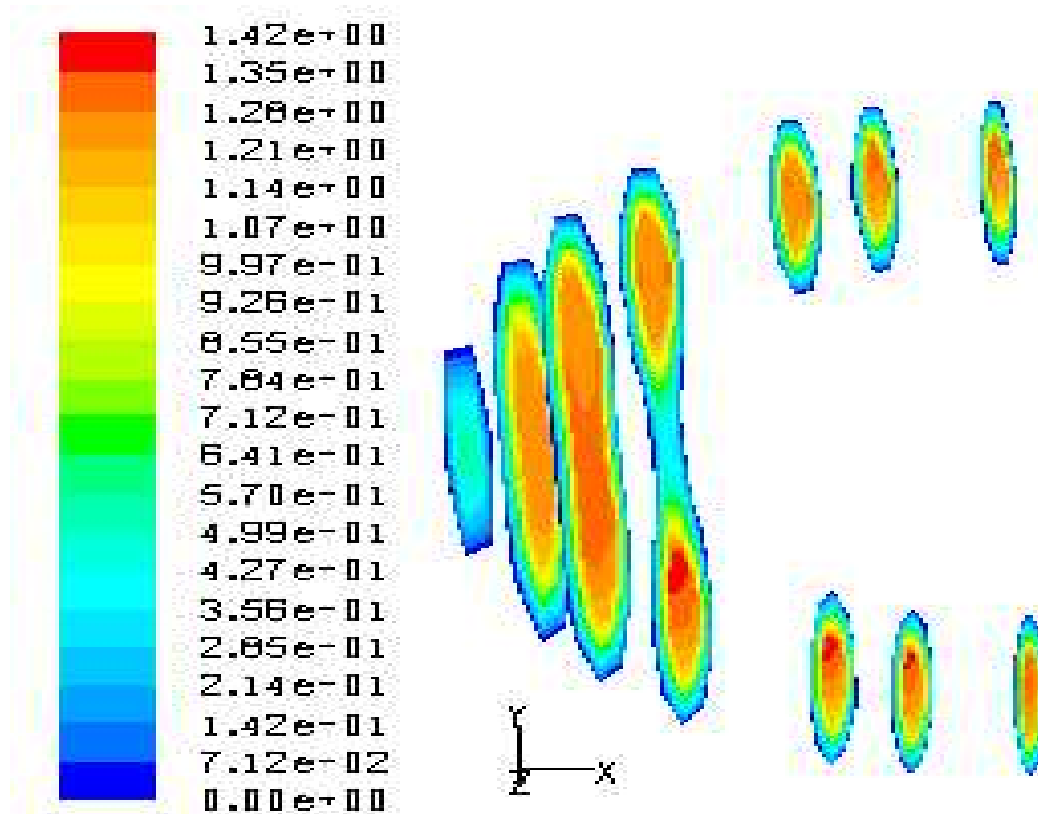


Fig. 3.58 Contour plot of velocity, mixture for U-bend at radius of curvature 0.06 m at different points in the bend,

water velocity (m/s): 0.933, gas velocity (m/s): 1.365, gas fraction, r_g : 0.59

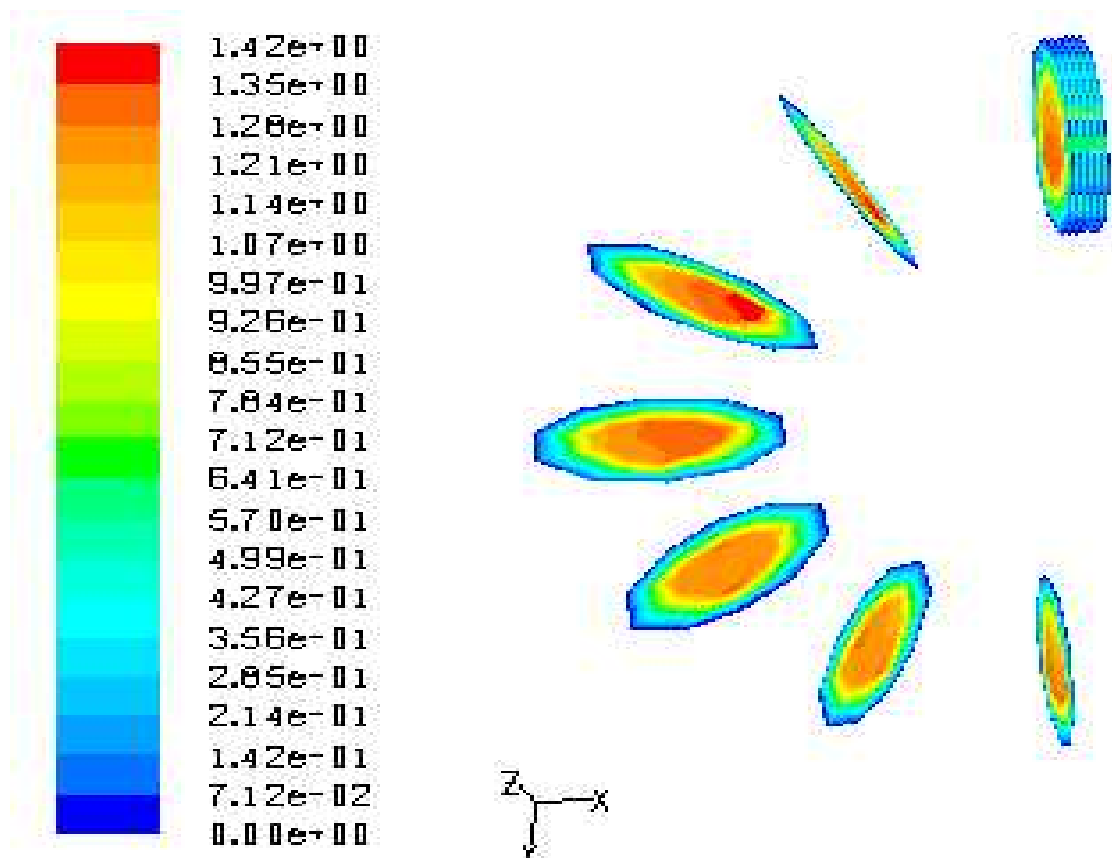
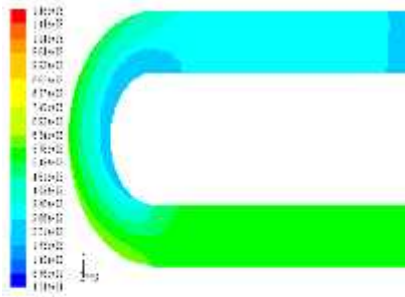
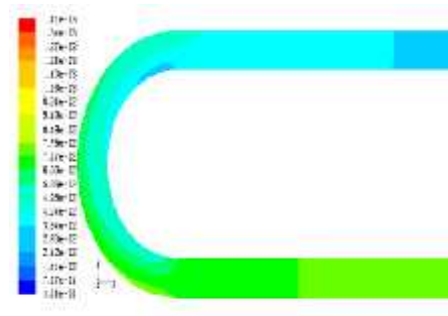


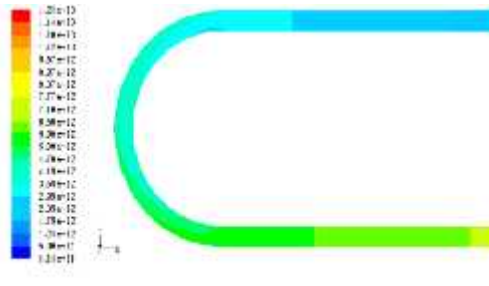
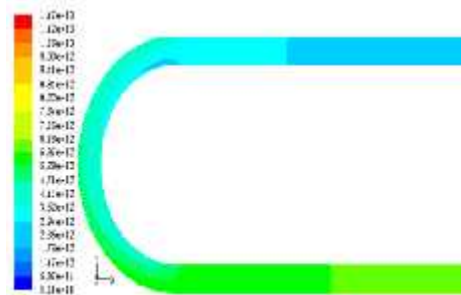
Fig. 3.59 Contour plot of velocity, mixture for U-bend at radius of curvature 0.06 m at different angular points in the bend, water velocity (m/s): 0.933, gas velocity(m/s): 1.365, gas fraction, r_g : 0.59



a) Radius of curvature 0.06 m



(b) Radius of curvatures 0.11 m



(c) Radius of curvature 0.15 m

(d) Radius of curvatures 0.2 m

Fig. 3.60 Contour plot of static pressure for U-bends,
 water velocity (m/s): 0.933, gas velocity (m/s): 1.365, gas fraction, r_g : 0.59

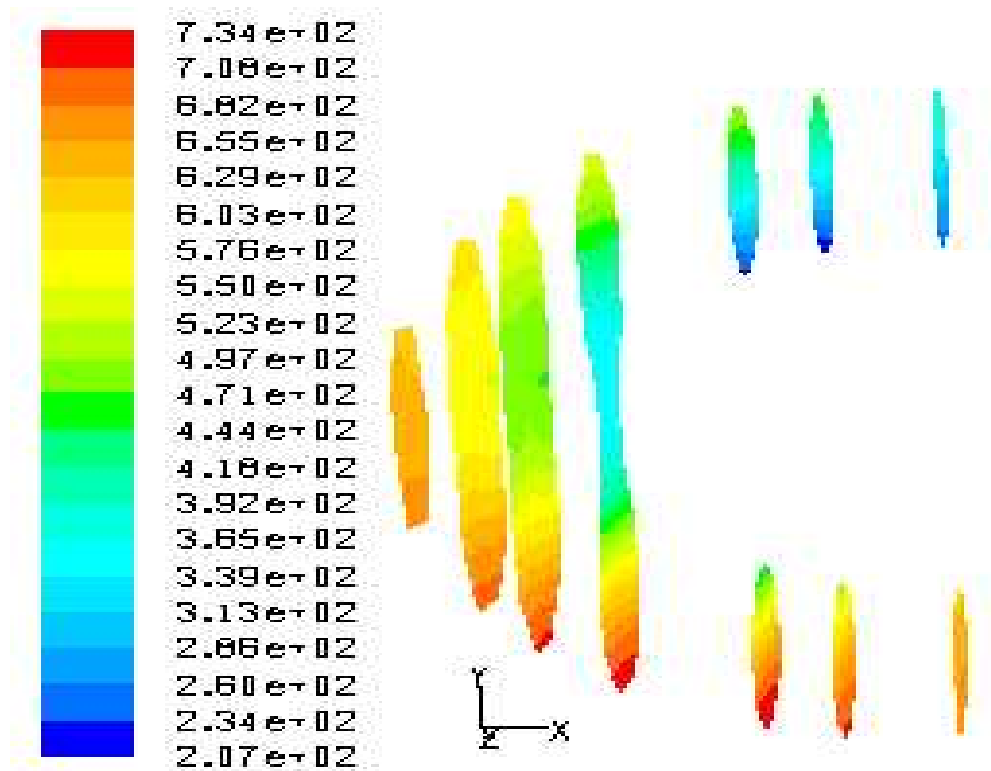


Fig. 3.61 Contour plot of static pressure, mixture for U – bend at radius
 of curvature 0.06 m at different points in the bend,
 water velocity (m/s):0.933, Gas velocity (m/s):1.365, gas fraction, r_g : 0.59

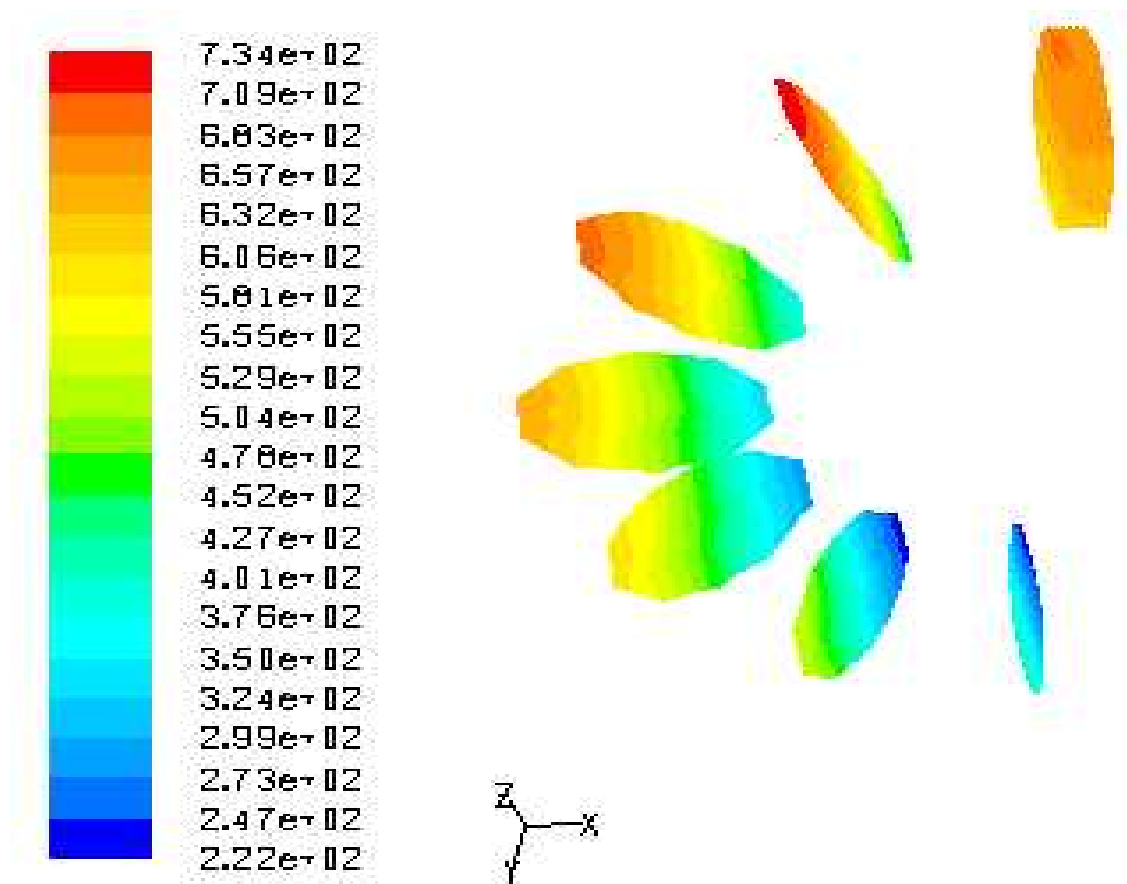
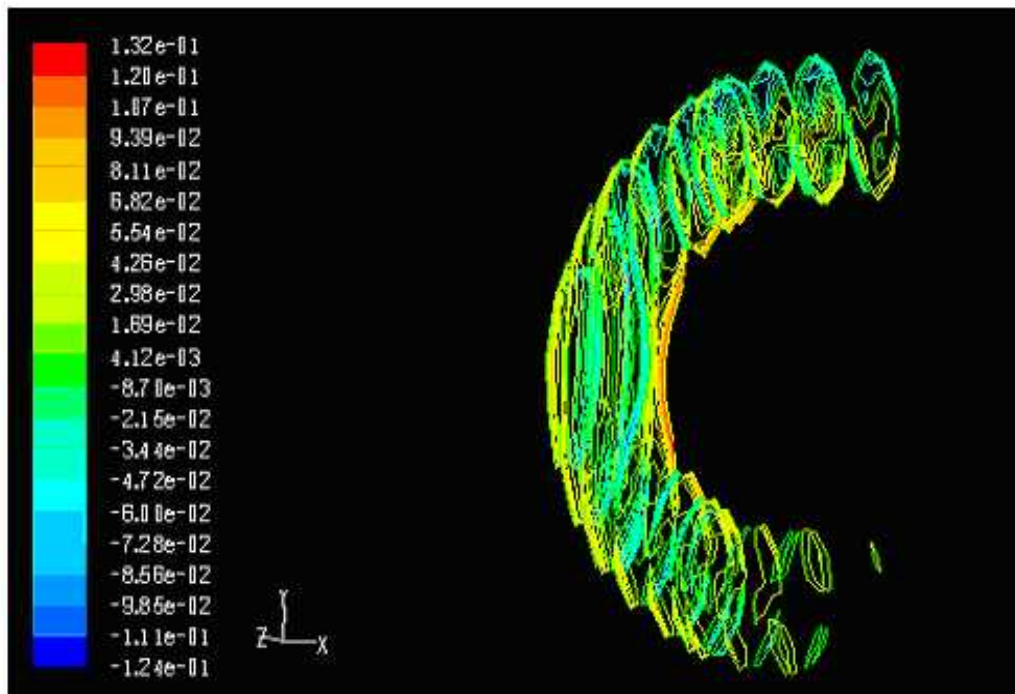


Fig. 3.62 Contour plot of static pressure, mixture for U – bend at radius of curvature 0.06 m at different angular points in the bend, water velocity (m/s): 0.933, gas velocity (m/s): 1.365, Gas fraction, r_g : 0.59



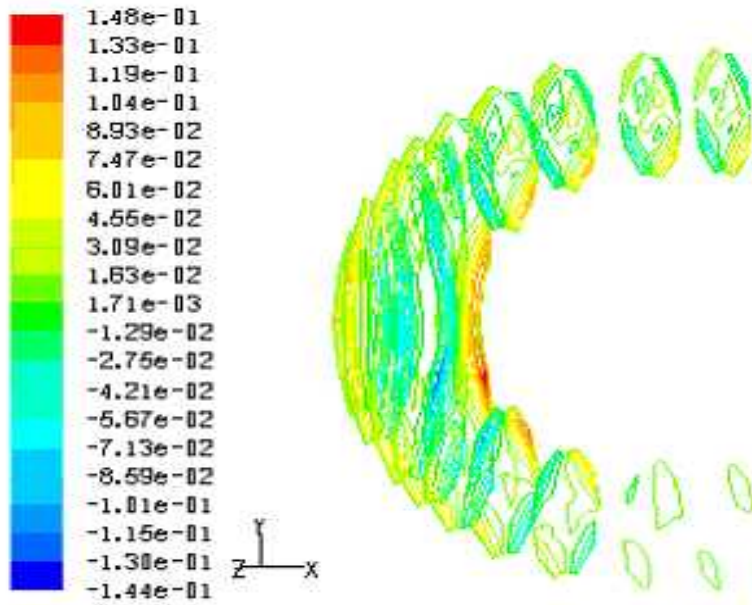
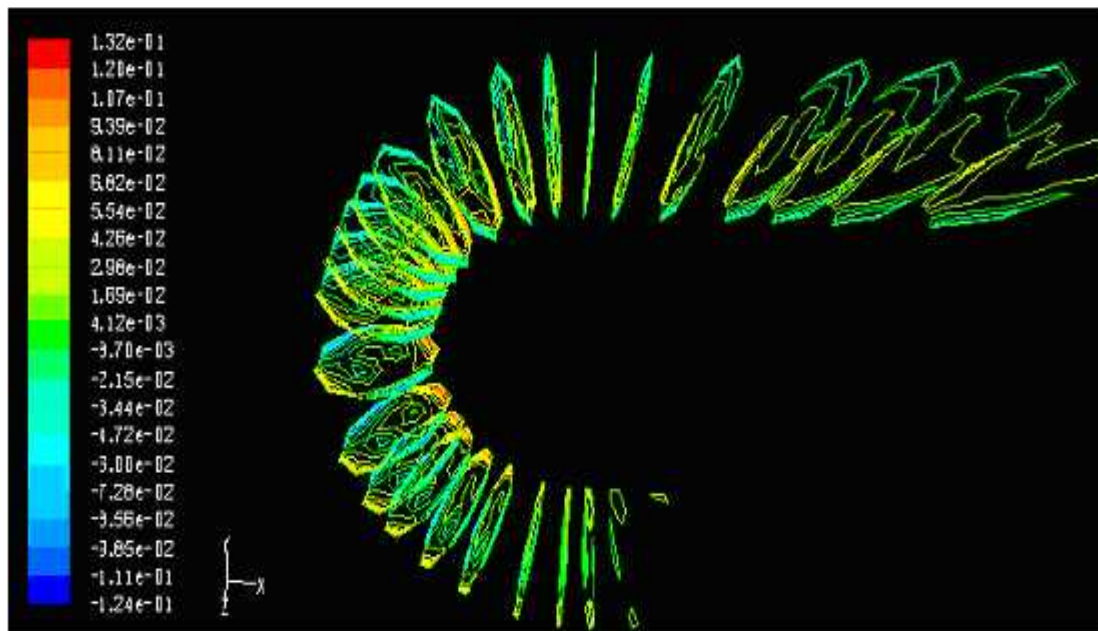


Fig. 3.63 Contour velocity plot inside the different points of U-bend, water velocity: 0.933 m/s, gas velocity (m/s): 1.365, Gas fraction, r_g : 0.59, radius of curvature: 0.06 m



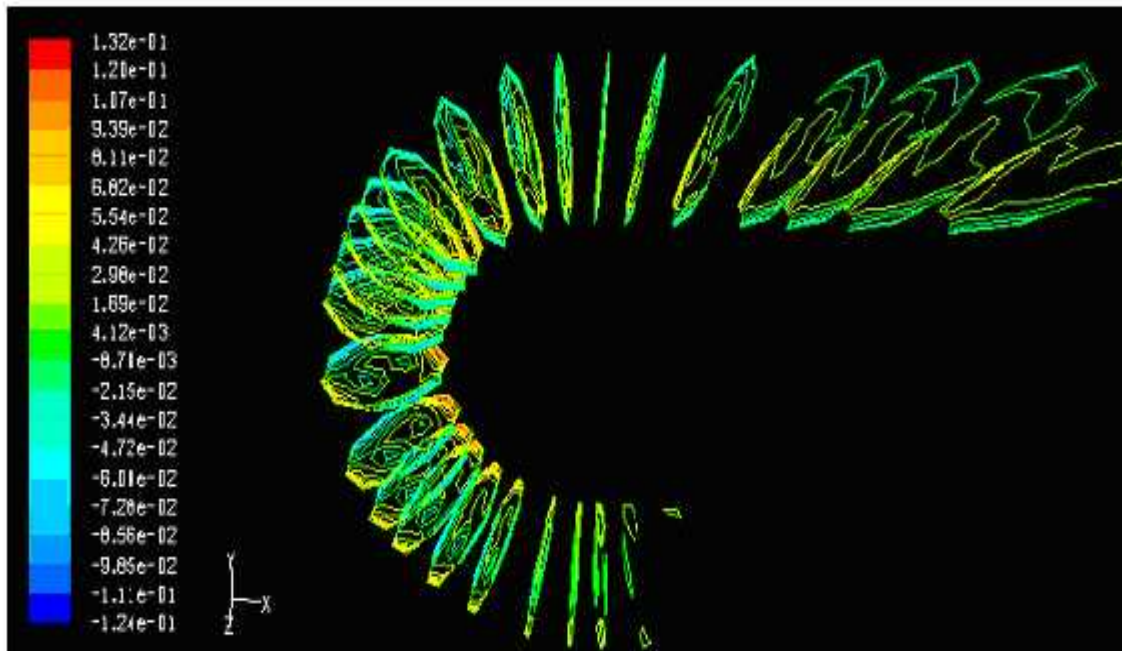


Fig. 3.64 Contour velocity plot inside the different angular points of U-bend
water velocity: 0.933 m/s, gas velocity (m/s): 1.365, Gas fraction, r_g : 0.59, radius of
curvature: 0.06 m

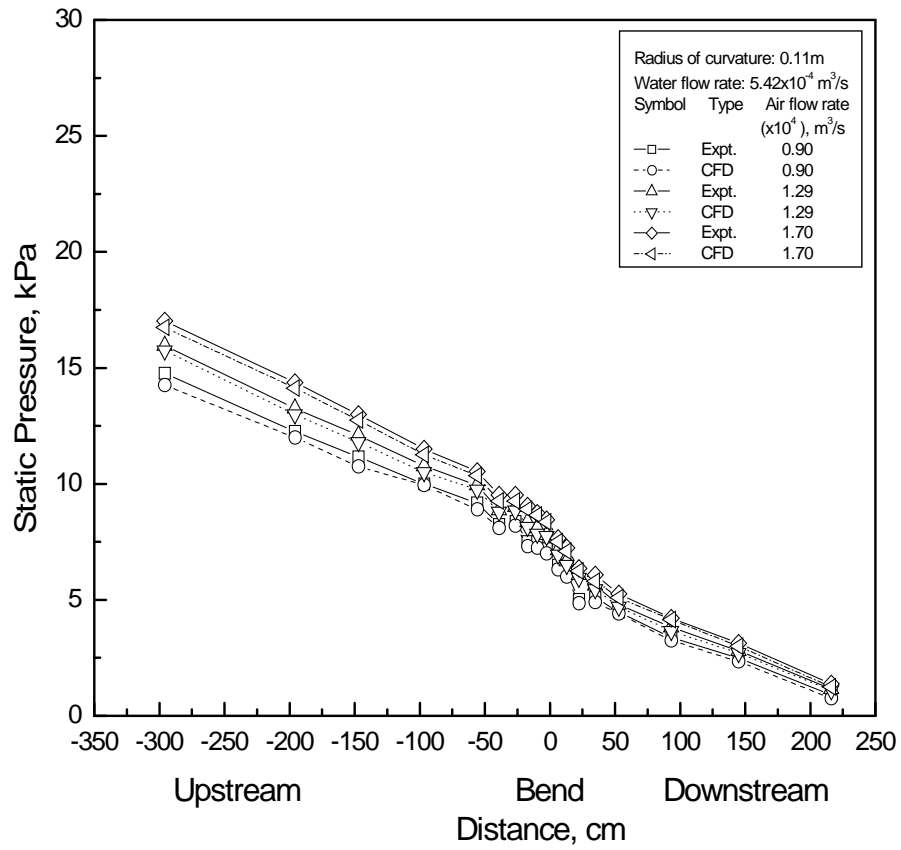


Fig. 3.65 Experimental and CFD static pressure distribution

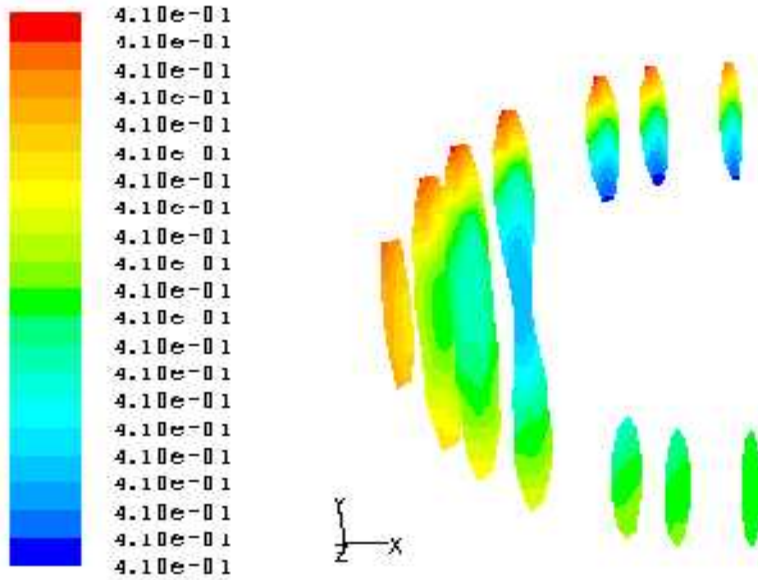
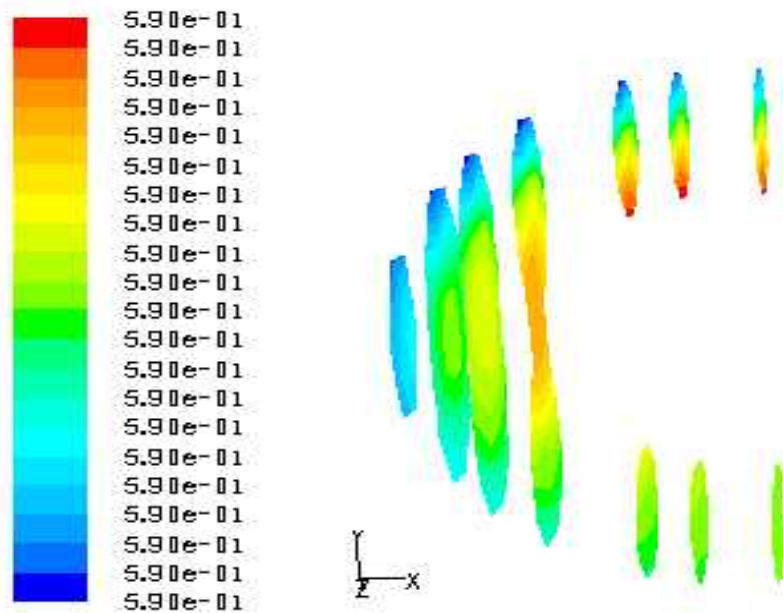


Fig. 3.66a Contour plot of volume fraction for water at different points in the bend, radius of curvature 0.06 m, water velocity (m/s): 0.933, gas velocity (m/s): 1.365, gas fraction, $r_g : 0.59$



(b) air

Fig. 3.66b Contour plot of volume fraction for air at different points in the bend, radius of curvature 0.06 m, water velocity (m/s): 0.933, gas velocity (m/s): 1.365, gas fraction, $r_g : 0.59$

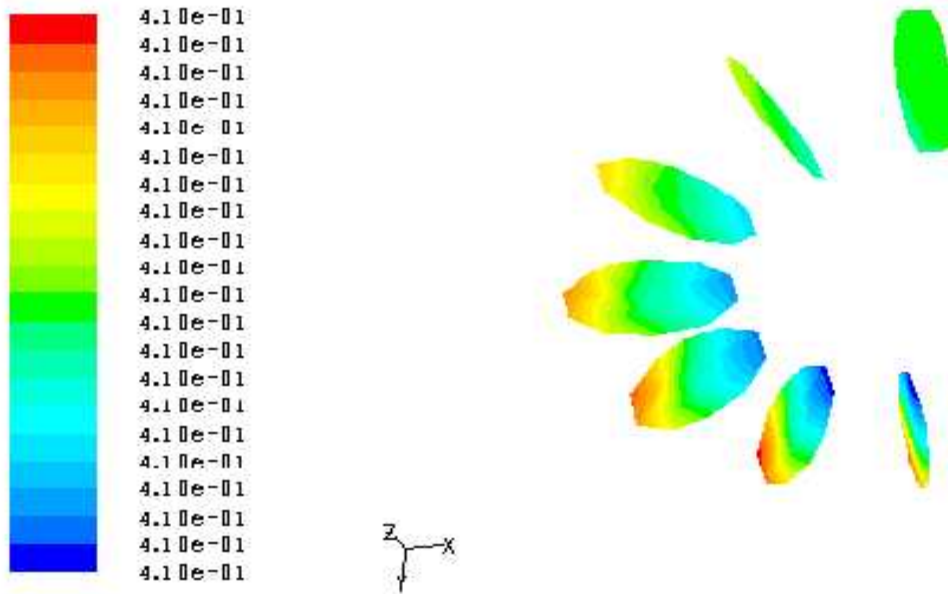


Fig. 3.67a Contour plot of volume fraction for water at different angular points in the bend, radius of curvature 0.06 m, water velocity (m/s): 0.933, gas velocity (m/s): 1.365, gas fraction, r_g : 0.59

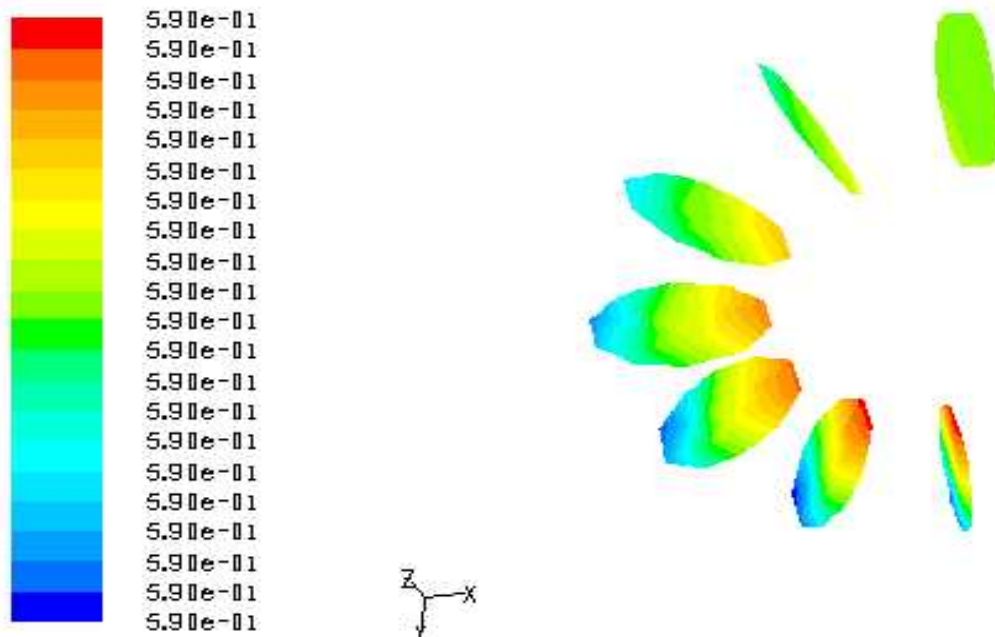


Fig. 3.67b Contour plot of volume fraction for air at angular coordinates in the bend, radius of curvature 0.06 m, water velocity (m/s): 0.933, gas velocity (m/s): 1.365, gas fraction, r_g : 0.59

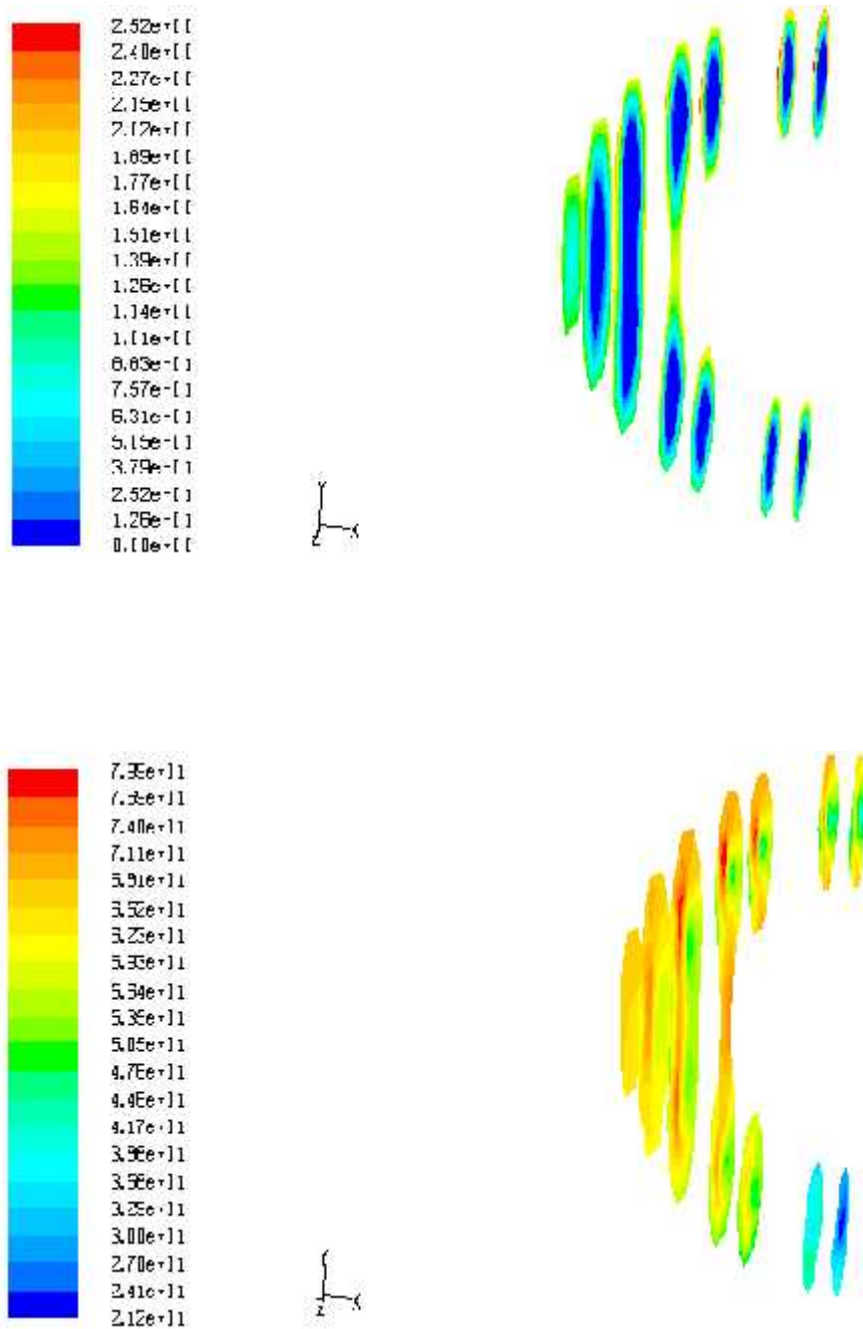


Fig. 3.68 Contour plot of shear stress and shear strain for U-bend, radius of curvature 0.06 m at different points in the bend, water velocity (m/s): 0.933, Gas velocity (m/s): 1.365, Gas fraction, Γ_g : 0.59

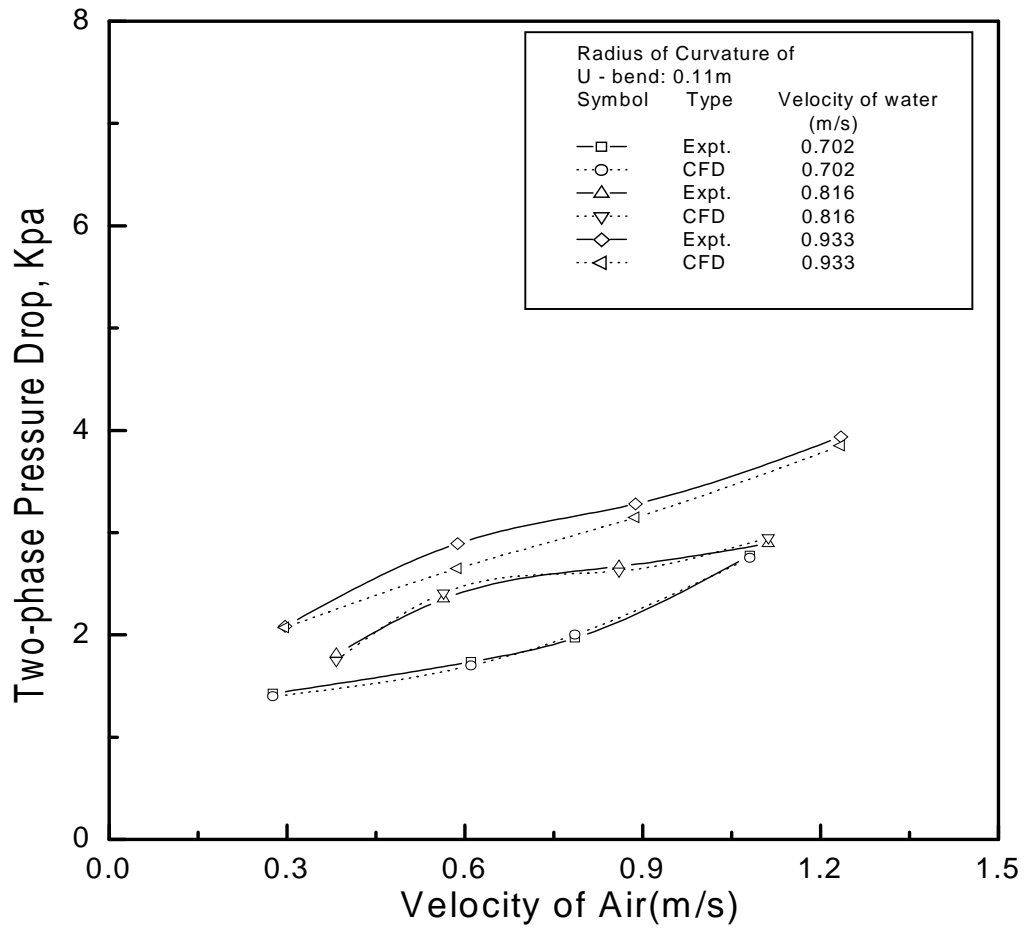


Fig. 3.69 Comparison plot of the experimental data and CFD modeling for two-phase air-water flow

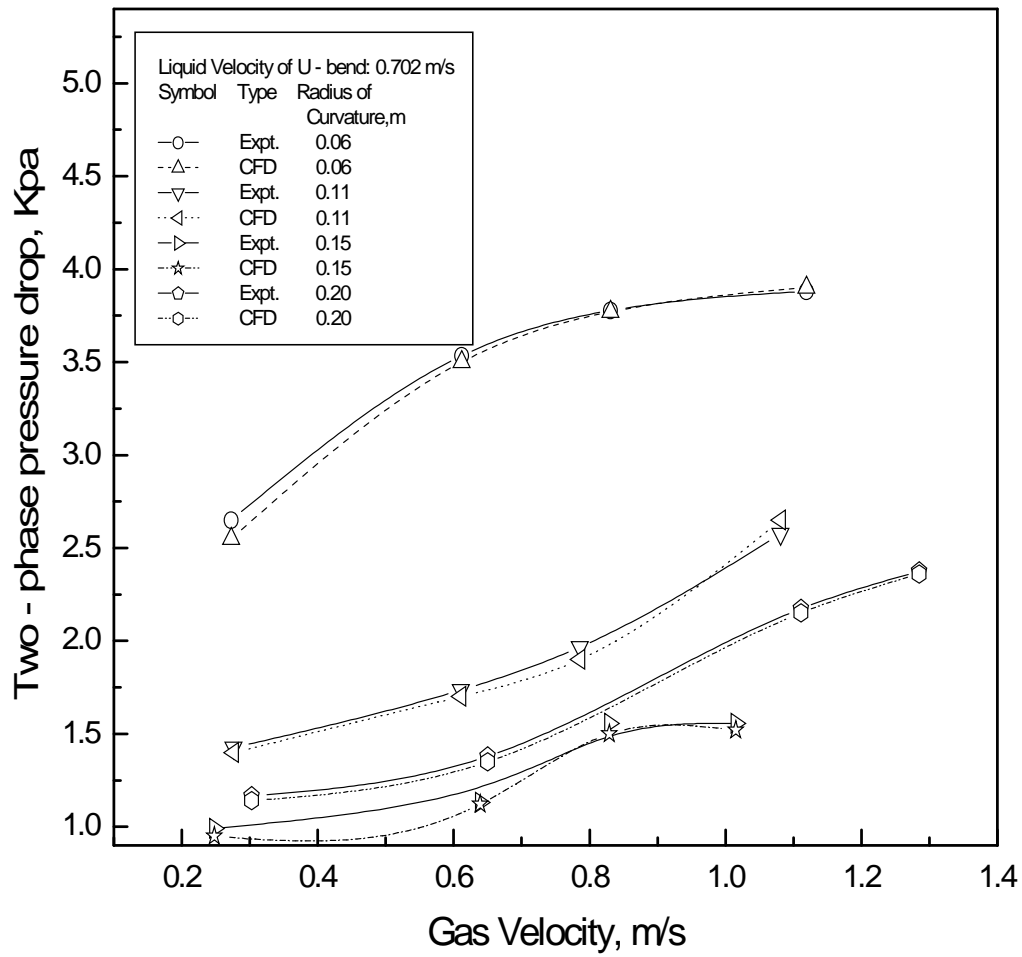


Fig. 3.70 Comparison plot of the experimental data and CFD modeling of two-phase air-water flow

Table 3.1 Dimensions of the U-bends used in the experiments

Sl. No.	Radius of curvature, m	Length of the bend, m
1.	0.06	0.1885
2.	0.11	0.3456
3.	0.15	0.4712
4.	0.20	0.6283

Table 3.2 Range of variables used in the experiments

U-bends	
Measurement Type	Range
Diameter (m)	0.01905
Radius of curvature (m)	0.06 R_b 0.20
Liquid and Flow properties	
Water Flow Rate $Q_l \times 10^{-4} (\text{m}^3/\text{s})$	2.000 to 4.65
Air Flow Rate $Q_g \times 10^{-5} (\text{m}^3/\text{s})$	5.936 to 56.1189

Table 3.3 Comparison of the pressure drop across the U-bends, Experimental and CFD analysis data

Sl. No.	Water velocity V_1 m/s	Pressure drop, experimental $\Delta P_{b,Expt.}$ kPa	Pressure drop, CFD $\Delta P_{b,CFD}$ kPa
Radius of curvature of U-bend: 0.06m			
1	0.702	0.25	0.2
2	0.816	0.45	0.4
3	0.933	0.58	0.5
4	1.049	0.75	0.72
5	1.281	0.95	0.9
6	1.512	1.00	0.96
Radius of curvature of U-bend: 0.11m			
7	0.702	0.15	0.13
8	0.816	0.35	0.30
9	0.933	0.40	0.35
10	1.049	0.70	0.68
11	1.281	0.85	0.80
12	1.512	0.90	0.88
Radius of curvature of U-bend: 0.15m			
13	0.702	0.10	0.08
14	0.816	0.25	0.22
15	0.933	0.30	0.25
16	1.049	0.60	0.50
17	1.281	0.75	0.70
18	1.512	0.80	0.75
Radius of curvature of U-bend: 0.2m			
19	0.702	0.05	0.04
20	0.816	0.20	0.17
21	0.933	0.22	0.20
22	1.049	0.40	0.35
23	1.281	0.60	0.55
24	1.512	0.70	0.65

Table 3.4 Comparison of the two-phase pressure drop across the U-bends, Experimental and CFD analysis

Sl. No.	Air velocity V_g m/s	Two-phase pressure drop $\Delta P_{tplb, Expt.}$ kPa	Two-phase pressure drop $\Delta P_{tplb, CFD}$ kPa
Water velocity, V_1 : 0.702 m/s Radius of crvature: 0.06m			
1	0.273	2.651	2.55
2	0.612	3.535	3.5
3	0.831	3.777	3.77
4	1.119	3.882	3.9
Water velocity, V_1 : 0.702 m/s Radius of curvature: 0.11m			
5	0.276	1.427	1.4
6	0.611	1.735	1.7
7	0.786	1.967	1.9
8	1.081	2.577	2.65
Water velocity, V_1 : 0.702 m/s Radius of curvature: 0.15m			
9	0.248	0.99	0.95
10	0.639	0.131	1.12
11	0.829	1.555	1.5
12	1.015	1.555	1.52
Water velocity, V_1 : 0.702 m/s Radius of curvature: 0.2m			
13	0.303	1.166	1.14
14	0.65	1.379	1.35
15	1.111	2.174	2.15
16	1.285	2.374	2.36

Chapter 4

*Non-Newtonian fluid flow through piping components –
experimental investigation*

Experimental investigation have been carried out to evaluate the frictional pressure drop across different piping components such as orifices, gate and globe valves, elbows and bends in 0.0127 m piping components for non-Newtonian liquid flow. Empirical correlations have been developed for the prediction of the frictional pressure drop in terms of the various physical and dynamic variables of the system.

4.1 Introduction

Pipe fittings like valves, bends, elbows, tees, reducers, expander etc. are the integral part of any piping system. Flow through piping components is more complex than the straight pipes. The problem of determining the pressure losses in pipe fittings is important in design and analysis of the fluid machinery. Forcing a fluid through pipe fittings consumes energy detected by the drop in pressure across the fittings. The friction between the fluid and the fitting wall causes this pressure drop. The problem of predicting pressure losses in pipe fittings is much more uncertain than for the pipe because,

1. The mechanism of flow is not clearly defined. At least two types of losses are superposed – skin friction and loss due to change in flow direction, and
2. There are very few experimental data available in the literature.

Edwards et al. (1985) studied the frictional head loss of different fittings like 90° elbows, gate valves, square plug and circular plug globe valves, expansions and contractions, orifice plates in 2.54 cm and 5 cm pipeline for the flow of non-Newtonian liquids. They observed that the loss coefficient depends on the size of the pipe fittings. Das et al. (1991b) reported the experimental investigation of the pressure loss across different types of bends in the horizontal plane for non-Newtonian liquids. They

developed generalized correlation for pressure drop. Banerjee et al. (1994) studied the non-Newtonian liquid flow through gate and globe valves and developed empirical correlation for pressure drop. Turian et al. (1998) reported the frictional losses for the flow of non-Newtonian suspension of concentrated slurries of laterite and gypsum through 2.5 cm and 5 cm bends, fittings, valves and venture meters. They observed that the resistance coefficient for laminar flow was depends on the size of the fittings and inversely proportional to the Reynolds number. Telis-Romero (2000) studied the friction loss coefficients for laminar flow of xanthan gum solutions through full and half opening ball and angle vales, 90° elbows. They developed empirical correlations for each fitting. Polizelli et al. (2003) studied the pressure drop for 2.54 cm, 38.1 cm and 50.8 cm pipe fittings and valves for laminar and turbulent flow of aqueous solutions of sucrose and xanthan gum. They measured the friction losses in fully and partially open butterfly and plug valves, bends and unions and the loss coefficients were correlated as a function of Reynolds number by two-k method. Bandala-Rocha et al. (2005) measured the pressure drop across various pipe fittings for the flow of non-Newtonian liquids. Since the design of piping and pumping systems for chemical, petroleum refinery and petrochemical, pharmaceutical and food processing industries requires knowledge of the pressure drop due to flow in straight segments and through valves and fittings. The fluid often behaves as non-Newtonian in nature in these industries. However, data or equations for pressure drops through pipe fittings are meager. Since most non-Newtonian liquids are highly viscous in nature and the laminar flow is of greatest practical interest (Das et al., 1989). The present study aims at generating experimental data, which may be used to provide

numerical correlations to predict pressure, drop through different pipe fittings for laminar flow of non-Newtonian liquids.

4.2 The experimental setup

The schematic diagram of the experimental setup consists of elbow is shown in Fig. 4.1. It consists of a liquid storage tank (0.45 m^3), test section, control and measuring systems for flow rates, pressure and other accessories. The test section consists of a horizontal upstream straight tube of 4.5 m length, a test section and a horizontal downstream straight tube of 3 m length. The reason for having long horizontal upstream and downstream portions before and after the test section was to achieve fully developed flow conditions to facilitate the measurement of pressure across the test section. The test section was connected to the upstream and downstream portions with the help of flanges. The entrance and exit lengths were 2.0 m and 1.4 m respectively, which were more than 50 pipe diameters to ensure fully developed flow. Before the test section, a 0.5 m length Perspex tube of the same diameter was incorporated in the system for flow visualization. The rest of the test section was fabricated from mild steel. The test section was fitted horizontally with the help of a leveling gauge. It was provided with pressure taps (piezometric ring) at different points in the upstream and downstream sections of the pipe. Different types of pipe fittings have been used and their dimensions are given in Table 4.1. The elbows and orifices used were specially manufactured in order to ensure uniform internal diameter, constant curvature and roundness. The gate and globe valves used in the experiments are made of steel used in petroleum, petrochemical and allied industries and they satisfy the Indian standard IS: 10605-1983 and IS : 11335-1984 respectively.

The experimental liquids were dilute solutions of SCMC (sodium salt of carboxy methyl cellulose, high viscous grade, Loba Chemie Pvt. Ltd., Bombay, India). The test liquids were prepared by dissolving the required amount of SCMC in tap water and stirring until a homogeneous solution was obtained and kept for about 15 h for ageing. Adding trace amounts of formaline prevented biological degradation. A cooling coil incorporated in the liquid storage tank controlled the liquid temperature. The liquid and air temperature used were closed to the atmospheric temperature, $31 \pm 2^\circ \text{C}$. Four aqueous solutions of SCMC of approximate concentrations $0.2 - 0.8 \text{ kg/m}^3$ were used as the non-Newtonian liquid.

Rheological properties and density of the solutions were measured experimentally by pipeline viscometer and by specific gravity bottle. Rheological and physical properties of the test liquids are given in Table 4.2. The dilute SCMC solutions displayed shear thinning behaviour and followed Power law model. Pseudoplastic power law fluid calculations are carried out on the basis of the effective viscosity, \sim_{eff} which is given as,

$$\sim_{eff} = K' \left[\frac{8V}{D} \right]^{n'-1} \quad (4.1)$$

Ranges of variables investigated are shown in Table 4.3.

4.3 Results and discussion

4.3.1 Evaluation of the pressure drop across the piping component

Variation of static pressure along the tube are schematically shown in Fig. 4.2 in which AC and DF correspond to the upstream and downstream portion of the test section and CD corresponds to the pipe fittings. The curve a-b-c-d-e-f is the static pressure distribution in the straight upstream portion, pipe fitting portion and downstream portion

of the test section. Pressure drop across the pipefitting, ΔP_{pf} , was obtained from the difference between the static pressure of the upstream, and the static pressure of the downstream. Thus, ΔP_{pf} , the frictional pressure drop across the pipe fitting for the flowing fluid through a passage of length equal to the axis of the pipe fitting and the additional pressure loss due to irreversibility. The typical static pressure distribution curves are shown in Figs. 4.3 - 4.6.

4.3.2 Effect of non-Newtonian characteristics on the pressure drop across the piping components

Figs. 4.7 - 4.10 show the pressure drop across the different pipe fittings as a function of liquid flow rate. It is clear from the graphs that as n' decreases the pressure drop increases at constant liquid flow rate.

4.3.3 Problem analysis

For flow of non-Newtonian fluid through a straight pipe, the steady state Z-component equation of motion in cylindrical coordinate system in a horizontal pipe may be written as

$$\dots \left(V_r \frac{\partial V_z}{\partial r} + \frac{V_r}{r} \frac{\partial V_z}{\partial r} + V_z \frac{\partial V_z}{\partial Z} \right) = -\frac{\Delta P}{\partial Z} - \left\{ \frac{1}{r} \dots (r \ddagger_{rz}) + \frac{1}{r} \frac{\partial \ddagger_{rz}}{\partial r} + \frac{\partial \ddagger_{zz}}{\partial Z} \right\} \quad (4.2)$$

This equation is dimensionally homogeneous and is true for laminar flow only. The dimensional equality (numerically not true) for the equation may be written as,

$$\left(\frac{V^2}{L} \right) = -\frac{\Delta P}{\dots L} + \frac{\epsilon V}{L} \quad (4.3)$$

this equation is made dimensionless by dividing by V^2/L which suggests that the functional relationship of ΔP with other parameters is as follows :

$$\frac{\Delta P}{\dots V^2} = F\left(\frac{V \dots D}{\sim}\right) \quad (4.4)$$

Equation (4) is only true for flow in a horizontal straight pipe.

4.3.3.1 Elbow

Fluid flowing through a straight pipe attains a characteristic velocity profile that is independent of the distance along the pipe, i.e., the flow becomes fully developed. If the flow direction is changed with a curved pipe, the flow structure of the fluid is completely changed. The fluid is subjected to varying degrees of centrifugal forces from the neighborhood of the curved wall to the center of the pipe. Due to the interaction primarily between centrifugal and viscous forces in the curved portion of the flow, certain characteristic motion, known as secondary flow, is generated which causes shifting of the maximum velocity from the inner portion of the curved pipe to the outer portion of the curved pipe. Dean (1927, 1928b) showed that a dimensionless parameter, De , expressed as the ratio of the square root of the product of inertia and centrifugal forces to the viscous forces, is important in considering this interaction. Since the Dean number takes into account the interaction of centrifugal and viscous forces, hence for the curved pipe, we have,

$$\frac{\Delta P}{\dots V^2} = F(De) \quad (4.5)$$

In Equation (4.5) the Dean number really plays the same role as the Reynolds number does in the straight pipes. The friction factor, f_{pf} , for flow through elbow is defined by the Fanning friction equation

$$f_{pf} = \frac{D\Delta P_{pf}}{2V^2 \dots L_{pf}} \quad (4.6)$$

S, Equation (4.6) can be modified to

$$f_{pf} = F(De) \quad (4.7)$$

In order to extend the applicability of Equation (4.7) to all the different elbows in the horizontal plane, an angle factor has been introduced in the functional relationship as follows

$$f_{pf} = F\left(De, \frac{r}{135}\right) \quad (4.8)$$

In the limiting case when $\alpha \rightarrow 0$ or $R_c \rightarrow \infty$, i.e., when the elbow becomes straight, the friction factor, f_{pf} , given by equation (8) should be the friction factor, f_s , in a straight pipe.

To incorporate this limiting condition, Equation (4.8) has been modified as follows:

$$\left(\frac{f_{pf}}{f_s} - 1\right) = F\left(De, \frac{r}{135}\right) \quad (4.9)$$

4.3.3.2 Orifice

Initially, using water as test liquid tested each orifice and the relationship between the orifice coefficient and Reynolds number for each orifice was in the same form as recommended by ASME Research Committee (1959) (Gadiyar and Das, 1993). In the case of the flow through orifices, the sudden reduction of the flow path and is followed by re-establishment of the flow path. Hence, the functional relationship should incorporate the diameter ratio, D_0/D_t , as follows,

$$\frac{\Delta P_{pf}}{\dots V^2} = F\left(\text{Re}, \frac{D_0}{D_t}\right) \quad (4.10)$$

4.3.3.3 Valves

In the case of the flow through gate and globe valves the percentage opening of the valves obstructs the flow path. Hence the functional relationship should incorporate the ratio of the valve opening to the full opening of the valve as follows,

$$\frac{\Delta P_{pf}}{\dots V^2} = F(\text{Re}, \varsigma) \quad (4.11)$$

4.3.4 Pressure drop

4.3.4.1 Analysis of the Experimental pressure drop

Initially, pressure drop was measured for a straight horizontal tube and the results were found to be in close agreement (within $\pm 5\%$) with the conventional resistance formula applied for non-Newtonian liquid flow through a straight pipe in laminar flow condition, i.e.,

$$f_s = \frac{16}{\text{Re}} \quad (4.12)$$

which signifies the accuracy of the experimental procedure and technique.

The total pressure drop across the pipe fitting for non-Newtonian liquid flow is the same as the frictional pressure drop across the pipe fitting because the hydrostatic head component and the acceleration component are both negligible.

There are two approaches for analysis of the pressure drop across the pipe fittings equivalent length and velocity head. In the equivalent length method the fitting is treated as a piece of straight pipe of some physical length, i.e., equivalent length that has the same total loss as the fitting. The main drawback of this simple approach is that the equivalent length for a given fitting is not constant but depends on Reynolds number and roughness as well as size and geometry (Hooper, 1991). In the case of the other method,

the velocity head is the amount of potential energy (head) necessary to accelerate a fluid to its flowing velocity. The number of velocity head (H) in a flowing fluid can be calculated directly from the velocity of the fluid (V) as

$$H = \frac{V^2}{2g} \quad (4.13)$$

Flow through a piping component in a pipeline also cause a reduction in static head, which may be expressed in terms of velocity head and the resistance coefficient, K as,

$$H = K \frac{V^2}{2g} \quad (4.14)$$

Friction losses for fittings are often expressed in terms of the resistance coefficient, *K*. It can be shown, using dimensional analysis, that for incompressible fluids *K* is a dimensionless function of Reynolds number and of dimensionless geometric ratios characteristic of the fitting. Figs 4.11 - 4.14 illustrate the comparison between the experimental values and the correlations available in the literature in terms of the resistance coefficient. It is clear from these figures that the experimental data deviates from the correlations available in the literature. These differences are attributed by the size of pipe fittings, rheological behaviour of the liquid, the circuit employed in transporting the liquid and so-called “mutual influence effect” of the pipe fittings (Bandala-Rocha et al., 2005). So the analysis of the experimental pressure drop data across the pipefitting is carried out by means of dimensional analysis. Parameters influencing the friction loss or pressure drop are the physical and operating variables of the system. The physical variables include the radius of the tube, the characteristics dimension of the piping component (radius of curvature of the elbow, percentage opening of the valves and the orifice etc) and the physical properties of the fluid. However, the

operating variables are limited to the flow rate of the fluid. The final generalized correlations for the different pipe fittings are given below,

Elbows

$$\left(\frac{f_{pf}}{f_s} - 1 \right) = 7.94 \times 10^{-2} De^{0.718} \left(\frac{r}{135} \right)^{-0.519} \quad (4.15)$$

$$\text{for, } 40 < Re < 2200$$

$$30 < De < 2150$$

$$45^\circ < r < 135^\circ$$

Gate valve

$$\frac{\Delta P_{pf}}{\dots V^2} = 1.905 Re^{-0.197} S^{-1.987} \quad (4.16)$$

$$\text{for, } 45 < Re < 2200$$

$$0.25 < S < 1.0$$

Globe valve

$$\frac{\Delta P_{pf}}{\dots V^2} = 8.266 Re^{-0.061} S^{-0.797} \quad (4.17)$$

$$\text{for, } 45 < Re < 2200$$

$$0.25 < S < 1.0$$

Orifice

$$\frac{\Delta P_{pf}}{\dots V^2} = 0.601 Re^{-0.048} \left(\frac{D_o}{D_t} \right)^{-4.379} \quad (4.18)$$

$$\text{for, } 45 < Re < 2200$$

$$0.4646 < D_o/D_t < 0.7087$$

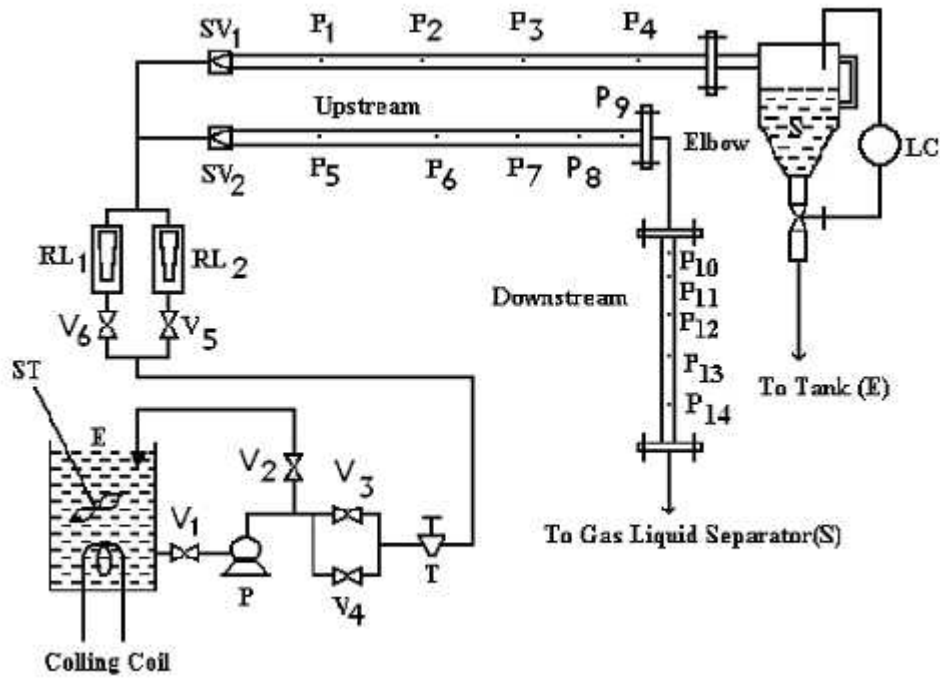
4.3.4.2 Stream-wise pressure drop due to piping components

To determine the pressure drop across the fitting, the static pressure was measured in the long upstream and long downstream portion of the fitting. The static pressure starts to deviate from the steady value within 5 to 8 (5 for elbow and 8 for globe valve) pipe diameter of the inlet of the pipe fitting and the pressure recovery lengths were also found to be within 5 to 8 (5 for elbow and 8 for globe valve) pipe diameter.

4.4 Conclusions

Experimental investigations have been carried out to evaluate the pressure drop across the piping components for non-Newtonian pseudoplastic liquid flow in laminar condition.

Generalized empirical correlations have been developed to predict the frictional pressure drop across the different pipe fittings in the horizontal plane, for non-Newtonian pseudo plastic liquid in laminar flow.



E – tank; P – pump; S – separator; P₁ – P₁₄ – manometer tappings; LC – level controller;
 RL₁ – RL₂ – rotameters; ST – stirrer; SV₁ – SV₂ – solenoid valves;
 V₁ – V₆ – valves

Fig. 4.1 Schematic diagram of the experimental setup

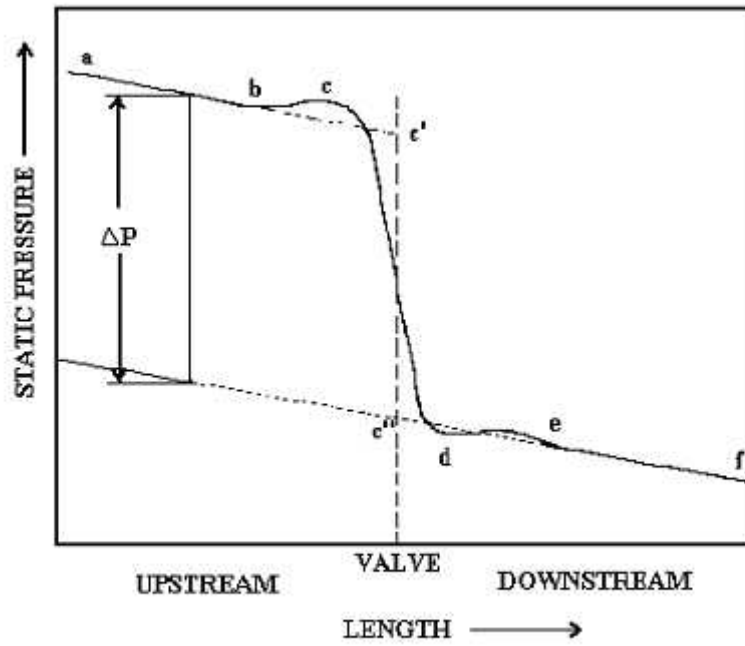


Fig. 4.2 Static pressure distribution curve across the valve

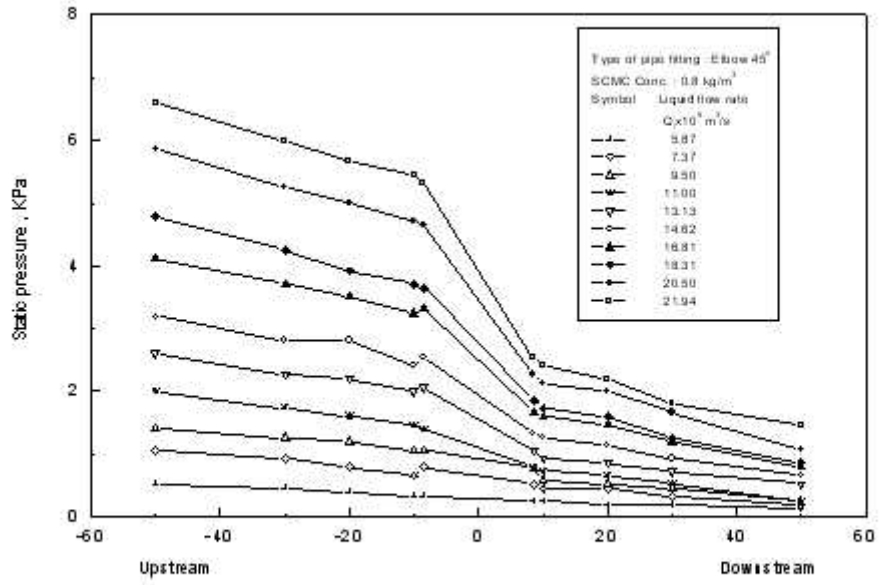


Fig. 4.3 Typical static pressure distribution curve for elbow

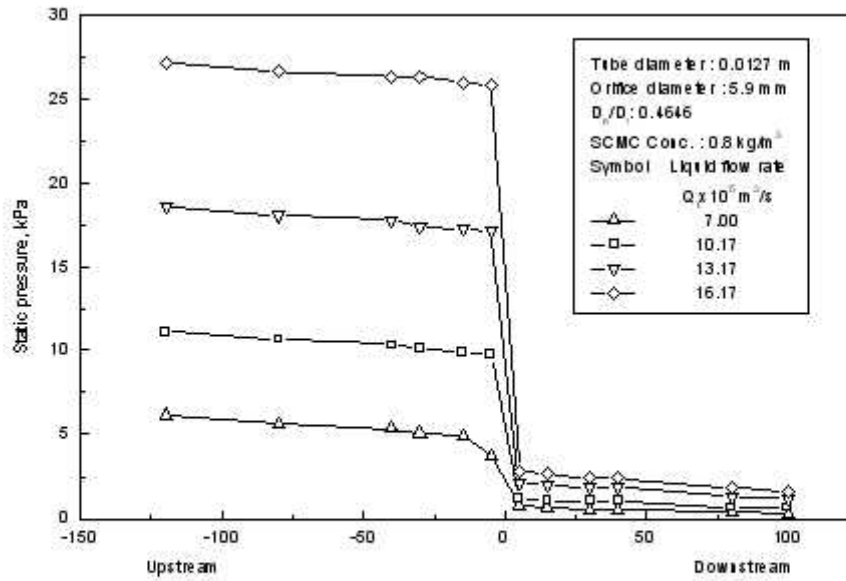


Fig. 4.4 Typical static pressure distribution curve for orifice

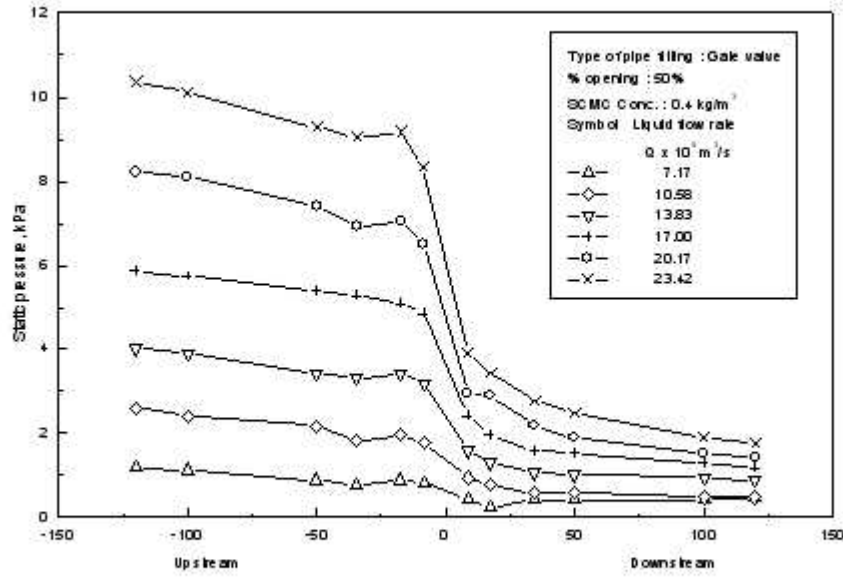


Fig. 4.5 Typical static pressure distribution curve for gate valve

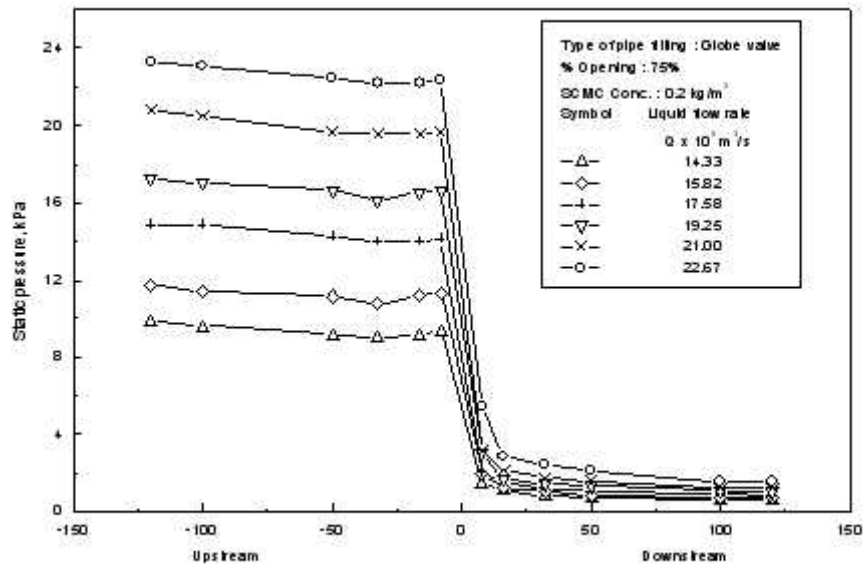


Fig. 4.6 Typical static pressure distribution curve for globe valve

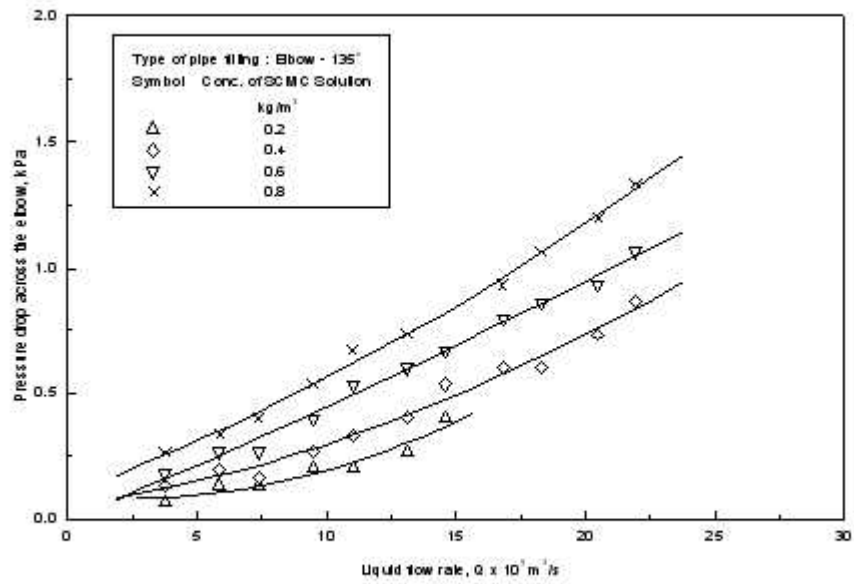


Fig. 4.7 Variation of the pressure drop across the elbow with liquid flow rate

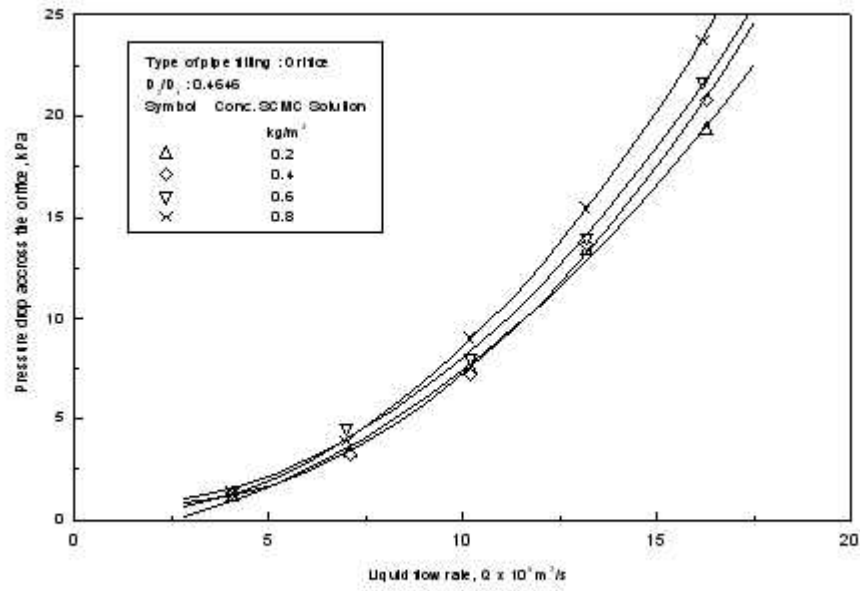


Fig. 4.8 Variation of the pressure drop across the orifice with liquid flow rate

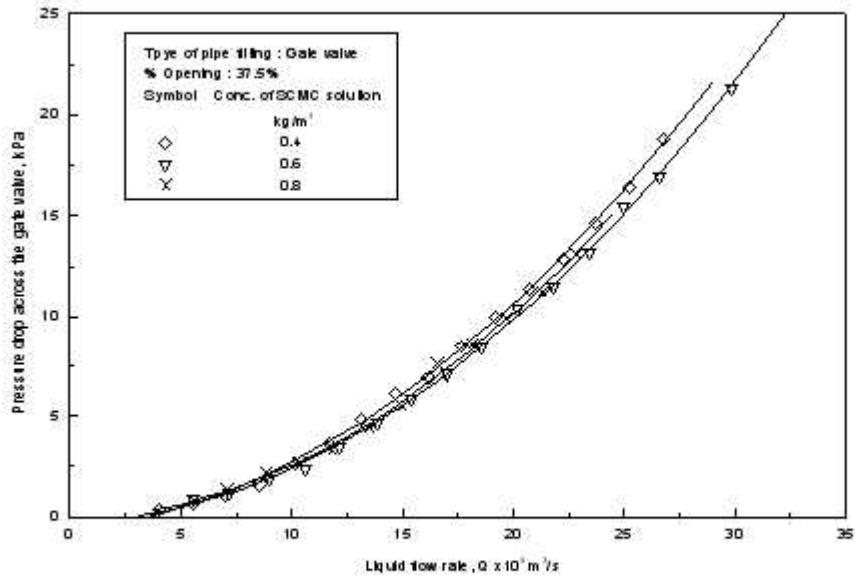


Fig. 4.9 Variation of the pressure drop across the gate valve with liquid flow rate

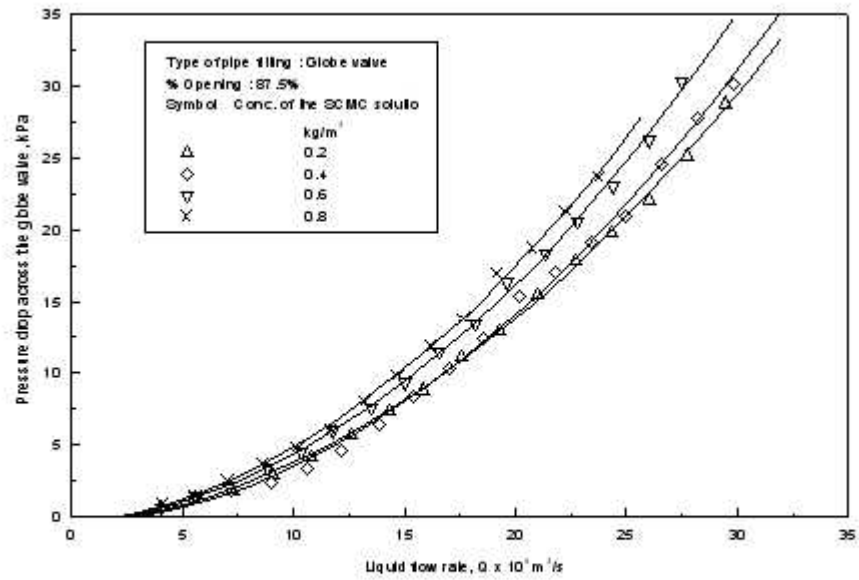


Fig. 4.10 Variation of the pressure drop across the globe valve with liquid flow rate

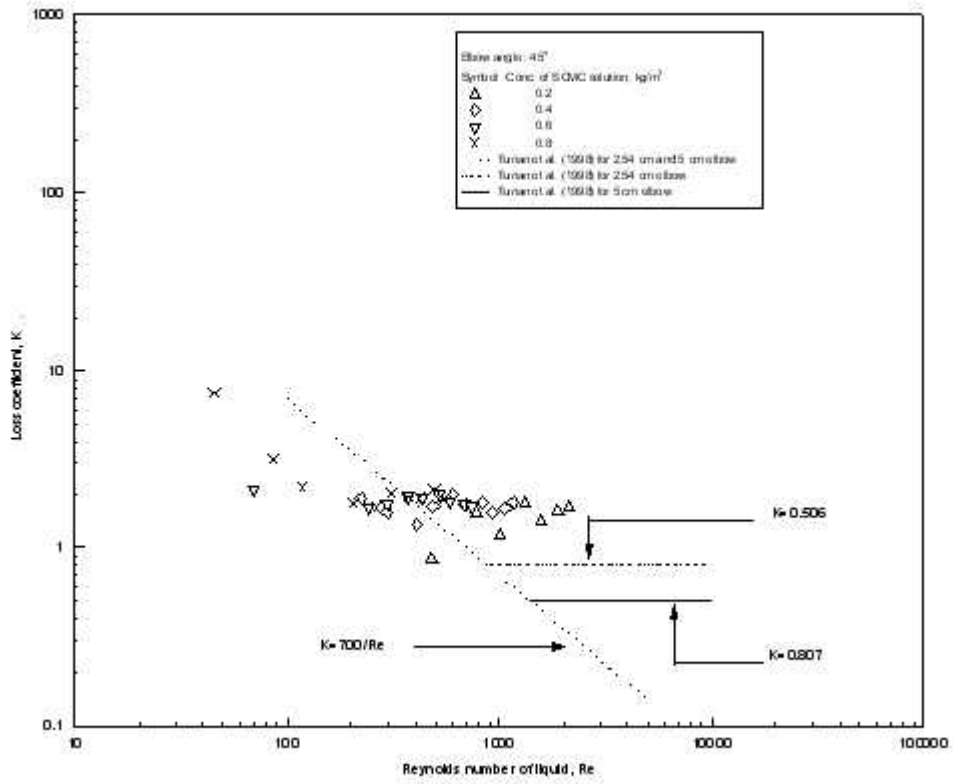


Fig. 4.11 Comparison of the experimental pressure drop across 45° elbow with Turian et al. (1998) correlation

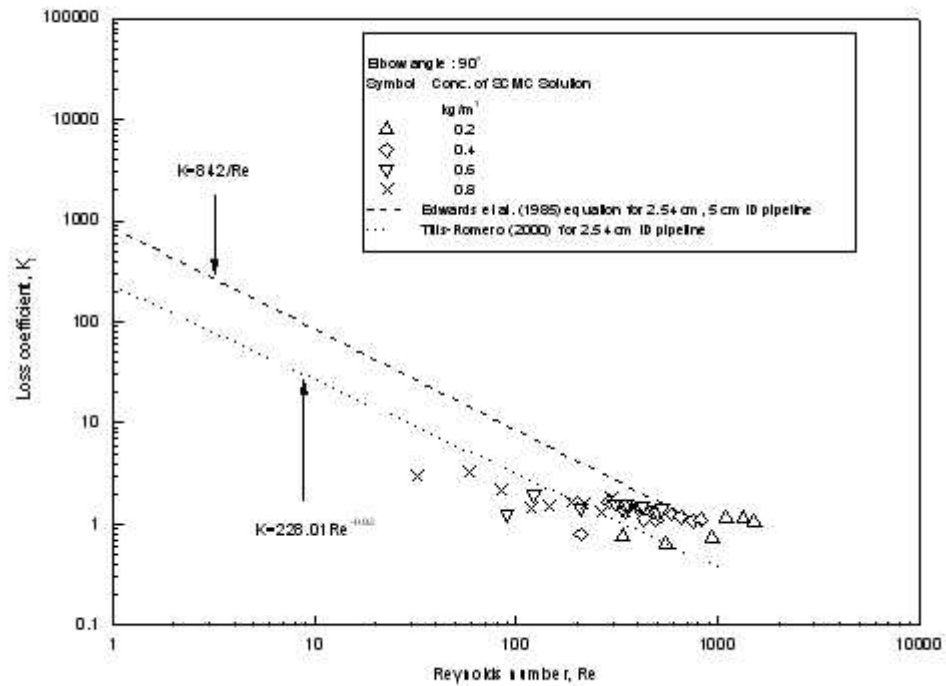


Fig. 4.12 Comparison of the experimental pressure drop across 90° elbow with Edwards et al. (1985) and Telis-Romero et al. (2000) correlation

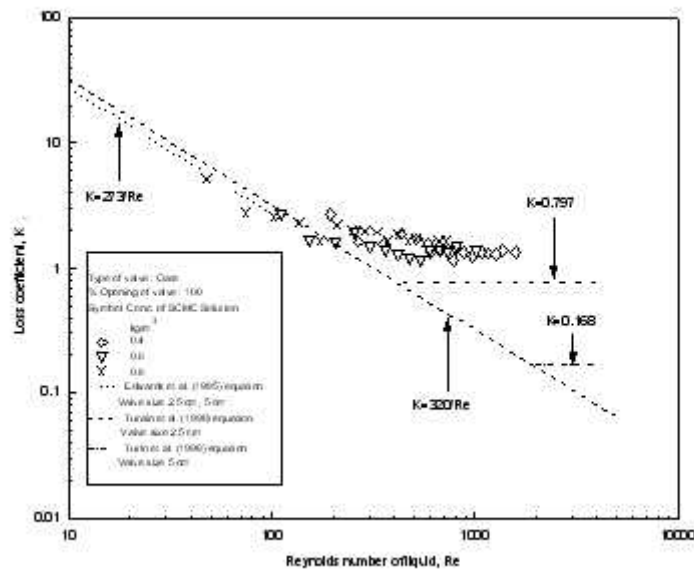


Fig. 4.13 Comparison of the experimental pressure drop across gate valve with Edwards et al. (1985) and Turian et al. (1998) correlation

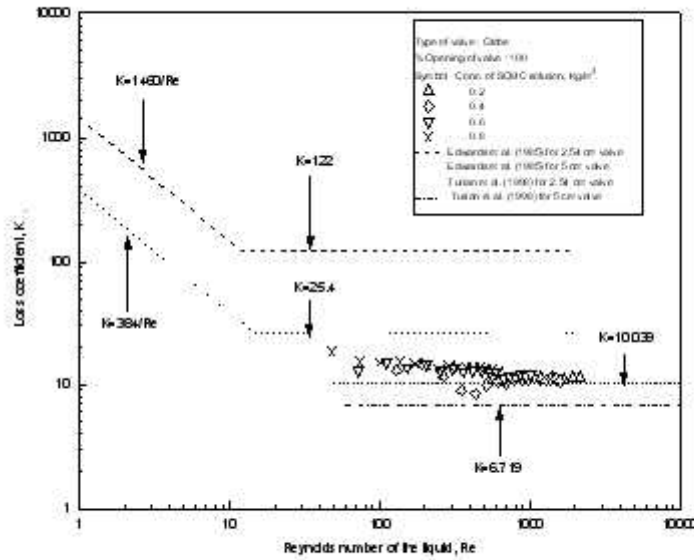


Fig. 4.14 Comparison of the experimental pressure drop across globe valve with Edwards et al. (1985) and Turian et al. (1998) correlation

Table 4.1 Dimension of the piping components

Type of pipe fitting : Elbow		
Elbow angle θ deg.	Radius of curvature R_c , m	Linear length of the elbow L, m
45	0.011	0.014
90	0.022	0.011
135	0.017	0.016
Type of pipe fitting : Orifice		
Orifice diameter D_0 , mm	Ratio of orifice diameter to pipe diameter D_0/D_t	
5.9	0.4646	
7.6	0.5984	
9.0	0.7087	

Table 4.2 Physical properties of the SCMC solution

Concentration kgm^{-3}	Flow behaviour index n'	Consistency index K' $Ns^{n'} m^{-2}$	Density ρ_l kgm^{-3}
0.2	0.9013	0.0142	1001.69
0.4	0.7443	0.1222	1002.13
0.6	0.6605	0.3416	1002.37
0.8	0.6015	0.7112	1003.83

Table 4.3 Range of variables

Measurement Type	Range
Liquid and Flow properties	
Flow behavior index	0.6015 n' 0.9013
Consistency index (Ns^n/m^2)	0.0142 K' 0.7112
Density (kg/m^3)	1001.69 1003.83
Concentration of SCMC Solution (kg/m^3)	0.2 to 0.8
Liquid Flow Rate $Q_1 \times 10^5 (m^3/s)$	3.75 to 29.83
Reynolds Number	47.51 Re 2234.21
Dean Number	32.41 De 2130.23
Pressure Drop (Experimental) (kPa)	0.0333 P 36.933
Elbow	
Angle of Elbow	45° to 135°
45° elbow	Radius of curvature = 0.011m Linear length of the elbow = 0.014m
90° elbow	Radius of curvature = 0.022m Linear length of the elbow = 0.011m
135° elbow	Radius of curvature = 0.017m Linear length of the elbow = 0.016m
Orifice	
Diameter of orifice (m)	0.0059, 0.0038, 0.0045
Diameter ratio of Orifice to pipe diameter	0.4646 D_o/D_t 0.7087
Gate valve	
Valve opening (%)	50, 75, 100
Ratio of the valve opening to the full opening of valve	0.50 1.00
Globe Valve	
Valve opening (%)	50, 75, 100
Ratio of the valve opening to the full opening of valve	0.50 1.00

Chapter 5

*Non-Newtonian liquid flow through small diameter piping
components – CFD analysis*

Computational Fluid Dynamics (CFD) analysis have been carried out to evaluate the frictional pressure drop across the horizontal pipeline and different piping components, like elbows, orifices, gate and globe valves for non-Newtonian liquid through 0.0127m pipe line. The mesh generation is done using Gambit 6.3 and FLUENT 6.3 is used for CFD analysis. The CFD results show the very good agreement with the experimental values.

5.1 Introduction

The integral part of any piping systems are valves, bends, elbows, orifices, tees, reducers, expander etc. Flow through piping components is more complex than the straight pipes. The complex nature arises due to the presence of constriction and expansion, change of flow direction etc. Consumption of energy across pipe fittings gives pressure losses which expressed as a pressure drops. The friction between the fluid and the fitting wall causes this pressure drop. Pressure drop across the pipe fittings is important in design and analysis of the fluid machinery. Process engineers are dealing with non-Newtonian fluids mainly in food processing, paints, pharmaceutical, paper, and petroleum industry for production and transportation of foods, paints, glues, colors, fiber solutions, polymer solutions through piping components.

Computational Fluid Dynamics (CFD) can serve to evaluate the frictional losses in piping systems, secondary flow effects can be visualized to aid in better understanding of the flow phenomena and can be applied to improve flow characteristics and equipment design. However CFD analysis often requires fine tuning by comparison with the reliable experimental data. CFD is a useful tool for studying non-Newtonian flows. The improvements in computer performance, matched by the developments in numerical

methods, have resulted in a growing confidence in the ability of CFD to model complex fluid flows. CFD techniques have been used on a broad scale in the process industry to gain insight into various flow phenomena, examine different equipment designs or compare performance under different operating conditions (Abbott and Basco, 1989, Xia and Sun, 2002). The use of viscous non-Newtonian fluids in industry poses a number of challenges. Highly viscous fluids require much energy to flow in pipelines and processing equipments.

Numerical simulation of gas-solid flow in a U-bend was reported by Hidayat and Rasmuson (2002). Etemad and Sunden (2004) studied numerical analysis of turbulent convective heat transfer in a square-sectioned U-bend duct. Marn and Ternik (2006) numerically studied laminar flow of shear-thickening electrostatic ash-water mixture through 90° pipe bend. Edwards et al. (1998) developed a CFD based model to predict erosion in piping system in slurry pipeline. Numerical simulations are performed for the dilute gas-solid flow through rectangular duct containing a horizontal to vertical bend of 90° angle by Kuan et al. (2003). Brown (2006) has been used to investigate the cause of highly localized erosion in slurry pipeline in an aluminium refinery through CFD and subsequently used for the development of the newer pipeline. Saha and Jain (2008) used CFD analysis for slurry pipeline to investigate the erosion in the pipeline. Wu and Chen (2008) used commercial CFD code to simulate the flow fields of lab-scale, scale-up and pilot-scale anaerobic digesters. Their simulated results were validated against the experimental data from literature using liquid as Newtonian and non-Newtonian in nature. Manzar and Shah (2009) reported the CFD analysis for straight and coils tubes using different Newtonian and non-Newtonian liquids.

The CFD has been used for many steady flow engineering devices such as pipe junction (Sierra-Espinosa et al., 2000a and b), pipeline design (Famiyesin et al., 2002) etc. The use of CFD to study the effect of modifying valve geometry on flow characteristics is also very important in valve design and performance. Roorda (1998) and Davis and Stewart (1998) reported their work on this direction for the control valve design. In any use of CFD for improving component design, it is vital that suitable validation studies be undertaken.

In this paper, the CFD modeling of the hydrodynamics of non-Newtonian flow through straight pipe, elbows, orifices, gate and globe valves are described. The Fluent 6.3 is used as CFD code. The applicability of the Fluent 6.3 software in the flow of non-Newtonian liquid through small diameter pipeline and the piping components are investigated. The numerical results are compared with the results as shown in Chapter 4.

5.2 Experimental

The detail experimental set up, techniques and results are given in Chapter 4.

5.3 Mathematical Model

The detailed mathematical methods used for the CFD analysis is given in Chapter 2. Dilute solution of SCMC follows the non-Newtonian pseudoplastic Power law model. In general for non-Newtonian liquids the effective viscosity is used for calculation and defined as,

$$\tilde{\nu}_{eff} = K' \left(\frac{8v}{d} \right)^{n'-1} \tag{5.1}$$

The governing equation is the Navier – Stokes equation as,

$$\dots \frac{\partial v}{\partial t} + \dots v \cdot \nabla v = \tilde{\nu}_{eff} \nabla^2 v - \nabla P \tag{5.2}$$

and the continuity equation is

$$\nabla v = 0 \quad (5.3)$$

where,

$$\nabla = i \frac{\partial}{\partial x} + j \frac{\partial}{\partial y} + k \frac{\partial}{\partial z} \quad (5.4)$$

As the flow of liquid is laminar in all cases the viscous model, i.e., laminar non-Newtonian Power Law model is used for the CFD analysis. These equations are solved subject to the following boundary conditions,

(i) The pipeline and piping components walls are assumed rigid and a no-slip condition is imposed.

(ii) At the outlet, the velocities are free but the normal and tangential stresses are constrained to be zero and the gauge pressure is set to zero.

(iii) At the inlet, a uniform velocity profile is used with a time varying forcing function representative of flow in the left portion of the piping components.

5.4 Computational fluid dynamics (CFD) Procedure

Geometries for the straight pipe, elbows, orifices, valves and are created in Gambit 6.3 preprocessor. A typical mesh has about $3 \times 10^3 - 2 \times 10^5$ order unstructured tetrahedral mesh for elbows and unstructured boundary layer hexahedral mesh for straight pipe, orifices and valves are used. Inlet and outlet are located at each end of the piping system. The inlet is used to specify the inlet velocity and outlet is used to specify pressure outlet. These geometries of the pipeline and piping components are imported into Fluent 6.3 in a Cartesian co-ordinate system. Fluent 6.3 solved the governing equations in 3-D geometry. Laminar non-Newtonian Power Law model have been used for simulation. The model solves for Navier-stokes equation at prescribes velocities. The governing equations are non linear and several iterations of loop must be performed

before a convergent solution is obtained. The first-order upwind scheme is used in the discretization of set of governing equations, standard interpolation schemes is used for calculating cell-face pressures for using the Segregated solver in Fluent 6.3. Pressure-velocity coupling refers to the numerical algorithm which uses a combination of continuity and momentum equations to derive an equation for pressure (or pressure correction) when using the segregated solver. Simple algorithm is used in Fluent 6.3 domain.

The general procedure to simulate SCMC flow through pipe and different piping components based on Gambit 6.3 and Fluent 6.3 software is outlined below,

1. Perform meshing under Gambit 6.3 :
 - Create a computational domain at the flow region,
 - The grids were generated using boundary layer hexahedral and t-grid (tetrahedral) meshes,
 - Controlling a smooth change in the mesh size by size functions,
 - Specify boundary and continuum types,
 - Examine the mesh to ensure that the high skewness is below 0.5 for hexahedral and below 0.9 for tetrahedral meshes.
2. Import the mesh file to Fluent 6.3 and check the mesh.
3. Define a 3-D, unsteady, implicit, and pressure-based solver.
4. Activate the single phase laminar non-Newtonian power law model.
5. Define a laminar non-Newtonian power law model.
6. Enable the liquid properties with laminar flow conditions using the text command: `define/models/viscous/laminar`. Putting the non-Newtonian fluid

values: flow behavior index, consistency index, temperature and effective viscosity values at the inlet velocity.

7. Define the phase by setting liquid as the single phase. Define the operating conditions by turning on gravity and specify the operating density.
8. Solution control methodology – Under relaxation factors – 0.5 for pressure, 0.3 for momentum, and default values for the other parameters. Standard schemes – STANDARD for momentum and 1st order upwind for other variables. Pressure-velocity SIMPLE coupling used;
9. Initialize the solution – velocity;

Enable the plotting of residuals during the calculation, and kept the default convergence criteria, 1×10^{-5} for all residuals except for the transport equation which residual was set at 10^{-3} .

5.5 Results and discussion

5.5.1 Convergence and grid independency

The convergence criterions were set at 10^{-5} for all equations except for the transport equation which residual was set at 10^{-3} . A computational domain L 200D was used to ensure fully developed flow results could be obtained for all pipe and piping components. In general the final results depend upon mesh geometries. Subsequent decrement and increment in mesh resolution by 50% were applied to evaluate if the employed mesh resolution was adequate to obtain accurate solutions. It was observed that when the mesh resolution was decreased by 50% the axial velocity profile was 7-12% of the currently employed mesh velocity profile for pipe and different piping components. As the present mesh resolution was increased by 50% the axial velocity profile changes

1-3% for pipe and different piping components. These results suggest that the current mesh resolution is sufficient to obtain grid independent solutions for the proposed model.

5.5.2 Straight pipe

Boundary layer and hexahedral mesh is fitted with the geometry of pipe as shown in Fig. 5.1. Fig. 5.2 shows the contour plot of pressure field for straight pipe. At the inlet of the pipe pressure is high and gradually decreases at the outlet due to friction with the top and bottom walls. Fig. 5.3 shows the plot of velocity field for straight pipe. It shows that at the centre of the pipe velocity is high and at the wall velocity is near to zero. Fig. 5.4 shows the comparison plot of the single-phase pressure drop across the straight pipe for experimental and CFD analysis and it is clear that these two match very well.

5.5.3 Elbows

Fig. 5.5 shows the mesh generated for different elbows. Unstructured t-grid (tetrahedral) is fitted well for the cases of elbows due to its curved structure. Fig. 5.6 shows that plot of velocity field. Fig. 5.7 shows the vector field inside the different points. Fig. 5.8 shows that the velocity magnitude inside the different points. Fig. 5.9 shows the plot of X-velocity. Fig. 5.10 shows the contours plot of static pressure. Fig. 5.11 shows the contours plot of static pressure inside the different points. Fig. 5.12 shows the contours plot of total pressure inside the different points.

As the fluid flows through the straight pipe and then enters into the elbow section, the pressure which is uniform across the flow in the straight section, must adjust in the elbow to counter the centrifugal force. The pressure is greatest at the outer wall furthest from the centre of curvature and least at the inner wall nearest to the centre of curvature.

At the inlet of the elbow a low pressure exists in the inner wall and high pressure exists at the outer wall, it is clearly indicated in Figs. 5.10 - 5.12. This initial pressure gradient resulting from the change from straight to curve flow, a cross stream pressure gradient exists in the elbow, at the elbow inlet the boundary layer on the outer wall experiences the effect of an the adverse stream wise pressure gradient which may be sufficiently strong for 45° elbow than compare to 135° elbow and produce local separation and the inner wall boundary layer is accelerated (Figs. 5.6 - 5.8). The reverse occurs at the exit of the elbow where local pressure gradients of the opposite sign appear as the flow adjust to uniform pressure condition of the downstream. The impacts of the curve geometry into the straight section were extended 5 pipe diameter upstream of the elbow and also 5 pipe diameter downstream of the elbow. This impacts depends on the velocity of the flow and also the elbow angle and effect is maximum for the 45° elbow and minimum for the 135° elbow. Thus the flow at the entrance of the elbow differs considerably from a fully developed pipe flow. The flow in elbow is influenced by centrifugal force due to its curvature. This centrifugal force is, in principle, balanced by a pressure gradient in the plane of curvature. However, near the wall where the velocity is small, this pressure gradient can no longer be balanced and consequently fluid in the middle of the pipe moves at the outer wall and then turns to move inward along the wall. The flow on the outer wall and separation at the inner wall make flow very complex (Fig. 5.9). The result is a secondary flow superimposed in the main flow in the plane perpendicular to the main flow. The magnitude and direction of the flow depends on Dean number. The direct effect of secondary flow is to displace the region of maximum velocity to the centre towards the outer wall as it is shown in Figs. 5.6 - 5.7. For the elbow entrance the mean

axial velocity profile significantly altered with respect to the fully developed profile in the straight pipe and the location of the maximum velocity is shifted towards the inner wall of the elbow, as shown in Figs. 5.6 - 5.8. This explained by the fact that no centrifugal forces due to redirection of flow are present at the entrance of the flow.

The flow in 90° elbow is always developing in nature in which the velocity distribution do not attain other forms that are more or less independent of the position along the pipe axis. For 45° elbow exist the axial velocity moves further towards the outer radius as clearly shown in Figs. 5.6 - 5.7. The secondary motion can be seen clearly in the Fig. 5.9. At the elbow entrance the centrifugal forces are very weak to balance the pressure gradient which results in an inward flow as shown in Figs. 5.6 – 5.7. With increasing deflection that is flow through inside the elbows the centrifugal forces increases and counter rotating vortices that circulate in the outer direction in the central part of the pipe. This is shown in Fig. 5.9. It is more pronounced in the 45° elbow than other elbows. As the flow passes to the elbow this vortices shifted towards the inner wall (Fig. 5.9) and then the static pressure starts to deviate from steady value within 15 pipe diameter in the upstream of the inlet of the elbows, depending on the flow rate. In the downstream of the elbow, the pressure recovery lengths were found to be within 20 pipe diameter for all elbows, depending on the flow rate. Similar results are obtained by Kuan et al. (2003), Berrouk and Laurence (2008), Kumar et al. (2008) and Zhang et al. (2010).

Figs. 5.13 - 5.14 show the comparison plot of the pressure drop across the elbows for experimental and CFD analysis. It is clear from the figure that the non-Newtonian liquid flow through elbows, the experimental pressure drop data matches well with the CFD simulated results.

5.5.4 Orifices

Boundary layer and hexahedral mesh is fitted well with the geometry of the orifice (Fig. 5.15). Fig. 5.16 shows the contour plot of pressure field of the orifice and Fig. 5.17 shows the contour plot of static pressure at different points of the orifice. Similar plot observed for the case of other orifices. It shows that flow through orifices, the sudden reduction of the flow path is followed by re-establishment of the flow path. The velocity is a maximum near the orifice. According to Bernoulli's principle, this region of high velocity is also a region of low pressure. Hence the pressure, shear stress and shear strain increases with increasing the flow area with increasing the diameter ratio, D_0/D_t . Pressure drop decreases with increasing the diameter ratio, D_0/D_t . Fig. 5.18 shows the plot of velocity vector field of the orifice. Fig. 5.19 shows the plot of velocity vector field at the different points of the orifice. Fig. 5.20 shows the plot of velocity magnitude at the different points of the orifice. Similar plot observed for the case of other orifices. It shows that due to gradual decreasing of D_0/D_t ratio from 0.7087 to 0.4646, i.e., narrowing of flow area velocity is increased. Figs. 5.21 - 22 shows the comparison plot of the pressure drop across the orifices for experimental and CFD analysis. Results are matches well.

5.5.5 Gate valve

Fig. 5.23 shows that boundary layer hexahedral mesh for 50% opening gate valve. The valve is drawn in somewhat simplified manner with intact its internal dimensions. Fig. 5.24 shows that contour plot of static pressure and Fig. 5.25 shows that contour plot of total pressure for 50% opening gate valve. The contour plot of pressure field shows that the pressure drop decreases with increasing the percentage opening of the valve. The

shear strain and shear stress gradually decreases with increase in flow area, i.e., percentage opening of the valve. The pressure drop increases with increasing liquid concentration, i.e., pseudoplasticity of the liquid at constant liquid flow rate. Figs. 5.26 and 5.27 show that plot of velocity magnitude and velocity vector field. The velocity is increases due to the presence of orifice, i.e., by decreasing the flow area, and again reestablished the lower velocity. Figs. 5.28 - 5.29 show that comparison plot of the pressure drop across the gate valves for experimental and CFD analysis. It is clear from the figure that pressure drop matches well. However the simplified figure has drawn for meshing due to the large pressure drop experimental and CFD data matches well

5.5.6 Globe valve

Boundary layer and hexahedral mesh is fitted well with the geometry of Globe Valve. Fig. 5.30 shows the mesh geometry of the globe valve and the geometry are simplified with intact its entire internal dimension. The pressure drop across the valve behaves similar to the gate valve, but only different is a change in the flow direction occurs. Fig. 5.31 shows the plot of velocity field. The change of flow direction is clearly observed in the figure. Figs. 5.32 - 5.33 show the comparison plot which gives good agreement with the CFD simulated values, but differ slightly and it may be due to its simplified geometry taken in this studies.

5.6 Conclusions

Commercially available software FLUENT 6.3 was used to calculate pressure drops in pipeline and piping components for non-Newtonian liquid flow. The numerical simulated results are verified with experimental data and it gives excellent agreement. The numerical simulated results also provide detail information of the flow field in

pipeline and piping components. It gives better physical insights and understanding of the flow phenomena. This study demonstrated the Computational fluid dynamics (CFD) application as an effective tool for design in the pipeline and piping components.

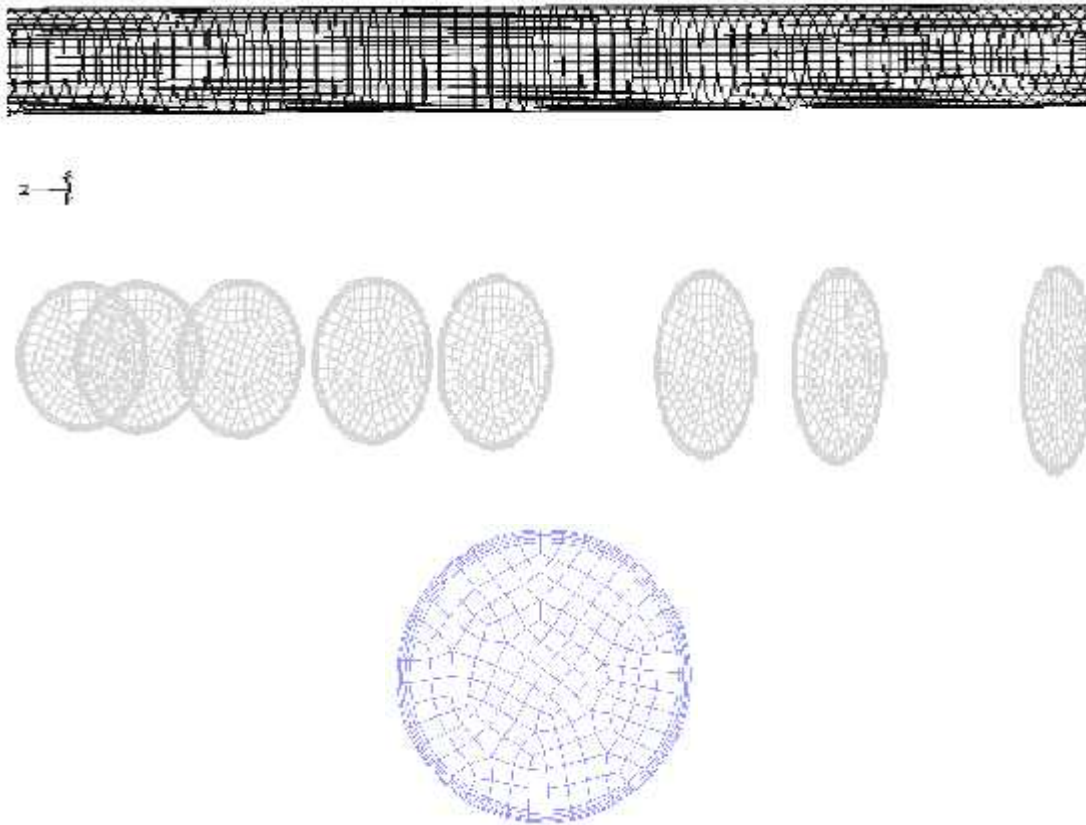


Fig. 5.1 Unstructured boundary layer hexahedral grid of straight pipe
Grid Size: No. of cells = 200633; No. of faces = 615032, No. of nodes = 214428
1 cell zone, 4 face zones



Fig. 5.2 Contour plot of static pressure for straight pipe
 Concentration of SMC solution (kg/m^3): 0.8, Liquid velocity (m/s): 0.3199

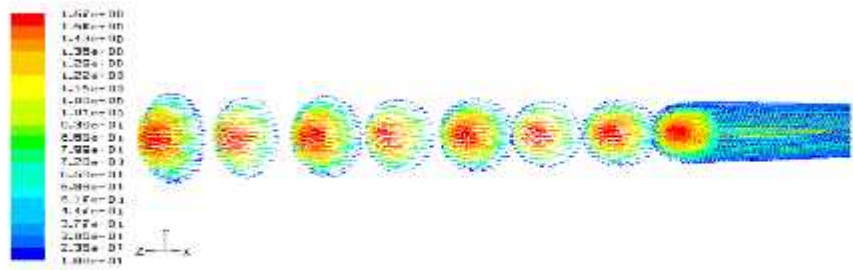


Fig. 5.3 Contour plot of velocity vector for straight pipe
 Concentration of SMC solution (kg/m^3): 0.8, Liquid velocity (m/s): 0.3199

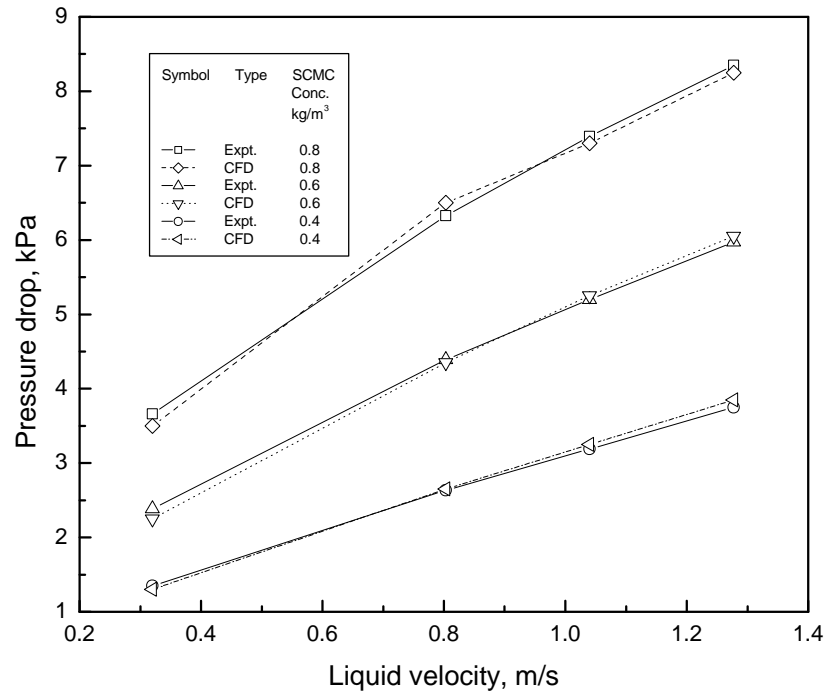


Fig. 5.4 Comparison of the experimental data and CFD modeling for straight pipe

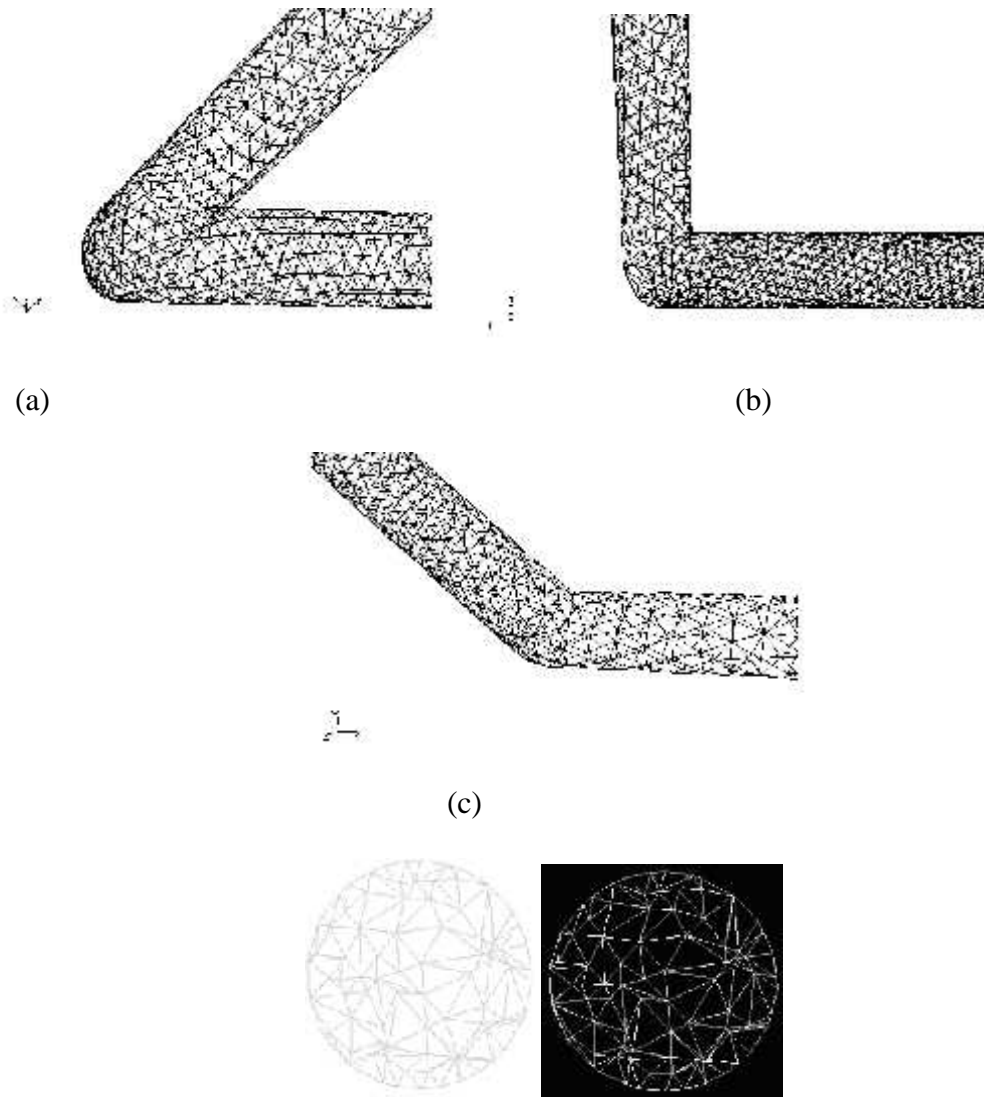


Fig. 5.5 Mesh geometry - Unstructured Tetrahedral grid

(a) 45° elbow

Grid Size: No. of cells = 25985; No. of faces = 57149, No. of nodes = 7310

1 cell zone, 4 face zones

(b) 90° elbow

Grid Size: No. of cells = 29157; No. of faces = 64167, No. of nodes = 8208

1 cell zone, 4 face zones

(c) 135° elbow

Grid Size: No. of cells = 4427; No. of faces = 9778, No. of nodes = 1279

1 cell zone, 4 face zones

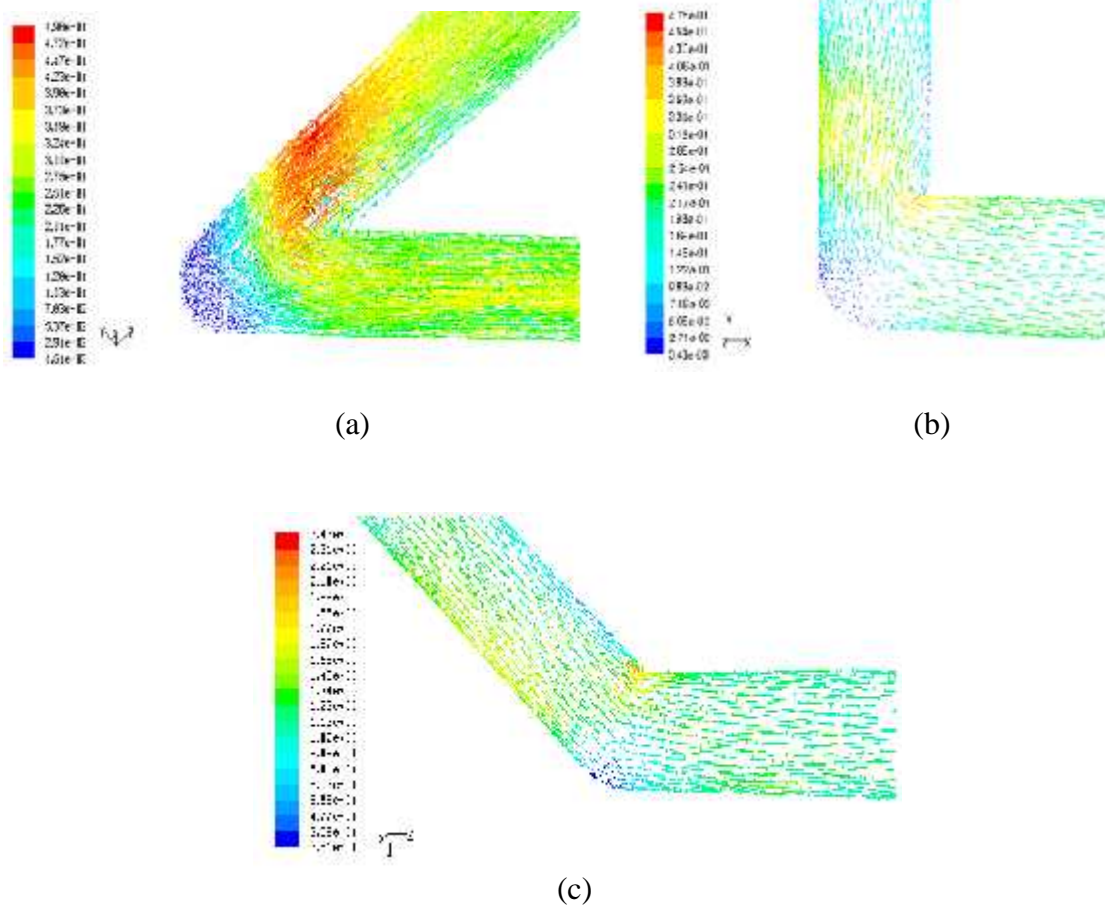


Fig. 5.6 Plot of velocity vector

(a) 45⁰ elbow

Concentration of SCMC solution (kg/m³): 0.2, Liquid velocity (m/s): 0.296

(b) 90⁰ elbow

Concentration of SCMC solution (kg/m³): 0.2, Liquid velocity (m/s): 0.296

(c) 135⁰ elbow

Concentration of SCMC solution (kg/m³): 0.8, Liquid velocity (m/s): 1.733

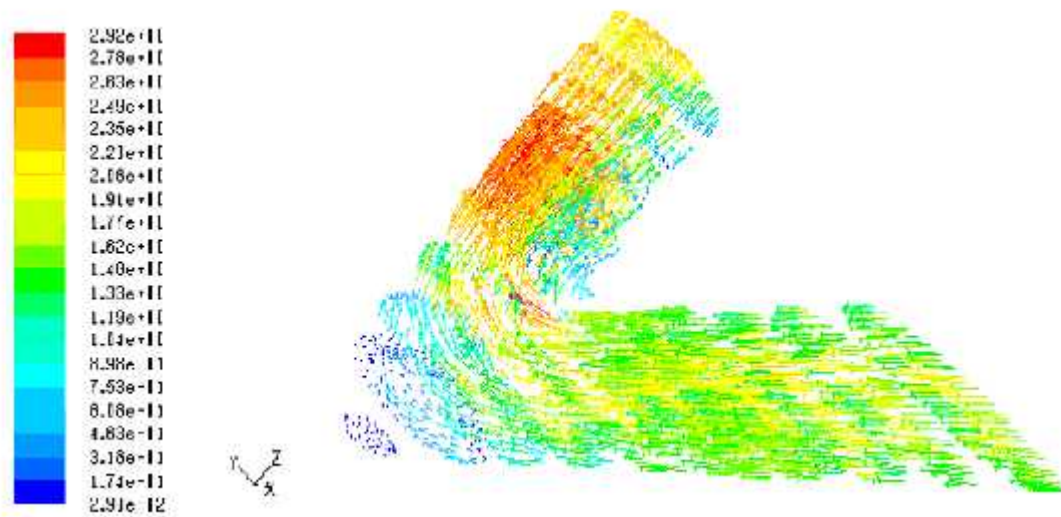
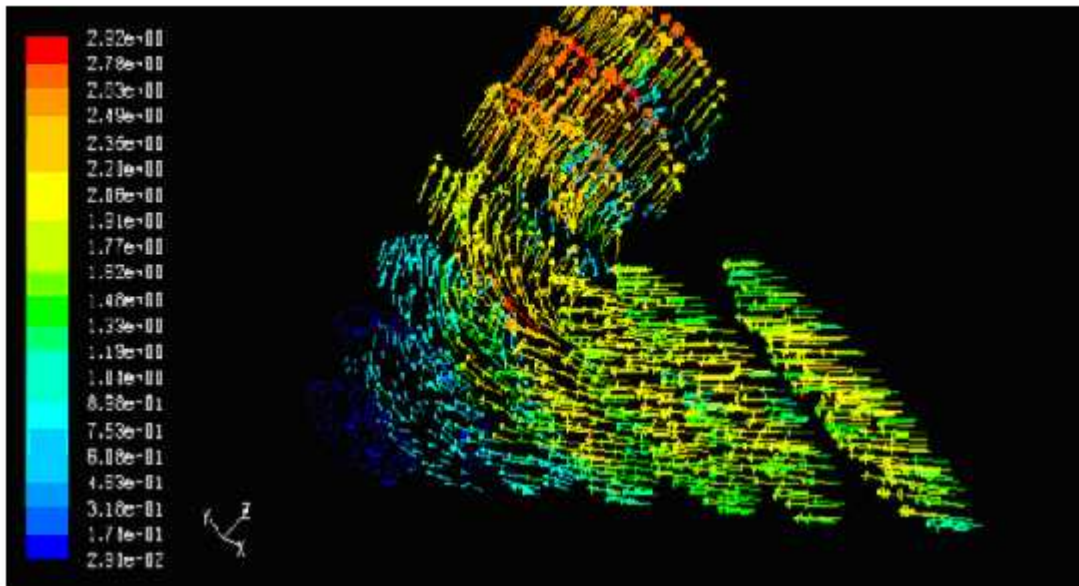


Fig. 5.7a Contours plot of velocity vector inside the different points of 45⁰ elbow
 Concentration of SMC solution (kg/m³): 0.8, Liquid flow rate, Q_l(m³/s): 21.94x10⁻⁵

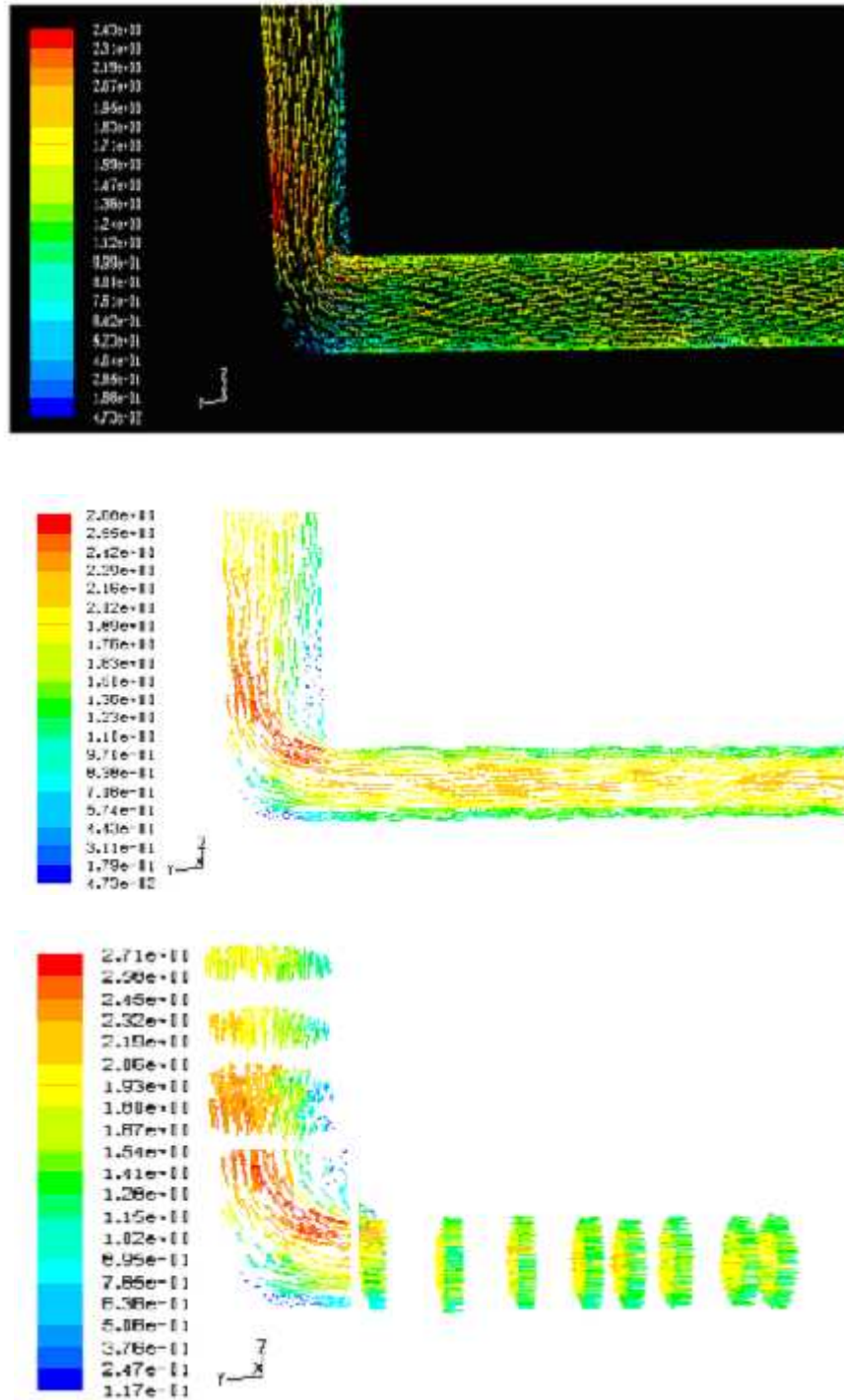


Fig. 5.7b Contour plot of velocity vector inside the different points of 90° elbow
 Concentration of SMC solution (kg/m^3): 0.8, Liquid flow rate, Q_1 (m^3/s): 21.94×10^{-5} , Liquid velocity, V_1 (m/s): 1.733

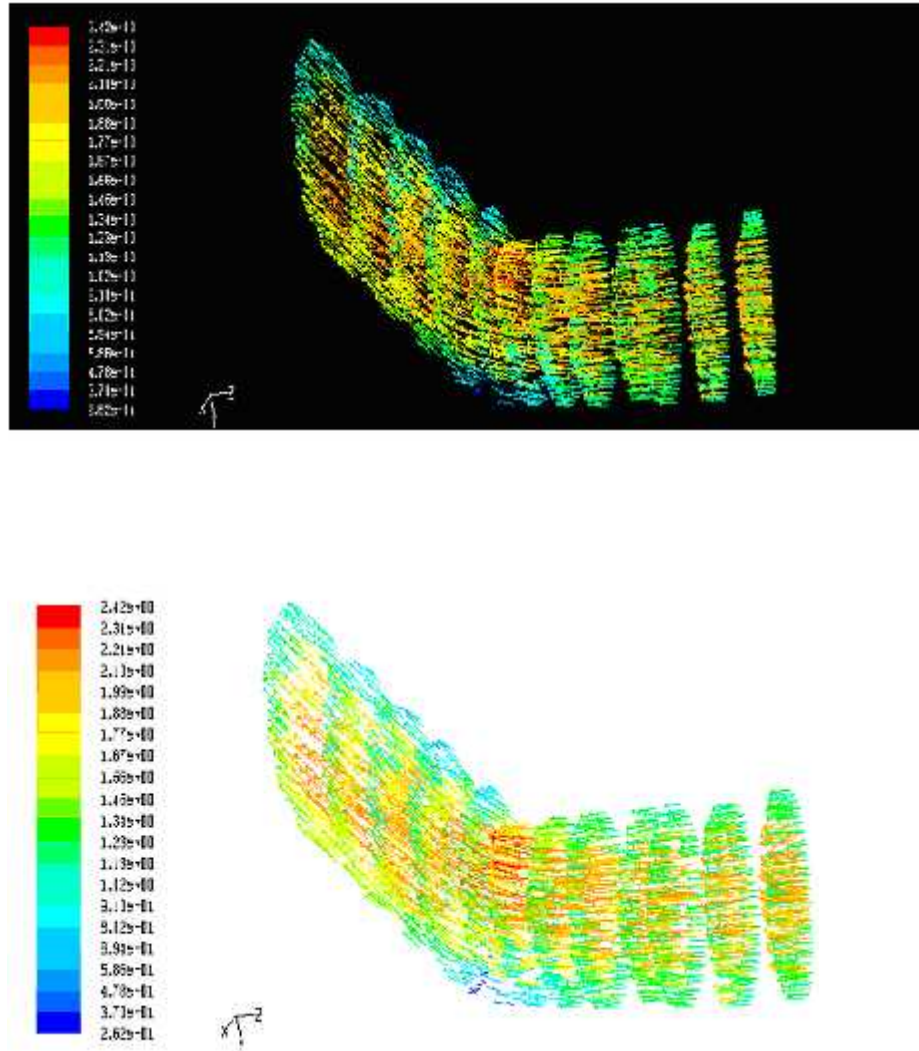


Fig. 5.7c Contour plot of velocity vector inside the different points of 135° elbow
 Concentration of SMC solution (kg/m^3): 0.8, Liquid flow rate, $Q_1(\text{m}^3/\text{s})$: 21.94×10^{-5} , Liquid
 velocity, $V_1(\text{m/s})$: 1.733

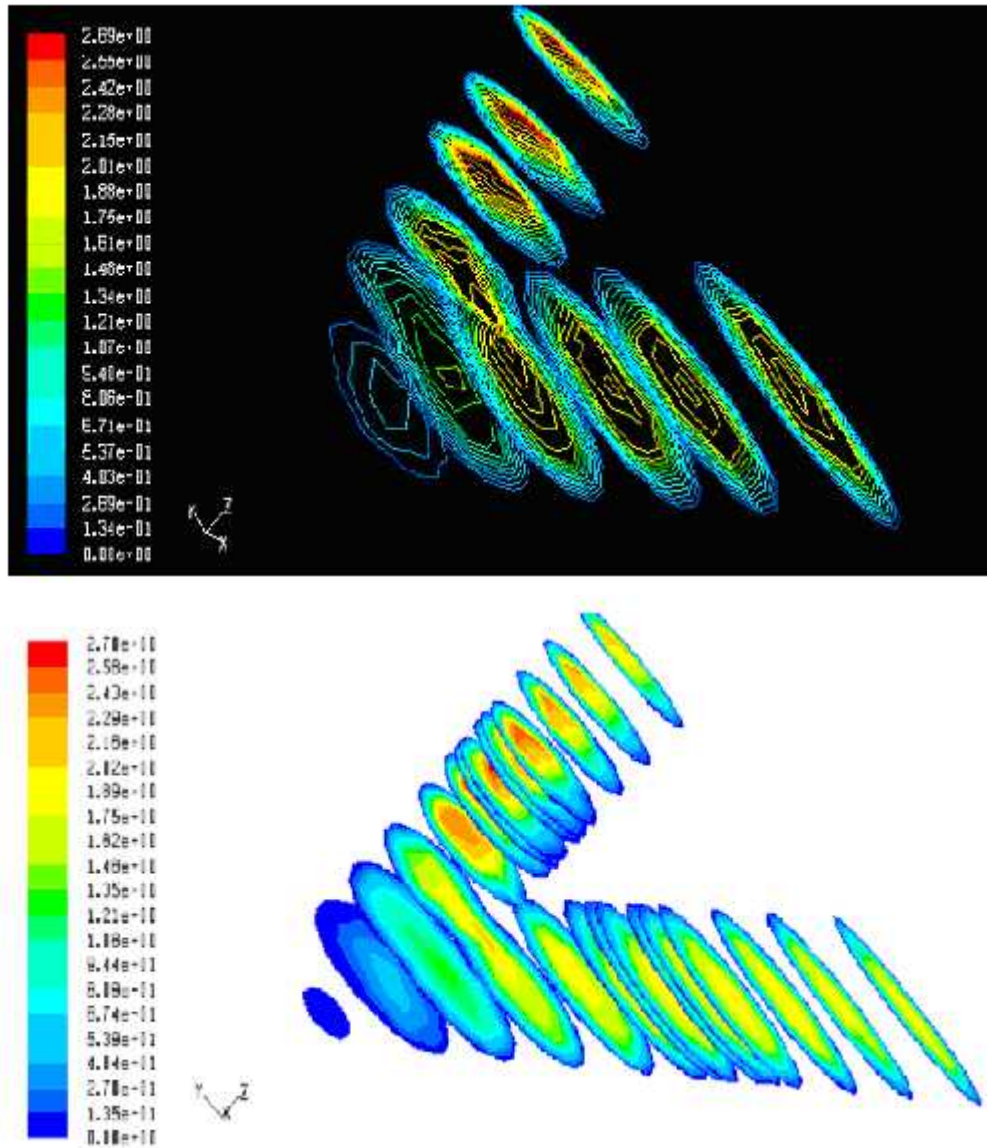


Fig. 5.8a Contours plot of velocity magnitude inside the different points of 45⁰ elbow, Concentration of SMC solution (kg/m³): 0.8, Liquid flow rate, Q_l(m³/s): 21.94x10⁻⁵, Liquid velocity, V_l(m/s): 1.733

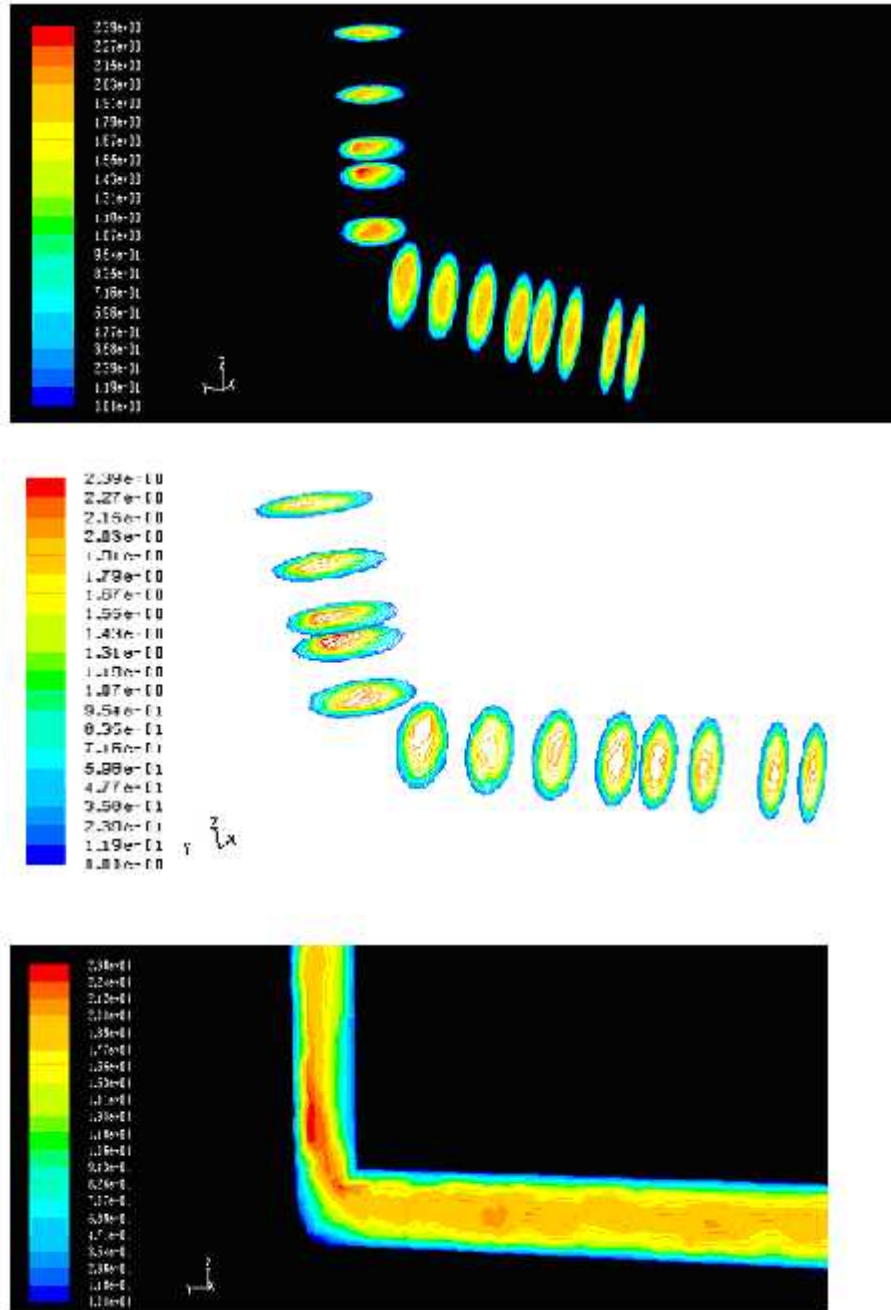


Fig. 5.8b Contour plot of velocity magnitude inside the different points of 90° elbow

Concentration of SCMC solution (kg/m^3): 0.8, Liquid flow rate, $Q_1(\text{m}^3/\text{s})$: 21.94×10^{-5} , Liquid velocity, $V_1(\text{m/s})$: 1.733

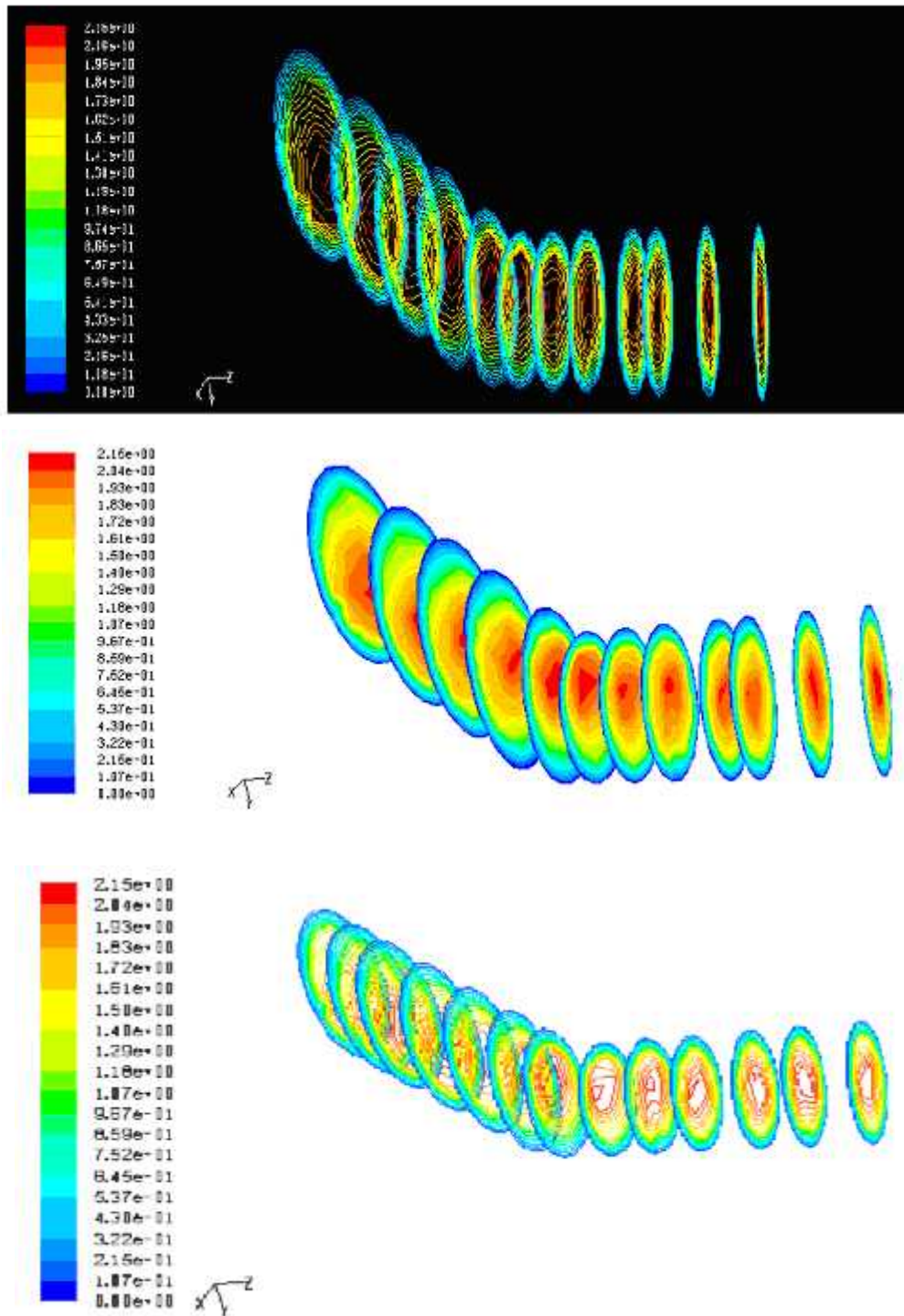


Fig. 5.8c Contour plot of velocity magnitude inside the different points of 135° elbow, Concentration of SCMC solution (kg/m^3): 0.8, Liquid flow rate, $Q_1(\text{m}^3/\text{s})$: 21.94×10^{-5} , Liquid velocity, $V_1(\text{m/s})$: 1.733

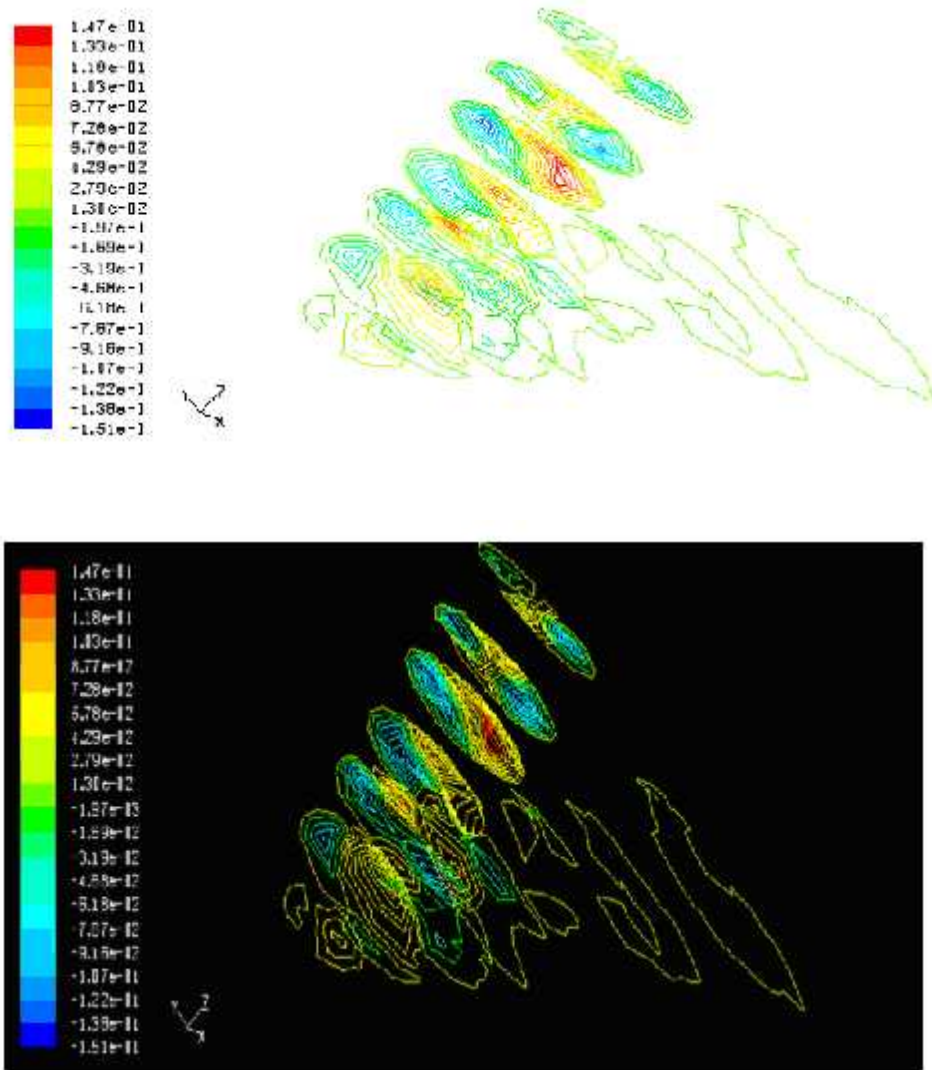


Fig .5.9a Contour plot of X-velocity inside the different points of 45⁰ elbow
 Concentration of SCMC solution (kg/m³): 0.8, Liquid flow rate, Q_l(m³/s): 21.94x10⁻⁵, Liquid
 velocity, V_l(m/s): 1.733

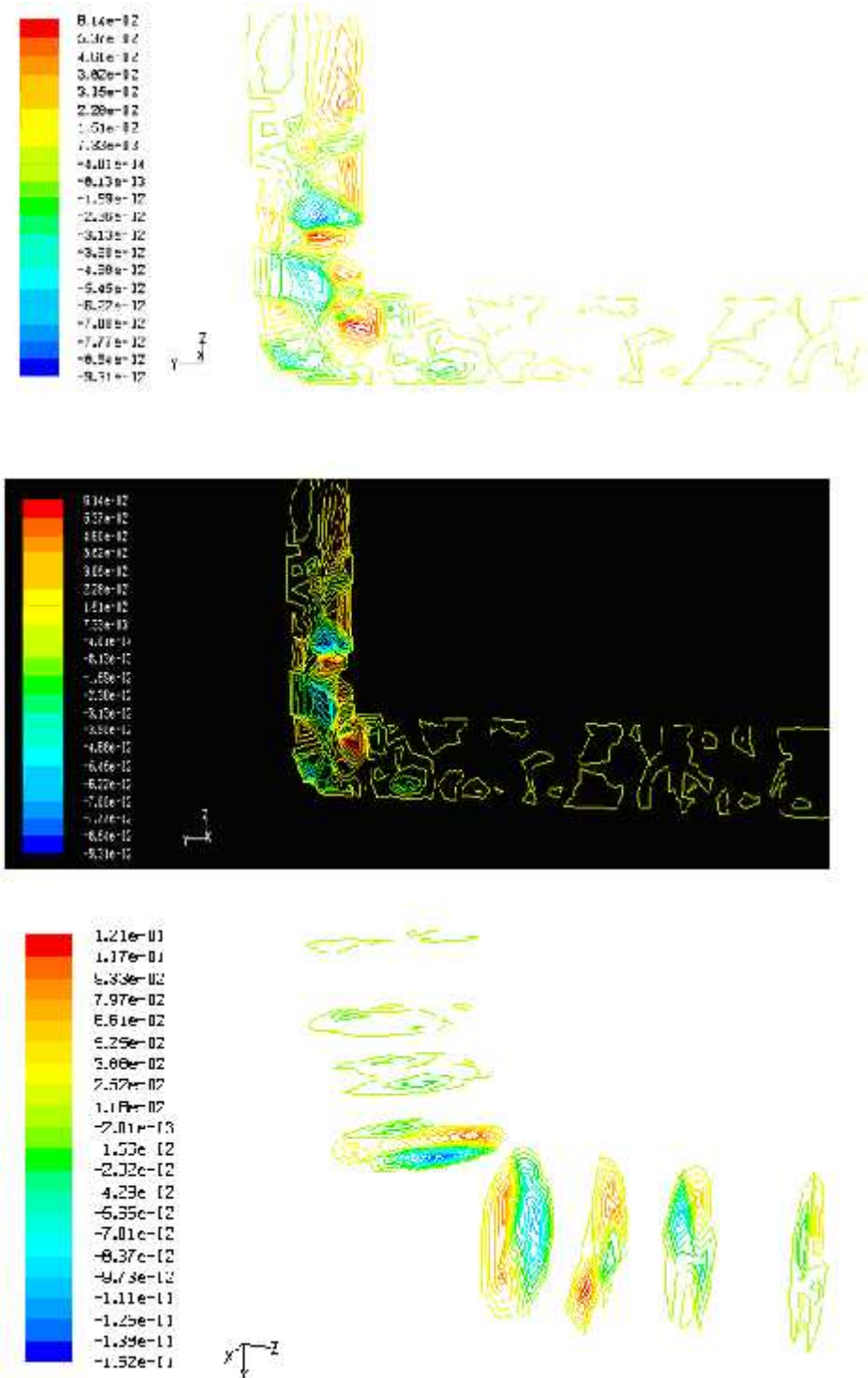


Fig. 5.9b Contour plot of X-velocity inside the different points of 90° elbow
 Concentration of SMC solution (kg/m^3): 0.8, Liquid flow rate, $Q_1(\text{m}^3/\text{s})$: 21.94×10^{-5} , Liquid velocity, $V_1(\text{m}/\text{s})$: 1.733

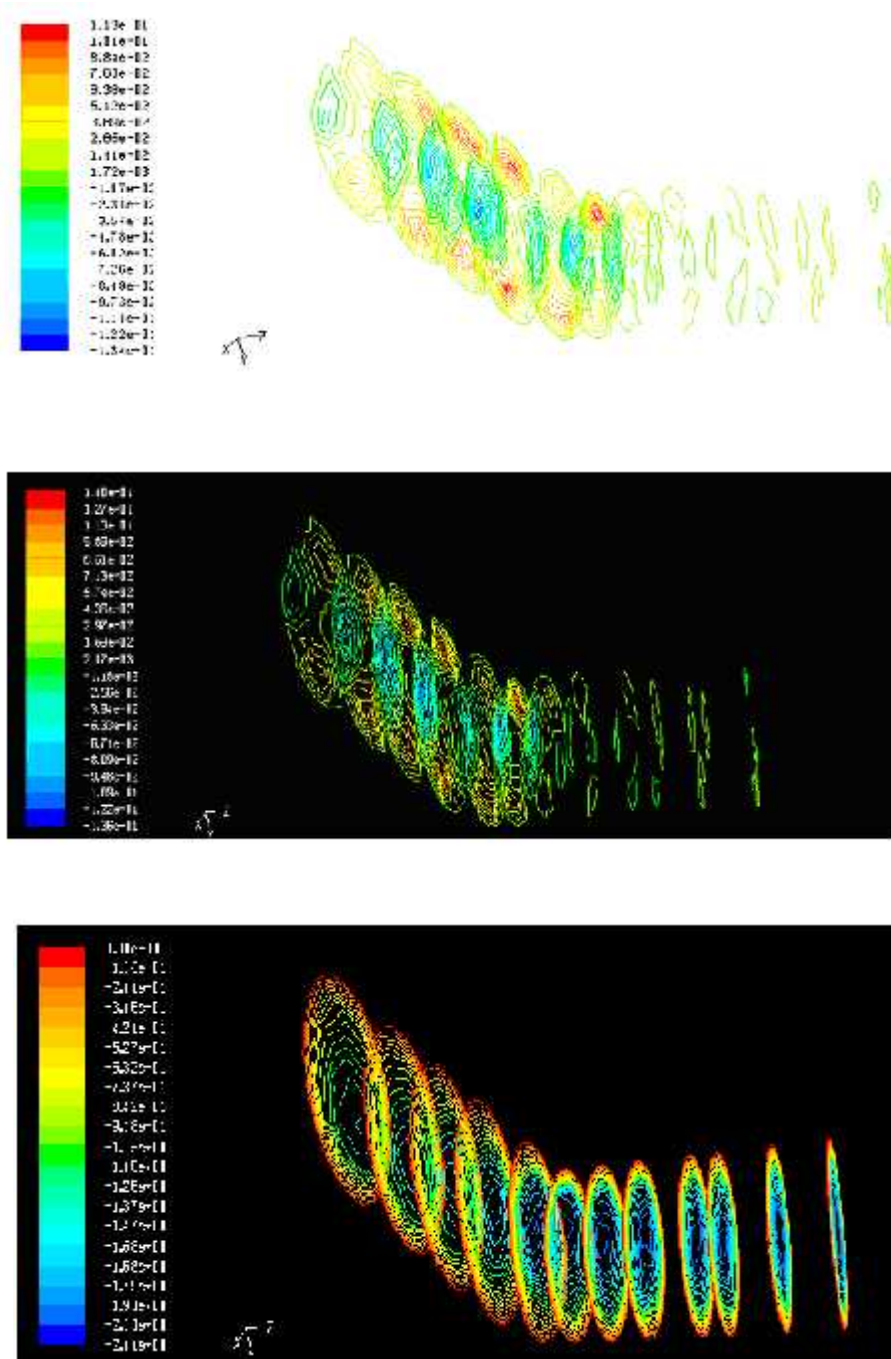


Fig. 5.9c Contour plot of X-velocity inside the different points of 135⁰ elbow
 Concentration of SMC solution (kg/m³): 0.8, Liquid flow rate, Q₁(m³/s): 21.94x10⁻⁵, Liquid
 velocity, V₁(m/s): 1.733

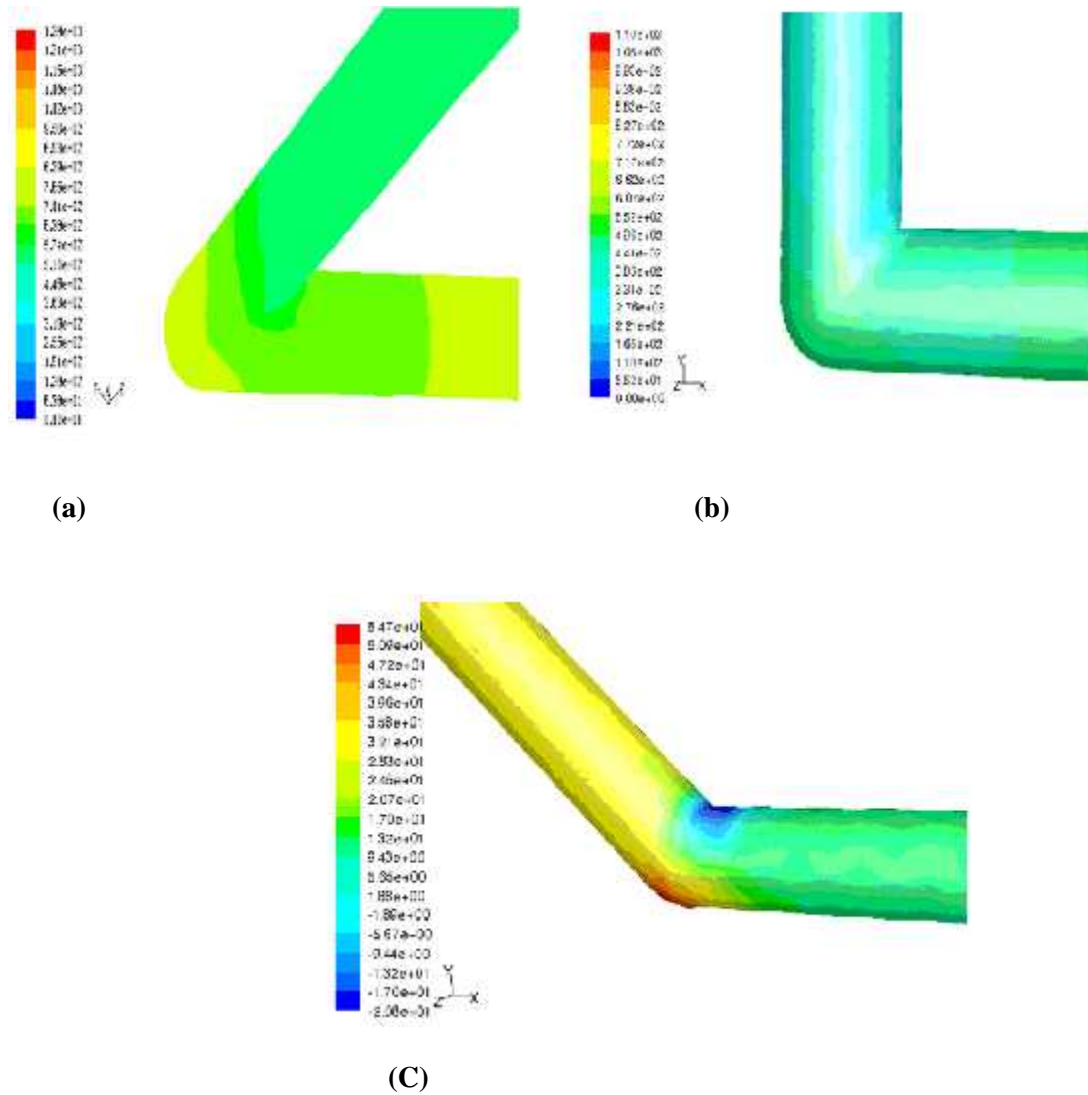


Fig. 5.10 Contour plot of static pressure

(a) 45° elbow

Concentration of SCMC solution (kg/m³): 0.2, Liquid velocity (m/s): 0.296

(b) 90° elbow

Concentration of SCMC solution (kg/m³): 0.2, Liquid velocity (m/s): 0.296

(c) 135° elbow

Concentration of SCMC solution (kg/m³): 0.4, Liquid velocity (m/s): 0.296



Fig. 5.11a Contours plot of static pressure inside the different points of 45⁰ elbow
 Concentration of SMC solution (kg/m³): 0.8, Liquid flow rate, Q₁(m³/s): 21.94x10⁻⁵, Liquid velocity, V₁(m/s): 1.733

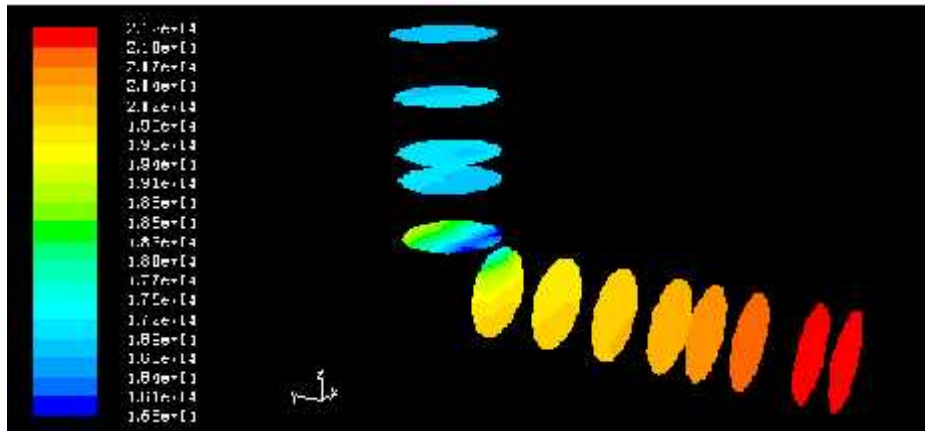


Fig. 5.11b Contours plot of static pressure inside the different points of 90⁰ elbow
 Concentration of SMC solution (kg/m³): 0.8, Liquid flow rate, Q₁(m³/s): 21.94x10⁻⁵, Liquid velocity, V₁(m/s): 1.733

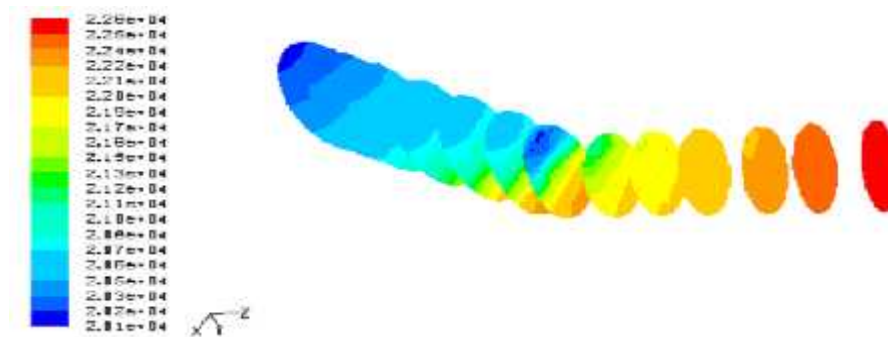


Fig. 5.11c Contour plot of static pressure inside the different points of 135⁰ elbow
 Concentration of SMC solution (kg/m³): 0.8, Liquid flow rate, Q₁(m³/s): 21.94x10⁻⁵, Liquid velocity, V₁(m/s): 1.733

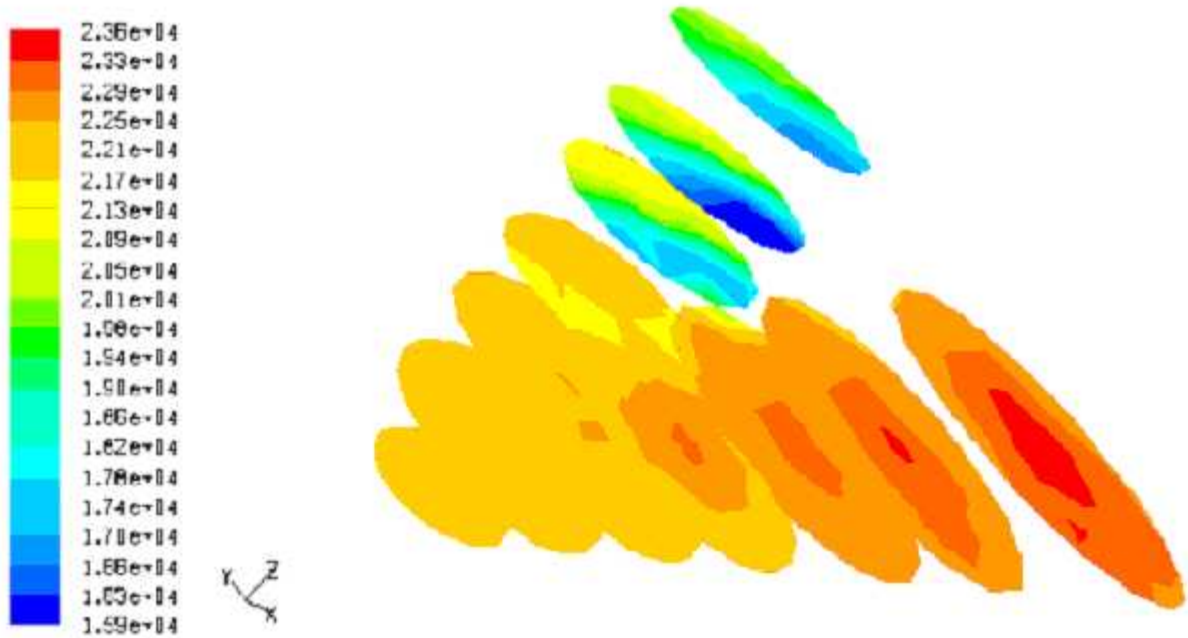


Fig. 5.12a Contour plot of total pressure inside the different points of 45° elbow, Concentration of SCMC solution (kg/m^3): 0.8, Liquid flow rate, Q_1 (m^3/s): 21.94×10^{-5} , Liquid velocity, V_1 (m/s): 1.733

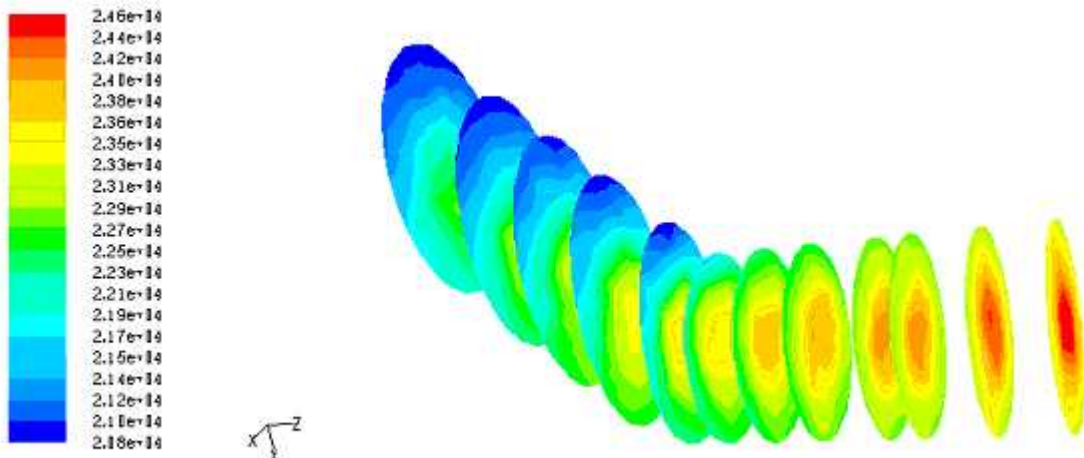


Fig. 5.12b Contour plot of total pressure inside the different points of 135° elbow, Concentration of SCMC solution (kg/m^3): 0.8, Liquid flow rate, Q_1 (m^3/s): 21.94×10^{-5} , Liquid velocity, V_1 (m/s): 1.733

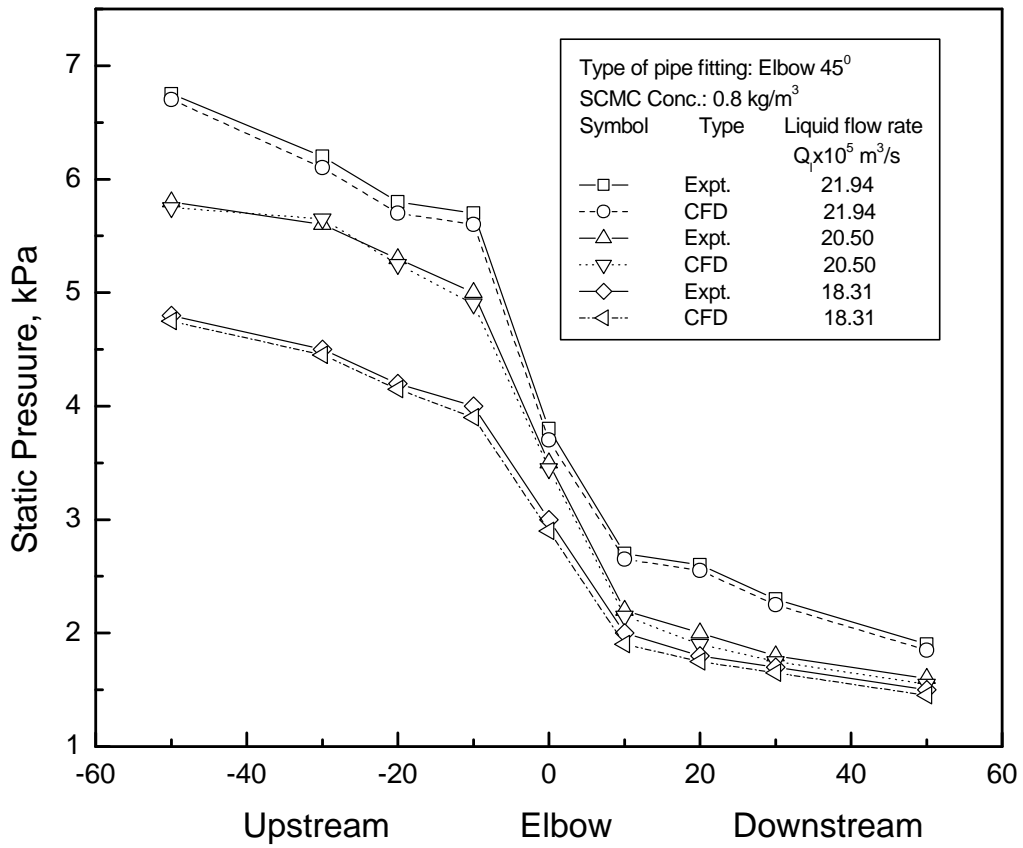


Fig.5.13 Comparison plot of experimental and CFD for 45° elbow

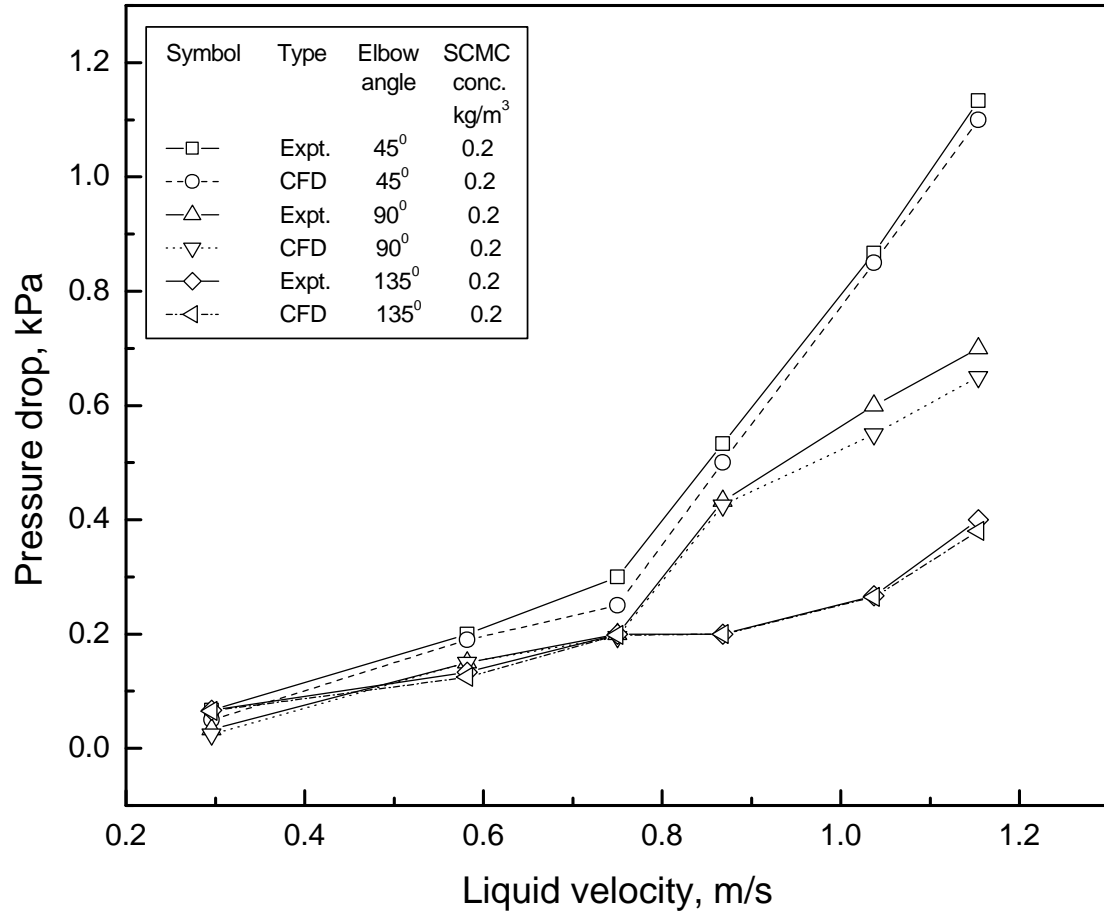


Fig. 5.14 Comparison of the experimental data and CFD modeling for elbows

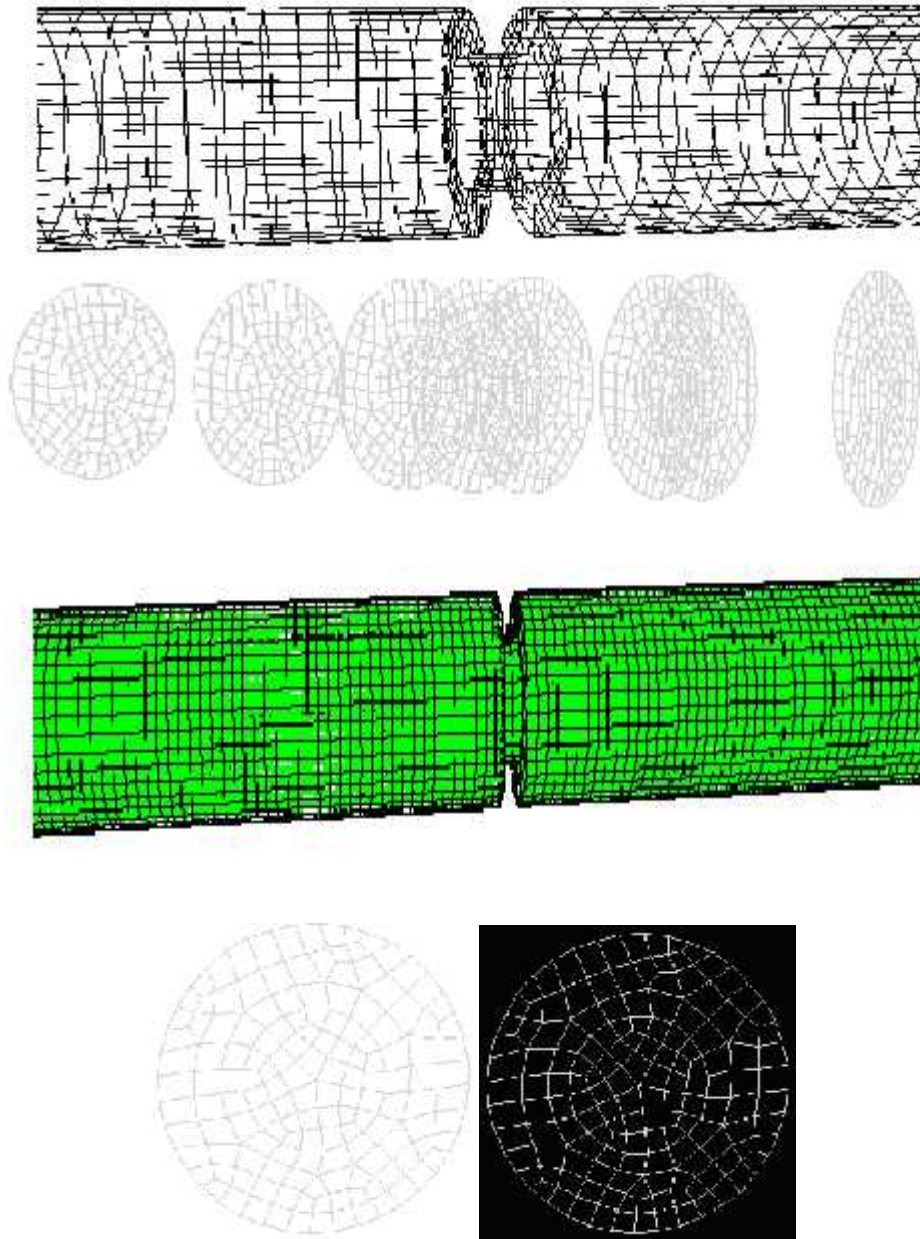


Fig. 5.15 Unstructured boundary layer hexahedral grid of orifice, $D_0/D_t = 0.5984$
Grid Size: No. of cells = 4427; No. of faces = 9778, No. of nodes = 1279
1 cell zone, 4 face zones

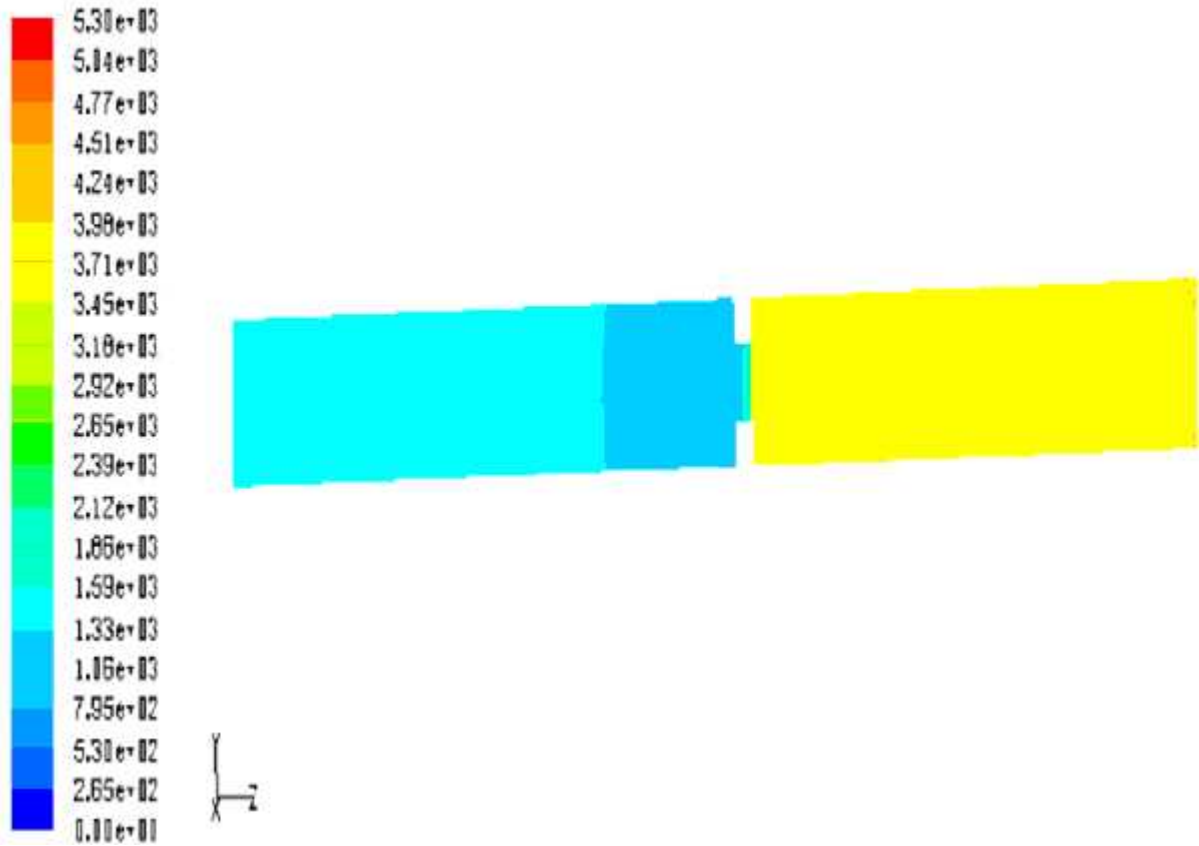


Fig. 5.16 Contour plot of static pressure for $D_0/D_t = 0.4646$ orifice
Concentration of SMC solution (kg/m^3): 0.8, Liquid velocity (m/s): 0.3199

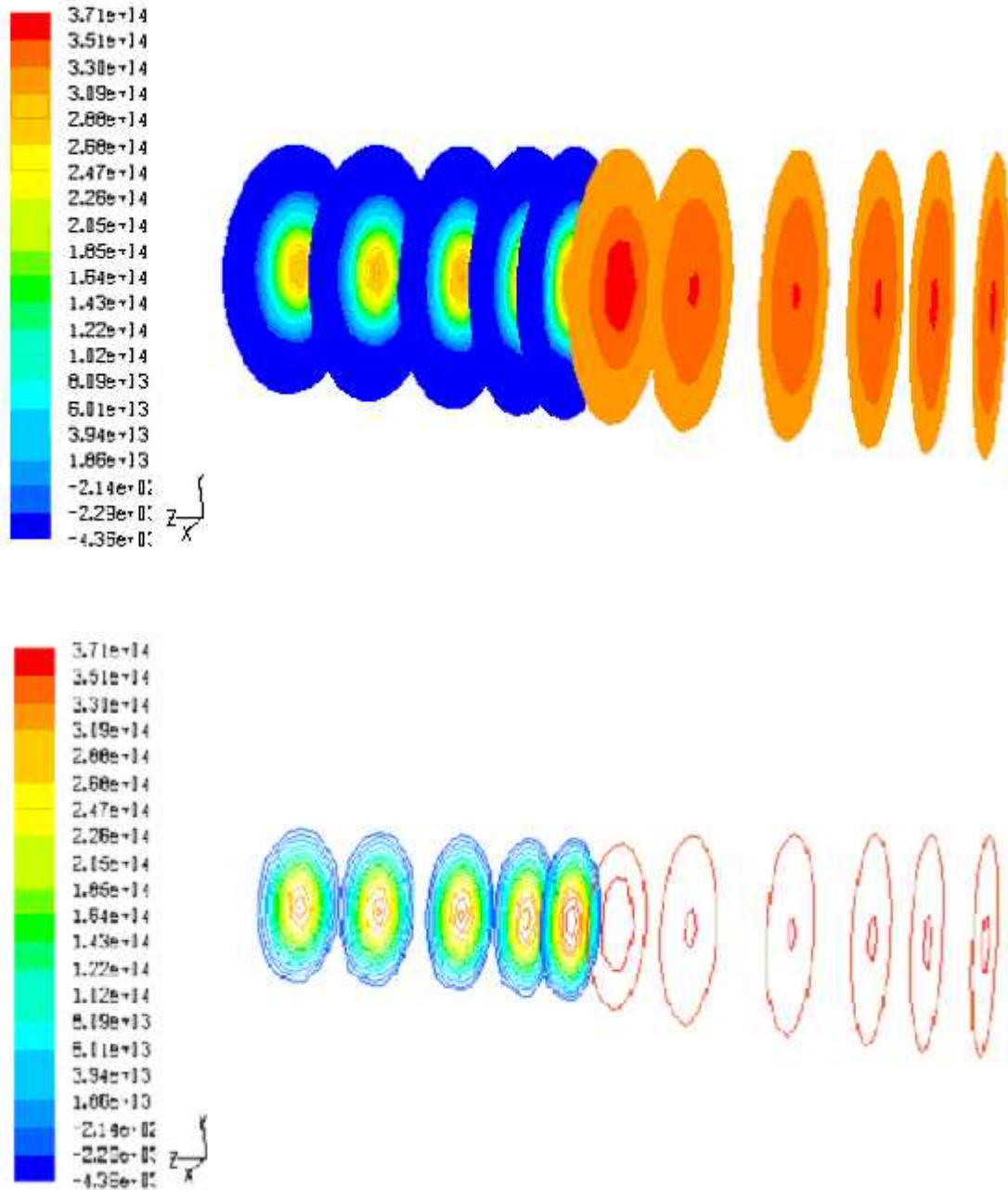


Fig. 5.17 Contour plot of static pressure at different points of $D_0/D_t = 0.5984$ orifice
 Concentration of SMC solution (kg/m^3): 0.8, Liquid velocity (m/s): 1.2772

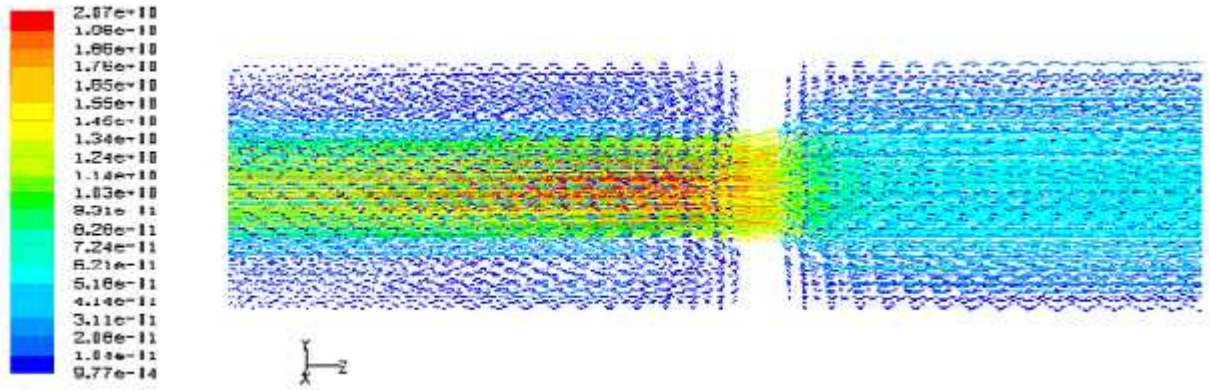


Fig. 5.18 Plot of velocity vector for $D_0/D_t = 0.4646$ orifice
 Concentration of SCMC solution (kg/m^3): 0.8, Liquid velocity (m/s): 0.3199

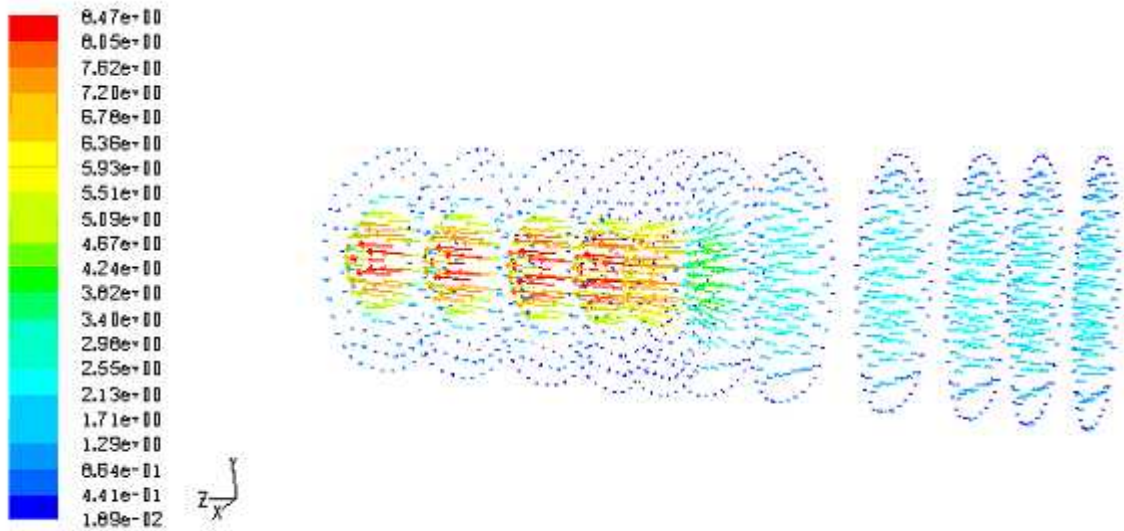


Fig. 5.19 Plot of velocity vector at different points of $D_0/D_t = 0.5984$ orifice
 Concentration of SCMC solution (kg/m^3): 0.8, Liquid velocity (m/s): 1.2772

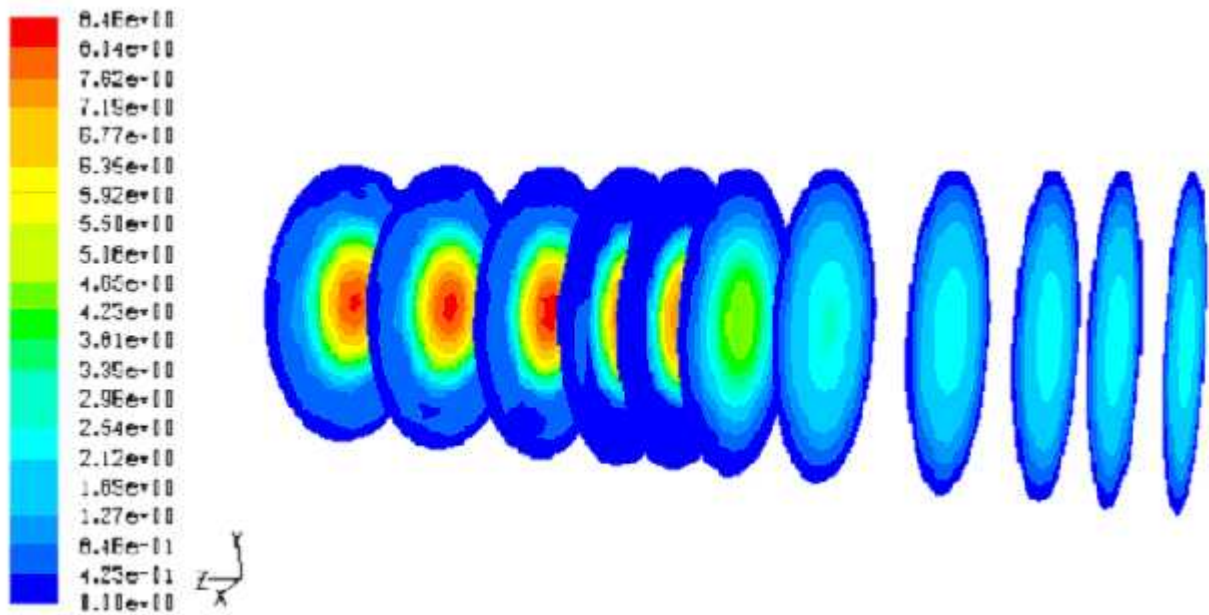


Fig. 5.20 Plot of velocity magnitude for $D_0/D_t = 0.5984$ orifice
Concentration of SCMC solution (kg/m^3): 0.8, Liquid velocity (m/s): 1.2772

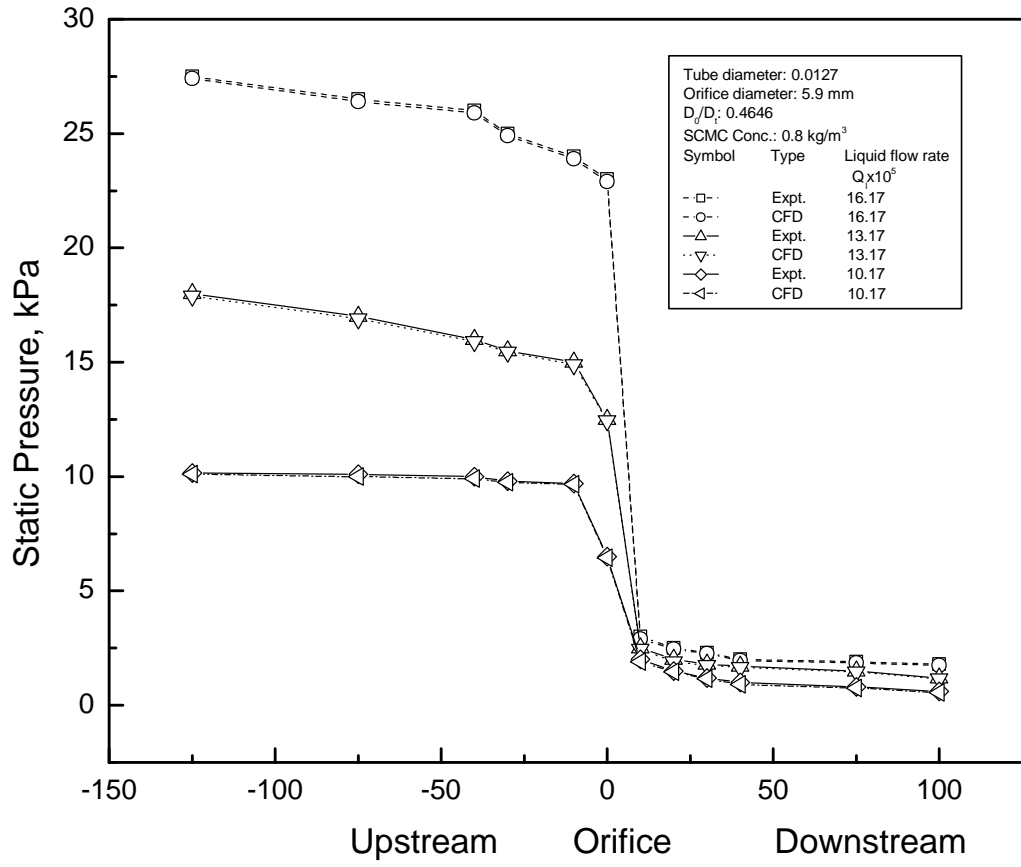


Fig. 5.21 Comparison plot of experimental and CFD for orifice

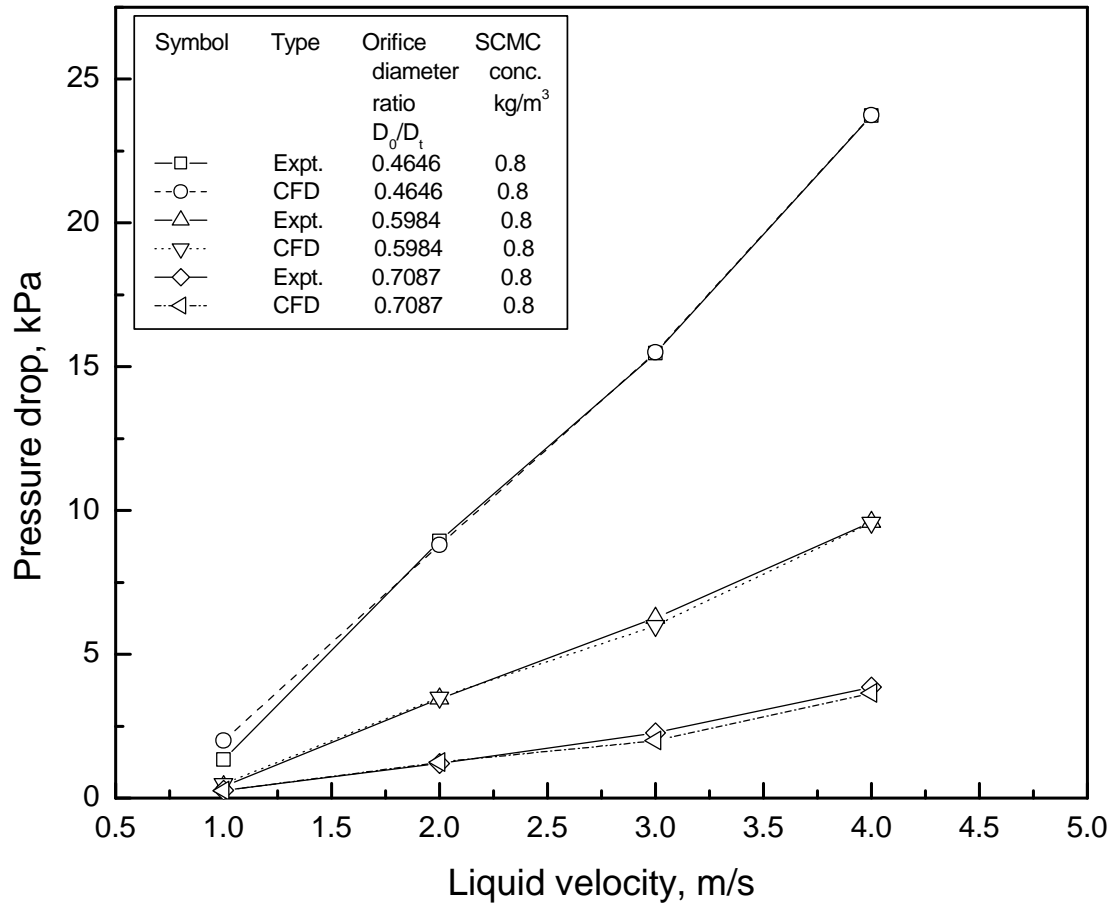


Fig. 5.22 Comparison of the experimental data and CFD modeling for orifices

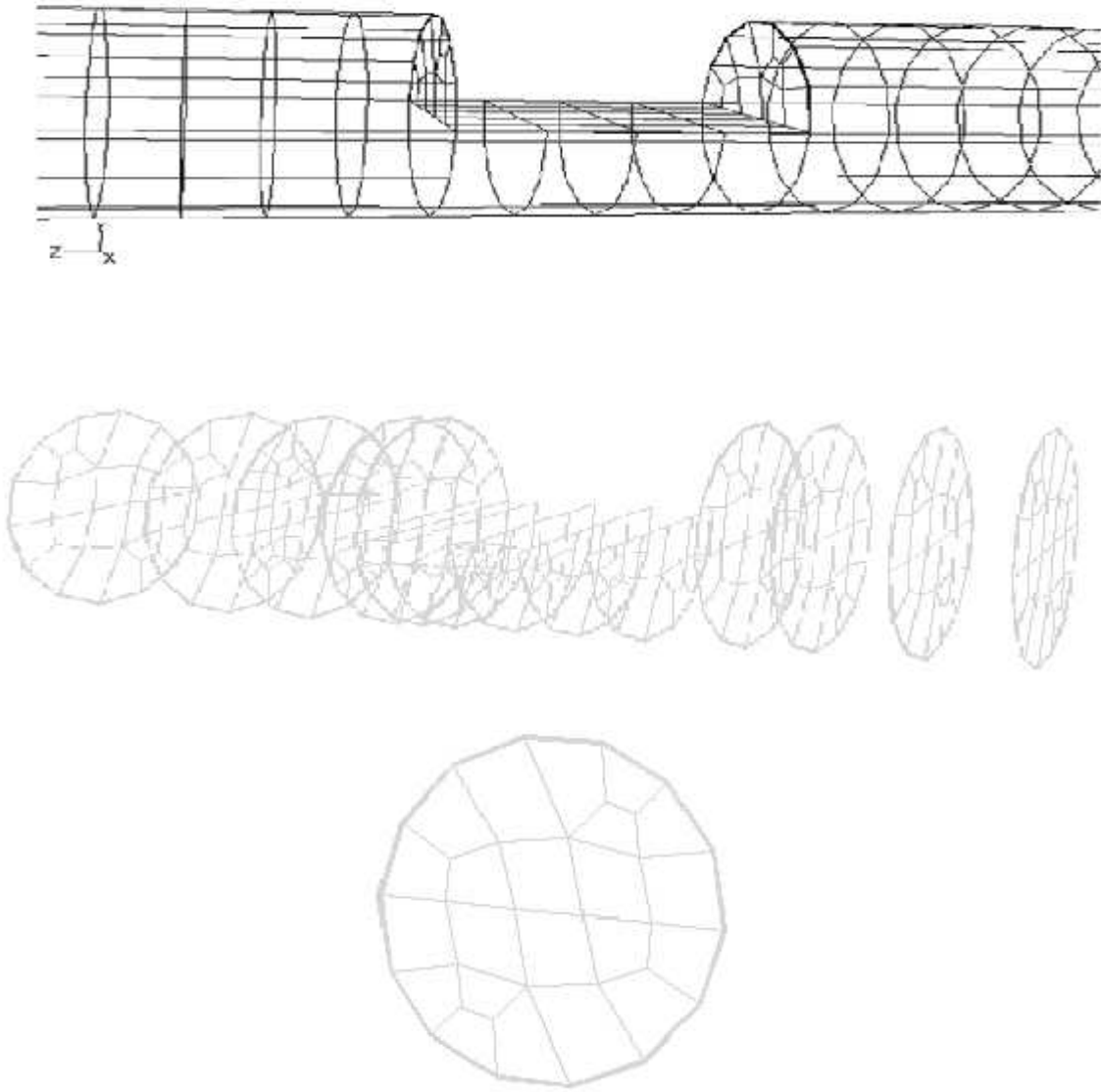


Fig. 5.23 Grid for 50% opening gate valve

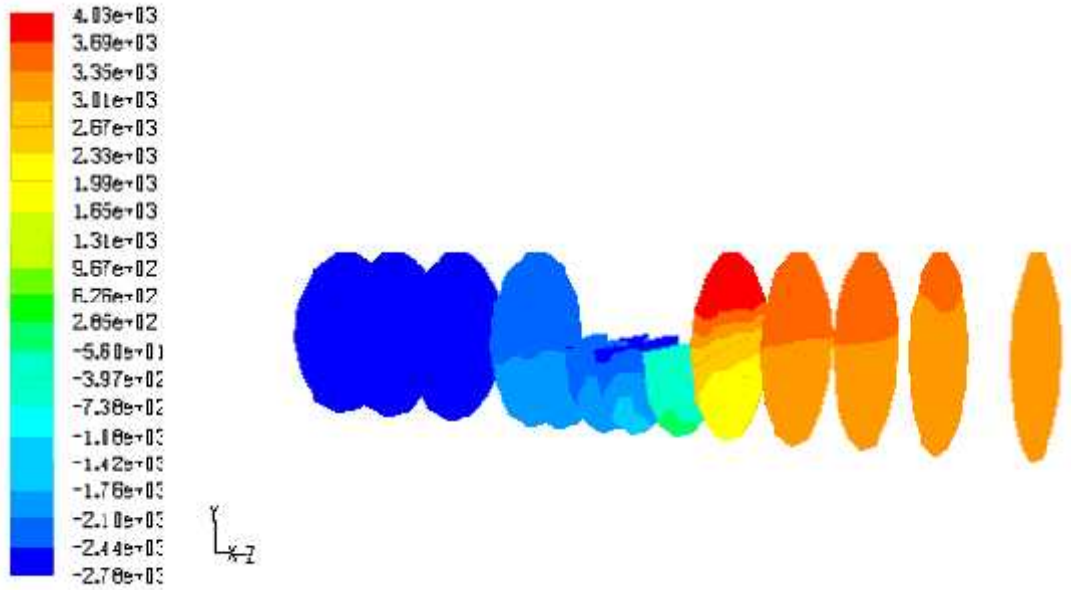


Fig. 5.24 Plot of static pressure for 50% opening gate valve
Concentration of SMC solution (kg/m^3): 0.8, Liquid velocity (m/s): 1.5142

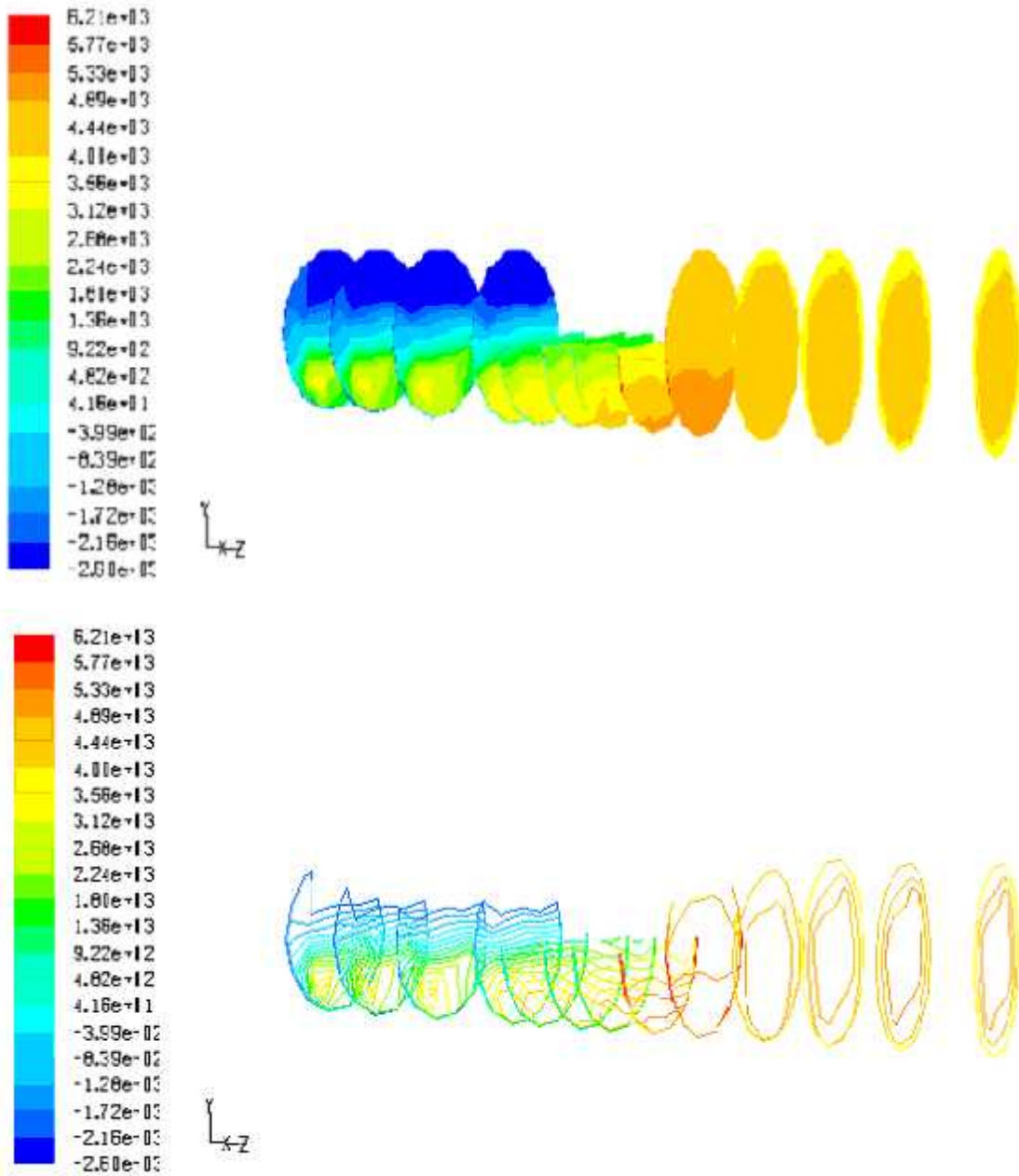


Fig. 5.25 Plot of total pressure for 50% opening gate valve
 Concentration of SCMC solution (kg/m^3): 0.8, Liquid velocity (m/s): 1.5142

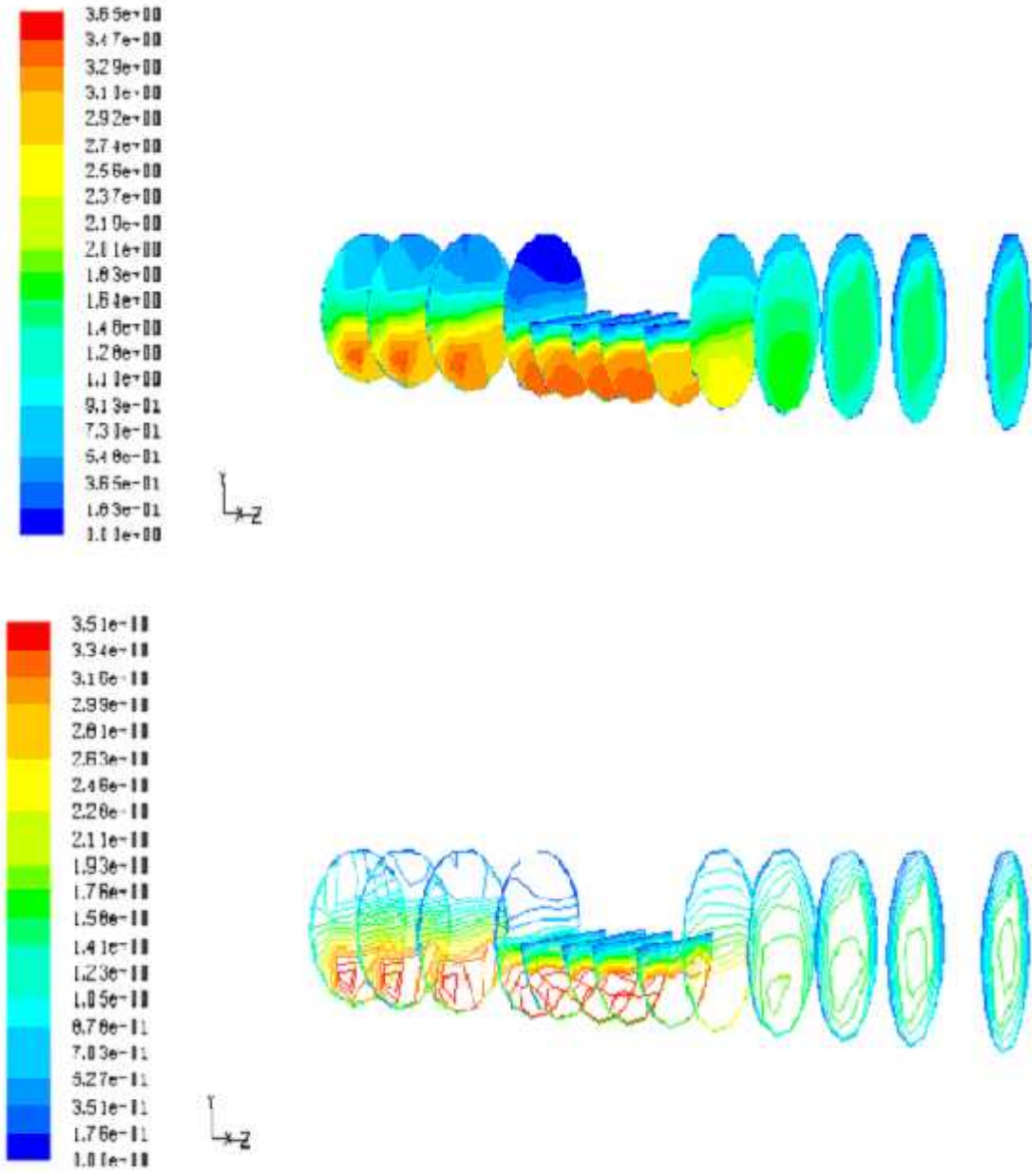


Fig. 5.26 Plot of velocity magnitude for 50% opening gate valve
 Concentration of SCMC solution (kg/m^3): 0.8, Liquid velocity (m/s): 1.5142

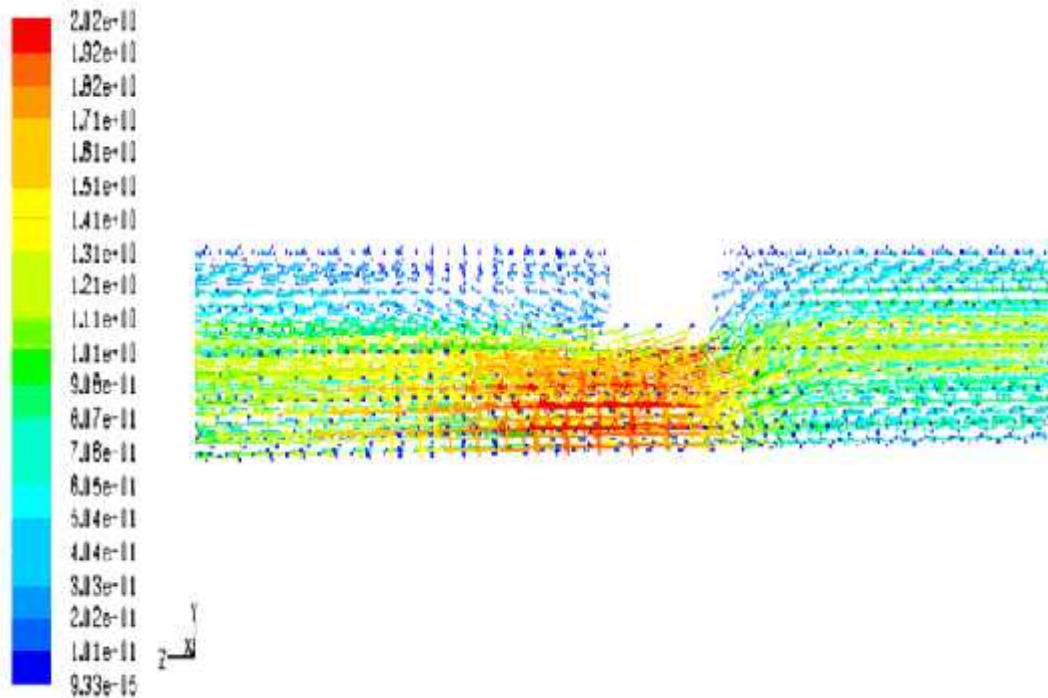


Fig. 5.27 Plot of velocity vector for 50% opening gate valve
Concentration of SMC solution (kg/m^3): 0.8, Liquid velocity (m/s): 0.8033

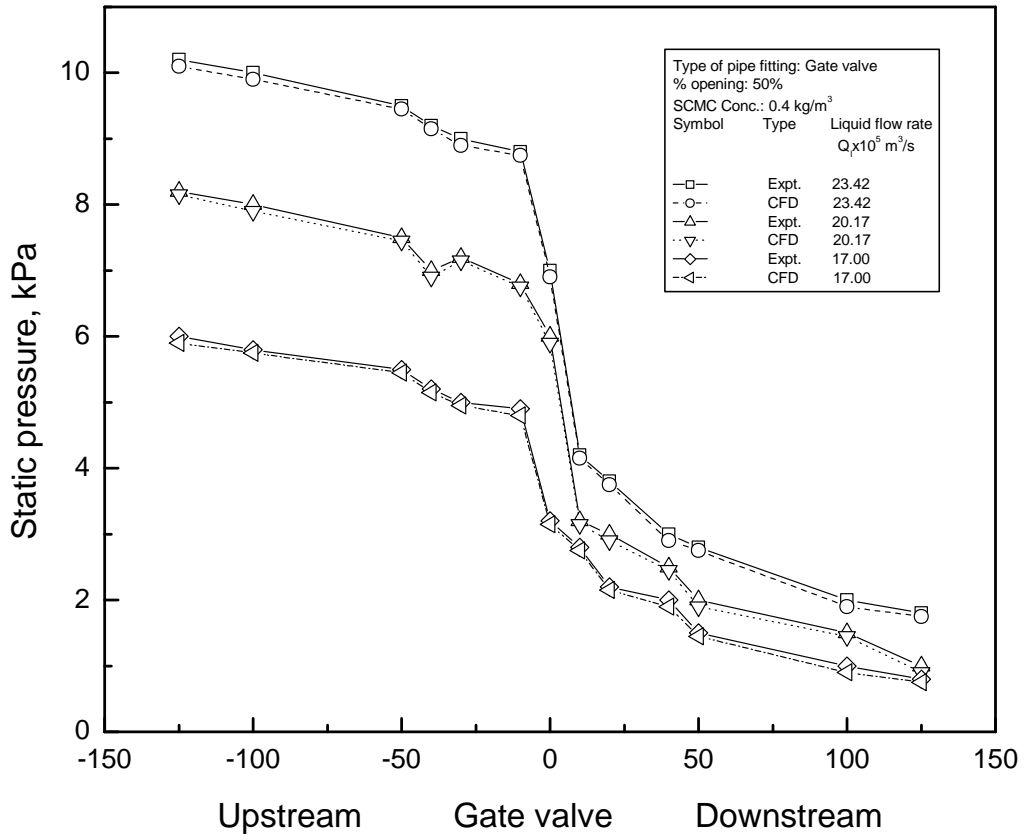


Fig. 5.28 Comparison plot of experimental and CFD for gate valve

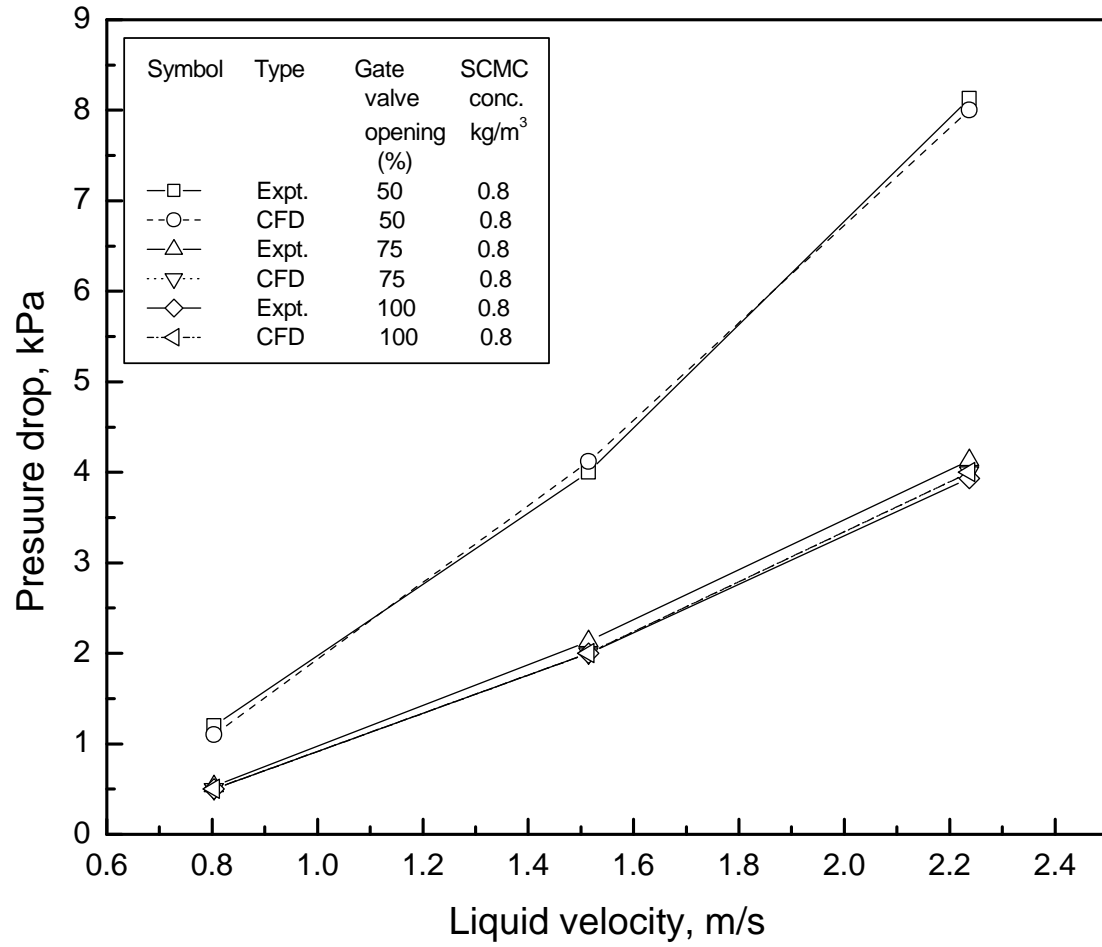


Fig. 5.29 Comparison of the experimental data and CFD modeling for gate valve

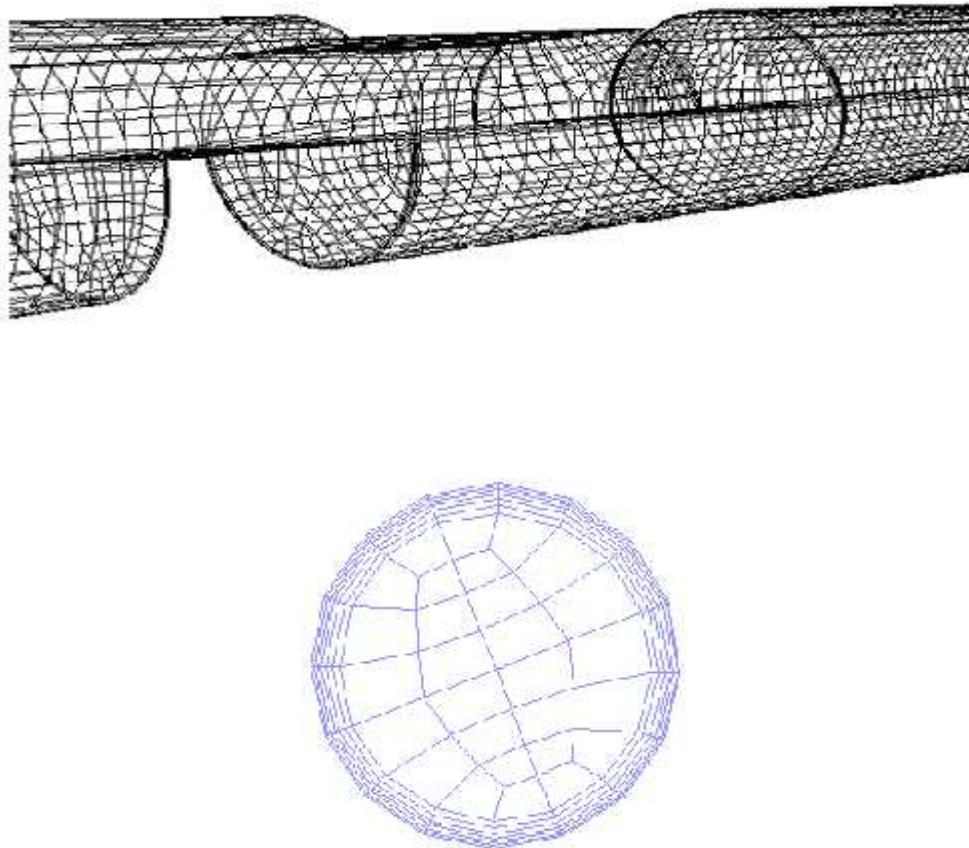


Fig. 5.30 Unstructured boundary layer hexahedral grid of 75% opening globe valve
Grid Size: No. of cells =348633; No. of faces = 1077668, No. of nodes = 381741
1 cell zone, 4 face zones

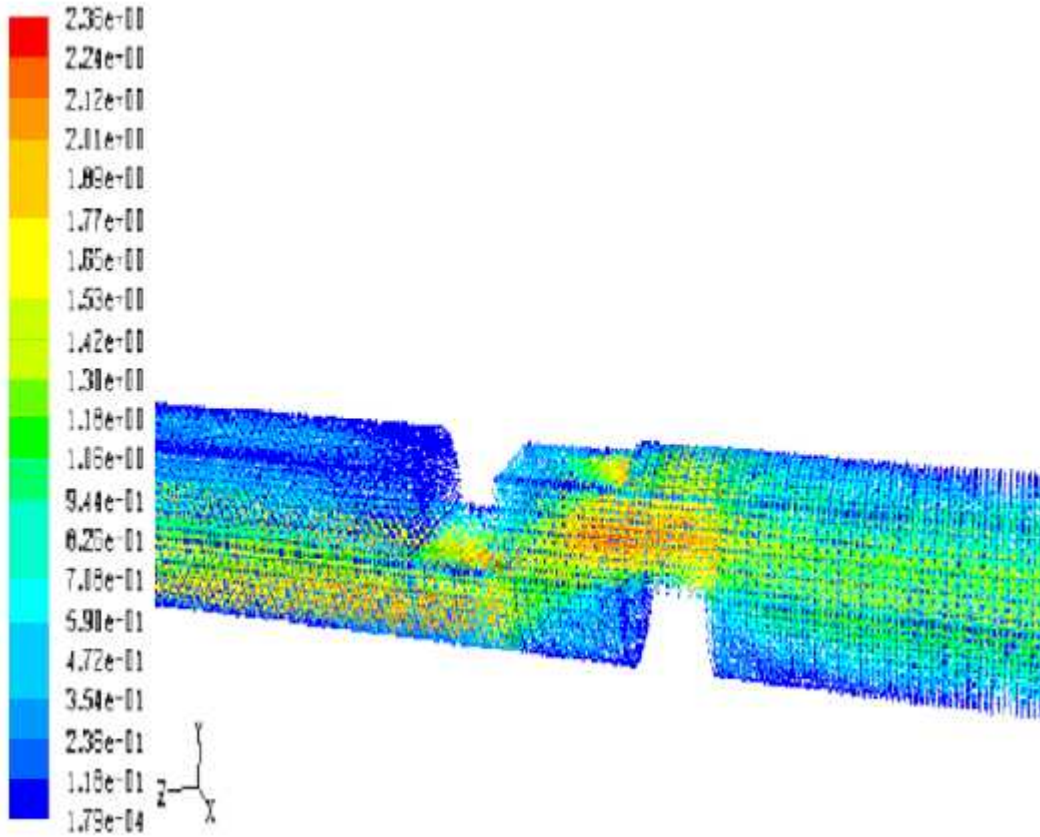


Fig. 5.31 Plot of velocity vector for 75% opening globe valve
Concentration of SCMC solution (kg/m^3): 0.8, Liquid velocity (m/s): 0.8033

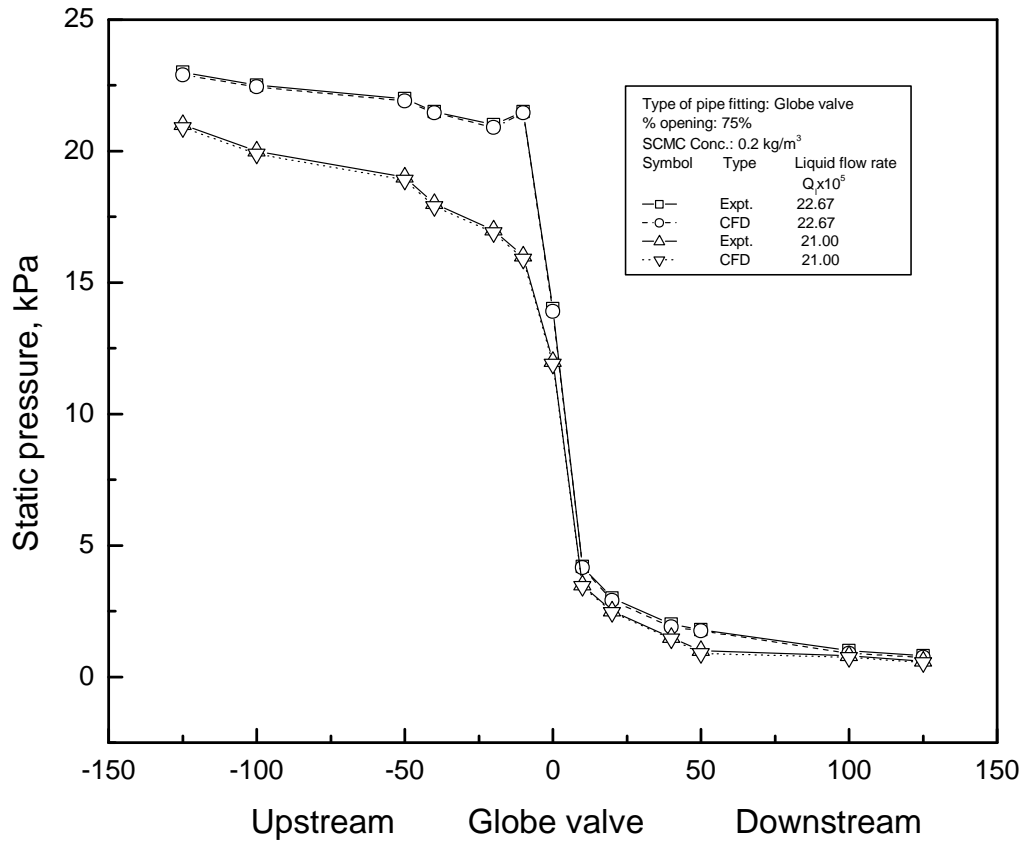


Fig. 5.32 Comparison plot of experimental and CFD for globe valve

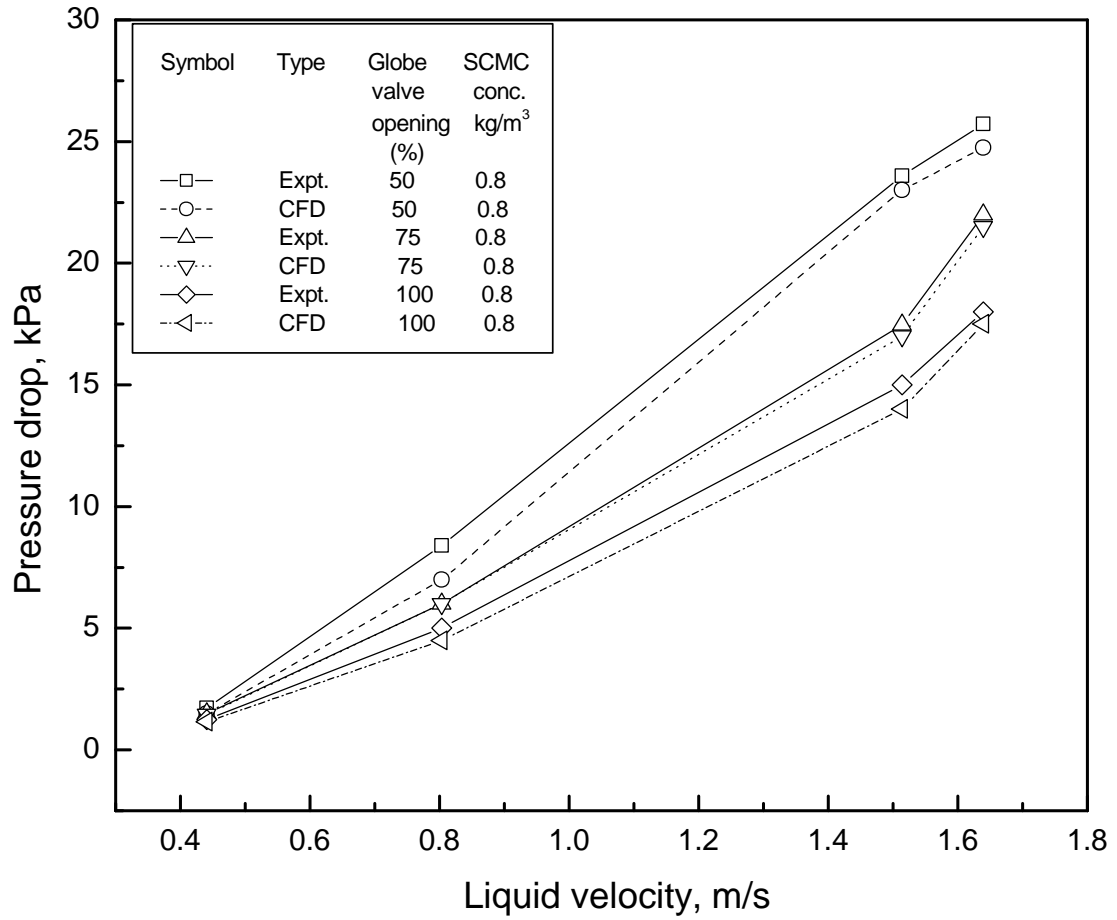


Fig. 5.33 Comparison of the experimental data and CFD modeling for globe valve

Table 5.1 Comparison of experimental and CFD analysis data for straight pipe

Sl. No.	Liquid flow rate Q_1 m^3/s	Single-phase pressure drop, experimental $\Delta P_{st, Expt.}$ kPa	Single-phase pressure drop CFD $\Delta P_{st, CFD}$ kPa
SCMC concentration(kg/m^3):0.8			
1	0.3199	3.659	3.5
2	0.8033	6.325	6.5
3	1.0402	7.39	7.3
4	1.2772	8.35	8.25
SCMC concentration(kg/m^3):0.6			
5	0.3199	2.385	2.25
6	0.8033	4.39	4.35
7	1.0402	5.199	5.25
8	1.2772	5.97	6.05
SCMC concentration(kg/m^3):0.4			
9	0.3199	1.348	1.3
10	0.8033	2.636	2.65
11	1.0402	3.19	3.25
12	1.2772	3.748	3.85

Table 5.2 Comparison of experimental and CFD analysis data for elbows,
Concentration of SCMC solution (kg/m³): 0.2

Sl. No.	Liquid flow rate Q _l m ³ /s	Single-phase pressure drop, experimental $\Delta P_{eb,Expt.}$ kPa	Single-phase pressure drop CFD $\Delta P_{eb,CFD}$ kPa
Concentration of SCMC solution (kg/m ³):0.2 Elbow angle: 45 ⁰			
1	0.296	0.0667	0.05
2	0.582	0.2	0.19
3	0.75	0.3	0.25
4	0.868	0.5333	0.5
5	1.037	0.8667	0.85
6	1.154	1.1333	1.1
Concentration of SCMC solution (kg/m ³):0.2 Elbow angle: 90 ⁰			
7	0.296	0.0333	0.025
8	0.582	0.15	0.15
9	0.75	0.2	0.195
6	0.868	0.4333	0.425
7	1.037	0.6	0.55
8	1.154	0.7	0.65
Concentration of SCMC solution (kg/m ³):0.2 Elbow angle: 135 ⁰			
9	0.296	0.0667	0.065
10	0.582	0.1333	0.125
11	0.75	0.2	0.198
12	0.868	0.2	0.2
13	1.037	0.2667	0.265
14	1.154	0.4	0.38

Table 5.3 Comparison of experimental and CFD analysis data for orifice, Concentration of SCMC solution (kg/m^3): 0.8

Sl. No.	Liquid flow rate Q_1 m^3/s	Single-phase pressure drop, experimental $\Delta P_{0,Expt.}$ kPa	Single-phase pressure drop CFD $\Delta P_{0,CFD}$ kPa
Concentration of SCMC solution (kg/m^3):0.8 Orifice diameter ratio, D_0/ D_t : 0.4646			
1	0.296	2	1.98
2	0.582	8.933	8.88
3	0.75	15.5	15.4667
4	0.868	23.75	23.73
Concentration SCMC solution (kg/m^3):0.8 Orifice diameter ratio, D_0/ D_t : 0.5984			
5	0.296	0.5	0.4
6	0.582	3.5	3.46
8	0.75	6.26	6
7	0.868	9.6	9.58
Concentration of SCMC solution (kg/m^3):0.2 Orifice diameter ratio, D_0/ D_t : 0.7087			
8	0.296	0.2666	0.25
9	0.582	1.25	1.2
10	0.75	2.266	2.2
11	0.868	3.866	3.65

Table 5.4 Comparison of experimental and CFD analysis data for gate valve,
Concentration of SMC solution (kg/m³): 0.8

Sl. No.	Liquid flow rate Q _l m ³ /s	Single-phase pressure drop, experimental $\Delta P_{gate,Expt.}$ kPa	Single-phase pressure drop CFD $\Delta P_{gate,CFD}$ kPa
Concentration of SMC solution (kg/m ³):0.8 Gate Valve, % opening: 50			
1	0.8033	1.2	1.1
2	1.5142	4	4.12
3	2.2377	8.13	8
Concentration of SMC solution (kg/m ³):0.8 Gate Valve, % opening: 75			
5	0.8033	0.533	0.5
6	1.5142	2.133	2
7	2.2377	4.133	4
Concentration of SMC solution (kg/m ³):0.8 Gate Valve, % opening: 100			
8	0.8033	0.5	0.5
9	1.5142	2	2
10	2.2377	3.93	4

Table 5.5 Comparison of experimental and CFD analysis data for globe valve, Concentration of SCMC solution (kg/m³): 0.8

Sl. No.	Liquid flow rate Q_1 m ³ /s	Single-phase pressure drop, experimental $\Delta P_{globe, Expt.}$ kPa	Single-phase pressure drop CFD $\Delta P_{globe, CFD}$ kPa
Concentration of SCMC solution (kg/m ³):0.8 Globe Valve, % opening: 50			
1	0.4407	1.733	1.5
2	0.8033	8.4	7
3	1.5142	23.6	23
4	1.639	25.73	24.75
Concentration of SCMC solution (kg/m ³):0.8 Globe Valve, % opening: 75			
5	0.4407	1.5	1.45
6	0.8033	6	6
7	1.5142	17.46	17
8	1.639	22	21.5
Concentration of SCMC solution (kg/m ³):0.8 Globe Valve, % opening: 100			
9	0.4407	1.25	1.15
10	0.8033	5	4.5
11	1.5142	15	14
12	1.639	18	17.5

Chapter 6

***CFD analysis on two-phase gas-non-Newtonian liquid flow
through piping components***

This chapter deals with the CFD analysis using commercial software Fluent 6.3 was used for the analysis of gas-non-Newtonian liquid flow through piping components in the horizontal plane. The CFD analysis was tested from our published experimental results Bandyapadhyay (2002) and Bandyopadhyay et al. (2000).

6.1 Introduction

Pipe fittings like valves, bends, elbows, tees, reducers, expander etc. are the integral part of any piping system. Flows through piping components are more complex than the straight pipes. The problem of determining the pressure losses in elbows is important in design and analysis of the fluid machinery. Forcing a fluid through elbows consumes energy provided by the drop in pressure across the elbows. The friction between the fluid and the fitting wall causes this pressure drop. Edwards et al. (1985) and Das et al. (1991), Banerjee et al. (1994), Bandyopadhyay and Das (2007) reported experimental studies of non-Newtonian liquid flow through various piping components and empirical correlation were suggested for individual piping components. However, data or equations for pressure drops through elbows are meager. Since most non-Newtonian liquids are highly viscous in nature and the laminar flow is of greatest practical interest (Das et al., 1989).

Struiver (1955), Cohen (1957), Castillo (1957), Straub and Silbeman (1960) and Spedding and Benard (2007) pointed out the difficulties in understanding the pressure characteristics in bends. Chenoweth and Martin (1955) showed that the two-phase pressure drops across the bends were higher than the single phase flow and Lockhart-Martinelli (1949) model correlated the experimental data. Fitzsimmons (1964) reported two-phase pressure drop across the bend in terms of equivalent length technique and also

Lockhart-Martinelli (1949) correlation and observed that the experimental data were very poorly correlated using these techniques. Sekoda et al. (1969) reported the flow characteristics in the inlet and outlet region of 90° bend. They also observed that the two-phase pressure drop was independent of the pipe diameter but depends on the ratio of D_o/d . Bruce (1971) observed that the two-phase pressure drop across the bends was over predicted by using the conventional Lockhart-Martinelli (1949) correlation for the vapour liquid R_{12} refrigerant flow through bends. Engineering Science Data Unit (1977) reported model for two-phase flow through piping components. Maddock et al. (1974) reported the structure of two-phase flow in curved geometry. Hoang and Davies (1984) showed that flow regime changes from bubbly inlet flow to stratified flow at the outlet of the 180° bend. Deobold (1962) claimed that the horizontal bend, horizontal to vertical up bend and the vertical down to horizontal bend all gave the same bend pressure loss. However, a horizontal to vertical down bend had a pressure drop was 35% less. Xin et al. (1996) reported the numerical modeling of turbulent single-phase and two-phase flow in curved pipe and observed discrepancies between the prediction and observed values in two-phase flow. Azzi et al. (2000) and Azzi et al. (2002) pointed out that no model describes the properties of the two-phase gas-liquid flow through bends. Supa-Amornkul et al. (2005) reported the CFD modeling of two-phase air water flow through pipe bends. They observed that the simulation for two-phase flow was significantly different from the experimental data. i.e., the overall pressure drop across the test section was significantly less for the simulation than for the experimental data. Spedding et al. (2007) correlated the two-phase pressure drop across the elbow in terms of total Reynolds number.

The availability of the literature for gas-non-Newtonian liquid flow through piping components is very sporadic (Das et al., 1991). Das et al. (1991), Banerjee and Das (1998), Samanta et al. (1999) and Bandyopadhyay et al. (2000) reported the experimental investigation for gas-non-Newtonian liquid flow through bends, valves, orifices and elbows. They developed empirical correlation for predicting the frictional pressure drop across the piping components. In order to achieve optimum performance, an accurate design technique is necessary for the prediction of the pressure drop for gas-non-Newtonian liquid through piping components.

The use of CFD in designing engineering devices has increased over the last few years due to availability of commercial codes featuring state-of-the-art robust models and the ability to run the code on desktop PCs. Evaluating two-phase pressure losses across the piping components using continuum and particulate phase in the Eulerian/Lagrangian approach or as a homogeneous fluid in the Eulerian/Eulerian approach. The objective of this chapter is to validate the CFD model of the commercial code Fluent 6.3 for predicting the two-phase gas-non-Newtonian pressure drop across the straight pipe and the piping components and tested the model with our previous experimental data from our laboratory by Bandyopadhyay (2002) and Bandyopadhyay et al. (2000).

6.2 The experimental setup

Details of the experimental (Fig. 6.1) investigation for gas-non-Newtonian liquid flow through piping components are reported in our earlier work published by Bandyopadhyay (2002) and Bandyopadhyay et al. (2000). The ranges of variables investigated are shown in Tables 6.1.

6.3 Mathematical Model

Governing equations and numerical methods are explained in chapter 2.

Dilute solution of SCMC follows the non-Newtonian pseudo plastic Power law model. In general for non-Newtonian liquids the effective viscosity is used for calculation and defined as,

$$\mu_{eff} = K' \left(\frac{8u}{d} \right)^{n'-1} \quad (6.1)$$

As the flow of liquid is laminar, non-Newtonian Power Law model is used as viscous model and Euler Ian model is used as multiphase model for the CFD analysis. These equations are solved subject to the following boundary conditions,

- (i) The pipeline and piping components walls are assumed rigid and a no-slip condition is imposed.
- (ii) At the outlet, the velocities are free but the normal and tangential stresses are constrained to be zero and the gauge pressure is set to zero.
- (iii) At the inlet, a uniform velocity profile is used with a time varying forcing function representative of flow in the left portion of the piping components.

6.3.1 Computational fluid dynamics (CFD) Procedure

Geometries for the straight pipe, elbows, orifices, valves and are created in Gambit 6.3 preprocessor. A typical mesh has about $3 \times 10^3 - 2 \times 10^5$ order unstructured t-grid and unstructured boundary layer hex-wedge cooper schemes are used. Inlet and outlet are located at each end of the piping system. The inlet is used to specify the inlet velocity and outlet is used to specify pressure outlet. These geometries of the pipeline and piping components are imported into Fluent 6.3 in a Cartesian co-ordinate system. Fluent 6.3 solved the governing equations in 3-D geometry. Laminar non-Newtonian Power

Law model have been used for simulation. The model solves for Navier-stokes equation at prescribes velocities. The governing equations are non linear and several iterations of loop must be performed before a convergent solution is obtained. The first-order upwind scheme is used in the discretization of set of governing equations, standard interpolation schemes is used for calculating cell-face pressures for using the Segregated solver in Fluent 6.3. Pressure-velocity coupling refers to the numerical algorithm which uses a combination of continuity and momentum equations to derive an equation for pressure (or pressure correction) when using the segregated solver. Simple algorithm is used.

A general procedure to simulate the two-phase gas-non-Newtonian fluid flow through pipe and piping components based on Gambit 6.3 and Fluent 6.3 software is outlined below,

1. Perform meshing under Gambit 6.3.
 - Create a computational domain at the flow region,
 - The grids were generated using boundary layer hexahedral meshes and t-grid (tetrahedral grid),
 - Controlling a smooth change in the mesh size by size functions,
 - Specify boundary and continuum types,
 - Examine the mesh to ensure that the high skewness is below 0.5 for hexahedral and below 0.9 for tetrahedral mesh.
2. Import the mesh file to Fluent 6.3 and check the mesh.
3. Define a 3-D, unsteady, implicit, and pressure-based solver.
4. Activate the Eulerian laminar non-Newtonian power law multiphase model.
5. Define Eulerian laminar model. Slip velocity is added.

6. Enable the liquid (SCMC) properties with laminar flow conditions using the text command: define/models/viscous/laminar
7. Define the phases by setting liquid (SCMC) as the primary phase and gas as the secondary phase, and keeping the default selection of Schiller-Naumann drag model in the phase interaction panel.
8. Define the operating conditions by turning on gravity and specify the operating density.
9. Solution control methodology – Under relaxation factors – 0.5 for pressure, 0.3 for momentum, 0.1 - 0.9 for volume fraction, and default values for the other parameters. Standard schemes – STANDARD for momentum and volume fraction, and 1st order upwind for other variables. Pressure-velocity SIMPLE coupling used;
10. Initialize the solution – velocity;

Enable the plotting of residuals during the calculation, and kept the default convergence criteria, 1×10^{-3} for continuity and 1×10^{-5} all residuals.

6.3.2 Assumptions for air-SCMC flow through piping components

The following concepts and assumptions were made:

1. The solution temperature is constant at 30⁰C, and each phase is an isothermal and incompressible fluid;
2. A single pressure is shared by both phases;
3. Momentum and continuity equations are solved for each phase;

4. Our system behaves like a plug and slug flow regimes. But we assumed two-phase flow as a bubbly flow due to simplicity of calculation in which liquid (SCMC) is treated as the primary phase while gas is treated as the secondary phase;
5. The secondary phase consists of uniform and unchanging bubbles dispersed in a continuous phase;
6. The bubbles size is assumed to be small, 0.1mm spherical in size;
7. Two-phase Eulerian laminar non-Newtonian power law model is used;
8. Physical properties are uniform throughout;
9. Different phases move at different velocities (slip velocities);
10. The drag force from liquid (SCMC) phase acting on the gas bubbles is included into the interphase momentum exchange;
11. There are no external body force and virtual mass force, and the effect of lift force on the bubbles is negligible.

6.4 Results and discussion

6.4.1 Convergence and grid independency

The convergence criterions were set at 10^{-5} for all equations except for the transport equation which residual was set at 10^{-3} . A computational domain L 200D was used to ensure fully developed flow results could be obtained for all pipe and piping components. In general the final results depend upon mesh geometries. Subsequent decrement and increment in mesh resolution by 50% were applied to evaluate if the employed mesh resolution was adequate to obtain accurate solutions. It was observed that when the mesh resolution was decreased by 50% the axial velocity profile was 7-12% of the currently employed mesh velocity profile for pipe and different piping components.

As the present mesh resolution was increased by 50% the axial velocity profile changes 1-3% for pipe and different piping components. These results suggest that the current mesh resolution is sufficient to obtain grid independent solutions for the proposed model.

6.4.2 Computational fluid dynamics (CFD) analysis for air-non-Newtonian liquid flow through straight pipe

Fig. 6.2 shows the contour plot of velocity vector in the air-SCMC mixture for straight pipe. It illustrates that velocity is maximum at centre and velocity is minimum near the wall of the pipe. Figs. 6.3 and 6.4 show the velocity vector plot of liquid phase and air phase in the mixture for straight pipe. It indicates that heavier density liquid phase more at the nearer to the wall and lighter air phase more at the centre of the pipe. Fig. 6.5 shows that contours of velocity magnitude at the different points of straight pipe. It illustrates that velocity is maximum at centre and velocity is minimum near the wall of the pipe. Fig. 6.6 shows that contours of axial velocity at the different points of straight pipe. It indicates that some air pockets observed with the liquid.

Figs. 6.7 and 6.8 show the Contour plot of static pressure and total pressure (mixture) at the different points of the straight pipe. It indicates that static pressure and total pressure gradually decreases from inlet to outlet of the pipe due to fluid-pipe friction. This effect is more with increasing the liquid concentration. Figs. 6.9 and 6.10 show that the contours plot of volume fraction at liquid and air phase. It indicates that air concentration is more at the centre and liquid concentration is more neighboring position of the centre and nearer to the wall.

Fig. 6.11 indicates that two-phase frictional pressure drop increases with increasing liquid flow rate.

Fig. 6.12 indicates that two-phase frictional pressure drop increases with increasing SCMC concentration in the liquid, i.e., pseudoplasticity of the liquid.

Fig.13 shows that comparison of experimental results with CFD simulated results for different liquid flow rate. In both cases experimental results matches well with the CFD simulated results. From this plot we see that both result matches with error% ± 10 .

6.4.3 Computational fluid dynamics (CFD) analysis for air-non-Newtonian liquid flow through elbows

Fig.6.14 illustrates the contour plot of velocity for the gas-liquid mixture for 45° elbows. Fig. 6.15 (a-c) shows that contour plot of velocity at different points in the elbows. It is clear from these figures the mixture velocity is higher at the centre position and inner side of the elbow and lowers at the outer wall. As the mixture enters to the elbows due to centrifugal action heavier density phase that is liquid moves to the outer wall and lower density phase, air moves to the inner wall. Fig. 6.16 clearly demonstrates that the liquid velocity is higher at the outer wall. Fig. 6.17 illustrates that the air velocity at the inner wall is higher and practically zero at the outer wall. The inlet flow regime is intermittent in nature (plug and slug). At inlet the existence of air is at the top. Due to slip exist between the liquid and air and the existence of the pressure gradient across the cross-section air velocity increases compare to the liquid velocity, due to centrifugal action the liquid is shifted towards the outer wall and a stratified flow condition attain within the elbows.

Fig. 6.18 shows the static pressure profile of elbows. The 45° elbow shows higher pressure drop than comparing with the other elbows and it is due to faster dispersion of rope and a shorter developing flow exist. Fig. 6.19 shows that contour plot of static pressure at different points in the elbows. It shows that pressure is high at outer wall as

heavier density liquid phase goes to outer wall due to centrifugal force and low at the inner wall when the air phase exists. Due to this pressure gradient at any cross section of the elbow the air is accelerated more than the liquid phase. Due to this acceleration maximum velocity is shifted for the mixer.

The secondary flow originated in a pair of counter rotating vortices at the just inside of the elbow as shown in Fig. 6.20 for 45⁰ elbows. These vortices continue up to the downstream of the elbow, merged in the just outlet of the elbow and downstream flow return slowly to the steady state.

Fig. 6.21 shows that volume fraction of the liquid (SCMC) and air at different point in the 90⁰ elbow. It shows that heavier density phase liquid (SCMC) goes to outer wall side and lighter air goes to inner wall side due to centrifugal force.

Fig. 6.22 shows that comparison plot of static pressure experimental and CFD for 45⁰ elbows. Fig. 6.23 shows that comparison plot of experimental results with CFD simulated results at different elbow angles. In both cases experimental results matches well with the CFD simulated results.

The flow pattern is depended on the flow rate of each phase, their interactions the transport properties and the geometry of the elbows. The flow regime was difficult to determine in the two-phase region. In general an accumulation of air towards the inside of the wall, this originates from the start of the elbow. This could be caused by a radial pressure gradient generated by the lower density mixture causing the slow-moving liquid phase near the wall to move toward the inside wall of the elbow. Phenomenon at high gas flow rates was observed by Banerjee et al. (1967), Farukhi and Parker (1974), Maddock et al. (1974) and Usui et al. (1983).

6.4.4 Computational fluid dynamics (CFD) analysis for air-non-Newtonian liquid flow through orifices

Figs. 6.24 - 6.26 show that contour plot of velocity vector in the air-SCMC mixture at the different cross-section of orifices. It indicates that velocity is low at the inlet of the pipe and it increases more after passing the orifice plate. This is due to narrowing of the flow area. It affects more from large orifice diameter to small orifice diameter.

Figs. 6.27 - 6.29 show that contour plot of static pressure (mixture) for three orifices. It indicates that static pressure is high from inlet of the pipe to up to inlet of orifice and it decreases more after passing the orifice plate. This is due to narrowing of the flow area. It affects more from large orifice diameter to small orifice diameter. Figs. 6.30 – 6.32 show that velocity vector plot for mixture, liquid and air phase. Figs. 6.33 – 6.34 show that velocity magnitude and velocity at the different points of orifices. Figs. 6.35 – 6.36 show that static pressure and total pressure plot in the mixture at different points of orifice. Fig. 6.37 shows the contour of volume fraction for liquid phase at different cross section of the orifice. It indicates that liquid percentage is maximum at the centre of the orifice plate. It also indicates that after passing the orifice plate liquid percentage slightly decrease at the centre in compare to orifice plate but its surrounding place liquid percentage is very low. Fig. 6.38 shows the contour of volume fraction for air phase at different cross section of the orifice. It indicates that air percentage is minimum at the centre of the orifice plate. It also indicates that after passing through the orifice plate liquid percentage is slightly increase at the centre in compare to orifice plate due the presence of vena contracta.

Fig. 6.39 comparison of the experimental result with CFD simulated result with different liquid flow rate and fixed liquid concentration, fixed orifice dimension. It indicates that two-phase frictional pressure drop increases with increasing liquid flow rate. This is due to with increasing the flow rate, increasing the velocity and more increasing the velocity more increasing of kinetic energy causing loss as a form of pressure energy.

Fig. 6.40 shows that comparison of the experimental result with CFD simulated result with different orifice dimension and fixed liquid concentration, fixed liquid flow rate. It indicates that two-phase frictional pressure drop increases with decreasing orifice diameter. This is due to decreasing of flow area velocity increases and according to Bernoulli's conservation law pressure drop increase.

Fig. 6.41 shows that comparison plot of experimental results with CFD simulated results for different liquid flow rates. Fig. 6.42 shows that comparison of experimental results with CFD simulated results for different Orifice diameter ratios.

In both cases experimental results matches well with the CFD simulated results.

6.4.5 Computational fluid dynamics (CFD) analysis for air-non-Newtonian liquid flow through gate valve

Fig. 6.43 shows that plot of velocity vector in the air-non-Newtonian liquid mixture at different points of the 50% opening gate valve. It indicates that velocity increases at the position of the 50% opening gate valve. This is due to lowering of flow area. Similar velocity vector plot observed for 75% and 100% opening gate valve. It is noted that velocity increases from 100% opening valve to 50% opening valve. This is due to lowering of flow area which causing increasing of velocity. Figs. 6.44 - 6.45 show that contours of velocity magnitude and velocity in the air-non-Newtonian mixture at

different points of the 50% opening gate valve. It indicates that velocity increases at the valve position. This is due to narrowing the flow area. It is also observed that some secondary flow is observed.

Figs. 6.46 and 6.47 show that contour plot of static pressure and total pressure for 50% opening gate valve. It indicates that static pressure decreases after passing the valve. It affects more with increasing the obstruction i.e. decreasing the flow area, decreasing the valve and increasing the pseudoplasticity of the liquid. This is due to obstruction of flow causing increase of kinetic energy as a form of lowering of pressure. Similar plot observed for 75% and 100% opening gate valve. It is noted that static pressure decreases too much from 100% opening valve to 50% opening valve. This is due to lowering of flow area which causing decreasing of static pressure by increasing the velocity according to Bernoulli's conservation law. Fig. 6.48 and Fig. 6.49 show that contours of volume fraction for liquid phase and air-phase at the different points of the 50% opening gate valve. It indicates that at the valve position lighter density gas passing slightly lower than heavier density liquid phase.

Fig. 6.50 shows that comparison of experimental results with CFD simulated results for different liquid flow rates. It indicates that two-phase frictional pressure drop increases with increasing liquid flow rate. This is due to with increasing the flow rate, increasing the velocity and more increasing the velocity more increasing of kinetic energy causing loss as a form of pressure energy. Fig.6.51 shows that comparison of experimental results with CFD simulated results for different % opening of Gate valve. It indicates that two-phase frictional pressure drop increases with decreasing valve opening. This is due to decreasing of flow area velocity increases and according to Bernoulli's

conservation law pressure drop increases. In both cases Experimental results matches well with the CFD simulated results.

6.4.6 Computational fluid dynamics (CFD) analysis for air-non-Newtonian liquid flow through globe valve

Figs. 6.52 - 6.53 show that plot of velocity vector in the air-SCMC mixture at the different points of 50% opening globe valve. It indicates that velocity increases due to decreasing of flow area. Figs. 6.54 - 6.55 show that plot of velocity vector for liquid phase and air phase in the air-non-Newtonian mixture at the different points of 50% opening globe valve. It indicates that heavier density liquid phase goes to the wall side more at the valve position. Whereas lighter density air-phase more at the central position of valve. Figs. 6.56 - 6.57 show that Contour plot of velocity magnitude and axial velocity. It illustrates that velocity is more at the valve position due to lowering of flow area and also observed the secondary flow, vortices generated at the some position.

Figs. 6.58 - 6.59 show that Contour plot of static pressure and total pressure for 50%, opening globe valve. Similar plot is observed for 75%, 100% opening globe valve. It indicates that static pressure decreases more after passing the valve. This is due to increasing velocity, increasing of kinetic energy as a form of lowering of static pressure according to Bernoulli's conservation law. Both pressure decreases from 100%, 75%, 50% due to increasing of obstruction.

Figs. 6.60 - 6.61 show that contour plot of volume fraction for liquid phase and air phase in the air-non-Newtonian liquid mixture at the different points of 50% opening globe valve. It indicates that heavier density liquid phase goes to the wall side more at the valve position. Whereas lighter density air-phase more at the central position of valve.

Fig. 6.62 shows that comparison of the experimental result with CFD simulated result with different liquid flow rate and fixed liquid concentration, fixed valve dimension. It indicates that two-phase frictional pressure drop increases with increasing liquid flow rate. This is due to with increasing the flow rate, increasing the velocity and more increasing the velocity more increasing of kinetic energy causing loss as a form of pressure energy.

Fig. 6.63 shows that comparison plot of experimental results with CFD simulated results for different liquid flow rates. Fig. 6.64 shows that comparison plot of experimental results with CFD simulated results for different % opening of Globe valve. It indicates that two-phase frictional pressure drop increases with decreasing valve opening. This is due to decreasing of flow area velocity increases and according to Bernoulli's conservation law pressure drop increases.

In both cases Experimental results matches well with the CFD simulated results.

6.5 Conclusions

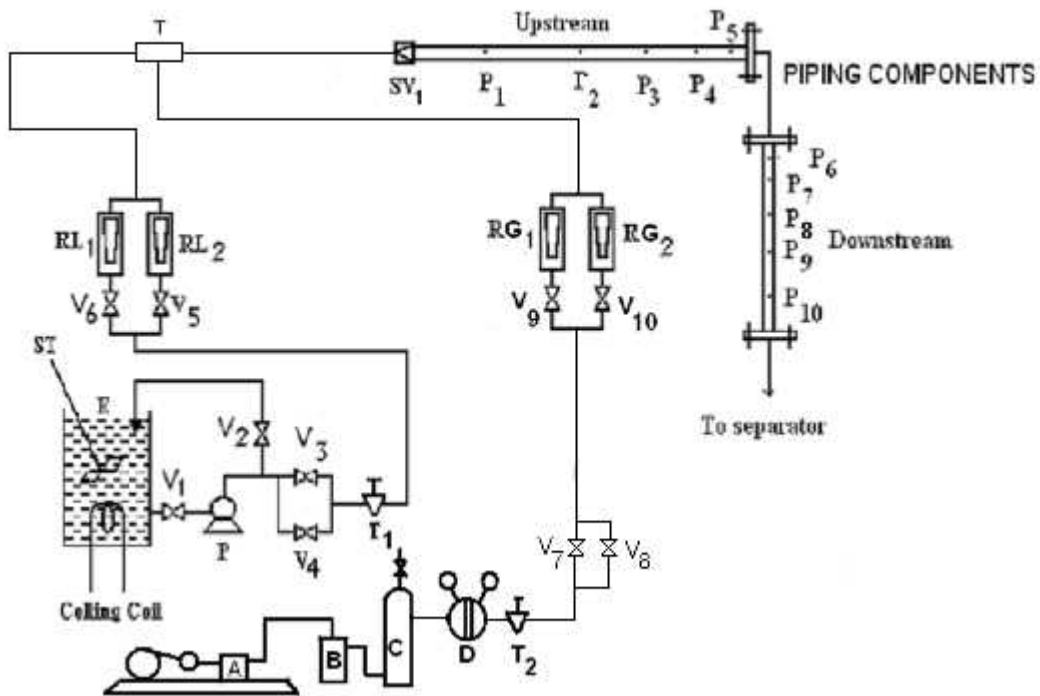
1. Computational Fluid Dynamics (CFD) analysis has been reported for gas-non-Newtonian liquids flow through straight pipe and piping components in the horizontal plane.
2. In case of gas-non-Newtonian liquid flow through horizontal pipe the CFD analysis predicts,
 - i. The velocity and pressure field at different points in the elbows for air-liquid mixture and individual phases.
 - ii The contour plots of velocity magnitude at the different points of straight pipe illustrates that velocity is maximum at centre and velocity is minimum near the

- wall of the pipe. The contour plots of the axial velocity at the different points of straight pipe indicate that some air pockets observed with the liquid.
- iii. Contour plots of static pressure and total pressure (mixture) at the different points of the straight pipe indicates that static pressure and total pressure gradually decreases from inlet to outlet of the pipe due to fluid-pipe friction. This effect is more with increasing the liquid concentration.
 - iv. Contour plots of volume fraction at liquid and air phase indicates that air concentration is more at the centre and liquid concentration is more neighboring position of the centre and nearer to the wall.
3. In case of gas-non-Newtonian liquid flow through elbows the CFD analysis predicts,
- i. The velocity and pressure field at different points in the elbows for air-SCMC mixture and individual phases.
 - ii. As the mixture enters to the elbows due to centrifugal action heavier density phase that is liquid moves to the outer wall and lower density phase, air moves to the inner wall. The static pressure profile of elbows show that for 45° elbow pressure drop is more comparing to the 135° elbow. Static pressure is high at outer wall as heavier density liquid phase goes to outer wall due to centrifugal force and low at the inner wall when the air phase exits.
 - iii. Contour plots of volume fraction show that heavier density liquid (SCMC) phase goes to outer wall side and lighter air goes to inner wall side.
4. In case of gas-non-Newtonian liquid flow through orifices the CFD analysis predicts
- i. velocity and pressure field at different points in the orifices for air-SCMC mixture and individual phases,

- ii. velocity is low at the inlet of the pipe and it increases more after passing the orifice plate. This is due to narrowing of the flow area. It affects more from large orifice diameter to small orifice diameter.
 - iii. Static pressure is high from inlet of the pipe to up to inlet of orifice and it decreases more after passing the orifice plate. This is due to narrowing of the flow area. It affects more from large orifice diameter to small orifice diameter.
 - iv. Contour plots of volume fraction for liquid phase at different cross section of the orifice indicates that liquid percentage is maximum at the centre of the orifice plate. It also indicates that after passing the orifice plate liquid percentage slightly decrease at the centre in compare to orifice plate but its surrounding place liquid percentage is very low. contour of volume fraction for air phase at different cross section of the orifice indicates that air percentage is minimum at the centre of the orifice plate. It also indicates that after passing through the orifice plate liquid percentage is slightly increase at the centre in compare to orifice plate due the presence of vena contracta.
5. In case of gas-non-Newtonian liquid flow through gate and globe valves the CFD analysis predicts,
- i. The velocity and pressure field at different points in the gate and globe valves for air-liquid mixture and individual phases.
 - ii. The velocity increases at the valve position. This is due to narrowing the flow area. It is also observed that some secondary flow is observed. Velocity is more for 50% opening gate and globe valve. Static pressure decreases after passing the valve. It affects more with increasing the obstruction, i.e., decreasing the flow

area, decreasing the valve and increasing the pseudoplasticity of the liquid. This is due to obstruction of flow causing increase of kinetic energy as a form of lowering of pressure. Static pressure decreases too much from 100% opening valve to 50% opening valve. This is due to lowering of flow area which causing decreasing of static pressure by increasing the velocity according to Bernoulli's conservation law.

- iv. The volume fraction for liquid phase and air-phase at the different points of the 50% opening gate and globe valve indicates that at the valve position lighter density gas passing slightly lower than heavier density liquid phase.



A: Compressor, B: Oil Tray, C: Gas Cylinder, D: Gas Regulator, E: Storage tank, P: Pump, P1 – P10: Manometer, RL₁ – RL₂: Liquid Rota meter, RG₁ – RG₂: Gas Rota meter, ST: Stirrer, T: T – Mixer, T₁ – T₂: Thermometer, V₁ – V₁₀: Valves, SV1: Solenoid valve

Fig. 6.1 Schematic diagram of the experimental setup

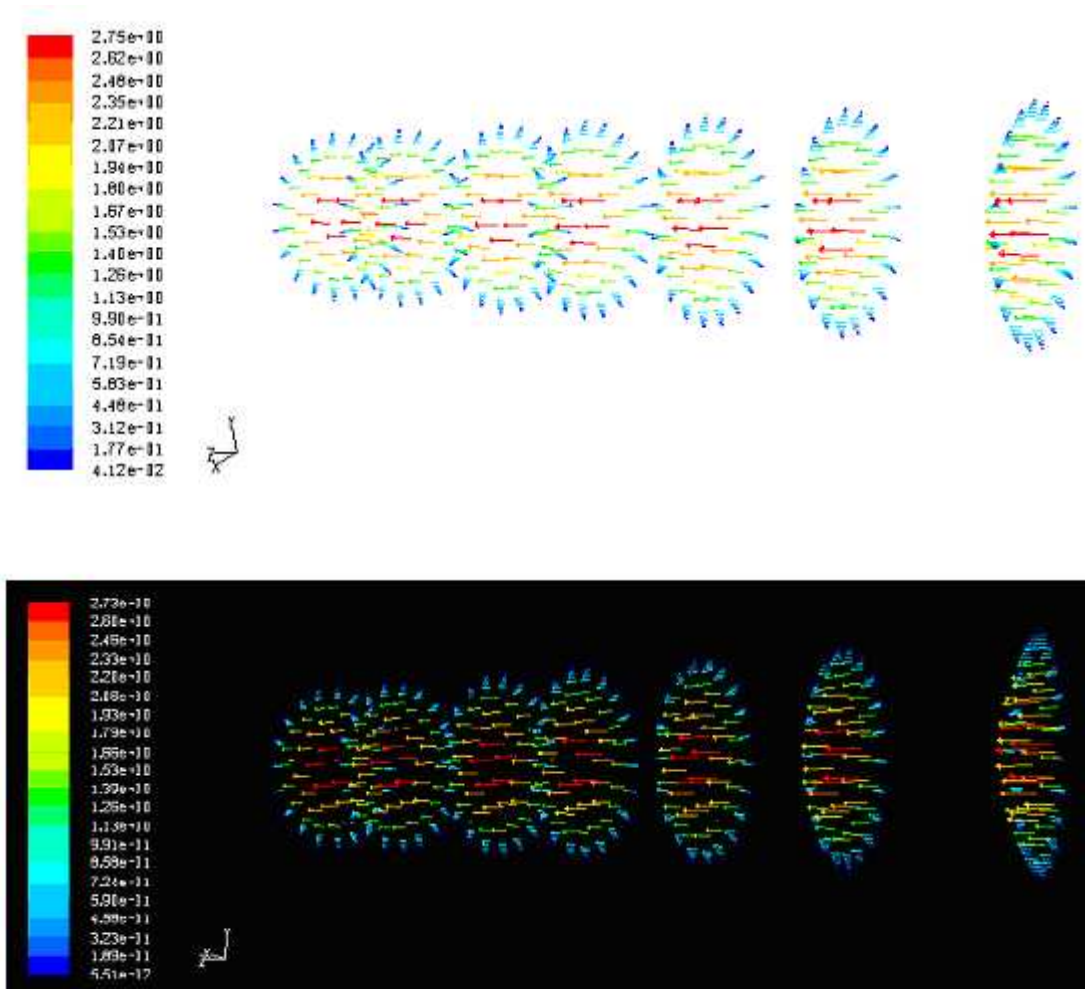


Fig. 6.2 Contour plot of velocity vector in the air-SCMC mixture at different points of straight pipe, concentration of SCMC solution (kg/m^3): 0.8, Liquid velocity (m/s): 1.2772, Gas velocity (m/s): 1.9842, Gas fraction, Γ_g : 0.3086

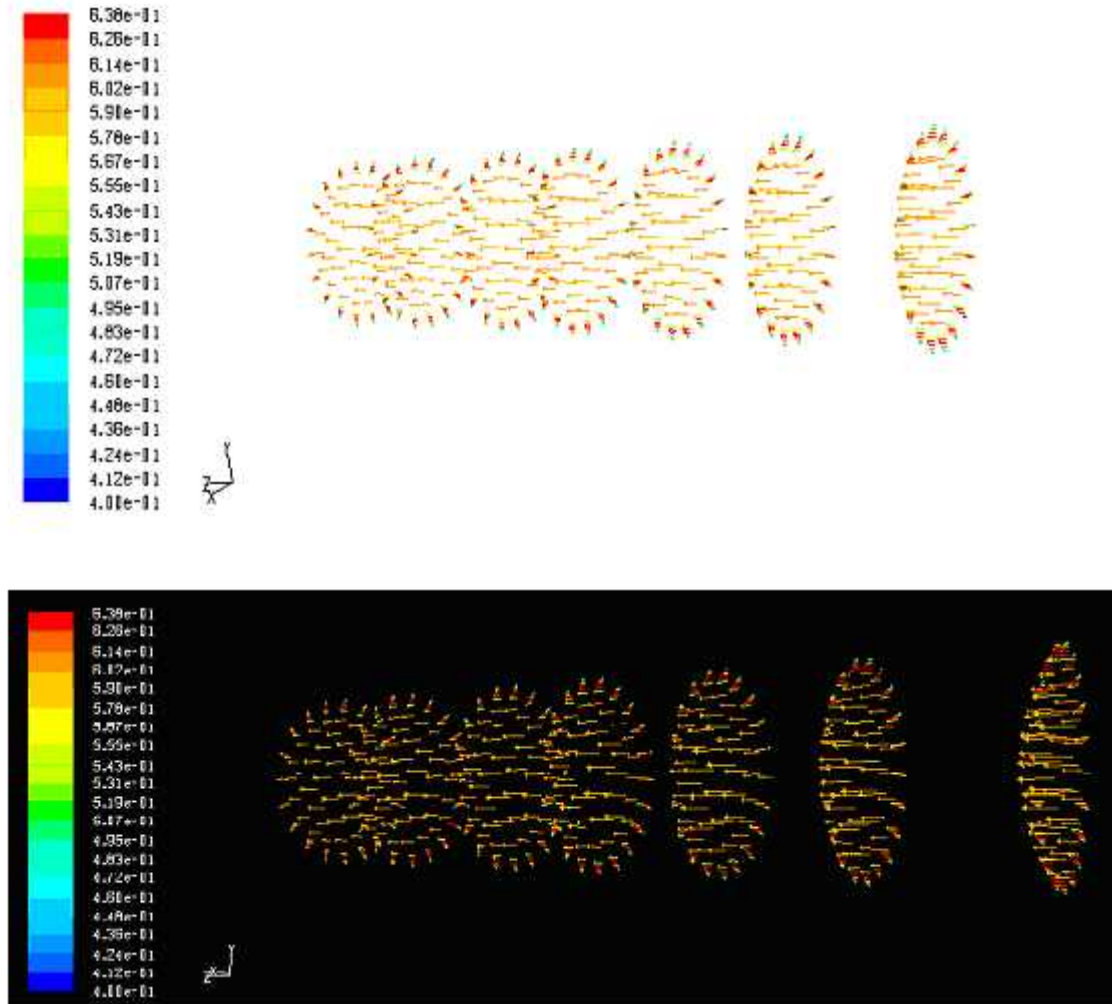


Fig. 6.3 Contour plot of velocity vector for SCMC phase in the mixture at different points of straight pipe, SCMC concentration (kg/m^3): 0.8, Liquid velocity (m/s): 1.2772, Gas velocity (m/s): 1.9842, Gas fraction, τ_g : 0.3086

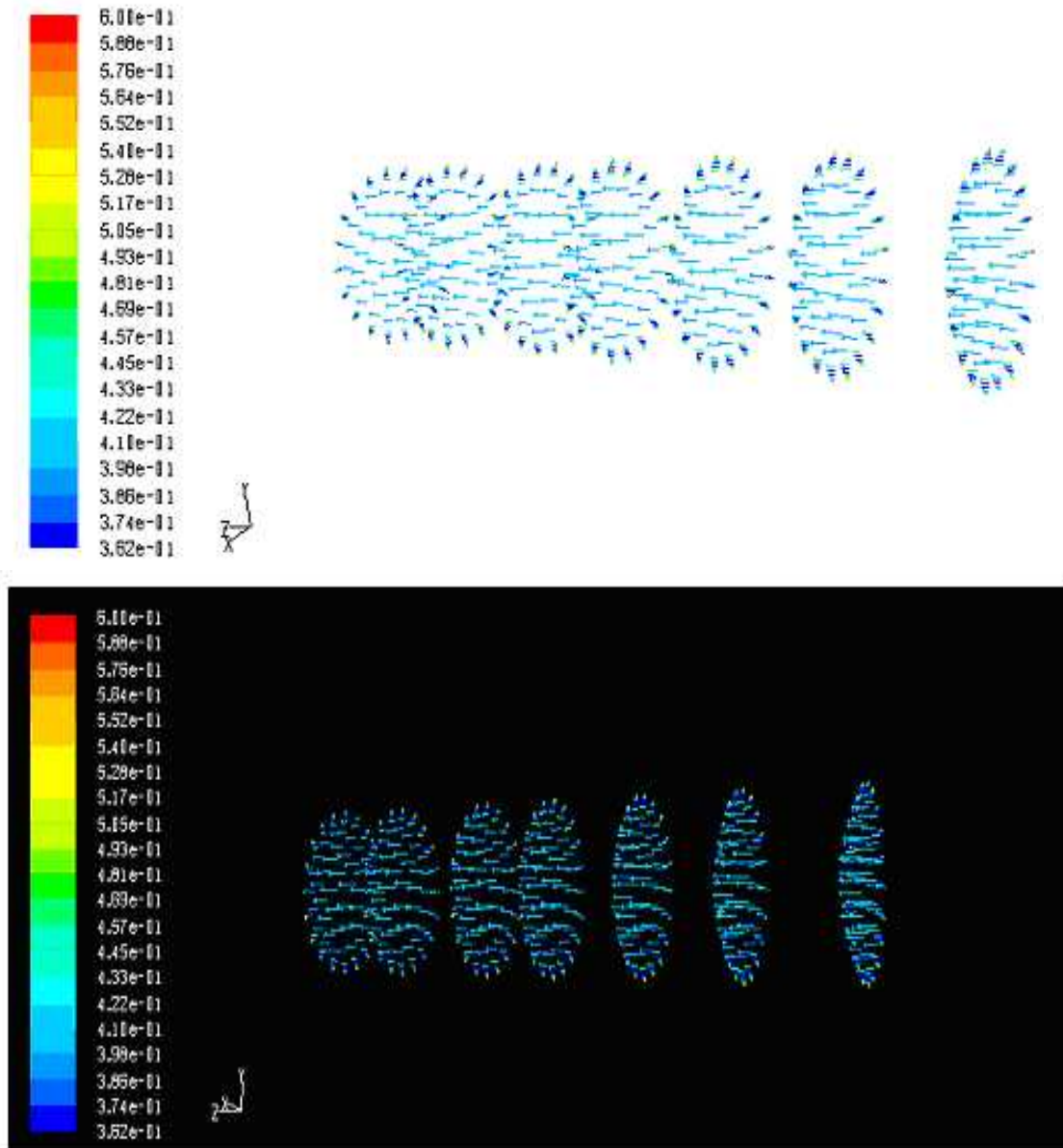


Fig. 6.4 Plot of velocity vector for air phase in the mixture at different points of straight pipe, concentration of SCMC solution (kg/m^3): 0.8, Liquid velocity (m/s): 1.2772, Gas velocity (m/s): 1.9842, Gas fraction, Γ_g : 0.3086

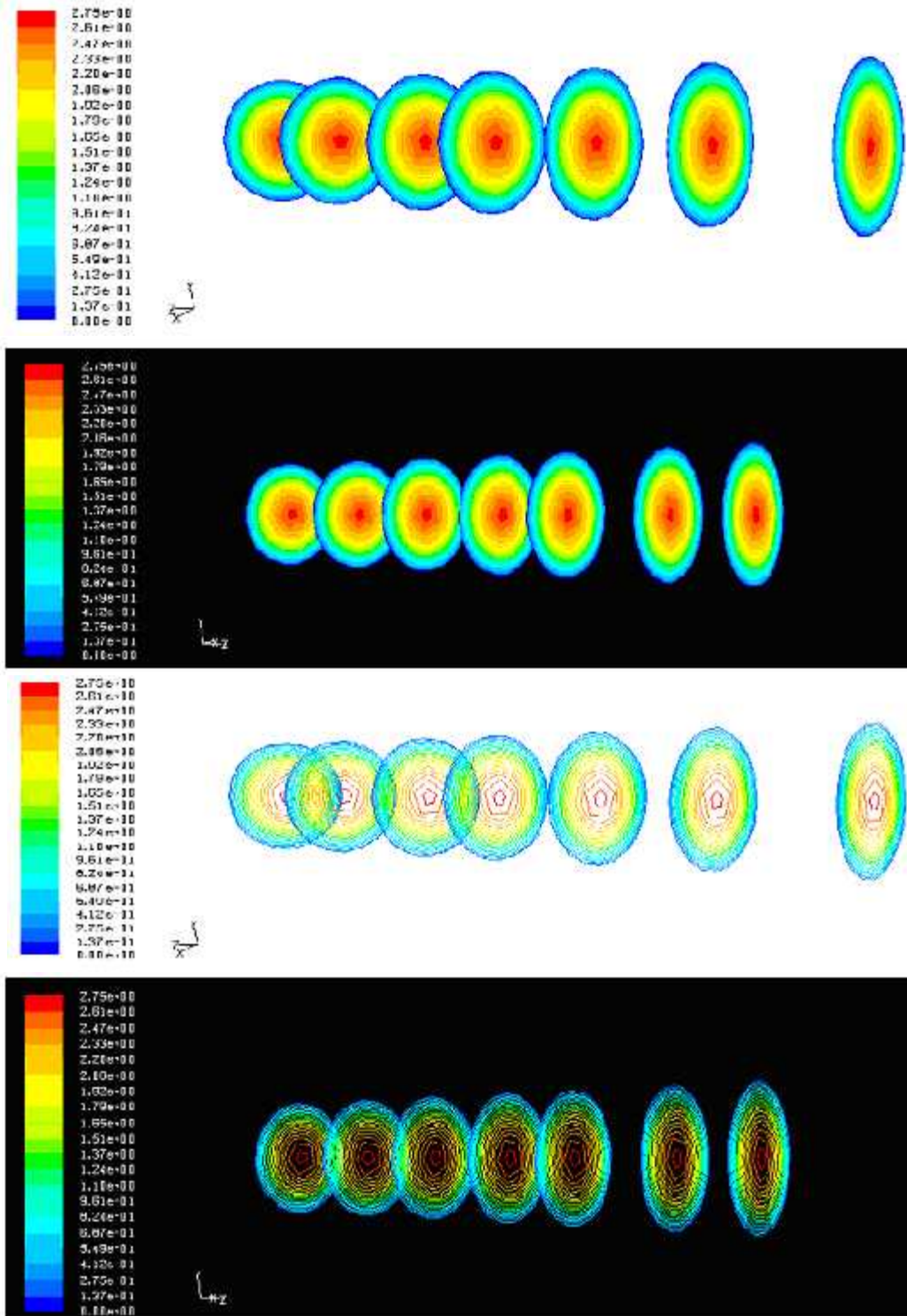


Fig. 6.5 Contour plot of velocity magnitude in air-SCMC mixture at different points of straight pipe, concentration of SCMC solution (kg/m^3): 0.8, Liquid velocity (m/s): 1.2772, Gas velocity (m/s): 1.9842, Gas fraction, γ_g : 0.3086

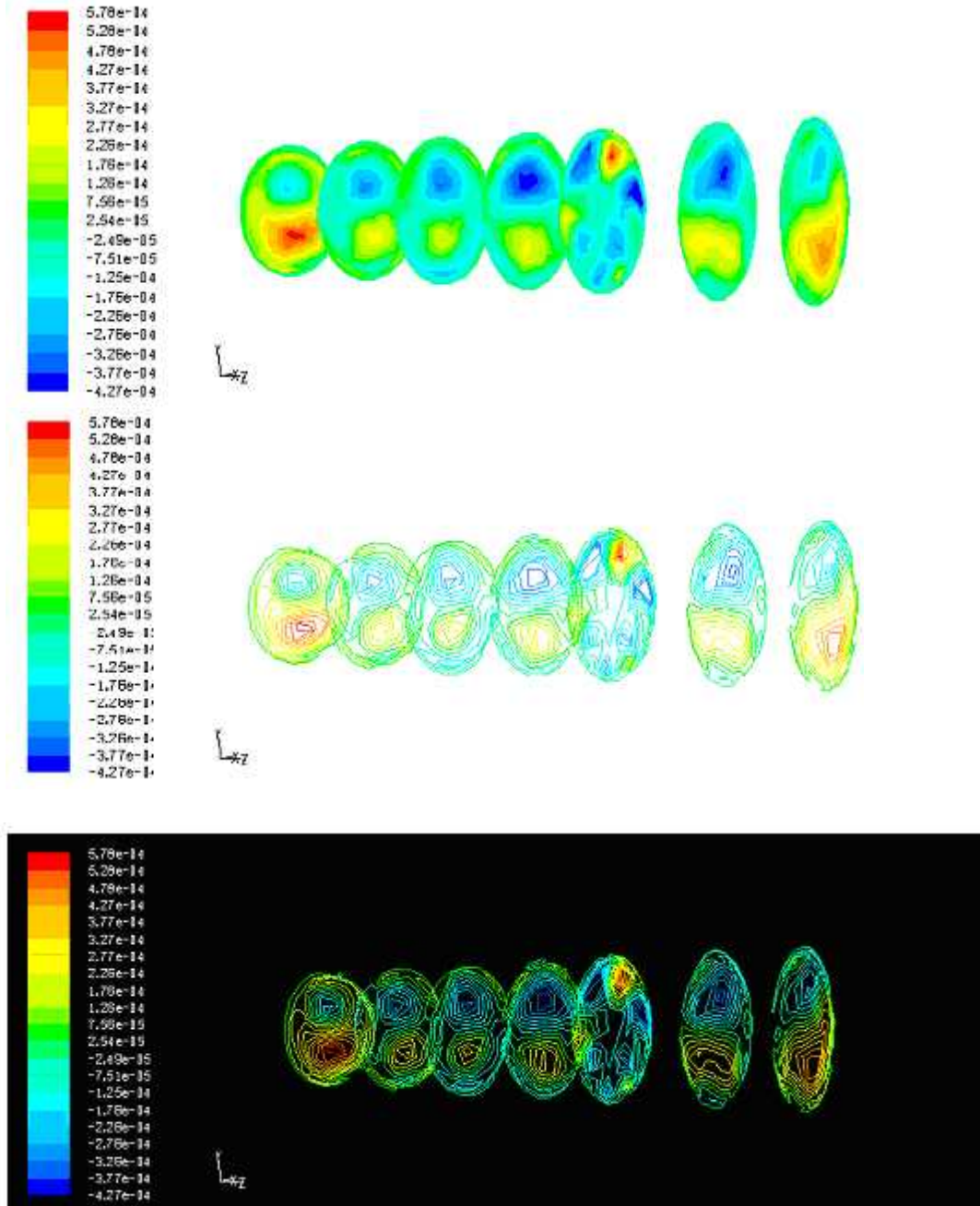


Fig. 6.6 Contour plot of axial velocity inside the different points of straight pipe, Concentration of SCMC solution (kg/m^3): 0.8, Liquid velocity (m/s): 1.2772, Gas velocity (m/s): 1.9842, Gas fraction, τ_g : 0.3086

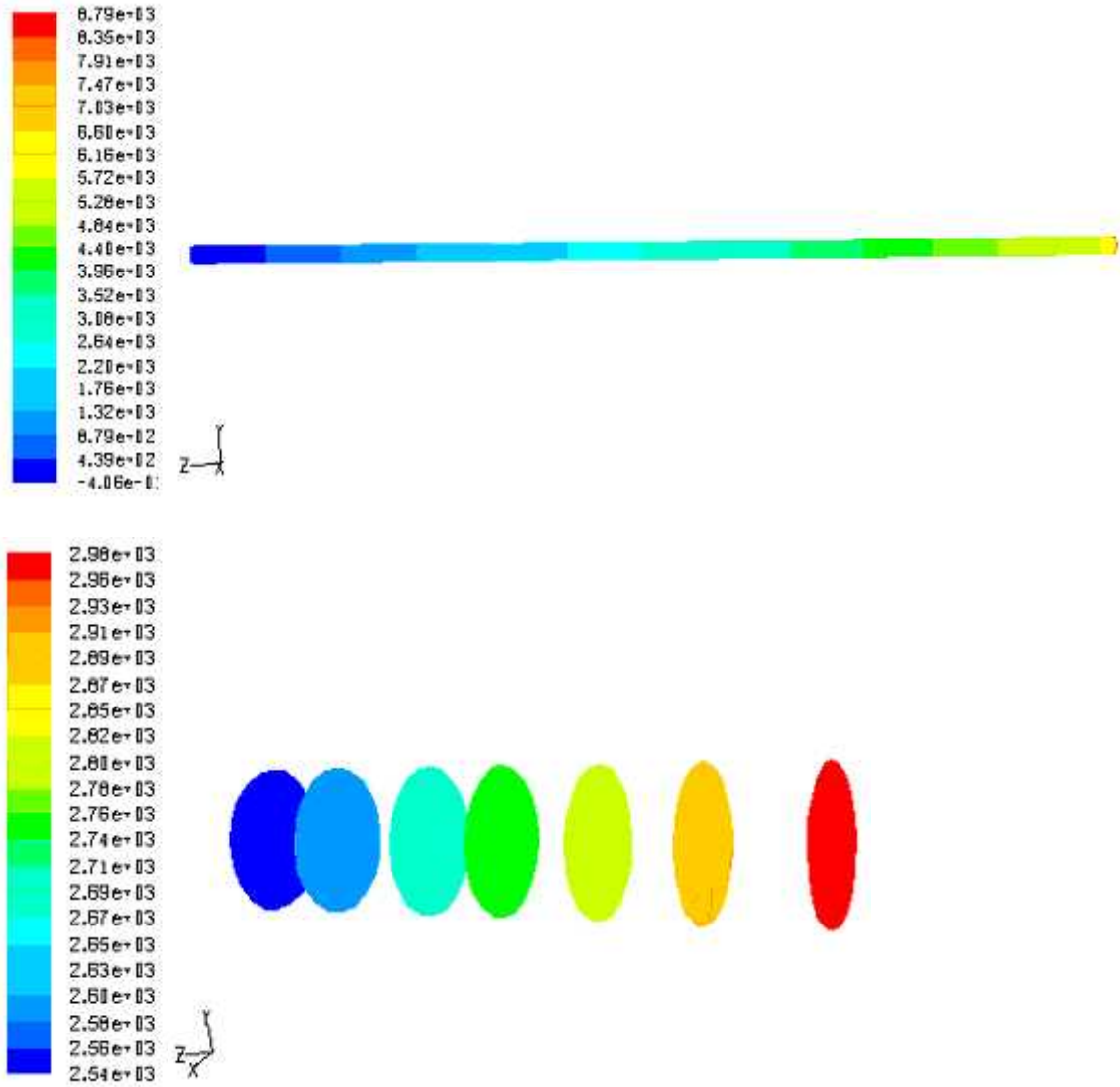


Fig. 6.7 Contours of static pressure inside the different points of straight pipe, Concentration of SCMC solution (kg/m^3): 0.8, Liquid velocity (m/s): 1.2772, Gas velocity (m/s): 1.9842, Gas fraction, r_g : 0.3086

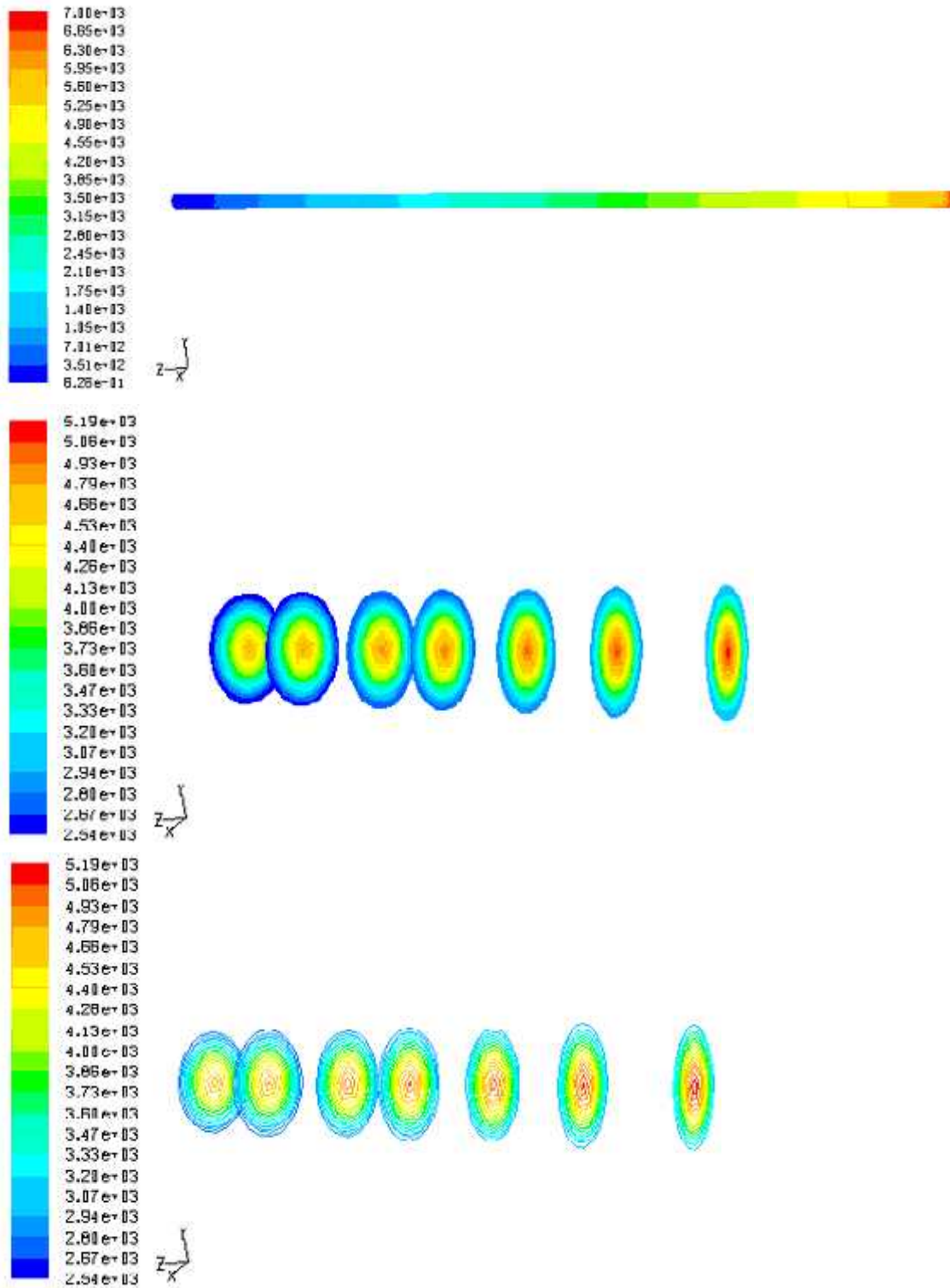


Fig. 6.8 Contours of total pressure inside the different points of straight pipe, Concentration of SCMC solution (kg/m^3): 0.8, Liquid velocity (m/s): 1.2772, Gas velocity (m/s): 1.9842, Gas fraction, r_g : 0.3086

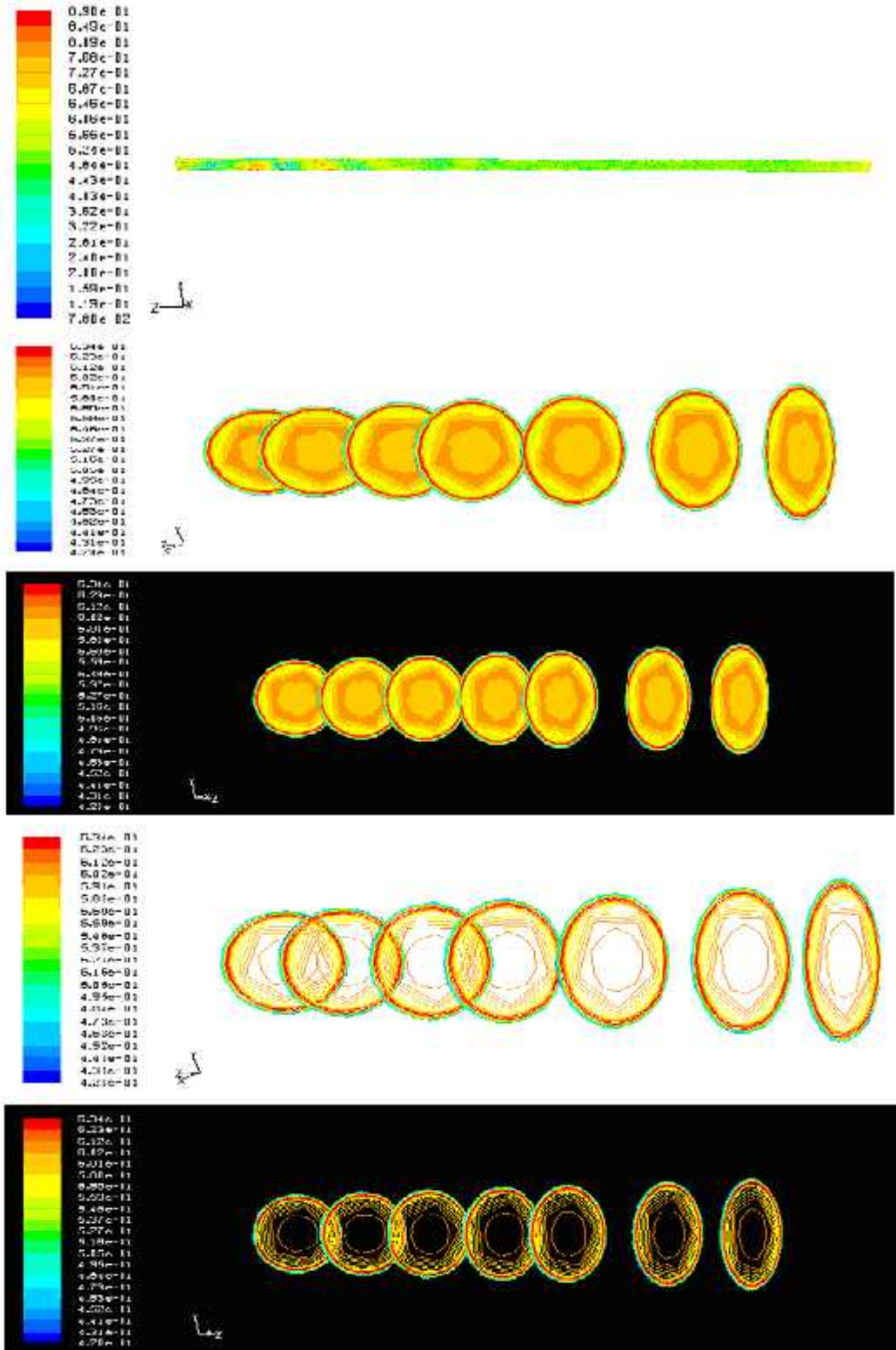


Fig. 6.9 Contours of SCMC phase volume fraction at different points of straight pipe, concentration of SCMC solution (kg/m^3): 0.8, Liquid velocity (m/s): 1.2772, Gas velocity (m/s): 1.9842, Gas fraction, Γ_g : 0.3086

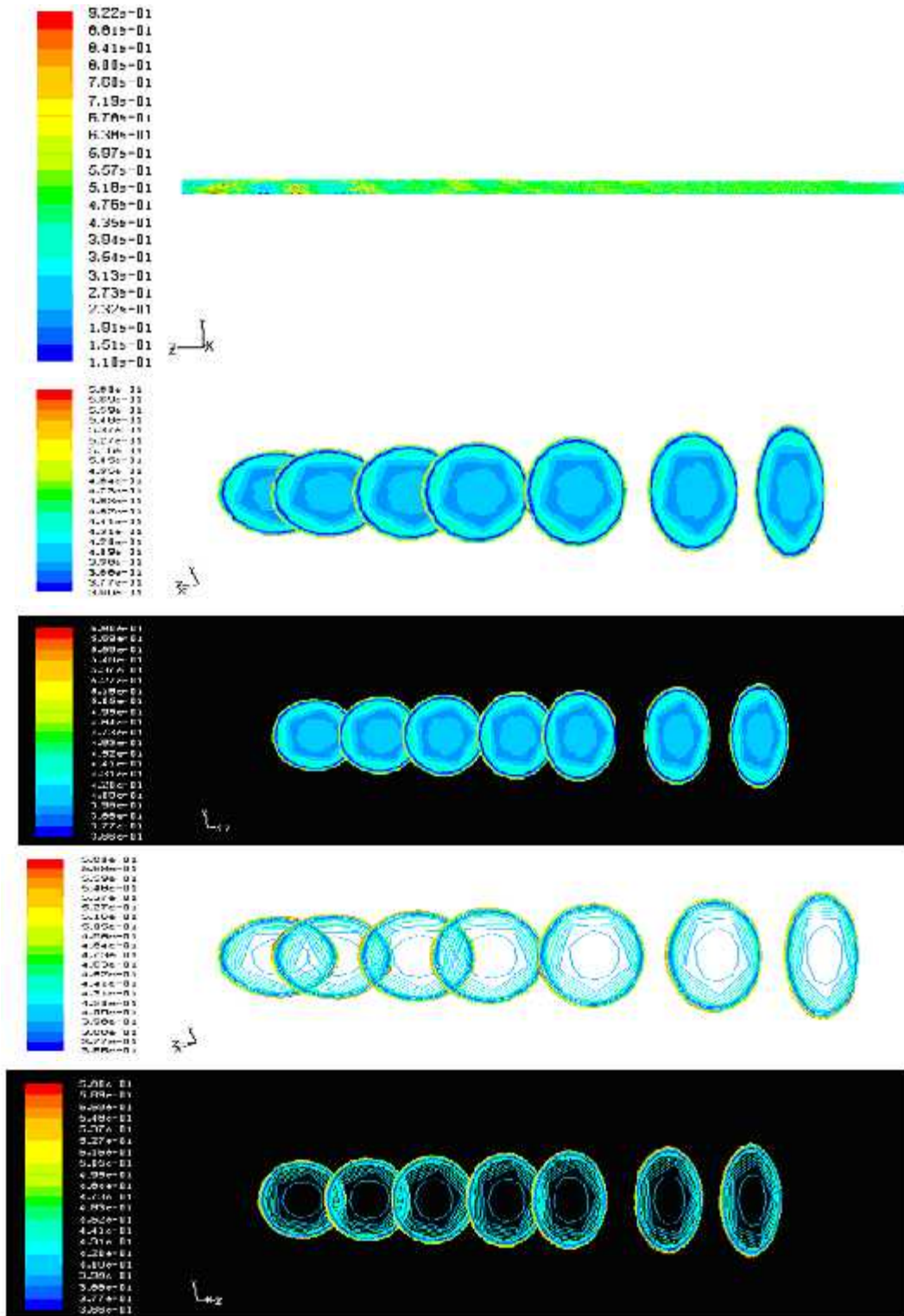


Fig. 6.10 Contours of air phase volume fraction at different points of straight pipe, concentration of SMC solution (kg/m^3): 0.8, Liquid velocity (m/s): 1.2772, Gas velocity (m/s): 1.9842, Gas fraction, r_g : 0.3086

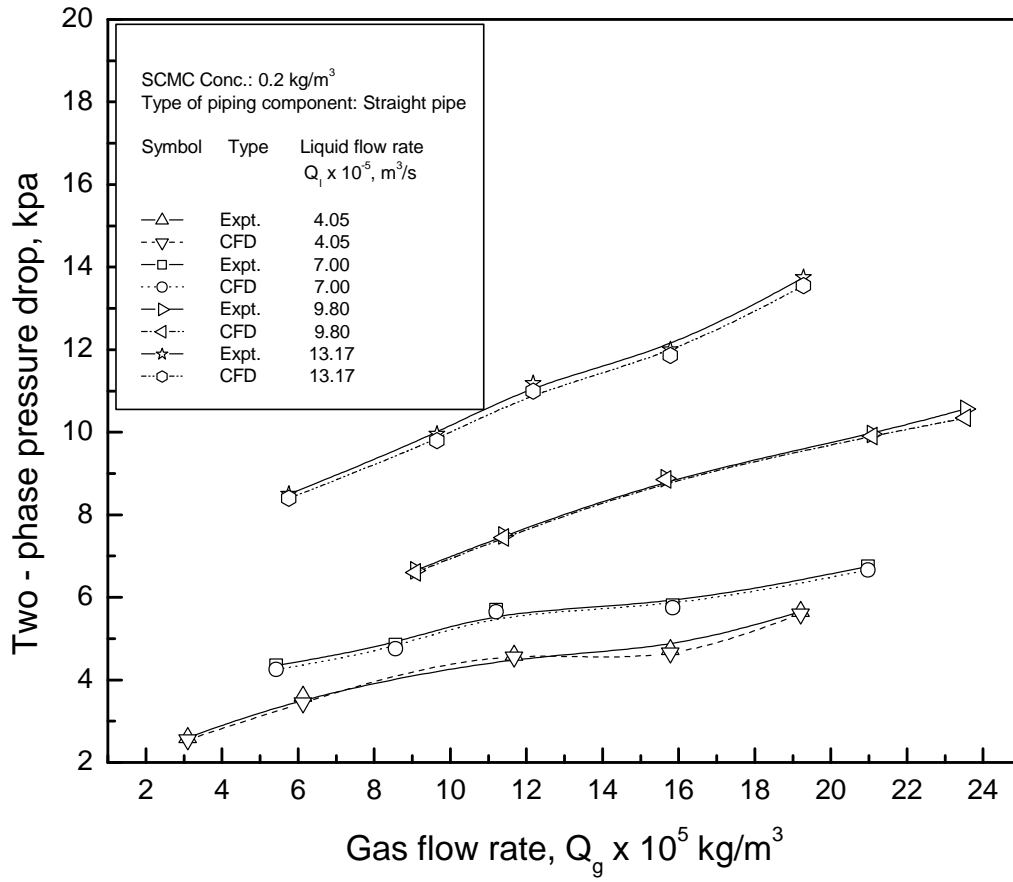


Fig. 6.11 Comparison of the experimental data and CFD modeling for straight pipe varying with liquid flow rate

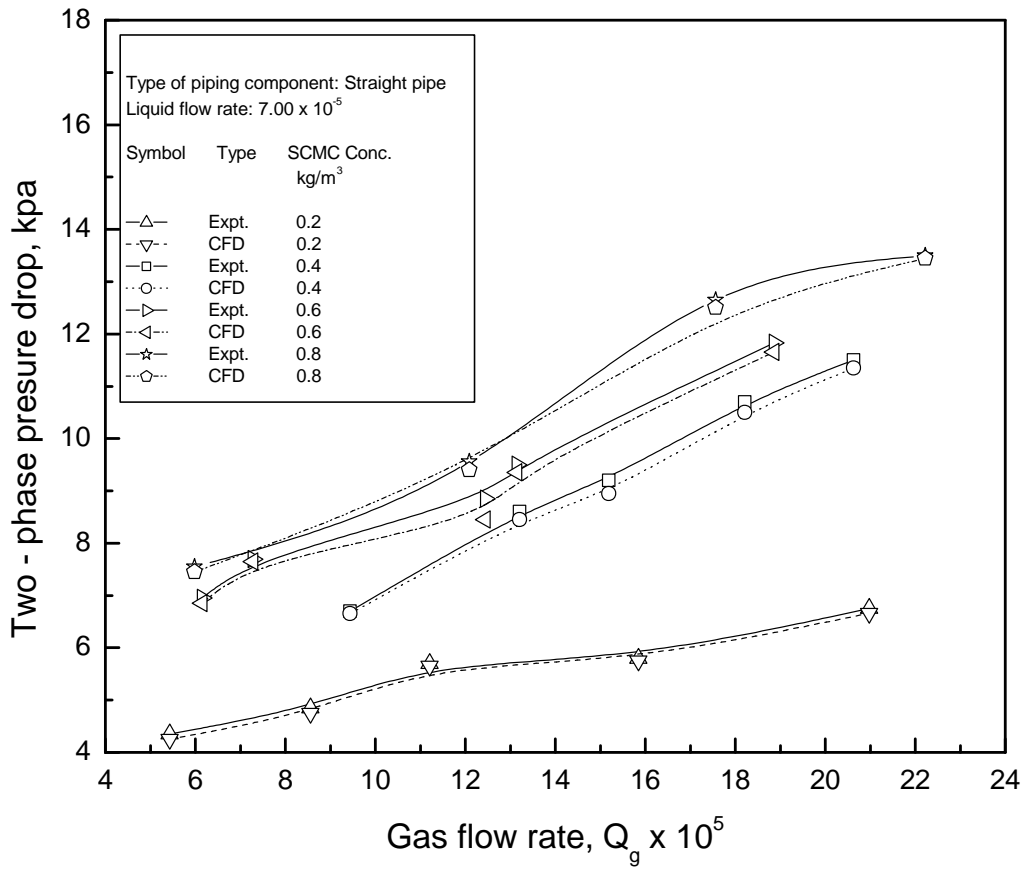


Fig. 6.12 Comparison of the experimental data and CFD modeling for straight pipe varying with SCMC solution concentration

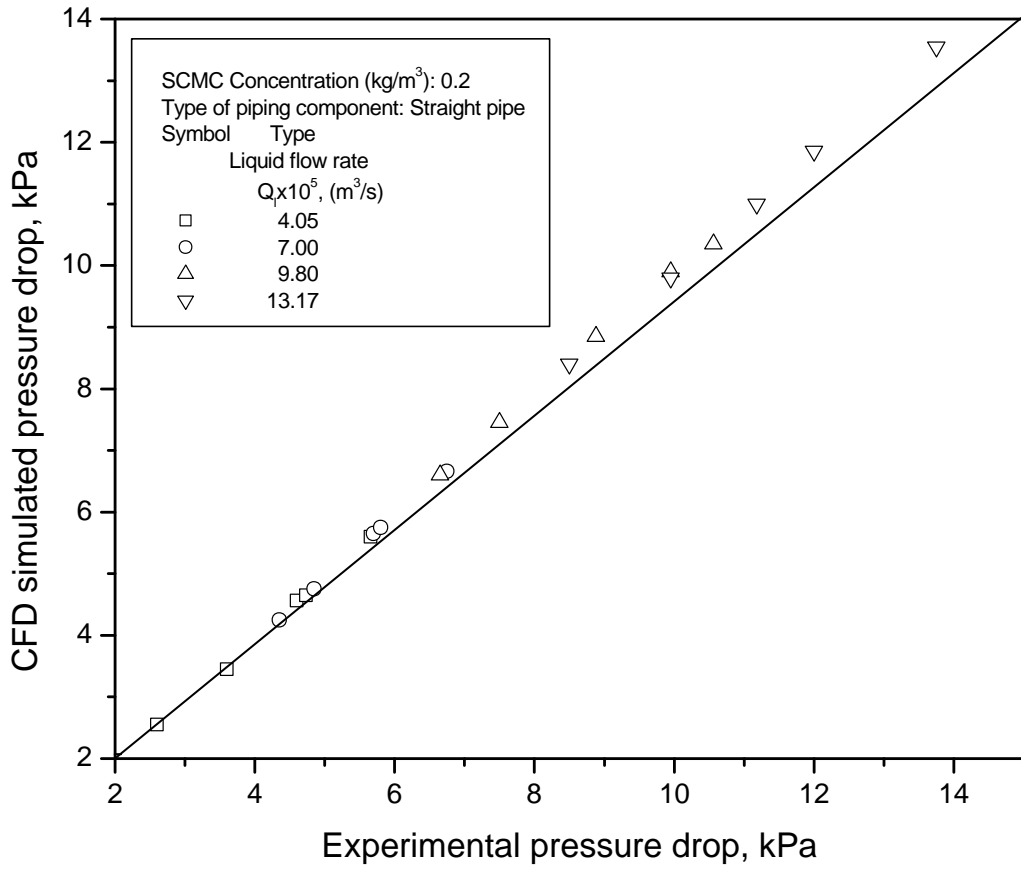


Fig. 6.13 Comparison of experimental results with CFD simulated results for different liquid flow rate

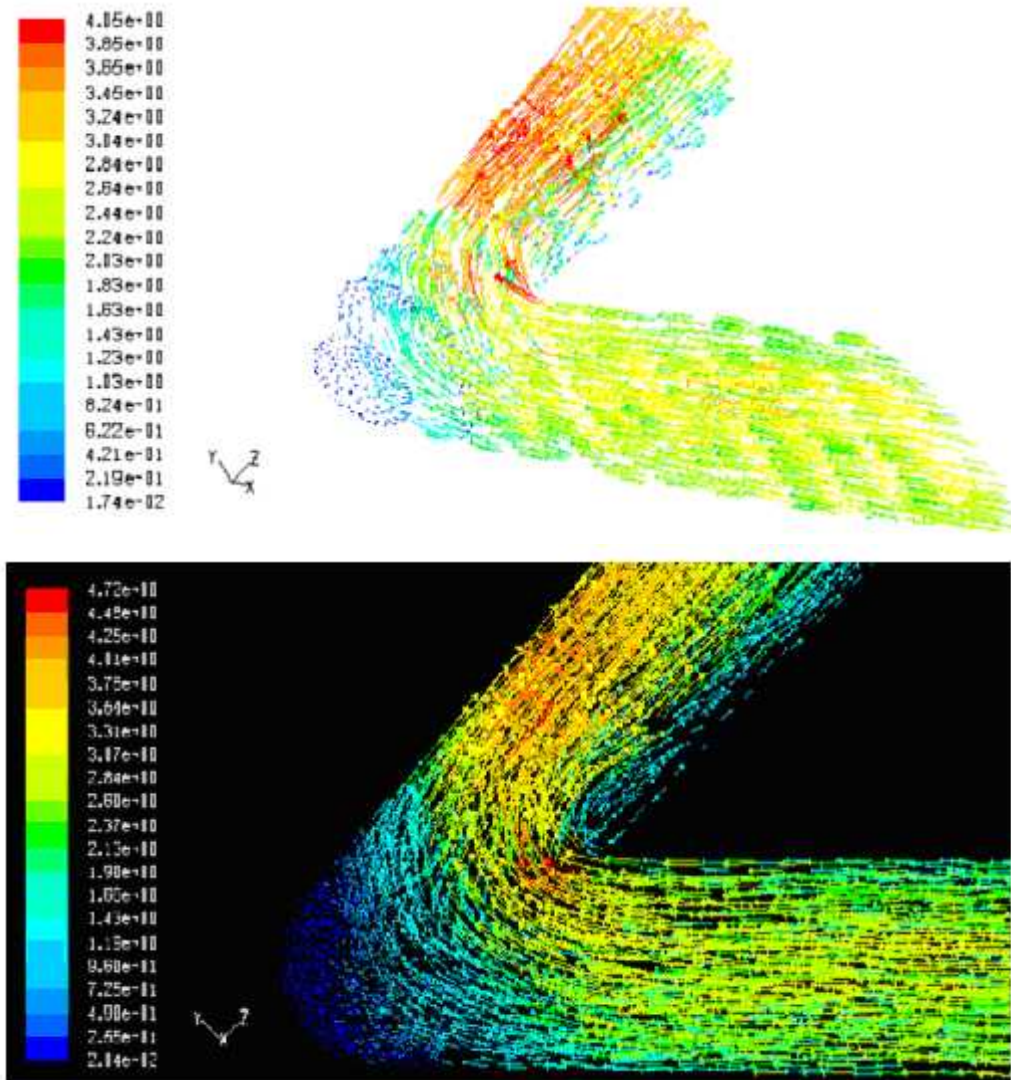


Fig. 6.14 Contour plot of velocity vector for air-SCMC mixture at different points in 45° elbow,
 Concentration of SCMC solution (kg/m³): 0.8, Liquid velocity (m/s): 1.733,
 Gas velocity (m/s): 3.167, Gas fraction, Γ_g : 0.64

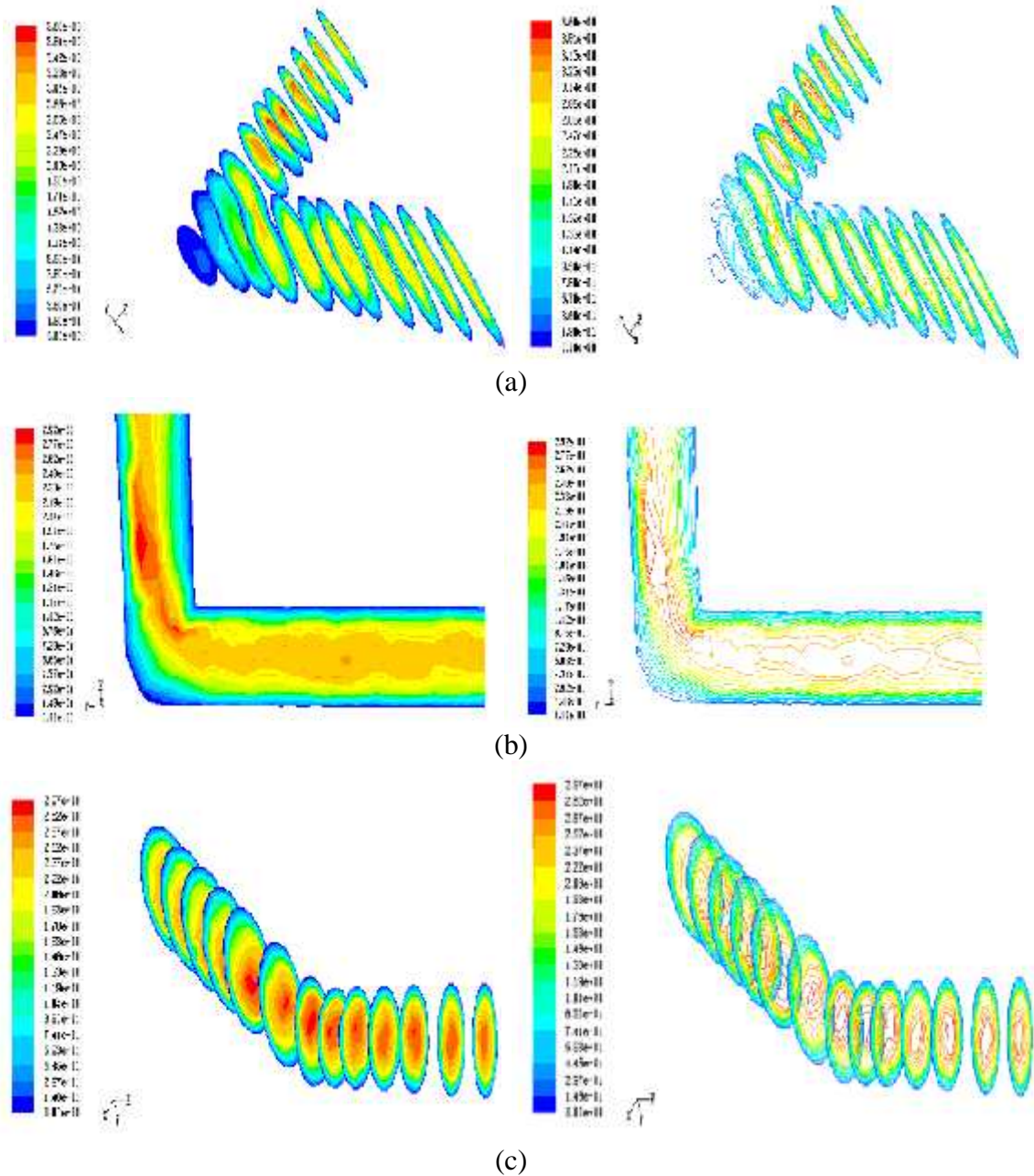


Fig. 6.15 Contour plot of velocity in the air-SCMC mixture at different points of elbows, concentration of SCMC solution (kg/m^3): 0.8, Liquid velocity (m/s): 1.733 (a) 45° , Gas velocity (m/s): 3.167, Gas fraction, r_g : 0.64
 (b) 90° , Gas velocity (m/s): 2.3933, Gas fraction, r_g : 0.58
 (c) 135° , Gas velocity (m/s): 2.867, Gas fraction, r_g : 0.62

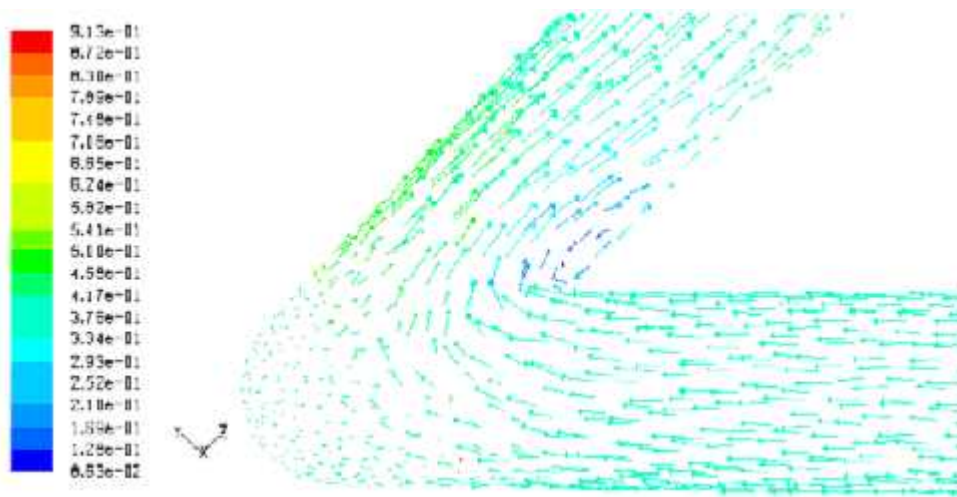


Fig. 6.16 Contour plot of velocity vector for SCMC in the mixture at different points in 45° elbow,
 Concentration of SCMC solution (kg/m^3): 0.8, Liquid velocity (m/s): 1.733,
 Gas velocity (m/s): 3.167, Gas fraction, Γ_g : 0.64

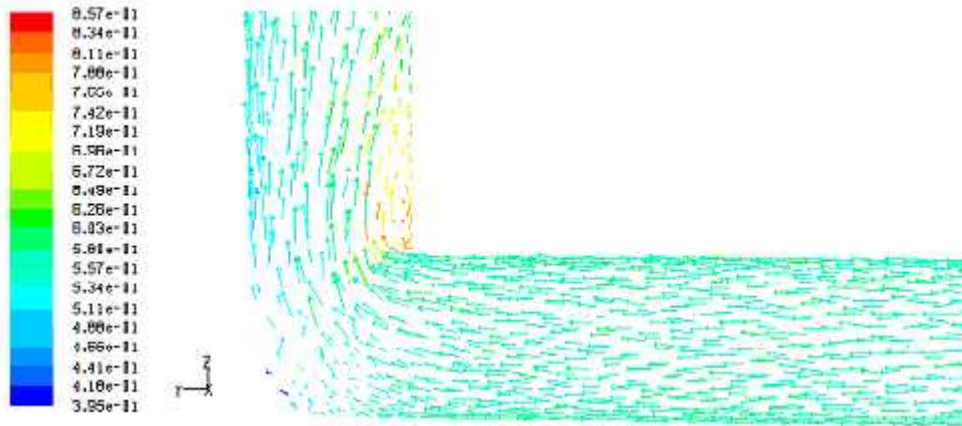


Fig. 6.17 Contour plot of velocity vector for air in the mixture at different points in 90° elbow,
 Concentration of SCMC solution (kg/m^3): 0.8, Liquid velocity (m/s): 1.733,
 Gas velocity (m/s): 2.3933, Gas fraction, Γ_g : 0.58

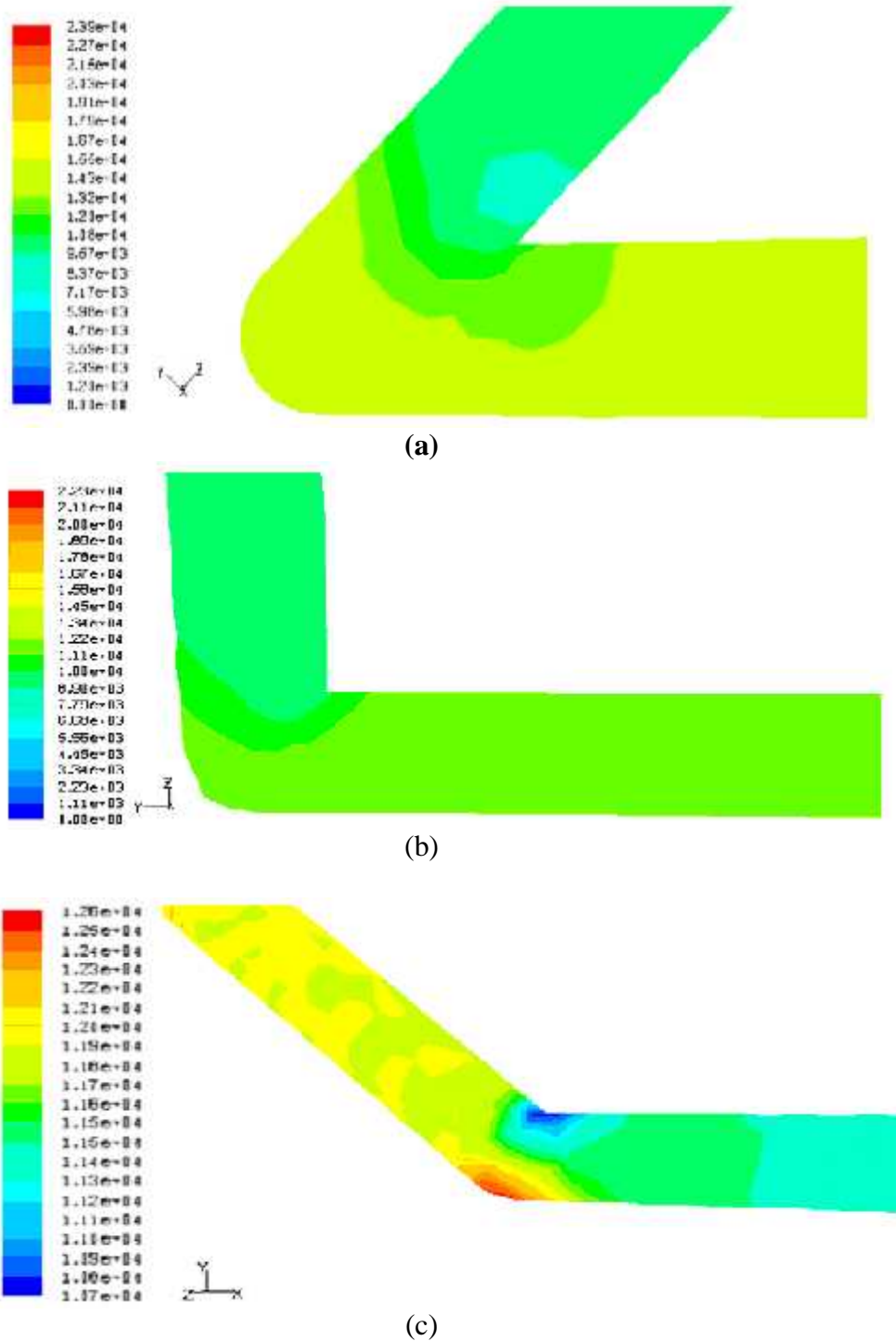


Fig. 6.18 Contours plot of static pressure for elbows, concentration of SCMC solution (kg/m^3): 0.8, Liquid velocity (m/s): 1.733 (a) 45° , Gas velocity (m/s): 3.167, Gas fraction, Γ_g : 0.64

(b) 90° , Gas velocity (m/s): 2.3933, Gas fraction, Γ_g : 0.58

(c) 135° , Gas velocity (m/s): 2.867, Gas fraction, Γ_g : 0.62

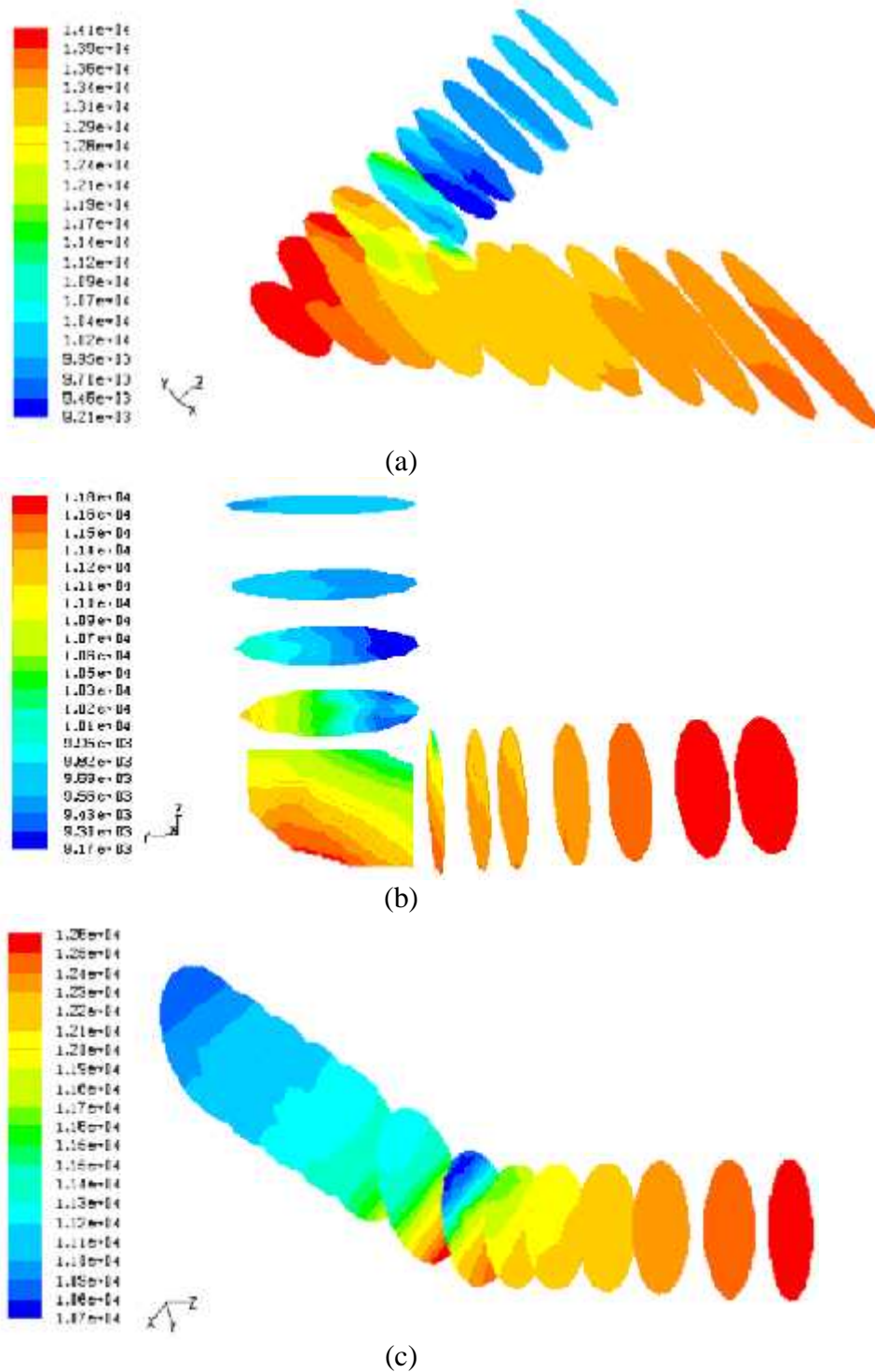


Fig. 6.19 Contour plot of static pressure, at different points in the elbows, concentration of SCMC solution (kg/m^3): 0.8, Liquid velocity (m/s): 1.733 (a) 45° , Gas velocity (m/s): 3.167, Gas fraction, r_g : 0.64
 (b) 90° , Gas velocity (m/s): 2.3933, Gas fraction, r_g : 0.58
 (c) 135° , Gas velocity (m/s): 2.867, Gas fraction, r_g : 0.62

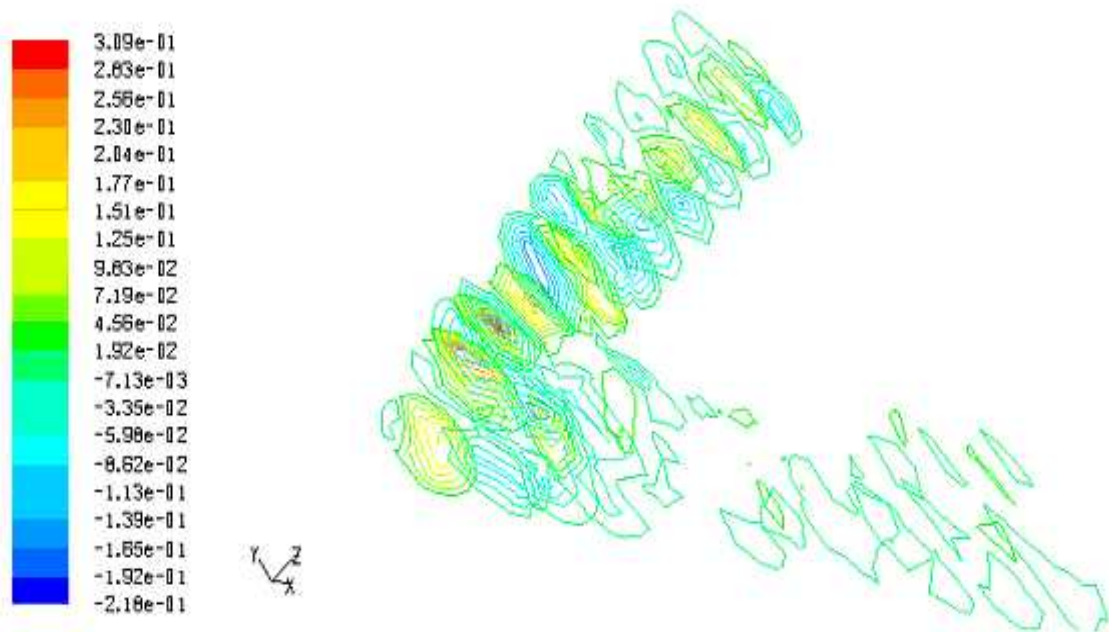
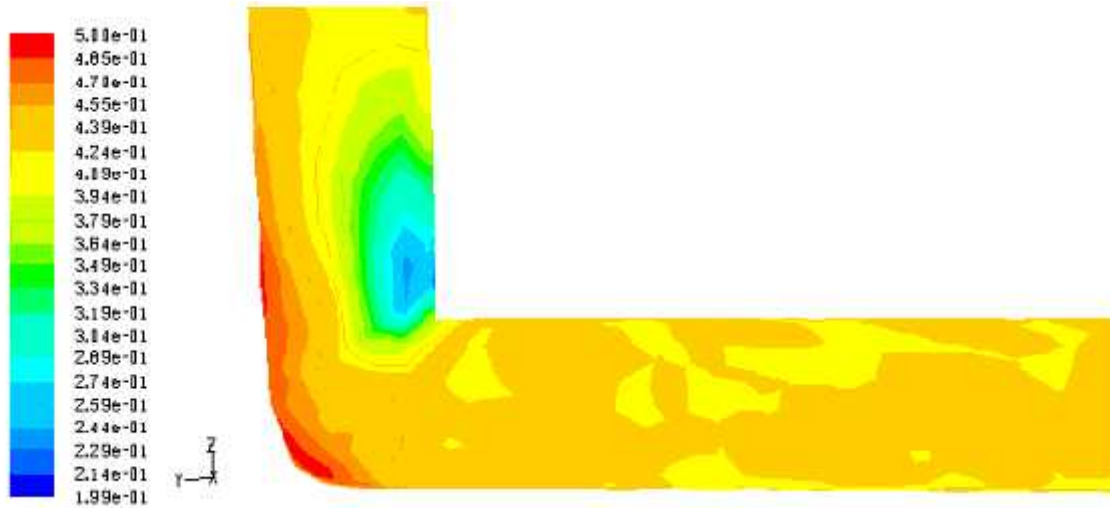
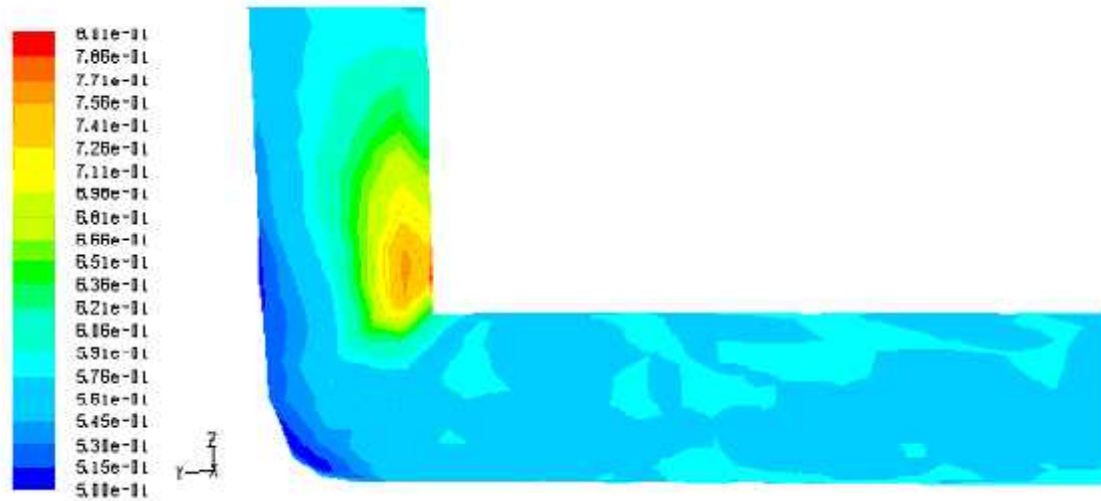


Fig. 6.20 Contour velocity plot inside different points of 45⁰ elbow
Concentration of SCMC solution (kg/m³): 0.8, Liquid velocity (m/s): 1.733,
Gas velocity (m/s): 3.167, Gas fraction, r_g : 0.64



(a) SCMC-phase



(b) air-phase

Fig. 6.21 Contours of volume fraction for 90⁰ elbow, concentration of SCMC solution (kg/m³): 0.8, Liquid velocity (m/s): 1.733, gas velocity (m/s): 2.3933, gas fraction, r_g : 0.58 (a) SCMC phase and (b) air phase

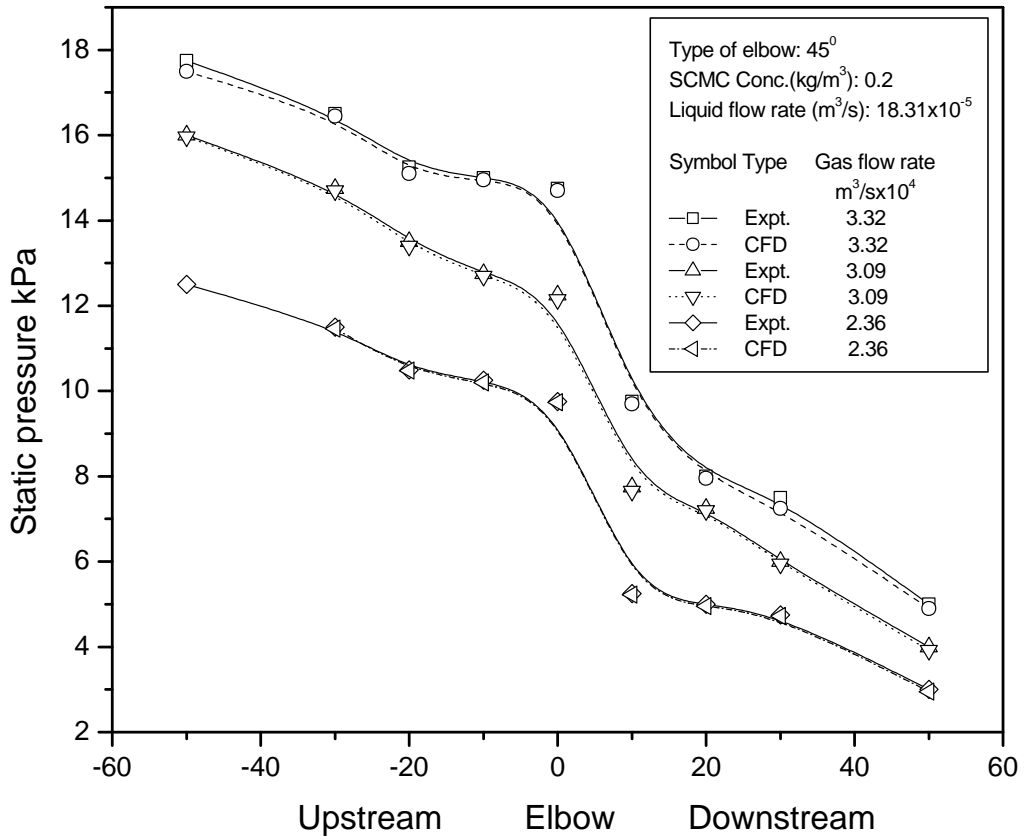


Fig. 6.22 Comparison plot of static pressure experimental and CFD for 45° elbow

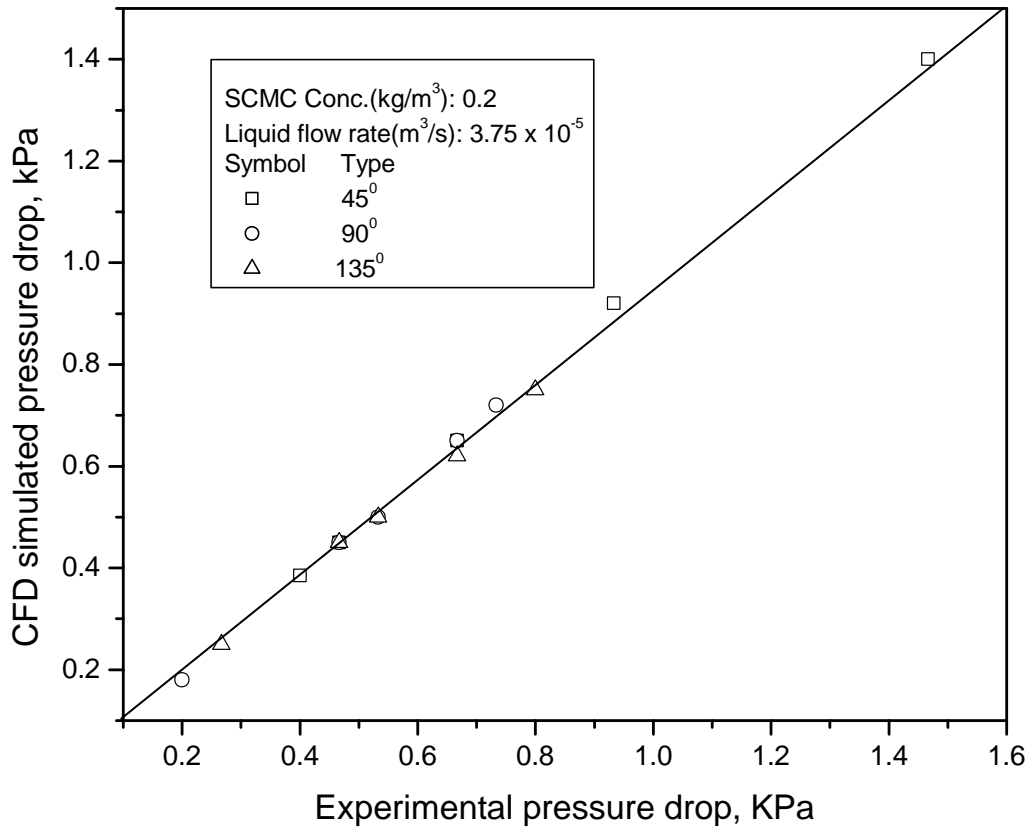


Fig. 6.23 Comparison of experimental results with CFD simulated results at different elbow angle

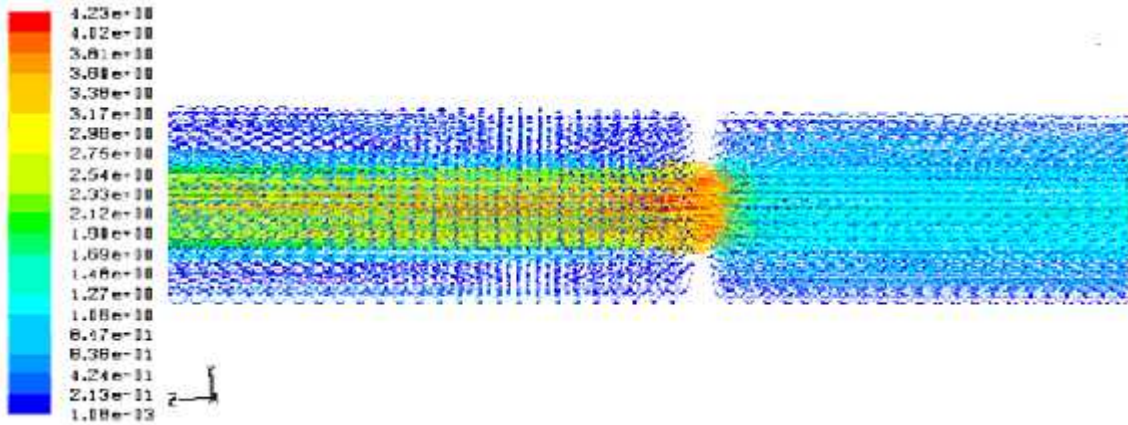


Fig. 6.24 Contour plot of velocity vector for $D_0/D_t = 0.4646$ orifice
 Concentration of SCMC solution (kg/m^3): 0.8, Liquid velocity (m/s): 0.8033, Gas velocity (m/s): 0.3552, Gas fraction, α_g : 0.30

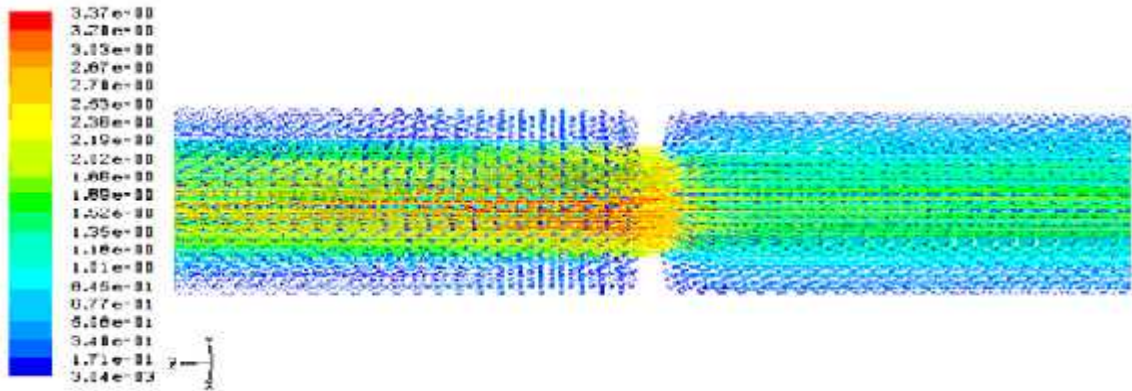


Fig. 6.25 Contour plot of velocity vector for $D_0/D_t = 0.5984$ orifice
 Concentration of SCMC solution (kg/m^3): 0.8, Liquid velocity (m/s): 0.8033, Gas velocity (m/s): 0.3552, Gas fraction, α_g : 0.30

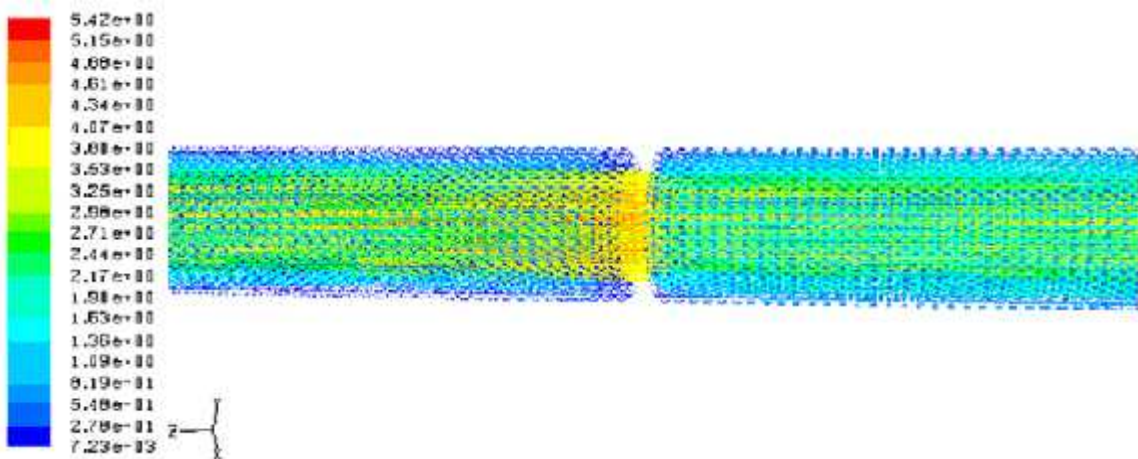


Fig. 6.26 Contour plot of velocity vector for $D_0/D_t = 0.7087$ orifice
 Concentration of SCMC solution (kg/m^3): 0.8, Liquid velocity (m/s): 1.2772, Gas velocity (m/s): 2.4304, Gas fraction, α_g : 0.65

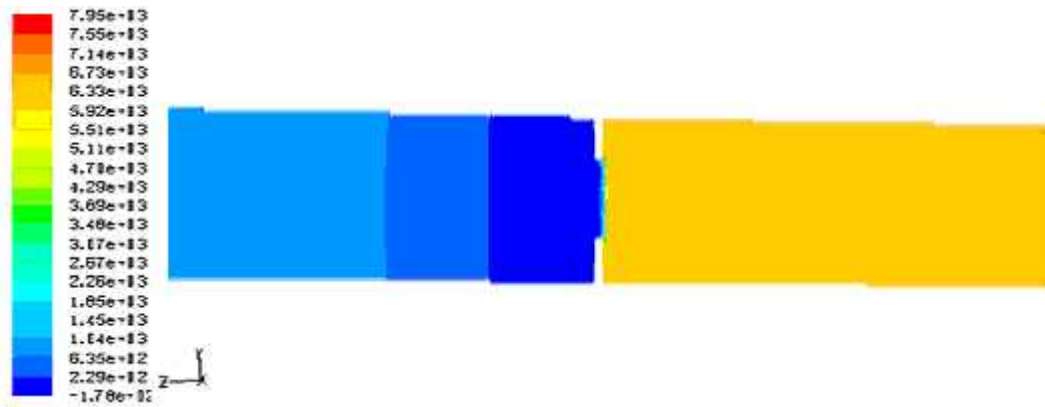


Fig. 6.27 Contour plot of static pressure for $D_0/D_t = 0.4646$ orifice
 Concentration of SCMC solution (kg/m^3): 0.8, Liquid velocity (m/s): 0.8033, Gas
 velocity (m/s): 0.3552, Gas fraction, ρ_g : 0.30

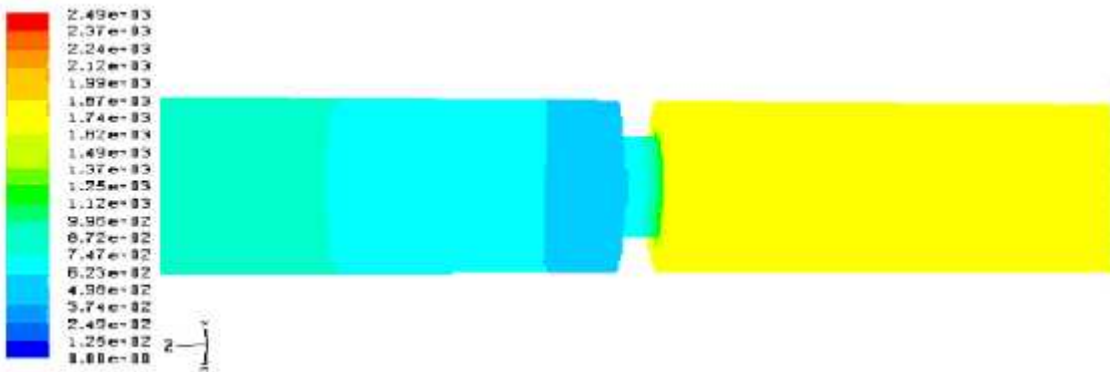


Fig. 6.28 Contour plot of static pressure for $D_0/D_t = 0.5984$ orifice
 Concentration of SCMC solution (kg/m^3): 0.8, Liquid velocity (m/s): 0.8033, Gas
 velocity (m/s): 0.3552, Gas fraction, ρ_g : 0.30

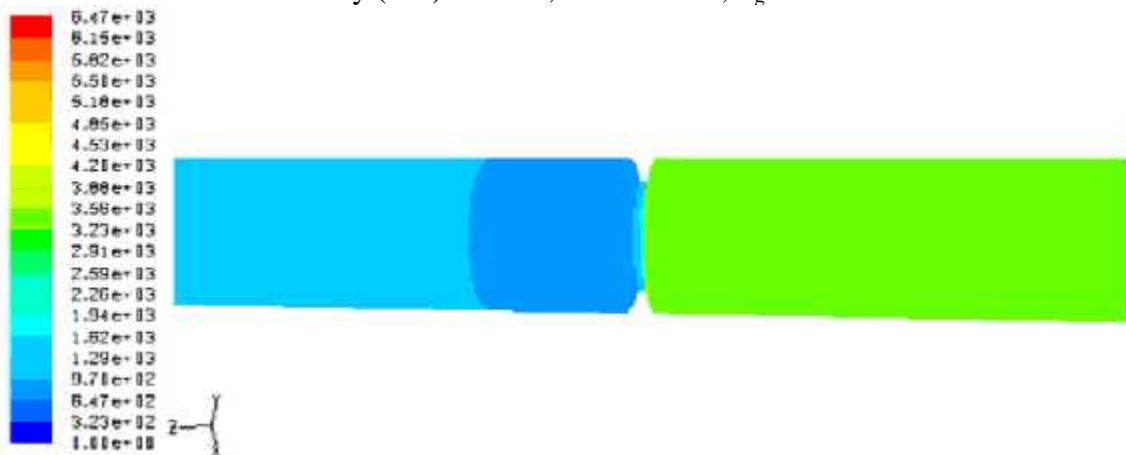


Fig. 6.29 Contour plot of static pressure for $D_0/D_t = 0.7087$ orifice
 Concentration of SCMC solution (kg/m^3): 0.8, Liquid velocity (m/s): 1.2772, Gas
 velocity (m/s): 2.4304, Gas fraction, ρ_g : 0.65

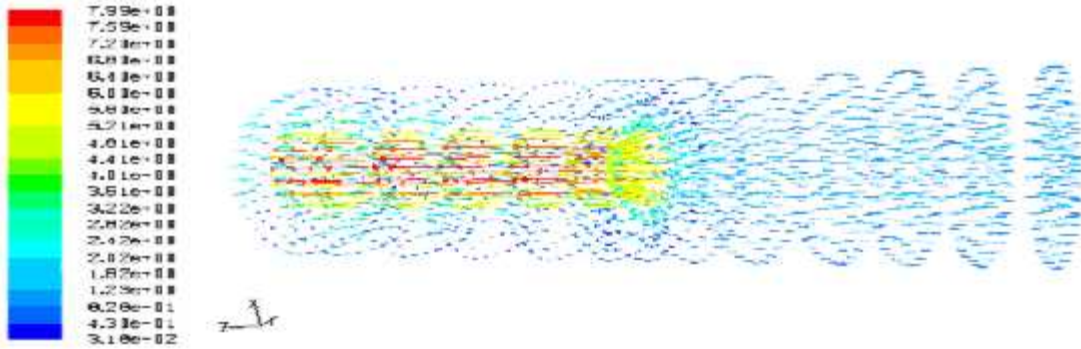


Fig. 6.30 Contour plot of velocity vector in air-SCMC mixture at different points for $D_0/ D_t = 0.4646$ orifice

Concentration of SCMC solution (kg/m^3): 0.8, Liquid velocity (m/s): 1.2772, Gas velocity (m/s): 1.1508, Gas fraction, γ_g : 0.46

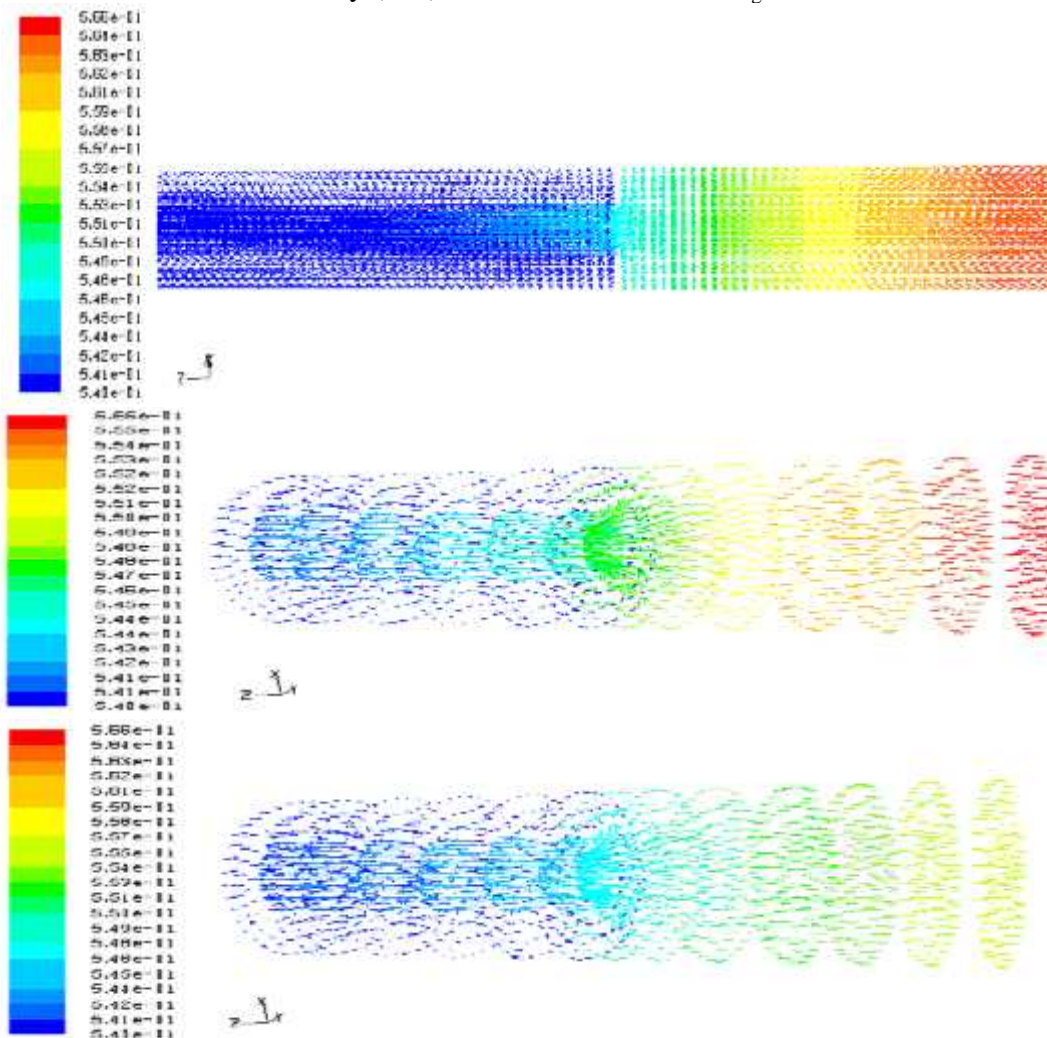


Fig. 6.31 Contour plot of velocity vector for SCMC phase in the mixture at different points for $D_0/ D_t = 0.4646$ orifice

Concentration of SCMC solution (kg/m^3): 0.8, Liquid velocity (m/s): 1.2772, Gas velocity (m/s): 1.1508, Gas fraction, γ_g : 0.46

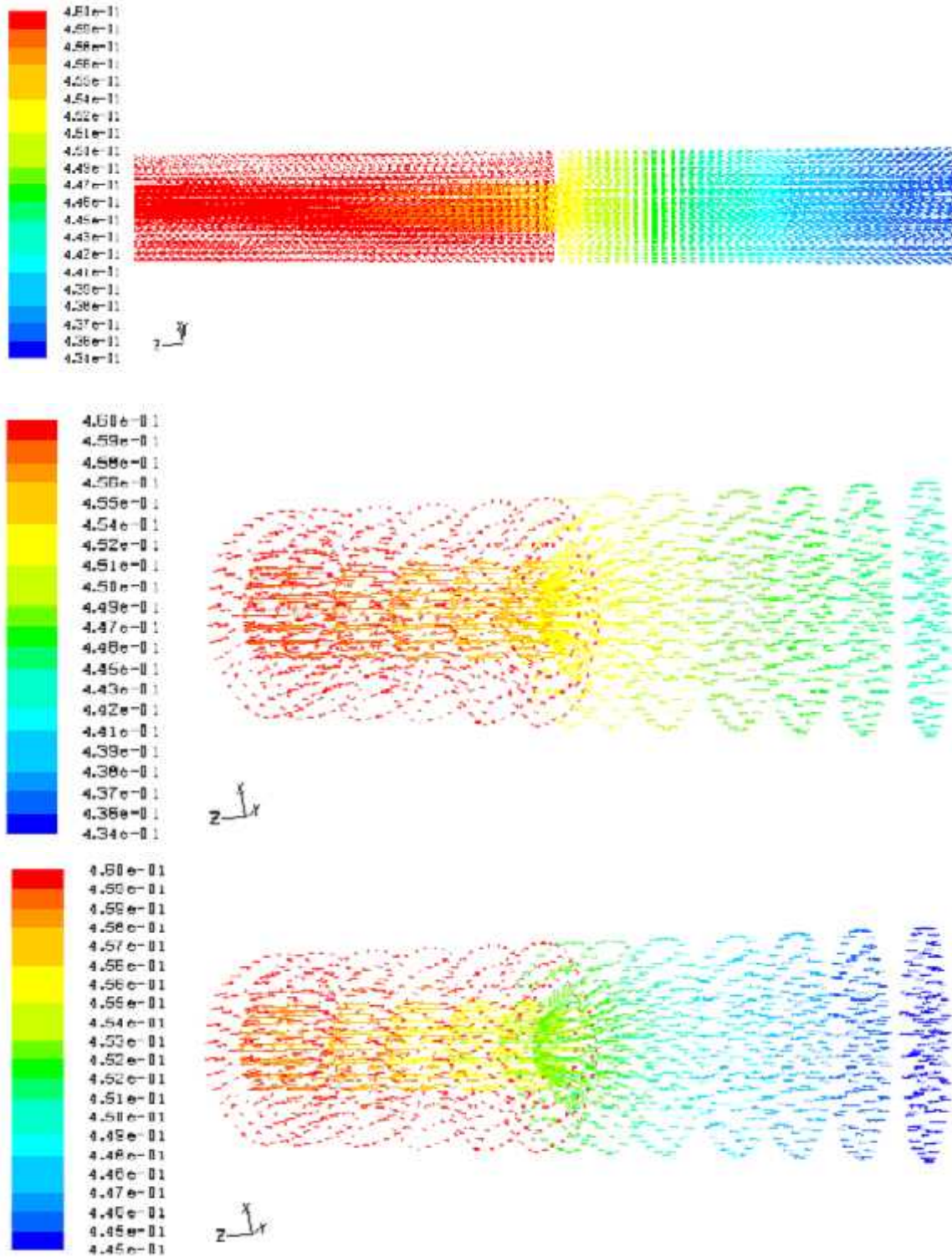


Fig. 6.32 Contour plot of velocity vector plot of air phase in the mixture at different points for $D_0/D_t = 0.4646$ orifice
 Concentration of SCMC solution (kg/m^3): 0.8, Liquid velocity (m/s): 1.2772, Gas velocity (m/s): 1.1508, Gas fraction, ρ_g : 0.46

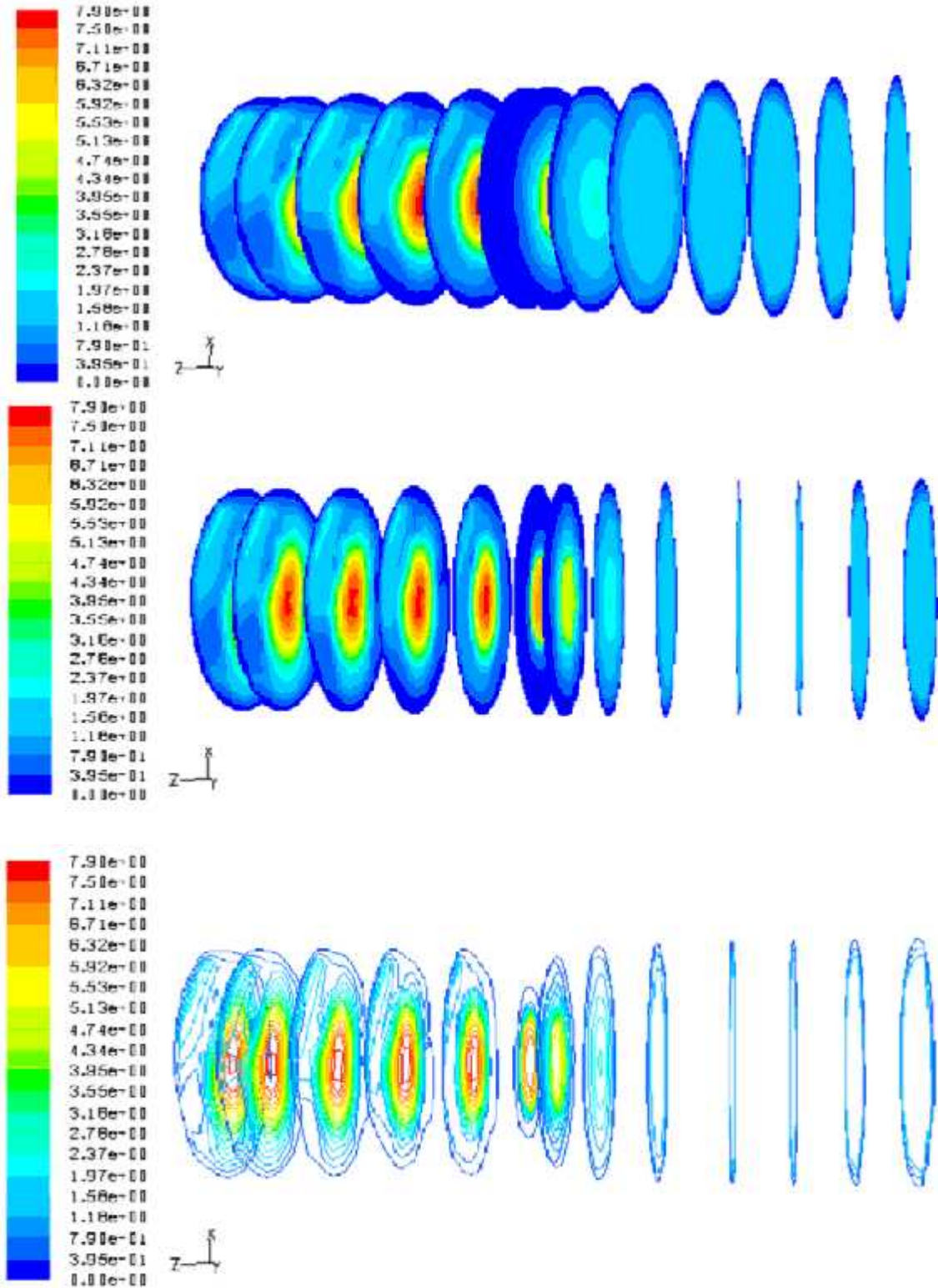


Fig. 6.33 Contours plot of velocity magnitude in the air-SCMC mixture at different points for $D_0/D_t = 0.4646$ orifice

Concentration of SCMC solution (kg/m^3): 0.8, Liquid velocity (m/s): 1.2772, Gas velocity (m/s): 1.1508, Gas fraction, α_g : 0.46

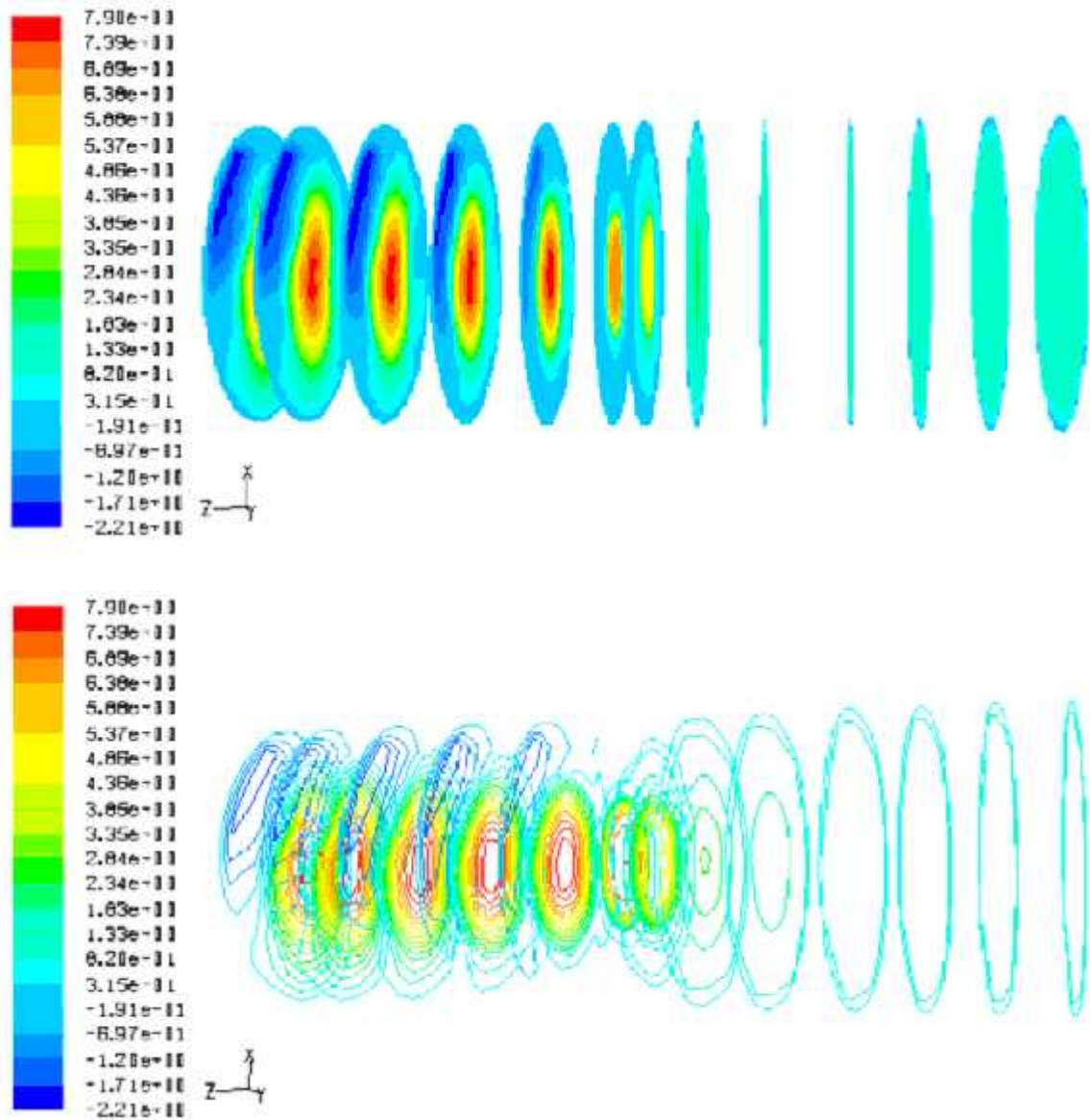


Fig. 6.34 Contours plot of velocity in the air-SCMC mixture inside the different points of $D_0/D_t = 0.4646$ orifice
 Concentration of SCMC solution (kg/m^3): 0.8, Liquid velocity (m/s): 1.2772, Gas velocity (m/s): 1.1508, Gas fraction, α_g : 0.46

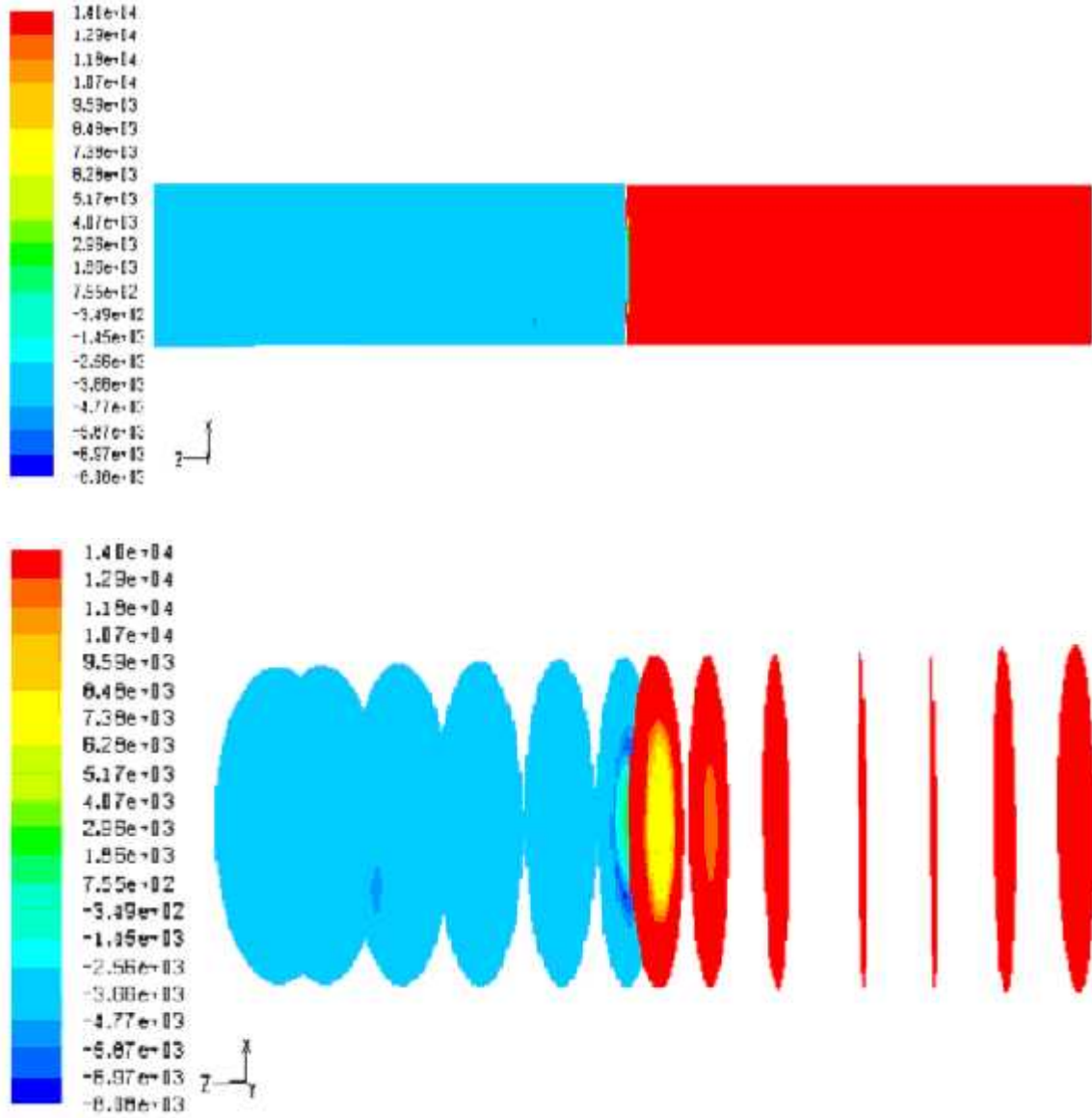


Fig. 6.35 Contours plot of static pressure in the air-SCMC mixture inside the different points of for $D_0/D_t = 0.4646$ orifice
 Concentration of SCMC solution (kg/m^3): 0.8, Liquid velocity (m/s): 1.2772, Gas velocity (m/s): 1.1508, Gas fraction, α_g : 0.46

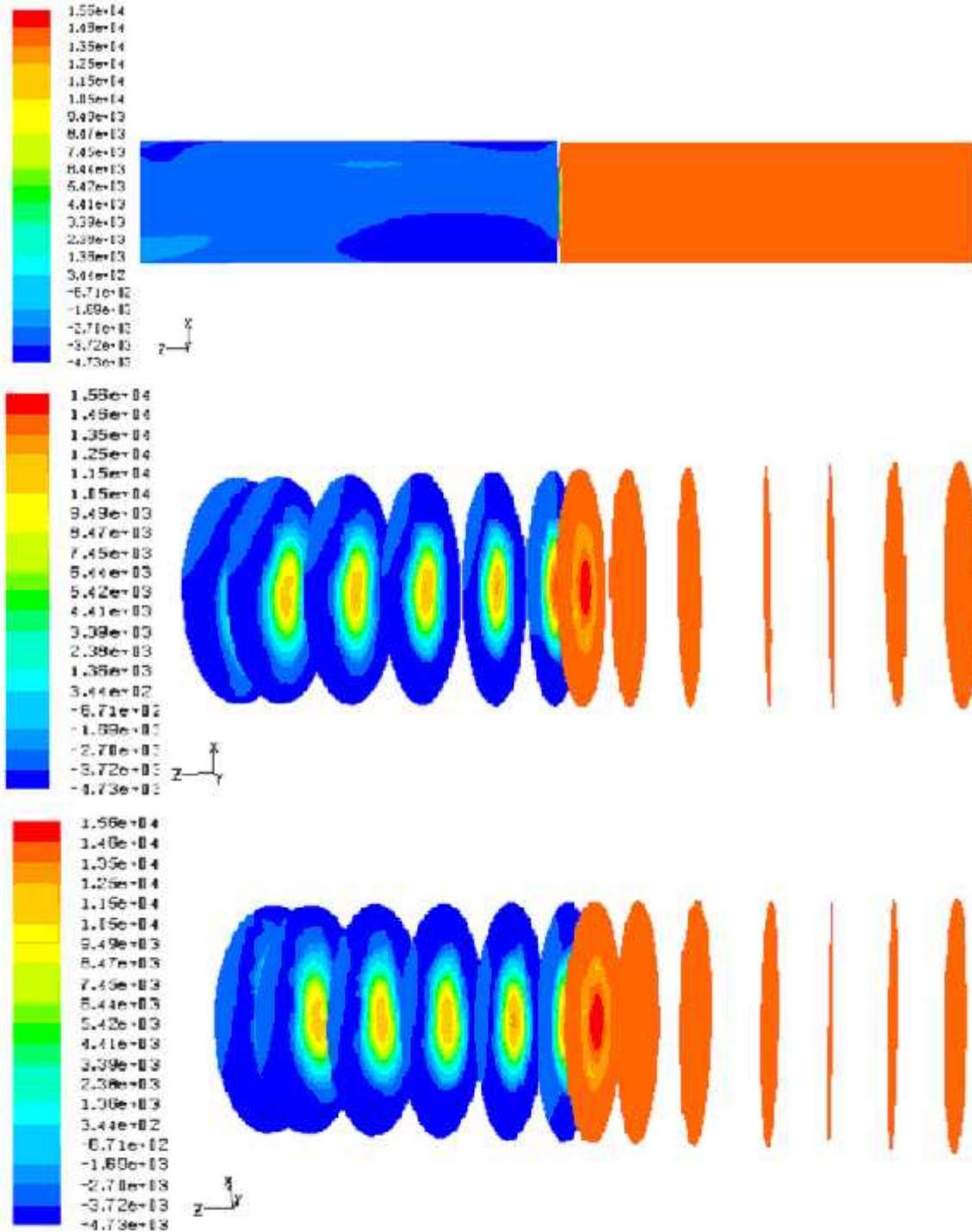


Fig. 6.36 Contours plot of total pressure in the air-SCMC mixture inside the different points of for $D_0/D_t = 0.4646$ orifice
 Concentration of SCMC solution (kg/m^3): 0.8, Liquid velocity (m/s): 1.2772, Gas velocity (m/s): 1.1508, Gas fraction, γ_g : 0.46

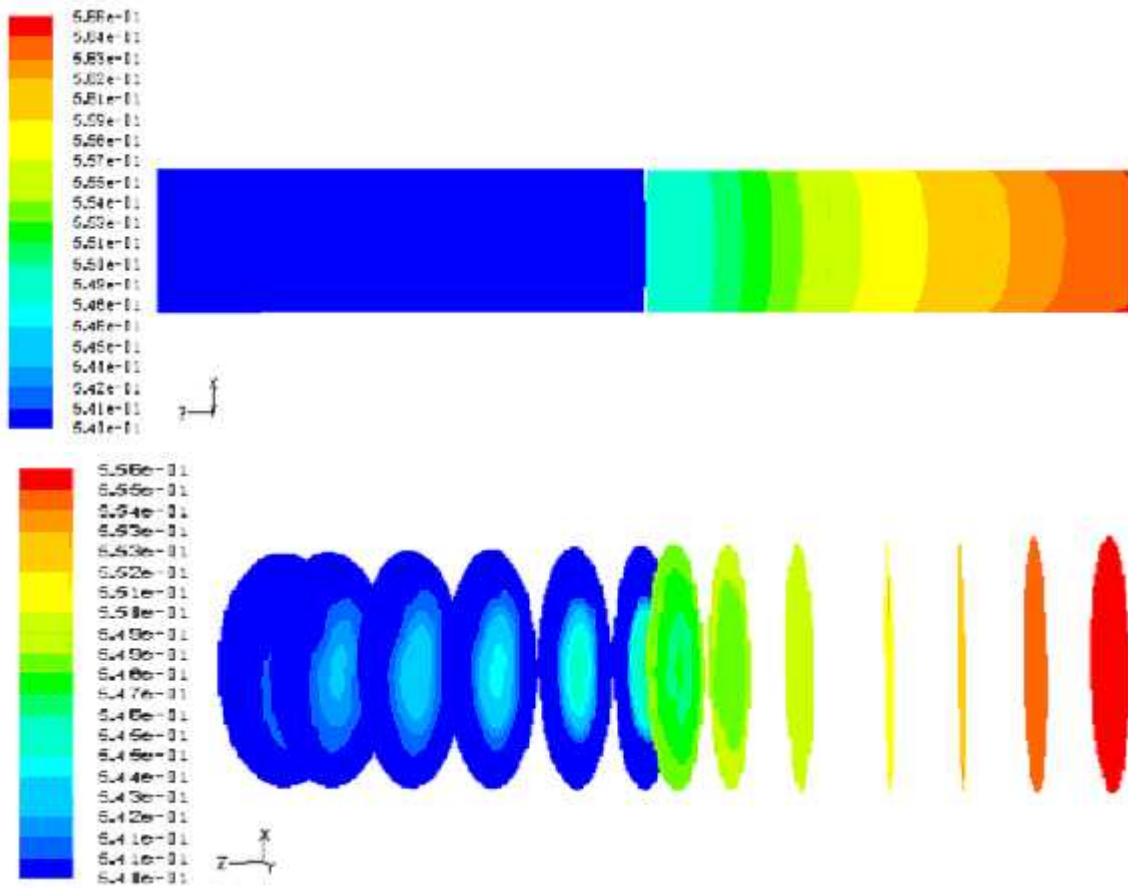


Fig. 6.37 Contours of plot of SCMC phase volume fraction in the mixture inside the different points of $D_0/D_t = 0.4646$ orifice
 Concentration of SCMC solution (kg/m^3): 0.8, Liquid velocity (m/s): 1.2772, Gas velocity (m/s): 1.1508, Gas fraction, α_g : 0.46

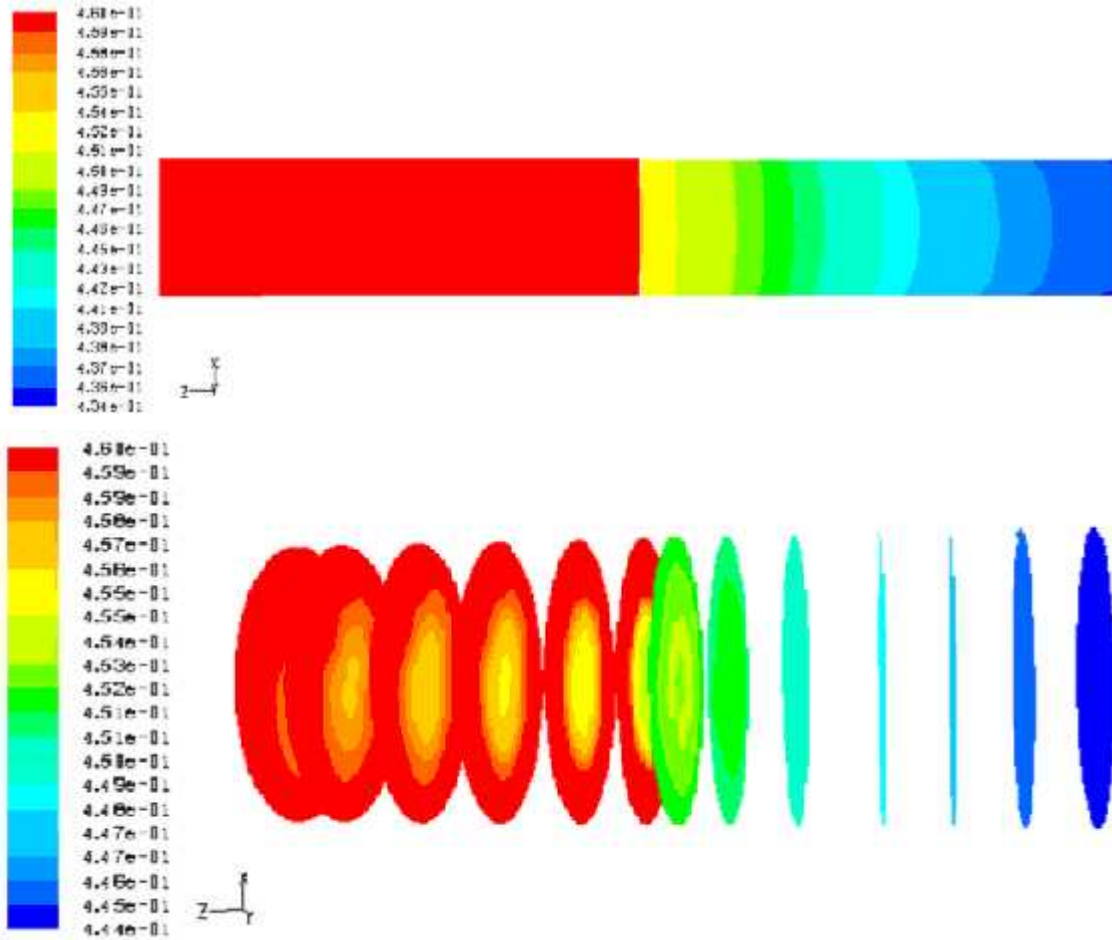


Fig. 6.38 Contours plot of air phase volume fraction in the mixture inside the different points of $D_0/D_t = 0.4646$ orifice
 Concentration of SCMC solution (kg/m^3): 0.8, Liquid velocity (m/s): 1.2772, Gas velocity (m/s): 1.1508, Gas fraction, α_g : 0.46

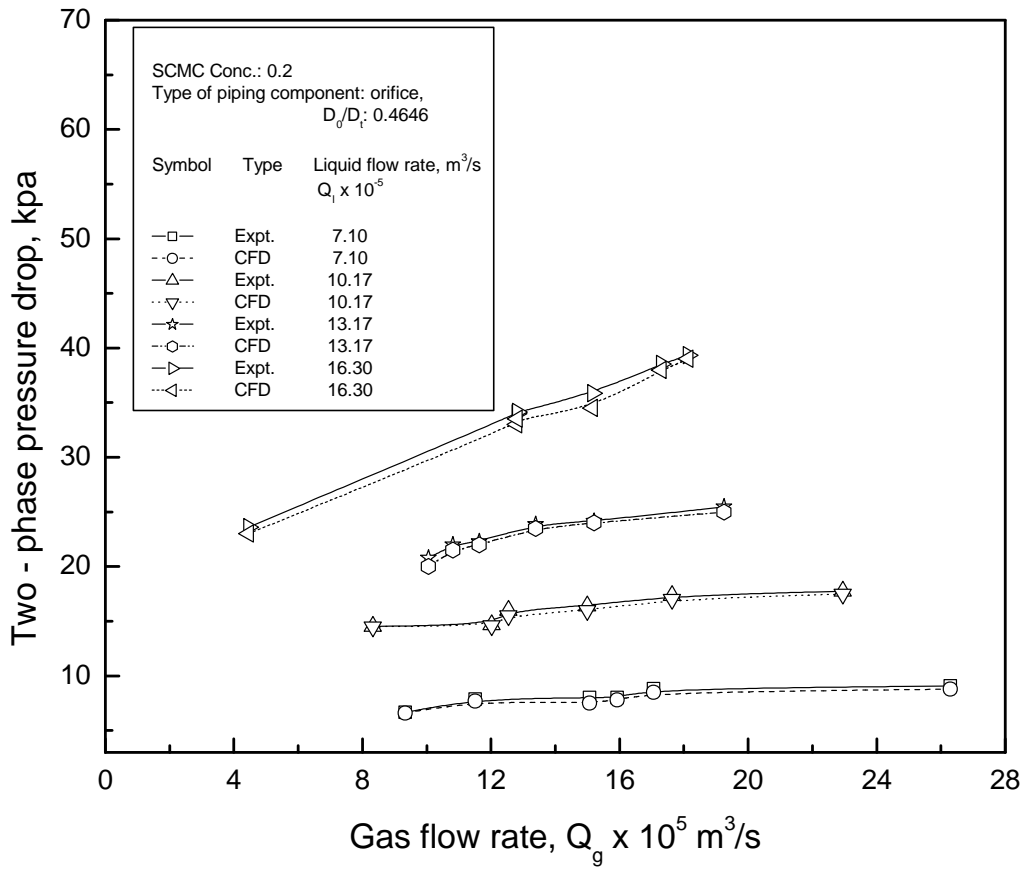


Fig. 6.39 Comparison of the experimental result with CFD simulated result with different liquid flow rate and fixed liquid concentration, fixed orifice dimension

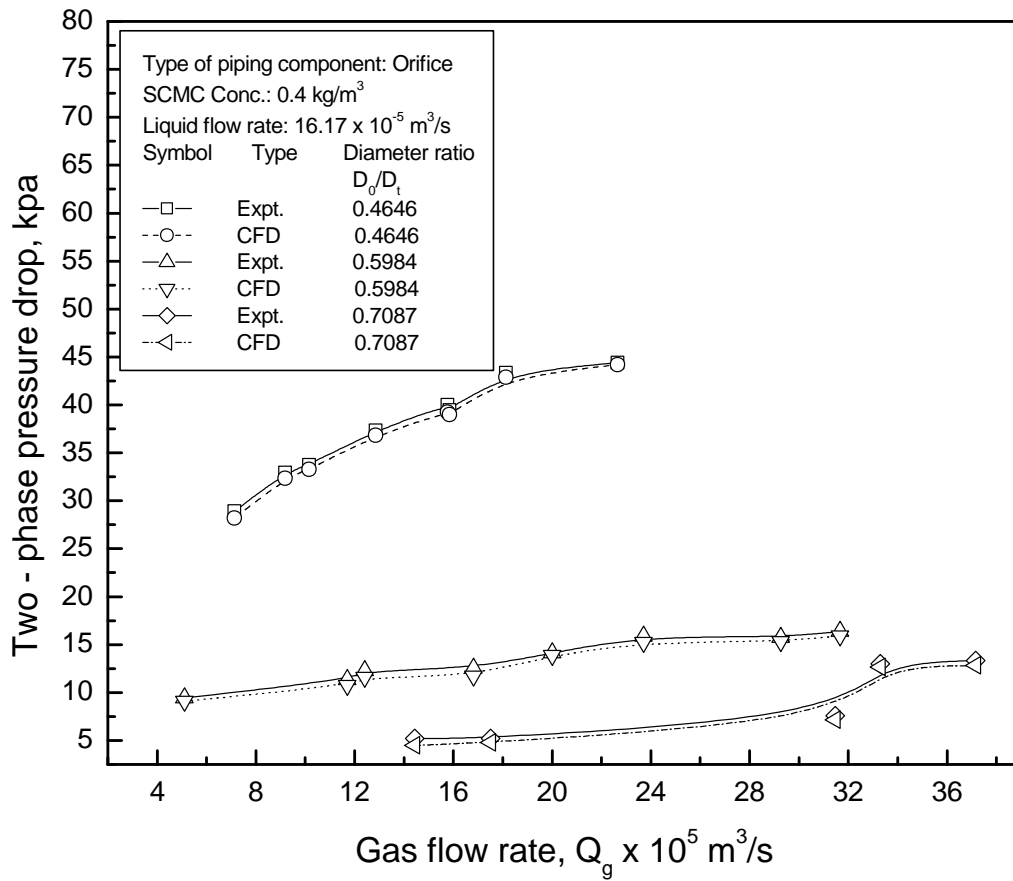


Fig. 6.40 Comparison of the experimental result with CFD simulated result with different orifice dimension and fixed liquid concentration, fixed liquid flow rate

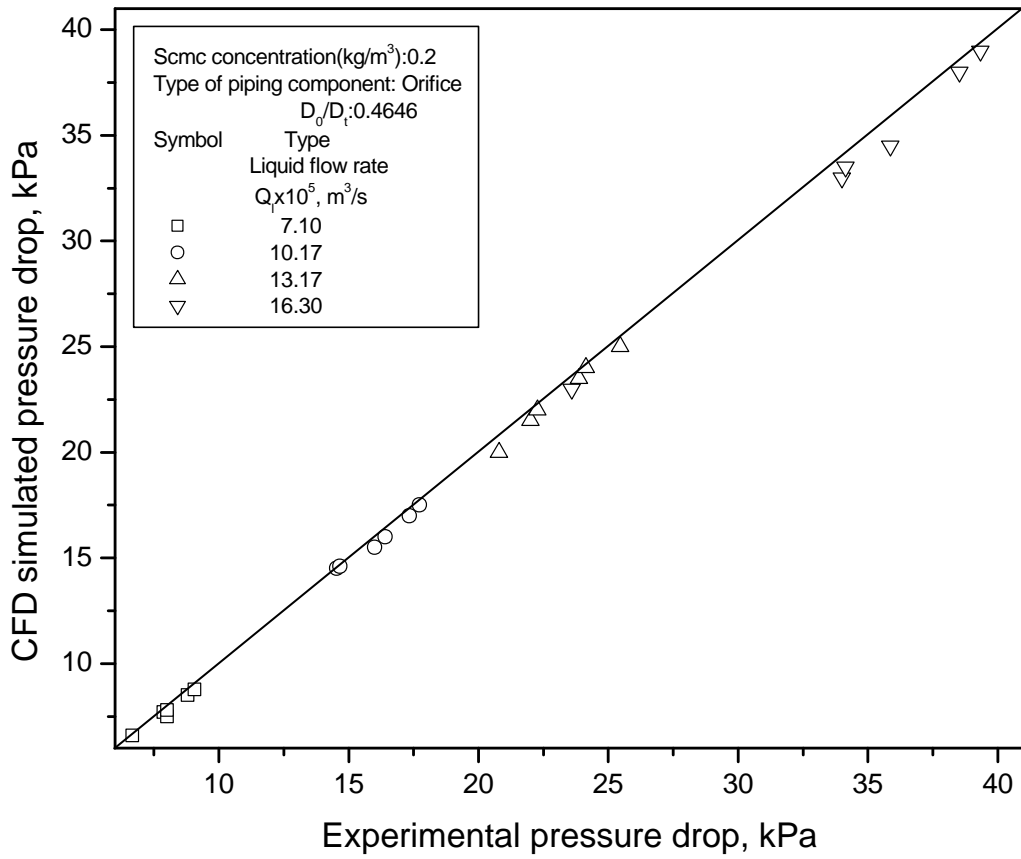


Fig. 6.41 Comparison of experimental results with CFD simulated results for different liquid flow rates

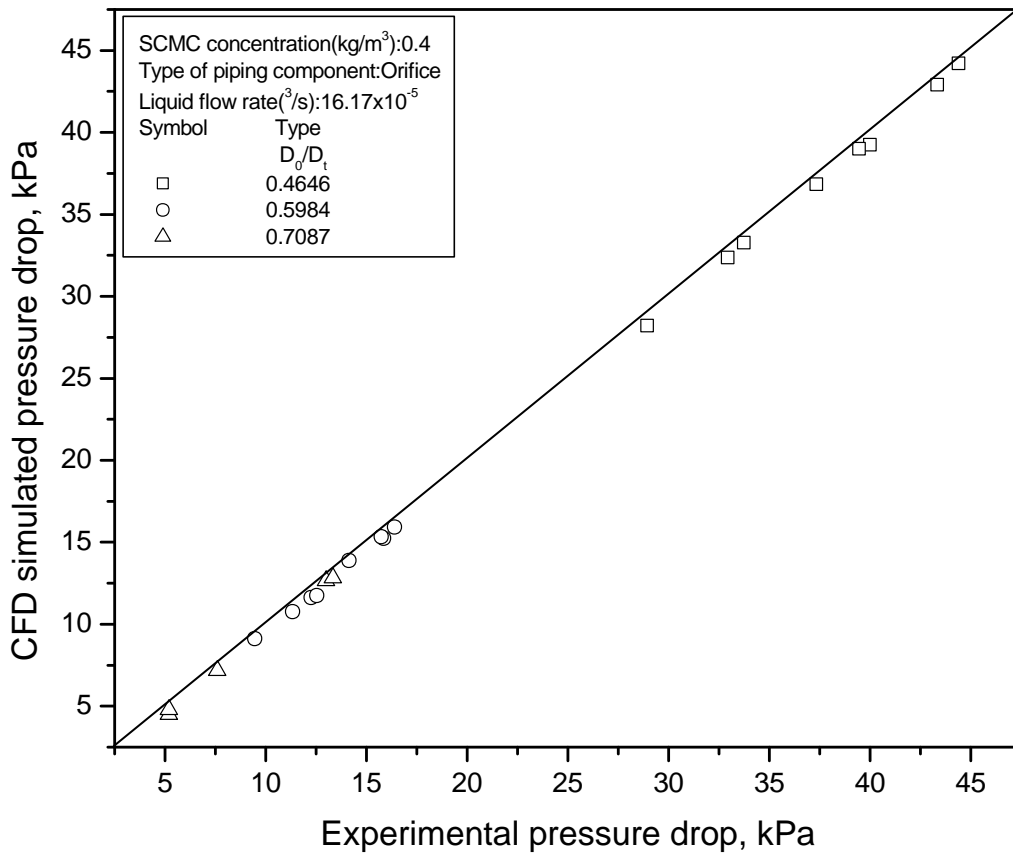


Fig. 6.42 Comparison of experimental results with CFD simulated results for different orifice diameter ratios

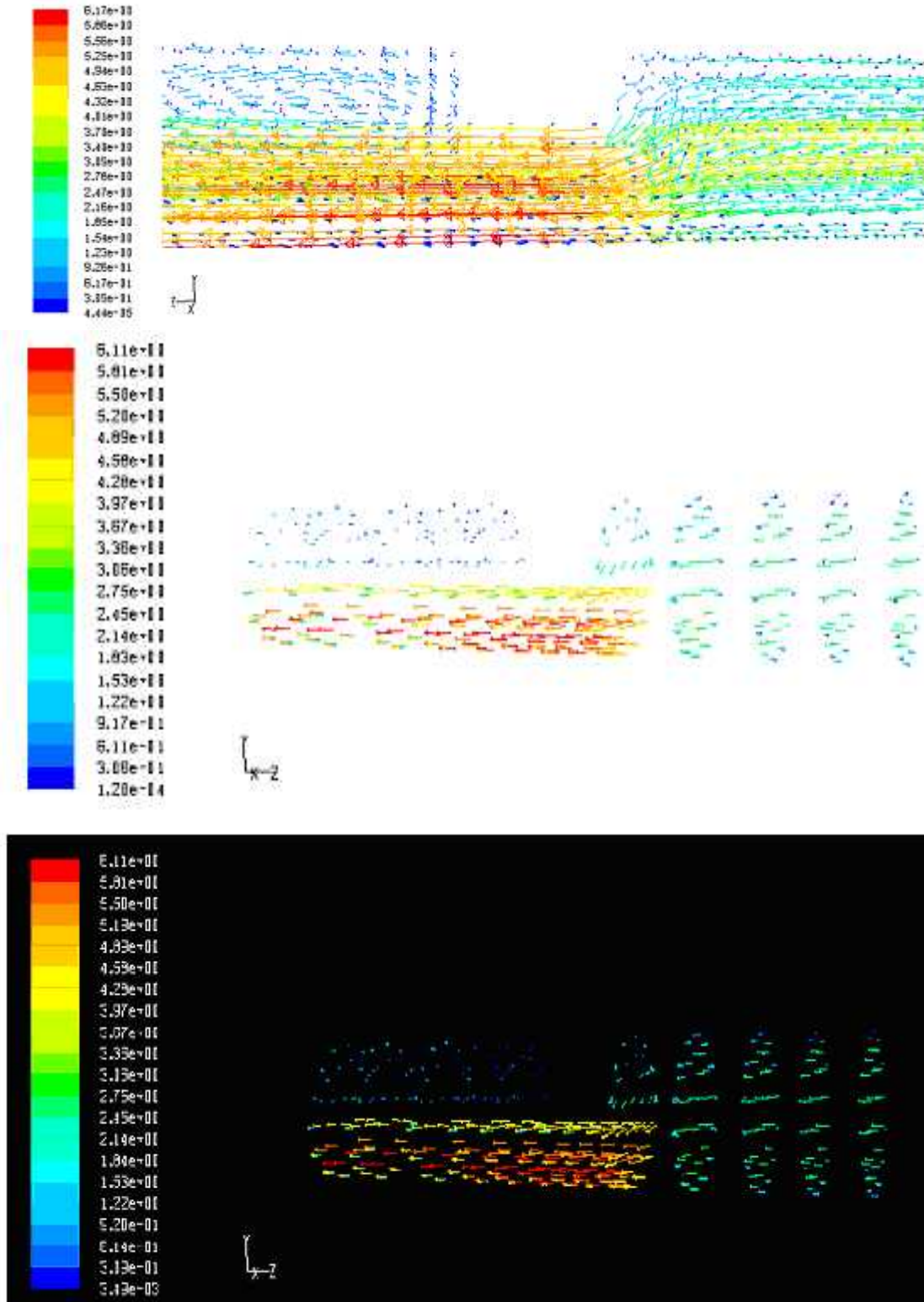


Fig. 6.43 Contours plot of velocity vector in the air-SCMC mixture at the different points of 50% opening gate valve, Concentration of SCMC solution (kg/m^3): 0.8, Liquid velocity (m/s): 1.5142, Gas velocity (m/s): 3.0516, Gas fraction, ρ_g : 0.668

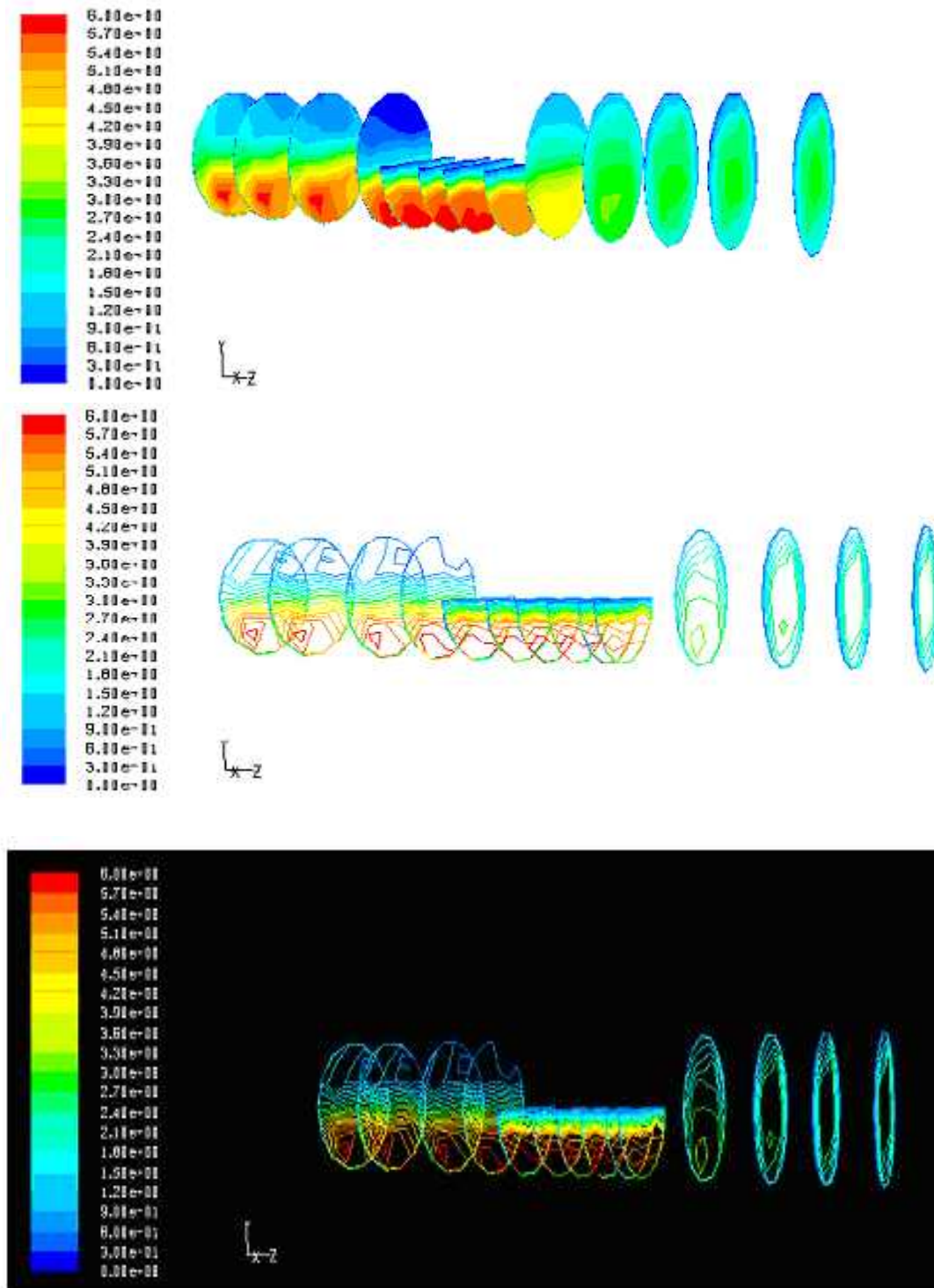


Fig. 6.44 Contours plot of velocity magnitude in the air-SCMC mixture at the different points of 50% opening gate valve, Concentration of SCMC solution (kg/m^3): 0.8, Liquid velocity (m/s): 1.5142, Gas velocity (m/s): 3.0516, Gas fraction, γ_g : 0.6683

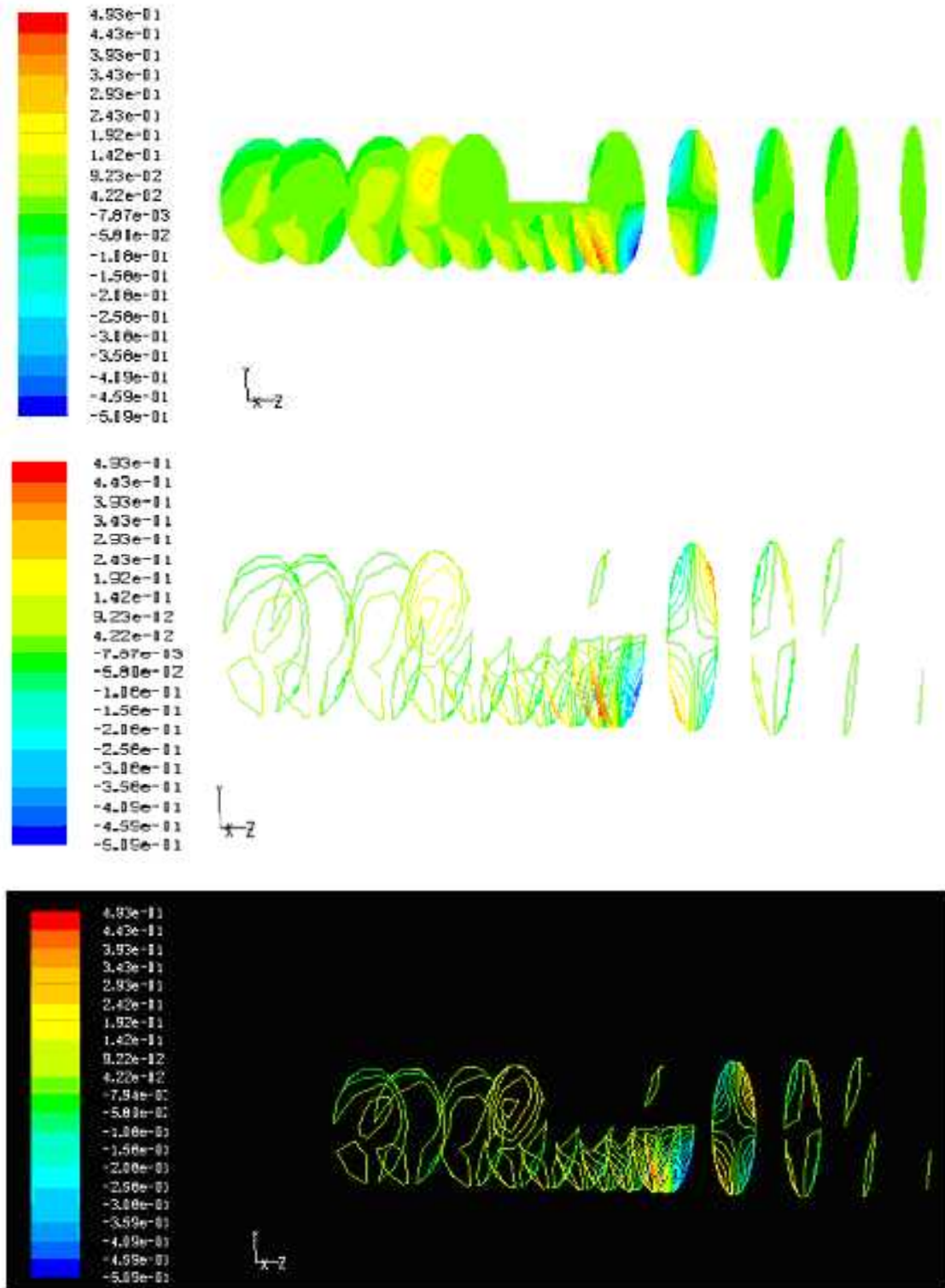


Fig. 6.45 Contours plot of velocity in the air-SCMC mixture at the different points of 50% opening gate valve, Concentration of SCMC solution (kg/m^3): 0.8, Liquid velocity (m/s): 1.5142, Gas velocity (m/s): 3.0516, Gas fraction, ρ_g : 0.6683

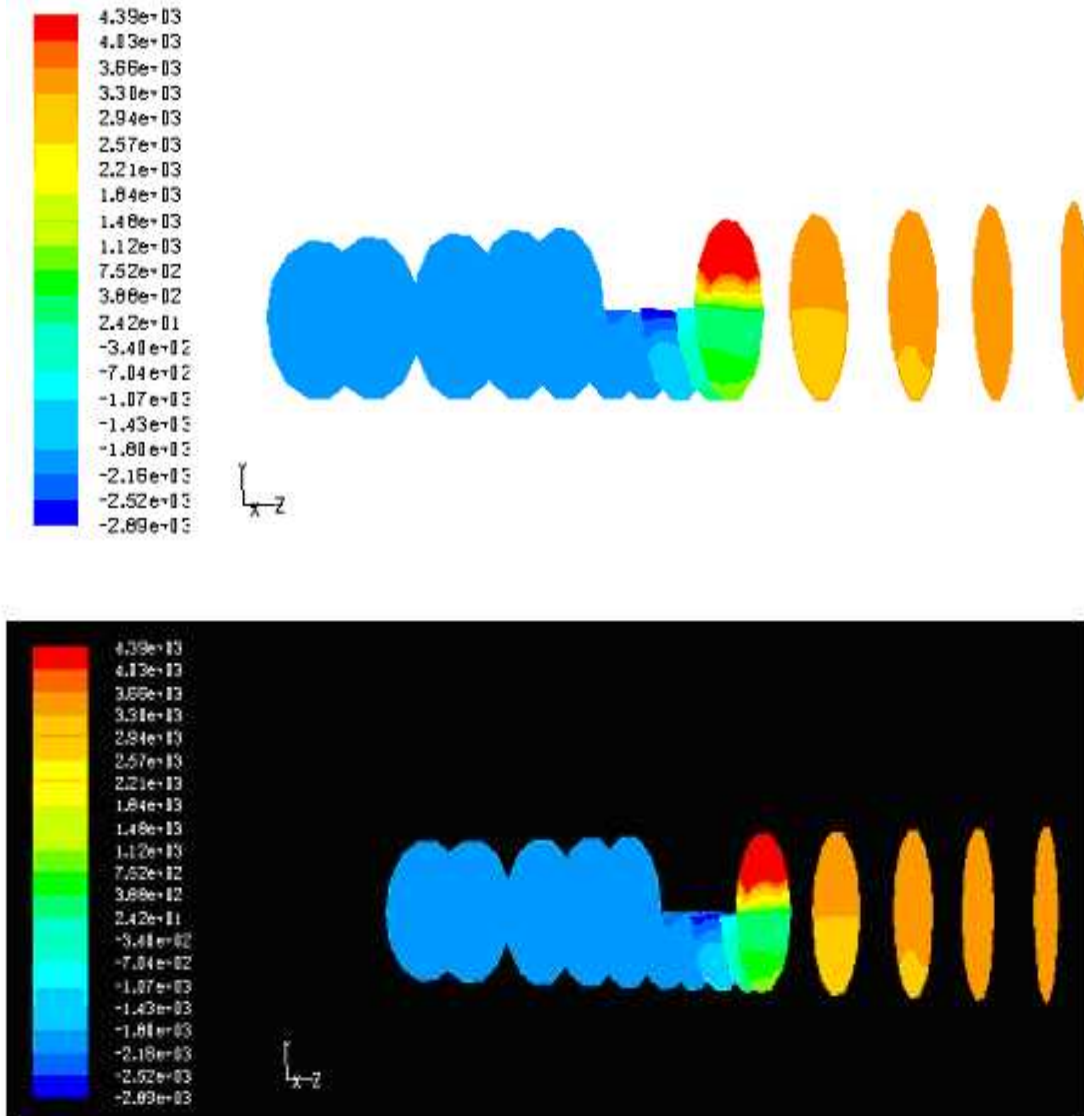


Fig. 6.46 Contours plot of static pressure in the air-SCMC mixture at the different points of 50% opening gate valve, Concentration of SCMC solution (kg/m^3): 0.8, Liquid velocity (m/s): 1.5142, Gas velocity (m/s): 3.0516, Gas fraction, γ_g : 0.6683

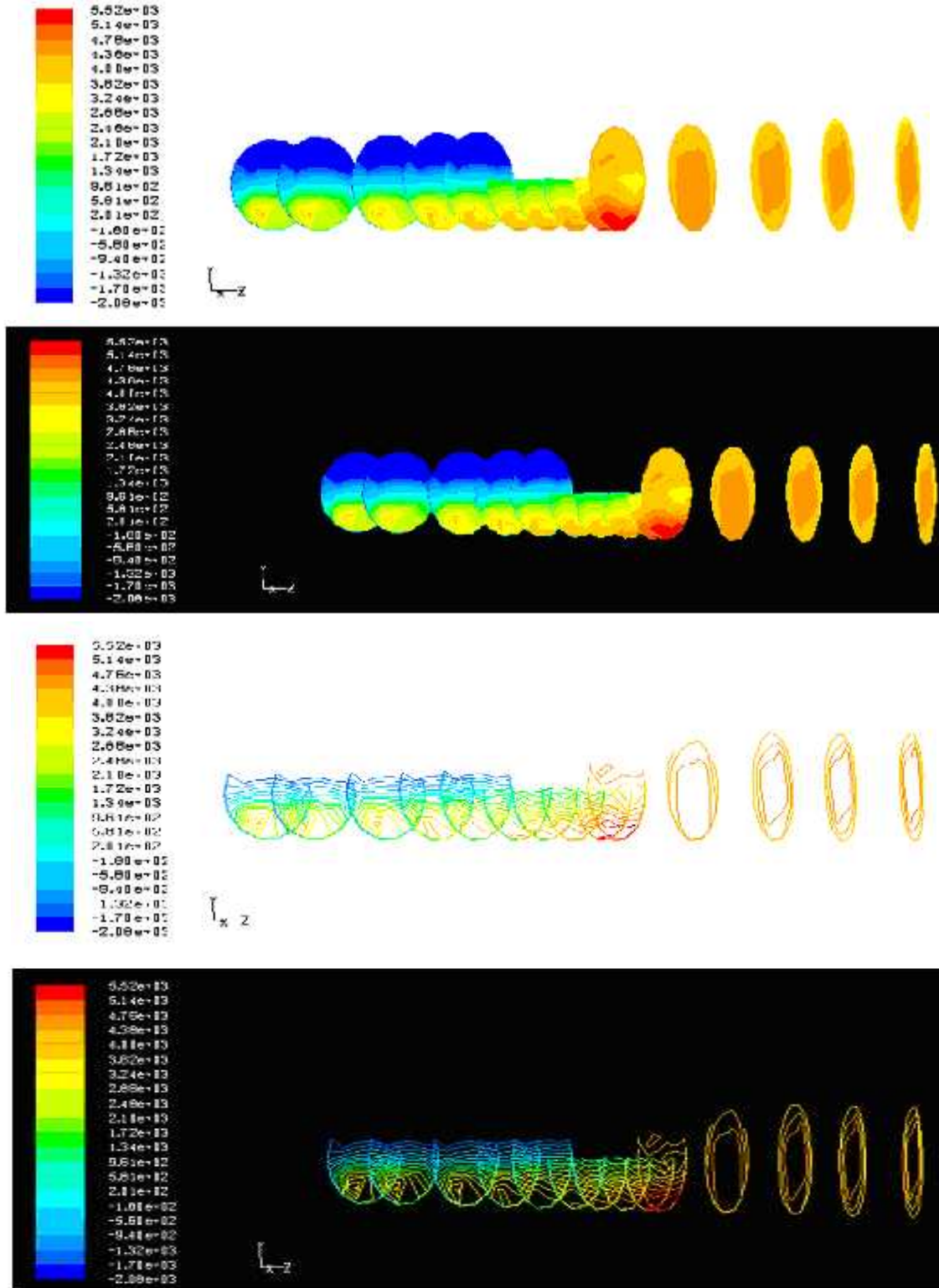


Fig. 6.47 Contours plot of total pressure in the air-SCMC mixture at the different points of 50% opening gate valve, Concentration of SCMC solution (kg/m^3): 0.8, Liquid velocity (m/s): 1.5142, Gas velocity (m/s): 3.0516, Gas fraction, α_g : 0.6683

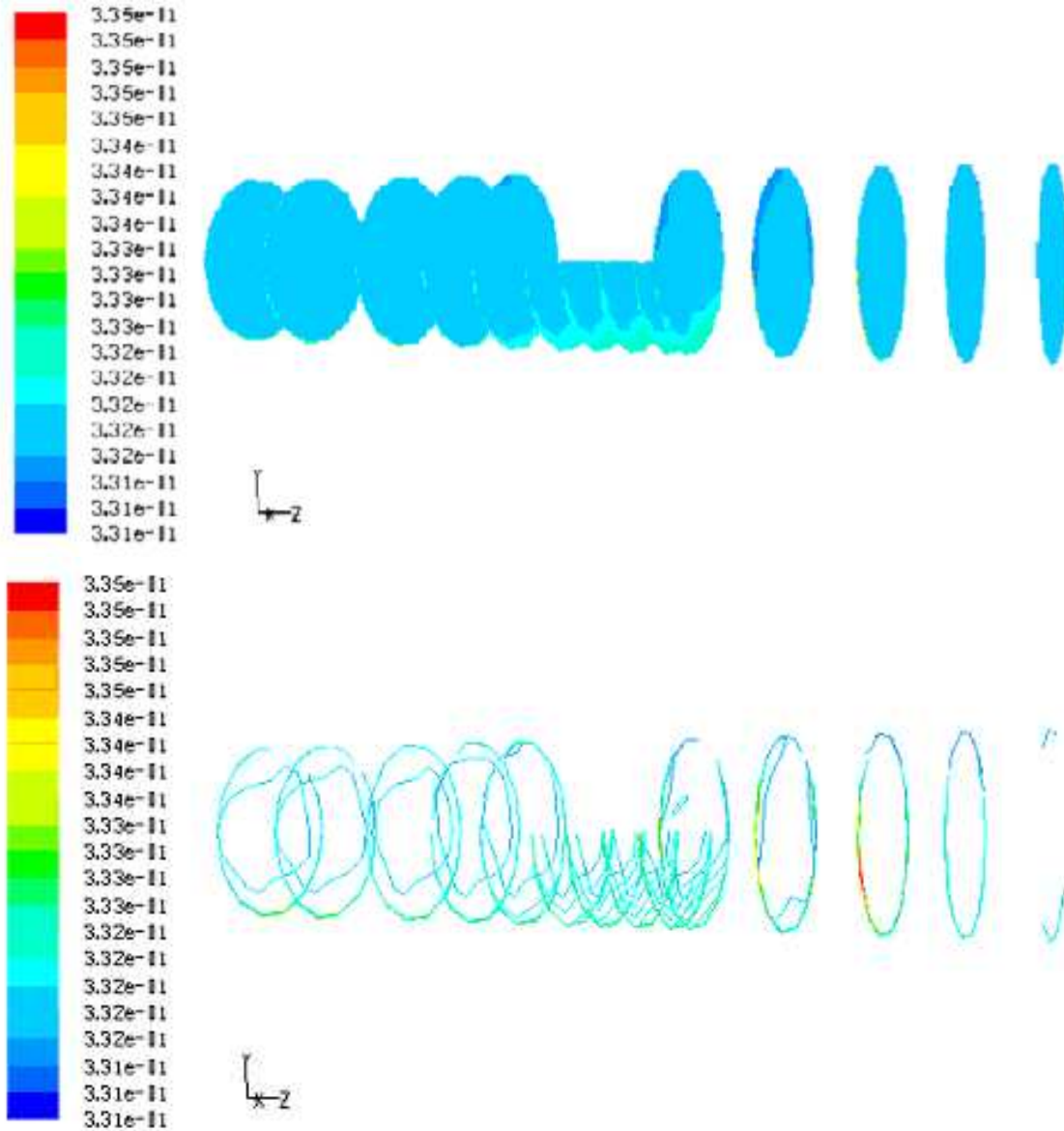


Fig. 6.48 Contours plot of SCMC phase volume fraction in the air-SCMC mixture at the different points of 50% opening gate valve, Concentration of SCMC solution (kg/m^3): 0.8, Liquid velocity (m/s): 1.5142, Gas velocity (m/s): 3.0516, Gas fraction, α_g : 0.6683

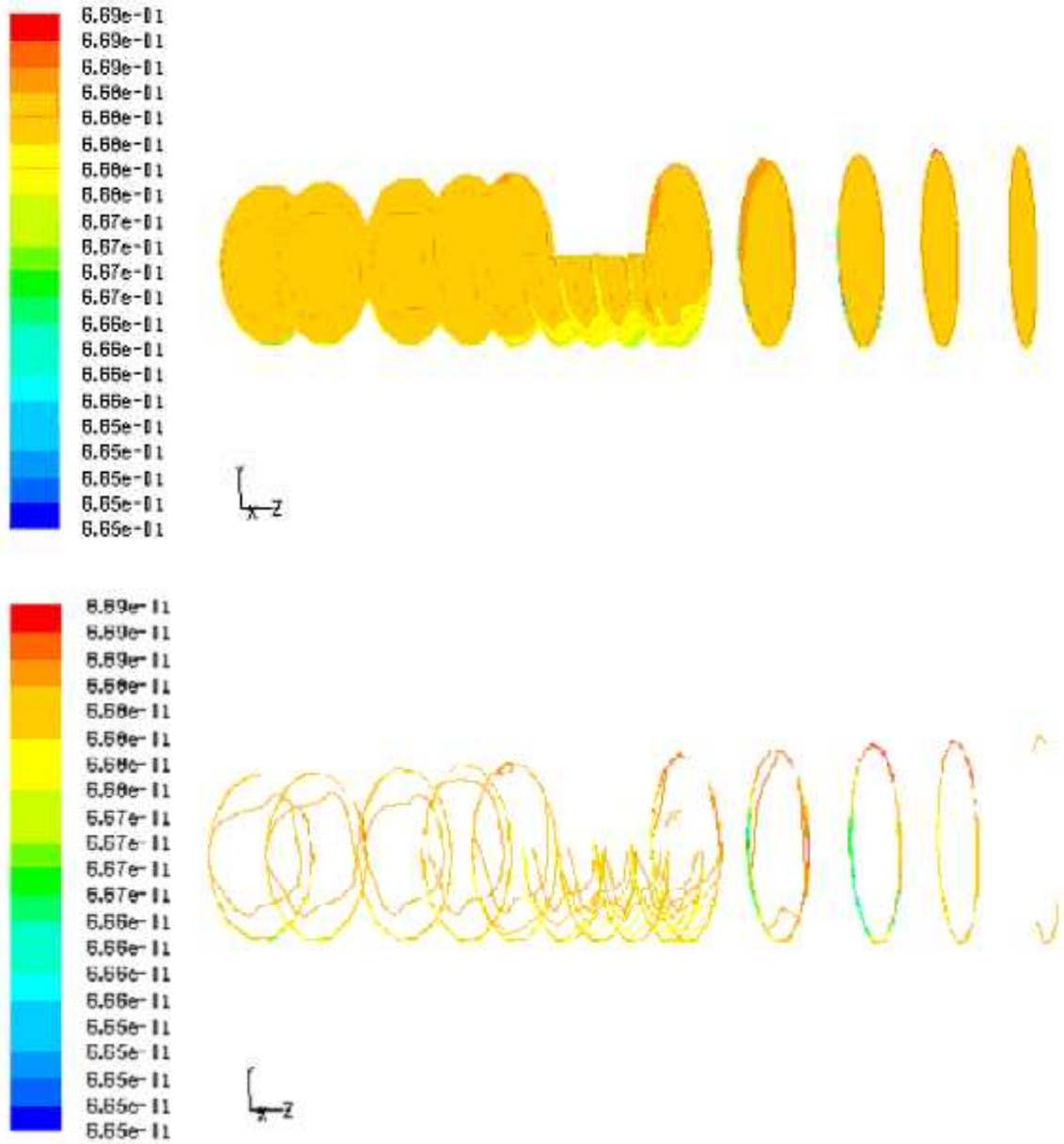


Fig. 6.49 Contours plot of air phase volume fraction in the air-SCMC mixture at the different points of 50% opening gate valve, Concentration of SCMC solution (kg/m^3): 0.8, Liquid velocity (m/s): 1.5142, Gas velocity (m/s): 3.0516, Gas fraction, ρ_g : 0.6683

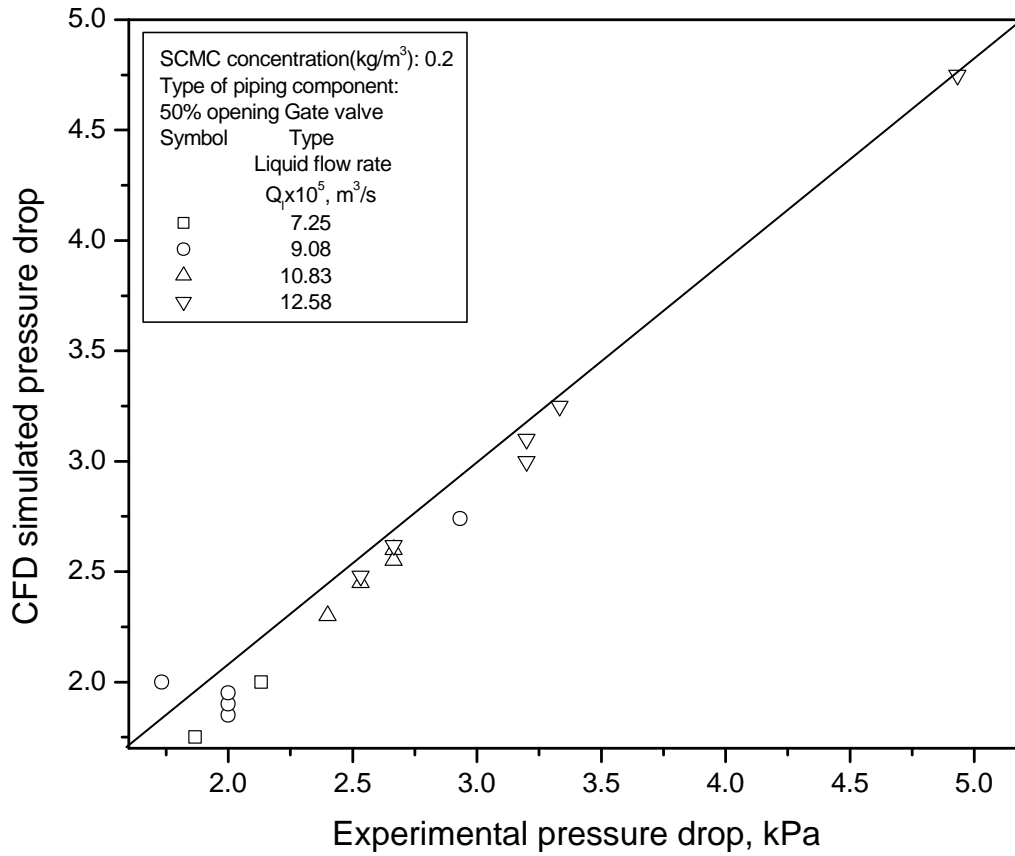


Fig. 6.50 Comparison of experimental results with CFD simulated results for different liquid flow rates

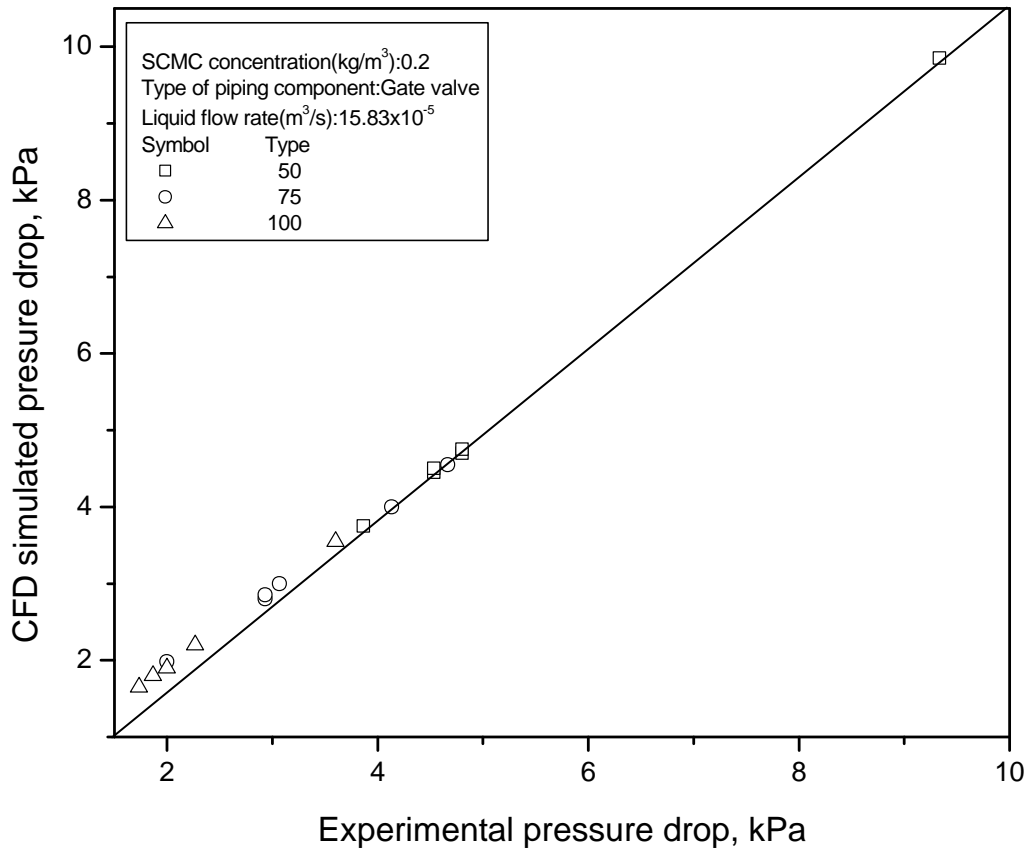


Fig.6.51 Comparison of experimental results with CFD simulated results for different % opening of Gate valve

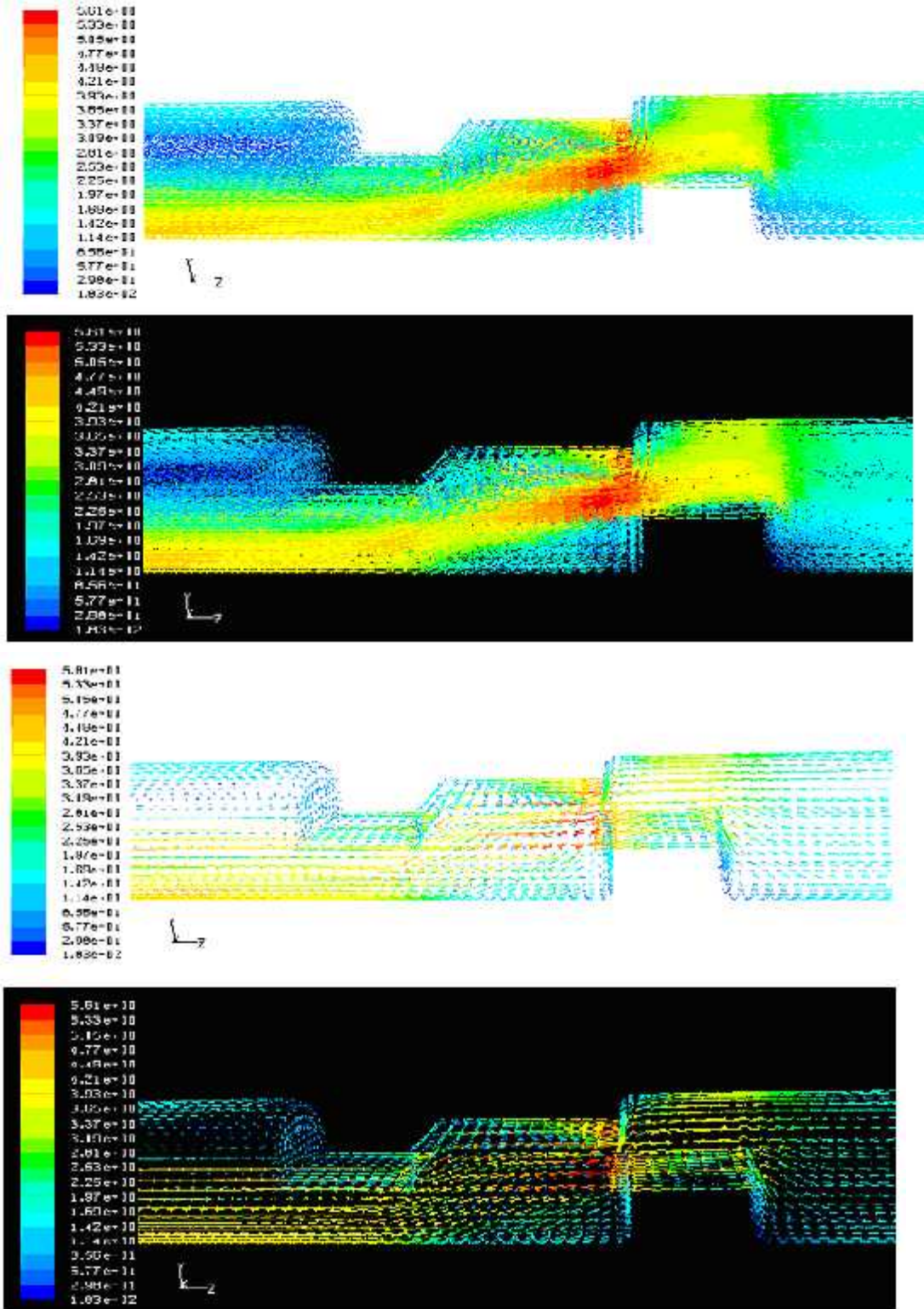


Fig. 6.52 Contours plot of velocity vector in the air-SCMC mixture for 50% opening globe valve, Concentration of SCMC solution (kg/m^3): 0.8, Liquid velocity (m/s): 1.5142, Gas velocity (m/s): 1.7265, Gas fraction, γ_g : 0.5

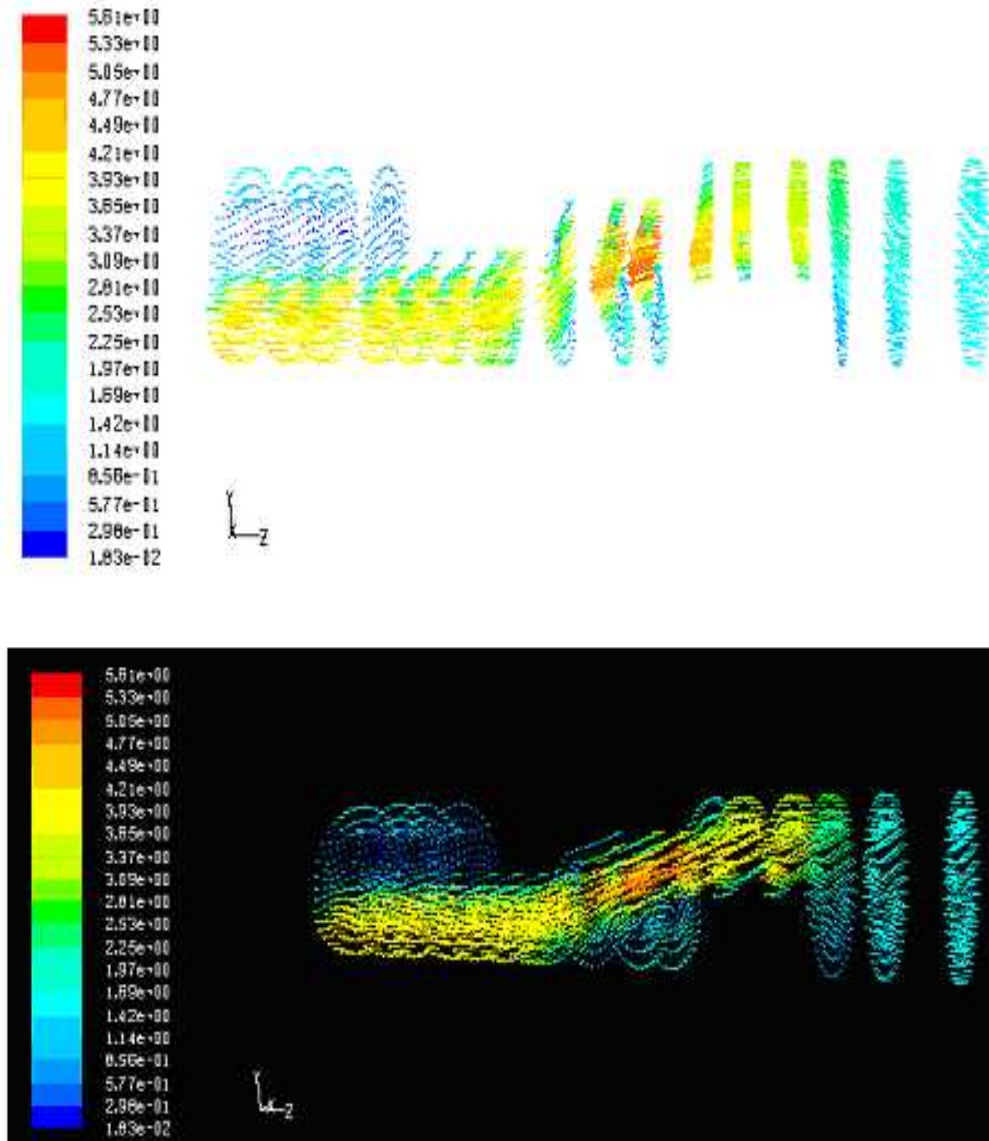


Fig. 6.53 Contours plot of velocity vector in the air-SCMC mixture at the different points of 50% opening globe valve, Concentration of SCMC solution (kg/m^3): 0.8, Liquid velocity (m/s): 1.5142, Gas velocity (m/s): 1.7265, Gas fraction, γ_g : 0.5

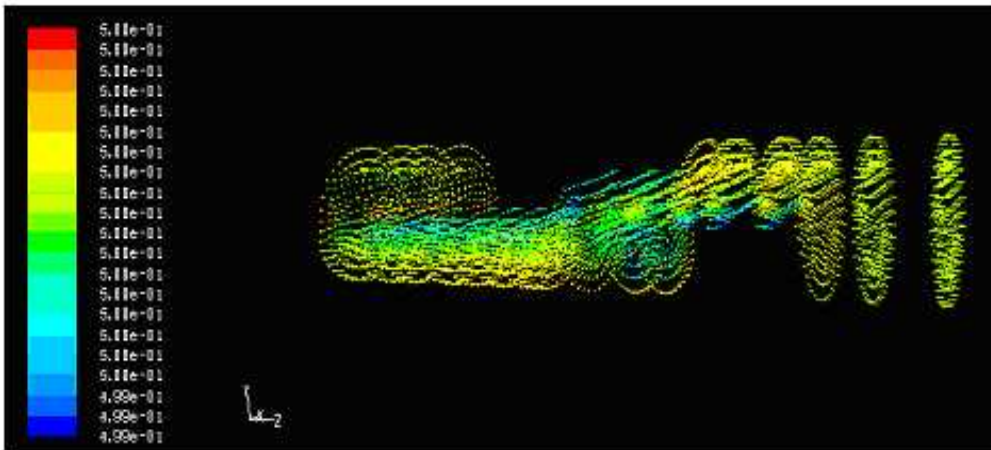
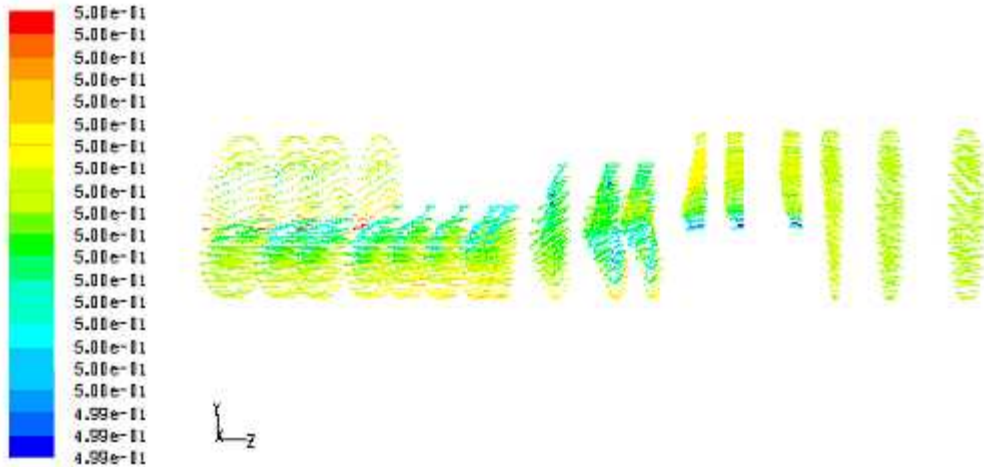


Fig. 6.54 Contours plot of velocity vector for SCMC phase in the air-SCMC mixture at the different points of 50% opening globe valve, Concentration of SCMC solution (kg/m^3): 0.8, Liquid velocity (m/s): 1.5142, Gas velocity (m/s): 1.7265, Gas fraction, ϕ_g : 0.5

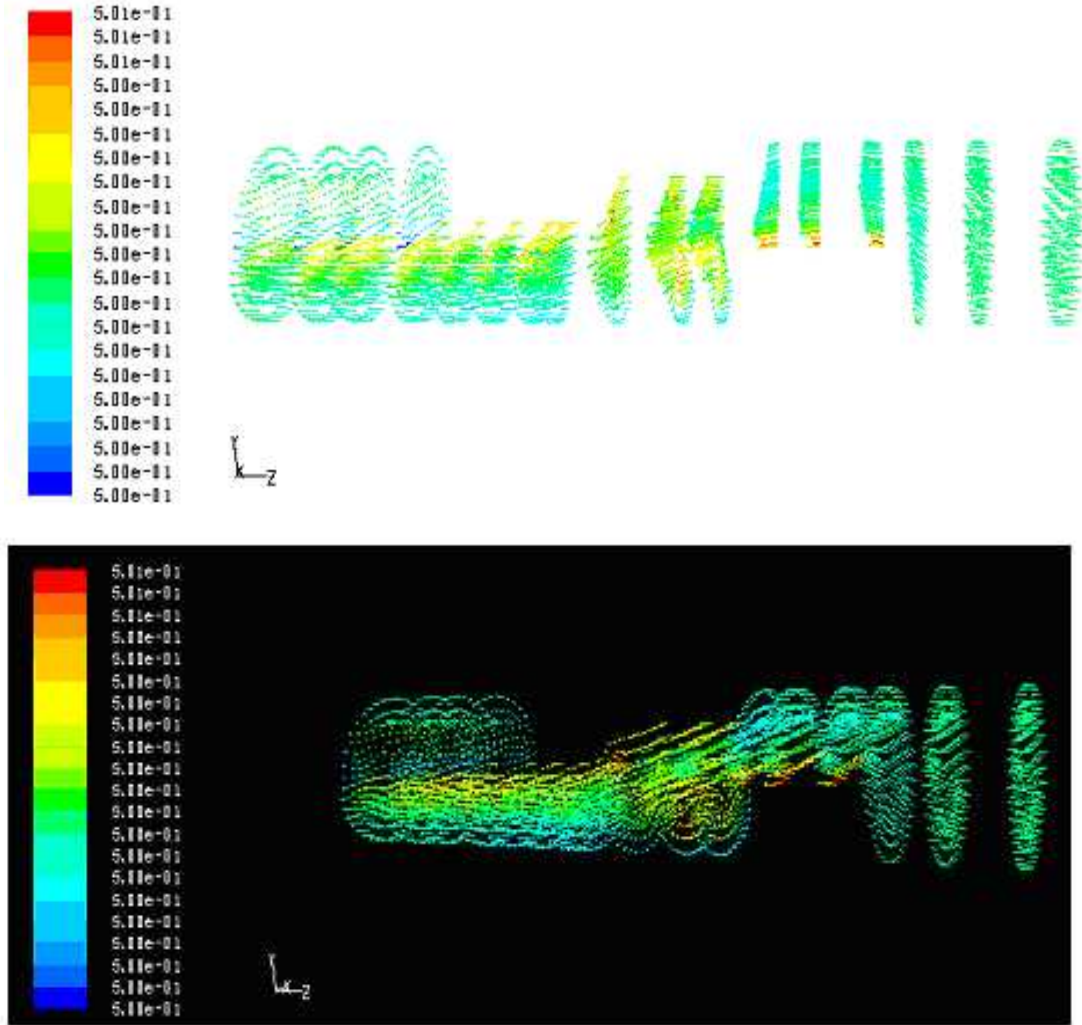


Fig. 6.55 Contours plot of velocity vector for air phase in the air-SCMC mixture at the different points of 50% opening globe valve, Concentration of SCMC solution (kg/m^3): 0.8, Liquid velocity (m/s): 1.5142, Gas velocity (m/s): 1.7265, Gas fraction, γ_g : 0.5

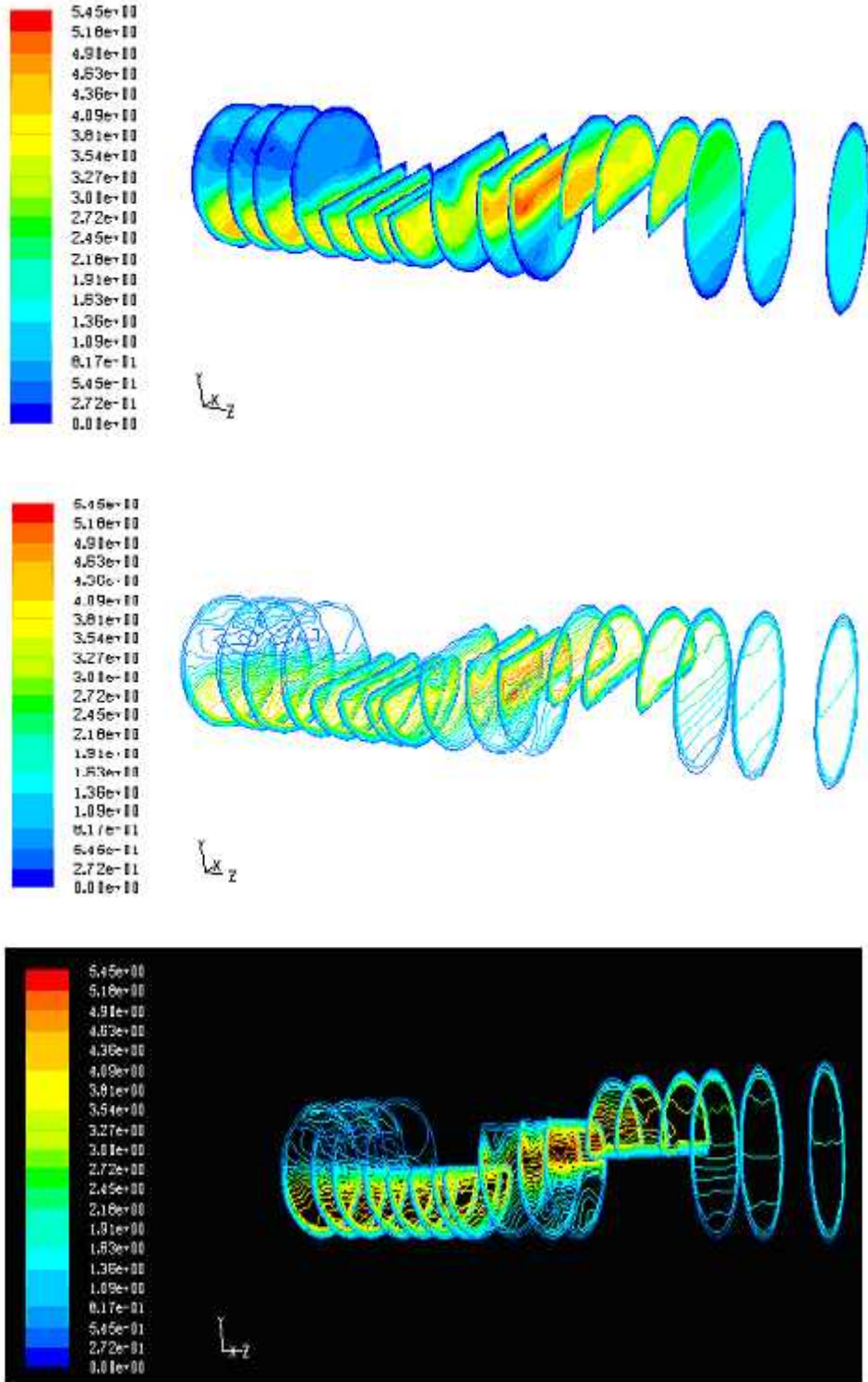


Fig. 6.56 Contours plot of velocity magnitude in the air-SCMC mixture at the different points of 50% opening globe valve, Concentration of SCMC solution (kg/m^3): 0.8, Liquid velocity (m/s): 1.5142, Gas velocity (m/s): 1.7265, Gas fraction, g : 0.5

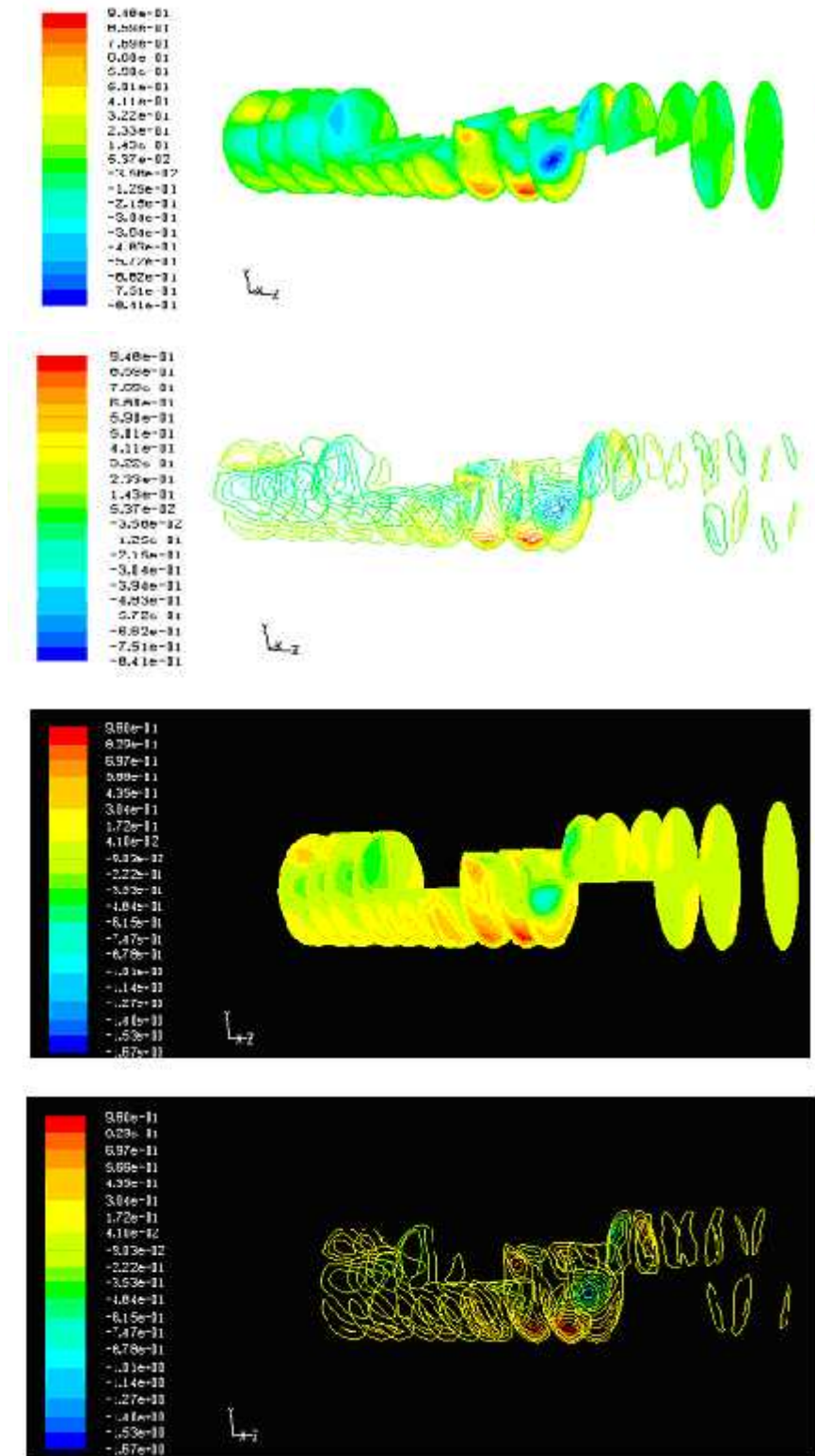


Fig. 6.57 Contours plot of axial velocity in the air-SCMC mixture at the different points of 50% opening globe valve, Concentration of SCMC solution (kg/m³): 0.8, Liquid velocity (m/s): 1.5142, Gas velocity (m/s): 1.7265, Gas fraction, α_g : 0.5

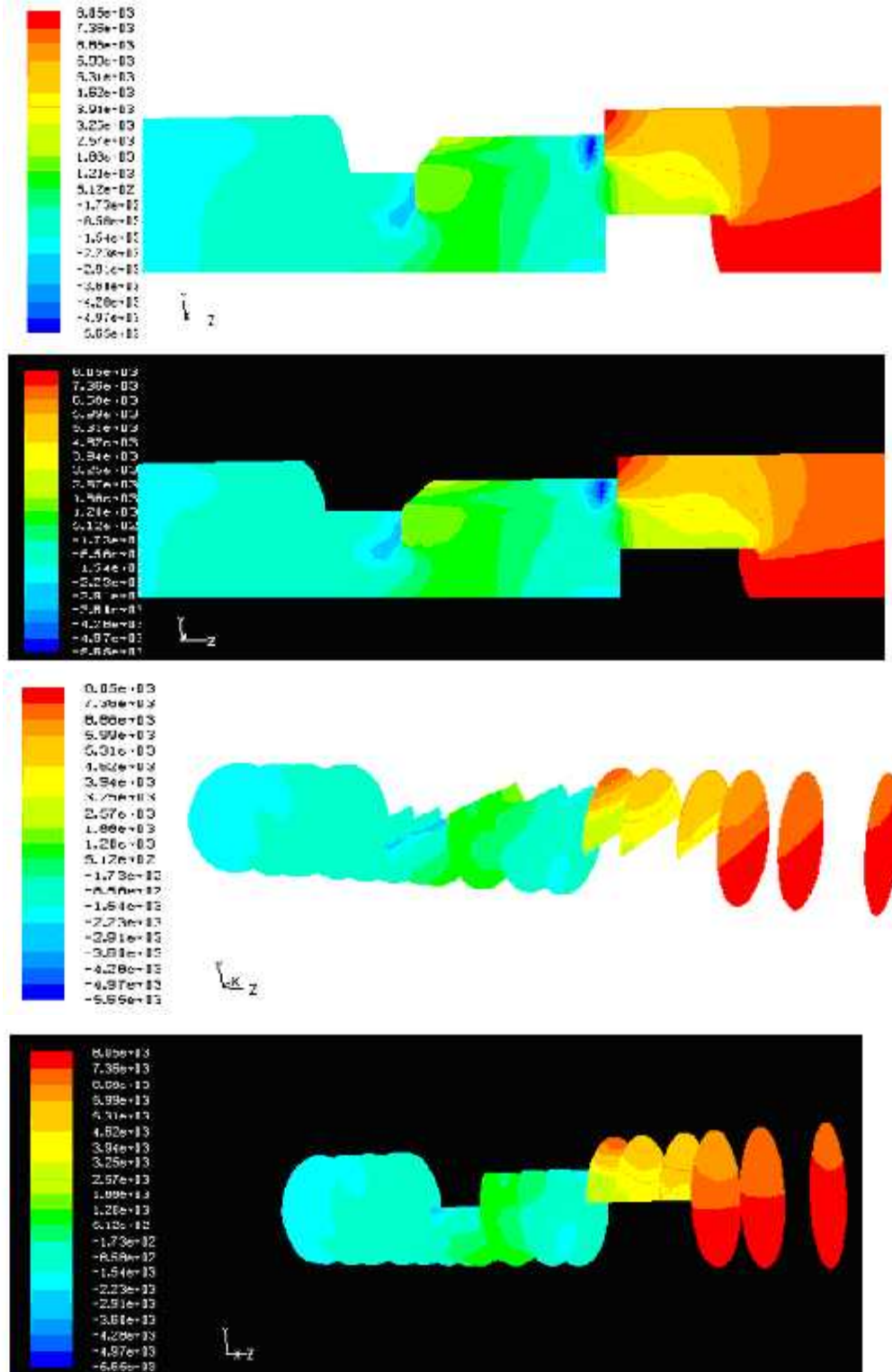


Fig. 6.58 Contours plot of static pressure in the air-SCMC mixture at the different points of 50% opening globe valve, Concentration of SCMC solution (kg/m^3): 0.8, Liquid velocity (m/s): 1.5142, Gas velocity (m/s): 1.7265, Gas fraction, α_g : 0.5

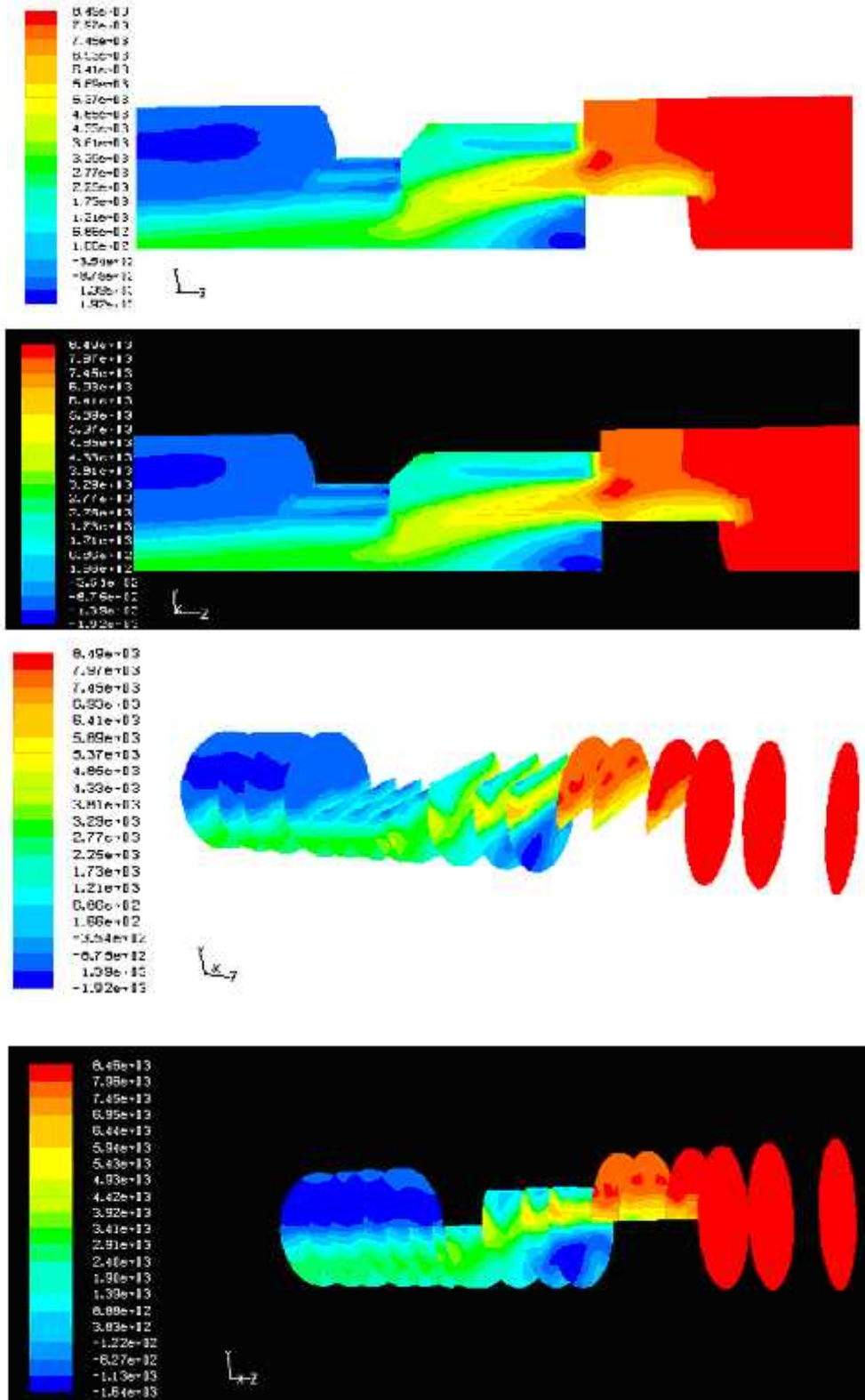


Fig. 6.59 Contours plot of total pressure in the air-SCMC mixture at the different points of 50% opening globe valve, Concentration of SCMC solution (kg/m^3): 0.8, Liquid velocity (m/s): 1.5142, Gas velocity (m/s): 1.7265, Gas fraction, ρ_g : 0.5

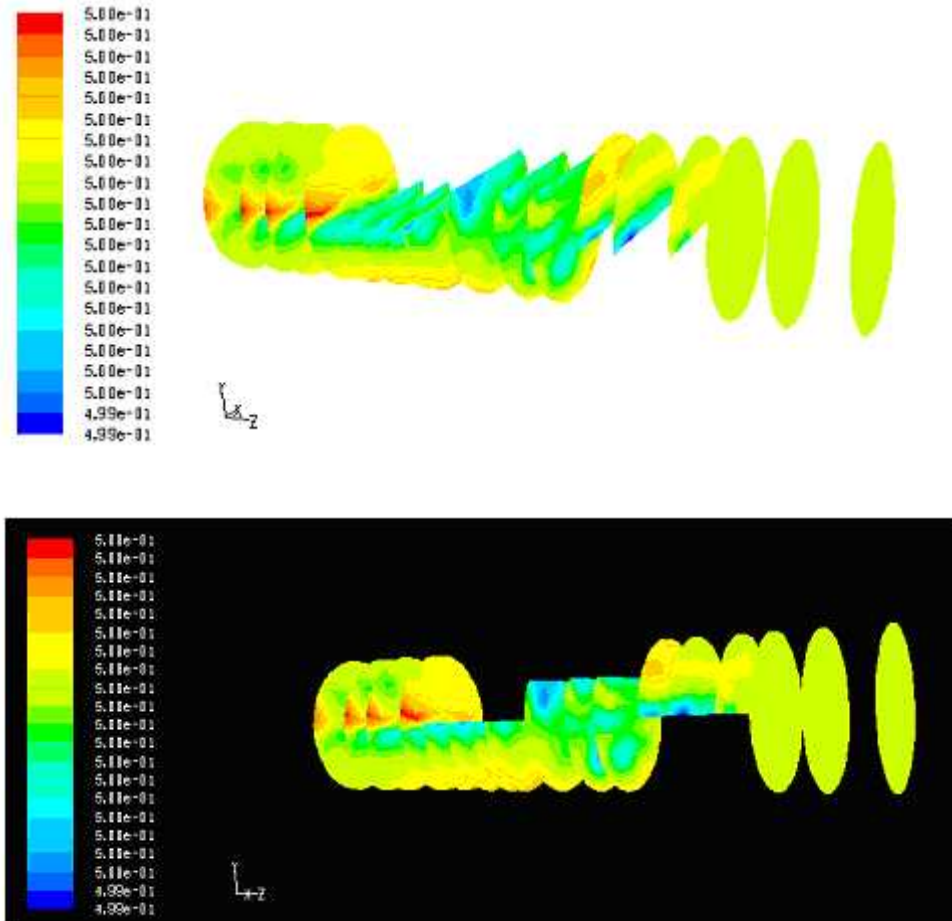


Fig. 6.60 Contours plot of SMC phase volume fraction in the air-SCMC mixture at the different points of 50% opening globe valve, Concentration of SMC solution (kg/m^3): 0.8, Liquid velocity (m/s): 1.5142, Gas velocity (m/s): 1.7265, Gas fraction, γ_g : 0.5

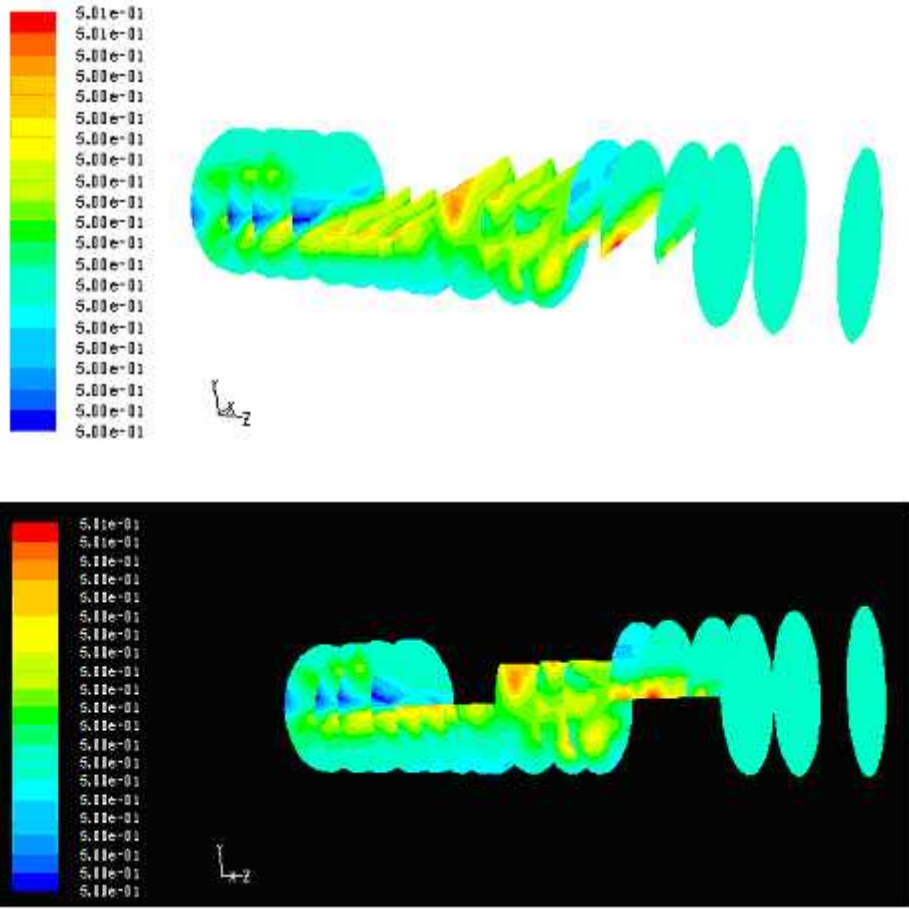


Fig. 6.61 Contours plot of air phase volume fraction in the air-SCMC mixture at the different points of 50% opening globe valve, Concentration of SCMC solution (kg/m^3): 0.8, Liquid velocity (m/s): 1.5142, Gas velocity (m/s): 1.7265, Gas fraction, γ_g : 0.5

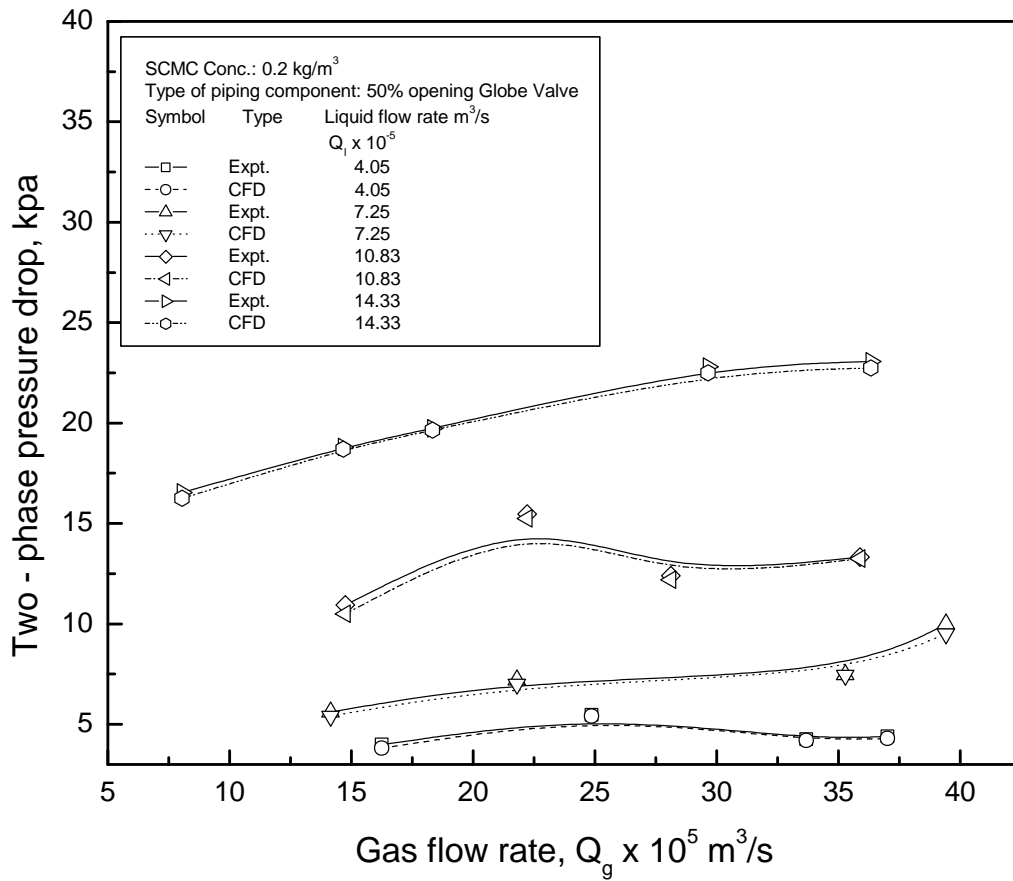


Fig. 6.62 Comparison of experimental and CFD simulated result at different liquid flow rate and fixed liquid concentration, fixed opening of the Globe valve

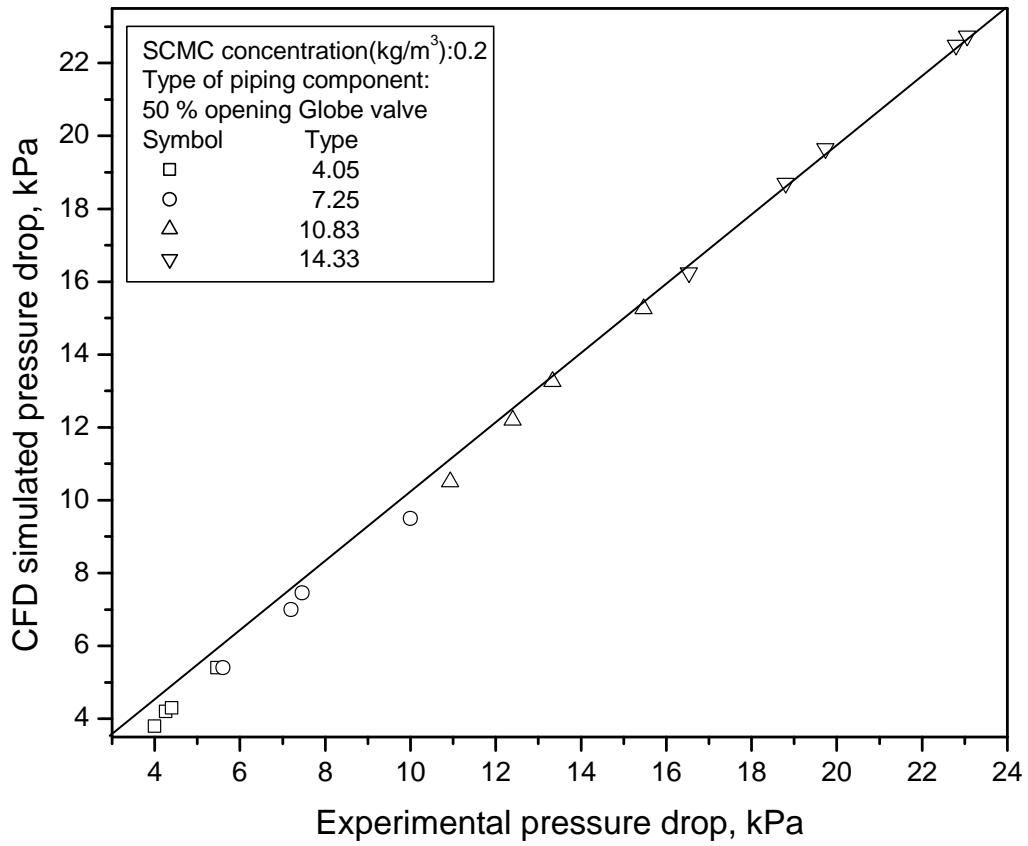


Fig. 6.63 Comparison of experimental results with CFD simulated results for different liquid flow rates

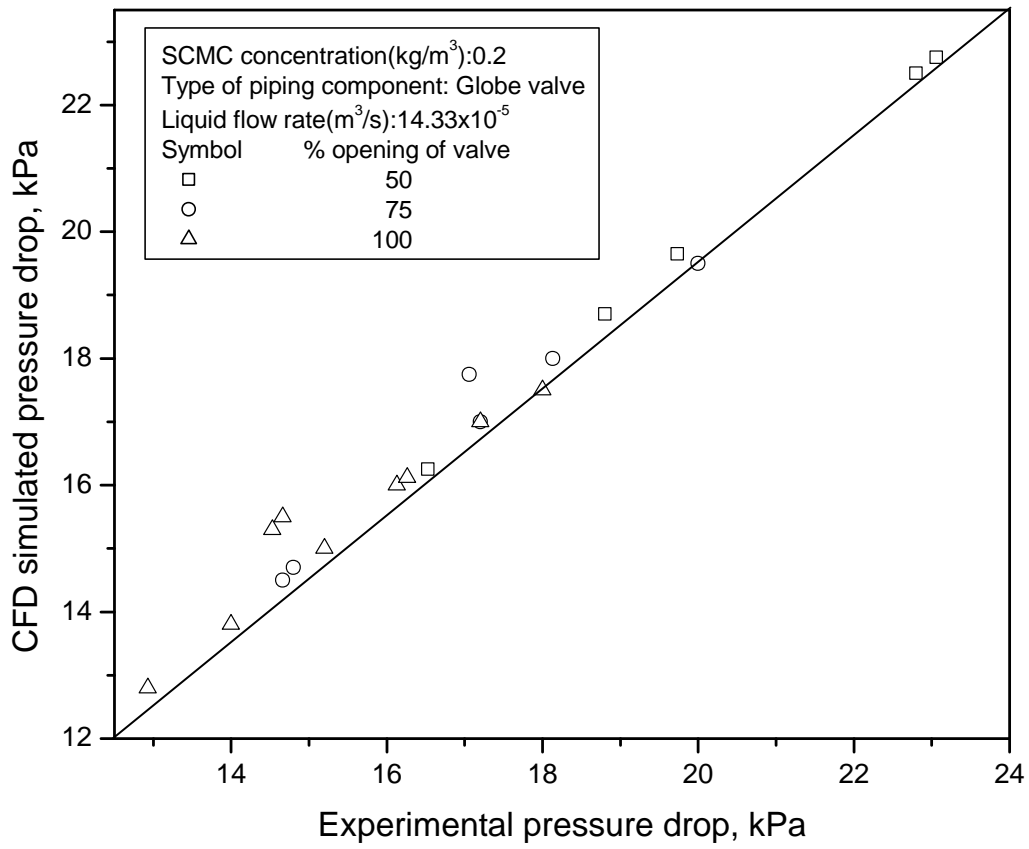


Fig. 6.64 Comparison of experimental results with CFD simulated results for different % opening of Globe valve

Table 6.1 Range of variables

Measurement Type	Range
Liquid and Flow properties	
Flow behavior index	0.6015 n' 0.9013
Consistency index (Ns^n/m^2)	0.0142 K' 0.7112
Density (kg/m^3)	1001.69 1003.83
Concentration of SCMC Solution (kg/m^3)	0.2 to 0.8
Liquid Flow Rate $Q_l \times 10^5 (m^3/s)$	3.75 to 29.83
Gas Flow Rate $Q_g \times 10^5 (m^3/s)$	2.90 to 44.75
Reynolds Number	47.51 Re 2234.21
Dean Number	32.41 De 2130.23
Pressure Drop (Experimental) (kPa)	0.1333 P 45.46
Elbow	
Angle of Elbow	45° to 135°
45° elbow	Radius of curvature = 0.011m Linear length of the elbow = 0.014m
90° elbow	Radius of curvature = 0.022m Linear length of the elbow = 0.011m
135° elbow	Radius of curvature = 0.017m Linear length of the elbow = 0.016m
Orifice	
Diameter of Orifice (m)	0.0059, 0.0038, 0.0045
Diameter ratio of Orifice to pipe diameter	0.4646 D_o/D_t 0.7087
Gate valve	
Valve opening (%)	50, 75, 100
Ratio of the valve opening to the full opening of valve	0.50 1.00
Globe Valve	
Valve opening (%)	50, 75, 100
Ratio of the valve opening to the full opening of valve	0.50 1.00

Table 6.2

Comparison of the experimental and CFD analysis data of two-phase pressure drop through straight pipe for different flow rate

Sl. No.	Air flow rate $Q_1 \times 10^5$ m^3/s	Two-phase pressure drop, experimental (ΔP_{tp}) Straight pipe, Expt. kPa	Two-phase pressure drop, CFD (ΔP_{tp}) straight pipe, CFD kPa
Liquid flow rate, $Q_1 : 4.05 \times 10^{-5} m^3/s$; SCMC Concentration(kg/m^3): 0.2			
1	3.1	2.6	2.55
2	6.13	3.6	3.45
3	11.68	4.6	4.56
4	15.78	4.73	4.65
5	19.21	5.66	5.6
Liquid flow rate, $Q_1 : 7.00 \times 10^{-5} m^3/s$; SCMC Concentration(kg/m^3): 0.2			
6	5.43	4.35	4.25
7	8.56	4.85	4.75
8	11.21	5.7	5.65
9	15.85	5.8	5.75
10	20.98	6.75	6.66
Liquid flow rate, $Q_1 : 9.80 \times 10^{-5} m^3/s$; SCMC Concentration(kg/m^3): 0.2			
11	9.09	6.65	6.6
12	11.4	7.5	7.45
13	15.67	8.88	8.85
14	21.09	9.95	9.9
15	23.54	10.56	10.35
Liquid flow rate, $Q_1 : 13.17 \times 10^{-5} m^3/s$; SCMC Concentration(kg/m^3): 0.2			
16	5.76	8.5	8.4
17	9.65	9.95	9.8
18	12.18	11.18	11
19	15.78	12	11.86
20	19.28	13.75	13.55

Table 6.3

Comparison of the experimental and CFD analysis data of two-phase pressure drop through straight pipe for different SCMC concentration

Sl. No.	Air flow rate $Q_1 \times 10^5$ m^3/s	Two-phase pressure drop, experimental (ΔP_p) Straight pipe, Expt. kPa	Two-phase pressure drop, CFD (ΔP_p) Straight pipe, CFD kPa
Liquid flow rate, $Q_1 : 7.00 \times 10^{-5} m^3/s$; SCMC Concentration(kg/m^3): 0.2			
1	5.43	4.35	4.25
2	8.56	4.85	4.75
3	11.21	5.7	5.65
4	15.85	5.8	5.75
5	20.98	6.75	6.66
Liquid flow rate, $Q_1 : 7.00 \times 10^{-5} m^3/s$; SCMC Concentration(kg/m^3): 0.4			
6	9.44	6.7	6.65
7	13.21	8.6	8.45
8	15.19	9.2	8.95
9	18.21	10.7	10.5
10	20.63	11.5	11.35
Liquid flow rate, $Q_1 : 7.00 \times 10^{-5} m^3/s$; SCMC Concentration(kg/m^3): 0.6			
11	6.15	6.95	6.85
12	7.28	7.69	7.65
13	12.44	8.85	8.45
14	13.15	9.5	9.35
15	18.86	11.83	11.65
Liquid flow rate, $Q_1 : 7.00 \times 10^{-5} m^3/s$; SCMC Concentration(kg/m^3): 0.8			
16	5.98	7.55	7.45
17	12.09	9.56	9.4
18	17.56	12.65	12.5
19	22.22	13.5	13.44

Table 6.4

Comparison of the experimental and CFD analysis data of two-phase pressure drop through elbows for different liquid flow rate

Sl. No.	Air flow rate $Q_1 \times 10^5$ m^3/s	Two-phase pressure drop, experimental (ΔP_p) elbow, Expt. kPa	Two-phase pressure drop, CFD (ΔP_p) elbow, CFD kPa
Type of elbow: 45 ⁰ , Liquid flow rate, $Q_1 : 3.75 \times 10^{-5} m^3/s$; SCMC Concentration(kg/m ³): 0.2			
1	0.153	0.4	0.385
2	0.193	0.4667	0.45
3	0.251	0.6667	0.65
4	0.351	0.9333	0.92
5	0.385	1.4667	1.4
Type of elbow: 45 ⁰ , Liquid flow rate, $Q_1 : 11.00 \times 10^{-5} m^3/s$; SCMC Concentration(kg/m ³): 0.2			
6	0.147	1.2	1.12
7	0.215	1.333	1.32
8	0.261	1.4667	1.45
9	0.287	1.7333	1.7
10	0.328	2.5333	2.5
Type of elbow: 45 ⁰ , Liquid flow rate, $Q_1 : 14.62 \times 10^{-5} m^3/s$; SCMC Concentration(kg/m ³): 0.2			
11	0.052	1.4667	1.45
12	0.121	2.2	2.12
13	0.157	2.2667	2.2
14	0.186	2.4667	2.45
15	0.271	2.6667	2.6

Table 6.5

Comparison of the experimental and CFD analysis data of two-phase pressure drop through elbows at different elbow angle

Sl. No.	Air flow rate $Q_1 \times 10^5$ m^3/s	Two-phase pressure drop, experimental (ΔP_{tp}) elbow, Expt. kPa	Two-phase pressure drop, CFD (ΔP_{tp}) elbow, CFD kPa
Type of elbow: 45° , Liquid flow rate, $Q_1 : 3.75 \times 10^{-5} m^3/s$; SCMC Concentration(kg/m^3): 0.2			
1	0.153	0.4	0.385
2	0.193	0.4667	0.45
3	0.251	0.6667	0.65
4	0.351	0.9333	0.92
5	0.385	1.4667	1.4
Type of elbow: 90° , Liquid flow rate, $Q_1 : 3.75 \times 10^{-5} m^3/s$; SCMC Concentration(kg/m^3): 0.2			
6	0.032	0.2	0.18
7	0.121	0.4667	0.45
8	0.16	0.5333	0.5
9	0.226	0.6667	0.65
10	0.313	0.7333	0.72
Type of elbow: 135° , Liquid flow rate, $Q_1 : 3.75 \times 10^{-5} m^3/s$; SCMC Concentration(kg/m^3): 0.2			
11	0.037	0.2667	0.25
12	0.289	0.4667	0.45
13	0.342	0.5333	0.5
14	0.355	0.6667	0.62
15	0.385	0.8	0.75

Table 6.6

Comparison of the experimental and CFD analysis data of two-phase pressure drop through orifices at different liquid flow rate

Sl. No.	Air flow rate $Q_1 \times 10^5$ m^3/s	Two-phase pressure drop, experimental (ΔP_p) orifice, Expt. kPa	Two-phase pressure drop, CFD (ΔP_p) orifice, CFD kPa
Orifice : $D_0/D_t = 0.4646$, Liquid flow rate, $Q_1 : 7.10 \times 10^{-5} m^3/s$; SMC Concentration(kg/m^3): 0.2			
1	9.329	6.6667	6.6
2	11.509	7.8667	7.7
3	15.075	8	7.5
4	15.923	8	7.8
5	17.064	8.8	8.5
6	26.292	9.0667	8.78
Orifice : $D_0/D_t = 0.4646$, Liquid flow rate, $Q_1 : 10.17 \times 10^{-5} m^3/s$; SMC Concentration(kg/m^3): 0.2			
7	8.327	14.5333	14.5
8	12.021	14.6667	14.6
9	12.549	16	15.5
10	14.996	16.4	16
11	17.631	17.3333	17
12	22.944	17.3333	17.5
Orifice : $D_0/D_t = 0.4646$, Liquid flow rate, $Q_1 : 13.17 \times 10^{-5} m^3/s$; SMC Concentration(kg/m^3): 0.2			
13	10.053	20.8	20
14	10.81	22	21.5
15	11.634	22.2667	22
16	13.392	23.8667	23.5
17	15.213	24.1333	24
18	19.255	25.4667	25
Orifice : $D_0/D_t = 0.4646$, Liquid flow rate, $Q_1 : 16.30 \times 10^{-5} m^3/s$; SMC Concentration(kg/m^3): 0.2			
19	4.456	23.6	23
20	12.804	34	33
21	12.815	34.1333	33.5
22	15.163	35.8667	34.5
23	17.301	38.5332	38
24	18.132	39.3332	39

Table 6.7

Comparison of the experimental and CFD analysis data of two-phase pressure drop through orifices at different orifice diameter ratio

Sl. No.	Air flow rate $Q_1 \times 10^5$ m^3/s	Two-phase pressure drop, experimental (ΔP_p) orifice, Expt. kPa	Two-phase pressure drop, CFD (ΔP_p) orifice, CFD kPa
Orifice : $D_0/D_t = 0.4646$, Liquid flow rate, $Q_1 : 16.17 \times 10^{-5} m^3/s$; SMC Concentration(kg/m^3): 0.4			
1	7.13	28.93	28.2
2	9.19	32.93	32.35
3	10.15	33.73	33.26
4	12.86	37.33	36.84
5	15.76	40	39.25
6	15.85	39.46	39
7	18.14	43.33	42.9
8	22.66	44.4	44.21
Orifice : $D_0/D_t = 0.5984$, Liquid flow rate, $Q_1 : 16.17 \times 10^{-5} m^3/s$; SMC Concentration(kg/m^3): 0.4			
9	5.11	9.46	9.11
10	11.7	11.33	10.76
11	12.41	12.26	11.61
12	16.81	12.53	11.73
13	20	14.13	13.87
14	23.7	15.86	15.24
15	29.26	15.73	15.34
16	31.66	16.4	15.91
17	14.44	5.2	4.5
18	17.5	5.2	4.78
19	31.47	7.6	7.17
20	33.29	13	12.65
21	37.15	13.33	12.81

Table 6.8
 Comparison of the experimental and CFD analysis data of two-phase pressure drop through gate valve at different flow rate

Sl. No.	Air flow rate $Q_1 \times 10^5$ m^3/s	Two-phase pressure drop, experimental $(\Delta P_{tp})_{gate}$ valve, Expt. kPa	Two-phase pressure drop, CFD $(\Delta P_{tp})_{gate valve}$, CFD kPa
Gate Valve : 50% opening, Liquid flow rate, $Q_1 : 7.25 \times 10^{-5} m^3/s$; SCMC Concentration(kg/m^3): 0.2			
1	14.25	1.8667	1.75
2	18.55	2.1333	2
Gate Valve : 50% opening, Liquid flow rate, $Q_1 : 9.08 \times 10^{-5} m^3/s$; SCMC Concentration(kg/m^3): 0.2			
3	11.98	2	1.85
4	17.08	2	1.9
5	19.52	2	1.95
6	20.29	1.733	2
7	36.14	2.933	2.74
Gate Valve : 50% opening, Liquid flow rate, $Q_1 : 10.83 \times 10^{-5} m^3/s$; SCMC Concentration(kg/m^3): 0.2			
8	13.43	2.666	2.6
9	16.46	2.4	2.3
10	23.21	2.533	2.45
11	35.82	2.666	2.55
Gate Valve : 50% opening, Liquid flow rate, $Q_1 : 12.58 \times 10^{-5} m^3/s$; SCMC Concentration(kg/m^3): 0.2			
12	8.21	2.666	2.62
13	11	2.5333	2.48
14	16	3.2	3
15	19.41	3.2	3.1
16	24.77	3.333	3.25
17	37.25	4.9333	4.75
Gate Valve : 50% opening, Liquid flow rate, $Q_1 : 14.33 \times 10^{-5} m^3/s$; SCMC Concentration(kg/m^3): 0.2			
18	9	2.9333	2.85
19	10.62	3.2	3.1
20	13.37	2.9333	2.9
21	13.56	3.6	3.5
22	16.53	4	3.95
23	23.21	4.133	4.1
24	40.5	4.8	4.6

Table 6.9

Comparison of the experimental and CFD analysis data of two-phase pressure drop at different opening of gate valve

Sl. No.	Air flow rate $Q_1 \times 10^5$ m^3/s	Two-phase pressure drop, experimental $(\Delta P_{ip})_{gate}$ valve, Expt. kPa	Two-phase pressure drop, CFD $(\Delta P_{ip})_{gate}$ valve, CFD kPa
Gate Valve : 50% opening, Liquid flow rate, $Q_1 : 15.83 \times 10^{-5} m^3/s$; SCMC Concentration(kg/m^3): 0.2			
1	9.23	3.8667	3.75
2	12.08	4.5333	4.45
3	14.12	4.5333	4.5
4	20.11	4.8	4.7
5	26.84	4.8	4.75
6	40.59	9.3333	9.85
Gate Valve : 75% opening, Liquid flow rate, $Q_1 : 15.83 \times 10^{-5} m^3/s$; SCMC Concentration(kg/m^3): 0.2			
7	8.24	2	1.98
8	10.49	3.0667	3
9	12.6	2.9333	2.8
10	14.45	2.9333	2.85
11	19.84	4.1333	4
12	26.18	4.6667	4.55
Gate Valve : 100% opening, Liquid flow rate, $Q_1 : 15.83 \times 10^{-5} m^3/s$; SCMC Concentration(kg/m^3): 0.2			
13	5.514	1.8667	1.8
14	8.324	1.7333	1.65
15	11.655	2	1.9
16	17.198	2.2667	2.2
17	22.831	3.6	3.55

Table 6.10

Comparison of the experimental and CFD analysis data of two-phase pressure drop at different opening of globe valve

Sl. No.	Air flow rate $Q_1 \times 10^5$ m^3/s	Two-phase pressure drop, experimental $(\Delta P_{tp})_{globe}$ valve, Expt. kPa	Two-phase pressure drop, CFD $(\Delta P_{tp})_{globe}$ valve, CFD kPa
Globe Valve : 50% opening, Liquid flow rate, Q_1 : $14.33 \times 10^{-5} m^3/s$; SCMC Concentration(kg/m^3): 0.2			
1	8.05	16.53	16.25
2	14.66	18.8	18.7
3	18.33	19.73	19.65
4	29.65	22.8	22.5
5	36.33	23.06	22.75
Globe Valve : 75% opening, Liquid flow rate, Q_1 : $14.33 \times 10^{-5} m^3/s$; SCMC Concentration(kg/m^3): 0.2			
6	9.72	14.66	14.5
7	13.62	14.8	14.7
8	17.88	17.2	17
9	18.66	14.8	14.5
10	24.45	17.06	17.75
11	30.49	18.13	18
12	36.73	20	19.5
Globe Valve : 100% opening, Liquid flow rate, Q_1 : $14.33 \times 10^{-5} m^3/s$; SCMC Concentration(kg/m^3): 0.2			
13	9.43	12.93	12.8
14	11.58	14	13.8
15	16.08	15.2	15
16	16.08	14.53	15.3
17	16.62	14.66	15.5
18	20.27	16.13	16
19	24.59	16.26	16.12
20	30.2	17.2	17
21	34.28	18	17.5

Chapter 7

Non-Newtonian liquid flow through helical coils – CFD analysis

Experimental investigation has been carried out for non-Newtonian liquid flow through helical coils. The Computational Fluid Dynamics (CFD) analysis using Fluent 6.3 software evaluates the frictional pressure drop across the helical coils. The CFD results compare with the experimental data.

7.1 Introduction

Helical coils are extensively used in compact heat exchangers, heat exchanger networks, heating or cooling coils in piping systems, intake in air crafts, fluid amplifiers, coil steam generators, refrigerators, nuclear reactors, thermosiphones, other heat-transfer equipment and chemical plants, as well as in the food and drug industries. But non-Newtonian fluid flows through helical coils are mainly used in pulp and paper, paints, tooth-paste industries. One of the main advantages in the use of helical coiled tubes as chemical reactors or heat exchangers lies in the fact that considerable lengths of tubing can be contained in a space-saving configuration that can easily be placed in a temperature-controlled environment. The heat and mass transfer coefficients in helical coiled tubes are higher than those in straight tubes. When fluid flows through a curved pipe, the presence of curvature generates a centrifugal force that acts at right angles to the main flow, resulting in secondary flow. The strength of the secondary flow depends on the curvature of the surface. A literature survey indicates that numerous studies dealing with flow phenomena and pressure drop in single-phase flow through helical coils have been published. These are well summarized in Berger et al. (1983), Shah and Joshi (1987) and Das (1996). Coiled tubes are basically Dean-vortex-based systems, in which the curvature directly induces secondary flows to enhance the radial mixing. The formation of centrifugal instabilities in the flow creates higher vorticity and also shear

rates at the wall of the coil thus stronger mixing effect generates than the normal Taylor vortices (Tiwari et al. 2004; Gelfgat et al., 2003). The use of Dean vortices were utilized in the various membrane module configuration. U-bend and helical tubes are the most commonly used geometries (So et al., 1991; Chung et al., 1996; Yamamoto et al., 1994; Moulin et al., 2001, etc.). Moulin et al. (2001) studied the wall shear stress by using four types of tube geometry, i.e., straight, torus, helical and woven, and concluded that the helical geometry gives more wall shear stress. Guan and Martonen (2000) simulated by using CFD to observed the developing length of velocity patterns and transitional character of fluid flowing in curved geometry.

In order to achieve optimum performance, an accurate design technique is necessary for the prediction of two-phase pressure drop through helical coil tube. This chapter deals with the computational fluid dynamics technique, FLUENT 6.3, to predict the pressure drop in helical coil tubes.

7.2 The experimental setup

The detail experimental set up is shown in Fig. 7.1. The experimental apparatus consisted of a solution tank, heat exchanger, centrifugal pumps, a test section, control and measuring systems for flow rate, pressure drop and other accessories.

The liquid storage tank was a cylindrical vessel of 0.45 m³ capacity and was fitted with a propeller type of stirrer for uniform mixing of sodium salt of carboxymethyl cellulose (SCMC) solutions. The test liquids were prepared by dissolving the required amount of SCMC in tap water, stirring until a homogeneous solution was obtained and kept around 15hr. for aging. Adding trace amounts of formalin prevented biological

degradation. Content of the tank was kept at a constant temperature by circulating water through a copper coil.

Thick walled flexible, transparent PVC pipes with internal diameter of 0.00933 – 0.01200 m having the total length of the tube as 15 m was used as experiment. The PVC pipes were wound round a cylindrical hard PVC frame of known diameter to form a helical coil. The helical coils were fixed and carefully tightened with clamps in order to avoid deformation of the tube. Changing the diameter of the frame and diameter of the tube will vary coil diameter. The tubes were wound in closed packed fashion so that the pitch is equal to the outer diameter of the tube and maintained constant for all cases. Helix angle of 0° was used for experiment. The entire test section was vertically mounted on frame to prohibit vibration. Detailed dimensions of the coils used in the experiments are given in Table 7.1.

The test liquid was circulated from the tank by means of a centrifugal pump to the helical coil test section. Its flow rate was controlled by bypass valves and was measured by a set of rotameters (RL1 and RL2) [Transducers and Controls Pvt. Ltd., Hyderabad, India, Accuracy $\pm 2\%$] connected in parallel. The liquid was discharged in the level control tank and was returned to the liquid storage tank.

The level control tank diameter 0.25 m and height 0.6 m was made from mild steel sheet. The liquid level in the level control tank was always kept below the test section. The level of liquid in the control tank was controlled with the help of a level controller.

The pressure taps were located at the middle of the vertical helical coils. The upstream pressure tap was mounted after 4 to 6 coil turns in order to reduce the effect of

the upstream flow and downstream pressure tap also mounted before 4 to 6 coils turns to reduce the down stream flow. The two pressure tap were adjusted to ensure that they were on the same vertical line. A simple U-tube manometer containing mercury beneath the water measured the pressure difference.

Four aqueous solutions of SCMC (Loba Cheme Pvt. Ltd., Mumbai, India) of approximate concentrations 0.2 kg/m^3 , 0.4 kg/m^3 , 0.6 kg/m^3 and 0.8 kg/m^3 , were used as non-Newtonian liquids. The properties of the non-Newtonian liquids were measured by standard techniques, i.e., viscosity was measured by pipeline viscometer, surface tension by Dunouy tensiometer and density was measured by specific gravity bottles. For non-Newtonian liquids the effective viscosity is used for calculation and defined as,

$$\mu_{eff} = K' \left(\frac{8v}{d} \right)^{n'-1} \quad (7.1)$$

7.3 Mathematical Model

The present work considers a coiled tube with circular cross-sectional diameter, d , coiled diameter D_c , pitch=0 and curvature ratio= D_c/d . The axis of the coil is vertical Fig. 2. The cartesian coordinate system was used to represent (X, Y, Z) a coiled tube in the numerical simulation Fig. 3.

The detailed mathematical methods used for the CFD analysis is given in Chapter 2. As the flow of liquid is laminar in all cases the viscous model, i.e., laminar non-Newtonian Power Law model is used for the CFD analysis. These equations are solved subject to the following boundary conditions,

(i) The vertical helical coils walls are assumed rigid and a no-slip condition is imposed.

(ii) At the outlet, the velocities are free but the normal and tangential stresses are constrained to be zero and the gauge pressure is set to zero.

(iii) At the inlet, a uniform velocity profile is used with a time varying forcing function representative of flow in the left portion of the coils. Since fluid flowing in the upward direction against the gravity, negative gravitational acceleration -9.8 m/s^2 is added.

7.4 Computational fluid dynamics (CFD) Procedure

Geometries for vertical helical coil created in Gambit 6.3 preprocessor. Two types of mesh have been used, about 3×10^4 – 1.2×10^5 order unstructured tetrahedral and boundary layer hexahedral mesh are used (Figs.7.4 - 7.5). Inlet and outlet are located at each end of the coils. The inlet is used to specify the inlet velocity and outlet is used to specify pressure outlet. These geometries of the coils are imported into Fluent 6.3 in a cartesian co-ordinate system. Fluent 6.3 solved the governing equations in 3-D geometry. Laminar non-Newtonian Power Law model have been used for simulation. The model solves for Navier-stokes equation at prescribes velocities. The governing equations are non linear and several iterations of loop must be performed before a convergent solution is obtained. The first-order upwind scheme is used in the discretization of set of governing equations, standard interpolation schemes is used for calculating cell-face pressures for using the segregated solver in Fluent 6.3. Pressure-velocity coupling refers to the numerical algorithm which uses a combination of continuity and momentum equations to derive an equation for pressure (or pressure correction) when using the segregated solver. Simple algorithm is used in Fluent 6.3 domain.

The general procedure to simulate liquid flow through coils based on Gambit 6.3 and Fluent 6.3 software is outlined below,

1. Perform meshing under Gambit 6.3 :
 - (a) Create a computational domain at the flow region,
 - (b) The grids were generated using boundary layer hexahedral and t-grid (tetrahedral) meshes,
 - (c) Controlling a smooth change in the mesh size by size functions,
 - (d) Specify boundary and continuum types,
 - (e) Examine the mesh to ensure that the high skewness is below 0.5 for hexahedral and below 0.9 for tetrahedral meshes.
2. Import the mesh file to Fluent 6.3 and check the mesh.
3. Define a 3-D, unsteady, implicit, and pressure-based solver.
4. Activate the single phase laminar non-Newtonian power law model.
5. Define a laminar non-Newtonian power law model.
6. Enable the SCMC properties with laminar flow conditions using the text command: `define/models/viscous/laminar`. Putting the non-Newtonian fluid values: flow behavior index, consistency index, temperature and effective viscosity values at the inlet velocity.
7. Define the operating conditions by turning on gravity and specify the operating density.
8. Solution control methodology – Under relaxation factors – 0.5 for pressure, 0.3 for momentum, and default values for the other parameters. Standard schemes –

STANDARD for momentum and 1st order upwind for other variables. Pressure-velocity SIMPLE coupling used;

9. Initialize the solution – velocity; enable the plotting of residuals during the calculation, and kept the default convergence criteria, 1×10^{-5} for all residuals except for the transport equation which residual was set at 10^{-3} .

7.5 Results and discussion

7.5.1 Convergence and grid independency

The convergence criterions were set at 10^{-5} for all equations except for the transport equation which residual was set at 10^{-3} . A computational domain $L = 200D$ was used to ensure fully developed flow results could be obtained for all coils. In general the final results depend upon mesh geometries. Subsequent decrement and increment in mesh resolution by 50% were applied to evaluate if the employed mesh resolution was adequate to obtain accurate solutions. It was observed that when the mesh resolution was decreased by 50% the axial velocity profile was 5-10% of the currently employed mesh velocity profile for coils. As the present mesh resolution was increased by 50% the axial velocity profile changes 1-4% for coils. These results suggest that the current mesh resolution is sufficient to obtain grid independent solutions for the proposed model.

7.5.2 Computational fluid dynamics (CFD) analysis

Figs.7.4 - 7.5 show the tetrahedral and hexahedral grid for helical coil.

Figs. 7.6 - 7.7 show the contour plot of static pressure and total pressure. Figs. 7.8 - 7.9 show the contours of static pressure and total pressure at various planes along the length of the coil. It indicates that static pressure decreases gradually after passing the coil turn and its effect more with increasing the liquid concentration i.e., as pseudo

plasticity increases. Figs. 7.10 - 7.11 show that contour of static pressure and total pressure at the different angular plane and at different turn or height of the coil. Figs. 7.12 - 7.13 show that contour of static pressure and total pressure at the different angular plane and at the fixed turn (1st turn) of the coil. It indicates that the static pressure decreases with angle and coil turn. But at particular coil turn and angle fully developed flow was achieved. It is also observed that the pressure is more at the outer side wall and less at the inner wall. This is due to the action of centrifugal force. Figs. 7.14 - 7.19 show the contour plot of dynamic pressure. It indicates that the dynamic pressure is more at the outside of the coil wall than the inner wall of the coil due to centrifugal force. For the first turn of the coil fully developed flow observed after angle $270^{\circ} - 330^{\circ}$ and for higher turn it is achieved after $240^{\circ} - 330^{\circ}$.

Figs. 7.20 - 7.32 show that contour plot of velocity magnitude and velocity varying with angle and coil turn. It can be seen from these figures that the maximum velocity is shifted towards the outer wall of the coiled tube. Velocity starts to change from angle 30° up to 150° . It can also depict that the flow gets almost fully developed at angle 240° to 330° . Since the velocity profiles have minor changes. As angle is increased, the axial velocity becomes asymmetrical. Due to the unbalanced centrifugal forces on the main flow, the maximum velocity is shifted towards the outer wall of the pipe. At a fixed angle and with increasing coil turn the velocity profiles have very minor changes. Secondary flow and vortices observed from the velocity profile. Figs. 7.33 - 7.36 show the plot of velocity vector. It indicates that the velocity is high at the outer wall due to centrifugal force. It is clear from the velocity vector plot that the liquid is more at the outer wall than in the inner side of the wall. Fully developed flow observed at angle 240°

to 330° . Since the velocity profiles have minor changes. Figs. 7.37 - 7.39 show the contour plot of helicity, vorticity and cell Reynolds number. It indicates that all effects are more at the outer wall of the coil due to centrifugal force. Figs. 7.40 - 7.43 show that strain rate and wall shear stress are both high at outer wall due to centrifugal force.

Fig. 7.44 indicates that the frictional pressure drop per unit length of coil increases with increasing SCMC concentration. The experimental result matches well with CFD simulated result for hexahedral grid than the tetrahedral grid.

Fig. 7.45 indicates that the frictional pressure drop per unit length of coil increases with increasing coil diameter. The experimental result matches well with CFD simulated result for hexahedral grid than the tetrahedral grid.

Fig. 7.46 shows the dimensionless wall shear stress and pressure drop at hexahedral and tetrahedral grid.

When a fluid flows inside a coiled tube, secondary flow develops due to centrifugal forces. These centrifugal and shear forces move the fluid flowing near the centerline to outward direction and the fluid near the walls towards inward direction, resulting in secondary flow known as Dean vortices. Dean vortices represent centrifugal and shear instabilities that occur when a viscous fluid flows in a coil.

Since the secondary flows, are induced by centrifugal force, and their interactions are primarily with the viscous force which is a measure of the magnitude of the secondary flow. Even if the inlet conditions correspond to a fully developed flow, the velocity profile along the flow immediately starts changing due to the centrifugal force induced by the duct curvature. This centrifugal force initiates a secondary flow. After a

sufficient distance (i.e., entry length from the inlet), a steady fully developed velocity profile may be reached, although different from that for a straight tube.

The computed secondary flow structure is observed from Figs. 7.24, 7.26, 7.30 and 7.32 and 7.35-7.36. Circulation is observed towards the outer wall of the coiled tube where velocity is higher due to higher intensity of centrifugal forces. Figs. 7.24, 7.30 show the calculated stream wise velocity contours at velocity 1.708 m/s. The velocity field is characterized by two types of vortices, axial and longitudinal. The fluid at the inner wall has low velocity and outer wall has high velocity due to unbalanced centrifugal forces.

Fig. 7.47 (a) and (b) show that velocity magnitude profiles at different cross-sectional planes in (a) horizontal and (b) vertical centerline for the similar conditions. In each figure the left side indicates the inner wall of the coiled tube and right side as the outer wall. It can be seen from the figure that the maximum velocity is shifted towards the outer wall of the coiled tube. It can also be depicted that the flow gets almost fully developed at angles 240° - 330° . At angles 90° to 240° velocity profiles have very minor changes. As angle is increased, the axial velocity becomes asymmetrical. Due to the unbalanced centrifugal forces on the main flow, the maximum velocity is seen to shift towards the outer wall of the pipe, in the horizontal centerline.

Fig. 7.48 shows that effect of liquid velocity on development of axial velocity profile in curved tube at curvature ratio $(D_c/d) = 28$, coil turn = 2. It indicates that location of the maximum velocity profile shifts towards the outer wall of the coiled tube due to centrifugal force effect. The velocity profile flattens when the velocity is increased.

Fig. 7.49 shows the effect of coil turn or height on the development of axial velocity profile in (a) horizontal centerline and (b) vertical centerline. It indicates that at height = 0, the velocity contours are symmetrical to the centerline of the tube. As the coil turn or height is increased the velocity contours becomes asymmetrical. The axial velocity profiles for coiled tube at different angular planes are shown in Fig.7.49 (a) for horizontal centerline and Fig. 7.49 (b) for vertical centerline. In the horizontal centerline, the maximum velocity shifts towards the outer wall of the pipe due to unbalanced centrifugal forces on the main flow. It can be seen that the velocity profiles tends to flatten as the value of coil turn or height decreases for the vertical and horizontal centerline.

Fig. 7.50 shows that effect of curvature ratio on the development of axial velocity profile in (a) horizontal centerline (b) vertical centerline. It indicates that as the curvature ratio is increased, it approach towards a straight tube (curvature ratio ∞). This minimizes the curvature effect as centrifugal forces become less predominant for higher curvature ratio coils. This is evident from this figure as the velocity profiles flattens in the case of curvature ratio $(D_c/d) = 18$, due to action of strong centrifugal force.

7.6 Comparison with the data available in the literature

Mishra and Gupta (1979) performed elaborate experiments to generate experimental data on the non-Newtonian liquid flow through helical coils. They developed empirical correlation for laminar flow as

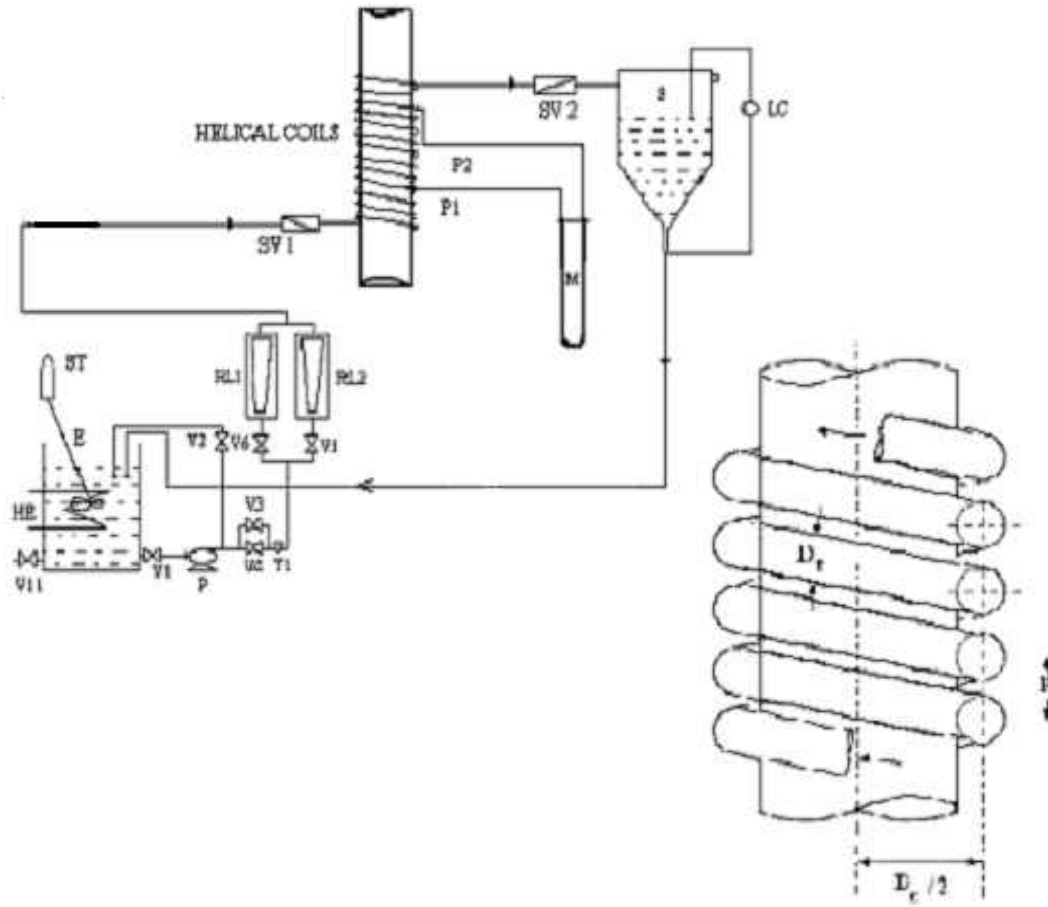
$$\frac{f_c}{f_{sl}} = 1 - 0.033(\log De)^{4.0} \quad (7.2)$$

Fig. 7.51 compared the experimental data friction factor with the Mishra and Gupta (1979) correlation and with the CFD simulated data. It is clear that the experimental data

matches well with the Mishra and Gupta (1979) correlation and also the CFD simulated data. However, the hexahedral grid gives the better results than the tetrahedral grid.

7.7 Conclusions

1. Experiments have been carried out to evaluate the frictional pressure drop for non-Newtonian liquid flow through helical coils.
2. CFD analysis has been carried out for non-Newtonian liquid flow through helical coils. Commercial software Fluent 6.3 has been used for simulation. For simulation two types of grid have been generated, i.e., tetrahedral and hexahedral grid used for simulation purpose and compare their suitability.
3. Flow phenomena inside the coils has been analyzed and observed,
 - (i) due to action of centrifugal force the maximum velocity shifted towards the outer wall,
 - (ii) maximum pressure also shifted towards the outer wall due to centrifugal action,
 - (iii) creation of the vortices in different location.
4. CFD analysis clearly predicts the effect of liquid concentration i.e., pseudo plasticity, effect of coil diameter on frictional pressure drop.
5. CFD analysis also visualized the effect of liquid velocity at different position in the coils.
6. CFD analysis also provides the visualized the effect of the coil turn or height and curvature ratio on the local velocity.
7. The experimental frictional pressure drop matches with the CFD analysis. However, hexahedral grid gives the better agreement.



E: Solution Tank, HE: Heat Exchanger, LC: Level Controller, P: Pump, P1, P2: Pressure Tapping, RL1, RL2: Liquid Rotameter, S: Separator, ST: Stirrer, T1, T2: Thermometer, V1-V11: Valves

Fig. 7.1 Schematic diagram of helical coil

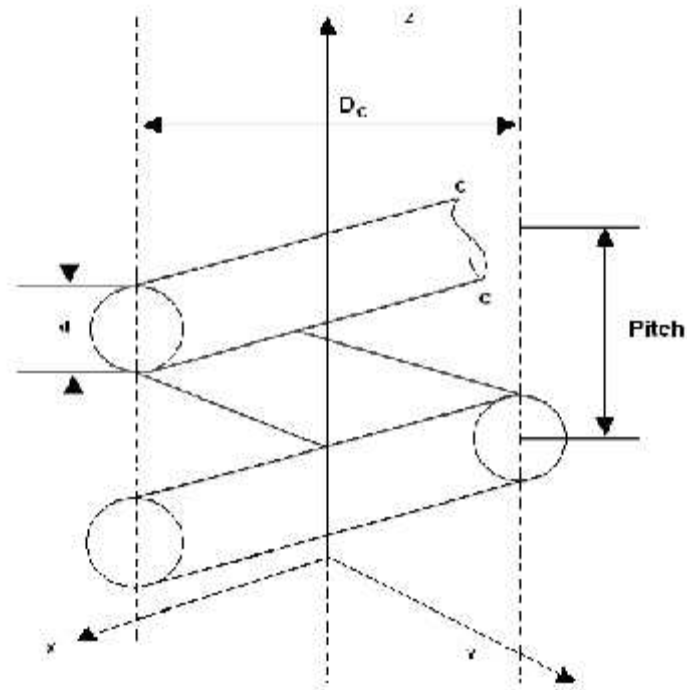


Fig. 7.2 Schematic geometry of the coil, pitch = 0

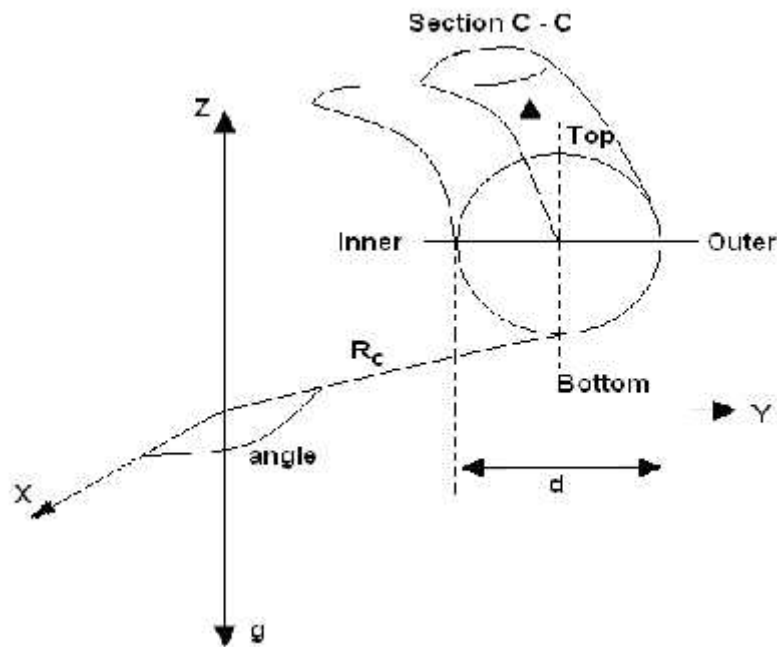
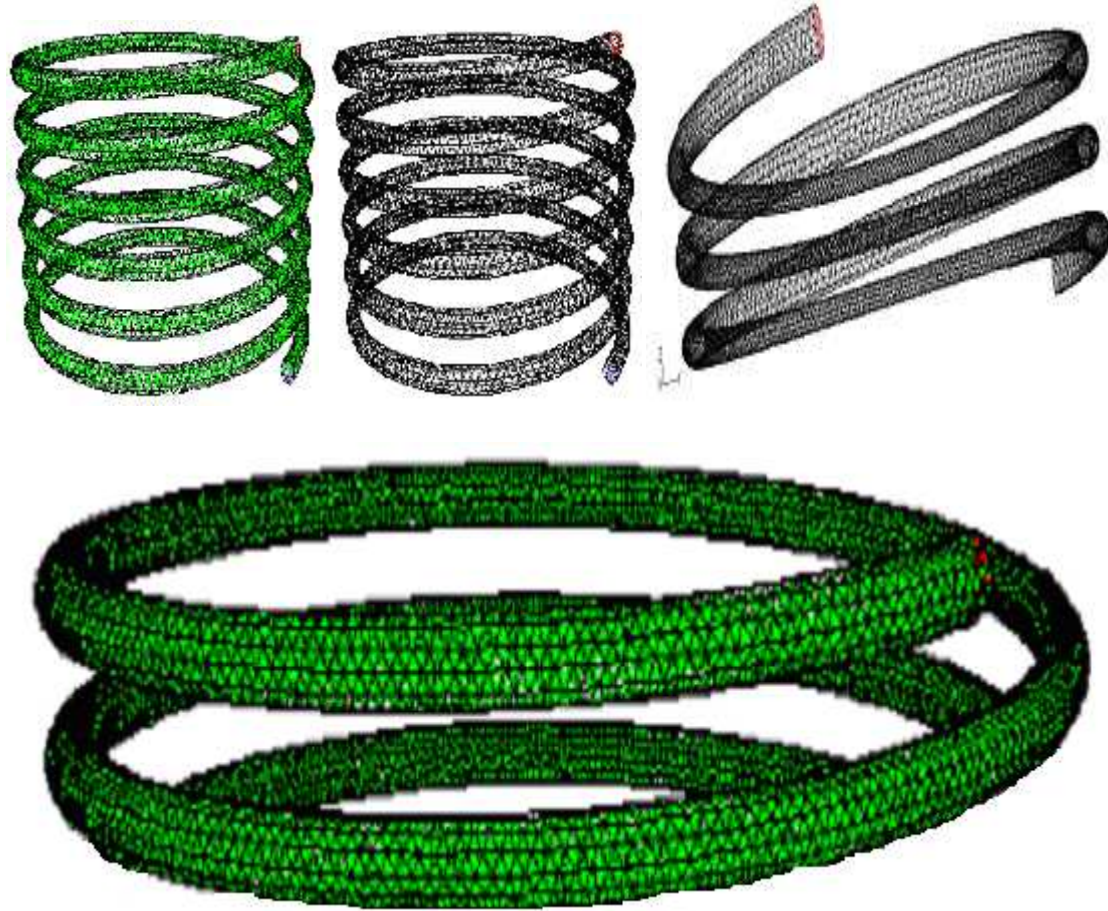


Fig. 7.3 Co-ordinates of the coiled tube



Grid Size Level 0, Cells 108263, Faces 237397, Nodes 30060, Partitions 1, 1 cell zone, 4 face zones

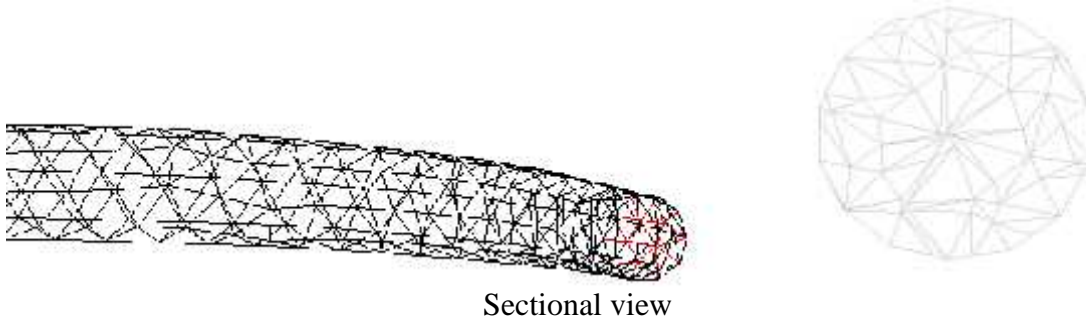
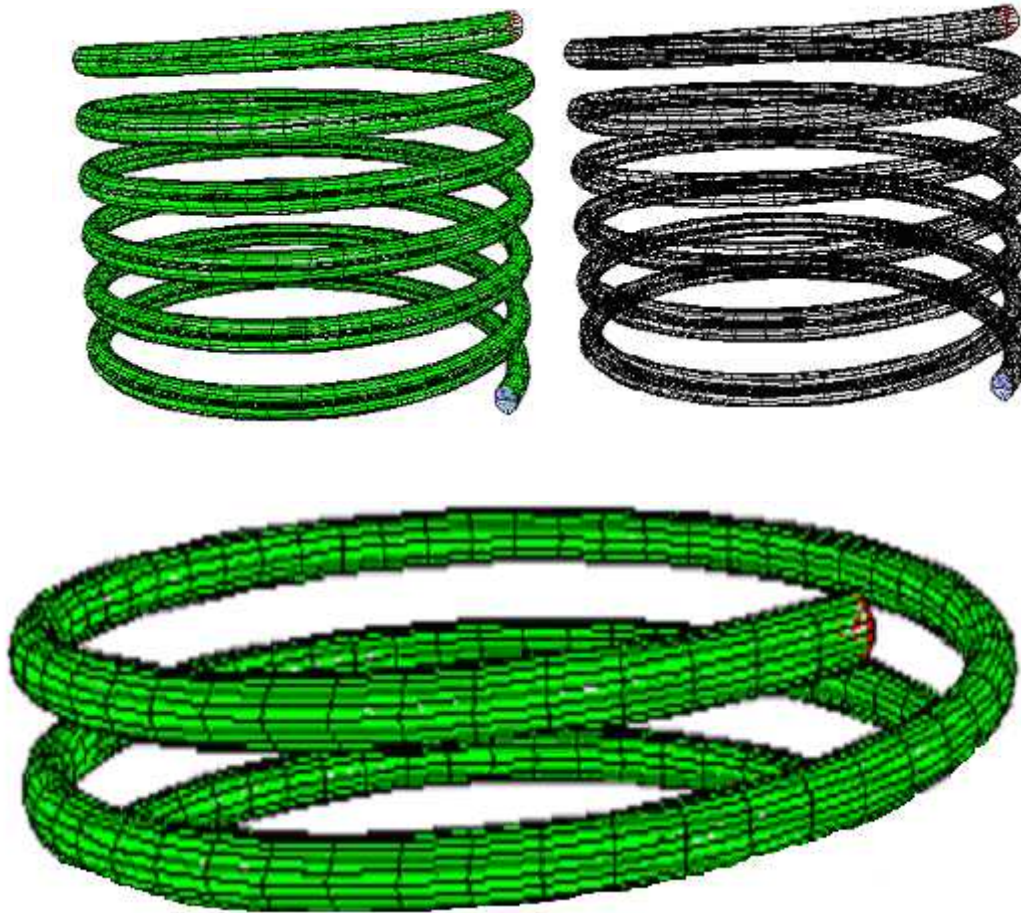
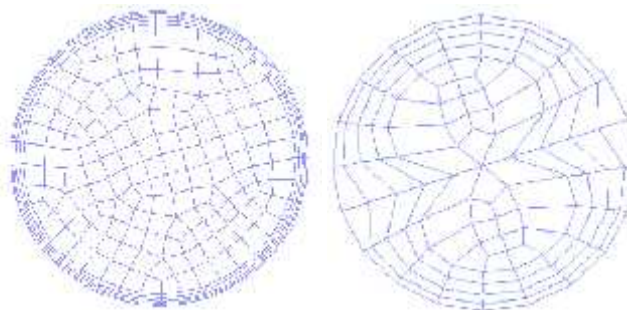


Fig. 7.4 Tetrahedral grid for coil
Coil dimension D_t : 0.00933m, D_v/D_c : 0.0529, D_c : 0.2662 m, Total length: 5.01m, Turn: 6



Grid Size Level 0, Cells 36594, Faces 113106, Nodes 40250, Partitions1, 1 cell zone, 4 face zones



Inlet Middle
Sectional view

Fig.7.5 Hexahedral grid for coil
Coil dimension D_t : 0.00933m, D_t/D_c : 0.0529, D_c : 0.2662 m, Total length: 5.01m, Turn: 6

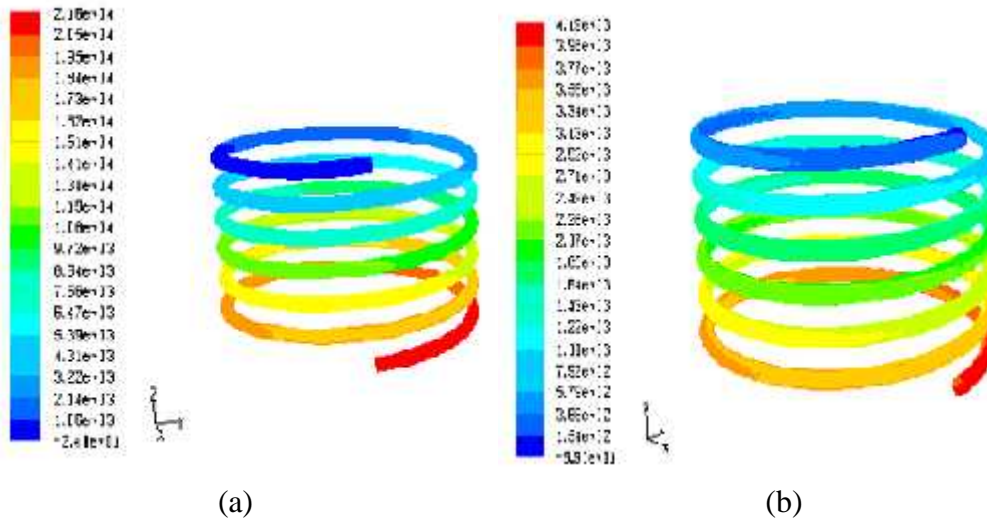


Fig.7.6 Contour plot of static pressure at (a) hexahedral (b) tetrahedral grid, Coil dimension, D_t : 0.00933 m, D_t/D_c : 0.0529, D_c : 0.2662 m, Total length: 5.01 m, Turn: 6, Liquid velocity (m/s): 1.7086 and concentration of SCMC solution (kg/m^3): 0.8

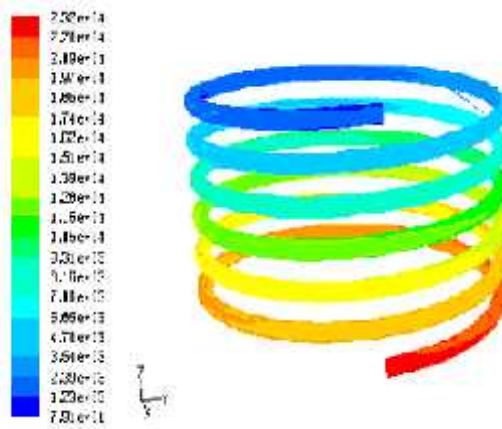


Fig. 7.7 Contours plot of total pressure at hexahedral grid, Coil dimension, D_t : 0.00933 m, D_t/D_c : 0.0529, D_c : 0.2662 m, Total length: 5.01 m, Turn: 6, Liquid velocity (m/s): 1.7086 and concentration of SCMC solution (kg/m^3): 0.8

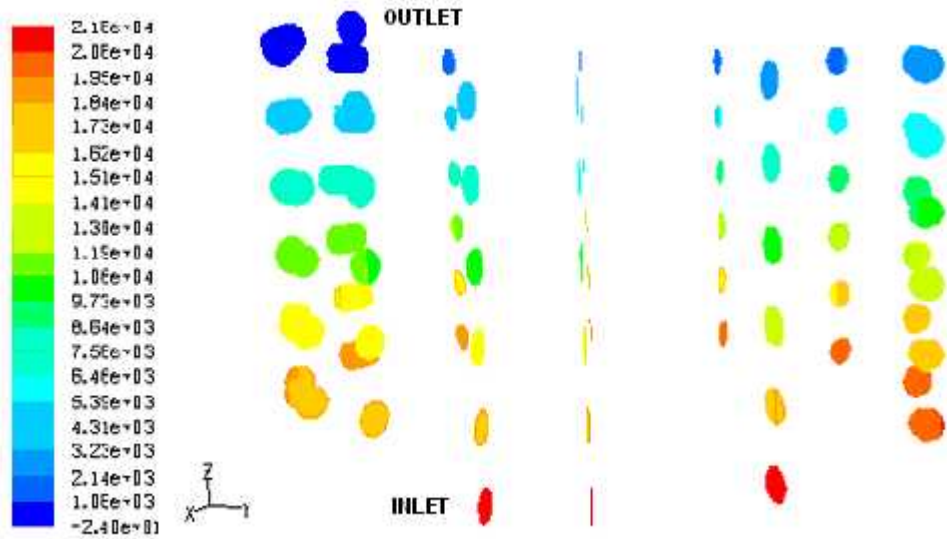


Fig. 7.8 Contours plot of static pressure at various planes along the length coil at hexahedral grid,
 Coil dimension, D_t : 0.00933 m, D_t/D_c : 0.0529, D_c : 0.2662 m, Total length: 5.01 m, Turn: 6, Liquid velocity (m/s): 1.7086 and concentration of SCMC solution (kg/m^3): 0.8

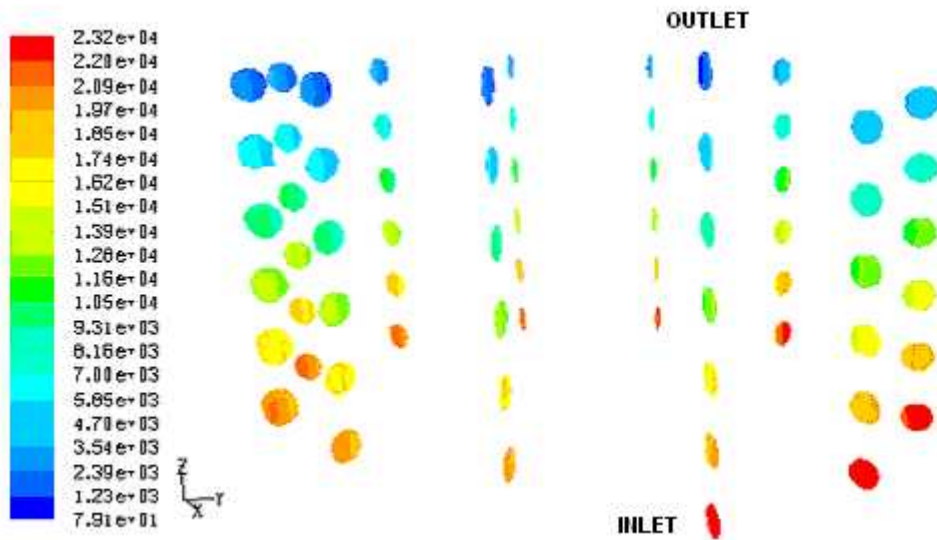


Fig. 7.9 Contours plot of total pressure at various planes along the length of the coil at hexahedral grid,
 Coil dimension, D_t : 0.00933 m, D_t/D_c : 0.0529, D_c : 0.2662 m, Total length: 5.01 m, Turn: 6, Liquid velocity (m/s): 1.7086 and concentration of SCMC solution (kg/m^3): 0.8

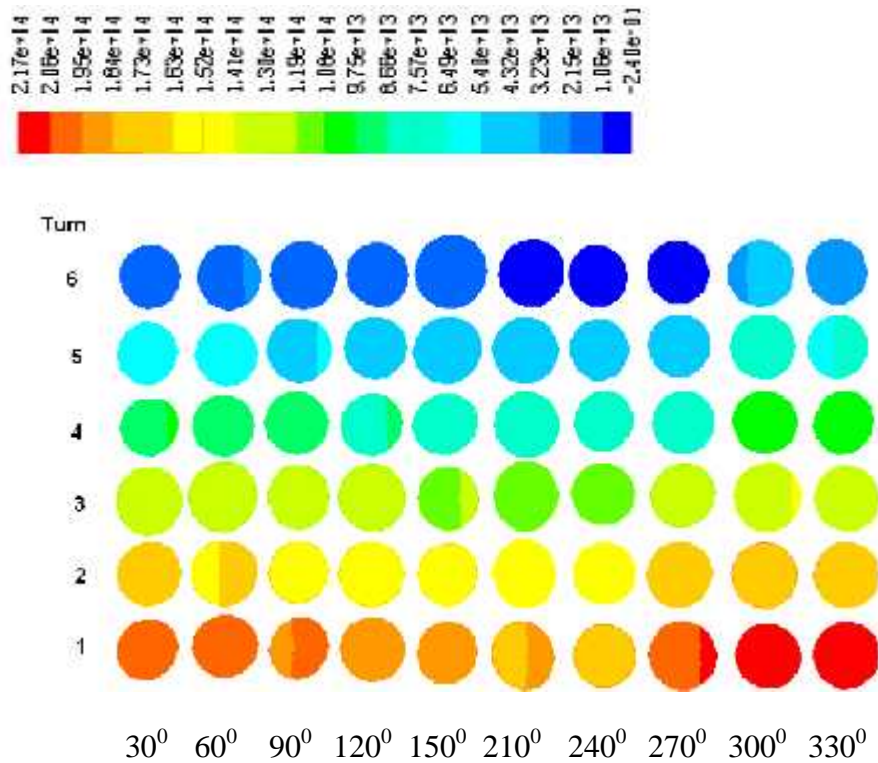


Fig. 7.10 Contour plot of static pressure at the different angular plane and at different turn of the coil
 Coil dimension, D_i : 0.00933 m, D_i/D_c : 0.0529, D_c : 0.2662 m, Total length: 5.01 m, Turn: 6, Liquid velocity (m/s): 1.7086 and concentration of SCMC solution (kg/m^3): 0.8

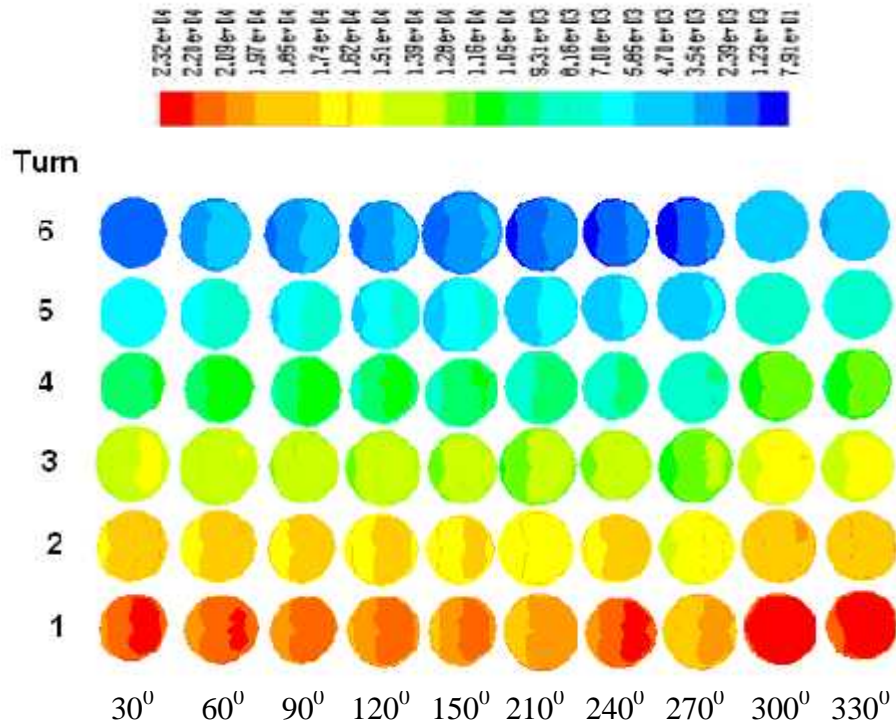


Fig. 7.11 Contour plot of total pressure at the different angular plane and at different turn of a coil at hexahedral grid

Coil dimension, D_i : 0.00933 m, D_i/D_c : 0.0529, D_c : 0.2662 m, Total length: 5.01 m, Turn: 6, Liquid velocity (m/s): 1.7086 and concentration of SCMC solution (kg/m^3): 0.8

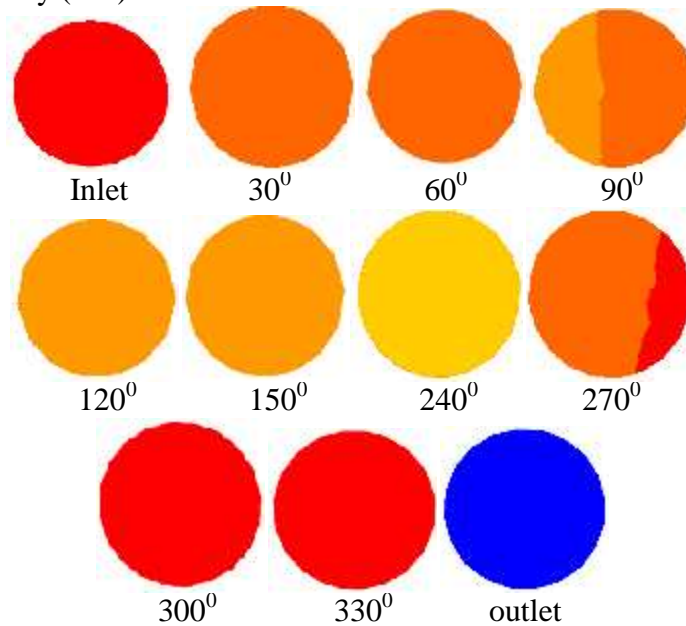


Fig. 7.12 Contour plot of static pressure at the different angular plane and at the fixed turn1 of the coil

Coil dimension, D_i : 0.00933 m, D_i/D_c : 0.0529, D_c : 0.2662 m, Total length: 5.01 m, Turn: 6, Liquid velocity (m/s): 1.7086 and concentration of SCMC solution (kg/m^3): 0.8

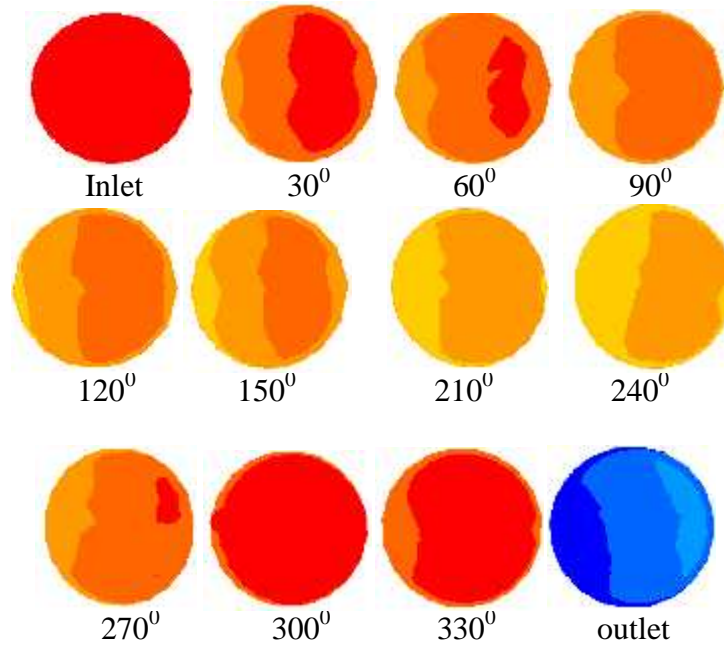


Fig. 7.13 Contour plot of total pressure at the different angular plane and at the fixed turn1 of the coil
 Coil dimension, D_t : 0.00933 m, D_t/D_c : 0.0529, D_c : 0.2662 m, Total length: 5.01 m, Turn: 6, Liquid velocity (m/s): 1.7086 and concentration of SCMC solution (kg/m^3): 0.8

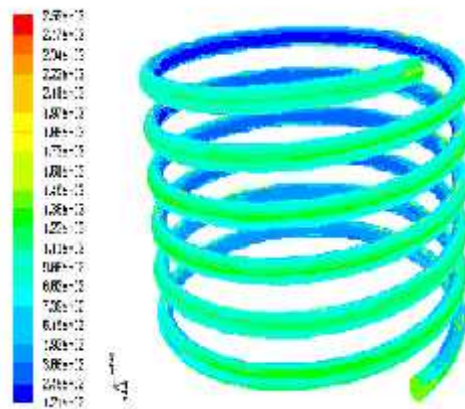


Fig. 7.14 Contour plot of dynamic pressure at hexahedral grid,
 Coil dimension, D_t : 0.00933 m, D_t/D_c : 0.0529, D_c : 0.2662 m, Total length: 5.01 m, Turn: 6, Liquid velocity (m/s): 1.7086 and concentration of SCMC solution (kg/m^3): 0.8

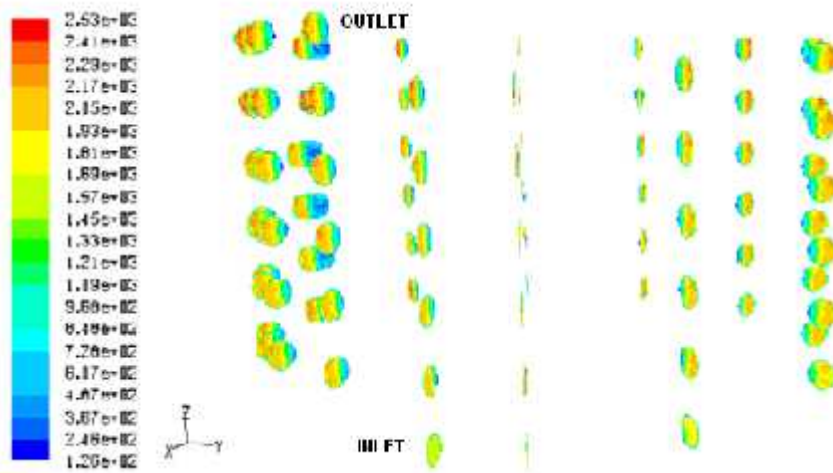


Fig. 7.15 Contour plot of dynamic pressure at various planes along the length of the coil for hexahedral grid,
 Coil dimension, D_t : 0.00933 m, D_t/D_c : 0.0529, D_c : 0.2662 m, Total length: 5.01 m, Turn: 6, Liquid velocity (m/s): 1.7086 and concentration of SMC solution (kg/m^3): 0.8

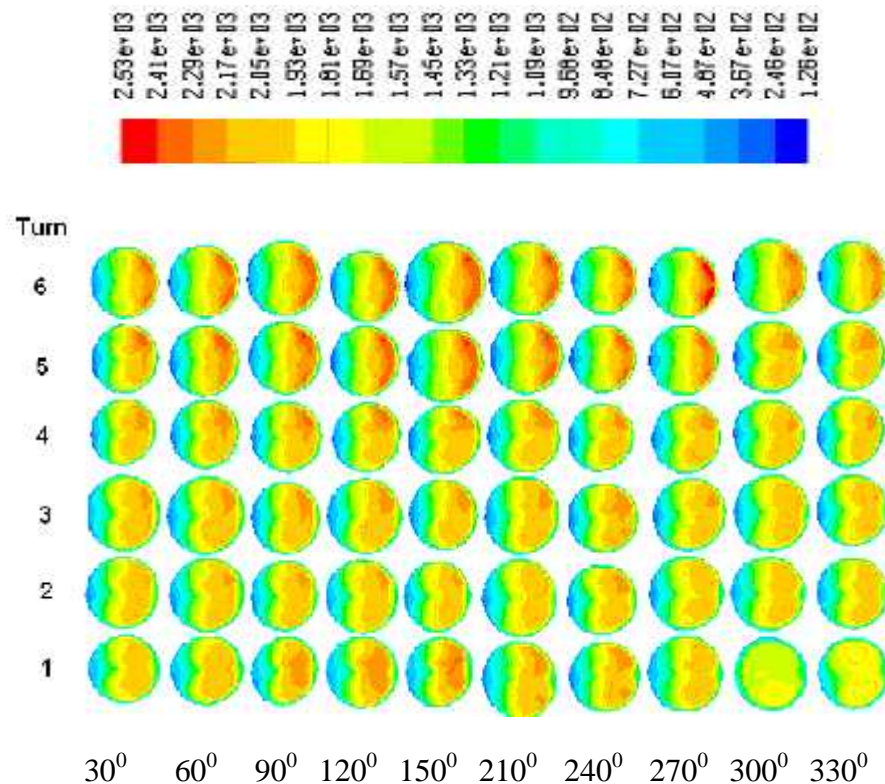


Fig. 7.16 Contour plot of dynamic pressure at the different angular plane and at different turn or height of the coil at hexahedral grid,
 Coil dimension, D_t : 0.00933 m, D_t/D_c : 0.0529, D_c : 0.2662 m, Total length: 5.01 m, Turn: 6, Liquid velocity (m/s): 1.7086 and concentration of SMC solution (kg/m^3): 0.8

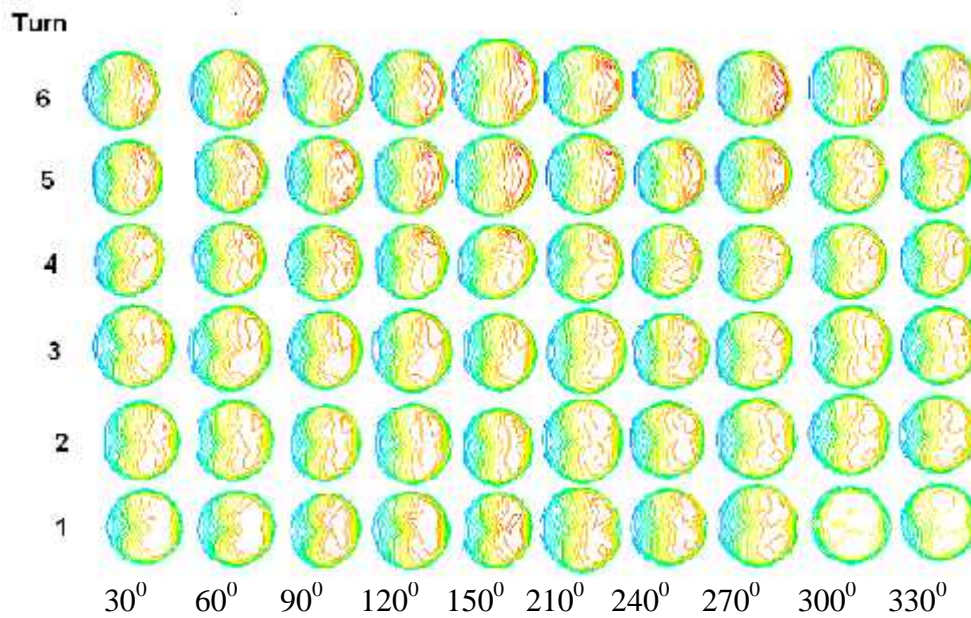


Fig. 7.17 Contour plot of dynamic pressure at the different angular plane and at different turn or height of the coil at hexahedral grid, Coil dimension, D_i : 0.00933 m, D_i/D_c : 0.0529, D_c : 0.2662 m, Total length: 5.01 m, Turn: 6, Liquid velocity (m/s): 1.7086 and concentration of SCMC solution (kg/m^3): 0.8

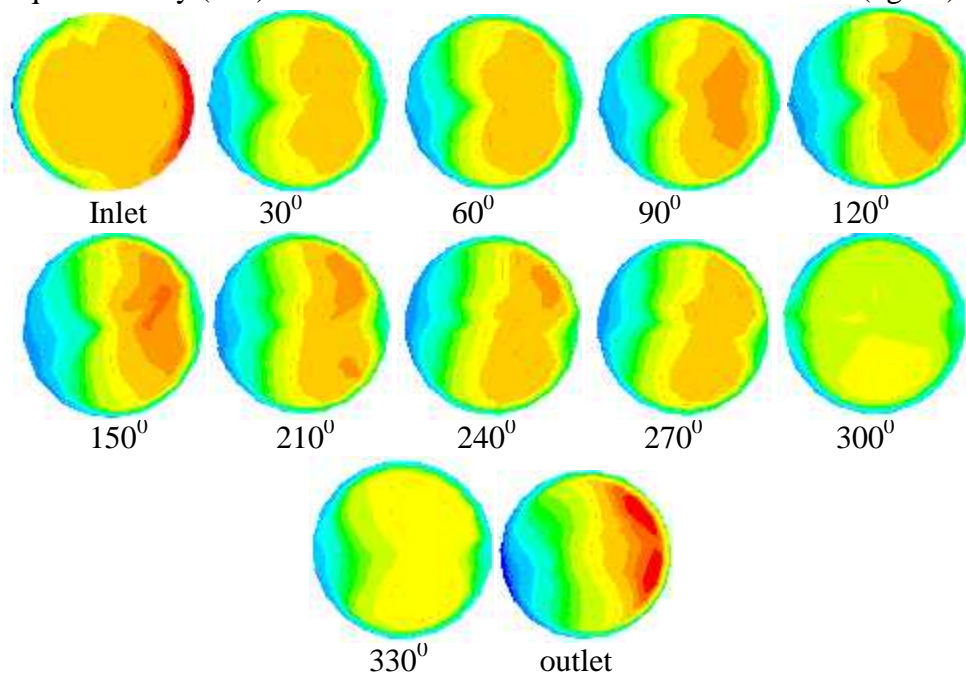


Fig. 7.18 Contour plot of dynamic pressure at the different angular plane and at the fixed turn1 of the coil at hexahedral grid, Coil dimension, D_i : 0.00933 m, D_i/D_c : 0.0529, D_c : 0.2662 m, Total length: 5.01m, Turn: 6, Liquid velocity (m/s): 1.7086 and concentration of SCMC solution (kg/m^3): 0.8

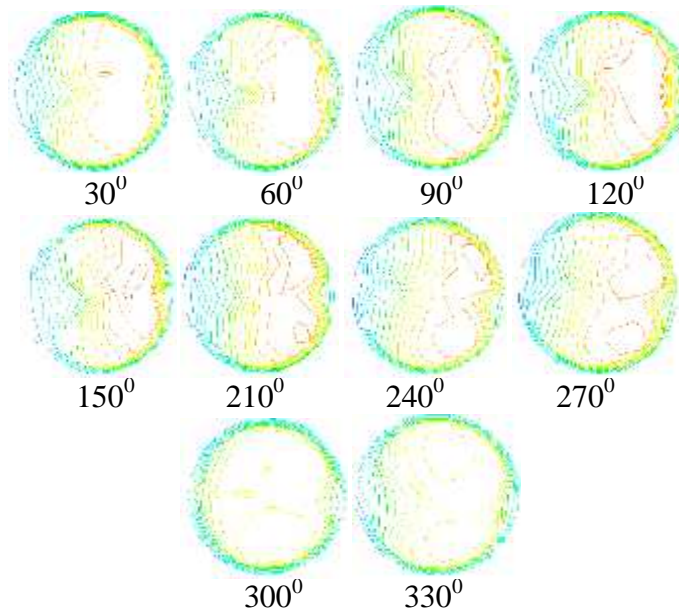


Fig. 7.19 Contour plot of dynamic pressure at the different angular plane and at the fixed turn1 of the coil at hexahedral grid,
 Coil dimension, D_t : 0.00933 m, D_t/D_c : 0.0529, D_c : 0.2662 m, Total length: 5.01 m, Turn: 6, Liquid velocity (m/s): 1.7086 and concentration of SMC solution (kg/m^3): 0.8

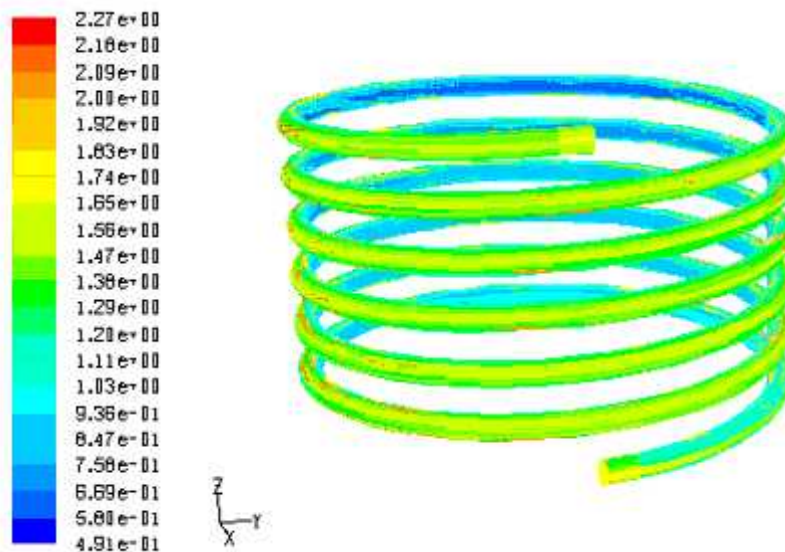


Fig. 7.20 Contours plot of velocity magnitude for helical coil at hexahedral grid,
 Coil dimension, D_t : 0.00933 m, D_t/D_c : 0.0529, D_c : 0.2662 m, Total length: 5.01m, Turn: 6, Liquid velocity (m/s): 1.7086 and concentration of SMC solution (kg/m^3): 0.8

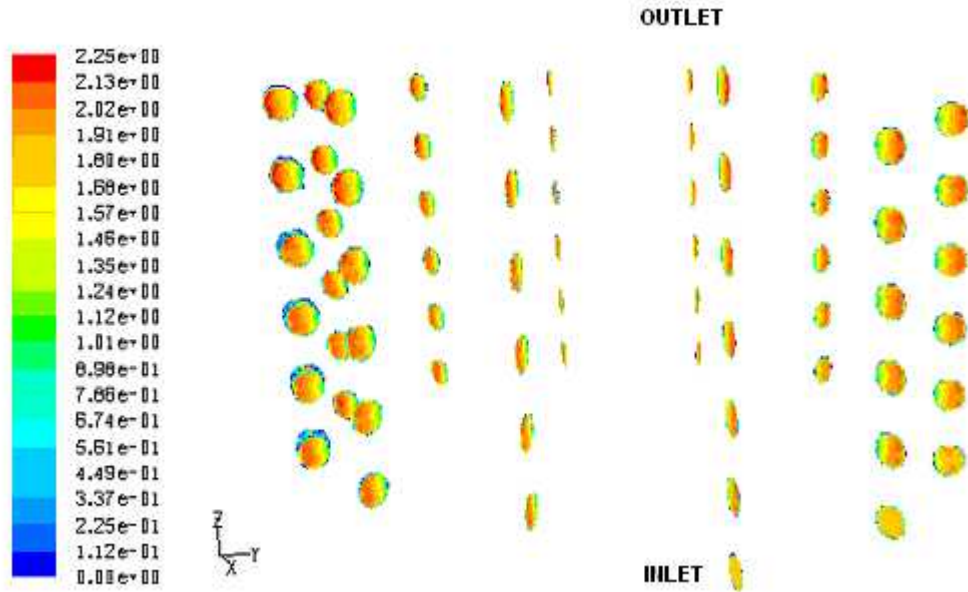


Fig. 7.21 Contours plot of velocity magnitude at various planes along the length coil for helical coil at hexahedral grid, Coil dimension, D_i : 0.00933 m, D_i/D_c : 0.0529, D_c : 0.2662 m, Total length: 5.01 m, Turn: 6, Liquid velocity (m/s): 1.7086 and concentration of SCMC solution (kg/m^3): 0.8

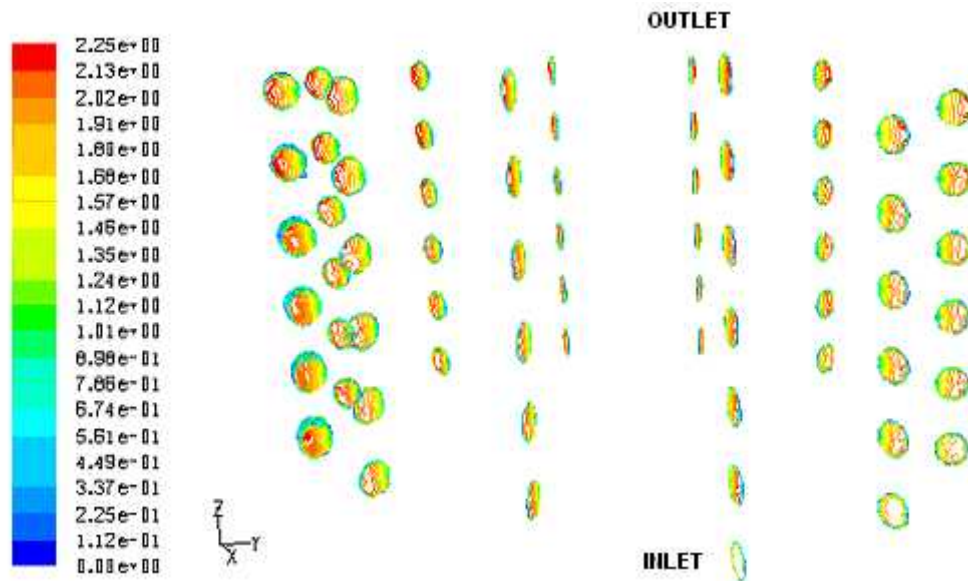


Fig. 7.22 Contours plot of velocity magnitude at various planes along the length coil for helical coil at hexahedral grid, Coil dimension, D_i : 0.00933 m, D_i/D_c : 0.0529, D_c : 0.2662 m, Total length: 5.01 m, Turn: 6, Liquid velocity (m/s): 1.7086 and concentration of SCMC solution (kg/m^3): 0.8

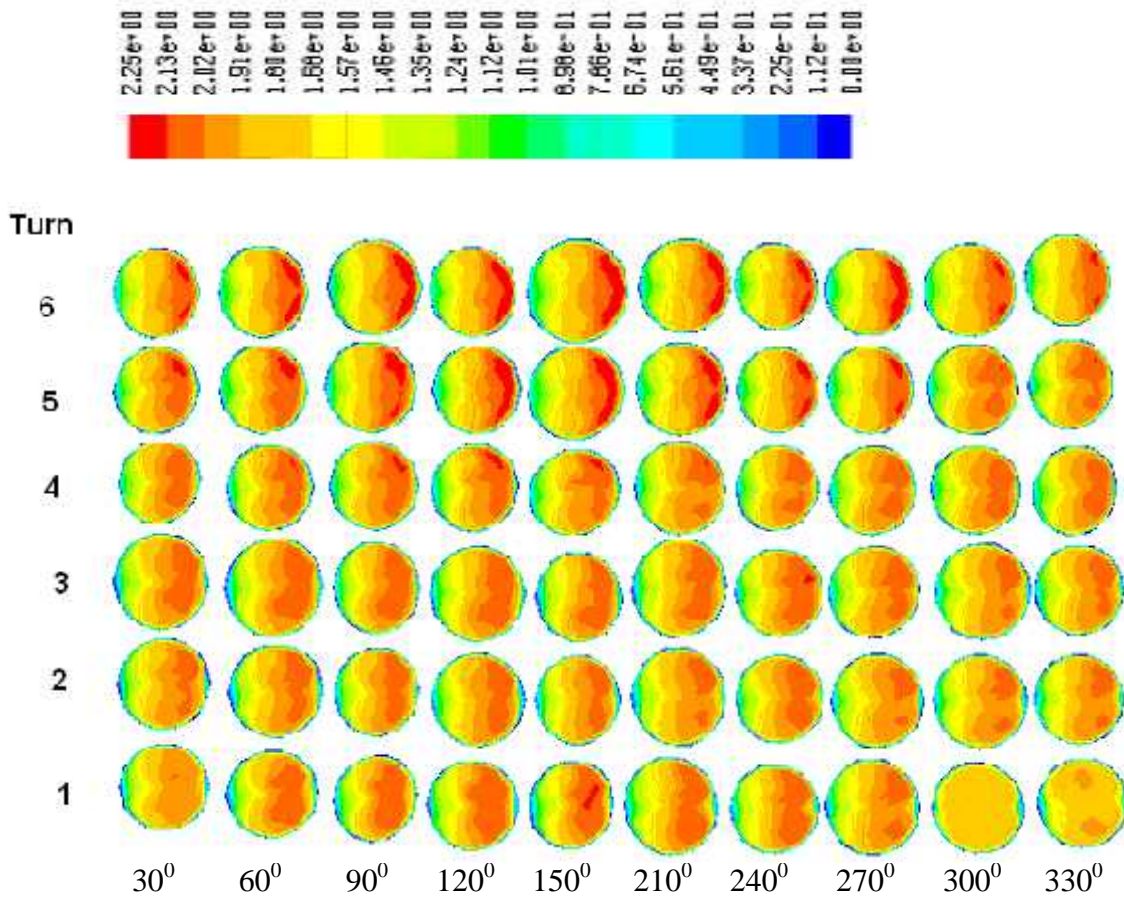


Fig. 7.23 Contours plot of velocity magnitude at various planes along the length of the coil at hexahedral grid,
 Coil dimension, D_i : 0.00933 m, D_i/D_c : 0.0529, D_c : 0.2662 m, Total length: 5.01 m, Turn: 6, Liquid velocity (m/s): 1.7086 and concentration of SCMC solution (kg/m^3): 0.8

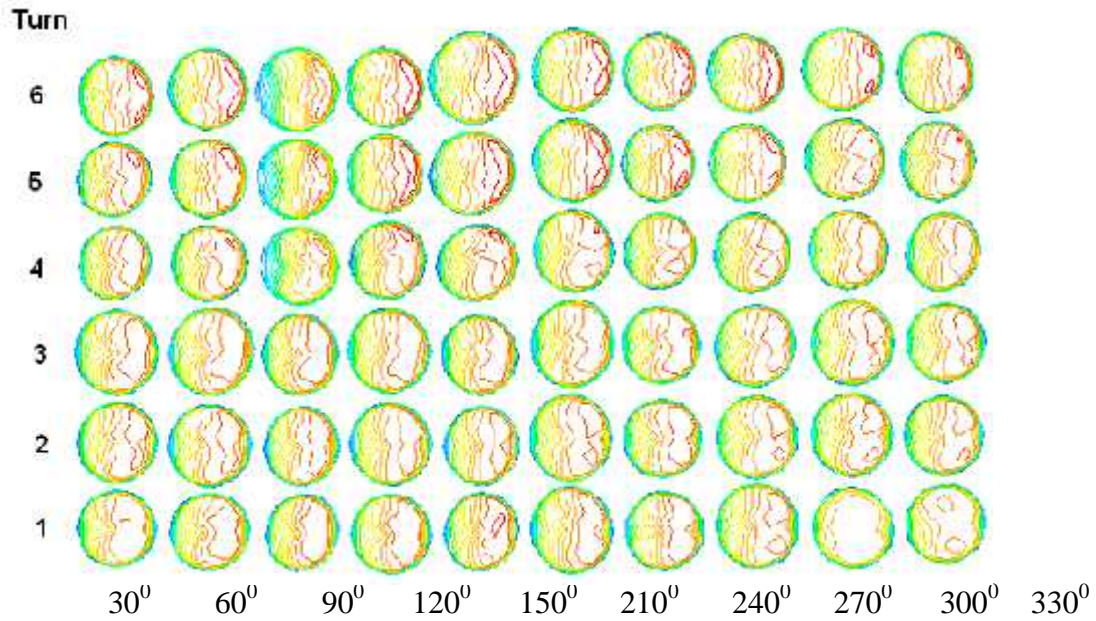


Fig. 7.24 Contour plot of velocity magnitude at the different angular plane and at different turn or height of the coil at hexahedral grid,
 Coil dimension, D_t : 0.00933 m, D_t/D_c : 0.0529, D_c : 0.2662 m, Total length: 5.01 m, Turn: 6, Liquid velocity (m/s): 1.7086 and concentration of SCMC solution (kg/m^3): 0.8

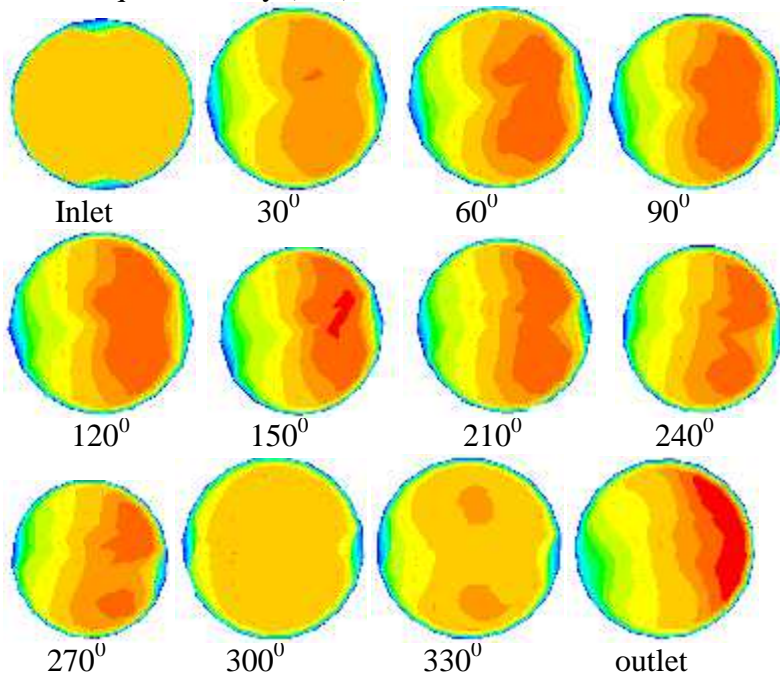


Fig. 7.25 Contour plot of velocity magnitude at the different angular plane and at the fixed turn1 of the coil at hexahedral grid,
 Coil dimension, D_t : 0.00933 m, D_t/D_c : 0.0529, D_c : 0.2662 m, Total length: 5.01 m, Turn: 6, Liquid velocity (m/s): 1.7086 and concentration of SCMC solution (kg/m^3): 0.8

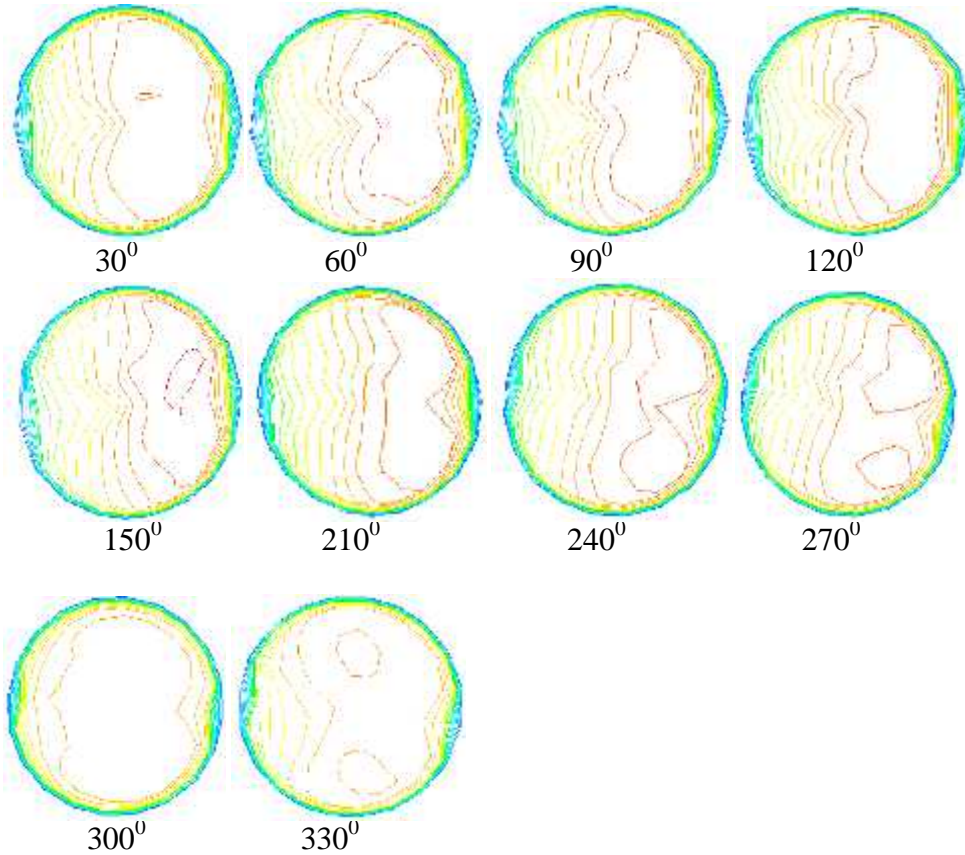


Fig. 7.26 Contour plot of velocity magnitude at the different angular plane and at the fixed turn1 of the coil at hexahedral grid, Coil dimension, D_t : 0.00933 m, D_t/D_c : 0.0529, D_c : 0.2662 m, Total length: 5.01 m, Turn: 6, Liquid velocity (m/s): 1.7086 and concentration of SCMC solution (kg/m^3): 0.8

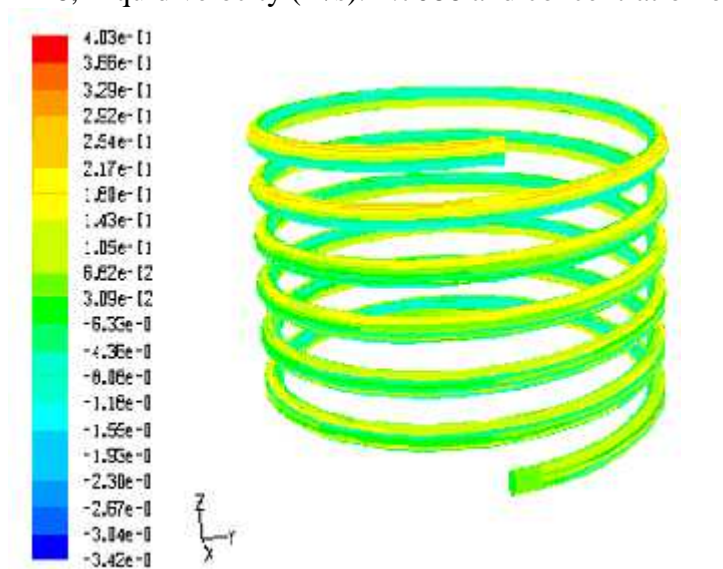


Fig. 7.27 Contours plot of velocity for helical coil at hexahedral grid, Coil dimension, D_t : 0.00933 m, D_t/D_c : 0.0529, D_c : 0.2662 m, Total length: 5.01 m, Turn: 6, Liquid velocity (m/s): 1.7086 and concentration of SCMC solution (kg/m^3): 0.8

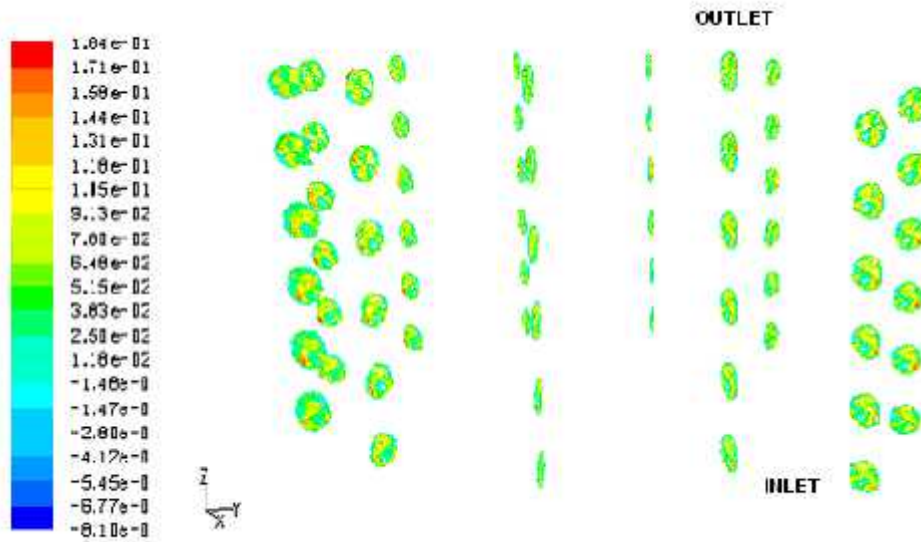


Fig. 7.28 Contours plot of velocity at various planes along the length coil for helical coil at hexahedral grid,

Coil dimension, D_i : 0.00933 m, D_i/D_c : 0.0529, D_c : 0.2662 m, Total length: 5.01 m, Turn: 6, Liquid velocity (m/s): 1.7086 and concentration of SCMC solution (kg/m^3): 0.8

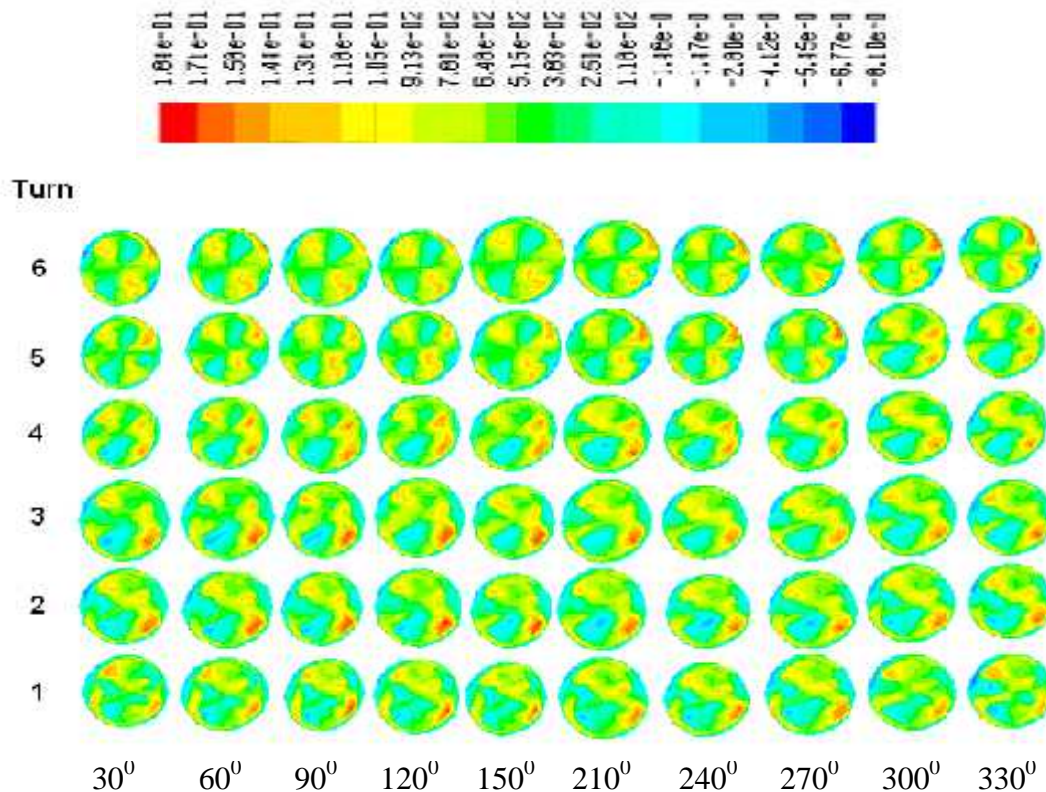


Fig. 7.29 Contour plot of velocity at the different angular plane and at different turn of the coil at hexahedral grid,

Coil dimension, D_i : 0.00933 m, D_i/D_c : 0.0529, D_c : 0.2662 m, Total length: 5.01 m, Turn: 6, Liquid velocity (m/s): 1.7086 and concentration of SCMC solution (kg/m^3): 0.8

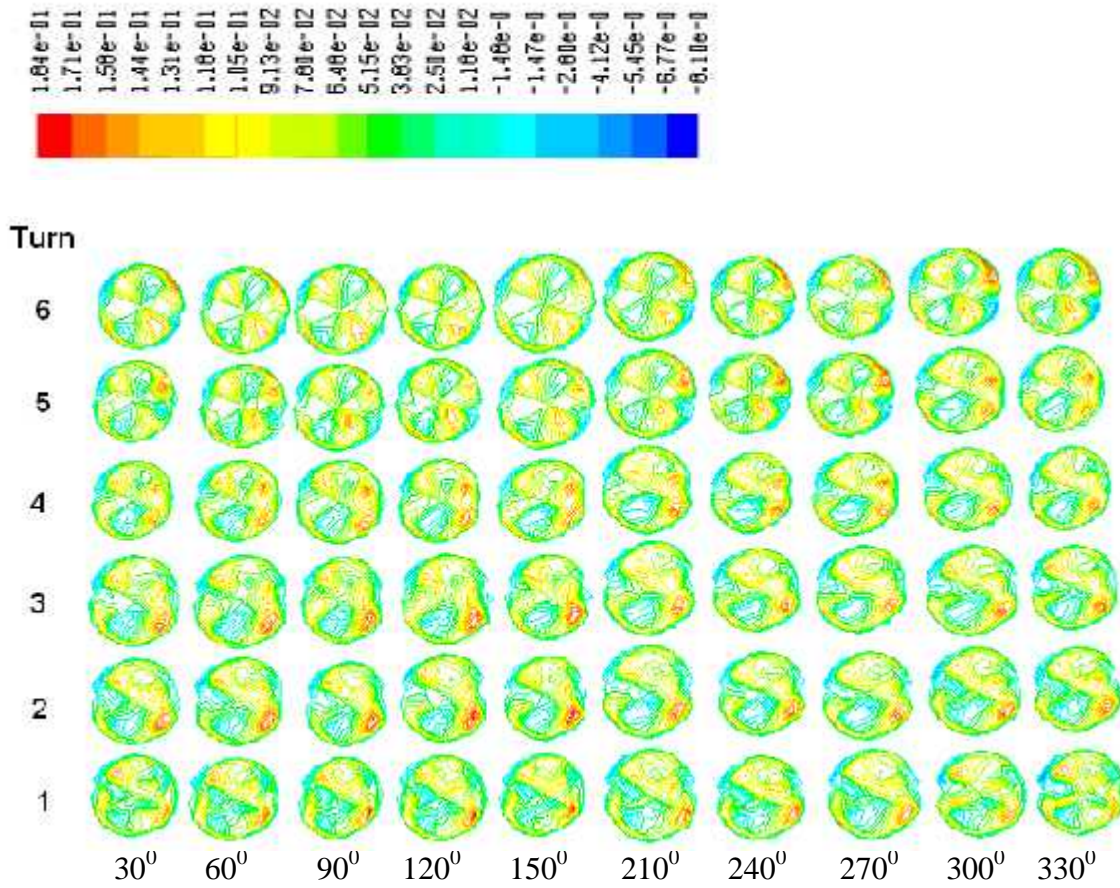


Fig. 7.30 Contour plot of velocity at the different angular plane and at different turn of the coil at hexahedral grid,
 Coil dimension, D_i : 0.00933 m, D_i/D_c : 0.0529, D_c : 0.2662 m, Total length: 5.01 m, Turn: 6, Liquid velocity (m/s): 1.7086 and concentration of SMC solution (kg/m^3): 0.8

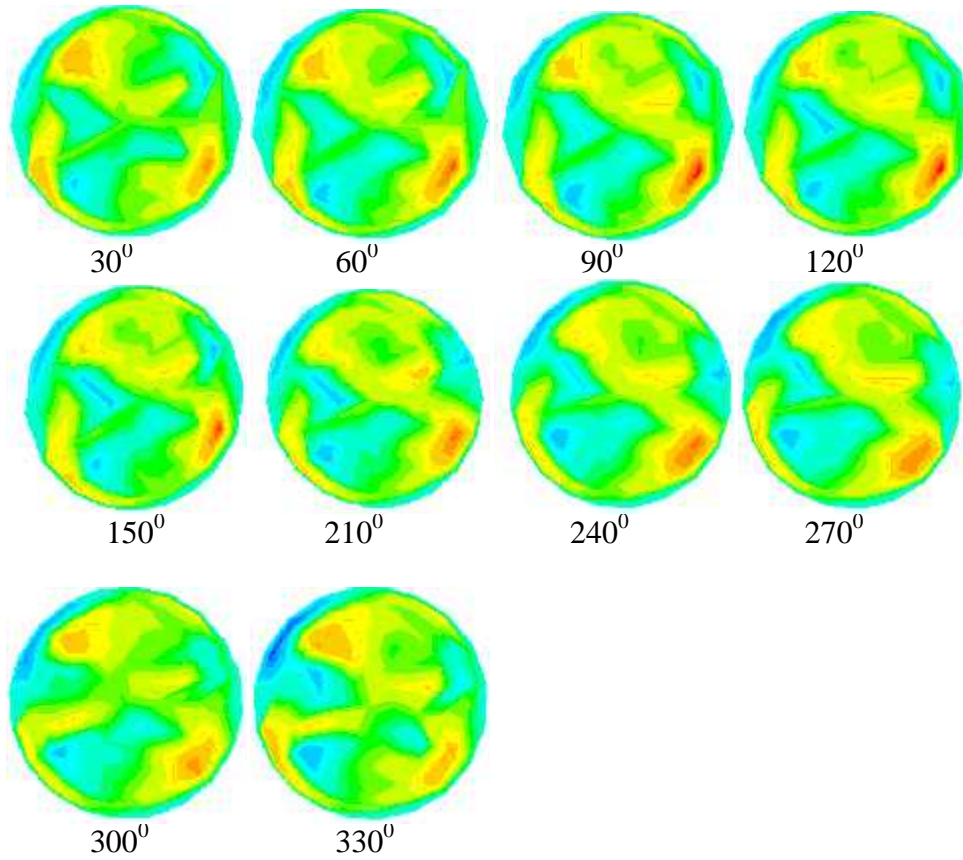


Fig. 7.31 Contour plot of velocity at the different angular plane and at the fixed turn1 of the coil at hexahedral grid,
Coil dimension, D_t : 0.00933 m, D_t/D_c : 0.0529, D_c : 0.2662 m, Total length: 5.01 m, Turn: 6, Liquid velocity (m/s): 1.7086 and concentration of SCMC solution (kg/m^3): 0.8

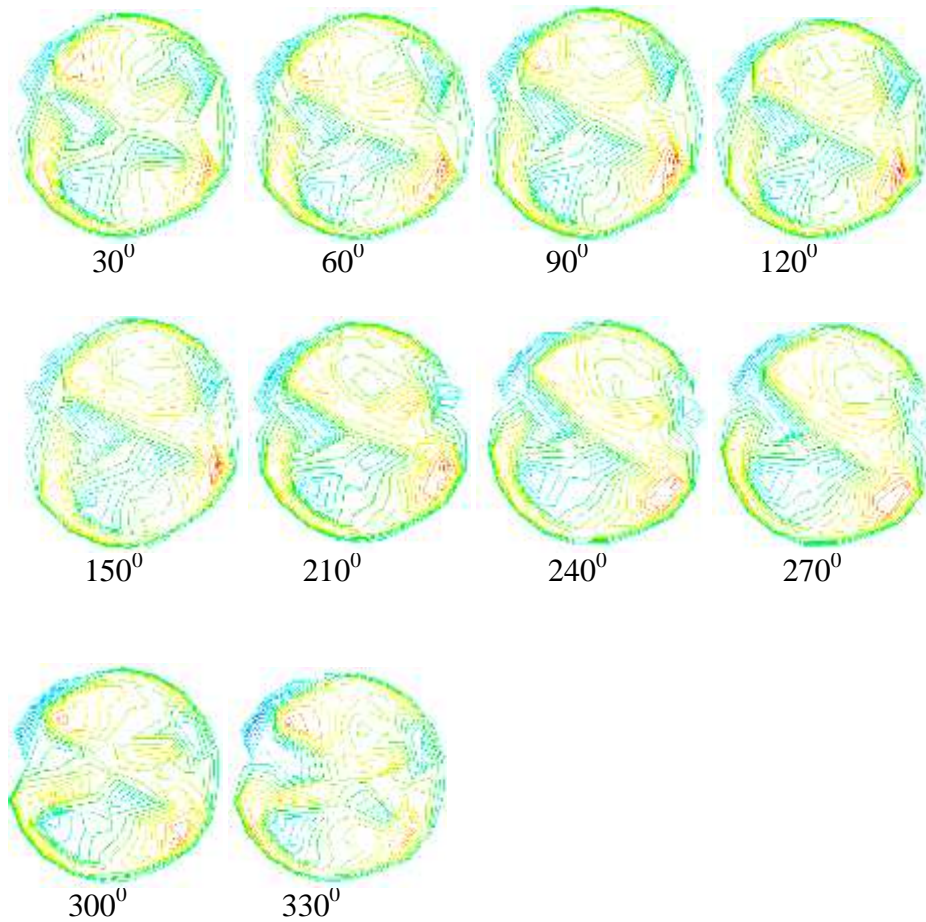
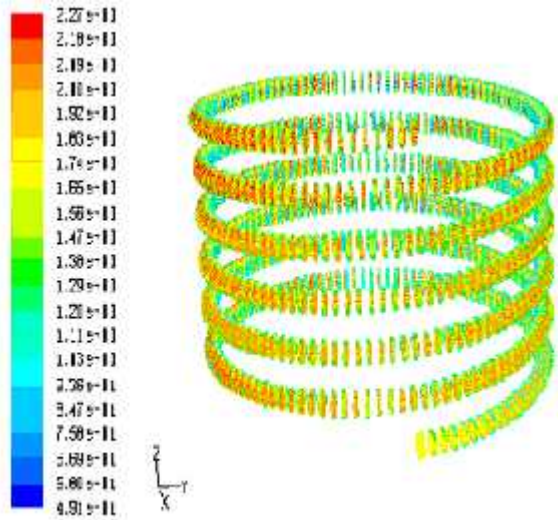
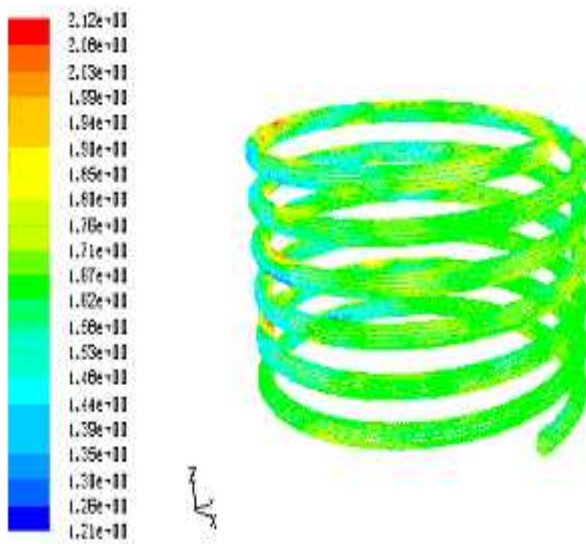


Fig. 7.32 Contour plot of velocity at the different angular plane and at the fixed turn1 of the coil at hexahedral grid,
Coil dimension, D_i : 0.00933 m, D_i/D_c : 0.0529, D_c : 0.2662 m, Total length: 5.01 m, Turn: 6, Liquid velocity (m/s): 1.7086 and concentration of SMC solution (kg/m^3): 0.8



(a)



(b)

Fig. 7.33 Contour plot of velocity vector for helical coil at (a) hexahedral grid (b) tetrahedral grid, Coil dimension, D_t : 0.00933 m, D_t/D_c : 0.0529, D_c : 0.2662 m, Total length: 5.01 m, Turn: 6, Liquid velocity (m/s): 1.7086 and concentration of SCMC solution (kg/m^3): 0.8

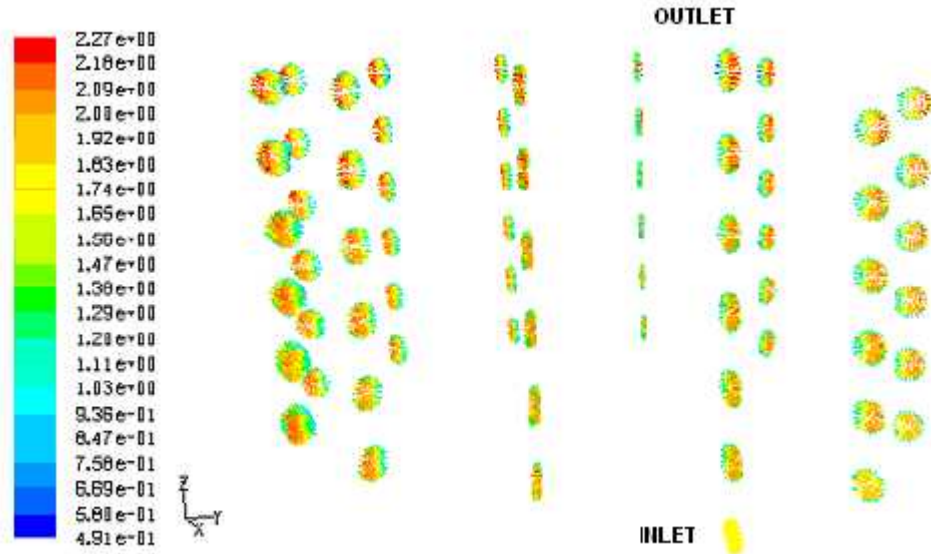


Fig. 7.34 Contour plot of velocity vector at the different angular plane of the coil at hexahedral grid,
 Coil dimension, D_t : 0.00933 m, D_t/D_c : 0.0529, D_c : 0.2662 m, Total length: 5.01 m, Turn: 6, Liquid velocity (m/s): 1.7086 and concentration of SCMC solution (kg/m^3): 0.8

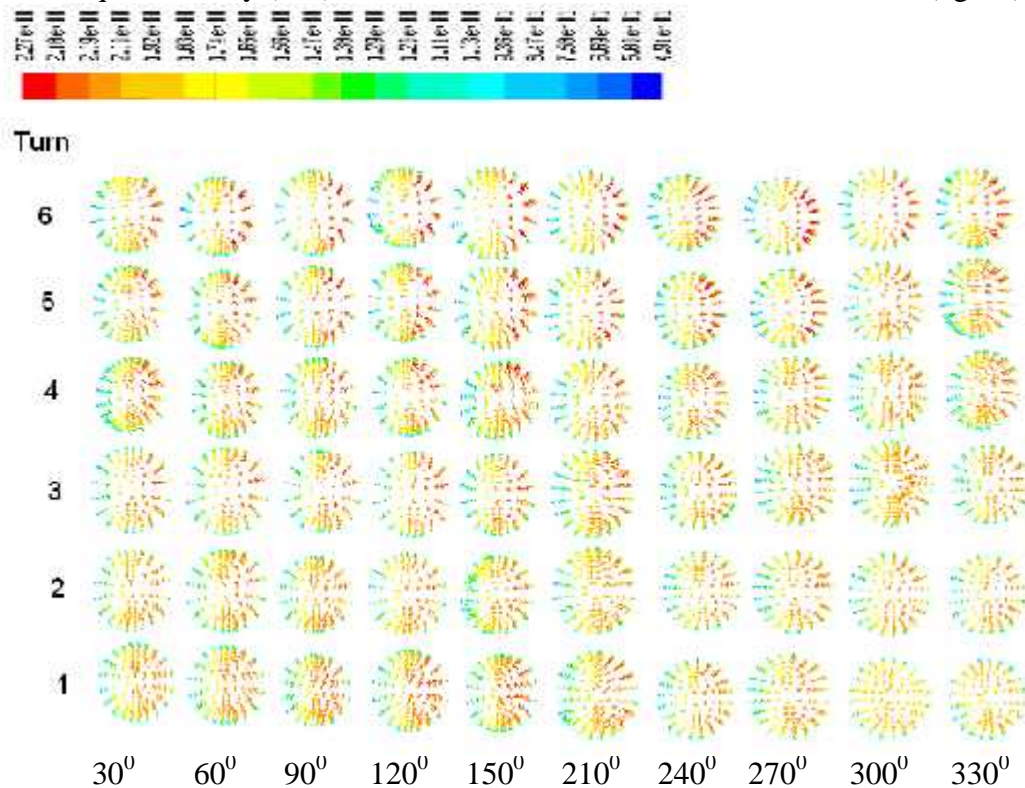


Fig. 7.35 Contour plot of velocity vector at the different angular plane and at different turn or height of the coil at hexahedral grid, Coil dimension, D_t : 0.00933 m, D_t/D_c : 0.0529, D_c : 0.2662 m, Total length: 5.01 m, Turn: 6, Liquid velocity (m/s): 1.7086 and concentration of SCMC solution (kg/m^3): 0.8

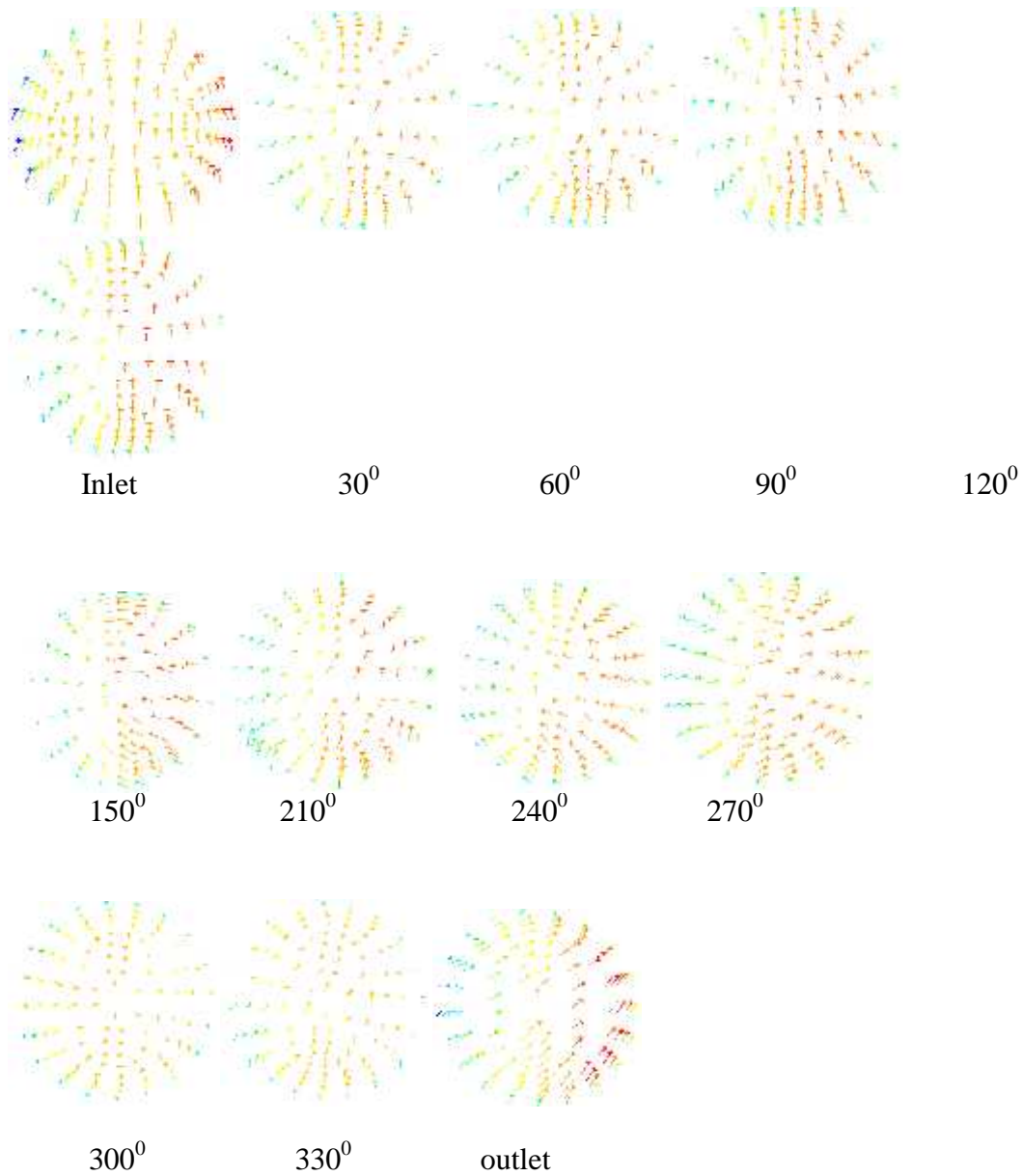


Fig. 7.36 Contour plot of velocity vector at the different angular plane and at the fixed turn1 of the coil at hexahedral grid, Coil dimension, D_i : 0.00933 m, D_i/D_c : 0.0529, D_c : 0.2662 m, Total length: 5.01 m, Turn: 6, Liquid velocity (m/s): 1.7086 and concentration of SCMC solution (kg/m^3): 0.8

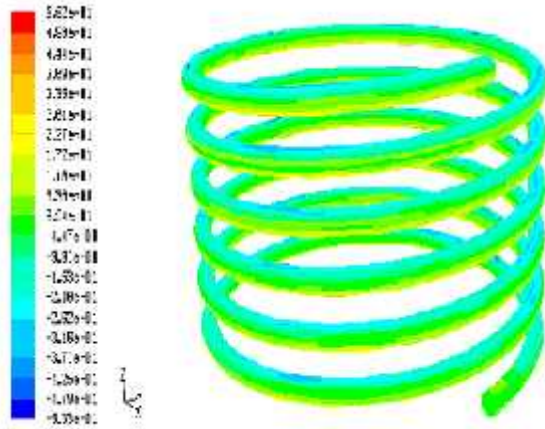


Fig. 7.37 Contour plot of helicity for helical coil at hexahedral grid, Coil dimension, D_t : 0.00933 m, D_t/D_c : 0.0529, D_c : 0.2662 m, Total length: 5.01 m, Turn: 6, Liquid velocity (m/s): 1.7086 and concentration of SCMC solution (kg/m^3): 0.8

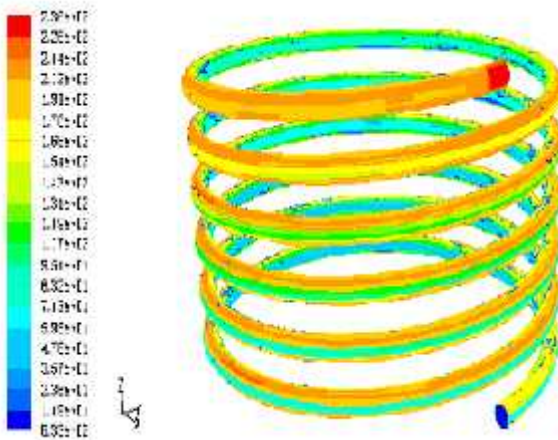


Fig. 7.38 Contour plot of vorticity for helical coil at hexahedral grid, Coil dimension, D_t : 0.00933 m, D_t/D_c : 0.0529, D_c : 0.2662 m, Total length: 5.01 m, Turn: 6, Liquid velocity (m/s): 1.7086 and concentration of SCMC solution (kg/m^3): 0.8

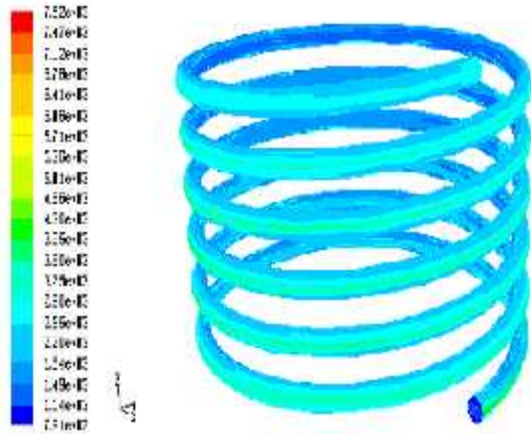


Fig. 7.39 Contour plot of cell Reynolds number for helical coil at hexahedral grid, Coil dimension, D_t : 0.00933 m, D_t/D_c : 0.0529, D_c : 0.2662 m, Total length: 5.01 m, Turn: 6, Liquid velocity (m/s): 1.7086 and concentration of SMC solution (kg/m^3): 0.8

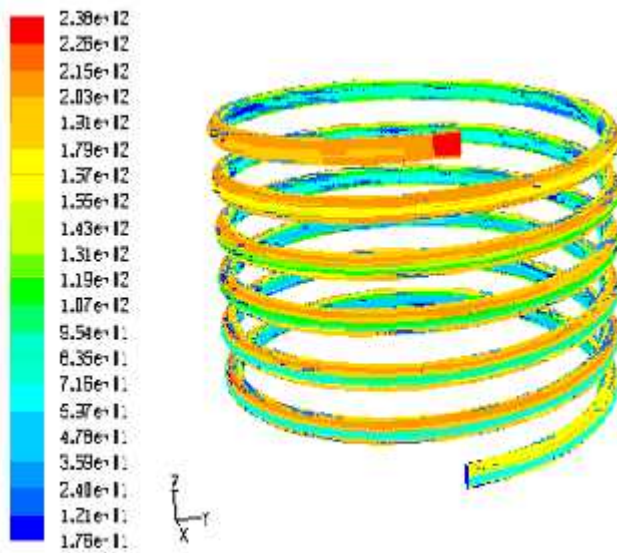


Fig. 7.40 Contour plot of strain rate at hexahedral grid, Coil dimension, D_t : 0.00933 m, D_t/D_c : 0.0529, D_c : 0.2662 m, Total length: 5.01 m, Turn: 6, Liquid velocity (m/s): 1.7086 and concentration of SMC solution (kg/m^3): 0.8

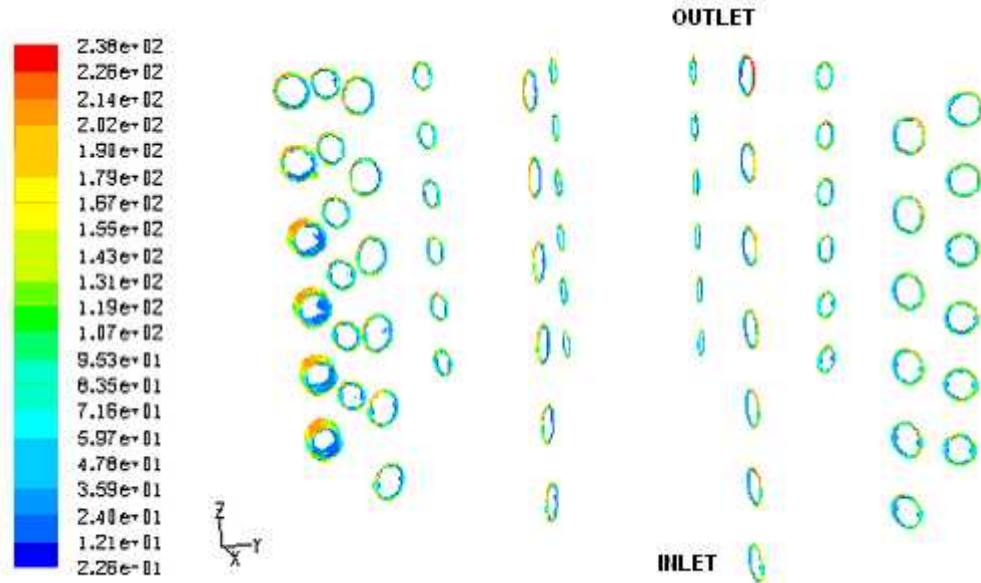


Fig. 7.41 Contour plot of strain rate at the different angular plane along the length of the coil at hexahedral grid,
 Coil dimension, D_t : 0.00933 m, D_t/D_c : 0.0529, D_c : 0.2662 m, Total length: 5.01 m, Turn: 6, Liquid velocity (m/s): 1.7086 and concentration SMC solution (kg/m^3): 0.8

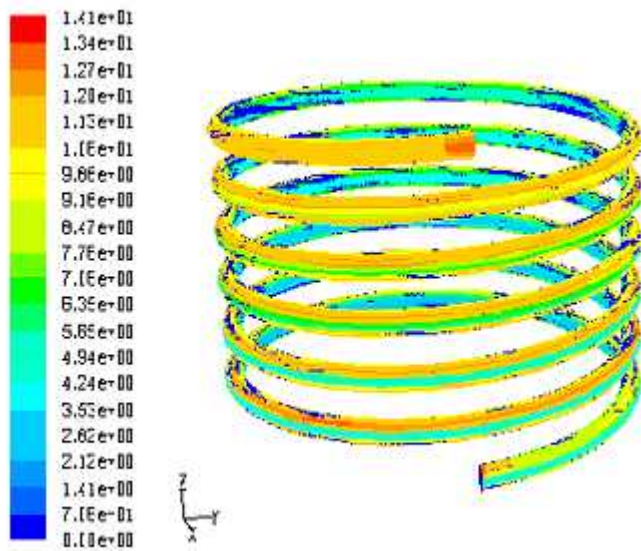


Fig. 7.42 Contour plot of shear stress for helical coil at hexahedral grid,
 Coil dimension, D_t : 0.00933 m, D_t/D_c : 0.0529, D_c : 0.2662 m, Total length: 5.01 m, Turn: 6, Liquid velocity (m/s): 1.7086 and concentration of SMC solution (kg/m^3): 0.8

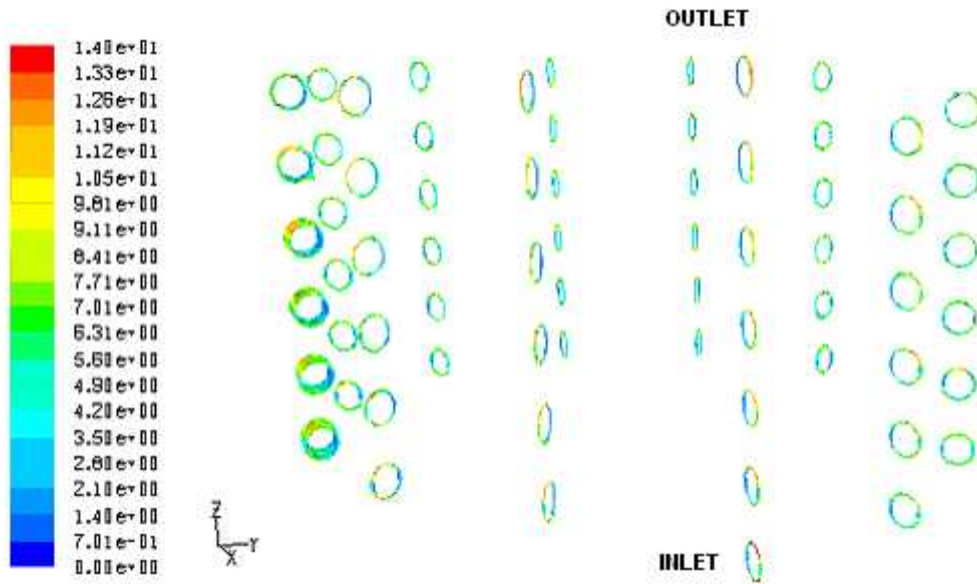


Fig. 7.43 Contour plot of shear stress at the different angular plane along the length of the coil at hexahedral grid,
 Coil dimension, D_t : 0.00933 m, D_t/D_c : 0.0529, D_c : 0.2662 m, Total length: 5.01 m, Turn: 6, Liquid velocity (m/s): 1.7086 and concentration of SCMC solution (kg/m^3): 0.8

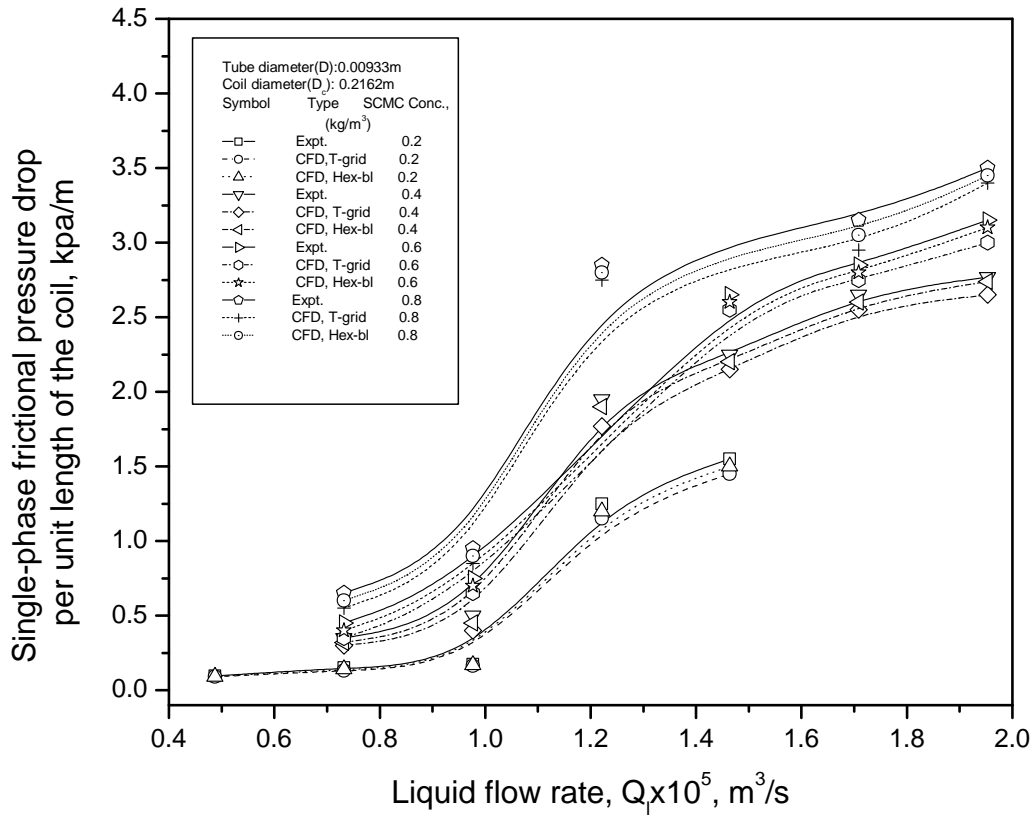


Fig. 7.44 Comparison plot of helical coil at different SMC concentration

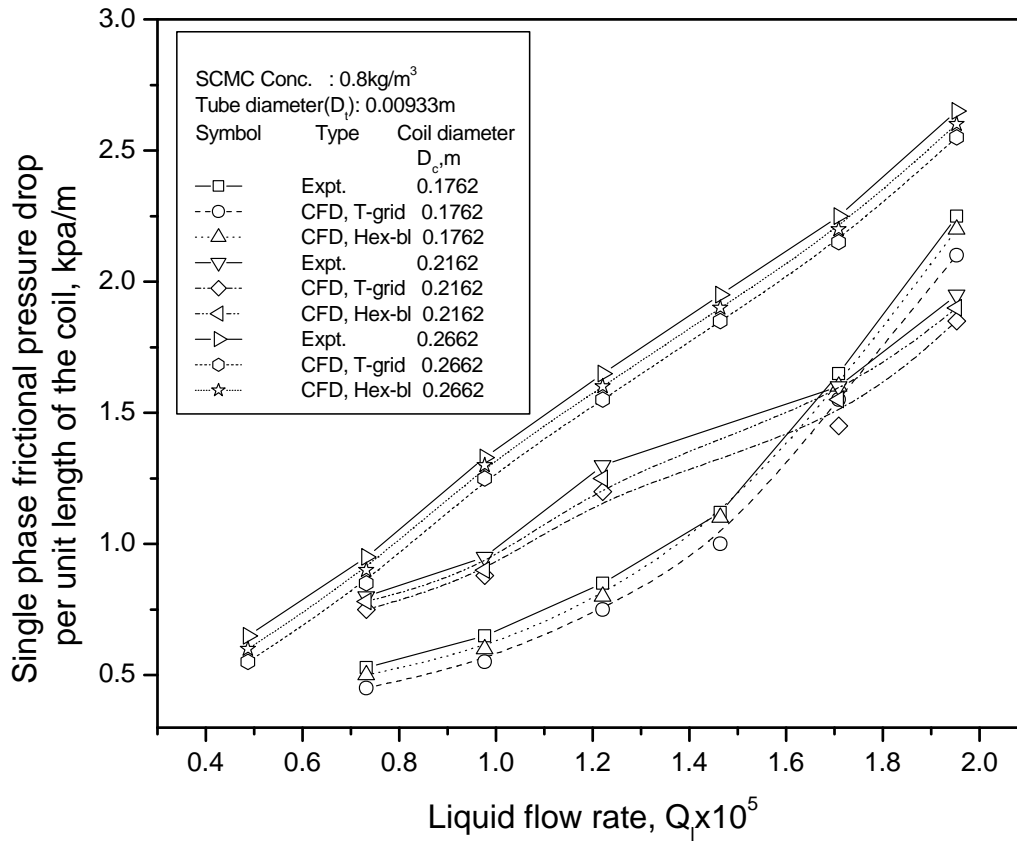
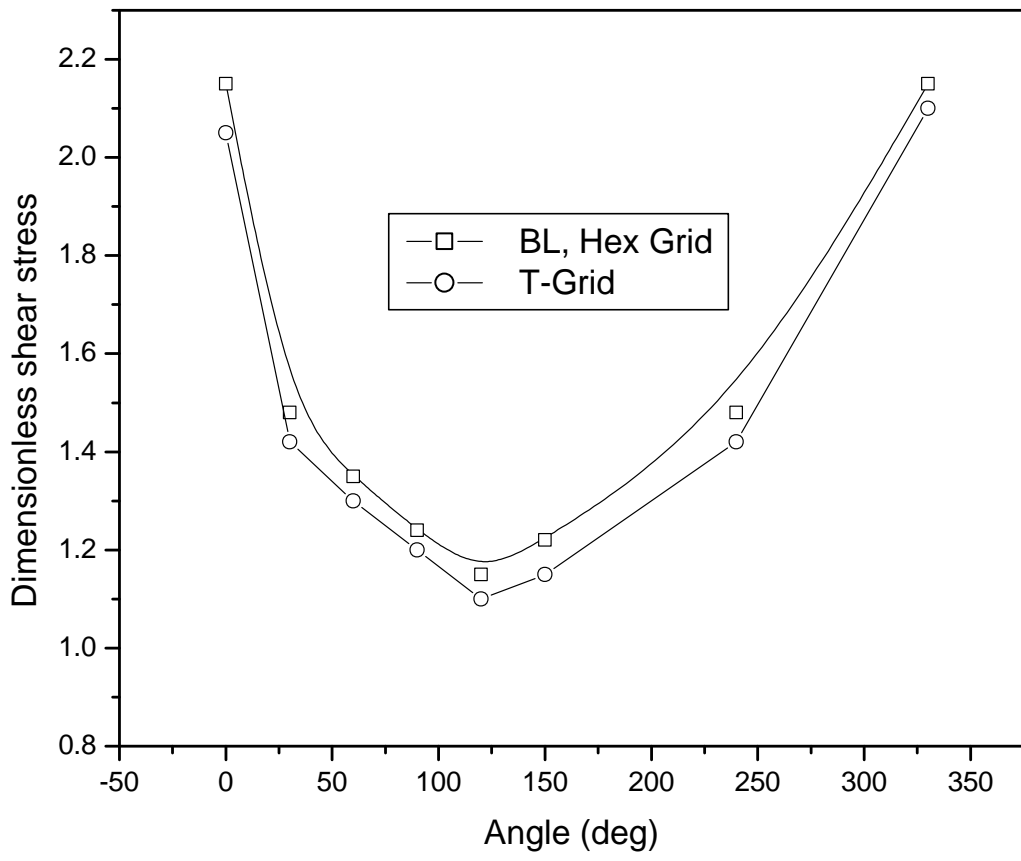
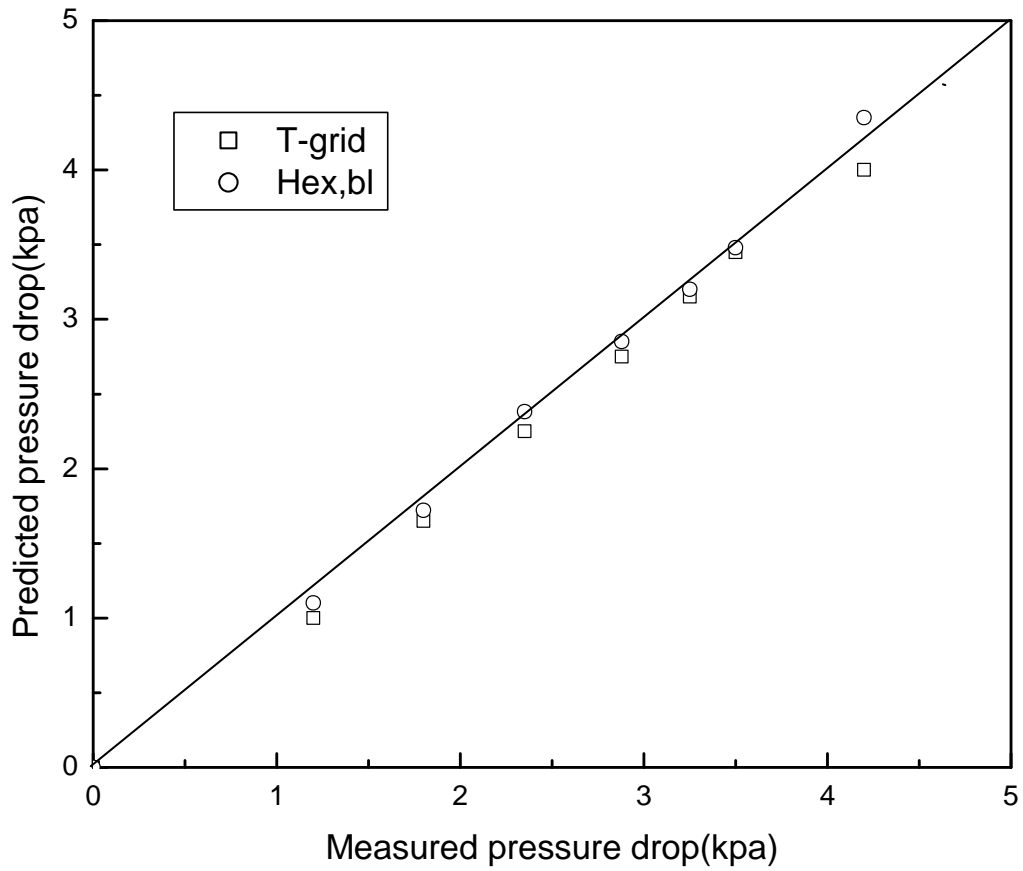


Fig. 7.45 Comparison plot of helical coil at different coil diameter

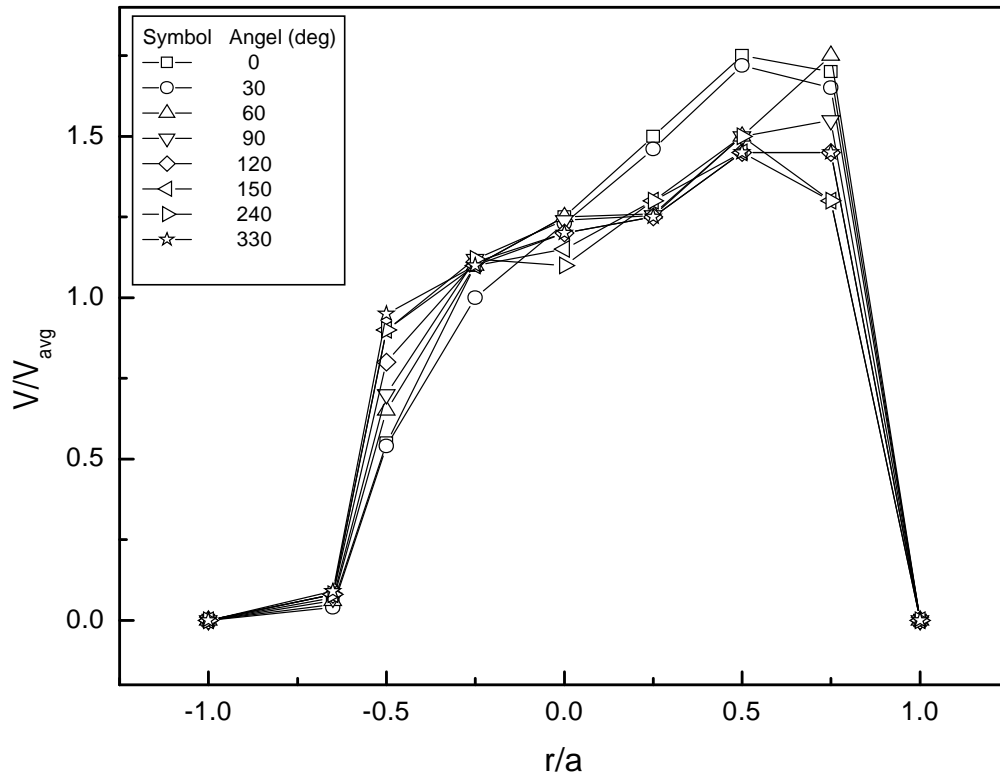


(a)

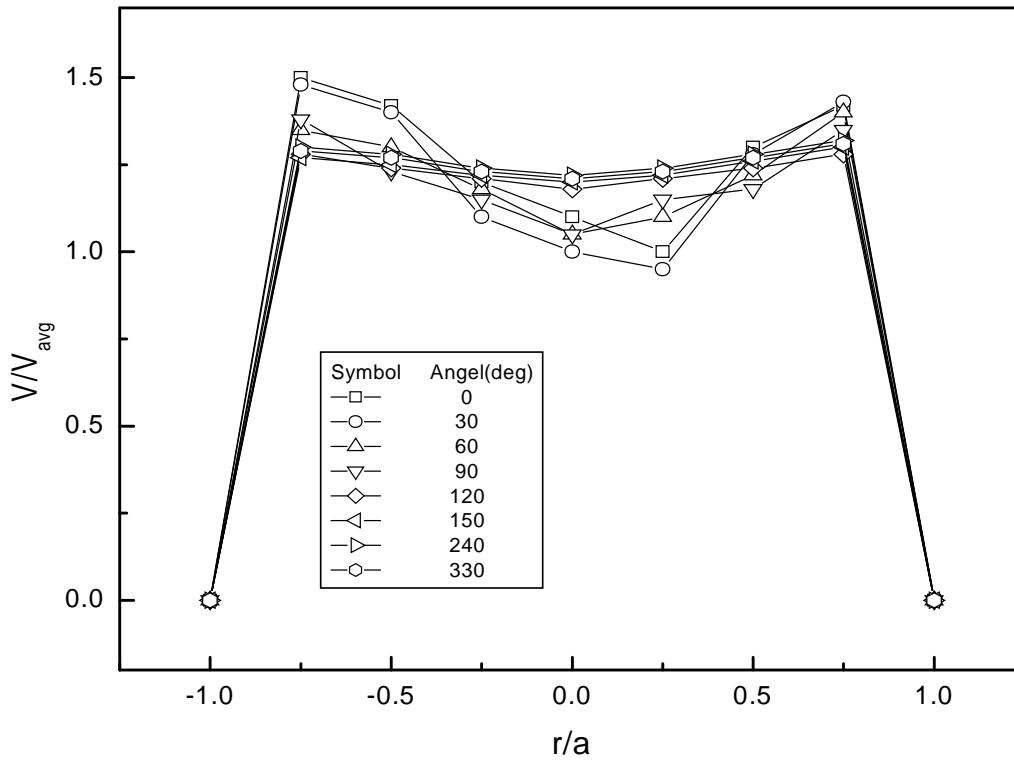


(b)

Fig. 7.46 Comparison of present prediction with the experimental data (a) dimensionless shear stress (b) pressure drop



(a)



(b)

Fig. 7.47 Development of axial velocity profile at different cross-sectional planes in curved tube at curvature ratio = 28, coil turn=2, $V_L=1.7086$ m/s, Liquid (SCMC) concentration (kg/m^3) =0.8 in (a) horizontal centerline and (b) vertical centerline

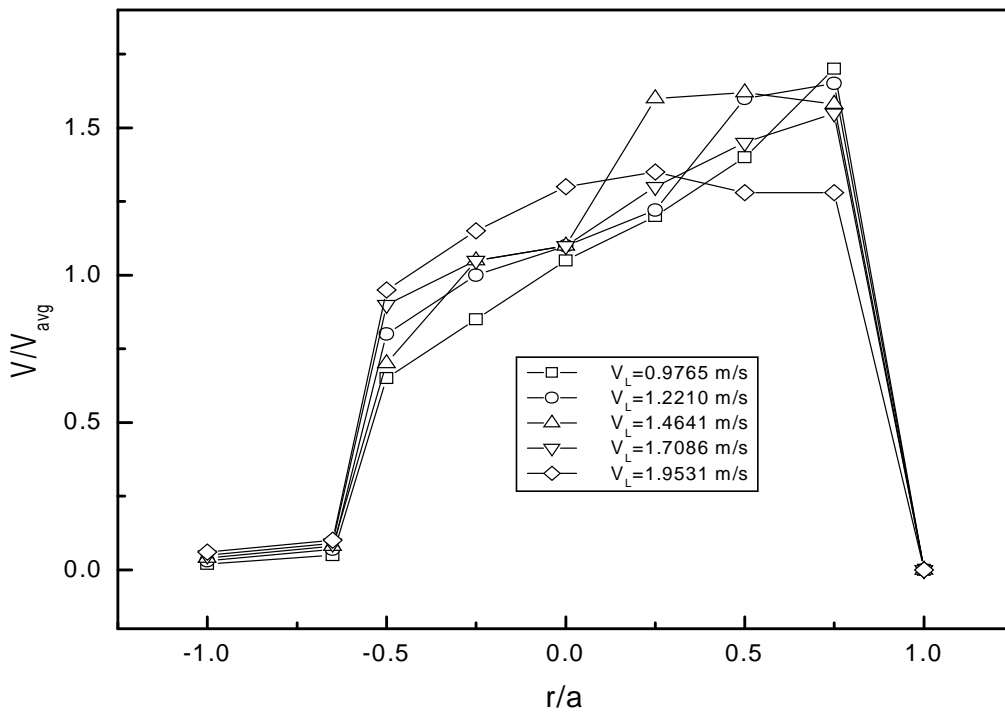
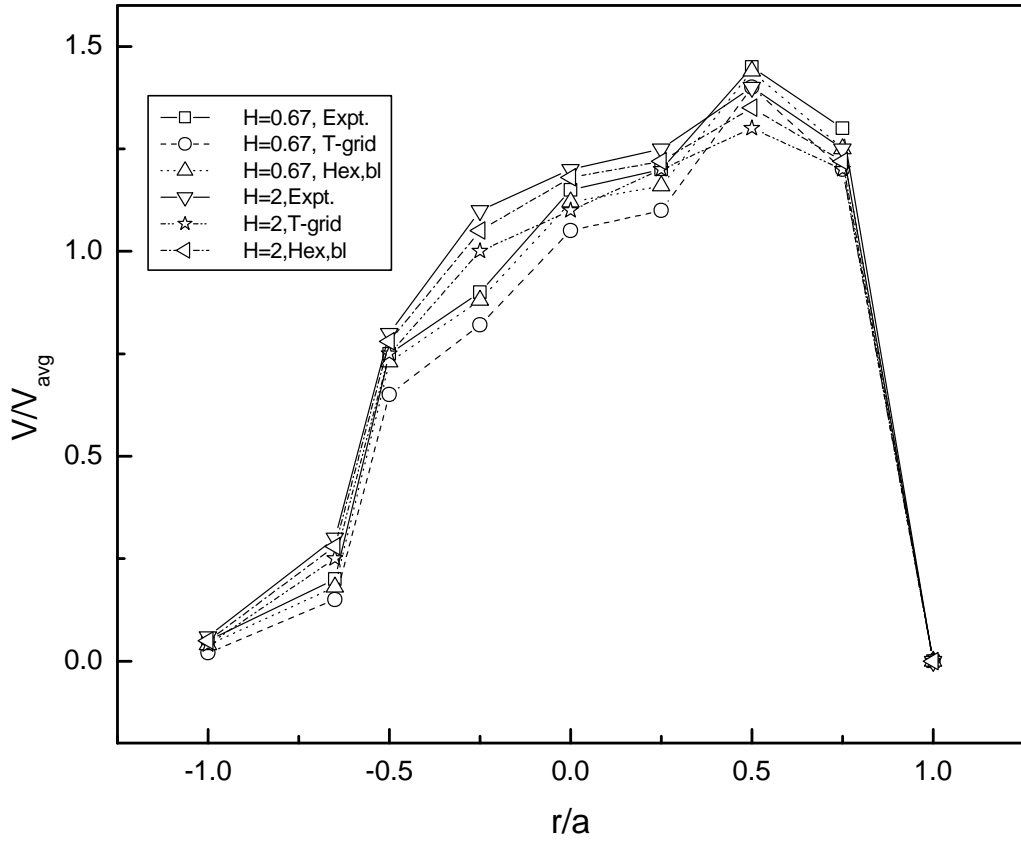
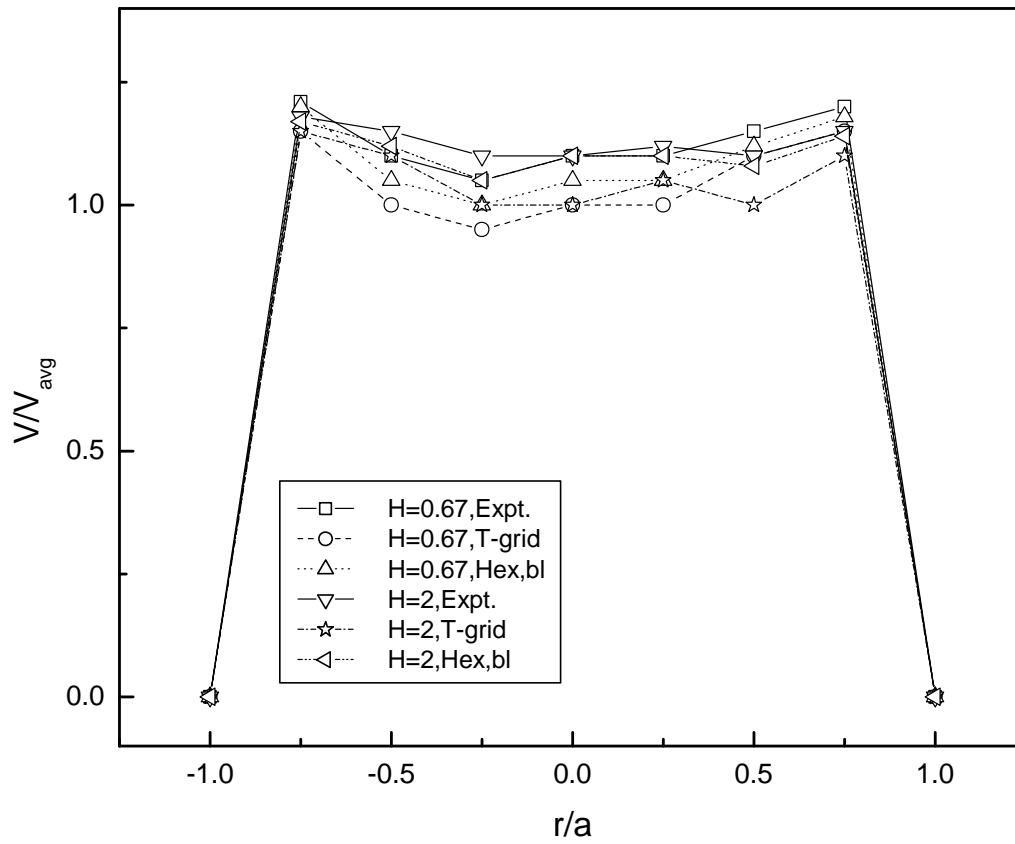


Fig. 7.48 Effect of liquid velocity on development of axial velocity profile in curved tube at curvature ratio=28, coil turn = 2

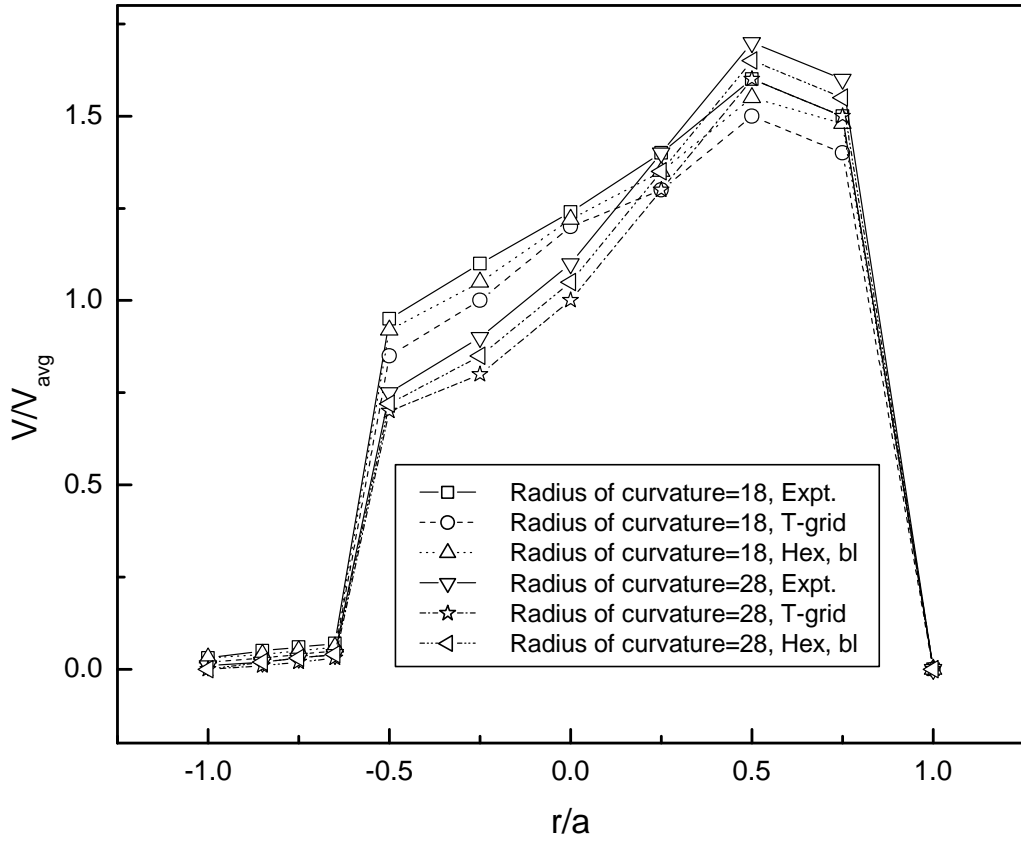


(a)

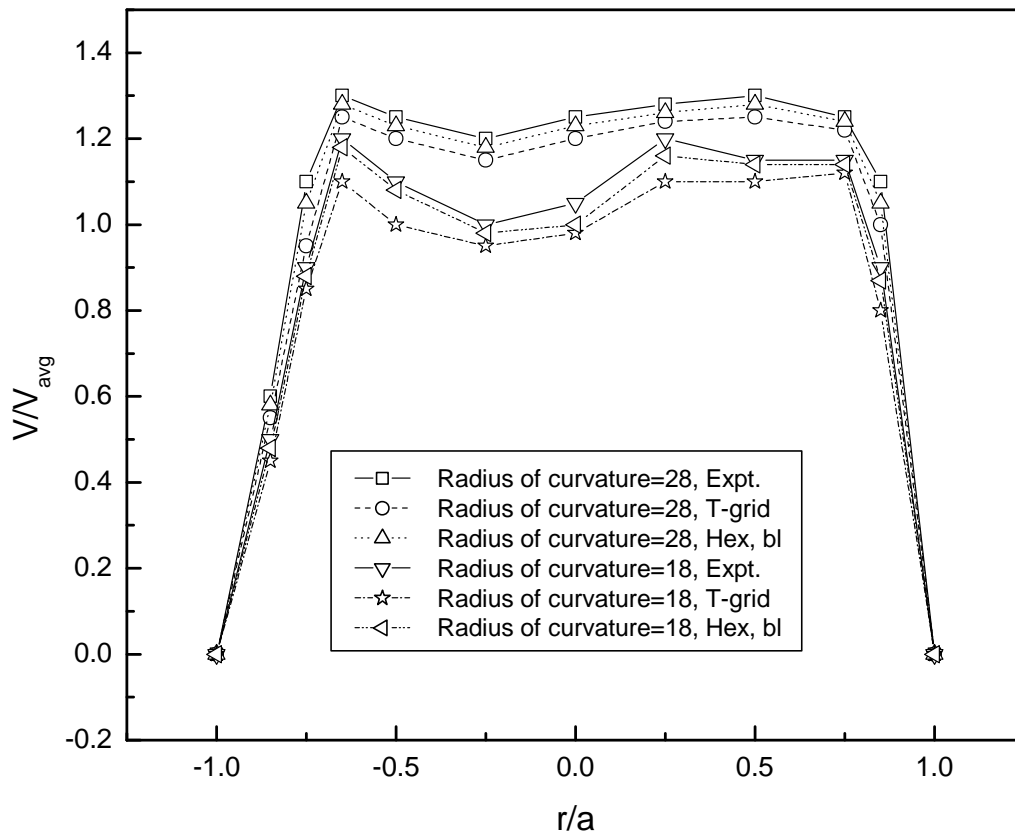


(b)

Fig. 7.49 Effect of coil turn or coil length, H on the development of axial velocity profile in (a) horizontal centerline (b) vertical centerline



(a)



(b)

Fig. 7.50 Effect of curvature ratio on the development of axial velocity profile in (a) horizontal centerline (b) vertical centerline, $V_L = 1.7086$ m/s, Liquid (SCMC) concentration (kg/m^3) = 0.8

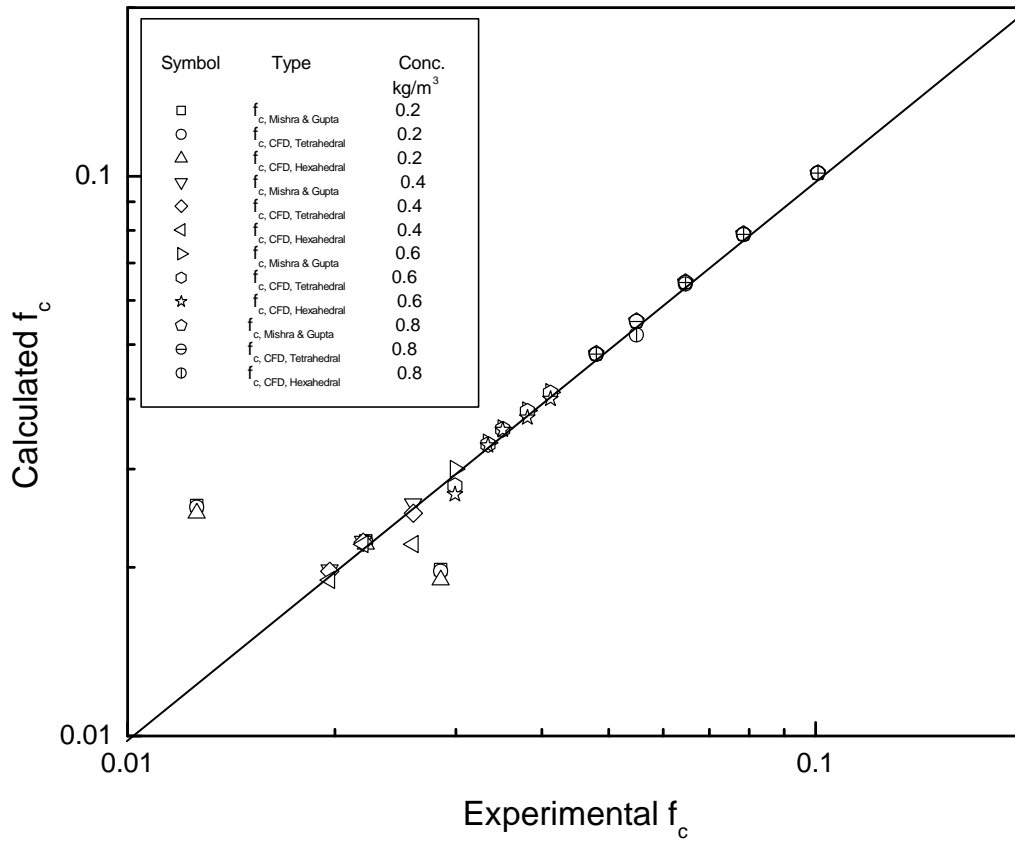


Fig. 7.51 Comparison plot of the experimental and calculated data for friction factor across the coil for different liquid (SCMC) concentration

Table 7.1 Range of variables investigated

Variables	Range
Liquid flow rate, m ³ /s	3.334 – 15.003 x10 ⁻⁵
Concentration of SCMC Solution (kg/m ³)	0.2 - 0.8
Flow behavior index of the liquid	0.6015 n' 0.9013
Consistency index (Ns ^{n'} /m ²) of the liquid	0.0142 K' 0.7112
Density of the liquid (kg/m ³)	1001.69 1003.83
Tube diameter, mm	9.33 – 12.00
Coil diameter, m	1.762 – 2.667
Number of turns	6 - 10

Table 7.2 Comparison of the experimental and CFD analysis data for the frictional pressure drop across the coil for different liquid (SCMC) concentration

Sl. No.	Liquid flow rate $Q_1 \times 10^5$ m^3/s	Frictional pressure drop per unit length, experimental $\left(\frac{\Delta P_c}{L_c}\right)$ Expt. kPa/m	Frictional pressure drop per unit length, $\left(\frac{\Delta P_c}{L_c}\right)$ CFD, T-grid kPa/m	Frictional pressure drop per unit length, $\left(\frac{\Delta P_c}{L_c}\right)$ CFD, Hex-BL grid kPa/m
1	2	3	4	5
SCMC Concentration(kg/m^3):0.2, Tube diameter(m): 0.00933, Coil diameter(m): 0.2162				
1	0.4875	0.095	0.09	0.092
2	0.732	0.15	0.13	0.14
3	0.9765	0.175	0.165	0.17
4	1.221	1.25	1.15	1.2
5	1.4641	1.55	1.45	1.5
SCMC Concentration(kg/m^3):0.4, Tube diameter(m): 0.00933, Coil diameter(m): 0.2162				
6	0.732	0.35	0.3	0.32
7	0.9765	0.5	0.4	0.45
8	1.221	1.95	1.77	1.9
9	1.4641	2.25	2.15	2.2
10	1.7086	2.65	2.55	2.6
11	1.9531	2.77	2.65	2.74
SCMC Concentration(kg/m^3):0.6, Tube diameter(m): 0.00933, Coil diameter(m): 0.2162				
12	0.732	0.45	0.35	0.4
13	0.9765	0.75	0.65	0.7
14	1.4641	2.65	2.55	2.6
15	1.7086	2.85	2.75	2.8
16	1.9531	3.15	3	3.1
SCMC Concentration(kg/m^3):0.8, Tube diameter(m): 0.00933, Coil diameter(m): 0.2162				
17	0.732	0.65	0.55	0.6
18	0.9765	0.95	0.85	0.9
19	1.221	2.85	2.75	2.8
20	1.7086	3.15	2.95	3.05
21	1.9531	3.5	3.4	3.45

Table 7.3 Comparison of the experimental and CFD analysis data for frictional pressure drop across the coil for liquid (SCMC) concentration of 0.8 kg/m³ and different coil diameters

Sl. No.	Liquid flow rate $Q_1 \times 10^5$ m^3/s	Frictional pressure drop per unit length, experimental $\left(\frac{\Delta P_c}{L_c}\right)_{\text{Expt.}}$ kPa/m	Frictional pressure drop per unit length, $\left(\frac{\Delta P_c}{L_c}\right)_{\text{CFD}}$ T-grid kPa/m	Frictional pressure drop per unit length, $\left(\frac{\Delta P_c}{L_c}\right)_{\text{CFD}}$ Hex-BL grid kPa/m
1	2	3	4	5
Tube diameter(m): 0.00933, Coil diameter(m): 0.1762				
1	0.732	0.529	0.45	0.5
2	0.9765	0.65	0.55	0.6
3	1.221	0.85	0.75	0.8
5	1.4641	1.12	1	1.1
6	1.7086	1.65	1.55	1.6
7	1.9531	2.25	2.1	2.2
Tube diameter(m): 0.00933, Coil diameter(m): 0.2162				
8	0.732	0.8	0.75	0.78
9	0.9765	0.95	0.88	0.9
10	1.221	1.3	1.2	1.25
11	1.7086	1.6	1.45	1.55
12	1.9531	1.95	1.85	1.9
13	0.4875	0.65	0.55	0.6
Tube diameter(m): 0.00933, Coil diameter(m): 0.2662				
14	0.732	0.95	0.85	0.9
15	0.9765	1.33	1.25	1.3
16	1.221	1.65	1.55	1.6
17	1.4641	1.95	1.85	1.9
18	1.7086	2.25	2.15	2.2
19	1.9531	2.65	2.55	2.6

Table 7.4 Comparison of the experimental and calculated data for friction factor across the coil for different liquid (SCMC) concentration

Sl. No.	Liquid flow rate $Q_1 \times 10^5$ m^3/s	Reynolds's number of liquid Re_1	Dean number of liquid De_1	Friction factor $f_{c, Expt.}$	Friction factor $f_{c, Mishra \& Gupta}$	Friction factor $f_{c, CFD, Tetrahedral}$	Friction factor $f_{c, CFD, Hexahedral}$
SCMC Concentration(kg/m^3):0.2, Tube diameter(m): 0.00933, Coil diameter(m): 0.2662							
1.	6.67	1247.11	233.47	0.0126	0.0258	0.0256	0.025
2.	8.34	1593.60	298.32	0.0222	0.0223	0.0222	0.022
3.	10.00	1947.05	0.0082	364.48	0.0198	0.0197	0.019
SCMC Concentration(kg/m^3):0.4, Tube diameter(m): 0.00933, Coil diameter(m): 0.2662							
1.	6.67	1247.11	233.45	0.0260	0.0260	0.025	0.022
2.	8.34	1593.60	298.32	0.0220	0.0223	0.0222	0.022
3.	10.00	1947.05	364.48	0.0196	0.0198	0.0197	0.019
SCMC Concentration(kg/m^3):0.6, Tube diameter(m): 0.00933, Coil diameter(m): 0.2662							
1.	6.67	417.29	78.11	0.0412	0.0411	0.041	0.04
2.	8.34	552.25	103.38	0.0351	0.0354	0.0353	0.0352
3.	10.00	694.32	129.97	0.0381	0.0381	0.038	0.037
4.	11.67	842.61	157.73	0.0334	0.0334	0.0332	0.033
5.	13.34	996.43	186.53	0.0299	0.0300	0.028	0.027
SCMC Concentration(kg/m^3):0.8, Tube diameter(m): 0.00933, Coil diameter(m): 0.2662							
1.	6.67	187.61	35.12	0.10069	0.10124	0.10123	0.10122
2.	8.34	256.32	47.08	0.0785	0.0788	0.0787	0.0786
3.	10.00	330.76	61.91	0.0647	0.0647	0.0646	0.0642
4.	11.67	410.33	76.81	0.0549	0.0551	0.055	0.052
5.	13.34	494.58	92.59	0.0480	0.0482	0.0481	0.048

Chapter 8

Gas-non-Newtonian liquid flow through helical coils – CFD analysis

This chapter deals with the Computational Fluid Dynamics (CFD) analysis to evaluate the frictional pressure drop for gas-non-Newtonian liquid through helical coils. The CFD analysis is verified with the experimental data obtained from our earlier experiments carried out by Biswas (2006) and Biswas & Das (2008).

8.1 Introduction

Two-phase flow through helical coil is much more complex in nature than that of straight pipes. Due to centrifugal action, when flow enters the curved position the heavier density phase, i.e., liquid is subjected to a larger centrifugal force which causes liquid to move away from the centre of curvature while the gas flows towards the centre of curvature. Despite various applications, the literature on two-phase flow through coiled tubes is rather scanty. The reasons for the lack of fundamental knowledge on two-phase flows are three-fold (Mandal and Das, 2003),

- i. Two-phase gas-liquid flow is a very complex physical phenomenon where many types flow regimes can exist (annular flow, jet flow, slug flow, bubbly flow, etc.);
- ii. The complex physical laws and mathematical treatment of phenomena occurring in the presence of the two phases (interface dynamics, coalescence, break-up, drag, etc.) are still largely undeveloped;
- iii. The numeric for solving the governing equations and closure laws of two-phase flows are extremely complex. Very often two-phase flows show inherent oscillatory behavior, requiring costly transient solution algorithms.

Owhadi et al. (1968) studied steam-water flow through coils and reported the two-phase frictional pressure drop agreed well the Lockhart-Martinelli (1949) correlation. Akagawa et al. (1971) studied gas-liquid flow through helically coiled tubes and

observed that the Lockhart-Martinelli (1949) correlation predicted their frictional pressure drop. Watanabe et al. (1986) studied air-water flow through helical coils and they experimentally found out the thickness of different points around the circumference. Unal et al. (1981) reported their experimental investigation on steam-water flow through coils and observed that the curvature ratio (D_c/d) had the very little influence on the two-phase pressure drop and proposed empirical correlation for the prediction of the two-phase pressure drop. Chen and Zhou (1981) tested the steam-water two-phase flow through vertical helical coils and proposed modified Lockhart-Martinelli (1949) correlation for their two-phase frictional pressure drop. Hart et al. (1988) studied single and gas-liquid flow through coils. Saxena et al. (1996) studied air-water flow through helical coils and observed that close similarities between the flow patterns in coiled tubes and those of the inclined tubes reported by Spedding et al. (1982). Czop et al. (1994) carried out experiments on two-phase SF₆-water flow through coil and observed that the Lockhart-Martinelli (1949) correlation gave the better prediction for the two-phase frictional pressure drop. Guo et al. (1994) studied steam-water flow through horizontal helical coils at high pressure and proposed empirical correlation for frictional pressure drop. Awaad et al. (1995) studied air-water flow through coils and observed superficial velocities of air or water had affect the pressure drop multiplier significantly, where as helix angle had insignificant effect on two-phase pressure drop. Saxena et al. (1996) proposed a model that describes the liquid residence time distribution for upward and downward co-current air-water two-phase flow in coiled tubes for turbulent and laminar liquid flow. Xin et al. (1997) reported air-water two-phase flow through coils and proposed a two-phase frictional pressure drop equation by modifying the Lockhart-

Martinelli (1949) parameter. They observed that the experimental holdup data matches well with the Lockhart-Martinelli (1949) correlation. Guo et al. (2001) studied steam-water two-phase flow through inclined helical coils and compared the two-phase pressure drop with the horizontal helical coils, and modified Chen's (1982) correlation to analyze their data. Gao et al. (2003) numerically simulated stratified oil-water two-phase flow in a horizontal tube. They proposed a new mechanistic approach to correlate the pressure drop in coils. Mandal and Das (2003) studied gas-Newtonian liquid flow through helical coils and proposed empirical correlations for two-phase friction factor and void fraction. Santini et al. (2008) proposed frictional two-phase pressure drop correlation based on the energy balance of the two-phase mixture for their experiments on the steam-water flow through helically coiled steam generator. Biswas and Das (2008) studied gas-non-Newtonian liquid flow through coils and developed empirical correlations for frictional pressure drop.

In order to achieve optimum performance, an accurate design technique is necessary for the prediction of two-phase pressure drop through helical coil tube. This chapter deals with the computational fluid dynamics technique, FLUENT 6.3, to predict the pressure drop in helical coil tubes.

8.2 Experimental

The detail experimental set up (Fig. 8.1), techniques and results (Table 8.1) are taken from published Ph. D. thesis of A. B. Biswas (2006) and their subsequent publication Biswas and Das (2008).

8.3 Mathematical Model

Governing equations and numerical methods are described in chapter 2. Laminar, non-Newtonian Power Law Eulerian model is used as multiphase model for the CFD analysis. These basic equations (as discussed in chapter 2) are solved subject to the following boundary conditions,

- (i) The helical coils walls are assumed rigid and a no-slip condition is imposed.
- (ii) At the outlet, the velocities are free but the normal and tangential stresses are constrained to be zero and the gauge pressure is set to zero.
- (iii) At the inlet, a uniform velocity profile is used with a time varying forcing function representative of flow in the left portion of the helical coils.
- (iv) Negative gravitational acceleration, -9.8 m/s^2 is added. Since flow is against the gravity.

8.3.1 Computational Fluid Dynamics (CFD) Procedure

Geometries for the helical coils are created in Gambit 6.3 preprocessor. A typical mesh has about $3 \times 10^4 - 2 \times 10^5$ order unstructured t-grid and unstructured boundary layer hex-wedge cooper schemes are used. Inlet and outlet are located at each end of the helical coil. The inlet is used to specify the inlet velocity and outlet is used to specify pressure outlet. These geometries of the coils are imported into Fluent 6.3 in a Cartesian coordinate system. Fluent 6.3 solved the governing equations in 3-D geometry. Laminar non-Newtonian Power Law model have been used for simulation. The model solves for Navier-stokes equation at prescribes velocities. The governing equations are non linear and several iterations of loop must be performed before a convergent solution is obtained. The first-order upwind scheme is used in the discretization of set of governing equations,

standard interpolation schemes is used for calculating cell-face pressures for using the Segregated solver in Fluent 6.3. Pressure-velocity coupling refers to the numerical algorithm which uses a combination of continuity and momentum equations to derive an equation for pressure (or pressure correction) when using the segregated solver. Simple algorithm is used.

A general procedure to simulate the two-phase gas-non-Newtonian fluid mixing in helical coil tubes are based on Gambit 6.3 and Fluent 6.3 software is outlined below,

1. Perform meshing under Gambit 6.3.
 - Create a computational domain at the flow region,
 - The grids were generated using boundary layer hexahedral meshes and t-grid (tetrahedral grid),
 - Controlling a smooth change in the mesh size by size functions,
 - Specify boundary and continuum types,
 - Examine the mesh to ensure that the high skewness is below 0.5 for hexahedral and below 0.9 for tetrahedral mesh.
2. Import the mesh file to Fluent 6.3 and check the mesh.
3. Define a 3-D, unsteady, implicit, and pressure-based solver.
4. Activate the Eulerian laminar non-Newtonian power law multiphase model.
5. Define a Eulerian laminar model. Slip velocity is added.
6. Enable the SCMC properties with laminar flow conditions using the text command: `define/models/viscous/laminar`

7. Define the phases by setting SCMC as the primary phase and gas as the secondary phase, and keeping the default selection of Schiller-Naumann drag model in the phase interaction panel.
8. Define the operating conditions by turning on gravity and specify the operating density.
9. Solution control methodology – Under relaxation factors – 0.5 for pressure, 0.3 for momentum, 0.1-0.9 for volume fraction, and default values for the other parameters. Standard schemes – STANDARD for momentum and volume fraction, and 1st order upwind for other variables. Pressure-velocity SIMPLE coupling used;
10. Initialize the solution – velocity;

Enable the plotting of residuals during the calculation, and kept the default convergence criteria, 1×10^{-3} for continuity and 1×10^{-5} all residuals.

8.3.2 Assumptions for air-SCMC flow through helical coils

The following concepts and assumptions were made:

1. The solution temperature is constant at 30⁰C, i.e., room temperature and each phase is an isothermal and incompressible fluid;
2. A single pressure is shared by both phases;
3. Momentum and continuity equations are solved for each phase;
4. Our system behaves like a plug and slug flow regimes. But we assumed two-phase flow as a bubbly flow due to simplicity of calculation in which SCMC is treated as the primary phase while gas is treated as the secondary phase;

5. The secondary phase consists of uniform and unchanging bubbles dispersed in a continuous phase;
6. The bubbles size is assumed to be small, 0.1mm spherical in size;
7. Two-phase Eulerian laminar non-Newtonian power law model is used;
8. Physical properties are uniform throughout;
9. Different phases move at different velocities (slip velocities);
10. The drag force from liquid phase acting on the gas bubbles is included into the interphase momentum exchange;
11. There are no external body force and virtual mass force, and the effect of lift force on the bubbles is negligible.

8.4 Results and discussion

8.4.1 Convergence and grid independency

The convergence criterions were set at 10^{-5} for all equations except for the transport equation which residual was set at 10^{-3} . A computational domain L 200D was used to ensure fully developed flow results could be obtained for all helical coil tubes. In general the final results depend upon mesh geometries. Subsequent decrement and increment in mesh resolution by 50% were applied to evaluate if the employed mesh resolution was adequate to obtain accurate solutions. It was observed that when the mesh resolution was decreased by 50% the axial velocity profile was 4-10% of the currently employed mesh velocity profile for helical coils. As the present mesh resolution was increased by 50% the axial velocity profile changes 1-5% for helical coils. These results suggest that the current mesh resolution is sufficient to obtained grid independent solutions for the proposed model.

8.4.2 Computational Fluid Dynamics (CFD) analysis

Tetrahedral and hexahedral grids are used in helical coils for the CFD analysis.

Figs. 8.2 – 8.3 illustrates the contour plot of static pressure for nine and six turn helical coil at hexahedral and tetrahedral grid. Fig. 8.4 shows that contour plot of static pressure at various planes along the length of the coil varying with turn of the coil. Fig. 8.5 shows that static pressure varying with angle and number of turn and length of the coil.

Fig. 8.6 shows that contour plot of static pressure (mixture) at the selected plane along the length of the coil for a first turn varying with angle. Figs. 8.7 – 8.9 show that contour plot of static pressure at the selected plane along the length of the coil varying angle and turn of the coil. Fig. 8.10 shows that contour plot of total pressure (mixture) varying with angle and coil turn or height. Fig. 8.11 shows that contour plot of total pressure (mixture) at the selected plane along the length of the coil for a first turn varying with angle. All these figures indicate that the static pressure decreases gradually after passing the coil turn. This effect is more with increasing the pseudoplasticity of the liquid, i.e., SCMC concentration in the liquid. In a particular turn the static pressure decreases from angle 0° to 240° and then the static pressure is almost constant from angle 240° - 330° , that is probably due to the fully developed flow condition attained. Due to the centrifugal force the lower density air phase shifted toward the inner side and gives lower pressure and the heavier density liquid phase at the outer side wall of the coil gives high pressure.

Fig. 8.12 shows that contours of velocity magnitude at various planes along the length of the coil. Fig. 8.13 shows that contour plot of velocity at the selected plane along

the length of the coil varying with angle and turn of the coil, from 1 – 9. Fig. 8.14 Contour of velocity magnitude at the different angular plane and at any fixed turn of the coil. Fig. 8.15 shows that contours plot of velocity magnitude for air-phase varying with angle and coil height and Fig. 8.16 shows that contours of velocity magnitude for air-phase at the first turn of the coil varying with angle at the selected plane along the length of the coil. Fig. 8.17 shows that contours plot of velocity magnitude for liquid phase varying with angle and coil height and Fig. 8.18 shows that contour of velocity magnitude for liquid phase at the first turn of the coil varying with angle for at the selected plane along the length of the coil. Fig. 8.19 illustrates the contour plot of velocity vector coil at hexahedral and tetrahedral grid. Fig. 8.20 shows that plot of velocity vector varying with angle and coil turn or height at hexahedral grid for helical coil and Fig. 8.21 shows that contours plot of velocity vector at the first turn of the coil varying with angle for hexahedral grid at the selected plane of the helical coil. Fig. 8.22 shows that contour plot of velocity vector for liquid phase. Fig. 8.23 shows that velocity vector plot for liquid phase varying with angle and coil height at hexahedral grid for helical coil. Fig. 8.24 Velocity vector plot for liquid phase varying with angle and coil turn1 at hexahedral grid at the selected plane of helical coil. Fig. 8.25 shows that contour plot of velocity vector for air phase at hexahedral grid for helical coil. Fig. 8.26 shows that velocity vector plot for air phase varying with angle and coil height at hexahedral grid for the helical coil. Fig. 8.27 shows that contours plot of velocity vector for air phase at the first turn of the coil varying with angle at hexahedral grid at the selected plane along the length of the coil.

These figures clearly indicates that heavier density goes to outer wall side of the coil and lower density air phase inner wall side of the coil due to centrifugal force and their also exists slip between the phases. The velocity changes smoothly to the with the increase of angle, 0° - 240° , for a particular coil turned and from the angle 240° - 330° it is remain unchanged probably due to fully developed flow condition established.

From these plots we observed that air phase shifts the location of the maximum velocity towards the outer wall of the coiled tube. The velocity profiles flatten when the velocity is increased until the developing stage is appeared. The developing stage starts from angle 240° and end at angle 330° . Since air is lighter, always stating at the inner upper side of the coil tube.

As fluid flows inside the coil tube a secondary flow develops due to centrifugal forces. These centrifugal and shear forces move the fluid near the centerline to outer and the fluid near the walls towards inward direction, resulting a secondary flow known as Dean vortices. Dean vortices represent centrifugal and shear instabilities that occur when a viscous fluid flows in a coil tube (Yao and Berger, 1975; Vashisth and Nigam (2009). It has been shown by Dean (1928b) that a non-dimensional parameter called Dean number characterizes these flow and defined as,

$$De = \frac{Re}{\left[\frac{D_c}{d} \right]^{0.5}} \quad (8.1)$$

The Dean number represents the ratio of the square root of the product of the inertial and centrifugal forces to the viscous force. Since the secondary flows are induced by the centrifugal force, and their interactions are primarily with the viscous force, the Dean number is the measure of the magnitude of the secondary flow. Fig. 8.14 clearly

characterized by longitudinal vortices and the axial velocity contours show the familiar C-shape. It also shows the velocity field shifted outer wall of the coil tube.

Fig. 8.28 shows that contour of volume fraction for air-liquid phase varying with angle and coil turn. Fig. 8.29 shows that volume fraction contours for liquid phase at various planes along the length of the coil. Fig. 8.30 shows that contours of volume fraction for liquid phase at the first turn of the coil varying with angle. Fig. 8.31 shows that contours plot of volume fraction for liquid phase varying with angle and coil height. Fig. 8.32 shows that contour of volume fraction for air phase at various planes along the length of the coil. Fig. 8.33 shows that contour plot of volume fraction for air phase at the first turn of the coil varying with angle. Fig. 8.34 contours plot of volume fraction for air phase varying with angle and coil height.

All these figures indicate that the volume fraction of the lighter phase, i.e., air, is gradually covers the top inner side of the coil as the number of turn increases and volume fraction of the liquid phase is more at the bottom side as turn increase comparing with the entering condition (Fig. 8.28). But heavier density liquid phase shifted towards the outer wall and lighter air phase shifted towards the inner wall side with increasing angle (Fig. 8.30 – 8.33).

Fig. 8.35 shows the liquid path lines in the mixture. It illustrates that heavier density liquid phase goes to outer wall side of the coil and lighter density air phase goes to inner side of the coil wall due to centrifugal force and slip existing between the mixtures.

Fig. 8.36 indicates the two – phase frictional pressure drop per unit length of coil increases with increasing liquid flow rate at constant SCMC concentration, tube and coil

diameter. The experimental results from Biswas and Das (2008) matches well with CFD simulated result for hexahedral grid than the tetrahedral grid.

Fig. 8.37 indicates the two-phase frictional pressure drop per unit length of coil increases with increasing the pseudoplasticity of the liquid. The experimental results Biswas and Das (2008) matches well with CFD simulated results. Fig. 8.38 indicates the two – phase frictional pressure drop per unit length of coil increases with increasing coil diameter. The experimental results Biswas and Das (2008) matches well with CFD simulated results. Fig. 8.39 indicates comparison of present prediction with the experimental data of Biswas and Das (2008) for the frictional pressure drop and the void fraction. The predicted data agree well with the experimental data with in an error of $\pm 15\%$.

Fig. 8.40 indicates effect of gas and liquid velocity on liquid volume fraction in curved tube at curvature ratio = 18 and coil length = 2 m. It can be seen from Fig.8.40 at $V_L = 0.72$ m/s when gas velocity increases from 0.8243 to 1.8243 m/s, the volume fraction of liquid reduces from 0.51 to 0.38. Fig. 8.41 shows that effect of gas and liquid velocity on development of axial velocity profile in curved tube at curvature ratio = 18 and coil length = 2 m, $V_L = 1.9531$ m/s, in horizontal centerline. It indicates that velocity profiles flatten when the liquid velocity is increased.

Fig. 8.42 shows the effect of coil turn or height on the development of axial velocity profile in (a) horizontal centerline and (b) vertical centerline. It indicates that at height = 0, the velocity contours are symmetrical to the centerline of the tube. As the coil turn or height is increased the velocity contours becomes asymmetrical. The axial velocity profiles for coiled tube at different angular planes are shown in Fig. 8.42(a) for

horizontal centerline and Fig. 8.42(b) for vertical centerline. In the horizontal centerline, the maximum velocity shifts towards the outer wall of the pipe due unbalanced centrifugal forces on the main flow. It can be seen that the velocity profiles tends to flatten as the value of coil turn or height decreases for the vertical and horizontal centerline.

Fig. 8.43 shows that effect of angle on the development of axial velocity profile in (a) horizontal centerline and (b) vertical centerline. It indicates that the maximum velocity is shifted towards the outer wall of the coiled tube. It can also state that the flow gets almost fully developed at angle 240° , since at 240° and 330° velocity profiles have very minor changes. As angle is increased, the axial velocity becomes asymmetrical. Due to the unbalanced centrifugal forces on the main flow, the maximum velocity shift towards the outer wall of the coil, in the horizontal centerline.

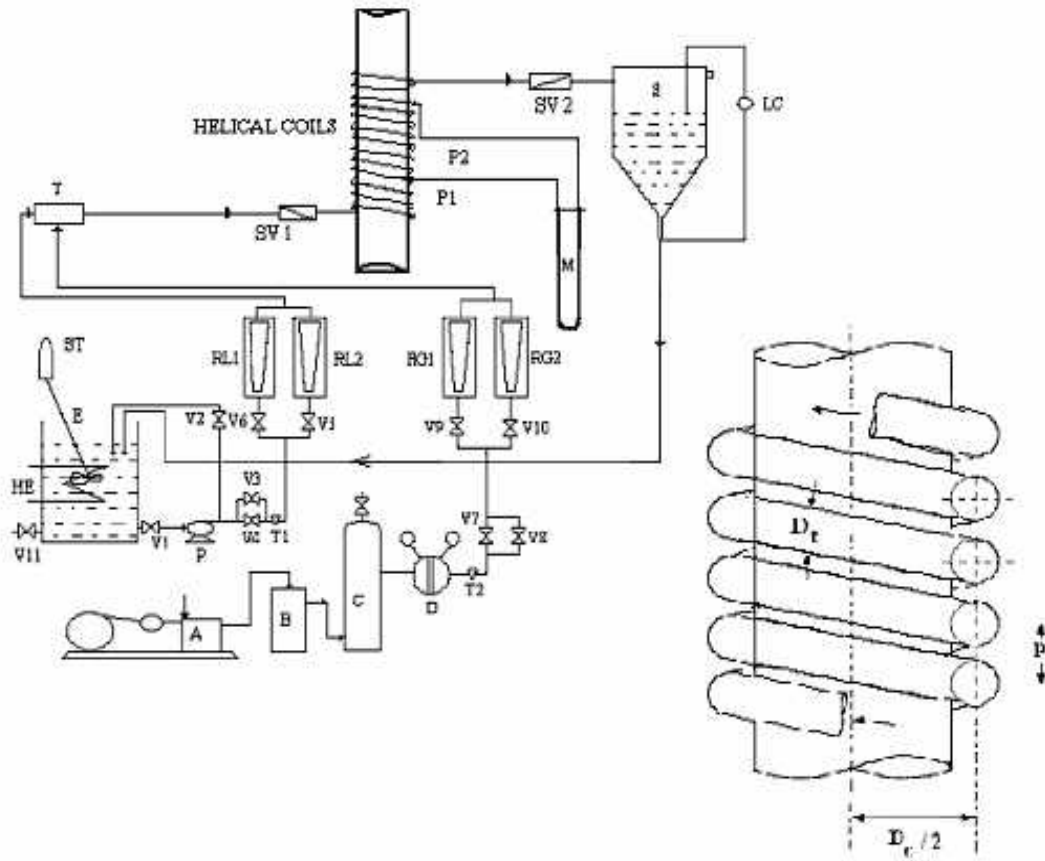
Fig. 8.44 shows the effect of curvature ratio on the development of axial velocity profile in (a) horizontal centerline and (b) vertical centerline, at $V_G = 0.8433$ m/s, $V_L = 1.9531$ m/s. It indicates that as the curvature ratio is increased, the coil approaches towards a straight tube (curvature ratio ∞). This minimizes the curvature effect as centrifugal forces become less predominant for higher curvature ratio coils. This is evident from the figure as the velocity profiles flattens in the case of curvature ratio = 18, due to action of strong centrifugal force.

8.5 Conclusions

1. Computational Fluid Dynamics (CFD) analysis is reported for different gas-non-Newtonian liquid flow through different coils. The experiments data are taken from

Biswas (2006) and their published paper Biswas and Das (2008) and these experiments are carried out in our laboratory.

2. The effect of secondary flow due to centrifugal forces is clearly demonstrated.
3. From the contour plots of volume fraction it demonstrated that existence of phase separation as the air liquid solution passes through the coil.
4. CFD analysis clearly predicts the effect of gas flow rate, liquid concentration, coil diameter on the two-phase frictional pressure drop, gas and liquid velocity on liquid volume fraction, gas and liquid velocity on the development of axial velocity profile, coil turn or height on the development of axial velocity profile, curvature ratio on the development of axial velocity profile, angle on the development of axial velocity profile
5. The CFD modeling for two phase pressure drop and void fraction matches well with the experimental results of Biswas (2006). It is also noted that simulated result for hexahedral grid very close to experimental result than tetrahedral grid.



A: Compressor, B: Oil Tray, C: Gas Cylinder, D: Gas Regulator, E: Solution Tank, HE: Heat Exchanger, LC: Level Controller, P: Pump, P1, P2: Pressure Tapping, RL1, RL2: Liquid Rotameter, RG1, RG2: Gas Rotameter, S: Separator, ST: Stirrer, T: T-Mixer, T1, T2: Thermometer, V1-V11: Valves

Fig. 8.1 Schematic diagram of helical coil

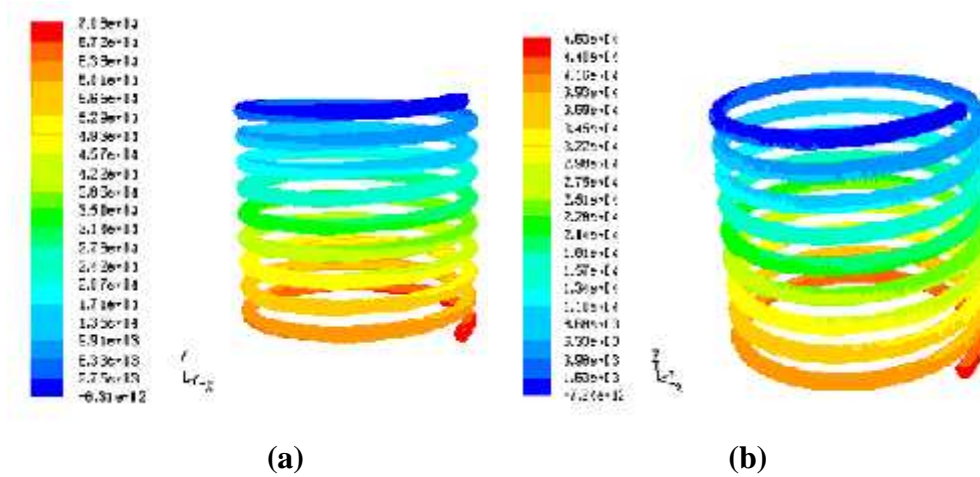


Fig. 8.2 Contour plot of static pressure mixture at (a) hexahedral and (b) tetrahedral grid, Coil dimension, D_t : 0.00933 m, D_t/D_c : 0.0431, D_c : 0.2162 m, Total length: 6.10 m, Turn: 9, Concentration of SCMC solution: 0.8 kg/m^3 , Liquid velocity: 1.9531 m/s, Gas velocity: 0.7218 m/s, Gas Fraction, r_g : 0.231

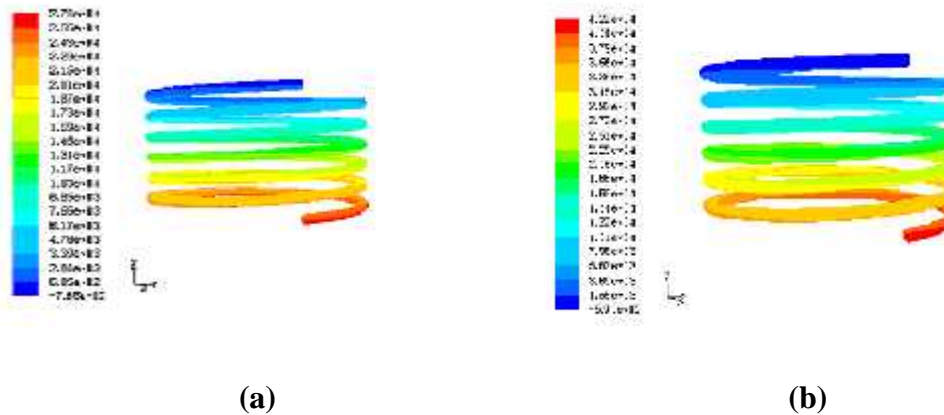


Fig. 8.3 Contour plot of static pressure at (a) hexahedral and (b) tetrahedral grid, Coil dimension, D_t : 0.00933 m, D_t/D_c : 0.0350, D_c : 0.2662 m, Total length: 5.01 m, Turn: 6, Concentration of SCMC solution: 0.8 kg/m^3 , Liquid velocity: 1.7086 m/s, Gas velocity: 0.9282 m/s, Gas fraction, r_g : 0.3750

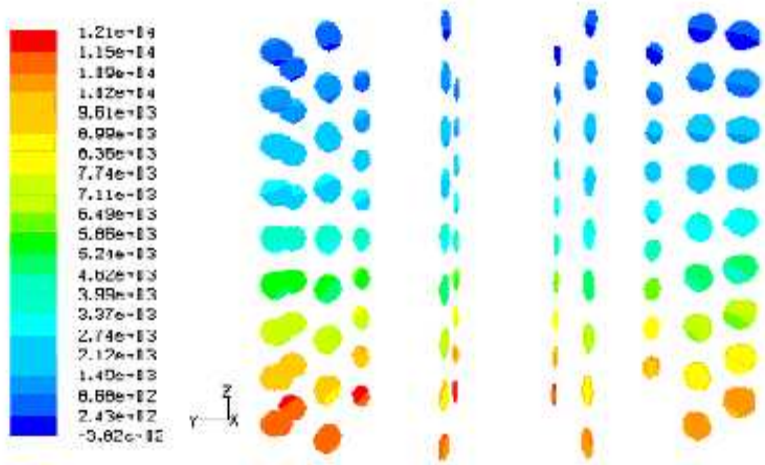


Fig. 8.4 Contour plot of static pressure mixture at various planes along the length of the coil at hexahedral grid,
 Coil dimension, D_t : 0.00933 m, D_t/D_c : 0.0431, D_c : 0.2162 m, Total length: 6.10 m, Turn: 9, Concentration of SCMC solution: 0.8 kg/m^3 , Liquid velocity: 1.9531 m/s, Gas velocity: 0.7218 m/s, Gas Fraction, r_g : 0.231

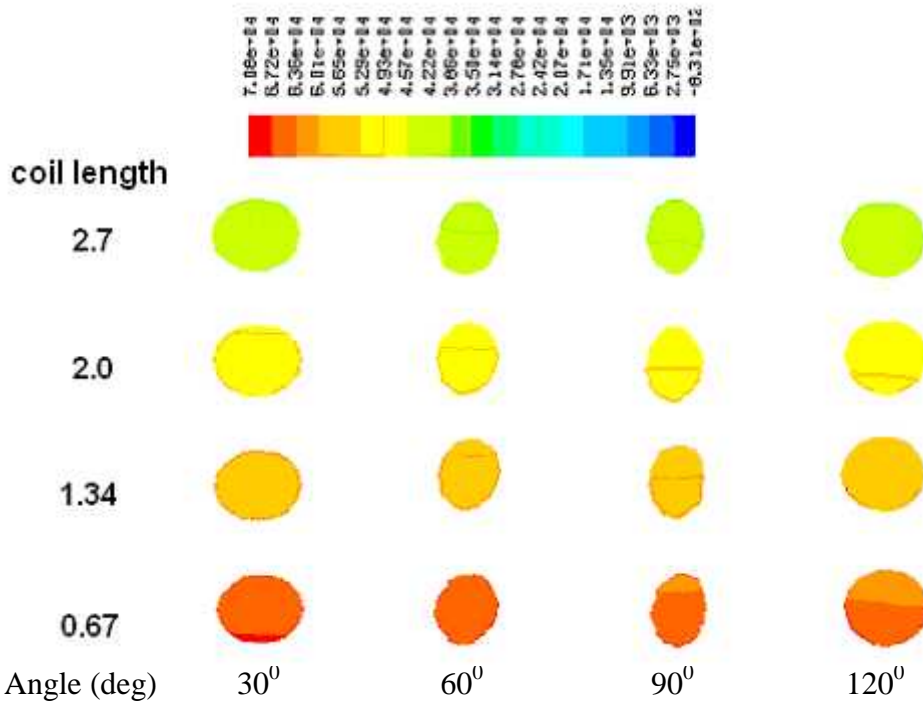


Fig. 8.5 Contour plot of static pressure, mixture at hexahedral boundary layer grid varying with coil turn, coil length and angle of the coil,
 Coil dimension, D_t : 0.00933 m, D_t/D_c : 0.0431, D_c : 0.2162 m, Total length: 6.10 m, Turn: 9, Concentration of SCMC solution (kg/m^3): 0.8, Liquid velocity, V_L (m/s): 1.9531, Gas velocity, V_g (m/s): 0.7218, Gas Fraction, r_g : 0.2310

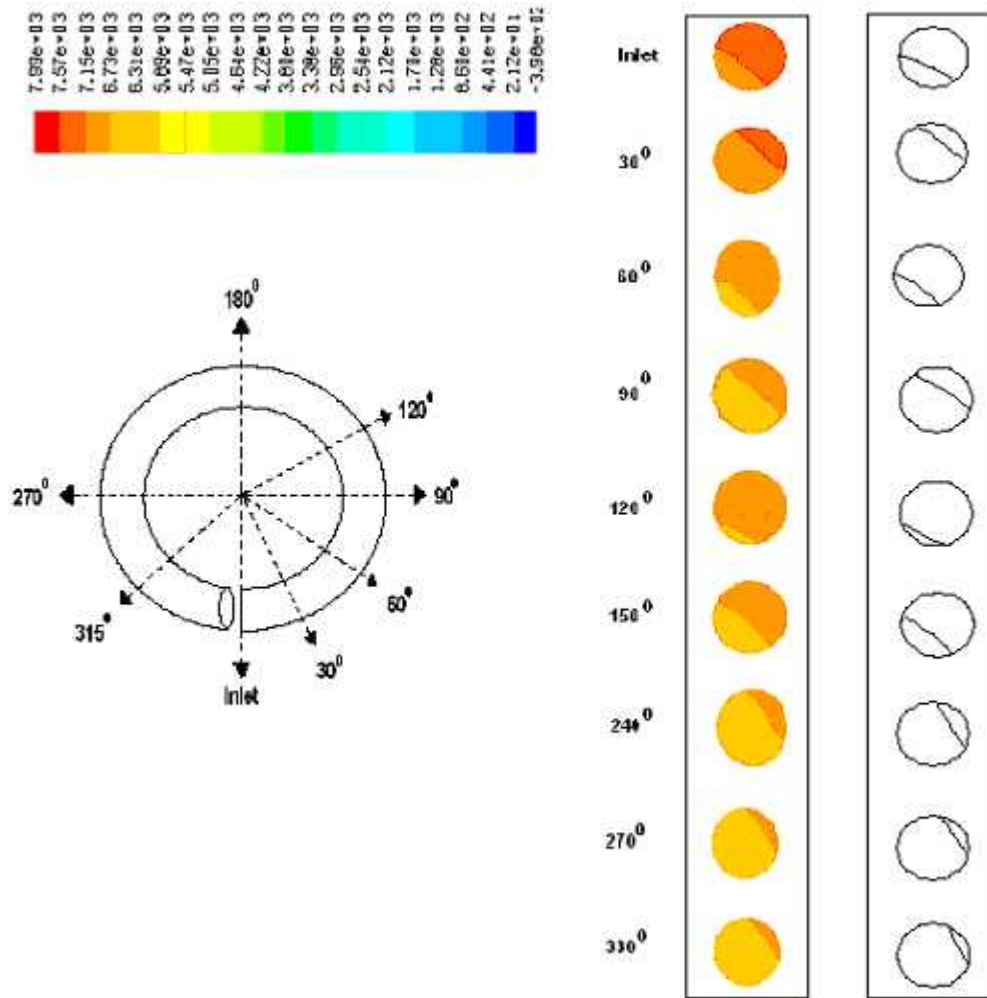


Fig. 8.6 Contour plot of static pressure (mixture) varying with angle at the first turn of the coil,

Coil dimension, D_i : 0.00933 m, D_i/D_c : 0.0431, D_c : 0.2162 m, Total length: 6.10 m, Turn: 9, Concentration of SMC solution (kg/m^3): 0.8, Liquid velocity, V_L (m/s): 1.9531, Gas velocity, V_g (m/s): 0.7218, Gas Fraction, r_g : 0.2310

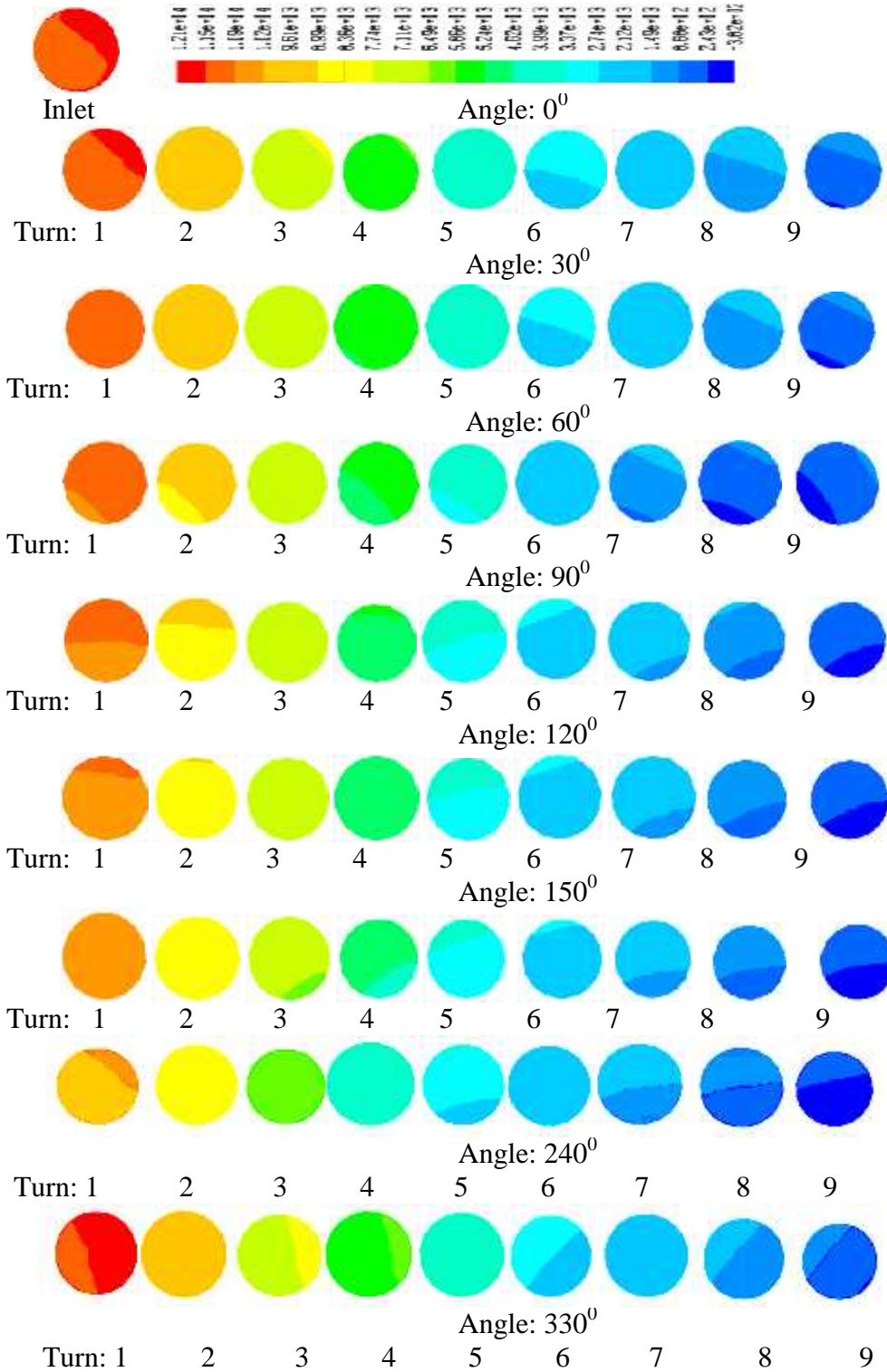


Fig. 8.7 Contour plot of static pressure at the selected plane along the length of the coil varying angle and turn of the coil, from 1-9,

Coil dimension, D_i : 0.00933 m, D_i/D_c : 0.0431, D_c : 0.2162 m, Total length: 6.10 m, Turn: 9, Concentration of SCMC solution (kg/m^3): 0.8, Liquid velocity, V_L (m/s): 1.9531, Gas velocity, V_g (m/s): 0.7218, Gas Fraction, Γ_g : 0.2310

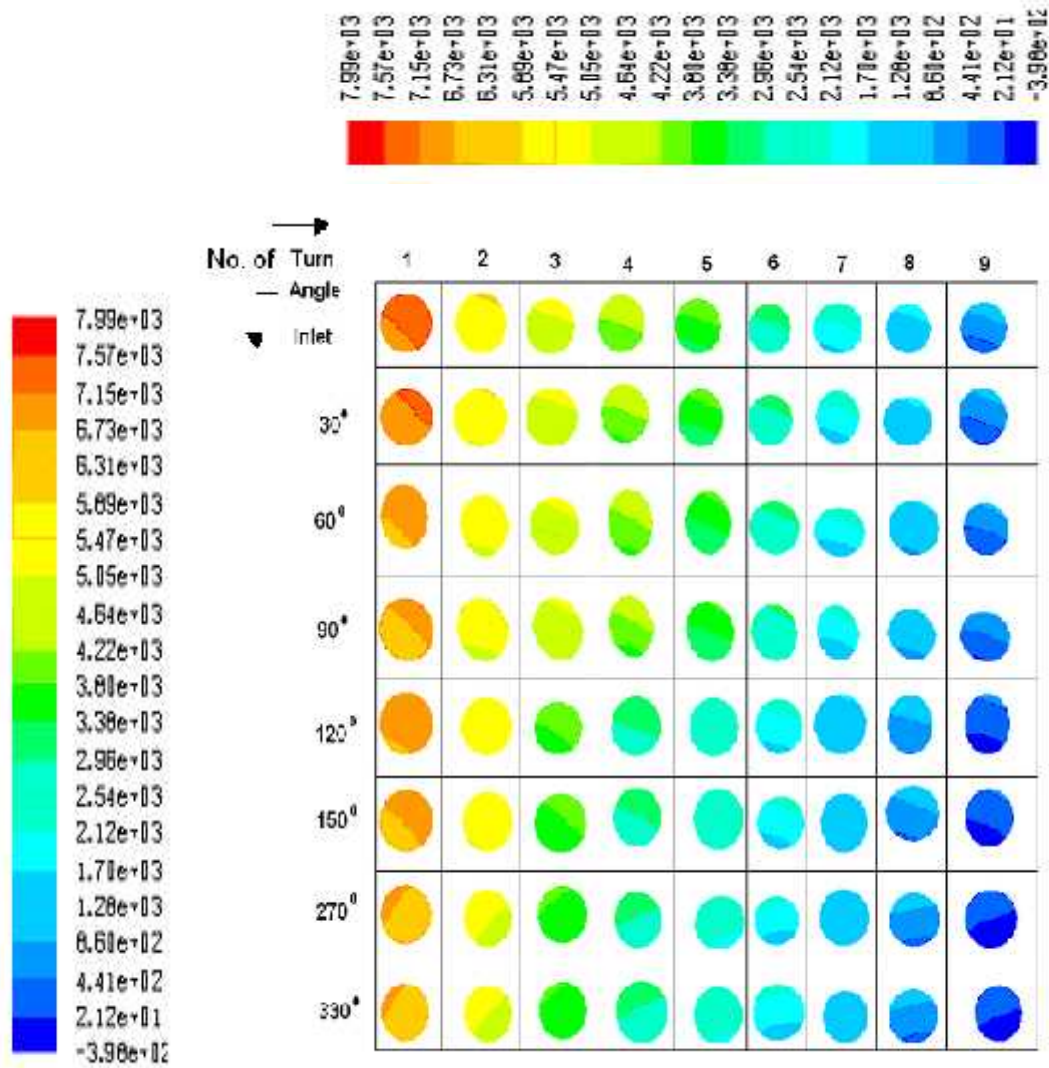


Fig. 8.8 Contour plot of static pressure varying with angle and number of turn of the coil, Coil dimension, Tube diameter (m): 0.00933, D_v/D_c : 0.0431, D_c : 0.2162 m, Total length: 6.10 m, Turn: 9
 Concentration of SCMC solution (kg/m^3): 0.8, Liquid velocity (m/s): 1.037, Gas velocity (m/s): 1.9531, Gas fraction, Γ_g : 0.2310 Turn: 9

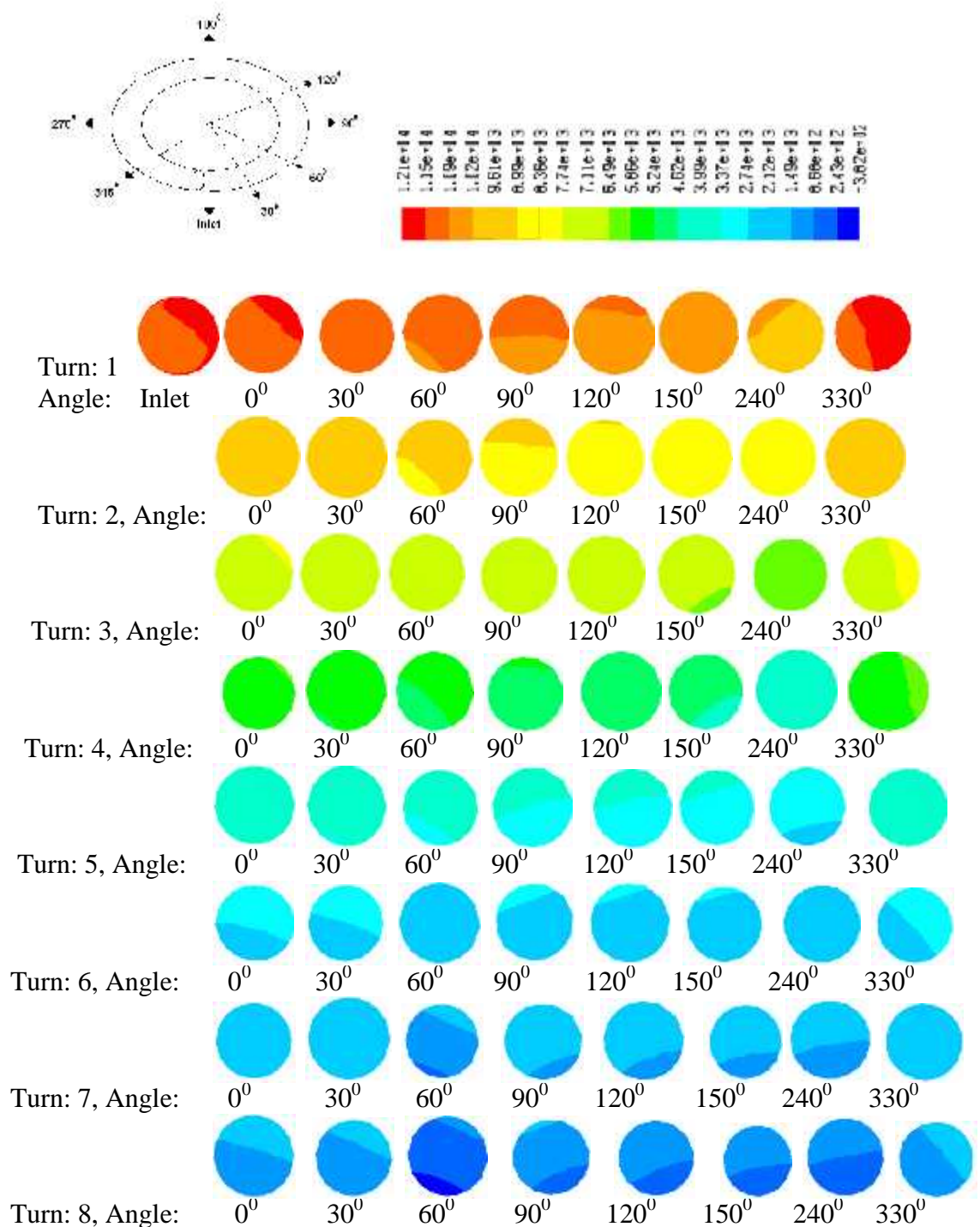
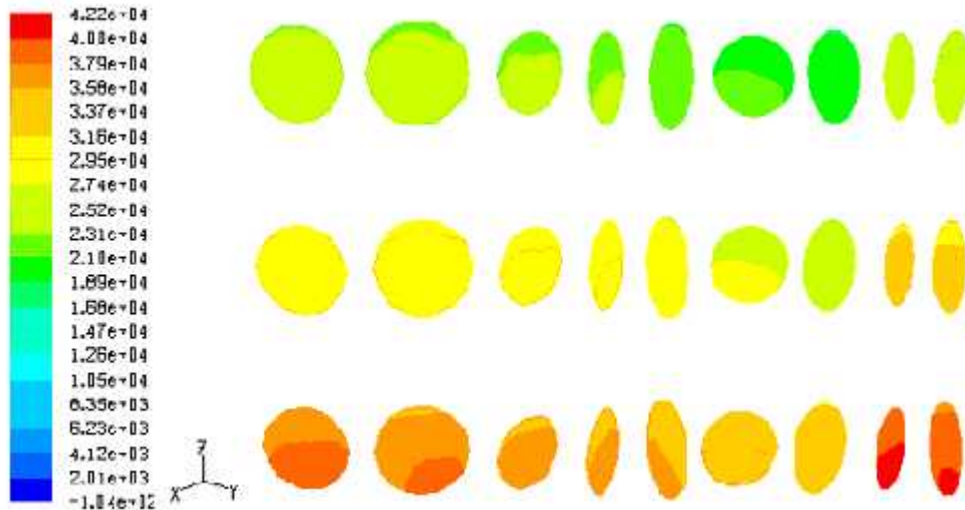


Fig. 8.9 Contour plot of static pressure at different angle and fixed turn of the coil, from 1-8 at the selected plane along the length of the coil,
 Coil dimension, Tube diameter (m): 0.00933, D_t/D_c : 0.0431, D_c : 0.2162 m, Total length: 6.10 m, Turn: 9, Concentration of SMC solution (kg/m^3): 0.8, Liquid flow rate (m^3/s): 13.34×10^{-5} , Gas flow rate (m^3/s): 4.93×10^{-5} , Gas fraction, r_g : 0.2310



Angle (deg): 30⁰ 60⁰ 90⁰ 120⁰ 150⁰ 240⁰ 270⁰ 300⁰ 330⁰

Fig. 8.10 Contours plot of total pressure varying with angle and coil height ,
 Coil dimension, D_t : 0.00933 m, D_t/D_c : 0.0350, D_c : 0.2662 m, Total length: 5.01 m, Turn:
 6, Concentration of SMC solution: 0.8 kg/m³, Liquid velocity: 1.7086 m/s, Gas
 velocity: 0.9282 m/s, Gas fraction, r_g : 0.3750

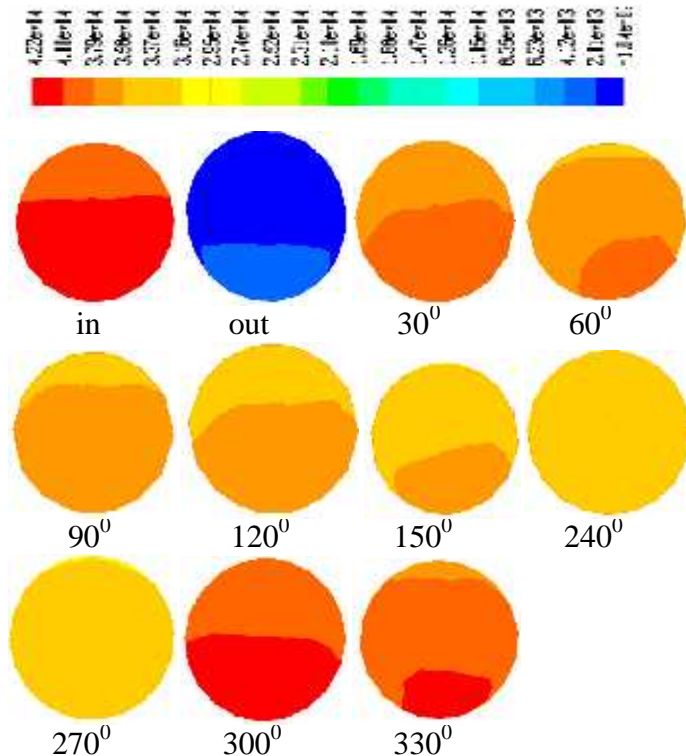


Fig. 8.11 Contours plot of total pressure (mixture) at the first turn of the coil varying with
 angle at the selected plane along the of the coil,

Coil dimension, D_t : 0.00933 m, D_t/D_c : 0.0350, D_c : 0.2662 m, Total length: 5.01 m, Turn:
 6, concentration of SMC solution: 0.8 kg/m³, Liquid velocity: 1.7086 m/s, Gas velocity:
 0.9282 m/s, Gas fraction, r_g : 0.3750

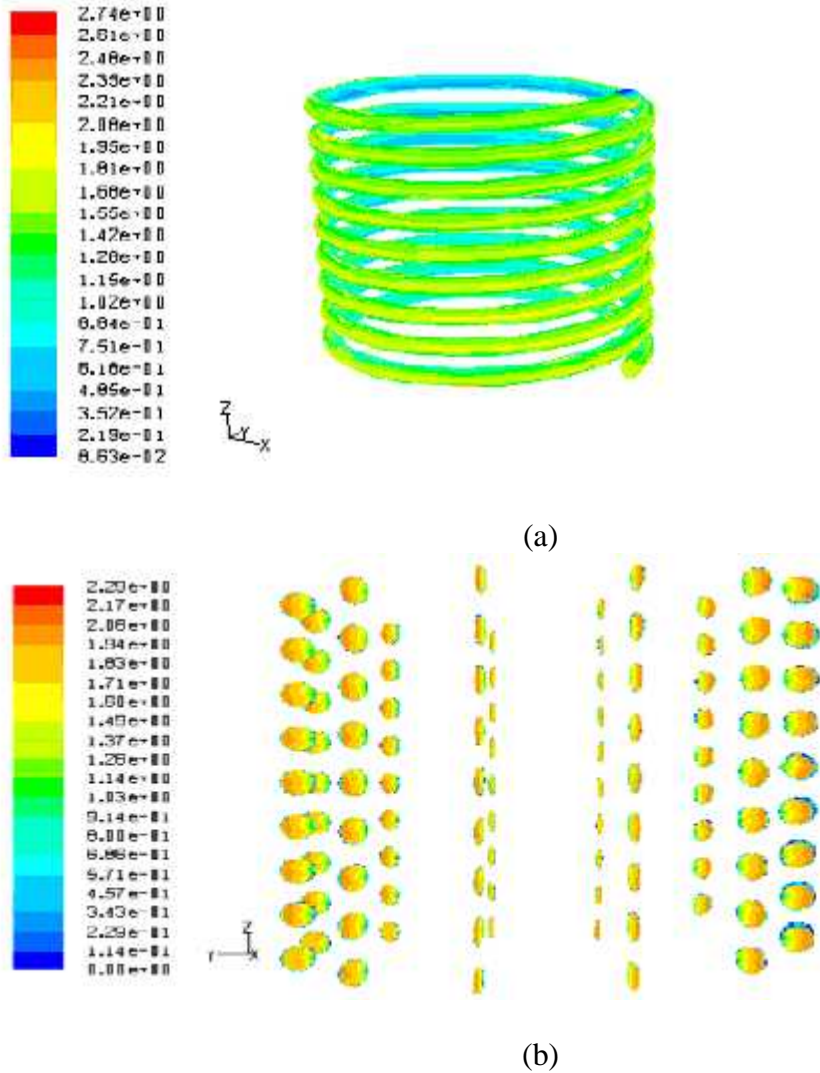


Fig. 8.12 (a) Contours plot of velocity magnitude for mixture and (b) Contours plot of velocity magnitude at various planes along the length of the coil at hexahedral grid,

Coil dimension, D_t : 0.00933 m, D_v/D_c : 0.0431, D_c : 0.2162 m, Total length: 6.10 m, Turn: 9, Concentration of SCMC solution: 0.8 kg/m^3 , Liquid velocity: 1.9531 m/s, Gas velocity: 0.7218 m/s, Gas fraction, r_g : 0.231

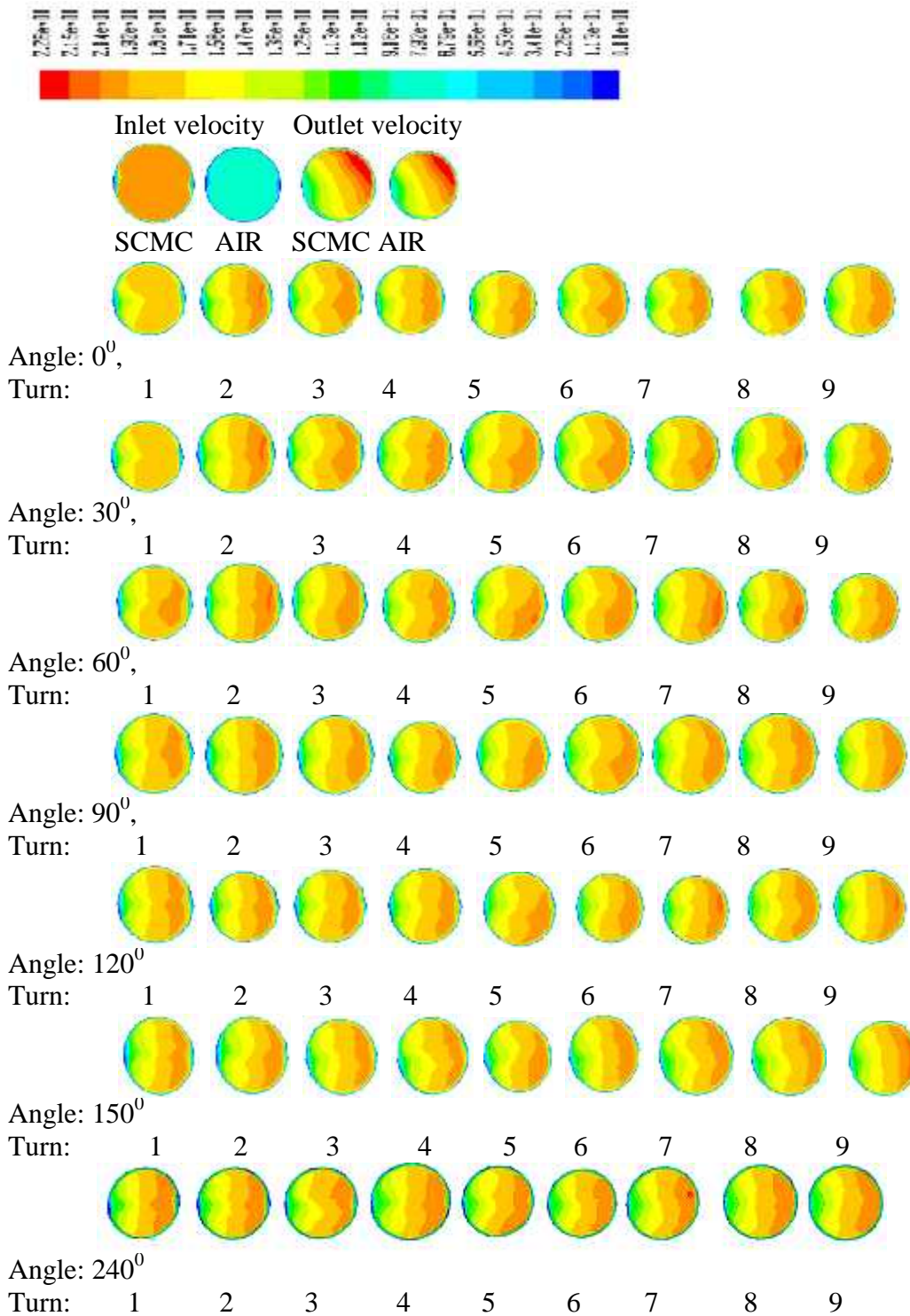


Fig. 8.13 Contour plot of velocity at the selected plane along the length of the coil varying with angle and turn of the coil from 1-9,

Coil dimension: D_t : 0.00933 m, D_t/D_c : 0.0431, D_c : 0.2162 m, Total length: 6.10 m, Turn: 9, concentration of SCMC solution: 0.8 kg/m^3 , Liquid velocity: 1.9531 m/s, Gas velocity: 0.7218 m/s, Gas fraction, Γ_g : 0.231

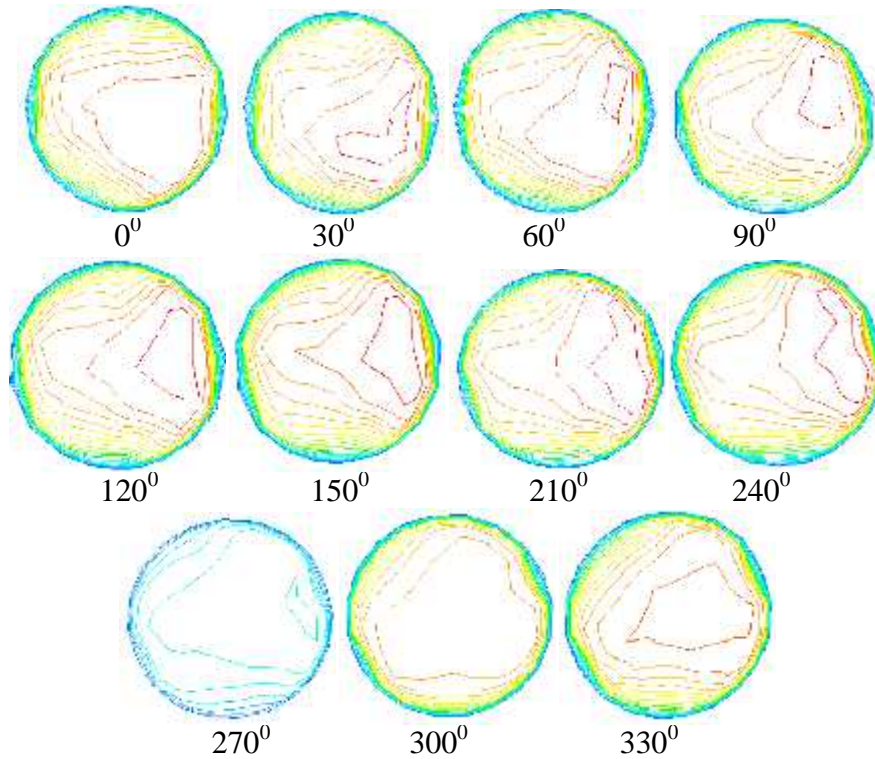
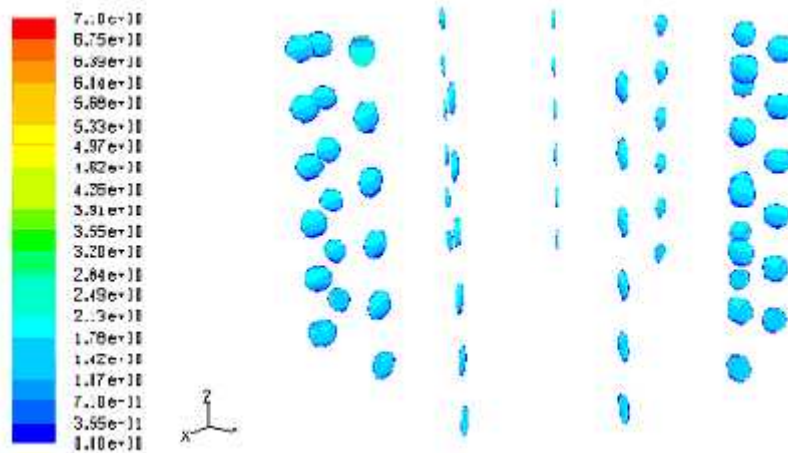


Fig. 8.14 Contour plot of velocity magnitude at the different angular plane and at the fixed turn1 of the coil,
 Coil dimension, D_i : 0.00933 m, D_i/D_c : 0.0350, D_c : 0.2662 m, Total length: 5.01 m, Turn: 6, concentration of SCMC solution: 0.8 kg/m^3 , Liquid velocity: 1.7086 m/s, Gas velocity: 0.9282 m/s, Gas fraction, r_g : 0.3750



(a)

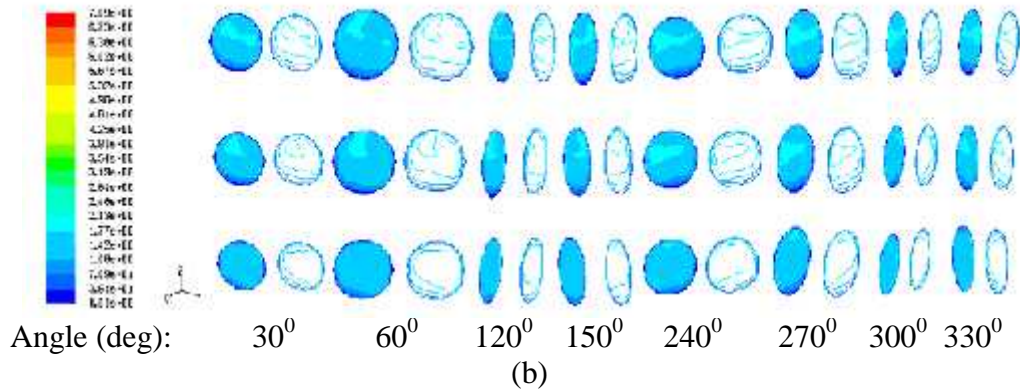


Fig. 8.15 (a) Contour plot of velocity magnitude for air phase at various planes along the length of the coil (b) Contours plot of velocity magnitude for air phase varying with angle and coil height

Coil dimension, D_t : 0.00933 m, D_t/D_c : 0.0350, D_c : 0.2662 m, Total length: 5.01 m, Turn: 6, concentration of SCMC solution: 0.8 kg/m^3 , Liquid velocity: 1.7086 m/s, Gas velocity: 0.9282 m/s, Gas fraction, r_g : 0.3750

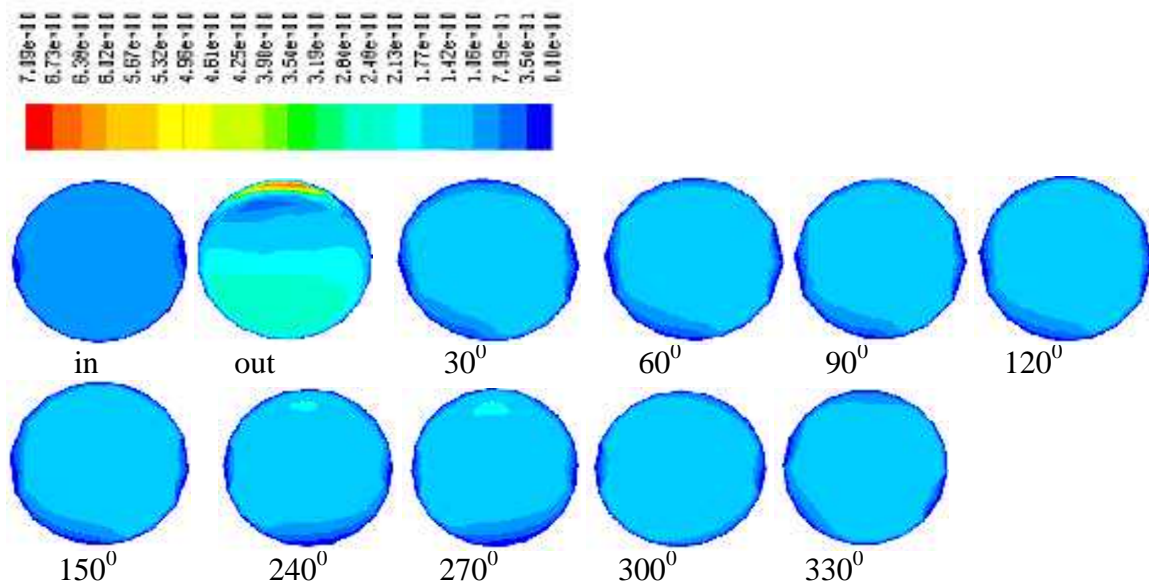


Fig. 8.16 Contours plot of velocity magnitude for air phase at the first turn of the coil varying with angle for hexahedral grid at the selected plane along the length of the coil, Coil dimension, D_t : 0.00933 m, D_t/D_c : 0.0350, D_c : 0.2662 m, Total length: 5.01 m, Turn: 6, concentration of SCMC solution: 0.8 kg/m^3 , Liquid velocity: 1.7086 m/s, Gas velocity: 0.9282 m/s, Gas fraction, r_g : 0.3750

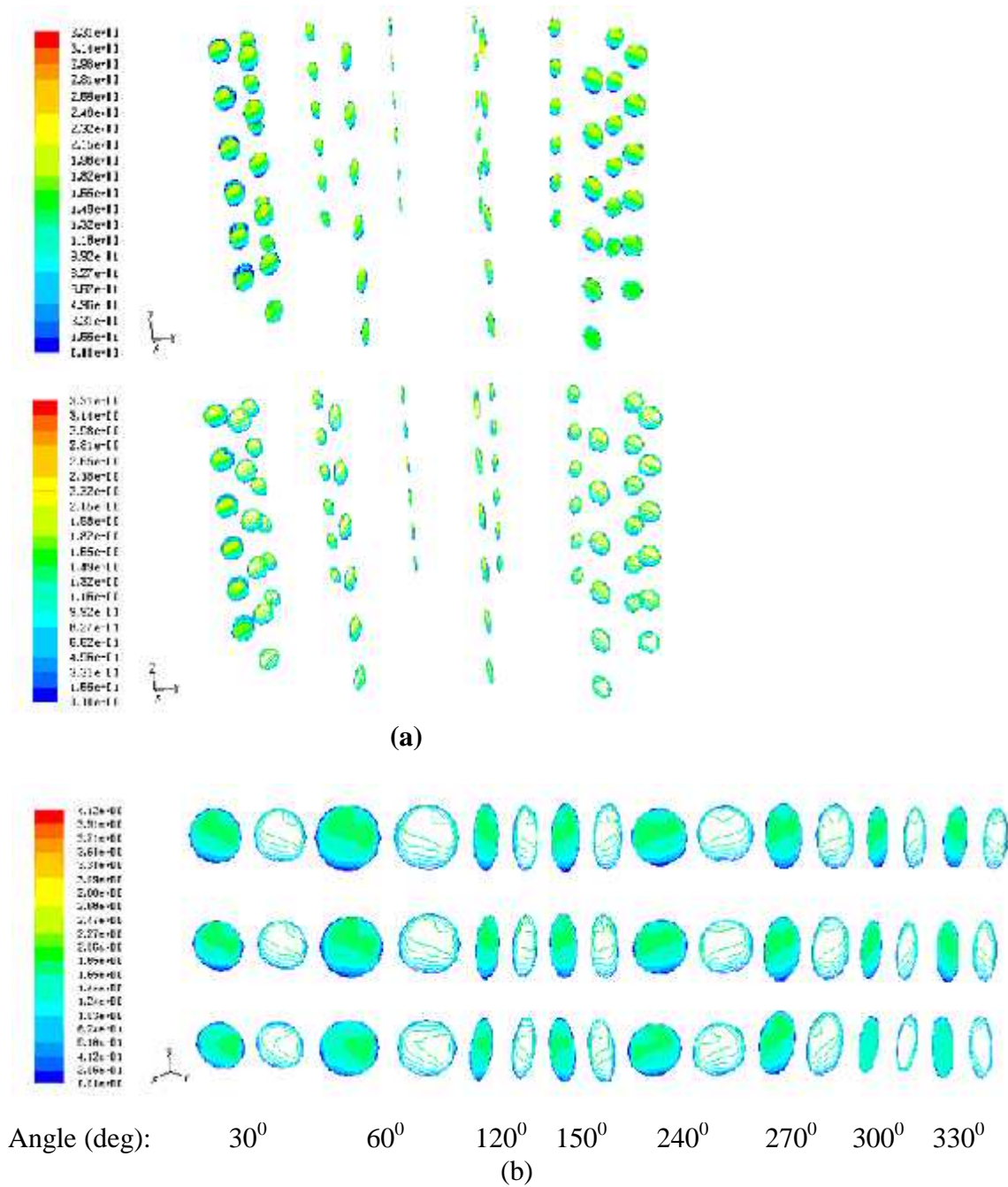


Fig. 8.17 (a) Contour plot of velocity magnitude for liquid phase at various planes along the length of the coil

(b) Contours plot of velocity magnitude for liquid phase varying with angle and coil height at hexahedral grid,

Coil dimension, D_t : 0.00933 m, D_t/D_c : 0.0350, D_c : 0.2662 m, Total length: 5.01 m, Turn: 6, concentration of SCMC solution: 0.8 kg/m^3 , Liquid velocity: 1.7086 m/s, Gas velocity: 0.9282 m/s, Gas fraction, r_g : 0.3750

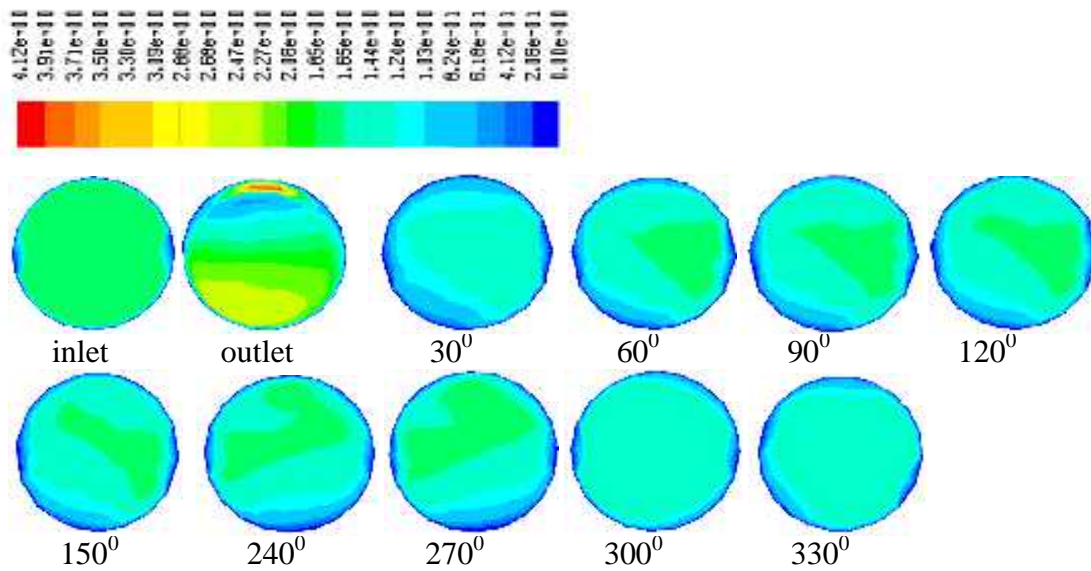


Fig. 8.18 Contours plot of velocity magnitude for liquid phase at the first turn of the coil varying with angle for hexahedral grid at the selected plane along the length of the coil, Coil dimension, D_t : 0.00933 m, D_t/D_c : 0.0350, D_c : 0.2662 m, Total length: 5.01 m, Turn: 6, concentration of SCMC solution: 0.8 kg/m^3 , Liquid velocity: 1.7086 m/s, Gas velocity: 0.9282 m/s, Gas fraction, r_g : 0.3750

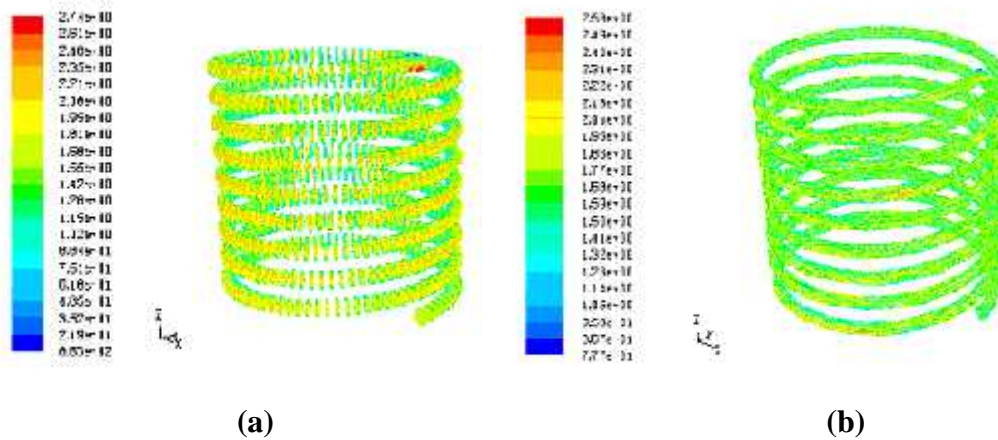
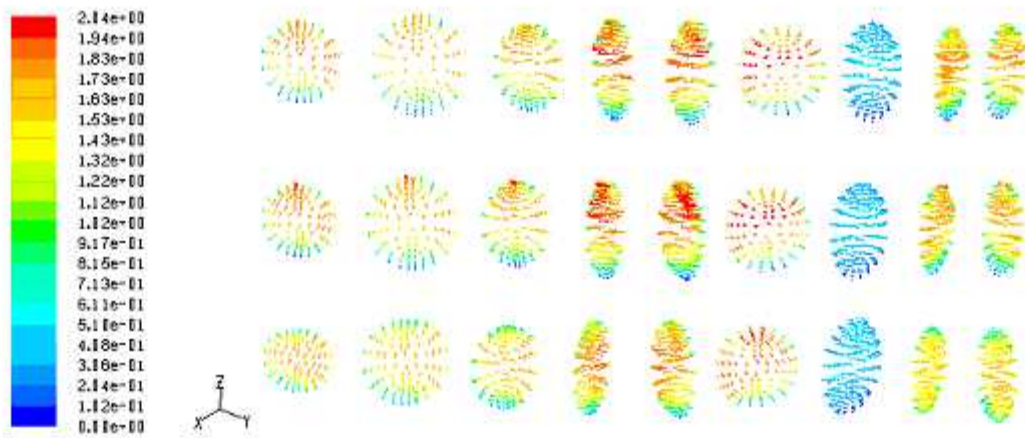


Fig. 8.19 Contour plot of velocity vector at (a) hexahedral and (b) tetrahedral grid, Coil dimension, D_t : 0.00933 m, D_t/D_c : 0.0431, D_c : 0.2162 m, Total length: 6.10 m, Turn: 9, concentration of SCMC solution: 0.8 kg/m^3 , Liquid velocity: 1.9531 m/s, Gas velocity: 0.7218 m/s, Gas fraction, r_g : 0.231



Angle (deg): 30⁰ 60⁰ 90⁰ 120⁰ 150⁰ 240⁰ 270⁰ 300⁰ 330⁰

Fig. 8.20 Contour plot of velocity vector varying with angle and coil turn or height at hexahedral grid,
 Coil dimension, D_t : 0.00933 m, D_t/D_c : 0.0350, D_c : 0.2662 m, Total length: 5.01 m, Turn: 6, concentration of SMC solution: 0.8 kg/m³, Liquid velocity: 1.7086 m/s, Gas velocity: 0.9282 m/s, Gas fraction, r_g : 0.3750

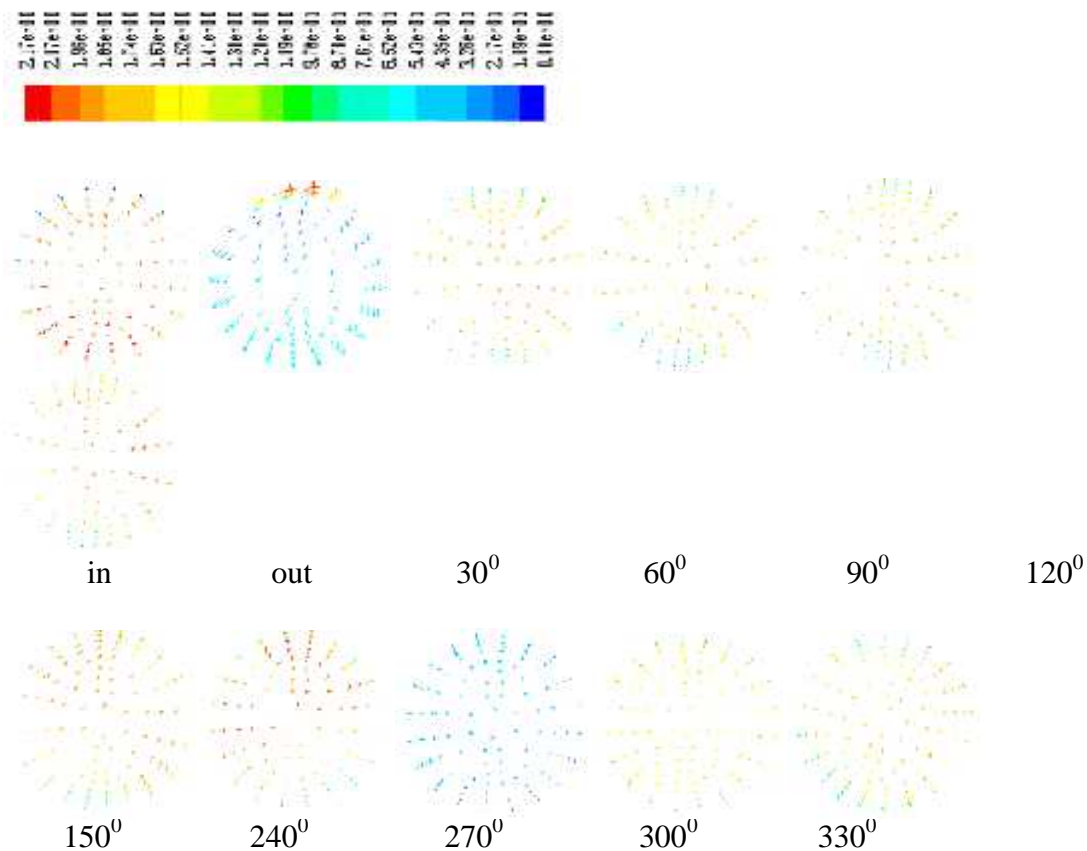
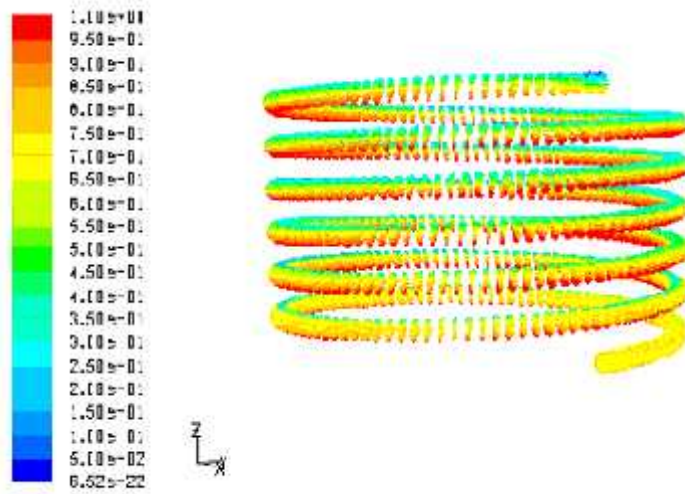
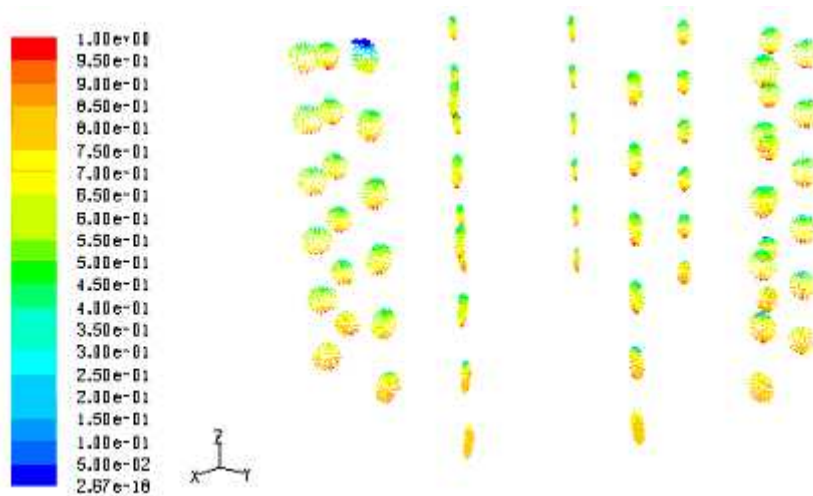


Fig. 8.21 Contours plot of velocity vector at the first turn of the coil varying with angle for hexahedral grid at the selected plane of the coil

Coil dimension, D_t : 0.00933 m, D_t/D_c : 0.0350, D_c : 0.2662 m, Total length: 5.01 m, Turn: 6, Concentration of SCMC solution : 0.8kg/m^3 , Liquid velocity: 1.7086 m/s, Gas velocity: 0.9282 m/s, Gas fraction, r_g : 0.3750



(a) Velocity vector plot for liquid phase



(b) Velocity vector plot for liquid phase at various planes along the length of the coil

Fig. 8.22 Contour plot of velocity vector for liquid phase at hexahedral grid, Coil dimension, D_t : 0.00933 m, D_t/D_c : 0.0529, D_c : 0.2662 m, Total length: 5.01 m, Turn: 6, Concentration of SCMC solution: 0.8 kg/m^3 , Liquid velocity: 1.7086 m/s, Gas velocity: 0.9282 m/s, Gas fraction, r_g : 0.3750

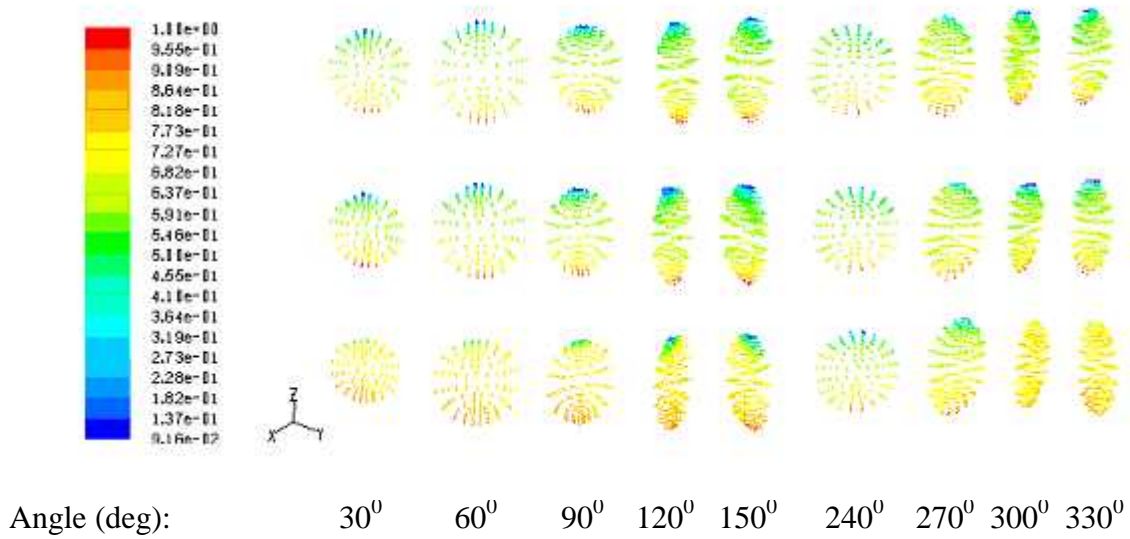


Fig. 8.23 Contour plot of velocity vector for liquid phase varying with angle and coil height at hexahedral grid,
 Coil dimension, D_i : 0.00933 m, D_i/D_c : 0.0350, D_c : 0.2662 m, Total length: 5.01 m, Turn: 6, Concentration of SMC solution: 0.8 kg/m³, Liquid velocity: 1.7086 m/s, Gas velocity: 0.9282 m/s, Gas fraction, r_g : 0.3750

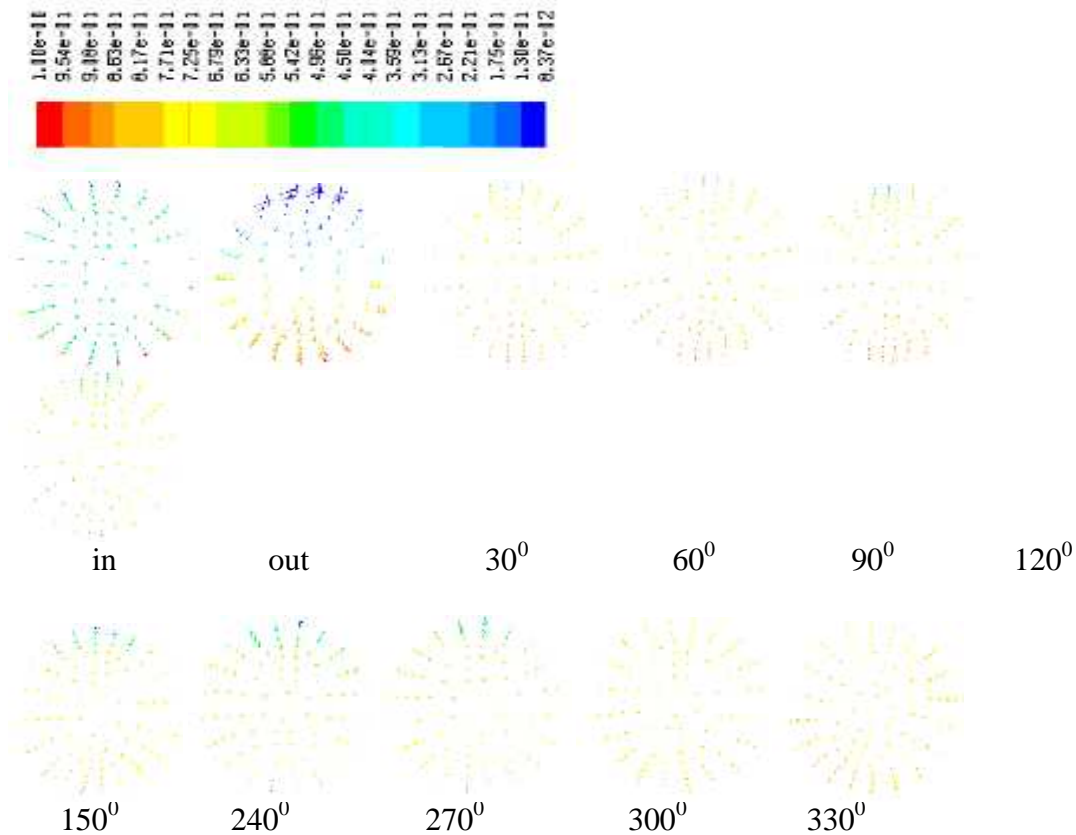
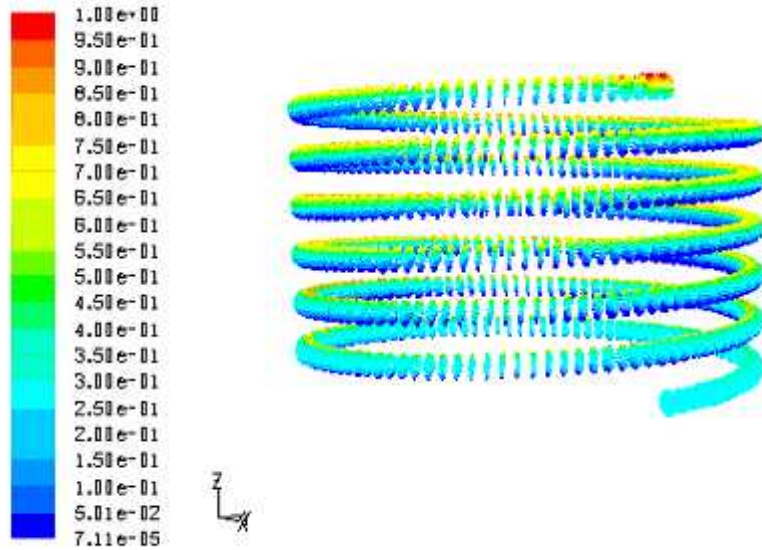
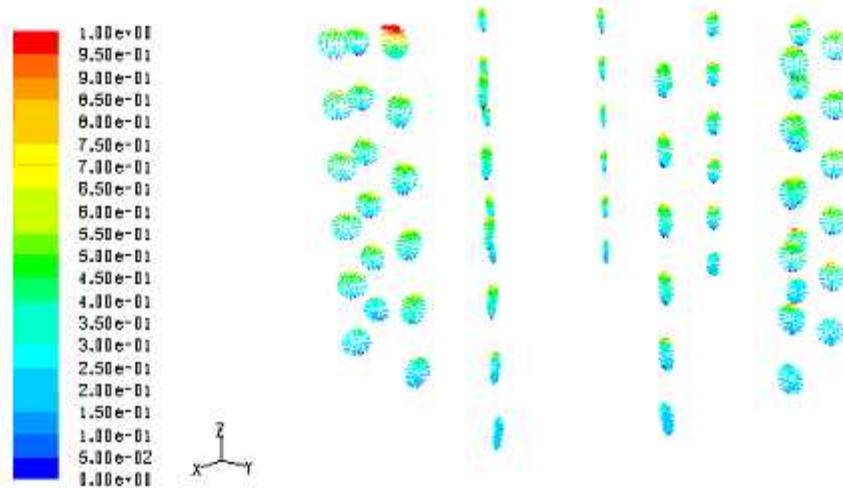


Fig. 8.24 Contour plot of velocity vector plot for liquid phase varying with angle and coil turn1 at hexahedral grid at the selected plane of the coil,
 Coil dimension, D_i : 0.00933 m, D_i/D_c : 0.0350, D_c : 0.2662 m, Total length: 5.01 m, Turn: 6, Concentration of SCMC solution: 0.8 kg/m^3 , Liquid velocity: 1.7086 m/s, Gas velocity: 0.9282 m/s, Gas fraction, Γ_g : 0.3750



(a)



(b)

Fig. 8.25 (a) Contour plot of velocity vector for air phase and (b) velocity vector plot for air phase at various plane along the length of the coil at hexahedral grid,
 Coil dimension, D_i : 0.00933 m, D_i/D_c : 0.0529, D_c : 0.2662 m, Total length: 5.01 m, Turn: 6, Concentration of SCMC solution: 0.8 kg/m^3 , Liquid velocity: 1.7086 m/s, Gas velocity: 0.9282 m/s, Gas fraction, Γ_g : 0.3750

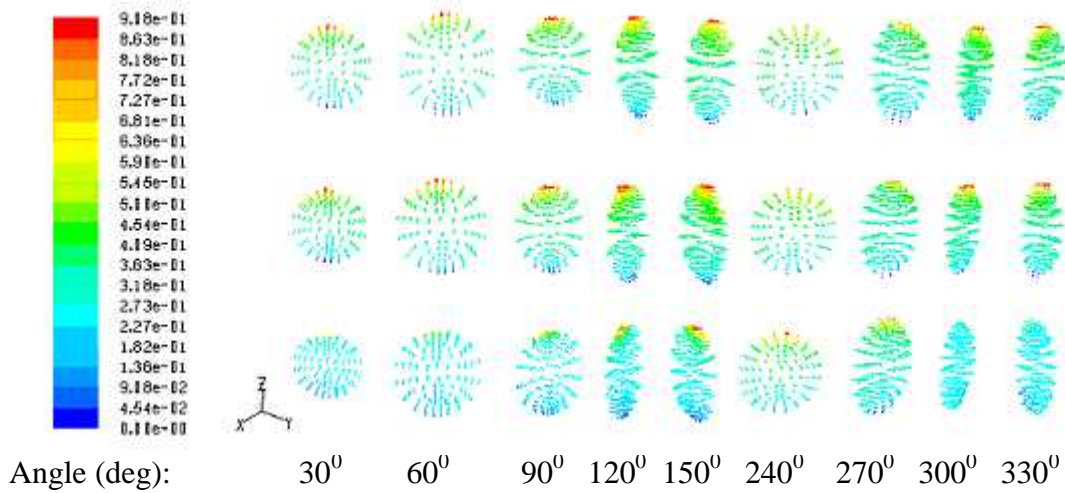


Fig. 8.26 Contour plot of velocity vector plot for air phase varying with angle and coil height at hexahedral grid,
 Coil dimension, D_i : 0.00933 m, D_i/D_c : 0.0350, D_c : 0.2662 m, Total length: 5.01 m, Turn: 6, Concentration of SCMC solution: 0.8 kg/m^3 , Liquid velocity: 1.7086 m/s, Gas velocity: 0.9282 m/s, Gas fraction: 0.3750

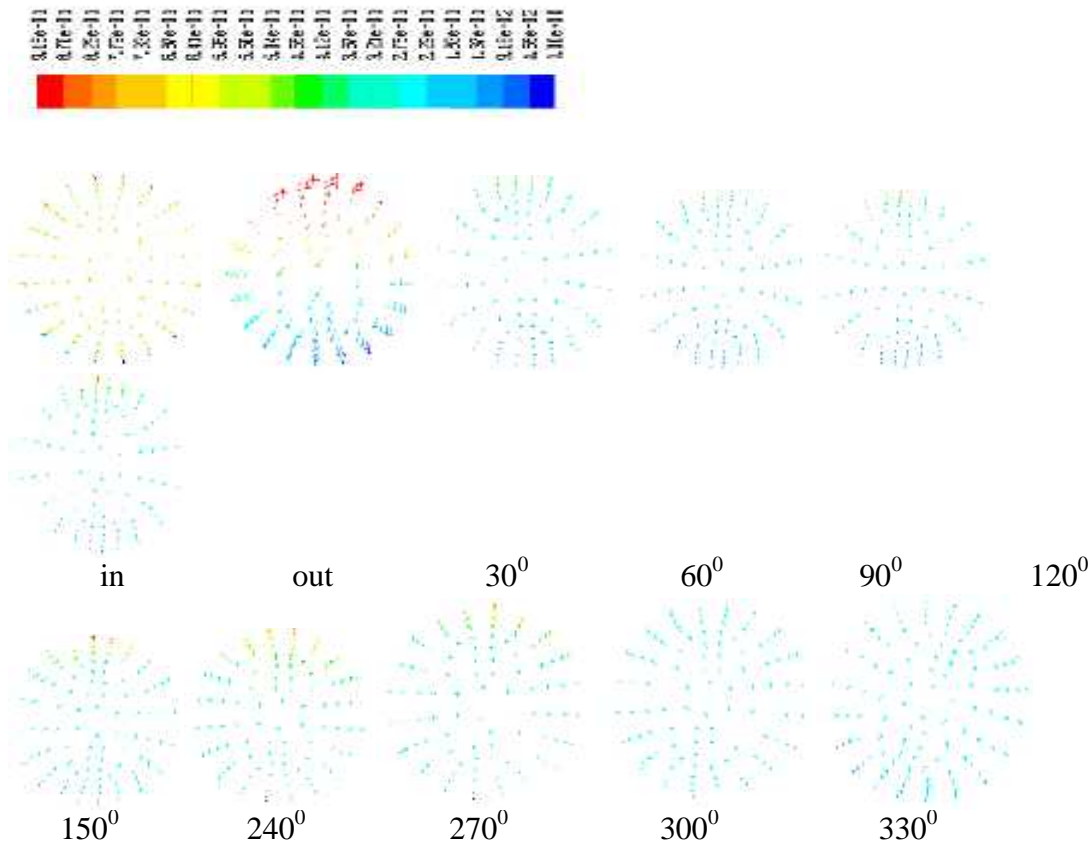


Fig. 8.27 Contours plot of velocity vector for air phase at the first turn of the coil varying with angle at hexahedral grid at the selected plane along the length of the coil, Coil

dimension, D_i : 0.00933 m, D_i/D_c : 0.0350, D_c : 0.2662 m, Total length: 5.01 m, Turn: 6, Concentration of SCMC solution: 0.8 kg/m^3 , Liquid velocity: 1.7086 m/s, Gas velocity: 0.9282 m/s, Gas fraction, r_g : 0.3750

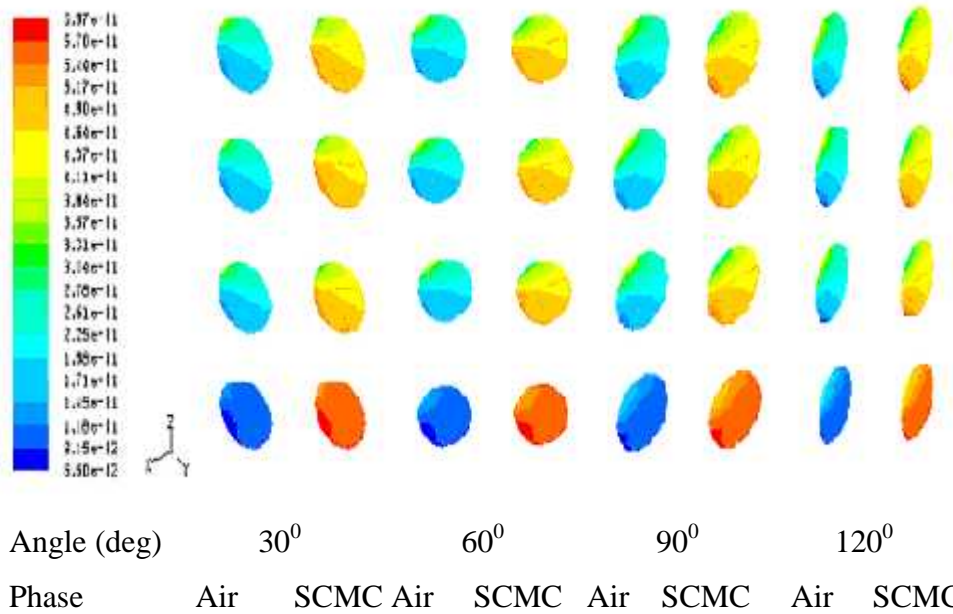
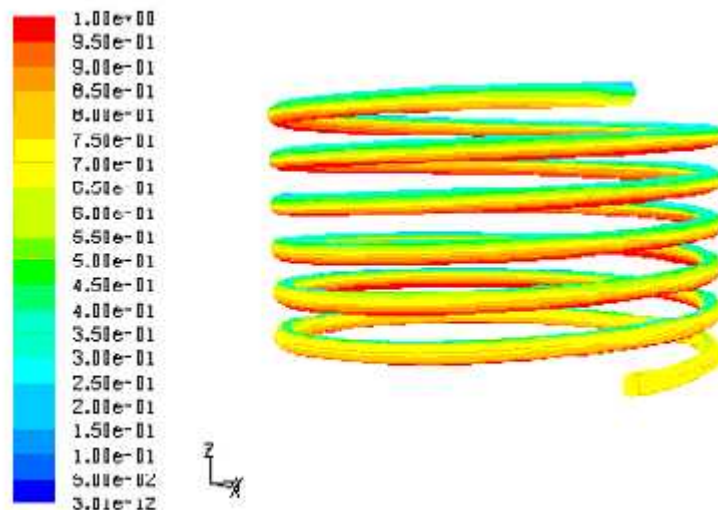
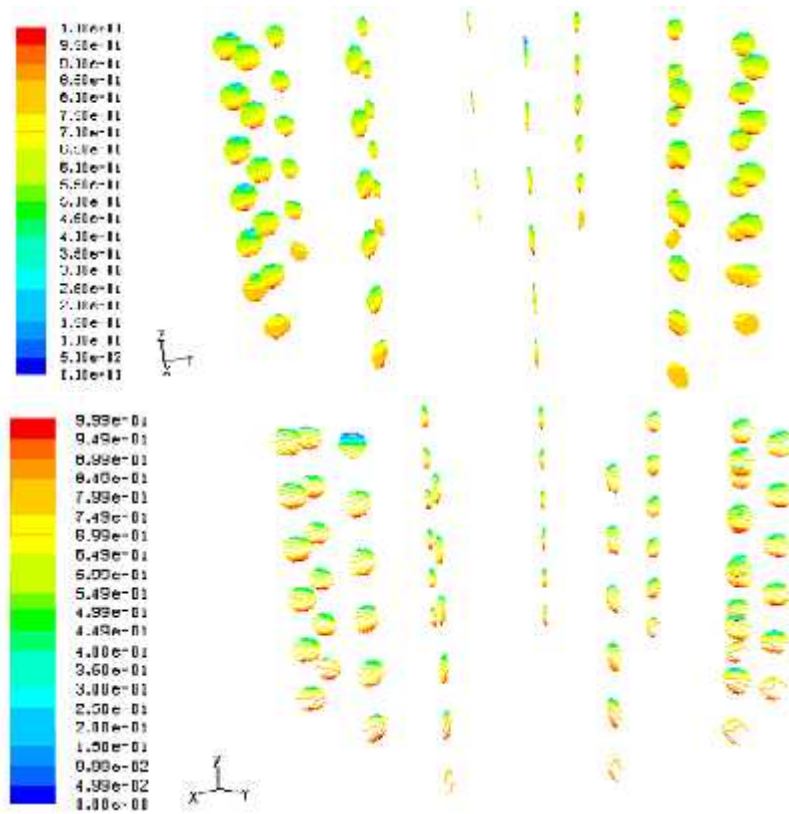


Fig. 8.28 Contour plot of volume fraction at the selected plane for air-SCMC phase varying with angle and coil turn at hexahedral boundary layer grid, Coil dimension, D_i : 0.00933 m, D_i/D_c : 0.0431, D_c : 0.2162 m, Total length: 6.10 m, Turn: 9, Concentration of SCMC solution (kg/m^3): 0.8, Liquid velocity, V_L (m/s): 1.9531, Gas velocity, V_g (m/s) :0.7218, Gas Fraction, r_g :0.2310



(a)



(b)

Fig. 8.29 (a) Contours plot of volume fraction for liquid phase and (b) Contour of volume fraction for liquid phase at various planes along the length of the coil at hexahedral grid at the selected plane along the length of the coil, Coil dimension, D_t : 0.00933 m, D_v/D_c : 0.0350, D_c : 0.2662 m, Total length: 5.01 m, Turn: 6, Concentration of SCMC solution: 0.8 kg/m^3 , Liquid velocity: 1.7086 m/s, Gas velocity: 0.9282 m/s, Gas fraction, r_g : 0.3750

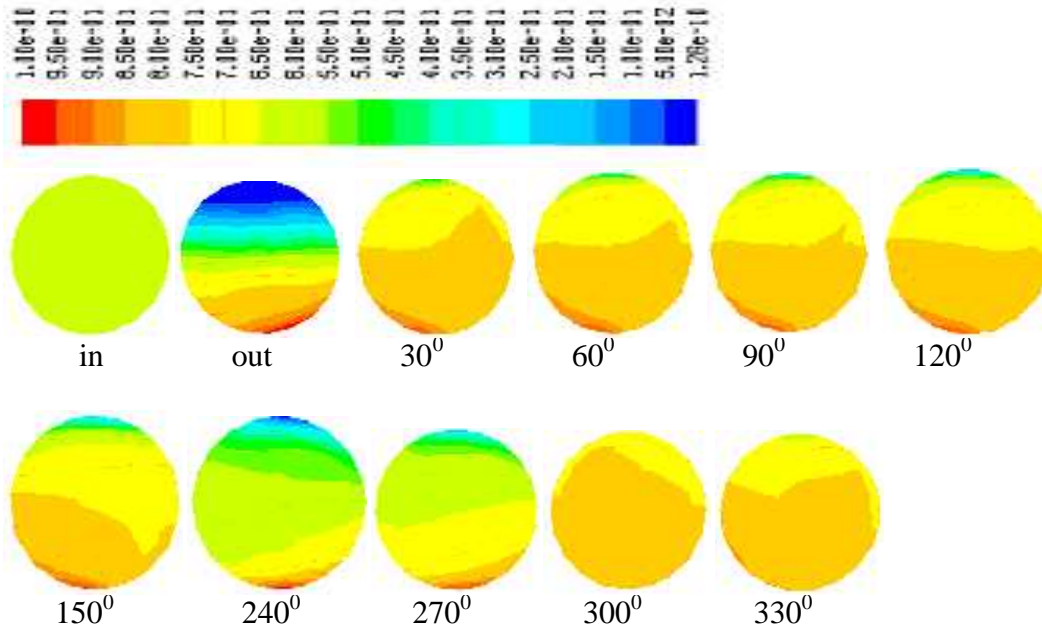


Fig. 8.30 Contours plot of volume fraction for liquid phase at the first turn of the coil varying with angle at hexahedral grid at the selected plane along the length of the coil, Coil dimension, D_t : 0.00933 m, D_t/D_c : 0.0350, D_c : 0.2662 m, Total length: 5.01 m, Turn: 6, Concentration of SCMC solution: 0.8 kg/m^3 , Liquid velocity: 1.7086 m/s, Gas velocity: 0.9282 m/s, Gas fraction, Γ_g : 0.3750

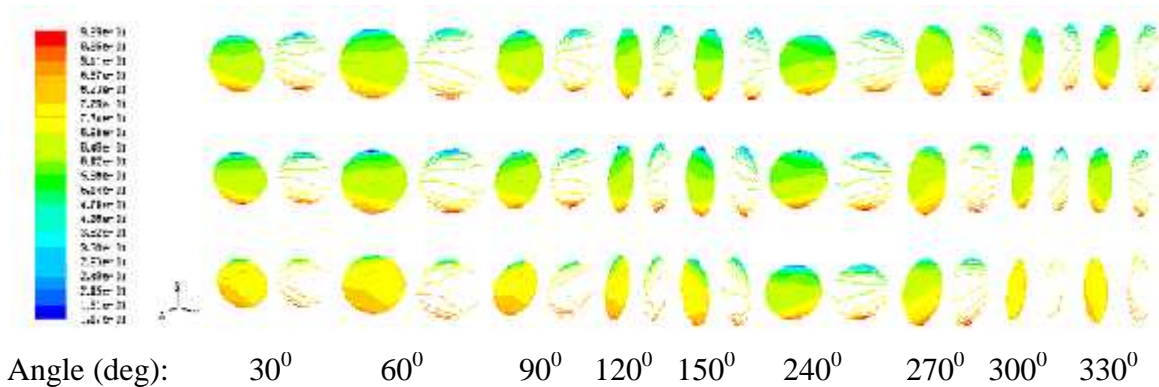


Fig. 8.31 Contours plot of volume fraction for liquid phase varying with angle and coil height at hexahedral grid, Coil dimension, D_t : 0.00933 m, D_t/D_c : 0.0350, D_c : 0.2662 m, Total length: 5.01 m, Turn: 6, Concentration of SCMC solution: 0.8 kg/m^3 , Liquid velocity: 1.7086 m/s, Gas velocity: 0.9282 m/s, Gas fraction, Γ_g : 0.3750

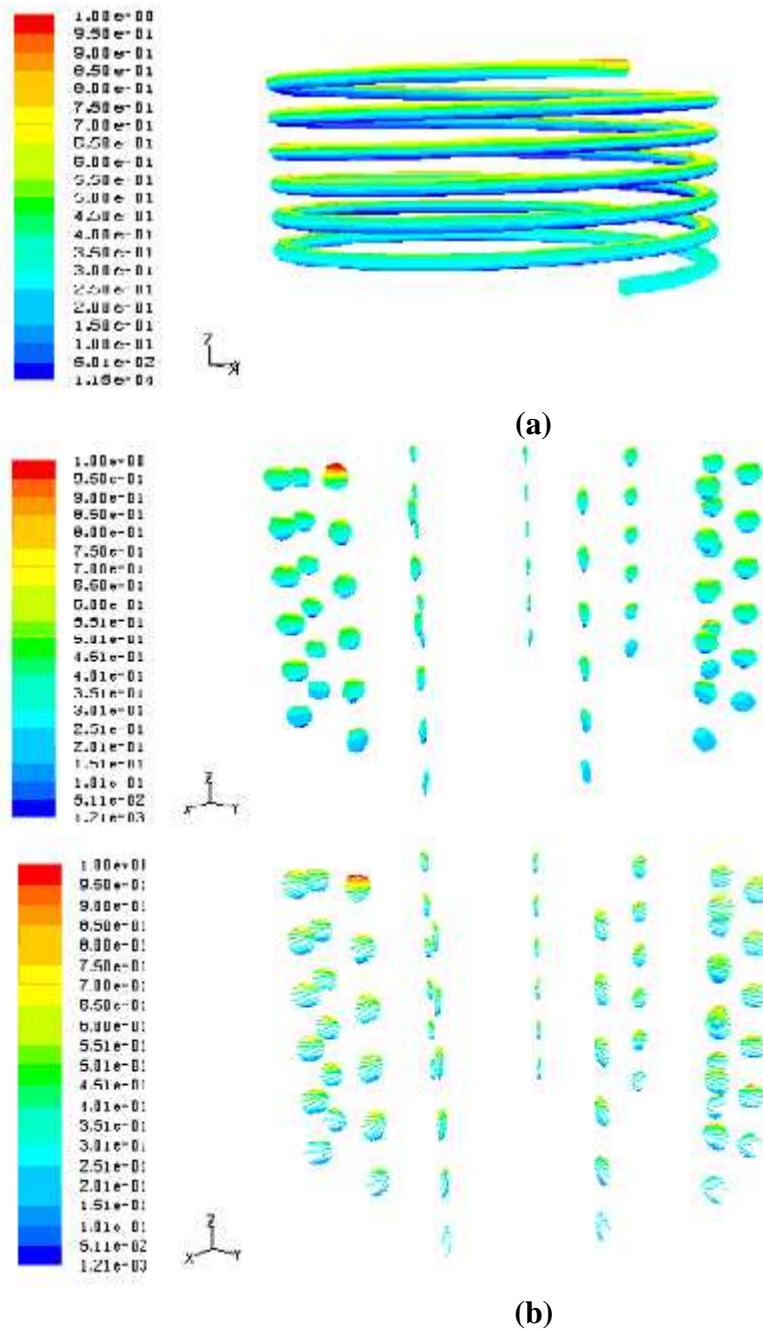


Fig. 8.32 (a) Contour plot of volume fraction for air phase (b) Contours of volume fraction for air phase at various planes along the length of the coil at hexahedral grid, Coil dimension, D_t : 0.00933 m, D_t/D_c : 0.0431, D_c : 0.2162 m, Total length: 6.10 m, Turn: 9, Concentration of SCMC solution: 0.8 kg/m^3 , Liquid velocity: 1.9531 m/s, Gas velocity: 0.7218 m/s, Gas fraction, Γ_g : 0.231

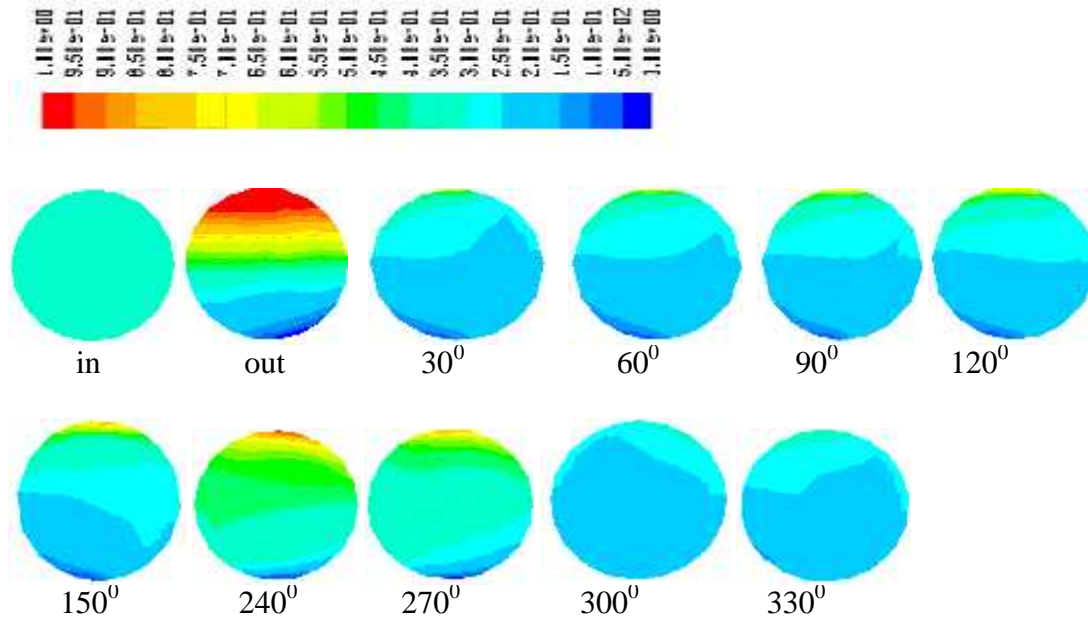


Fig. 8.33 Contour plot of volume fraction for air phase at the first turn of the coil varying with angle at hexahedral grid at the selected plane along the length of the coil, Coil dimension, D_t : 0.00933 m, D_t/D_c : 0.0529, D_c : 0.2662 m, Total length: 5.01 m, Turn: 6, Concentration of SCMC solution: 0.8 kg/m^3 , Liquid velocity: 1.7086 m/s, Gas velocity: 0.9282 m/s, Gas fraction, Γ_g : 0.3520

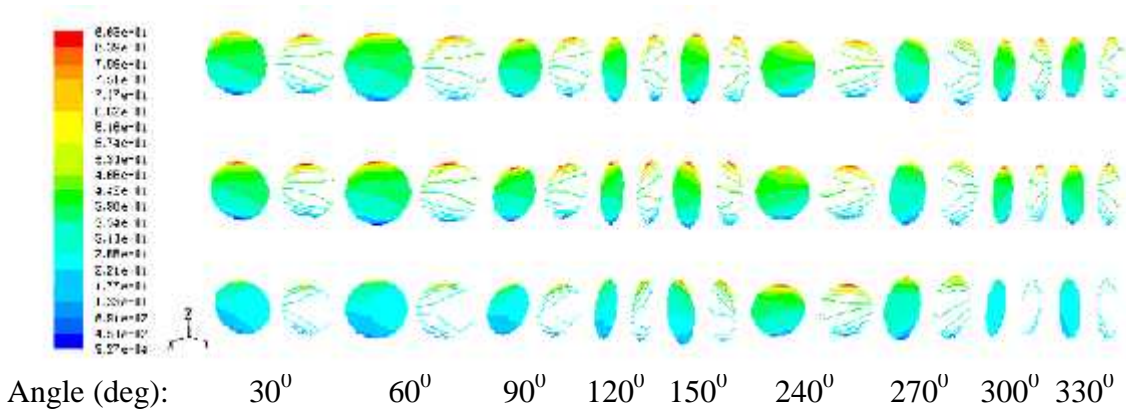


Fig. 8.34 Contours plot of volume fraction for air phase varying with angle and coil height, Coil dimension, D_t : 0.00933 m, D_t/D_c : 0.0350, D_c : 0.2662 m, Total length: 5.01 m, Turn: 6, Concentration of SCMC solution: 0.8 kg/m^3 , Liquid velocity: 1.7086 m/s, Gas velocity: 0.9282 m/s, Gas fraction, Γ_g : 0.3750

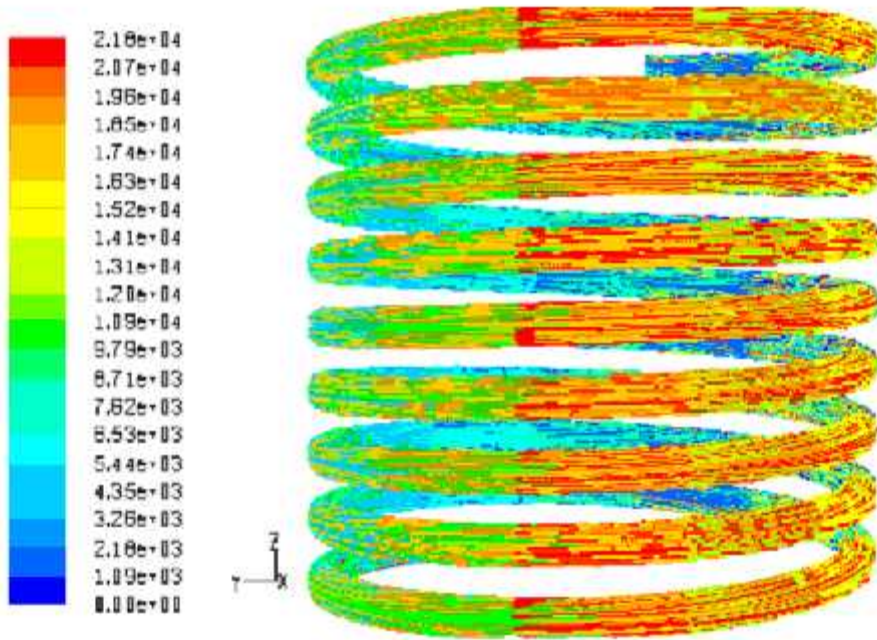


Fig. 8.35 Path lines of liquid in the mixture

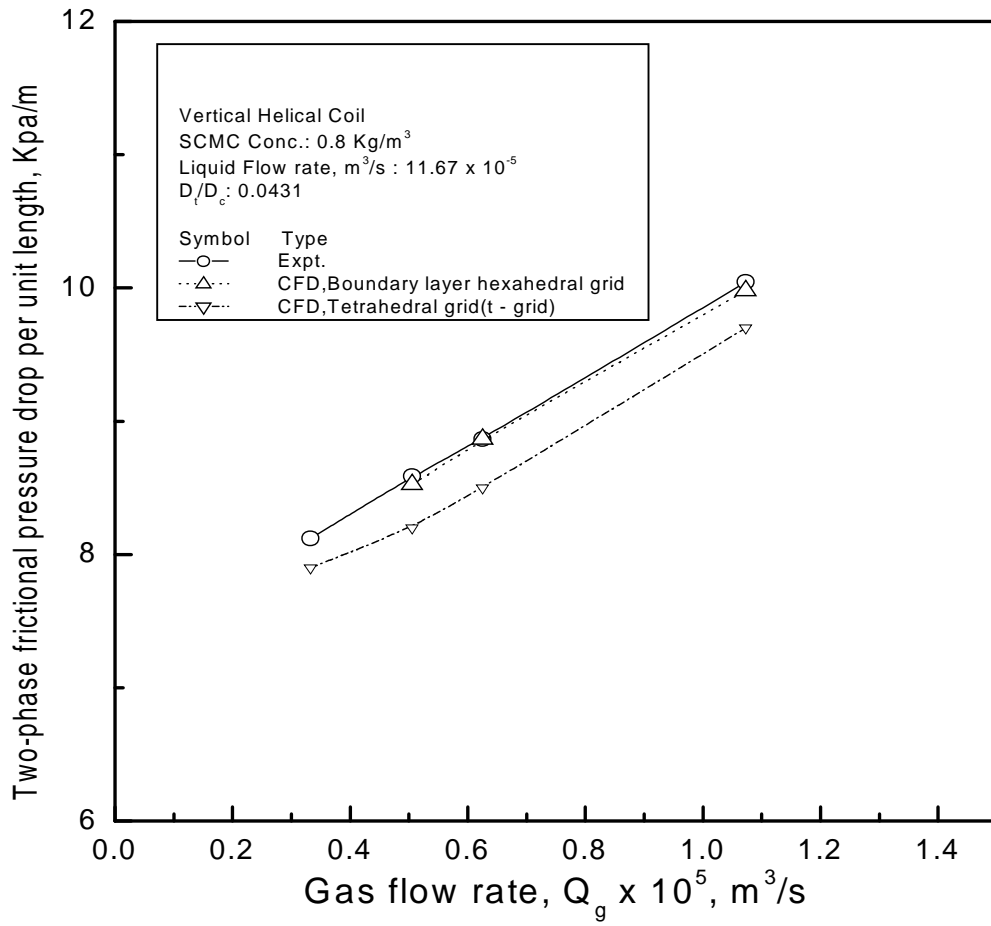


Fig. 8.36 Comparison plot for helical coil

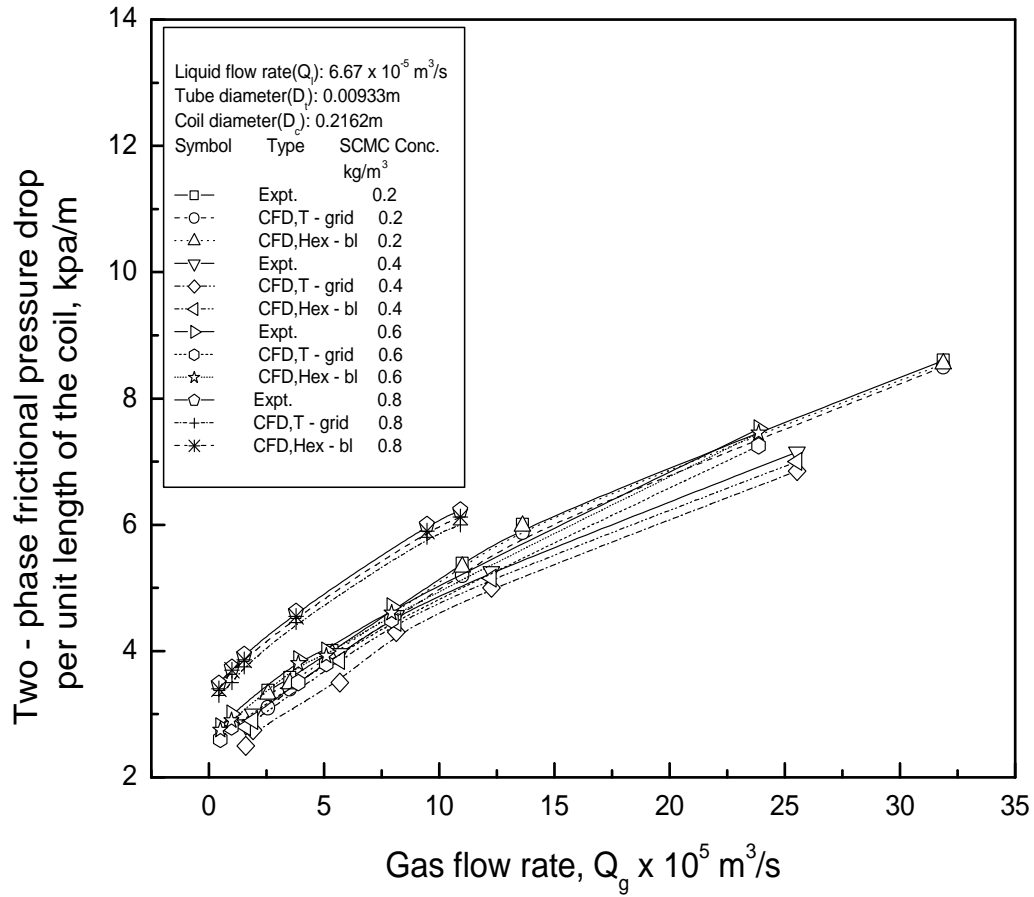


Fig. 8.37 Comparison plot for helical coil at different SCMC concentration

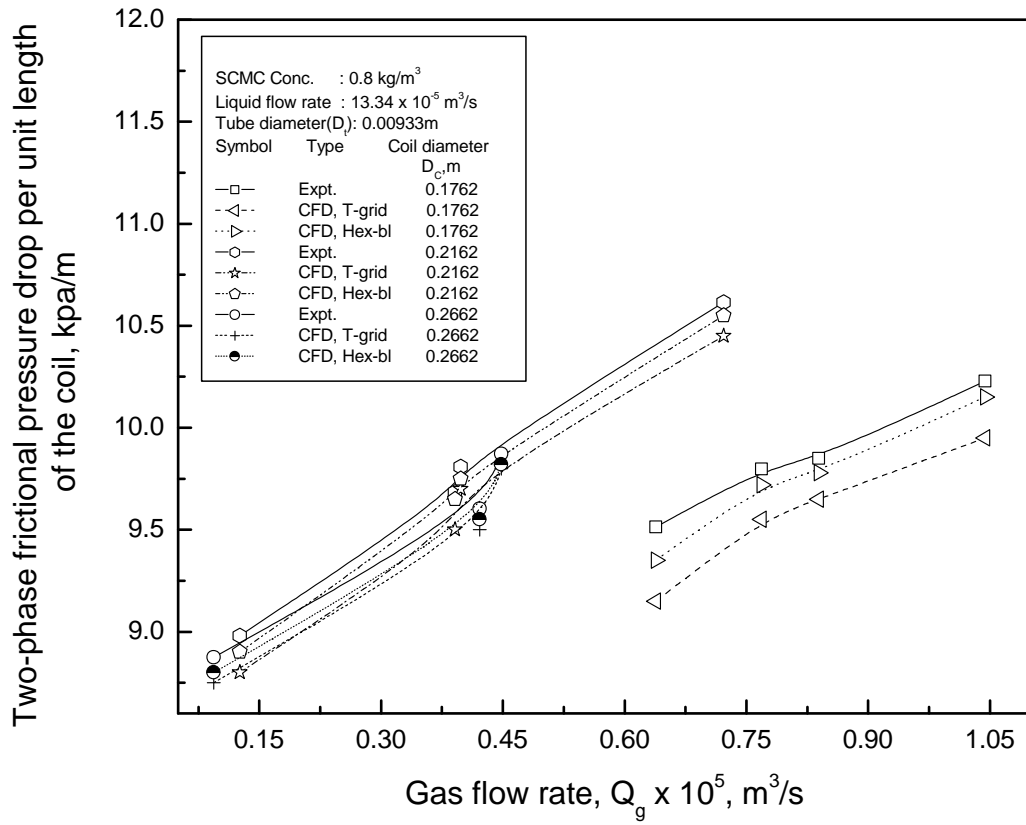
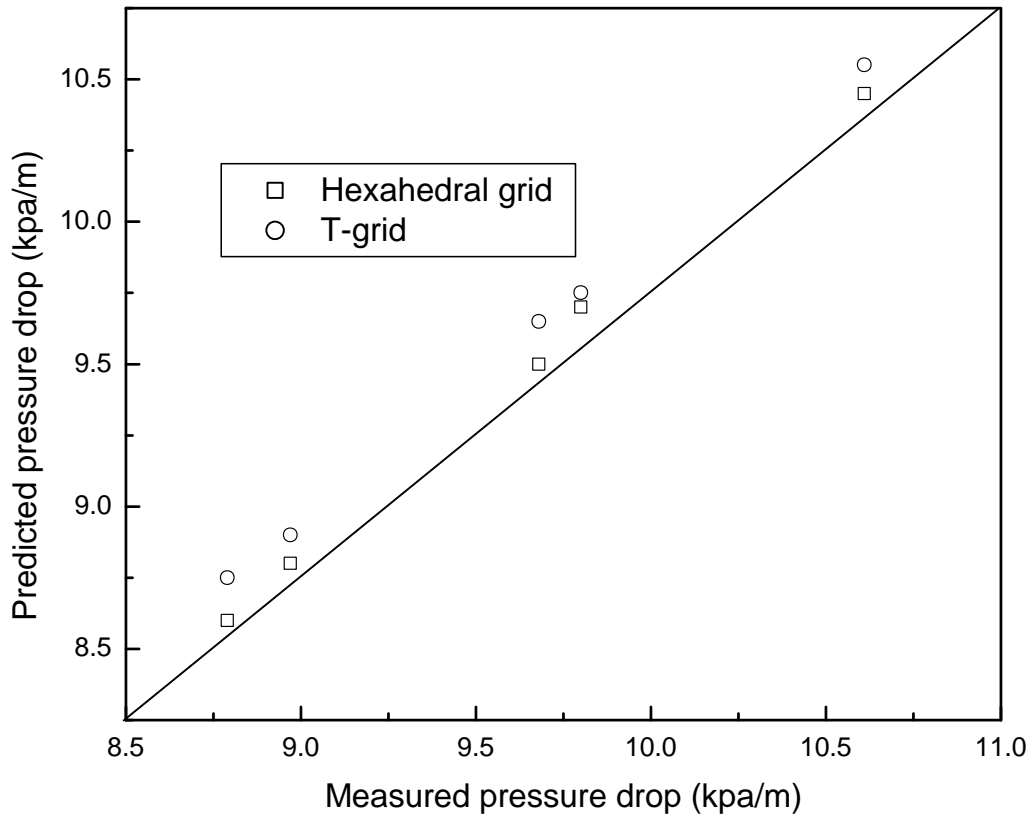
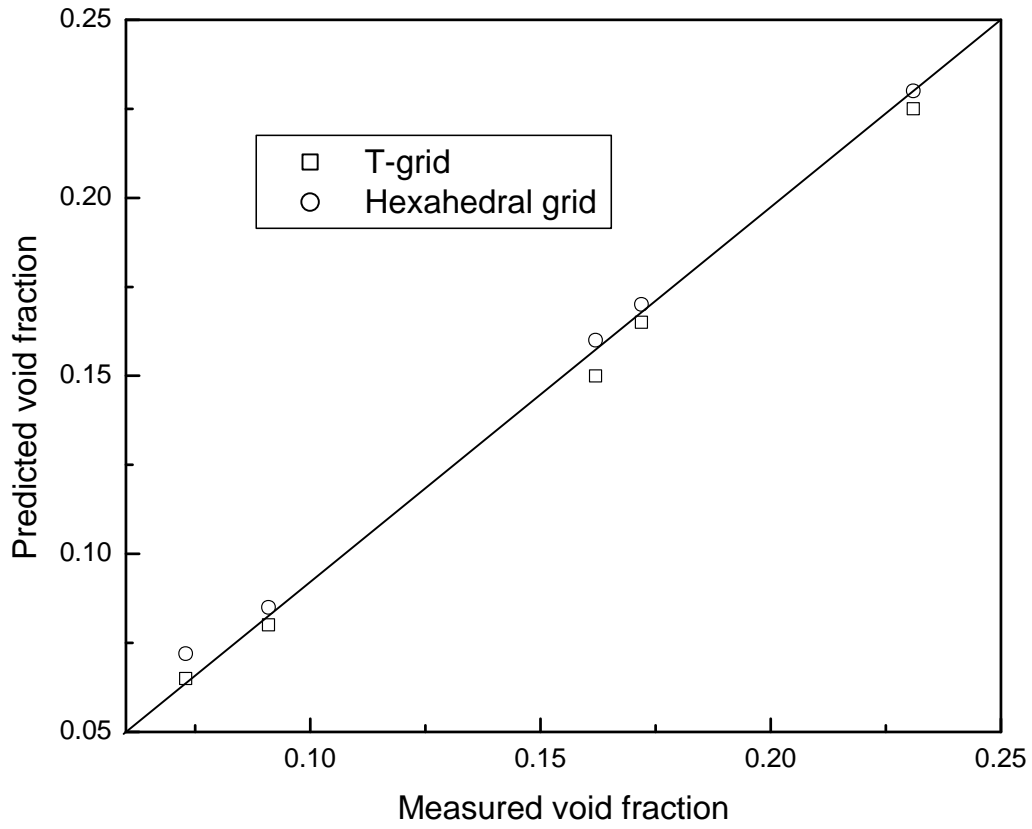


Fig. 8.38 Comparison plot of experimental data and CFD analysis for helical coil for two-phase frictional pressure drop per unit length of the coil with gas flow rate at constant liquid flow rate and constant SMC solution for different coil diameter



(a) Pressure drop

Fig. 8.39a Comparison of present prediction with the experimental data: pressure drop



(b) Void fraction

Fig. 8.39b Comparison of present prediction with the experimental data: void fraction

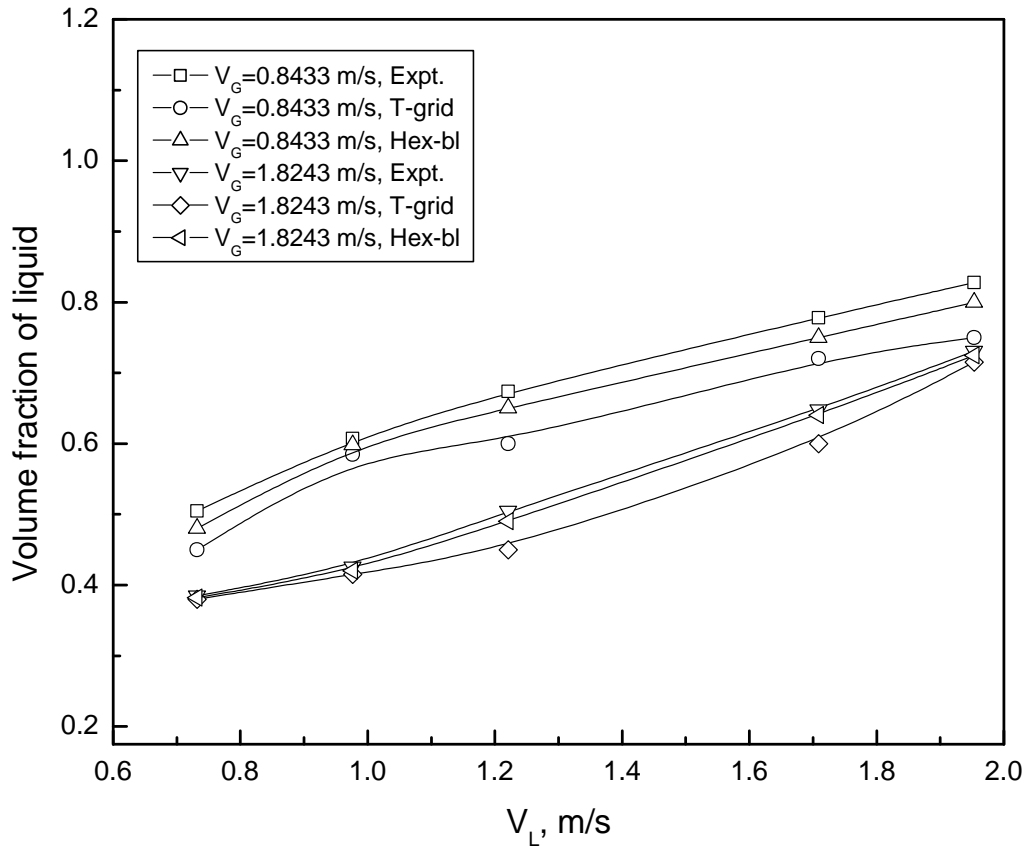


Fig. 8.40 Effect of gas and liquid velocity on liquid volume fraction in curved tube at curvature ratio = 18, coil turn = 2

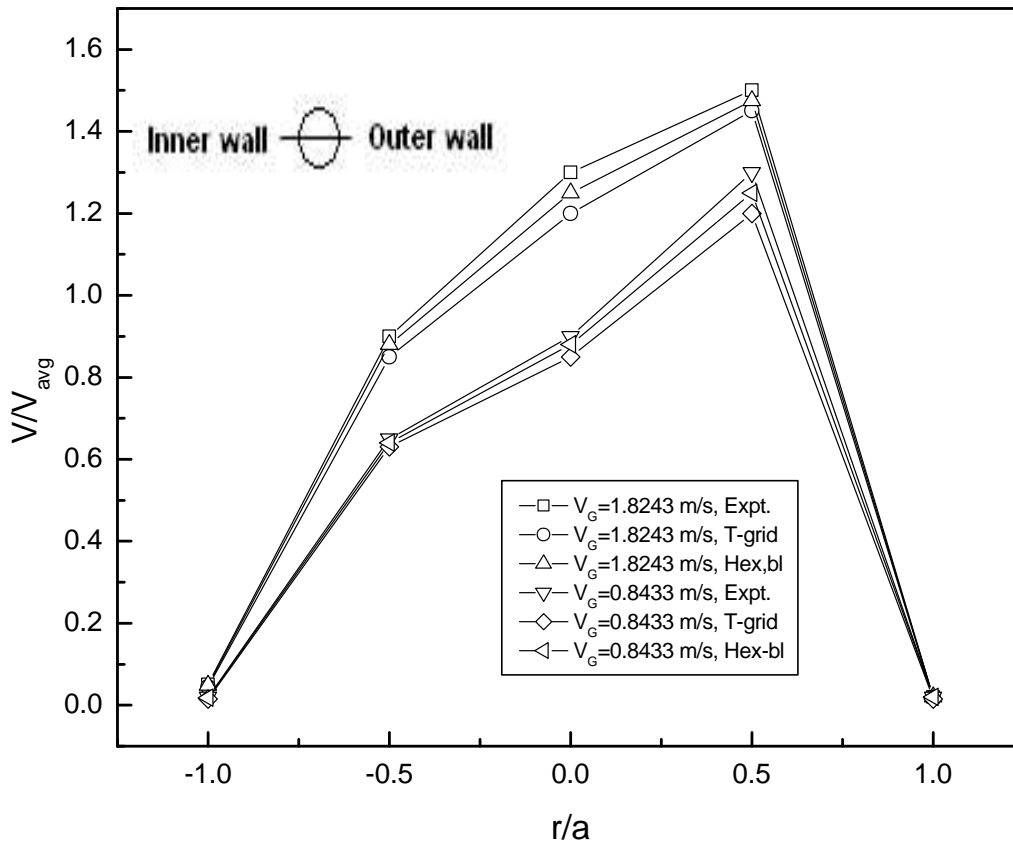
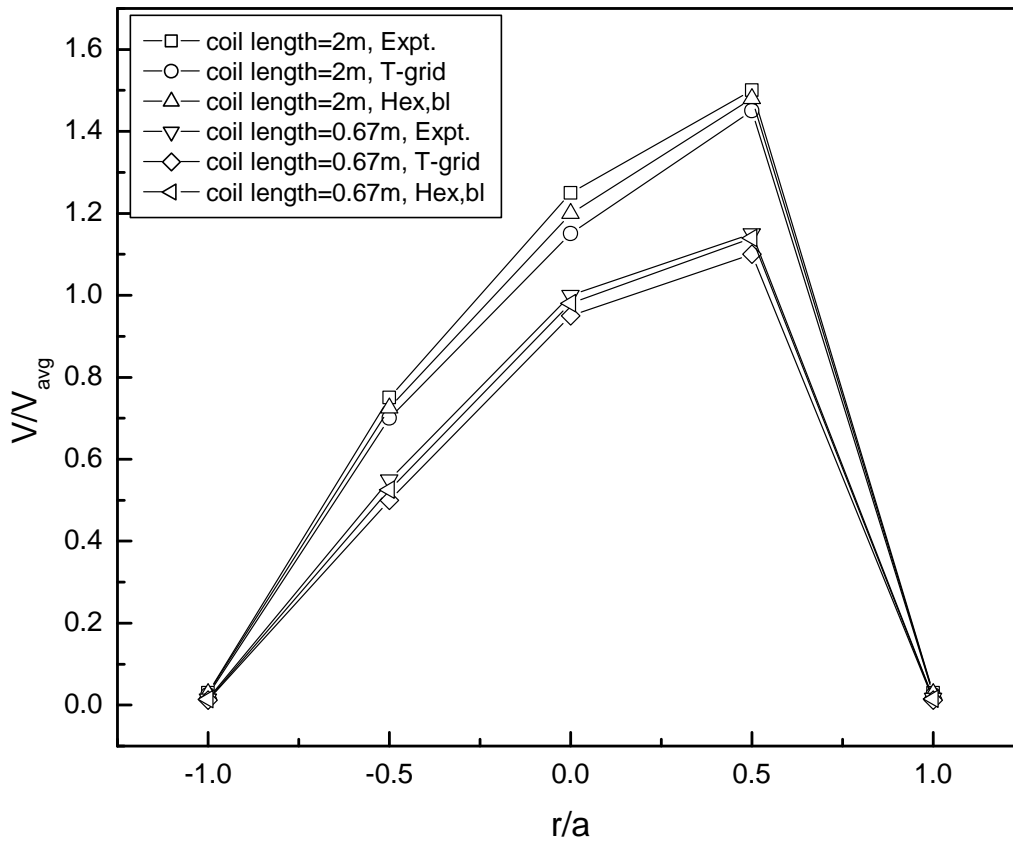
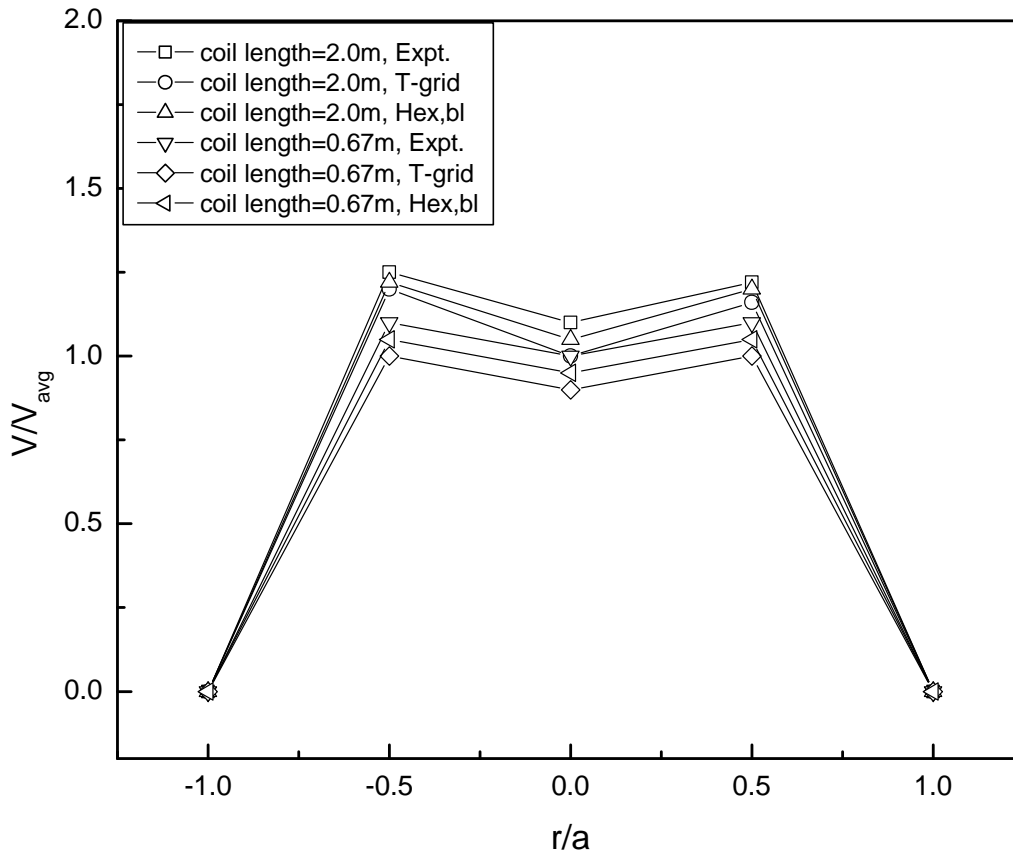


Fig. 8.41 Effect of gas and liquid velocity on development of axial velocity profile in curved tube at curvature ratio 18, coil turn = 2, $V_L = 1.9531$ m/s, in horizontal centerline



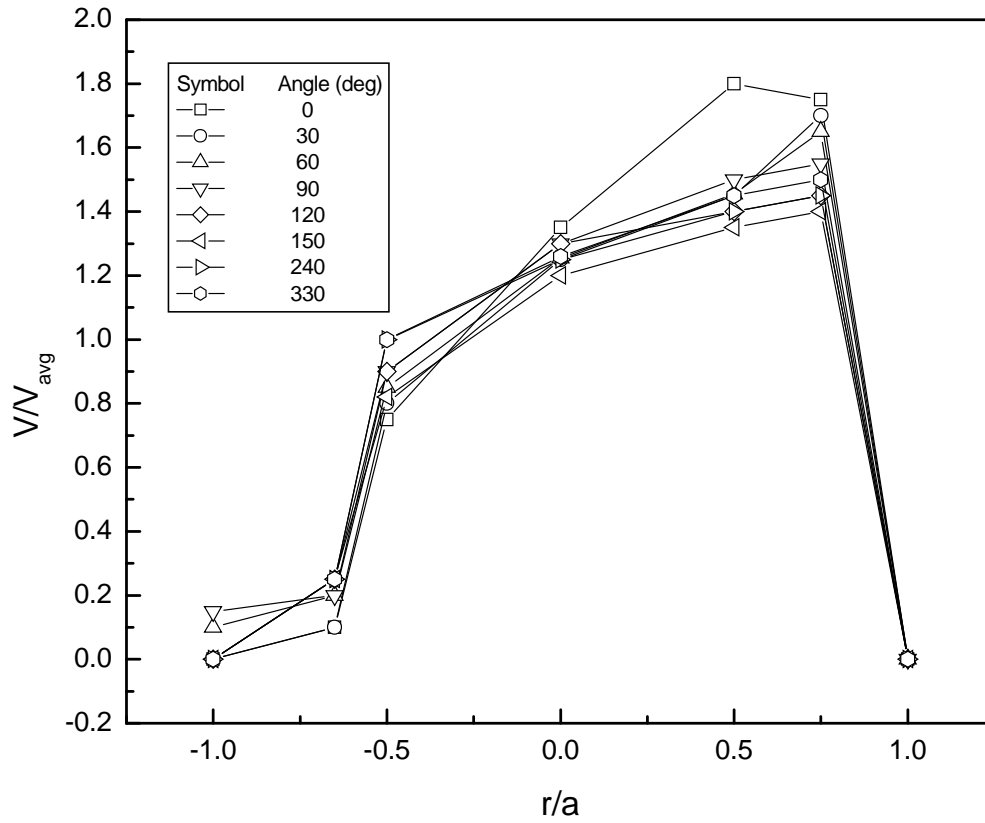
(a) Horizontal centerline

Fig. 8.42a Effect of coil turns or coil length on the development of axial velocity profile in horizontal centerline



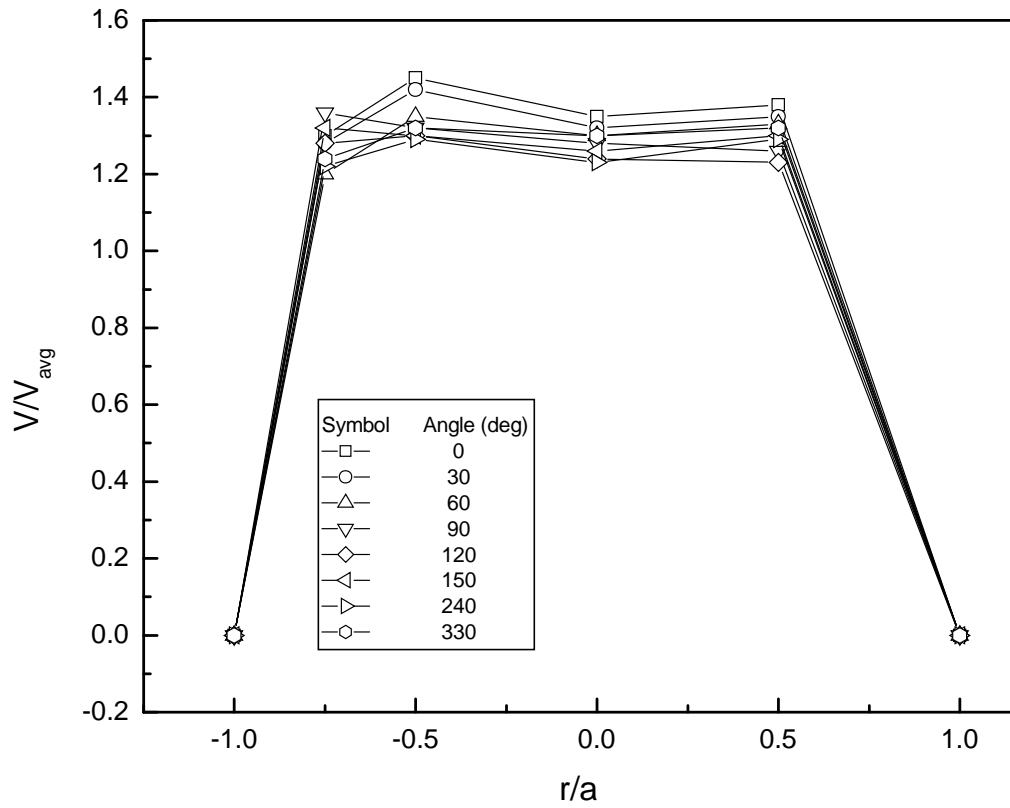
(b) Vertical centerline

Fig. 8.42b Effect of coil turns or coil length on the development of axial velocity profile in vertical centerline



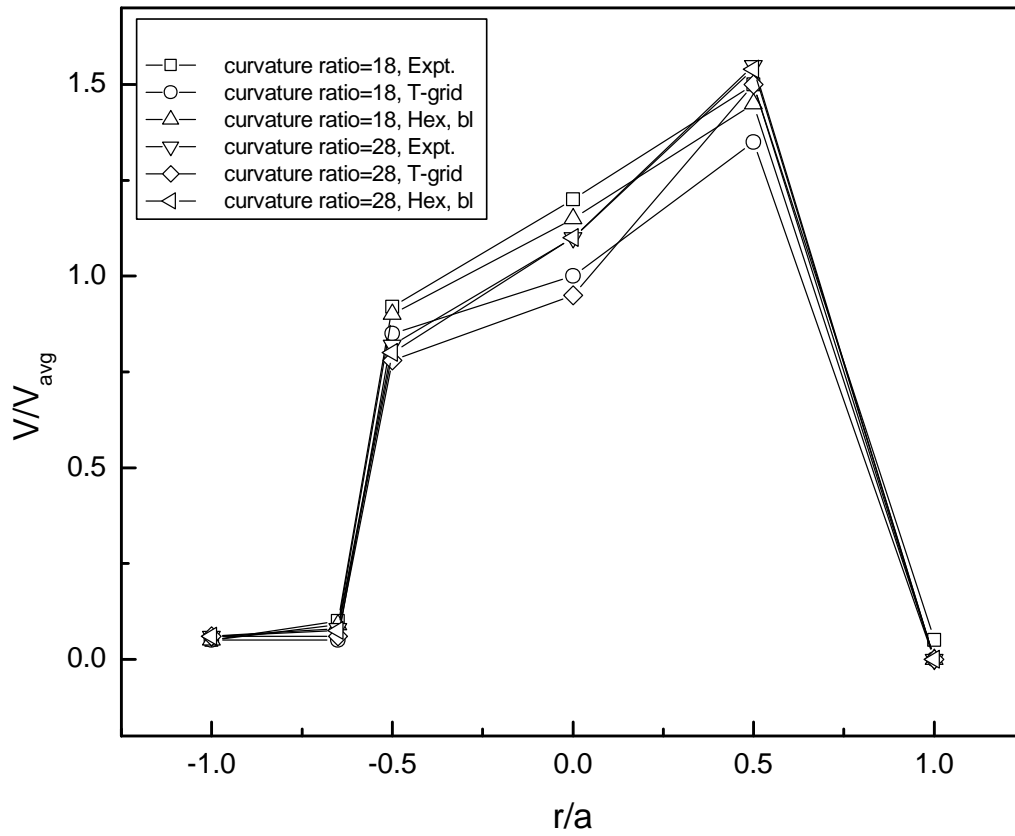
(a) Horizontal centerline

Fig. 8.43a Effect of angle on the development of axial velocity profile in horizontal centerline



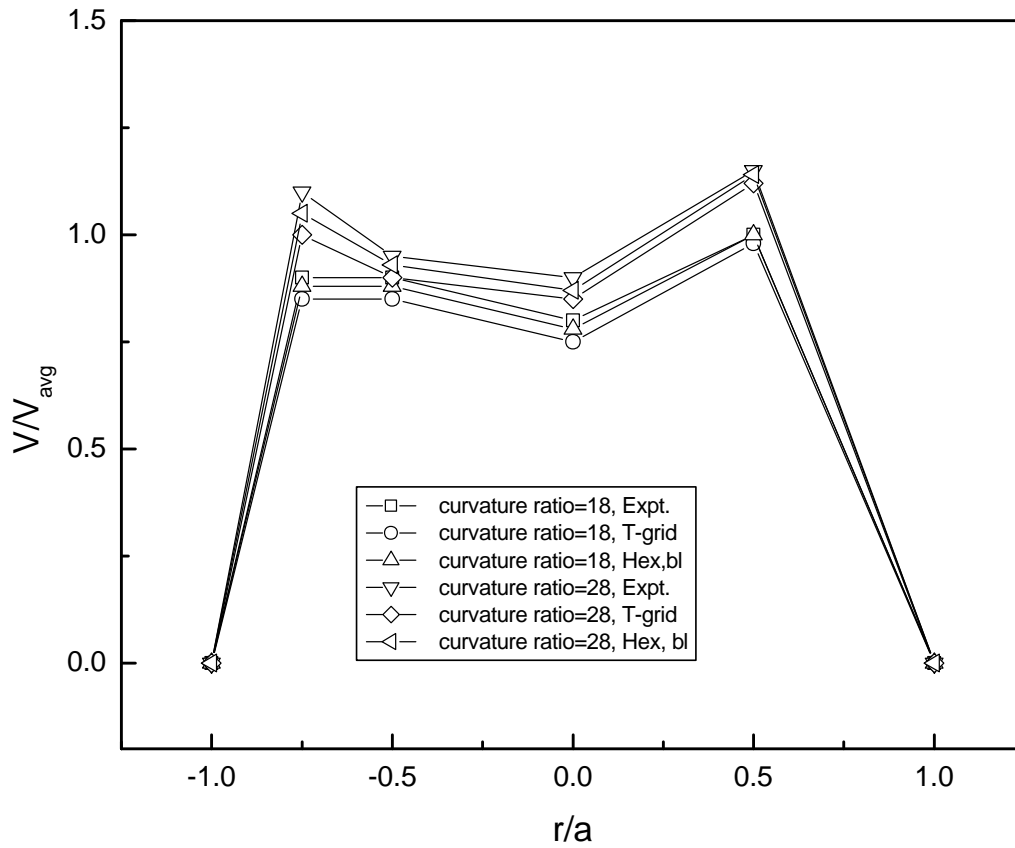
(b) Vertical centerline

Fig. 8.43b Effect of angle on the development of axial velocity profile in vertical centerline



(a) Horizontal centerline

Fig. 8.44a Effect of curvature ratio on the development of axial velocity profile in horizontal centerline at $V_G = 0.8433$ m/s, $V_L = 1.9531$ m/s



(b) Vertical centerline

Fig. 8.44b Effect of curvature ratio on the development of axial velocity profile in vertical centerline, at $V_G = 0.8433$ m/s, $V_L = 1.9531$ m/s

Table 8.1 Range of variables investigated

Variables	Range
Liquid flow rate, m ³ /s	3.334 – 15.003 x10 ⁻⁵
Gas flow rate, m ³ /s	0.440 – 42.030 x10 ⁻⁵
Concentration of SCMC Solution (kg/m ³)	0.2 to 0.8
Flow behavior index of the liquid	0.6015 n' 0.9013
Consistency index (Ns ⁿ /m ²)	0.0142 K' 0.7112
Density (kg/m ³)	1001.69 1003.83
Tube diameter, mm	9.33 – 12.00
Coil diameter, m	1.762 – 2.667
Turn	6 - 10

Table 8.2 Comparison of the experimental and CFD analysis data for frictional pressure drop across the coil for liquid (SCMC) concentration of 0.8 kg/m^3

Sl.No.	Air flow rate $Q_g \times 10^5$ m^3/s	Two-phase frictional pressure drop $(\Delta P_{fpc}/L)_{Expt.}$ kPa/m	Two-phase frictional pressure drop $(\Delta P_{fpc}/L)_{CFD}$ <i>Hex Grid</i> kPa/m	Two-phase frictional pressure drop $(\Delta P_{fpc}/L)_{CFD}$, <i>T-Grid</i> kPa/m
Liquid flow rate, $Q_l : 11.67 \times 10^{-5} \text{ m}^3/\text{s}$, $D_t/D_c : 0.0431$				
1	0.3323	8.1188	8.1	7.9
2	0.5051	8.5871	8.525	8.2
3	0.6251	8.864	8.865	8.5
4	1.0732	10.045	9.98	9.7

Table8.3 Comparison of the experimental and CFD analysis data for frictional pressure drop across the coil at different liquid (SCMC) concentrations

Sl.No.	Air flow rate $Q_g \times 10^5$ m ³ /s	Two-phase frictional pressure drop ($\Delta P_{fpc}/L$) <i>Expt.</i> kPa/m	Two-phase frictional pressure drop ($\Delta P_{fpc}/L$) <i>CFD Hex Grid</i> kPa/m	Two-phase frictional pressure drop ($\Delta P_{fpc}/L$) <i>CFD T-Grid</i> kPa/m
Liquid flow rate, Q_l :6.67x10 ⁻⁵ m ³ /s, Tube diameter(m):0.00933, Coil diameter(m):0.2162, SCMC Concentration (kg/m ³): 0.2, D_t/D_c : 0.0431				
1	2.57	3.37	3.32	3.1
2	3.51	3.57	3.48	3.4
3	5.35	4	3.95	3.9
4	11	5.38	5.33	5.2
5	13.61	6	5.98	5.88
6	31.88	8.6	8.55	8.5
Liquid flow rate, Q_l :6.67x10 ⁻⁵ m ³ /s, Tube diameter(m):0.00933, Coil diameter(m):0.2162, SCMC Concentration (kg/m ³): 0.4, D_t/D_c : 0.0431				
7	1.6	2.83	2.8	2.5
8	1.91	3	2.9	2.75
9	5.69	3.96	3.85	3.5
10	8.14	4.56	4.45	4.3
11	12.27	5.26	5.15	5.5
12	25.53	7.15	7	6.85
Liquid flow rate, Q_l :6.67x10 ⁻⁵ m ³ /s, Tube diameter(m):0.00933, Coil diameter(m):0.2162, SCMC Concentration (kg/m ³): 0.6, D_t/D_c : 0.0431				
13	0.5	2.8	2.75	2.6
14	0.99	3.	2.9	2.8
15	3.88	3.86	3.8	3.5
16	5.1	4	3.92	3.8
17	7.93	4.7	4.6	4.5
18	23.87	7.52	7.45	7.25
Liquid flow rate, Q_l :6.67x10 ⁻⁵ m ³ /s, Tube diameter(m):0.00933, Coil diameter(m):0.2162, SCMC Concentration (kg/m ³): 0.8, D_t/D_c : 0.0431				
19	0.44	3.48	3.4	3.3
20	1	3.74	3.7	3.5
21	1.54	3.94	3.86	3.75
22	3.79	4.62	4.55	4.45
23	9.47	6	5.9	5.8
24	10.92	6.23	6.12	6.0

Table 8.4 Comparison of the experimental and CFD analysis data for frictional pressure drop across the coil for liquid (SCMC) concentration of 0.8 kg/m^3 for different coil diameters

Sl. No.	Air flow rate $Q_g \times 10^5$ m^3/s	Two-phase frictional pressure drop $(\Delta P_{fpc}/L)$ <i>Expt.</i> kPa/m	Two-phase frictional pressure drop $(\Delta P_{fpc}/L)$ <i>CFD Hex Grid</i> kPa/m	Two-phase frictional pressure drop $(\Delta P_{fpc}/L)$ <i>CFD T-Grid</i> kPa/m
1	2	3	4	5
Liquid flow rate, $Q_l : 13.34 \times 10^{-5} \text{ m}^3/\text{s}$, Tube diameter(m):0.00933, Coil diameter(m):0.1762, Concentration of SCMC solution(kg/m^3): 0.8, D_t/D_c : 0.0431				
1	0.6383	9.5143	9.35	9.15
2	0.7686	9.7985	9.72	9.55
3	0.8389	9.8492	9.78	9.65
4	1.0439	10.2279	10.15	9.95
Liquid flow rate, $Q_l : 13.34 \times 10^{-5} \text{ m}^3/\text{s}$, Tube diameter(m):0.00933, Coil diameter(m):0.2162, Concentration of SCMC solution (kg/m^3): 0.8, D_t/D_c : 0.0431				
5	0.1259	8.9799	8.8	8.9
6	0.3909	9.6842	9.5	9.65
7	0.3982	9.8083	9.7	9.75
8	0.7218	10.6142	10.45	10.55
Liquid flow rate, $Q_l : 13.34 \times 10^{-5} \text{ m}^3/\text{s}$, Tube diameter(m):0.00933, Coil diameter(m):0.2662, Concentration of SCMC solution (kg/m^3): 0.8, D_t/D_c : 0.0431				
9	0.0937	8.875	8.75	8.8
10	0.4216	9.6025	9.5	9.55
11	0.448	9.8729	9.8	9.82

References

- Abbott, M. B. and Basco, D. R., Computational fluid dynamics: an introduction for engineers, *Longman Group UK Limited* (1989).
- Akagawa, N., Sakaguchi, T. and Ueda, M., Study on gas-liquid two-phase flow in helically coiled tubes, *Bull. JSME*, **14**, 564-571 (1971).
- Al-Rafai, W., Tridimas, Y. D. and Woolley, N. H., A study of turbulent flows in pipe bends, *Proc. Ins. Mech. Engers.*, **204**, 399-408 (1990).
- Alizadehdahkel, A., Rahimi, M, Sanjari, J. and Alsairafi, A. A., CFD and artificial neural network modeling of two-phase flow pressure drop, *Int. Commun. Heat Mass Transfer*, **36**, 850– 856 (2009).
- Anwer, M. and So, R. M. C., Rotation effects on a fully-developed turbulent pipe flow, *Expt. Fluids*, **8**, 33-40 (1989).
- Anwer, M., So, R. M. C. and Lai, Y.G, Perturbation by and recovery from bend curvature of a fully developed turbulent pipe flow, *Phys Fluids*, **A1**, 1387-1397 (1989).
- Anwer, M., So, R. M. C., Swirling turbulent flow through a curved pipe Part I; effect of swirl and bend curvature, *Expt. Fluids*, **14**, 85-96 (1993).
- Awwad, A., Xin, R. C., Dong, Z. F., Ebadin, M. A. and Soliman, H. M., Measurement and correlation of the pressure drop in air-water two-phase in horizontal helicoidal pipes, *Int. J. Multiphase Flow*, **21**, 607-619 (1995).
- Azzi, A., Friedel, L, and Balaadi, S., Two-phase gas/liquid flow pressure loss in bends, *Forsch. Im Ingenieurwesen*, **65(10)**, 309-318 (2000).
- Azzi, A., Friedel, L., Kibbona, R. and Shannak, B., Reproductive accuracy of two-phase flow pressure loss correlations for vertical 90° bends, *Forsch. im Ingenieurwesen*, **67(10)**, 109-166 (2002).
- Azzola, J., Humphery, J. A. C, Iacovides, H. and Launder, B. E., Developing turbulent flow in a U- bend of circular cross-section : measurement and computation, *Trans. J. Fluid Engg., ASME*, **108**, 214-221 (1986).
- Bandala-Rocha, M. R., Macedo, R. C., Ramirez and J. F., Velez-Ruiz, Valuación de coeficientes de fricción en el transporte de fluidos no-Newtonianos, *Informacion Tecnológica*, **16**, 73-80 (2005).
- Bandyopadhyay, T. K., Studies on non-Newtonian and gas-non-Newtonian liquid flow through horizontal tube and piping components, Ph. D., Thesis, C. U. (2002).

- Bandyopadhyay, T. K. and Das, S. K., Non-Newtonian pseudo plastic liquid flow through small diameter piping components, *J. Pet. Sci. Engg.*, **55**, 156–166 (2007).
- Bandyopadhyay, T. K., Banerjee, T. K. and Das, S. K., Gas-non-Newtonian liquid flow through elbows, *Chem. Engg. Comms.*, **182:1**, 21-33 (2000).
- Banerjee, T. K., Das, M. and Das, S. K., Non-Newtonian liquid flow through globe and gate valves, *Can. J. Chem. Engg.*, **72**, 207-211 (1994).
- Banerjee, S., Rhodes, E., and Scott, D. S., Film inversion of co-current two-phase flow in helical coils, *AIChE J.*, **13** 189-191(1967).
- Berger, S. A., Talbot, A. and Yao, L. S., Flow in curved pipes, *Ann. Rev. Fluid Mech.*, **15**, 461-512 (1983).
- Bergstrom, D. J., Bender, T., Adamopoulos, G. and Postlethwaite, J., Numerical prediction of wall mass transfer rates in turbulent flow through a 90° two-dimensional bend, *Can. J. Chem. Engg.*, **76**, 728-737 (1998).
- Berrouk, A. B. and Laurence, D., Stochastic modeling of aerosol deposition for LES of 90° bend turbulent flow, *Int. J. Heat and Fluid Flow*, **29**, 1010-1028 (2008).
- Biswas, A. B., Studies on two-phase gas-non-Newtonian liquid flow through helical coils, *Ph. D., Thesis*, C. U. (2006).
- Biswas, A. B. and Das, S. K., Two-phase frictional pressure drop of gas-non-Newtonian liquid flow through helical coils in vertical orientation, *Chem. Engg. Proc.*, **47(5)**, 816-826 (2008).
- Breuer, M., Baytekin, H. T. and Matida, E. A., Prediction of aerosol deposition in 90° bends using LES and an efficient Lagrangian tracking method, *J. Aerosol Sci.*, **37**, 1407-1428 (2006).
- Brockmann, J. E., Sampling and transport of aerosol, in aerosol measurement: principles, techniques, and applications, in *Baron P. A. and Willeke K., editors, New York, Van Nostrand Reinhold* (1993).
- Brown, Gary, Use of CFD to predict and reduce erosion in an Industrial slurry piping system, *5th Int. Conf. on CFD in the process industries CSIRO*, Melbourne, Australia, 13-15 December (2006).
- Bruce, J. M., Two-phase flow in straight pipe and 90° bends, *Ph. D. Thesis*, Univ. Aberdeen (1971).
- Castillo, J. R., Study of two-phase flow in pipe bends, M. Sc. Thesis, MIT (1957).

-
- Chen, L., Steam-water two-phase flow frictional pressure drop in straight tubes, in X. Chen(Ed.), *Selected Papers of Multiphase Flow and Heat Transfer*, **Paper 7**, Xi'an Jiaotong University Press., 7.1-7.6 (1982).
- Chen, Y. I., Wang, C. C. and Lin, S. Y., Measurement and correlations of frictional single-phase and two-phase pressure drops of R-410A flow in small U-type return bends, *Int. J. Heat Mass Transfer*, **47**, 2241–2249 (2004).
- Chen, X. J. and Zhou, F. D., An investigation of flow pattern and frictional pressure drop characteristics of air-water two-phase flow in helical coils, in *Proc. of the fourth Miami Int. Conf. on alternate energy sources*, 120-129 (1981).
- Cheng, G. C. and Farokhi, S., On turbulent flows dominated by curvature effects, *J. Fluids Engg.*, **114**, 52-57 (1992).
- Chenoweth, J. M. and Martin, M. W., Turbulent two-phase flow, *Pet. Ref.*, **34(10)**, 151-155 (1955).
- Chisholm, D. Two-phase Flow in Bends, *Int. J. Multiphase Flow*, **6**, 363–367 (1980).
- Cohen, M. I., An investigation of pressure drop in a two-phase two-component, flow in bends, *M. Sc. Thesis*, MIT (1957).
- Chung T. J., *Computational fluid dynamics*, Cambridge University Press, Cambridge, (2002).
- Chung, K. Y., Brewster, M. E. and Belfort, B., Dean Vortices with wall flux in a curved channel membrane systems, 2 - The velocity field, *AIChE J.*, **42(2)**, 347-358 (1996).
- Czop, V., Barbier, D. and Dong, S., Pressure drop, void fraction and shear stress measurements in an adiabatic two-phase flow in a coiled tube, *Nucl. Eng. Des.*, **149**, 323-333 (1994).
- Das, S. K., Water flow through helical coils in turbulent condition, in *Multiphase Reactor and Polymerization System Hydrodynamics*, N. P. Cheremisinoff Editor, Gulf Publication USA, Ch. 17, 379-403 (1996).
- Das, S. K., Biswas, M. N. and Mitra, A. K., Pressure losses in Two-phase Gas-non-Newtonian liquid flow in horizontal tube, *J. Pipelines*, **7**, 307-325 (1989).
- Das, S. K., Biswas, M. N. and Mitra, A. K., Friction factor for Gas-non-Newtonian Liquid Flow in Horizontal Bends, *Can. J. Chem. Engg.*, **69**, 179–187 (1991a).

-
- Das, S. K., Biswas, M. N. and Mitra, A. K., Non-Newtonian liquid flow in bends, *Chem. Eng. J.*, **45**, 165-171 (1991b).
- Davis, J. A. and Stewart, M., Geometry effects when using CFD analysis as a design tool to predict the control valve., *Dev. Theo. Appl. Mechanics*, **19**, 38-45 (1998).
- Dean, W. R., Note on the motion of fluid in a curved pipe, *Philos. Mag.*, **20**, 208-223 (1927).
- Dean, W.R., Fluid motion in a curved channel, *Proc. R. Soc. London*, **Vol. 121**, 402-420 (1928a).
- Dean, W. R., The Stream-line motion in curved pipes, *Philos. Mag.*, **30**, 673- 693, (1928b).
- Deobold T. L., An experimental investigation of two-phase pressure losses in pipe elbows, M. Sc., Univ. Idaho, *Chem., Eng. Rept.*, **HW-SA**, 2564 (1962).
- Domanski, P. A. and Christian, J. L. H., An improved correlation for two-phase pressure drop of R-22 and R-410A in 180° return bends, *Appl. Thermal Eng.*, **28**, 793–800 (2008).
- Edwards, M. F., Jadallah, M. S. and Smith, R., Head losses in pipe fittings at low Reynolds numbers, *Chem. Eng. Res. Dev.*, **63**, 43-50 (1985).
- Edwards, J. K., McLaury, B. S. and Shirazi, S. A., Supplementing a CFD code with erosion prediction capabilities, In *Proc. of ASME FEDSM'98: ASME Fluids Engineering Division Summer Meeting*, Washington D.C., June, 245 1-7 (1998).
- Enayet, M. M., Gibson, M. M., Taylor, A. M. K. P. and Yianneskis, M., Laser–doppler measurements of laminar and turbulent flow in a pipe bend, *Int. J. Heat Fluid Flow*, **3**, 213-219(1982).
- Engineering Science Data Unit Ltd., Pressure losses in curved duct, single bends, *ESDU*, Rept. No. 77008 (1977).
- Etemad, S. and Sunden, S., Numerical analysis of turbulent convective heat transfer processes in a square-sectioned U-bend duct, *15th Australasian Fluid Mechanics Conf.*, Sydney, Australia, 13-17 Dec. (2004).
- Eustice, J., Flow of water in curved pipes, *Proc. R. Soc. London*, **84**, 107-118, (1910).
- Famiyesin, O. O. R., Oliver, K. D. and Rodger, A. A., Semi-empirical equations for pipeline design by the finite element method, *Comp. & Structures*, **80**, 1369-1382 (2002).

-
- Faruki, N. M., and Parker, J. D., A visual study of air-water mixtures flowing inside serpentine tubes, *Proc. 5th Int. Heat Transfer Conf., JSME*, Tokyo, B5.5, pp 205-209, (1974).
- Ferziger, J. H. and Peric, M, *Computational methods for fluid dynamics*, Springer, Berlin, (1997).
- Fitzsimmons, P. E., Two phase pressure drop in pipe components, *General electric Res. Rept.*, **HW-80970**, Rev. 1 (1964).
- Fluent Users Guide, Version 6.2, Fluent India, Pune (2006).
- Fluent Users Guide, Version 6.3, Fluent India, Pune (2008).
- Flow Meters – Their theory and application, *Report of the ASME Research Committee on Fluid Meter*, ASME, New York, **5th Ed.**, (1959).
- Gadiyar, N. and Das, S. K., Pressure losses in two-phase air water flow in orifices, *Ind. J. Technol.*, **31**, 811-814(1993).
- Gao, H., Gu, Y. J. and Guo, L. J., Numerical study of stratified oil-water two-phase turbulent flow in a horizontal tube, *Int. J. Heat Mass Transfer*, **46**, 749-754 (2003).
- Geary, D. F., Return bend pressure drop in refrigeration systems, *ASHRAE Trans.* **81(1)**, 250–264 (1975).
- Gelfgat, A. Yu., Yarin, A. I. and Bar-Yoseph, P. Z., Dean vortices-induced enhancement of mass transfer through an interface separating two immiscible liquids, *Phys. Fluids*, **15(2)**, 330-347 (2003).
- Guan, X. and Martonen, T. B. Flow transition in bends and applications to airways, *J. Aero. Sci.*, **31**, 831-847 (2000).
- Guo, L. and Chen, X., An experimental investigation of the frictional pressure drop of steam-water two-phase flow in helical coils, *Int. J. Heat Mass Transfer*, **44(14)**, 2601-2610 (2001).
- Guo, L. J., Chen, X. J., Zhang, S. K. and Feng, Z. P., Correlation for predicting pressure drop of single and two-phase flow through horizontally helically coiled tubes, *in Proc. 3rd Int. Sym. Multiphase Flow and Heat Transfer*, 514-52, (1994).
- Hart, J., Ellenberger, J., and Hamersma, P. J., Single and two-phase flow through helically coiled tubes, *Chem. Engg. Sci.*, **43**, 775-783 (1988).

- Hidayat, M. and Rasmuson, A., Numerical investigation of gas-solid flow in a U-bend, *Proc. 13th Int. Drying Sym.*, **A**, 424-433, Beijing, China, IDS' (2002).
- Hoang, K. and Davis, M.,R., Flow Structure and Pressure Loss for Two Phase Flow in Return Bends, *7th Annual/Energy-Sources Technology Conf. and Exhibit*, New Orleans, U.S.A., Paper no. 84-FE-1, Feb. 11-17 (1984).
- Hooper, W. B., Piping design, fittings, pressure drop, *Encyclopedia of Chemical Processing and Design*, (Ed. J. J. Mcketta), **39**, 19-27 (1991).
- IS: 10605 – 1983, Steel globe valves (flanged and butt welded ends) for petroleum, petrochemical and allied industries (first revision), Bureau of Indian Standard, (1983).
- IS: 11335 – 1984, Cast Iron Gate valves, Bureau of Indian Standard, (1984).
- Ito, H., Friction factors for turbulent flow in curved pipes, *ASME J. of Basic Engg.*, **81**, 123-134 (1959).
- Jayanti, S., Hewitt, G. F. and Kightley, J. R., Fluid flow in curved ducts, *Int. J. Num. Methods in Fluids*, **10**, 567-589 (1990).
- Jayakumar, J. S., Mahajani, S. M., Mandal, J. C., Iyer, K. N. and Vijayan, P. K., Thermal hydraulic characteristics of air-water two-phase flows in helical pipes, *Chem. Engg. Res. Deg.*, **88**, 501-512 (2010).
- Joshi, J. B. and Ranade, V. V., Computational fluid dynamics for designing process equipment: expectation, current status, and path forward, *Ind. Eng. Chem. Res.*, **42**, 1115-1128 (2003).
- Kim, J. and Simon, T. W., Measurements of the turbulent transport of heat and momentum in convexly curved boundary layers : effects of curvature, recovery and free-stream turbulence, *J. Turbomachinery*, **110**, 81-87 (1988).
- Kuan, B., Yang, W. and Solnordal, C., CFD simulation and experimental validation of dilute particulate turbulent flows in a 90⁰ duct bend, *3rd Int. Conf. on CFD in the Minerals and Process Industries CSIRO*, Melbourne, Australia 10-12 December (2003).
- Kumar, A., Kaushal, D. R. and Kumar, U., Bend Pressure drop experiments compared with Fluent, *Eng. Computational Mech.*, **161**, 35-42 (2008).
- Lockhart, R. W. and Martinelli, R. C., Proposed correlation of data for isothermal two-phase two component flow in pipes, *Chem. Engg. Prog.*, **45**, 39 (1949).

-
- Maddock, C., Lacey, P. M. C. and Patrick, M. A., The structure of two-phase flow in a curved pipe in: *I. ChemE Symp. Ser.*, **38**, Paper J2, pp. 1-22 (1974).
- Mandal, S. N. and Das, S. K., Pressure Losses in Bends during Two-Phase Gas-Newtonian Liquid Flow, *Ind. Eng. Chem. Res.*, **40**, 2340–2351 (2001).
- Mandal, S. N. and Das, S. K., Gas-Liquid flow through helical coils in vertical orientation, *Ind. Eng. Chem. Res.*, **42**, 3487–3494 (2003).
- Manzar, M. A. and Shah, S. N., Particle distribution and erosion during the flow of Newtonian and non-newtonian slurries in straight and coiled pipes, *Engg. Applications Comp. Mech.*, **3**, 296-320 (2009).
- Marn, J. and Ternik, P., Laminar flow of a shear-thickening fluid in a 90° pipe bend, *Fluid Dynamics Res.*, **38**, 295-312 (2006).
- Mishra, P. and Gupta, S. N., Momentum transfer in curved pipes. 2. Non-Newtonian fluids, *Ind. Eng. Chem. Process Dev.*, **18**(1), 137-142 (1979).
- Moulin, Ph., Veyreth, D. and Charbit, D. F., Dean vortices: comparison of numerical simulation of shear stress and improvement of mass transfer in membrane processes at low permeation fluxes, *J. Membr. Sci.*, **183**, 149-162 (2001).
- Owhadi, A., Bell, K. J. and Crain, B., Forced convection boiling inside helically coiled tubes, *Int. J. Heat Mass Transfer*, **11**, 1779-1793 (1968).
- Patankar, S. V., *Numerical heat transport and fluid flow*, Taylor and Francis, New York, (1989).
- Pierre, B., Flow resistance with boiling refrigerants – Part II: Flow resistance in return bends, *ASHRAE J.*, 73–77 (1964).
- Polizelli, M. A., Menegalli, F. C., Telis, V. R. N. and Telis-Romero, J., Friction losses in valves and fittings for power-law fluids, *Brazilian J. Chem. Engg.*, **20**, 455-463 (2003).
- Pruvost, J., Legrand, J. and Legentilhomme, P., Numerical investigation of bend and turns flow, part I : effect of swirl motion on flow structure in U-bend, *Chem. Engg. Sci.*, **59**, 3345-3357 (2004).
- Pui, D. Y. H., Romay-Novas, F. and Liu, B.Y. H., Experimental study of particle deposition in bends of circular cross-section, *Aerosol Sci. Technol.*, **7**, 301-315 (1987).
- Ranade, V. V., *Computational flow modelling for chemical reactor engineering*, Academic Press: London (2002).

-
- Rowe, M., Measurements and computations of flow in pipe bends, *J. Fluid Mech.*, **43**(4), 771-783 (1970).
- Roorda, O., Computer simulation helps reduce pressure loss, *Water, Engg. Mag.*, **40**, 22-24 (1998).
- Samanta, A. K., Banerjee, T. K. and Das, S. K., Pressure losses in orifices for the flow of gas-non-Newtonian liquid, *Can. J. Chem. Engg.*, **77**, 579-583 (1999).
- Santini, L., Cioncolini, A., Lombardi, C. and Ricotti, M., Two-phase pressure drops in a helically coiled steam generator, *Int. J. Heat Mass transfer*, **51**, 4926-4939 (2008).
- Saxena, A. K., Nigam, K. D. P., Schumpe, A., Deckwer, W. D., Liquid phase residence time distribution for two-phase flow in coiled tubes, *Can. J. Chem. Eng.*, **74**, 861-866 (1996).
- Sekoda, K., Sato, Y. and Karyia, S., Horizontal two-phase air-water flow characteristics in the disturbed region due to a 90 degree bend, *J. Jpn. Soc. Mech. Eng.*, **35**(289), 2227-2333 (1969).
- Schiller, L. and Naumann, Z., A drag coefficient correlation, *Zait Ver Deutsch Ing*, **77**, 318-325 (1935).
- Shah, N. S. and Jain, S., Coiled tubing erosion during hydraulic fracturing slurry flow, *Wear*, **264**, 279-290 (2008).
- Shah, R. K. and Joshi, S. D., Convective heat transfer in curved ducts, in Handbook of single-phase convective heat transfer, Kakac, S., Shah, R. K., & Aung, W. (eds). (Wiley interscience, New York), Chapter 3, p. 1238 (1987).
- Sierra-Espinosa, F. Z., Bates, C. J. and O'Dherty T., urbulent flow in a 90° pipe junction Part 1 : decay of fluctuations upstream the flow bifurcation, *Comp. & Fluids*, **29**, 197-213 (2000a).
- Sierra-Espinosa, F. Z., Bates, C. J. and O'Dherty T., urbulent flow in a 90° pipe junction Part 2 : reverse flow at the branch exit, *Comp. & Fluids*, **29**, 215-233 (2000b).
- So, R. M. C., Zhang, H. S. and Lai, Y. G., Secondary cells and separation in developing laminar curved-pipe flows, *Theor. Comput. Fluid Dyn.*, **3**, 141-162 (1991).
- Spedding, P. I., Chen, J. J. J. and Nguyen, V. T., Pressure drop in two phase gas-liquid flow in inclined pipes, *Int. J. Multiphase flow*, **8**, 407-431 (1982).

- Spedding, P. L., Benard, E. and McNally, G. M., Fluid flow through 90 degree bends, *Dev. Chem. Eng. Min. Process*, **12**, 107-128 (2004).
- Spedding, P. L. and Benard, E., Gas-liquid two-phase flow through a vertical 90° elbow bend, *Exp. Thermal Fluid Sci.*, **31**, 761-769 (2007).
- Straub, L. G. and Silberman, E., Air-water mixture flow through orifices, bends and other fittings in a horizontal pipe, *St Anthony falls*, Hydraulic Lab., Univ. Minnesota Rept., **63** (1960).
- Struiver, W., Two phase fluid flow through bends and preliminary study of bends and preliminary study of pressure drop along pipe, *Dominion physical lab*, Newzeland, ANL, **R257**, 6734-1694 (1955).
- Sudo, K., Sumida, M. and Hibara, H., Experimental investigation on turbulent flow in a circular-sectioned 90-degrees bend, *Expt. Fluids*, **25**, 42-49 (1998).
- Sudo, K., Sumida, M. and Hibara, H., Experimental investigation on turbulent flow through a circular sectioned 180° bend, *Expt. Fluids*, **28**, 51-57 (2000).
- Supa-Amornkul, S., Steward, F., R. and Derek, H. L., Modeling Two-Phase Flow in Pipe Bends, *J. Press. Vessel Technol.*, **127**, 204-209 (2005).
- Telis-Romero, J., Gratao, A. C., Gacia-Cruz, C. H., Telis, V.R.N., Determinacao de coefficients de perda de carga atraves de valvulas e accessoris no escoamento laminar de fluidos naONewtonianos, *Ciencia & Engenharia*, **9**, 78-82 (2000).
- Thomson, J., On the origin of windings of rivers in alluvial plains, with remarks on the flow of water round bends in pipes, *Proc. R. Soc. London*, **25**, 5-8 (1876).
- Tiwari, P., Antal, S. P., Burgoyne, A., Belfort, G. and Podowski, M. Z., Multifid computational fluid dynamics model of particulate flow in curved circular tubes, *Theor. Comput. Fluid Dyn.*, **18**, 205-220 (2004).
- Tunstall, M. J. and Harvey, J. K., On the effect of a sharp bend in a fully developed turbulent pipe-flow, *J. Fluid. Mech.*, **34**, 595-608 (1968).
- Turian, R. M., Ma, T. W., F. L. G., Hsu, Sung, M. D. J. and Plackmann, G. W., Flow of concentrated non-Newtonian slurries : 2. friction losses in bends, fittings, valves and venture meters, *J. Multiphase Flow*, **24**, 243-269 (1998).
- Unal, H. C., Gasself, V. M. I. G., Versalt, P. M. and Dryout, Von't, Two-phase flow pressure drop in sodium heated helically coiled steam generators tubes at elevated pressure, *Int. J. Heat Mass Transer*, **24**, 285-298 (1981).

- Usui, K., Akoi, S. and Inoue, A., Flow behavior and phase distribution in two-phase flow around inverted U-bend, *J. Nucl. Sci. Technol.*, **20(11)** 33-46 (1983).
- Van de Vosse, F. N., Van Steenhoven, A. A., Sregak, A. and Janssen, J. D., A finite element analysis of the steady laminar entrance flow in a 90° curved tube, *Int. J. Num. Methods in Fluids*, **9**, 275-287 (1989).
- Vashisth, S. and Nigam, K. D. P., Prediction of flow profiles and interfacial phenomena for two-phase flow in coiled tubes, *Chem. Engg. and Proc. Proc. Intensification*, **48**, 452-463 (2009).
- Wang, C. C, Chen, I. Y, Yung, Y. W and Chang, Y. J., Two-phase flow pattern in small diameter tubes with the presence of horizontal return bend, *Int. J. Heat Mass Transfer*, **46**, 2975–2981 (2003).
- Wang, C. C, Chen, I. Y. and Huang, P. S., Two-phase slug flow across small diameter tubes with the presence of vertical return bend, *Int. J. Heat Mass Transfer*, **48**, 2342–2346, (2005).
- Wang, J. and Shirazi, S., A CFD based correlation for mass transfer coefficient in elbows, *Int. J. Heat Mass Transfer*, **44**, 1817-1822 (2001).
- Watanabe, O., Tajima, O. and Shimoya, O., Flow and heat transfer of gas and liquid two-phase flow in coils, *Trans. JSME*, **52** (476B), 1857-1864 (1986).
- Wilson, R. E., Mcadams, W. H. and Seltzer, M. The flow of fluids through commercial pipelines, *IEC*, **14**, 105-119 (1922).
- Wu, B. and Chen, S., CFD simulation of non-Newtonian fluid flow in anaerobic digesters, *Biotechnol. Bioeng.* **99**, 700-711 (2008).
- Xia, B. and Sun, D. W., Applications of computational fluid dynamics (CFD) in the food industry: a review, *Comp.Eelec. Agriculture*, **34**, 5-24 (2002).
- Xin, R. C., Dong, Z. F. and Ebadin, M. A., Three-Dimensional numerical modelling of turbulent single-phase and two-phase flow in curved pipes, *National Heat Transfer Conference, ASME*, **4**, 227-233 (1996).
- Xin, R. C., Awward, A., Dong, Z. F. and Ebadin, M. A., An experimental study of single-phase and two-phase flow pressure drop in annular helicoidal pipes, *Int. J. Heat Fluid Flow*, **18(5)**, 482-488 (1997).
- Yamamoto, K., Yanase, S. and Yoshida, T., Torsion effect on the flow in a helical pipe, *Fluid Dyn. Res.*, **14**, 259-273 (1994).

Yao, L. S. and Berger, S. A., Entry flow in a coiled pipe, *J. Fluid Mech.*, **67**, 177-196 (1975).

Zhang, P., Roberts, R. M., Benard, A. and Petty, C. A., Computational study of turbulent single phase and multiphase flows in 90⁰ Bends, *Proc. of the AIChE 2009 Annual Meeting*, **Paper 171080**, November (2009).

Zhang, P., Gros, Y., Roberts, R. M. and Benard, A., Modeling of turbulent flow with particle deposition in curved pipes, *Proc. 7th Int. Conf. on Multiphase flow ICMF 2010*, Tampa, FL USA, May 30-June 4 (2010).

Website

www.cfd-online.com available on 2nd Dec. 2010.

<http://www.chemicalvision2020.org/pdfs/compfluid.pdf> available on 4th Dec. 2010.